

# Modelling the age-depth and temperature profiles of deep ice cores from the Antarctic Peninsula and the Weddell Sea region

Ashleigh Massam



Department of Geography  
University of Durham



Ice Dynamics and Palaeoclimate  
British Antarctic Survey

A thesis submitted in partial fulfillment of the requirements for the University of  
Durham for the degree of Doctor of Philosophy

September 2017



# **Modelling the age-depth and temperature profiles of deep ice cores from the Antarctic Peninsula and the Weddell Sea region**

Ashleigh Massam

## **Abstract**

Three deep ice cores, obtained from Fletcher Promontory, Berkner Island, and James Ross Island across the Antarctic Peninsula (AP) and Weddell Sea region, preserve a climate record that can yield important information on the region. However, before this information can be interpreted, an accurate age-depth profile is required. This study seeks to develop optimal age-depth profiles for the three deep ice cores. The first branch of work is a modelling synthesis of the different physical relationships that reconstruct past surface temperature, accumulation, and the subsequent compaction of accumulation to annual layer thickness (thinning) at an ice-core site. From these relationships, one can estimate an age-depth profile for an ice core. The second half of the study includes the results of chemical analysis on the three deep ice cores. The results of these analyses yield observational data that has been used to assess the accuracy and reliability of the modelling results presented in this part of the study. The OptAcc age-depth model has been developed through this study; it uses an inverse approach to anchor reconstructed profiles of accumulation, thinning, and annual layer thickness profiles to observational data preserved in the ice core. This has been done for the deep ice cores from the AP and Weddell Sea region.

Interpretation of the results from this study provides information on the climate history of the region. In particular, the OptAcc model suggests that the coastal proximity of each ice core site leads to high inter-annual variability in accumulation that cannot be reconstructed using standard mathematical relationships. Additionally, an accurate surface temperature, accumulation and age-depth reconstruction for each ice-core site over the Holocene period suggests that an increase in the mean annual surface temperature of 1-3 K is sufficient to lead to significant deglaciation of the AP and Weddell Sea region.



# Contents

Title Page	i
Abstract	iii
Contents	v
List of figures	xv
List of tables	xxii
List of abbreviations	xxv
Declaration and statement of copyright	xxxii
Acknowledgements	xxxii
<b>1 Introduction</b>	<b>1</b>
1.1 Rationale	1
1.2 Aim of the project	4
1.2.1 Objectives	4
1.3 Study Area	5
1.4 Thesis Outline and Summary	8
1.4.1 Chapters 2 and 3	8
1.4.2 Chapter 4	8
1.4.3 Chapter 5	9
1.4.4 Chapters 6 and 7	10
1.4.5 Chapter 8	10
1.4.6 Chapter 9	10
<b>2 A review of Polar Ice Core Research</b>	<b>13</b>
2.1 Introduction	13

2.2	Developments in Ice-Core Research	13
2.3	Records of Climate	17
2.3.1	Stable Water Isotopes	18
2.3.1.1	Stable Water Isotopes and Precipitation	18
2.3.1.2	Deuterium Excess	18
2.3.2	Chemical Records in ice cores	19
2.3.3	Gas-phase ice-core records	22
2.3.4	Millennial-scale variability	24
2.4	Analysis of Ice-Core Records	28
2.5	Chronology of Ice-Core Records	31
2.5.1	Temperature	33
2.5.2	Accumulation	34
2.5.2.1	Arrhenius	34
2.5.2.2	Clausius-Clapeyron	34
2.5.2.3	Simple Exponential	35
2.5.2.4	Global Circulation Model	35
2.5.3	Thinning Functions	36
2.5.3.1	Nye Model	37
2.5.3.2	Dansgaard-Johnsen two-step thinning model	37
2.5.3.3	One-Dimensional Ice Flow	38
2.5.3.4	Phase-Sensitive Radio Echo Sounder (pRES)	40
2.5.4	Age-Depth Profile	40
2.5.5	Borehole Temperature Profiles	41
2.5.6	Inverse Probabilistic Approach	42
2.5.7	Perturbation Theory	44
2.6	Firn Compaction in the upper depths of an ice core	44

2.6.1	Densification of an ice core	45
2.6.2	Gas-phase age-depth profiles	46
2.7	Development of established ice-core chronologies	47
2.7.1	EPICA Dome C	48
2.7.2	Other deep ice cores	49
2.8	Summary	50
<b>3</b>	<b>Methodology</b>	<b>53</b>
3.1	Introduction	53
3.2	Site Details	53
3.2.1	Sampling Locations and Drilling Process	53
3.2.2	Borehole Temperature Measurements	56
3.3	Initial ice-phase chemical profiles	57
3.3.1	Continuous Flow Analysis (CFA)	58
3.3.2	Stable Water Isotopes	59
3.4	Laser Ablation Inductively-Coupled Plasma Mass Spectrometry	59
3.4.1	Sampling Strategy for LA ICP-MS	60
3.4.2	Cutting Process	61
3.4.3	Chemical Analysis using LA ICP-MS	62
3.4.4	Mitigation of Sampling Errors	64
3.5	Discrete Sampling at a high resolution	65
3.5.1	Sampling Strategy for Discrete Methods	66
3.5.1.1	Berkner Island	66
3.5.1.2	Fletcher Promontory	67
3.5.2	Cutting Process	68
3.5.2.1	Band Saw	68
3.5.2.2	Microtome Cutting	68

3.5.3	Chemical Analysis using Discrete Methods	70
3.5.4	Mitigation of Sampling Errors	70
3.5.4.1	Ensuring clean apparatus	70
3.5.4.2	Potential contamination in the sampling process using the microtome	71
3.5.4.3	Testing for contamination of outer core section	73
3.5.5	Potential uses of high-resolution analysis on ice cores	75
3.6	Development of ice-core modelling techniques	75
3.6.1	Inverse Probabilistic Approach	76
3.6.1.1	Monte Carlo Markov Chain (MCMC) algorithm	76
3.6.1.2	Directed Search Algorithm	77
3.6.1.3	Perturbed Accumulation Profile	77
3.6.2	Phase-Sensitive Radio Echo Sounding (pRES) Thinning Function	79
3.6.2.1	Steady-State Age-Depth Profile	79
3.6.2.2	Variable Accumulation History and pRES	79
3.6.3	Borehole Thermometry Profiles	81
3.7	Summary	82
<b>4</b>	<b>Results: Construction and analysis of age-depth models applied to the Fletcher Promontory deep ice core</b>	<b>85</b>
4.1	Introduction	85
4.2	Ice-Core Reconstructions	85
4.2.1	Observational Data	86
4.3	Empirical Reconstructions	87
4.3.1	Water-Equivalent Depth Conversion	88
4.3.2	Temperature Reconstruction	89

4.3.3	Accumulation Reconstructions	91
4.3.4	Thinning Functions	92
4.3.5	Age-Depth Profiles	94
4.4	Constrained Profiles	96
4.4.1	IceChrono	97
4.4.2	GCM	102
4.4.3	Direct Search	104
4.4.4	OptAcc	110
4.4.5	pRES	114
4.5	Discussion	117
4.5.1	Empirical Reconstructions	118
4.5.2	Constrained Models	119
4.5.2.1	Accumulation Reconstructions	119
4.5.2.2	Thinning Reconstructions	126
4.5.3	Optimal Dating Strategy	128
4.5.3.1	Assessment of the Modelling Approaches	129
4.5.3.2	Assessment of the Reconstructions of Accumulation and Thinning	130
4.6	Summary	132
<b>5</b>	<b>Results: A comparison of annual layer thickness model estimates with observational measurements using the Berkner Island ice core, Antarctica</b>	<b>135</b>
5.1	Summary	135
5.2	Abstract	136
5.3	Introduction	137
5.4	Methodology	140

5.4.1	Continuous Flow Analysis	140
5.4.2	LA ICP-MS and Discrete Sample Details	140
5.4.3	LA ICP-MS	141
5.4.4	Discrete Samples	142
5.4.5	Lower Resolution Discrete Sampling	142
5.5	Results	143
5.5.1	Model Estimates	143
5.5.2	CFA Results	144
5.5.3	LA ICP-MS Results	145
5.5.3.1	Mid-Holocene Ice from 5.5 ka BP (454 – 459 m)	145
5.5.3.2	Glacial Ice from 27.1 – 27.7 ka BP (694 – 697 m)	146
5.5.3.3	Glacial Ice from 29.7 – 31.2 ka BP (702 – 707 m)	148
5.5.4	Discrete Sampling	149
5.5.4.1	Mid-Holocene Ice from 5.5 ka BP (454 – 459 m)	150
5.5.4.2	Glacial Ice from 29.7 – 31.2 ka BP (702 – 707 m)	153
5.6	Discussion	155
5.6.1	Annual Layer Visibility in the LA ICP-MS Record	157
5.6.2	Annual Layer Visibility in Discrete Sampling Record	158
5.6.3	Assessment of the Annual Layer Thickness Model	158
5.7	Conclusions	160
5.8	Supplementary Material to the Chapter	161
5.8.1	Annual Layer Thickness Model Variables	161
5.8.2	Statistical Analysis of LA ICP-MS data	162
5.8.3	Modelled Annual Layer Thickness	164
<b>6</b>	<b>Results: The optimal age-depth profiles for the Berkner Island and Fletcher Promontory ice cores</b>	<b>167</b>

6.1	Introduction	167
6.2	Methods	168
6.3	Results	169
6.3.1	Observational Constraints	169
6.3.1.1	Berkner Island	169
6.3.1.2	Fletcher Promontory	171
6.3.2	Accumulation and Annual Layer Thickness	173
6.3.2.1	Berkner Island	173
6.3.2.2	Fletcher Promontory	178
6.3.3	Age-Depth Profiles	181
6.3.3.1	Berkner Island	181
6.3.3.2	Fletcher Promontory	183
6.4	Discussion	186
6.4.1	Inclusion of Annual Layer Thickness Measurements as Model Constraints	186
6.4.2	Age-Depth Profiles	188
6.4.3	Thinning Profiles	189
6.4.4	Accumulation Profiles	192
6.4.4.1	Industrial Era (1850 – Present Day)	192
6.4.4.2	Holocene	194
6.4.4.3	LGM	196
6.4.5	Stable Water Isotopes and Accumulation	197
6.4.5.1	Berkner Island	197
6.4.5.2	Fletcher Promontory	199
6.5	Summary	200

<b>7</b>	<b>Results: A revised chronology for the James Ross Island ice core</b>	<b>203</b>
	7.1 Introduction	203
	7.2 Methods	204
	7.2.1 Continuous Flow Analysis	205
	7.2.2 Age-Depth Profile	206
	7.3 Results	208
	7.3.1 Seasonality	208
	7.3.2 WAIS Divide tie points	209
	7.3.3 Accumulation and Annual Layer Thickness	212
	7.3.4 Age-Depth Profile	216
	7.4 Discussion	220
	7.4.1 Age-Depth Profile	220
	7.4.2 Thinning Profile	223
	7.4.3 Accumulation Profile	224
	7.4.3.1 Early Holocene Accumulation Record	225
	7.4.3.2 Climate of the Common Era	225
	7.4.3.3 Rapid Regional Warming	231
	7.4.4 Stable Water Isotopes and Accumulation	233
	7.5 Summary	235
<b>8</b>	<b>Results: Determination of geothermal heat flux from borehole temperature measurements in the Weddell Sea sector of Antarctica</b>	<b>237</b>
	8.1 Introduction	237
	8.2 Methods	240
	8.2.1 Site Description and Drilling	240
	8.2.2 Temperature Measurements	240
	8.2.3 The Inverse Model Approach	241

8.2.4	The Temperature Gradient Approach	241
8.3	Results	242
8.3.1	Optimal Values from the Inverse Model Approach	242
8.3.2	The Temperature Gradient Approach	246
8.4	Discussion	247
8.4.1	Comparison of GHF values estimated by the two approaches	247
8.4.2	Probability range of optimal values	247
8.4.3	Comparison with existing datasets	249
8.4.4	Surface Temperature Warming and Borehole Modelling	251
8.4.4.1	Extending the Borehole Model to Other Sites	251
8.4.4.2	Assessment of the Surface Temperature Records	254
8.4.4.3	Potential Improvements to the Method	255
8.5	Conclusions	256
<b>9</b>	<b>Wider Context</b>	<b>259</b>
9.1	Introduction	259
9.2	Integration of Results from Chapters 4-8	260
9.3	Wider Context	263
9.3.1	Stable Water Isotopes and Accumulation	263
9.3.2	Future Changes to the Surface Mass Balance of the Antarctic Peninsula	267
9.3.3	Mid-Holocene Ice Sheet Evolution	269
9.3.4	Last Interglacial GMSL and the WAIS Contribution	271
9.3.5	The OptAcc ice core model	272
9.4	Summary	274
<b>10</b>	<b>Conclusions</b>	<b>275</b>

10.1	Introduction	275
10.2	Achievement of Study Objectives	275
	10.2.1 Mathematical Modelling	275
	10.2.2 Chemical Analysis of BI, FP, and JRI	277
10.3	Summary of the Results in a Wider Context	278
	10.3.1 The Optimal Dating Strategy	279
	10.3.2 Climate Information Interpreted from the BI, FP, and JRI ice cores	279
10.4	Future Research	280
	10.4.1 Model Development	280
	10.4.2 High-Resolution Analysis	281
	10.4.3 WAIS Collapse Analysis	282
	10.4.4 Borehole Thermometry Modelling	283
10.5	Summary	284
<b>11</b>	<b>Appendix 1: Construction and analysis of age-depth models applied to the Berkner Island and James Ross Island ice cores</b>	<b>285</b>
<b>12</b>	<b>References</b>	<b>313</b>

## List of Figures

Figure 1.01	Map of the AP and Weddell Sea region showing the locations of the three ice cores used in this study.	6
Figure 2.01	Map of ice core sites across Greenland mentioned in the text.	15
Figure 2.02	Map of ice core sites across Antarctica mentioned in the text.	17
Figure 2.03a	Seasonal variation in the chemistry of ice over a 48-month cycle at the WAIS Divide ice core site.	21
Figure 2.03b	Example of annual layer counting in the B32 ice core, Antarctica.	21
Figure 2.04	1000-year record of atmospheric carbon dioxide from ice core records and the Mauna Loa Observatory.	23
Figure 2.05	Figure 2.05: Surface temperature, stable water isotope, and methane records from Antarctic ice cores with MIS and AIM events labelled.	25
Figure 2.06	Dansgaard-Oeschger events in the NGRIP ice core, Greenland.	27
Figure 2.07	Colle Gnifetti ice core data.	30
Figure 2.08	A flow chart outlining the construction of an age-depth profile and where each reconstruction or chemical measurement is incorporated.	32
Figure 2.09	Schematic cross-section of an ice sheet showing the coordinates used in the thinning functions.	37
Figure 3.01	Map showing the site locations of deep ice cores and short boreholes in the Antarctic Peninsula and Weddell Sea region.	55
Figure 3.02	Diagram of ice sampling from the archive material	62

Figure 3.03	The Sayre Cell TM system with labels	63
Figure 3.04	Cold room discrete sampling set-up	69
Figure 3.05	Diagram of the convex section of ice sampled in an experiment to test for contaminants from the drilling process (Figure taken from Thomas (2006)).	74
Figure 3.06	Factor increase of ion concentrations emanating from the centre of a section of the GRIP ice core (Figure taken from Thomas (2006)).	75
Figure 3.07	A flow diagram outlining an approach to reconstruct the accumulation, annual layer thickness, and age-depth profile using pRES measurements.	80
Figure 3.08	Flow chart outlining the methodological approach of the borehole temperature model.	81
Figure 4.01	Density Reconstruction for the FP ice core plotted against snow depth.	89
Figure 4.02	Temperature reconstructions for the FP ice core.	90
Figure 4.03	Accumulation reconstructions using empirical relationships.	92
Figure 4.04	Unconstrained thinning functions	93
Figure 4.05	Age-depth profiles calculated by a combination of empirical accumulation and thinning functions	94
Figure 4.06	Age-depth profiles constructed using the IceChrono model.	98
Figure 4.07	Accumulation and thinning profiles reconstructed using the IceChrono model approach, with a priori accumulation profiles.	101

Figure 4.08	Accumulation and thinning profiles reconstructed using the IceChrono model approach, with a priori thinning profiles.	102
Figure 4.09	Age-depth profiles using the Direct Search approach as calculated using four different accumulation history profiles.	106
Figure 4.10	Posterior thinning functions and associated uncertainty constrained using the Direct Search method.	108
Figure 4.11	Age-depth profiles using the Optimised Accumulation models with uncertainty (grey) and age horizons (black crosses).	112
Figure 4.12	Annual layer thickness profiles and accumulation estimated for FP ice core.	113
Figure 4.13	Perturbation profiles from the OptAcc model for the FP ice core using three different initial accumulation profiles.	114
Figure 4.14	Age-depth profile using the pRES model.	116
Figure 4.15	Accumulation and annual layer thickness derived from the pRES model.	117
Figure 4.16	Sensitivity change of accumulation reconstructions with respect to temperature.	118
Figure 4.17	Accumulation estimates from each model approach per millennia.	121
Figure 4.18	Changes in accumulation reconstructed using each model approach.	126
Figure 5.01	Berkner Island ice core isotopic and annual layer thickness profiles, with sample depths highlighted in pink.	144
Figure 5.02	Four-metre section analysed by CFA and DEP.	144
Figure 5.03	LA ICP-MS profiles for three sections of sample from 454 – 459 m with red dashed lines indicating a seasonal peak.	146

Figure 5.04	LA ICP-MS profiles for three sections of ice from 694-697 m with red dashed lines delineating a seasonal peak.	147
Figure 5.05	LA ICP-MS profiles for three sections of ice from 702-707 m with red dashed lines delineating a seasonal peak.	148
Figure 5.06	Three sections of ice originating from 455 – 459 m analysed by IC with red dashed lines indicating annual peaks.	151
Figure 5.07	Comparison of parallel sections of ice from 456.31 m – 456.51 m with seasonal peaks indicated by a grey line.	152
Figure 5.08	Comparison of parallel sections of ice from 458.51 - 458.71 m with seasonal peaks indicated by a grey line.	153
Figure 5.09	Comparison of parallel sections of ice from 703.2 - 703.22 m.	154
Figure 5.10	Comparison of parallel sections of ice from 706.3 - 706.38 m.	155
Figure S5.01	FFT power spectrum density plots for each section of ice analysed.	163
Figure 6.01	Sub-annual measurements on the Fletcher Promontory ice core.	172
Figure 6.02	Present-day (blue) and original annual layer thickness (red) for the BI ice core.	174
Figure 6.03	Perturbation profiles for the BI and FP ice core reconstructions.	175
Figure 6.04	Density distribution of the modelled annual layer thickness at depths corresponding to measured values in the BI ice core.	176
Figure 6.05	Thinning functions reconstructed using the OptAcc model for the BI and FP ice cores with the associated uncertainty.	177
Figure 6.06	Present-day and original annual layer thickness for the FP ice core.	179

Figure 6.07	Density distribution of the modelled annual layer thickness at depths corresponding to measured values in the FP ice core.	180
Figure 6.08	Age-depth profile of the BI ice core.	181
Figure 6.09	Probability distribution with the normal density function fitted of all age estimates at the depths corresponding to age constraints for BI.	182
Figure 6.10	Age-depth profile of the FP ice core.	184
Figure 6.11	Probability distribution with the normal density function fitted of all age estimates at the depths corresponding to age constraints for FP.	185
Figure 6.12	Comparison of the optimised accumulation and present-day annual layer thickness profiles of FP, reconstructed with and without annual layer thickness constraints.	187
Figure 6.13	Temperature reconstructions and accumulation reconstructions for FP and BI ice cores.	189
Figure 6.14	Comparison of the thinning function with pRES observations.	191
Figure 6.15	Accumulation and surface temperature reconstructions over the last 2000 years for each ice core.	194
Figure 6.16	Comparison of FP and BI accumulation records with records from WAIS Divide and Taylor Dome over 11.3 - 2 ka BP.	195
Figure 7.01	Map of JRI in the AP and Weddell Sea region	204
Figure 7.02	Seasonal cycles across a 5-m section of the JRI ice core.	209
Figure 7.03	The JRI stable water isotope profile at 357-363 m. Age constraints at circa 12.8 ka BP, 14.4 ka BP, and 17.5 ka BP are identified by blue dotted lines.	212

Figure 7.04	(a) Accumulation and annual layer thickness reconstructions; (b) the accumulation reconstructions from three techniques: inverted annual layer thickness measurements, empirical and inverse modelling.	213
Figure 7.05	Perturbation profile from the OptAcc model for the JRI ice core.	215
Figure 7.06	Thinning function for the JRI ice core with associated uncertainty in grey.	216
Figure 7.07	Age-depth profile for the JRI ice core.	217
Figure 7.08	Histogram distributions of modelled age estimates at depths corresponding to age horizons with a normal distribution function fitted.	219
Figure 7.09	Comparison of the JRI1 chronology with the JRI2 chronology.	223
Figure 7.10	Accumulation and surface temperature reconstructions over the last 15,000 years.	226
Figure 7.11	Accumulation and surface temperature reconstructions over the last 1,100 years.	228
Figure 7.12	LIA signatures in the chemical record of the JRI ice core from 1400 AD - 2000 AD.	230
Figure 7.13	Accumulation and surface temperature reconstructions for the JRI ice core for 1900 AD - 2000 AD	232
Figure 7.14	Comparison of annual accumulation at JRI with the Mean Annual SAM Index for 1955 - 2012.	234
Figure 8.01	Distribution of GHF values with a probability density function fitted for JRI, FP, and BI.	243
Figure 8.02	Distribution of surface temperature values with a probability density function fitted for JRI, FP, and BI.	244
Figure 8.03	Distribution of mean annual accumulation values with a probability density function fitted for JRI, FP, and BI.	244

Figure 8.04	Comparison of modelled borehole temperature profiles with measured temperatures for JRI, FP, and BI.	246
Figure 8.05	Spatial variability of GHF estimates across AP and Weddell Sea region, with calculated values overlaid for comparison.	250
Figure 8.06	Borehole temperature reconstructions (black line) for each borehole site, with measured borehole profiles in red crosses.	253
Figure 9.01	Temperature and Accumulation reconstructions for BI, FP, and JRI ice cores.	262
Figure 9.02	Initial and Optimised accumulation profiles for BI, FP, and JRI.	265
Figure 9.03	Reconstructed surface temperature anomaly over 11.3 - 0 ka BP for BI, FP, and JRI.	271

## List of Tables

Table 2.01	A list of trace element chemical species, the source before deposition, and the timing of seasonal deposition.	22
Table 3.01	Information pertaining to site specifications at each ice core drill site.	54
Table 3.02	Table outlining the application of different methods of chemical analysis to the three ice cores.	57
Table 3.03	BI sample depths for LA ICP-MS.	61
Table 3.04	Relative standard deviations used in the LA ICP-MS system calibration.	64
Table 3.05	BI sample depths for discrete sampling.	67
Table 3.06	FP sample depths for discrete sampling.	68
Table 3.07	Table of anion results for all instruments that come into contact with ice samples in the discrete sampling method.	72
Table 4.01	List of age horizons used to constrain the FP ice core age-depth profile.	87
Table 4.02	Site specific variables for the FP ice core.	88
Table 4.03	Age estimates at depths corresponding to age horizons in the FP ice core, using different empirical accumulation and thinning profiles.	95
Table 4.04	Age estimate and uncertainty for each IceChrono model scenario.	99
Table 4.05	GCM estimates of precipitation.	103
Table 4.06	Age estimates and uncertainty for each Direct Search model scenario.	107

Table 4.07	Glen exponent and p-parameter value for each Direct Search model scenario.	110
Table 4.08	Age estimates and uncertainty for each OptAcc model scenario.	111
Table 4.09	Glen exponent and p-parameter value for each OptAcc model scenario.	114
Table 4.10	Age estimate and uncertainty for the pRES model scenario.	115
Table 4.11	Precipitation estimates for every model approach per millennia.	123
Table 4.12	RMSE values for each model scenario for every model approach used.	129
Table 5.01	Comparison of the measured and modelled annual layer thickness at depths analysed using LA ICP-MS.	145
Table S5.01	List of parameters and the values used in calculating the annual layer thickness in the BI ice core.	161
Table S5.02	Known-age horizons along the Berkner Island ice core with associated error.	161
Table S5.03	Annual Layer Thickness estimates from every model combination, using a Clausius-Clapeyron accumulation reconstruction.	165
Table 6.01	BI age constraints and uncertainty.	170
Table 6.02	Observed annual layer thickness measurements used as constraints in the BI reconstructions.	170
Table 6.03	Observed annual layer thickness measurements used as constraints in the FP reconstructions.	173
Table 6.04	Modelled annual layer thicknesses and respective RMSE value for BI.	177
Table 6.05	Glen's exponent and p-parameter for the BI and FP ice cores.	178

Table 6.06	Modelled annual layer thicknesses and respective RMSE value for FP.	180
Table 6.07	Modelled ages and respective RMSE value for BI.	183
Table 6.08	Modelled ages and respective RMSE value for FP.	186
Table 7.01	List of chemicals measured using the BC-TE-CFA system at DRI.	205
Table 7.02	JRI age constraints and uncertainty.	210
Table 7.03	Modelled ages and respective RMSE value for JRI.	219
Table 8.01	Values of GHF, surface temperature and mean accumulation for JRI, FP, and BI.	242
Table 8.02	A list of GHF values estimated by methods outlined in this paper, and earlier studies for the three sites.	249
Table 8.03	Borehole results for each site.	253

## List of Abbreviations

$\theta$	Any parameter suffixed by a superscript theta indicates present-day conditions
$\alpha_c$	Thermal conductivity used in the calculation of $\alpha_D$
$\alpha_D$	Thermal diffusivity used in eq. 3.05
$\beta$	Free parameter in Simple Exponential accumulation relationship
$\delta D$	Deuterium isotope ratio
$\delta_{\text{grav}}$	Gravitational fractionation
$\delta^{18/16}\text{O}$	Oxygen isotope ratio
$\Delta\delta D$	Deviation between present-day and measured value of deuterium
$\Delta\text{age}$	Difference in age at a particular depth between ice-phase and gas-phase of an ice core
$\Delta\text{depth}$	Difference in depth at a particular age between ice-phase and gas-phase of an ice core
$\Delta m$	Difference in mass of two isotopes
$\varepsilon$	Perturbation term
$\dot{\varepsilon}\sigma$	viscous heating term
$\dot{\varepsilon}$	strain rate tensor
$\sigma$	stress rate tensor
$\lambda$	Layer Thickness
$\lambda_0$	Present-day annual layer thickness (equiv. to accumulation)
$\mu$	Geothermal heat flux in borehole temperature model
$\eta$	Thinning function
$\eta_D(\zeta)$	Vertical profile of deformation
$\rho$	Density
$\rho_i$	Density of ice
$\rho_D(d)$	probability density of a data space
$\rho_M(m)$	probability density of a model space
$\zeta$	Non-dimensional vertical co-ordinate
A	accumulation
ACR	Antarctic Cold Reversal
AIM	Antarctic Isotopic Maxima
AIS	Antarctic Ice Sheet
ANU	Australian National University

AOGCM	Atmosphere-Ocean General Circulation Model
age	age of a particle of ice in an ice column
AP	Antarctic Peninsula
Ar	Argon
A <sub>s</sub>	Constant used in eq. 2.14
AWS	Automatic Weather Station
b	mean present-day accumulation
B <sub>s</sub>	Constant used in eq. 2.14
BC	Black Carbon
BC-TE-CFA	Black Carbon Trace-Element Continuous Flow Analysis
Be	Beryllium
C	Constant used in eq. 2.31 for a change in density with depth
C	Specific Heat Capacity
C	Carbon
Co	constant in eq. 2.08
Ca	Calcium
CCI	Climate Change Institute
CFA	Continuous Flow Analysis
Cl	Chlorine
CL/x	A UHP water sample in an unsealed vial that was stored in clean room conditions
CL/Lx	A UHP water sample in a sealed vial that was stored in clean room conditions
CR/x	A UHP water sample in an unsealed vial that was stored in cold room conditions
CR/Lx	A UHP water sample in a sealed vial that was stored in cold room conditions
CH <sub>4</sub>	Methane
CO <sub>2</sub>	Carbon Dioxide
count s <sup>-1</sup>	Count per second
cps	Alternative abbreviation for count per second (used in publication in Chapter 5)
CRREL	Cold Regions Research and Engineering Laboratory
d	deuterium excess

DCH	Diffusive Column Height
DEP	Dielectric Profile
DMS	Dimethylsulphide
D-O	Dansgaard-Oeschger
DRI	Desert Research Institute
DS	Direct Search approach
dt	time step
dz	depth step
E	RMSE error value
EAIS	East Antarctic Ice Sheet
ECM	Electrical Conductivity Measurements
EDC	EPICA Dome C
EDML	EPICA Dronning Maud Land
ESF	European Science Foundation
EPICA	European Project for Ice Coring in Antarctica
F	Flouride
FFT	Fast Fourier Transform
g	gravitational acceleration
$G_{\theta}$	Temperature gradient
GCM	Global Circulation Model
GI	Greenland Interstadials
GISP	Greenland Ice Sheet Project
GMSL	Global Mean Seal Level
GRIP	GReenland Ice core Project
GrIS	Greenland Ice Sheet
h	Basal shear depth
H	total ice sheet thickness
H <sub>2</sub> O <sub>2</sub>	Hydrogen Peroxide
H-L	Herron and Langway model
HTM	Holocene Thermal Maximum
	International Atomic Energy Agency and the World Meteorological
IAEA-WMO	Organisation
IC	ion chromatography
ICP-MS	inductively-coupled plasma mass spectrometry

IRD	Ice Rafted Debris
IRMS	Isotope Ratio Mass Spectrometer
JRI1	First JRI chronology
JRI2	Second JRI chronology
k	Constant used in eq. 2.23
k	Thermal conductivity used in eq. 2.03
K	Potassium
LA ICP-MS	Ultra-violet laser ablation inductively-coupled plasma mass spectrometry
LF/x	A UHP water that was frozen in a plastic lay-flat bag and sampled from the centre of the UHP ice core
LGM	Last Glacial Maximum
LIA	Little Ice Age
LID	Lock-in depth
LIG	Last Interglacial
LIS	Laurentide Ice Sheet
m	Melting
MCMC	Monte Carlo Markov Chain
Mg	Magnesium
MIS	Marine Isotope Stage
MSA	Methanosulphonate
mweq	metres in water equivalent units
MWL	Meteoric Water Line
MWP	Medieval Warm Period
MQ	Milli-Q - alternative reference to UHP water
n	Glen's exponent
Na	Sodium
N/D	Not detected
NEEM	North Greenland Eemian site
NGRIP	North GRenland Ice core Project
NH <sub>4</sub>	Ammonium
NIGL	NERC Isotope Geochemistry Laboratory
N <sub>2</sub> O	Nitrous Oxide
NO <sub>3</sub>	Nitrate

NO <sub>x</sub>	Nitrate
nss-S	non sea salt Sulphur
OptAcc	Optimised Accumulation and Thinning model
p	parameter that controls the profile of deformation in the One-Dimensional thinning function
P-B	Pimienta-Barnola model
PB/x	A UHP water sample that has been in contact with the paintbrush
ppb	parts per billion
ppt	parts per trillion
P <sub>s</sub>	Saturation vapour pressure
PDD	Positive Degree Day
pRES	Phase-sensitive radio echo sounding
Q	activation energy
R	gas molar constant
R <sub>s</sub>	Stable Water Isotopes at a site
R <sub>SMOW</sub>	Stable Water Isotopes of the standard mean ocean water
s	sliding ratio
SAM	Southern Annular Mode
SIA	Shallow Ice Approximation
SLRS-5	Frozen river water reference material used to calibrate LA ICP-MS
SLP	Sea Level Pressure
SMB	Surface mass balance
SO <sub>4</sub>	Sulphate
SST	Sea Surface Temperatures
tf	time period
T	temperature
T/x	A UHP water that has been in contact with the tongs
T <sub>B</sub>	temperature at bedrock
T <sub>i</sub>	temperature at the inversion layer
T <sub>s</sub>	surface temperature
u	Velocity in eq. 2.03
UHP	Ultra high purity water
U <sub>o</sub>	Present-day mean surface temperature in borehole temperature modelling

UV	ultra-violet
U-Th	Uranium-Thorium
w	vertical velocity
WAIS	West Antarctic Ice Sheet
x	distance from the ice divide
z	Depth below surface
$\hat{z}$	Depth above the bed

## **Declaration and statement of copyright**

This copyright of this thesis rests with the author. No quotation from it should be published without the author's prior written consent and information derived from it should be acknowledged.

I confirm that no part of the material in this thesis has previously been submitted by me or any other person for a degree in this or any other university. In all cases, where is relevant, material from the work of others has been acknowledged.

Ashleigh Massam

Department of Geography

Durham University

## Acknowledgements

First and foremost, I must thank my supervisors, Dr Robert Mulvaney, Dr Pippa Whitehouse, and Professor Mike Bentley. Without your advice and comments, this thesis would be a shadow of itself. Throughout the course of the study, I must particularly thank Rob and Pippa for knowing me so well and supporting me at every step. This study has been funded by a NERC Algorithm scholarship, with additional funding from the Antarctic Science bursary.

Additional support in the completion of this study has been provided by colleagues at the British Antarctic Survey (BAS). Carlos Martin has acted as a proxy supervisor for much of the last four years and I am definitely indebted to him. Secondly, Laura Gerrish makes excellent maps. Also, I must thank the other scientists in the ice-core group for help, advice and support throughout the study: Dr Rebecca Tuckwell and Emily Ludlow, and fellow PhD student, Geoff Lee. External to BAS, I must thank colleagues from other institutions who have contributed to this study through collaboration. It has been fun, enlightening, and educational to work with you all.

I must thank my partner, Owen. He is consistently cheerful, supportive, and lovely. Throughout the study, you had insight, listened to my good and bad ideas, and regularly calmed me down when I got too anxious. Towards the end, when it was regular tears and tantrums, you calmed me down and kept me positive. I will never forget that, and I look forward to helping you in the same way when you write up your thesis next year. Mum and Dad, and my sister, Laura: you have behaved no differently throughout my PhD as you have done throughout my life. You are all great. Grandma – you are my Queen. I know it has been difficult, and I thank you for being so good.

Being based at BAS in Cambridge has been a brilliant. I want to thank Jim who welcomed me to Cambridge and continues to be one of my closest friends. Also, big thanks to the BAS Netball team, and the girls in my office – Jenny, Veronica, and Michelle. We went through everything together and I am so pleased we are all finishing this together. My housemates at Sedgwick Street – Heather, I have no words for our friendship. We got through this together. Polly: I loved coming home to your company! I am forever in debt to your wine – I drank more of it than you know.

Thank you to every one of you. You have all contributed – in either a big or a small way – to the last four years. This is for all of you.

# Chapter 1: Introduction

## 1.1 Rationale

In Polar Regions, ice sheets preserve a record of annual snowfall. When the snow falls on the ice sheet, the previous years of snowfall are compacted into ice due to the increasing load above. In Antarctica and Greenland, where the mean annual surface temperature remains below freezing and not all of the annual snow ablates away, the ice sheets preserve an uninterrupted history of snow deposition.

By drilling vertically downwards into the ice sheet, one can retrieve an ice core which provides a record of the past snowfall that can then be used to interpret the past climate conditions. An ice core can be used to interpret the past climatic conditions in two ways: (i) by measuring gases that are trapped within the ice matrix; and (ii) by interpreting the ice chemistry as a proxy for past climate.

Unreactive gases trapped in the ice matrix of an ice core yield records of past atmospheric conditions, and these are representative of the global atmosphere due to rapid rates of atmospheric mixing. The atmospheric conditions of at least the last eight glacial periods are preserved in deep Antarctic ice cores (Loulergue et al., 2008; Luthi et al., 2008), with records of greenhouse gases detailing the relationship of atmospheric composition to the orbital variations that define the glacial cycles of the planet (Hays et al., 1976; Imbrie and Imbrie, 1980).

The second method for interpreting the climate history preserved in an ice core analyses the chemical composition of annual snowfall and using the measurements to indirectly inform us of past climatic conditions on local and regional scales. The stable water isotopes that make up precipitation can be used to reconstruct a surface temperature and accumulation history (Dansgaard, 1953; 1964). In addition to the stable isotope profile, the seasonal flux of ion concentrations in the ice further provide a temporal view over the ice sheet and the region in which it is found, providing information on factors such as the sea ice evolution, wind sources, and humidity sources (Sommer et al., 2000; Curran et al., 2003; Abram et al., 2013).

In order to understand the records preserved in an ice core, it is necessary to construct a robust age-depth profile. For palaeoclimate reconstructions that are based on marine or terrestrial cores, absolute or radiometric dating methods can be directly employed on

organic materials found within these cores to obtain precise, site-specific age determinations. These methods are vital to palaeoclimate reconstructions, and can be used to constrain an age-depth profile by interpolation along the core (Blaauw, 2010; Bronk Ramsey, 1995). The lack of organic material present in glaciated regions of Antarctica creates a more complex situation for ice cores. For ice cores, an accurate ice-core chronology relies on a combination of methods to estimate the *in situ* annual layer thickness (the snowfall layer that has been compacted due to subsequent years of snowfall). At most sites, the uppermost layers can be dated by annual layer counting, but eventually a depth is reached where these become too thin to robustly count. After this depth, chemical analysis can be used to delineate the annual layers as many chemical species are deposited on an annual cycle in the snow. For ice cores obtained from regions of high mean annual accumulation, chemical analysis at the standard laboratory analytical resolution of ~10 mm, is sufficient to identify and count annual layer thicknesses throughout the ice core. This technique is used to reconstruct the age-depth profile of deep ice cores from Greenland and West Antarctica (Rasmussen et al., 2006; Sigl et al., 2016).

If one can assume that an Antarctic ice core preserves an uninterrupted, record of snowfall, one can also assume that the age of an ice particle at a particular depth is equal to the number of annual layers above it. It is also reasonable to assume that an ice-core record obtained from a site with a high mean annual accumulation will not extend as far back in time as an ice core of the same length from a site of lower mean annual accumulation, due to the greater *in situ* annual layer thickness in the ice core from a high annual accumulation site. For ice cores with an *in situ* annual layer thickness that is too thin to be determined from visual methods, annual layer thickness can be estimated using a combination of chemical analysis and modelling techniques.

In order to model an age-depth profile, an accumulation history must be reconstructed assuming a relationship between the stable water isotope profile preserved in the ice core and the rate of snowfall. This can be combined with a depth-varying expression (a 'thinning function') that reflects the amount by which annual layers along the ice core have been compacted since deposition, to give an estimate of current layer thickness along the length of the ice core. Accumulation and thinning functions can be reconstructed using a number of relationships. The modelled annual layer thickness and age-depth estimates can be constrained using observational data, preserved or measured in the ice core, by optimising one or more parameters in an inverse approach. Throughout the history of ice-core drilling

and analysis, several approaches have been used to estimate an age-depth profile for ice cores from Greenland and Antarctica (Dansgaard and Johnsen, 1969; Schwander et al., 2001; Parrenin et al., 2001; 2004; 2007a; 2007b). These modelled ice-core chronologies range from simplistic steady-state models to complicated ice-flow models. This leads to a lack of consensus across ice-core chronologies and the subsequent palaeoclimate analysis. One response to the differences between chronologies has been to develop age-depth model templates which can be applied to multiple cores within one iterative model in order to 'tune' chronologies and infer a temporal view of global atmospheric processes (Lemieux-Dudon et al., 2010; Bazin et al., 2012; Parrenin et al., 2015).

The ice-core records synchronised using the most recent modelling techniques include the accumulation records spanning multiple glacial cycles from the East Antarctic ice sheet (EAIS), and the annual-layer counted accumulation records from the Greenland ice sheet (GRIS) (Lemieux-Dudon et al., 2010; Bazin et al., 2012; Parrenin et al., 2015). Across these sites, longer records with low mean annual accumulation ( $< 40 \text{ mm yr}^{-1}$ ) have an effective resolution that does not preserve accumulation variability on a timeframe shorter than several thousand years. For Antarctica, the amount of snowfall across the ice sheet depends on the proximity to the coast and the sources of moisture, with higher annual rates of accumulation at coastal sites compared to the mean annual accumulation rates inland (Fudge et al., 2016; Schlosser et al., 2017; Steiger et al., 2017). As a result, the highest mean annual snowfall is found across the West Antarctic ice sheet (WAIS) and the Antarctic Peninsula (AP), where the mean annual accumulation is an order of magnitude greater than across the EAIS (Palermo et al., 2014). The higher mean annual accumulation across the WAIS results in an annual layer thickness record that covers a shorter timeframe over comparable ice core depths retrieved from the EAIS (Buizert et al., 2015; Sigl et al., 2016). As a result, the effective resolution of the accumulation record is much higher than EAIS ice core records, and hence the model strategy of synchronising ice-core records using common relationships is not always reliable due to the high natural variability in the accumulation and annual layer thickness records at individual WAIS and AP locations. To address this issue, alternative modelling approaches should be considered in order to accurately reconstruct the natural variability in a high-resolution ice-core record that impacts greatly upon the final age-depth profile.

## 1.2 Aim of the project

This study aims to explore and characterise the variety of options that can be chosen when reconstructing the accumulation, thinning, and hence annual layer thickness and age-depth profiles of an ice core. It seeks to highlight the variation in results by comparing possible combinations, before presenting the optimal dating strategy for three coastal ice cores originating from the AP and Weddell Sea region of Antarctica, and to make palaeoclimatic interpretations from them. The underlying rationale is that in order to improve our knowledge of palaeoclimate records, we must first understand the reliability of the methodological approach used in the construction of the age-depth profile.

### 1.2.1 *Objectives*

To achieve this aim, five objectives have been identified. These are designed to determine the optimal dating strategy for three ice cores retrieved from the AP and the Weddell Sea region. Specifically, the cores have been retrieved from James Ross Island (JRI), Fletcher Promontory (FP), and Berkner Island (BI). These cores have already been analysed for many proxies but in light of recent new data the identification of the optimal dating approach requires new analysis.

- i) Draw together and develop mathematical relationships that reconstruct accumulation and thinning in order to model the age scale for each ice core;
- ii) Make new laboratory measurements of annual layer thickness for the BI and FP ice cores to test the accumulation reconstructions derived under objective (i);
- iii) Use the results of the previous two objectives to develop the best combined dating model and establish a dating strategy for the AP and Weddell Sea ice cores;
- iv) Model the borehole thermometry profile to reconstruct an independent surface temperature history for the AP;
- v) Use newly dated ice cores to assess regional patterns of climate and ice sheet change in comparison to other regions of Antarctica.

### 1.3 Study Area

The three deep ice cores used in this study were drilled in the AP and Weddell Sea region, a region currently experiencing rapid regional warming leading to ice mass loss (Vaughan et al., 2003; Steig et al., 2009). The ice cores were drilled to bedrock in order to reconstruct the longest possible climate history of the region. These ice cores are: the JRI ice core, drilled to 364 m depth on the north-eastern tip of the AP, the 654 m-deep ice core drilled on FP, which is located in the southwestern Weddell Sea embayment, and the 947 m-deep ice core from BI, which is located east of Fletcher Promontory on a large ice rise in the eastern Weddell Sea embayment, embedded in the Ronne and the Filchner ice shelves (fig 1.01).

The AP is one of the most rapidly warming regions on Earth, with historical observations from Esperanza Station suggesting that average temperatures are currently increasing by as much as  $3.5 \text{ K (100 yr)}^{-1}$  (Mulvaney et al., 2014). Recently, mass loss has been particularly significant as a result of a series of ice shelf collapses (with consequent unbuttressing and acceleration of grounded ice), and the retreat of tidewater glaciers (Vaughan et al. 2003; Cook et al., 2005; 2016; Kunz et al., 2012). The impact of changes in glacier flow, particularly along narrow channels occupied by outlet glaciers along the AP, is thought to have a significant effect on the mass balance and the stability of the ice sheet. Mass loss, interpreted by remote sensing techniques such as radar interferometry, increased by 140% over 1996-2006 (Rignot et al., 2008; Shepherd et al., 2012).

Ice-shelf instability across the AP is a significant issue for understanding the ice-shelf stability across Antarctica, and the potential contribution of the Antarctic Ice Sheet (AIS) to future sea level rise. Potential instability at the Larsen C ice shelf, following the collapse of Larsen A and Larsen B in 1995 and 2002, respectively, threatens the removal of up to 12% of the Larsen C shelf area in a single calving event (Jansen et al., 2015). However, the growth and retreat of the ice shelves on the AP have not been determined only by the glacial-interglacial transitions, but instead they have continued to evolve throughout the Holocene (Domack et al., 2005; Pudsey et al., 2006). Assessment of a high-resolution ice core record from this region will help us understand the threshold limits on climate that have previously resulted in the retreat or disappearance of ice shelves in this region, with a view to interpreting and predicting future changes in response to the current rapid regional warming. An ice core from JRI provides an uninterrupted view of the Holocene period in a region where the ice shelf history can be used in forecasting the future stability of the AP ice shelves (Domack et al., 2005; Pudsey et al., 2006).

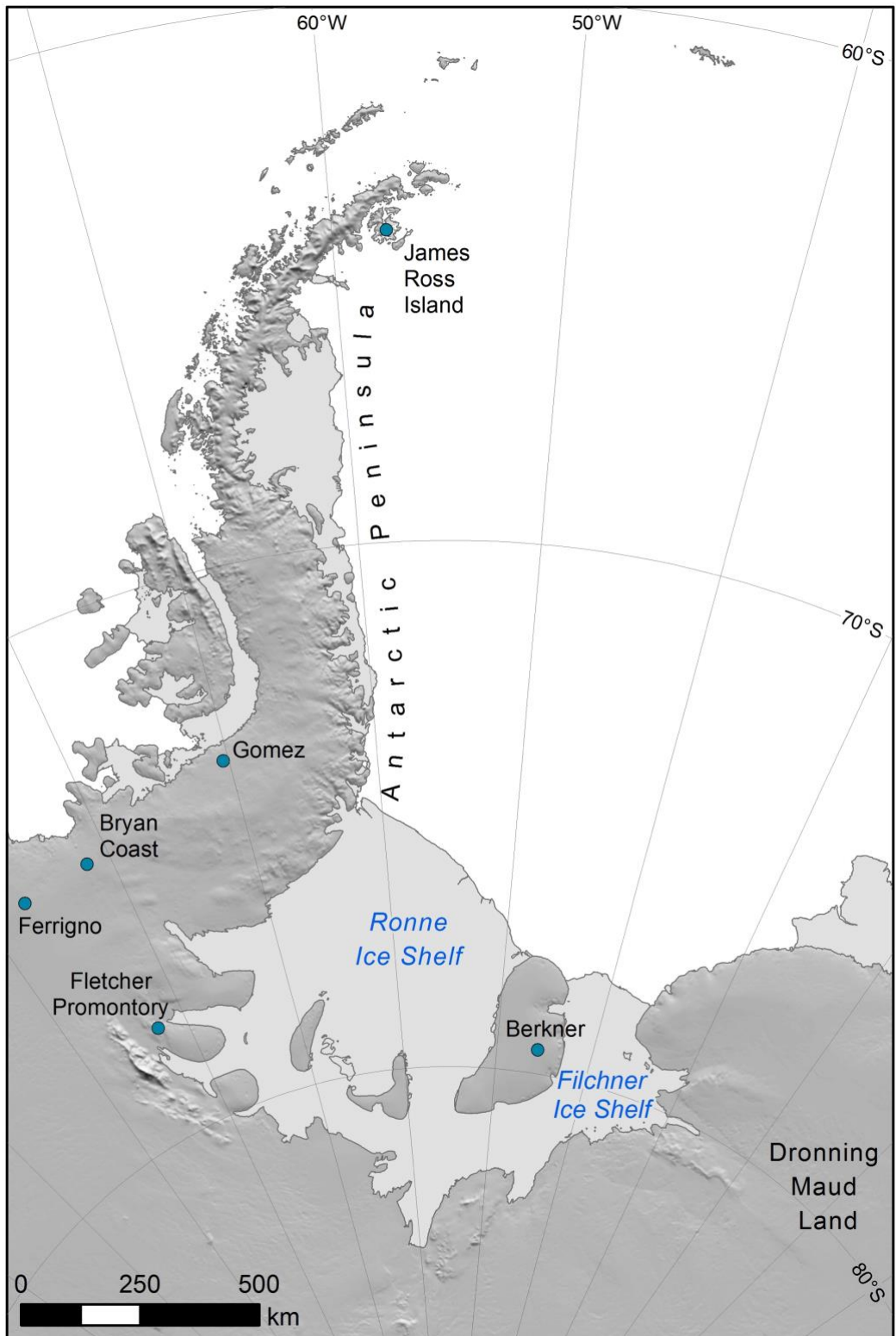


Figure 1.01: Map of the AP and Weddell Sea region showing the locations of the three ice cores drilled at Fletcher Promontory, Berkner Island, and James Ross Island. Also included in the map are the locations of short ice cores mentioned in this chapter. Dark grey areas indicate grounded ice, with pale grey surfaces extending from the grounding lines to the calving front of the ice shelves. The surrounding white area in map is open ocean.

In addition, records of past climate can provide insight into future sea level rise, when we combine marine, terrestrial and ice core records (McConnell et al., 2000; Dutton and Lambeck, 2012). During the last interglacial (LIG) global mean sea level (GMSL) was 6-9 m higher than the present-day level (Dutton et al., 2015). The contribution of the GrIS to this highstand is estimated to have been ~3 m (Dutton et al., 2015); the remainder of the sea level contribution would have come from thermal expansion of water masses and the Antarctic ice sheets. Of particular importance, the WAIS holds up to 5 m of GMSL, of which 3.3 m is located in areas of marine-grounded ice (Bamber et al., 2009). During the LIG, the North Greenland Eemian Ice Drilling (NEEM) ice core record in Greenland suggests that local mean annual surface temperature was up to 8 K warmer than the present-day interglacial (Landais et al., 2016). Globally, the mean annual surface temperature was 1-2 K warmer than pre-industrial climate conditions (McKay et al., 2011; Capron et al., 2014; Hoffman et al., 2017). Therefore it is hypothesized that warmer global mean surface temperatures contributed to ice mass loss, and thus the greater GMSL than present-day. However, the small GMSL contribution from non-Antarctic sources implies that a significant ice mass loss from Antarctica is required to agree with palaeoclimate data (Holloway et al., 2016).

Fletcher Promontory is located on a small ice dome that might be expected to disappear, or at least dramatically thin, in the event of WAIS collapse (Mulvaney et al., 2014) and so understanding the history of this site can provide insight into past WAIS stability. Berkner Island is a major ice rise separating the Filchner and Ronne Ice Shelves in the Weddell Sea embayment. Ice from Berkner Island flows into both ice shelves but at its northern end it also flows directly into the Weddell Sea, with ocean water able to flow in the sub-ice shelf cavity around the whole of the island (Mulvaney et al., 2007). Ice cores drilled at these locations, extending into the LIG, would provide direct information on the stability of the WAIS. Chemical analysis of the ice cores would yield proxy information allowing us to test whether the sites were surrounded by open ocean or sea ice, indicating the collapse/retreat, or the remaining presence, of the WAIS.

Future predictions of climate change estimated by global circulation models suggest that warming surface air temperatures could lead to an increase in precipitation over the Antarctic continent (Krinner et al., 2007; Bracegirdle et al., 2008; Palerme et al., 2016). Evidence to support these projections is found in shallow ice cores taken from the WAIS and the East Antarctic region of Dronning Maud Land. WAIS sites of Gomez, Ferrigno, and Bryan Coast record an increase in annual snowfall over the last century (Thomas et al., 2015).

Concurrently, an increase in surface mass balance (SMB – i.e. precipitation minus meltwater runoff, sublimation, and evaporation) is preserved in a record extending over the last 250 years in Dronning Maud Land, EAIS (Philippe et al., 2016). These ice core sites respond to the atmospheric transport of moisture from the oceans, which can make the accumulation rate at the site more responsive to local changes. This is true for WAIS and AP sites, due to their proximity to the coast, but it is not the case for EAIS ice core sites as they are often drilled in the interior of the ice sheet and hence far away from the coast.

The rapid regional warming across the AP and Weddell Sea region is contributing to ice mass loss on the ice shelves, with an increase in SMB across the interior of the AP region (Steig et al., 2009; Thomas et al., 2008; Cook et al., 2016). The potential effects of the increase in mean surface temperatures on the AP and Weddell Sea region, as well as the WAIS, can be better forecasted by answering key questions using the information preserved in ice cores. Principally, (i) What is the climate warming threshold for ice shelf stability on the AP? (ii) Did the WAIS collapse or significantly retreat during the LIG? Finally, (iii) Do the ice core records show evidence of increasing accumulation due to warming across the region?

#### 1.4 Thesis Outline and Summary

The following section details the work that is found in chapters 2-9 of this study. Some results have been published in a peer-reviewed scientific journal during the course of the study, or have been the result of international collaboration. Where there has been collaborative work, I have explicitly identified my contribution to that work in the chapter.

##### 1.4.1 *Chapters 2 and 3*

Chapter 2 is a comprehensive review of ice core science from the initial scientific experiments to the present-day state-of-the-art techniques. In particular, the chapter focuses on the development of ice core records and the relevant age-depth reconstructions. Within this literature review, the initial mathematical relationships used to reconstruct temperature, annual snowfall, compaction of annual layers and ultimately the age-depth profile are introduced. Chapter 3 then goes on to outline the novel methods used in the chemical analysis and numerical modelling of ice cores in this thesis.

##### 1.4.2 *Chapter 4*

Results of this study are presented from Chapter 4 onwards; Chapter 4 is a synthesis of all modelling combinations used in reconstructing temperature, accumulation, compaction of

annual layers, and age-depth profiles for the Fletcher Promontory ice core record. The reconstructions use stable water isotope data obtained externally to this study, and pRES measurements provided by Jonathan Kingslake. The reconstructions use techniques previously employed in existing age-depth profiles (Chapter 2) as well as the novel techniques (Chapter 3) developed during this study. Reconstructions using the same methods for the Berkner Island and James Ross Island ice core records are presented in Appendix 1. The decision to present only FP modelling results was due to the additional modelling approaches developed using data only available for the FP ice core. BI and JRI results were presented in Appendix 1 as the application of the modelling approaches to each ice core resulted in the same differences between model results due to the model development.

### 1.4.3 Chapter 5

Chapter 5 outlines the results of the novel application of ultra-violet laser ablation inductively-coupled plasma mass spectrometry (hereafter LA ICP-MS) on frozen samples from Berkner Island. The chapter is constituted by the manuscript that has been peer-reviewed and published in *Antarctic Science*. The article is the product of international collaboration with colleagues from the Climate Change Institute (CCI), University of Maine, and was funded by an *Antarctic Science* bursary in 2014. The author contributions are as follows: Ashleigh Massam prepared all samples of ice for analysis; furthered the development of the discrete sampling technique and contributed to discrete sampling work at BAS; assisted the LA ICP-MS analysis at the University of Maine; designed and wrote the annual layer thickness model; and wrote the manuscript. Geoff Lee contributed to the discrete sampling work at BAS; Sharon Sneed conducted the analysis of the ice samples using LA ICP-MS at University of Maine assisted by me; Rebecca Tuckwell assisted in the ion chromatography (IC) analysis of discrete samples assisted by me; Robert Mulvaney assisted in the design of the analysis, model and manuscript; Paul A. Mayewski developed the concept and approach of the LA ICP-MS system at the CCI; facilitated collaboration between BAS and CCI; Pippa Whitehouse assisted in the design of the analysis, model and manuscript. Some additional work that was not published is also presented at the end of this chapter, supplementary to the manuscript. The supplementary results provide information on the age-depth model, observational data and parameters that were used to model the ice core. Additionally, statistical assessment of the annual layer thickness data and the modelling approaches (introduced in Chapter 4 and Appendix 1) are included.

#### 1.4.4 *Chapters 6 and 7*

Chapter 6 presents the optimised profiles of accumulation, thinning, and hence annual layer thickness and age-depth, reconstructed for the ice cores retrieved from Fletcher Promontory and Berkner Island. The Berkner Island ice core record is constrained using known-age horizons and the annual layer thickness measurements described in Chapter 5. The FP record is constrained using known-age horizons and annual layer thickness measurements presented in Chapter 6. The annual layer thicknesses measured as part of this study are supplemented by additional stable water isotope data retrieved through a project separate to this study by Amy Pike.

Chapter 7 makes use of new high resolution chemistry data from JRI, measured by collaborators at the Desert Research Institute (DRI), Nevada, US, which allows layer counting of the JRI core to a greater depth than hitherto, and synchronisation to the well dated US WAIS core via volcanic horizons, and peaks in heavy metals. The JRI ice core was re-analysed at the DRI at a high resolution so that annual layers are resolved to 300 metres below the surface. The re-analysis of the ice core and the annual layer counting to 300 m was completed by colleagues, Monica Arienzo and Joe McConnell at DRI and Nerilie Abram at the Australian National University (ANU). The remainder (i.e. deeper than 300 m) of the JRI age-depth profile is constructed using the methods described in Chapter 6.

#### 1.4.5 *Chapter 8*

One objective of the study is to use borehole temperature profiles to provide an independent reconstruction of surface temperature. Borehole temperature measurements are provided by Rob Mulvaney and obtained prior to this study. Chapter 8 presents the results of this avenue of research, and was completed with the additional supervision of Carlos Martin at BAS.

#### 1.4.6 *Chapter 9*

Chapter 9 summarises and discusses the results of this study with a view to addressing the objectives listed in section 1.2.1. Particularly, the results of the study are used to interpret information on the modelling techniques developed and applied to the FP, BI, and JRI ice cores. Additionally, it discusses how the ice core and borehole temperature reconstructions presented in this study provide a context for the regional climate history of the AP and

Weddell Sea region. Finally, the outcomes of this research study are summarised alongside suggestions for future work.

Through nine chapters, this study will seek to address the five objectives introduced in section 1.2.1 in order to explore the variations in the relationships used to reconstruct ice-core profiles. In doing this, the optimal dating strategies for the three ice cores from the AP and Weddell Sea region will be presented.



## Chapter 2: A review of Polar Ice Core Research

### 2.1 Introduction

A key branch of palaeoclimate research involves the interpretation of data available in ice cores. The continuous records preserved in a polar ice sheet provide a record that can span multiple glacial cycles. Since the initial analysis of polar ice over 80 years ago (Sorge, 1935), there has been substantial development of drilling techniques, analysis and interpretation of the records preserved within the polar ice sheets. This chapter reviews polar ice core research and evaluates the latest analytical and modelling techniques for ice core interpretation.

### 2.2 Developments in Ice Core Research

The first attempts to understand the interior of an ice sheet employed shallow pits and cores in the Polar Regions (Sorge, 1935; Langway, 2008) but these yielded low quality ice, limiting the chemical analysis that could be carried out. It took until the 1950s to make further progress, with ice-core drill seasons in Greenland and Antarctica throughout the decade; between 1949 and 1952 a Norwegian-British-Swedish expedition drilled a 100 m ice core in Queen Maud Land, Antarctica (Swithinbank, 1957; Schytt, 1958). Further drilling was completed at Taku Glacier, Alaska, and two boreholes > 125 m long were drilled at Camp VI and Station Central, Greenland (Miller, 1954; Heuberger, 1954).

Throughout the 1960s and 1970s, five main nations focussed on the development of ice core drilling: Denmark, Switzerland, the US, the USSR, and France (Jouzel, 2013). The first deep ice core drilling was carried out by the US Army Cold Regions Research and Engineering Laboratory (CRREL) at Camp Century on the Greenland ice sheet (GrIS) (fig. 2.01), reaching the bed of the ice sheet at 1388 m in 1966 (Hansen and Langway, 1966; Dansgaard, 1969). The CRREL drill was then transferred to Antarctica, and in 1968 a 2160 m core to bedrock was recovered at Byrd Station in West Antarctica (Ueda and Garfield, 1969). Drilling in the north continued with the Greenland Ice Sheet Project (GISP - an international collaboration between the US, Denmark and Switzerland), which drilled several intermediate depth cores, and a 2038m core to the bedrock at Dye 3 in 1981 (Dansgaard, 1982). Chemical analysis of the composition of these deep ice cores revealed key climatic variations covering the last glacial period and the glacial-Holocene transition, and provided insight into the relationships between climate and oceanic processes (Oeschger, 1985). In 1988, a short ice core was

retrieved from Renland in East Greenland (fig. 2.01). Despite reaching bedrock at a depth of 324.35 m, the ice core record spans a full glacial cycle from the Holocene into the Eemian interglacial (LIG – the last interglacial) (Hansson, 1994). The success of deep ice core drilling on the GrIS led to the development of international collaboration between the US and European ice core teams and as a result, two new deep ice cores were drilled. A European-led project, the GRenland Ice core Project (GRIP), reached bedrock at 3028.8 m in 1992 with the support of the European Science Foundation (ESF) comprising of Belgium, Denmark, France, Germany, Iceland, Italy, Switzerland and the UK, while an American-led project, GISP2, reached bedrock at 3054 m a year later in 1993. Both ice cores reached the bed of the ice sheet, and yielded an ice core record of the LIG. However, disturbances to the flow of ice at an age greater than 110 ka BP limit the ice-core profiles of the LIG. The relatively high accumulation rate and surface temperature (compared to central Antarctica), the great depth of the ice and the geothermal heat flux combined to cause melting at the bed of the ice sheet which removed older ice. The failure to recover ice older than the last interglacial period (the Eemian) prompted further drilling of deep ice cores between 1999 and 2003 at North GRIP (NGRIP), 200 km north of the GRIP drill site, and during 2007-2011 at the North Greenland Eemian (NEEM) site. As a result, the oldest-dated Greenland ice core from NEEM now extends back to 128.5 ka BP (NEEM, 2013).



Figure 2.01: Map of ice core sites across Greenland mentioned in the text.

Development of deep ice core drilling in Antarctica came as a result of the success of the northern hemispheric attempts. The low accumulation rates across central Antarctica allow ice core records to extend further back in time than those from Greenland, producing climate profiles spanning multiple glacial-

interglacial cycles was drilled over a twelve-year period at the Vostok site by the Leningrad Mining Institute (fig. 2.02). This ice core ultimately reached 3623 m - spanning 420 kyr - after several attempts where drills were lost, and it ended close to sub-glacial Lake Vostok (Petit et al., 1999). The success at Vostok was eventually credited as an international collaboration, with support given by the US and France.

European collaboration continued following on from the success of GRIP and NGRIP, forming the European Project for Ice Coring in Antarctica (EPICA), consisting of GRIP members in addition to teams from the Netherlands, Norway and Sweden (Jouzel, 2013). Two sites of very low accumulation were chosen for deep drilling, producing the EPICA Dome C (EDC) and EPICA Dronning Maud Land (EDML) ice cores. Drilling finished in warm ice close to the bed at Dome C in 2005, at a depth of 3260 m, providing climate records spanning eight previous glacial cycles estimated to cover the last 800,000 years (Schwander et al., 2001; EPICA, 2004; Jouzel et al., 2007; Parrenin et al., 2007a). The second EPICA team successfully drilled the EDML ice core during a field season in 2005-2006, stopping short of the bedrock due to the ingress of sub-glacial water into the borehole at 2760 m. Current age-depth profiles estimate the climate record to span 150 ka BP (Ruth et al., 2007). Since these large-scale international collaborations, other efforts in deep ice coring have yielded climate records spanning more than 330 kyr at Dome Fuji (Japan) (Watanabe et al., 2003), and a 68 kyr record from the 3404 m-deep West Antarctic Ice Sheet (WAIS) Divide ice core (USA) (Buizert et al., 2015), as well as the joint British-French ice cores used within this research project at James Ross Island (JRI), Fletcher Promontory (FP), and Berkner Island (BI) (Mulvaney et al., 2002; Mulvaney et al., 2007; Mulvaney et al., 2012; Mulvaney et al., 2014).

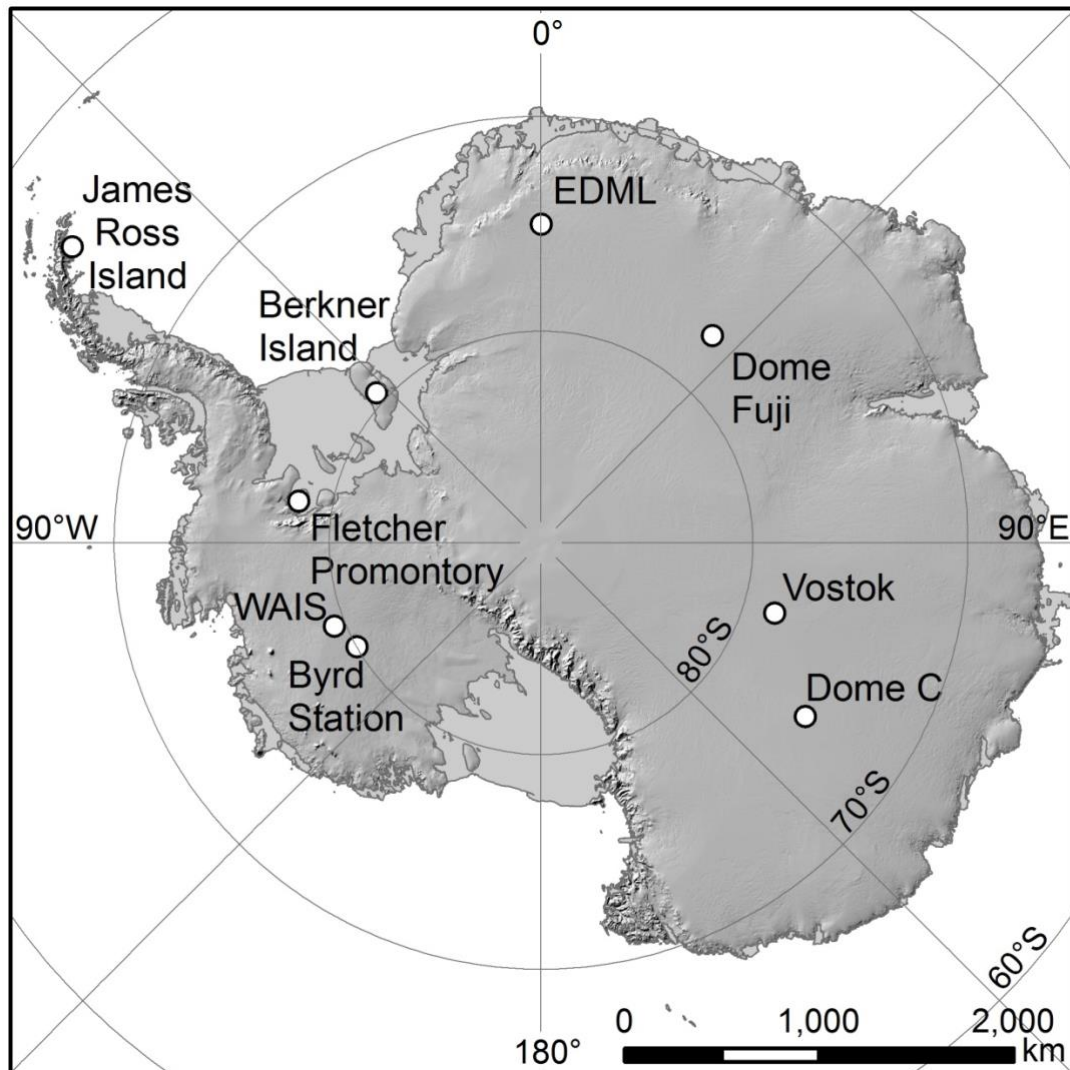


Figure 2.02: Map of ice core sites across Antarctica mentioned in the text.

### 2.3 Records of Climate

Characteristics of the climate and atmosphere above an ice sheet are recorded by the snowfall deposited on the surface. There is information available in the trace-element chemistry deposited on the snow surface, the gas bubbles occluded within the ice matrix, and the stable water isotopes that make up precipitation. High-resolution analysis of these chemical and gas records provides a clear and thorough reconstruction of past climate. The records reflect climatic changes on local, regional, and hemispheric scales. The following section will outline the main records made available to palaeoclimate research from ice cores, and the key processes and events that can be reconstructed by ice- and gas-phase proxies.

### 2.3.1 Stable Water Isotopes

#### 2.3.1.1 Stable Water Isotopes and Precipitation

First recognised by Dansgaard (1964), the potential of ice core records to record climate is dependent on the continuous accumulation of snowfall. Water masses, such as the oceans, have a nearly uniform isotopic composition of stable water isotopes, HDO, H<sub>2</sub><sup>18</sup>O, and H<sub>2</sub><sup>16</sup>O. Equilibrium fractionation, the closed-circuit evaporation and condensation cycle of water, follows a well-observed path in which heavier isotopic components evaporate less rapidly, and condense more readily from atmospheric water vapour, thus providing a proxy to reconstruct the natural cycles of precipitation in a continuous record (Paterson, 1981). The deviation,  $\delta$ , of the relative concentrations of stable water isotopes deposited at a site,  $R_S$ , are measured in parts per thousand (‰) relative to  $R_{SMOW}$ , the “standard mean ocean water” concentration, using the following relationship:

$$\delta = \frac{10^3(R_S - R_{SMOW})}{R_{SMOW}} \quad (2.01)$$

The principle of ice core interpretation rests on the assumption that there is a linear relationship between the isotopic composition of precipitation,  $\delta$ , and surface temperature,  $T_s$ . A trend between stable water isotopes and temperature was first observed on a global scale as part of a study commenced by the International Atomic Energy Agency and the World Meteorological Organisation (IAEA-WMO) (Dansgaard, 1953; 1964). A linear slope defining the relationship between isotopic composition values,  $\delta^{18}\text{O}$  (the deviation of the ratio of <sup>18</sup>O and <sup>16</sup>O in precipitation relative to the ratio in mean ocean water), and  $T_s$ , at a gradient of 0.67‰/K for Greenland sites and 0.76‰/K in Antarctica, was recognised to be the product of fractionation processes as water vapour travels from its source to the final precipitation site (Johnsen *et al.*, 1989).

#### 2.3.1.2 Deuterium Excess

The  $\delta^{18}\text{O}/T_s$  slope does not always hold because irreversible fractionation processes, which happen outside of the closed-circuit cycle, can alter the distribution of water isotopes (Jouzel & Merlivat, 1984). In contrast to  $\delta^{18}\text{O}$ , the ratio of stable hydrogen isotopes ( $\delta\text{D}$ ) remains largely unchanged by external phenomena and provides a more accurate representation of how precipitation varies with time. Following the principle that oceans, the major source of atmospheric water vapour, have nearly uniform isotopic composition, it can be assumed that  $\delta^{18}\text{O}$  and  $\delta\text{D}$  follow the meteoric water line (MWL) (Craig, 1961;

Merlivat & Jouzel, 1979; Paterson, 1961; Petit *et al.*, 1991); a linear relationship between  $\delta^{18}\text{O}$  and  $\delta\text{D}$  that holds on a global scale. Deviations from this relationship, referred to as the deuterium excess,  $d$ , can be used to determine variations in vapour source conditions of precipitation:

$$d = \delta\text{D} - 8 \cdot \delta^{18}\text{O} \quad (2.02)$$

Deuterium excess reflects external phenomena that affect the kinetic fractionation of  $\delta^{18}\text{O}$ , including wind effects and humidity (Jouzel *et al.*, 1982; Masson-Delmotte *et al.*, 2008). Humidity is related to the original source of vapour moisture in the air mass. As wind speed and humidity in the vapour source region can modify kinetic fractionation, the deuterium excess can be used as a proxy for the local wind and humidity conditions, as well as surface temperature in the source region (Jouzel *et al.*, 1982; Masson-Delmotte *et al.*, 2008).

### 2.3.2 Chemical records in ice cores

The deposition of chemical species on the ice sheet surface leads to a preserved record of local and regional source abundance and transport processes in the ice-phase of an ice core. The broad-ranging chemical profiles are found at sites in close proximity to the coast provide a clear record of sea-ice chemical proxies as well as atmospheric species. Common chemical components measured in ice include the cations sodium ( $\text{Na}^+$ ), magnesium ( $\text{Mg}^{2+}$ ), calcium ( $\text{Ca}^{2+}$ ), ammonium ( $\text{NH}_4^+$ ) and potassium ( $\text{K}^+$ ) and the anions chloride ( $\text{Cl}^-$ ), sulphate ( $\text{SO}_4^{2-}$ ), methansulphonate ( $\text{MSA}^-$ ), nitrate ( $\text{NO}_3^-$ ), and fluoride ( $\text{F}^-$ ), together with compounds such as hydrogen peroxide ( $\text{H}_2\text{O}_2$ ) and a wide range of ultra-trace elements including heavy metals, rare earth elements and black carbon. Chemical species are deposited continuously throughout a year either in precipitation or by dry deposition on the ice surface, but with variations in deposition inter-annually and seasonally. Analysis of these variations therefore reveals climate information depending on the source and pathway of the trace chemistry. For example, annual changes in sea-ice extent result in fluctuations in the deposition of chemical species present in sea-salt brine, such as sodium and chloride, in addition to the atmospheric oxidation product of dimethylsulphide (DMS), MSA (Sommer *et al.*, 2000; Rothlisberger *et al.*, 2003; Abram *et al.*, 2013). The annual advance and subsequent retreat of sea ice around the Antarctic continent leads to an increased deposition of chemical species originating from the oceans, peaking during the season of minimum sea ice extent (austral summer) (Curran *et al.*, 2003). Atmospheric production of nitrate species,  $\text{NO}_x$ , and sulphate, along with other atmosphere-borne species linked to insoluble dust, magnesium,

and calcium, are closely linked to sub-annual to multi-annual climate variability (Steffensen, 1997; Wagenbach et al., 1998; Rothlisberger et al., 2000a). In addition to the source production and transport information preserved in the seasonal deposition of these trace-chemical aerosols, the seasonal fluctuations provide a signal that can be counted annually as a method of dating the ice cores (fig. 2.03) (Fuhrer et al., 1999; Rothlisberger et al., 2000a; Curran et al., 2003). High-resolution analysis can be used to identify annual layers in an ice core and thus interpret annual accumulation (Sommer et al., 2000). An example of a chemical compound measured in the ice cores with a strong seasonal cycle is hydrogen peroxide, which provides one of the clearest signal for measuring and counting annual layers in the upper layers of an ice core. The origin of the seasonal cycle is the photolytic production of the hydrogen peroxide molecule which relies on the presence of sunlight, and is not locally produced in the total darkness during polar winter (Neftel et al., 1995). However, the signal tends to damp away with depth in the core as hydrogen peroxide is destroyed, probably by catalytic reactions in the ice. Table 2.01 and Fig 2.03a give other examples of trace-chemical species measured in an ice core, their source of production, and the timing of the annual peak in production and deposition. Included in figure 2.03(a) is a physical measurement of electrical conductivity (ECM – Electrical Conductivity Measurement) which also shows a clear seasonal cycle, and is related to the bulk acidity of the ice, which largely corresponds to the acidic sulphate, nitrate and methane sulphonate components, which are all predominantly deposited in the summer. Fig. 2.03b supplements fig. 2.03a, demonstrating sub-annual records in the B32 ice core, a shallow ice core drilled close to the deep EDML core (Sommer et al., 2000). The figure shows the additional trace species,  $\text{NH}_4$ ,  $\text{Ca}^{2+}$ ,  $\text{Na}^+$ , that are deposited inter-annually, and non-sea-salt conductivity, which can be used to identify four volcanic horizons over the period 1255-1293 AD.

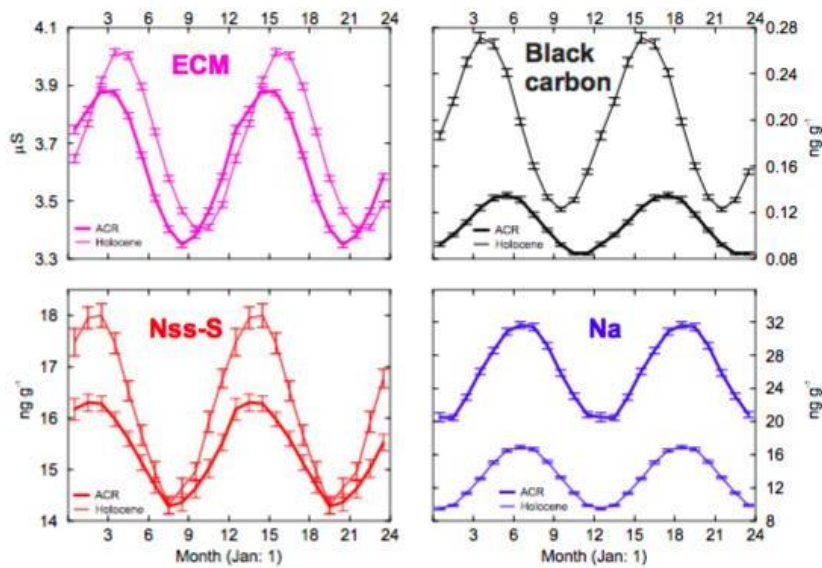


Figure 2.03(a): Seasonal variation in the chemistry of ice over a 48-month cycle at WAIS Divide ice core site: pink: electrical conductivity measurements (ECM); black: black carbon (BC); red: non-sea-salt Sulphur (nss-S); blue: Sodium (Na). The signal shown in a bold line presents the mean cycle during the Antarctic Cold Reversal (ACR), whilst the thin line is the mean Holocene signal. Figure taken from Sigl et al., 2015.

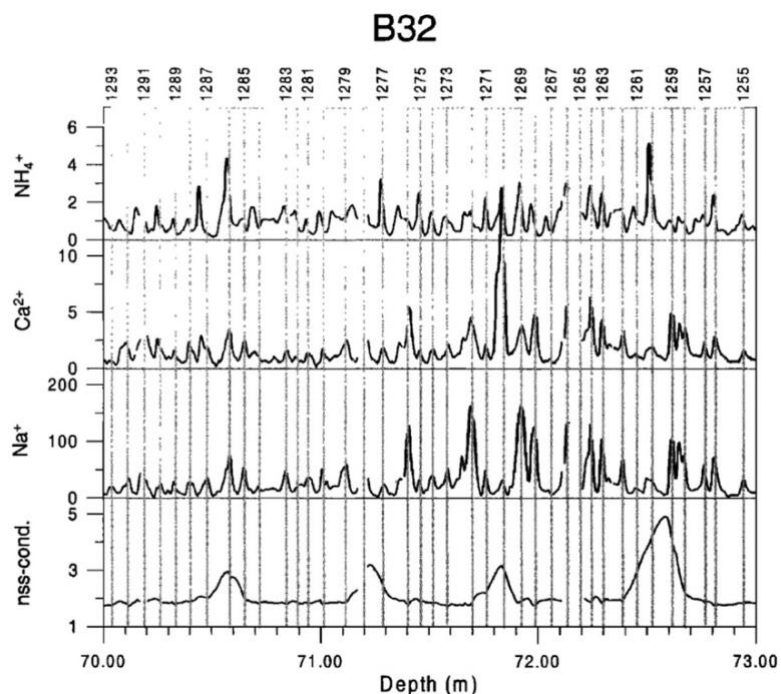


Figure 2.03(b): Example of annual layer counting using three aerosol components in parts per billion (ppb) (Sodium, Calcium, and Ammonium), and non-sea-salt conductivity measurement in the B32 ice core, Antarctica, across a 3 m section covering 1255 - 1293 AD (Sommer et al., 2000).

*Table 2.01: A list of trace chemical species, the source of each species before deposition in the ice sheet, and the approximate timing of the annual peak in concentration. Mg and Ca records occur bi-annually dependent on the component measured (dust or salt).*

<b>Chemical Species</b>	<b>Source</b>	<b>Timing of peak production</b>
Na	Sea salt aerosols	Winter
Ca	Insoluble dust and sea salt	Summer (dust), winter (salt)
Mg	Dust and sea salt	Summer (dust), winter (salt)
MSA <sup>-</sup>	Oxidation of biogenic DMS	Summer
Cl <sup>-</sup>	Sea salt aerosols	Winter
NO <sub>3</sub> <sup>-</sup>	Atmospheric production	Summer
SO <sub>4</sub> <sup>2-</sup>	Sea salt aerosols and biogenic DMS	Summer
H <sub>2</sub> O <sub>2</sub>	Photolytic production in atmosphere	Summer

### 2.3.3 Gas-phase ice-core records

In addition to the chemicals that make up the composition of ice, gas bubbles that are occluded within the ice matrix yield further proxies for climate reconstruction. Principally, carbon dioxide, CO<sub>2</sub>, methane, CH<sub>4</sub>, and nitrous oxide, N<sub>2</sub>O, are closely linked with temperature records (Barnola et al., 1987), and hence can be used to interpret the past climate history over the long glacial-interglacial time periods preserved in deep ice cores (Luthi et al., 2008). Atmospheric gas concentrations are globally mixed, and the concentrations preserved in the ice core are a direct measurement of past gas concentrations. As a result, ice core records can be used as a tool to extend back the record of directly-measured gas concentrations prior to 1956, when atmospheric measurements of CO<sub>2</sub> became routine, demonstrating that CO<sub>2</sub> concentrations have increased by 40% since 1800 AD (fig. 2.04).

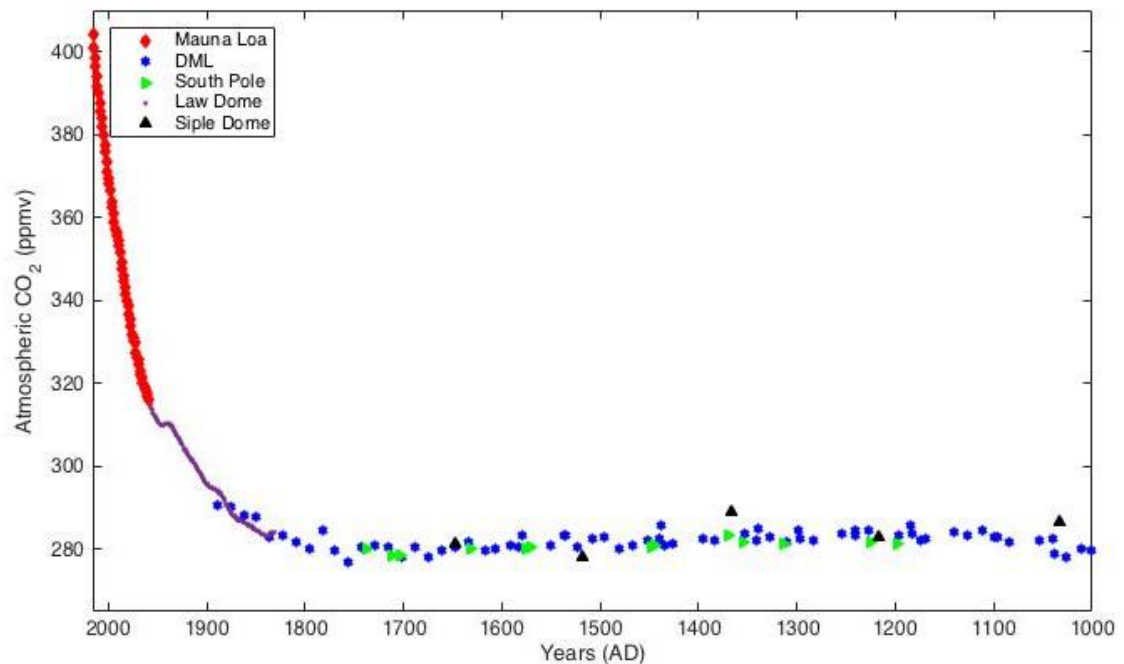


Figure 2.04: 1000-2016 AD record of atmospheric CO<sub>2</sub> concentrations from ice core records and Mauna Loa Observatory. Data has been obtained from [www.pangaea.de](http://www.pangaea.de) (Ahn, 2003; Siegenthaler et al., 2005; Etheridge, 2016; Tans, 2016).

In order to interpret the gas-phase records alongside ice-phase records, it is necessary to understand the processes that occur in the upper 80-100 m of an ice core. The weight of subsequent years of snowfall increases the vertical strain within the ice sheet, and leads to the compaction of the snowpack at the surface, which in turn leads to an increased density with depth. This process of increasing density, hereafter referred to as densification, continues until the snowpack is compacted and has the density of ice of  $\sim 0.917 \text{ Mg m}^{-3}$ . Until the snowpack densifies significantly, gas bubbles are free to move throughout the snowpack. The gas bubbles follow the physical laws of gravitational fractionation, where the heavier gases move downwards before being trapped within an ice matrix. The densification processes are explained in more detail in section 2.6. However, it is important to understand here that as the upper 80-100 m (the firn) is undergoing a snow-to-ice transition, present-day gas concentrations are trapped in ice of an older age, at a greater depth in the ice core. The age offset between the gas bubbles and the surrounding ice matrix, hereafter referred to as the  $\Delta$ age, must be reconstructed to accurately interpret both the gas- and ice-phase records.

#### 2.3.4 Millennial-scale variability

One of the main motivations for deep ice core drilling in the Antarctic is the chance to recover long-term climate records from the deep ice sheets. Low annual accumulation over the Antarctic Ice Sheet (AIS), coupled with the large ice sheet thickness, preserves the longest temporal records in the ice. The current longest record spans eight glacial cycles at EDC (EPICA, 2004). Comparison of climate and atmospheric conditions interpreted from long Antarctic ice-core records demonstrates the interplay between different climate relationships on a local, regional, and global scale. Local climate can be interpreted from the chemical ions deposited in the ice sheet from the nearby surroundings, as outlined in section 2.3.2. Regional and global climate can be interpreted through the comparison of multiple ice-core records. Fig. 2.05 compiles surface temperature reconstructions, measured stable water isotope profiles, and methane concentrations for four Antarctic ice cores. The ice cores have been obtained from sites across the Antarctic continent (fig. 2.02). Fig. 2.05 presents two distinct types of millennial-scale climate variability: (i) Marine Isotope Stages (MIS) occur on a cycle of 10s of thousands of years, and are highlighted in grey and white bands in fig. 2.05(a-c) (odd-numbered MIS events are labelled); (ii) Antarctic Isotope Maxima (AIM) events occur on a shorter millennial-scale variability (AIM 1, 8, 12, 14, 17, 18, 19, 21 are delineated in figure 2.05(d)).

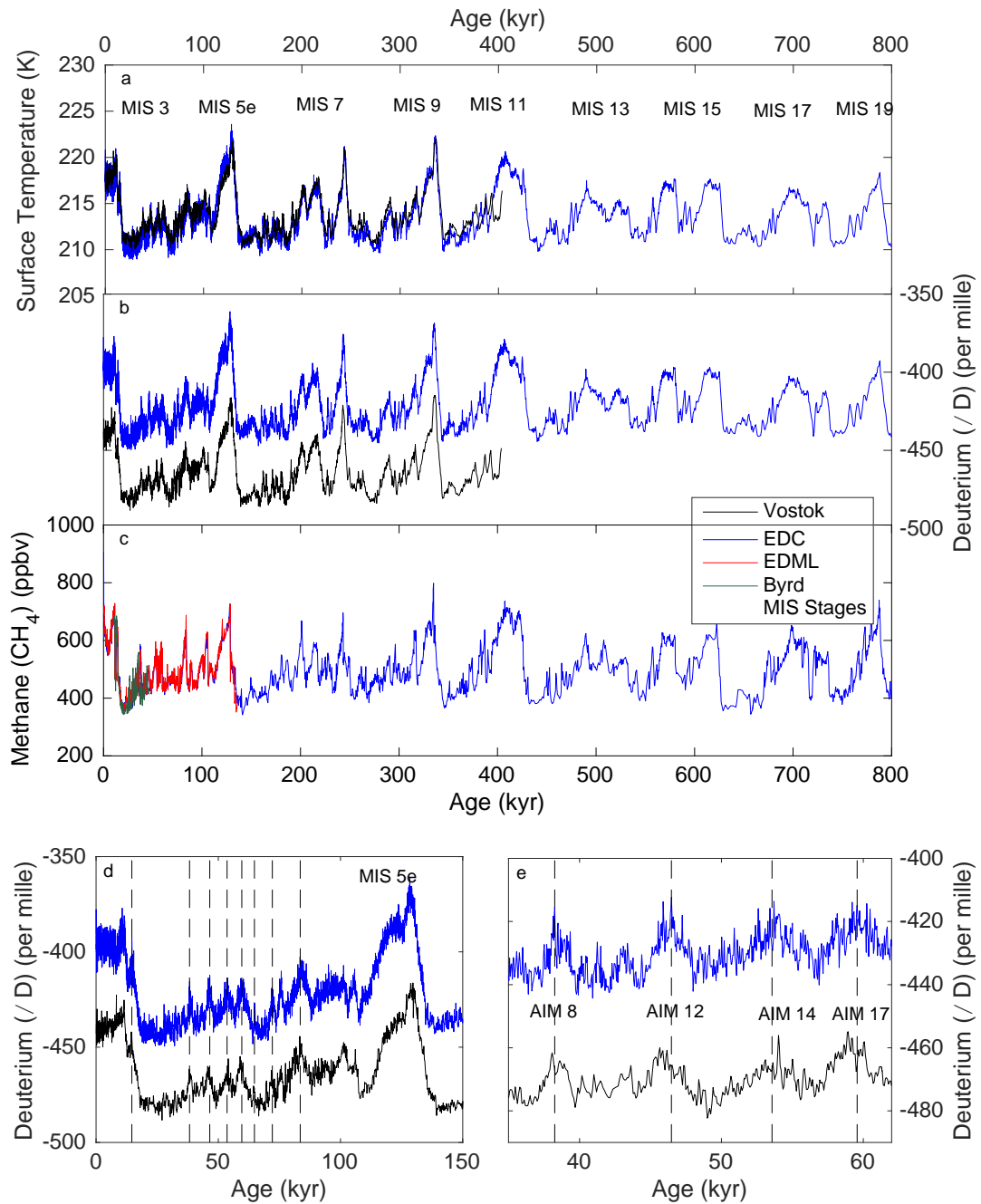


Figure 2.05: (a) Surface temperature reconstructions for the EDC and Vostok ice cores on a common timescale; (b) Stable water isotope profile for EDC and Vostok ice cores on a common timescale; (c) Methane profiles for the EDC, EDML, and Byrd ice cores on a common timescale. Odd-numbered Marine Isotope Stages (interglacials) are highlighted in grey and labelled in plot (a). Panels (d) and (e) are zoom-in plots of the stable water isotope profiles of EDC and Vostok (the pink highlighted section of plot (b), and the grey highlighted panel in plot (d), respectively). MIS 5e is highlighted as a grey band and labelled. Antarctic Isotope Maxima events are delineated by black dashed lines and labelled in plot (e).

Marine Isotope Stages (MIS) are globally synchronous events identified in the isotopic signatures of terrestrial and marine cores. The events alternate between warm and cold periods, interpreted as interglacial and glacial periods, and have been identified throughout the 5.3 million-year (Myr) record presented by Lisecki and Raymo (2005). Across the most recent 850 kyr, MIS events occur on a glacial-interglacial cycle of  $\sim 100$  kyr, in line with the periodicity of Earth's eccentricity based on the Milankovitch cycles (Imbrie and Imbrie, 1980; Imbrie et al., 1992). During an MIS event of the last 800 kyr, glacial periods typically last 70-90 kyr with end-member interglacial periods lasting 10-30 kyr. During the interglacial period (an odd-numbered MIS event), variations in surface temperature and atmospheric carbon concentrations occur synchronously as shown by increases in surface temperature, increases in stable water isotope concentrations, and increases in atmospheric carbon concentrations in ice-core records (fig. 2.05). MIS events are identified in records spatially distributed across Earth, and occur synchronously. Fig. 2.06 is taken from Wolff et al. (2010) and presents the millennial-scale variability in the NGRIP ice core from present-day, the last glacial period and extending into the LIG at 123 ka BP. Marine Isotope Stages (MIS) are indicated on the figure, with Greenland Interstadials (GI) numbered.

In addition to the globally-synchronous millennial-scale variability, a series of shorter millennial-scale climate events are evident in Antarctic ice core records. Ice core isotopic records indicate a cycle of warm interstadial periods throughout the last glacial period, and cyclical greenhouse gas records appear to be tied to the temperature trends of previous glacial and interglacial periods (fig. 2.05 and 2.06). 25 Greenland Interstadials (GI) (also referred to as Dansgaard-Oeschger (DO) events) punctuate the last glacial period as warming events and labelled in fig. 2.06. These climate events occur on a  $\sim 1500$  year periodicity and are characterized by 10-30 years of rapid warming followed by a slower period of cooling to original glacial conditions. Evidence of DO events is found in ice and marine cores in the northern hemisphere. The DO climate event leaves a signature of surface temperature warming in an ice-core stable water-isotope record. Alternatively, DO events are identified in marine-sediment cores by ice-rafted debris (IRD) released from the Laurentide Ice Sheet (LIS) as a result of the warming event. In the southern hemisphere, the climate is in antiphase with the northern hemispheric interstadials; the bipolar see-saw is a delay in the southern hemispheric response to climate forcing originating from the northern hemisphere (Severinghaus, 2009). The AIM events are in response to northern hemispheric DO events, and are identified in an out-of-phase chronology to the DO events as they are the effect of a

slowed-down transport of heat from the ocean circulation that has been affected by the initial pulse of freshwater from the LIS.

Fig. 2.05(d-e) are two plots of increasing resolution of stable water isotope profiles of Antarctic ice cores over the most recent 150 kyr; AIM events are delineated for comparison between ice core records. The signature of the AIM events is synchronous across the Antarctic continent. Isochronous events across the Antarctic continent are useful age horizons to synchronize ice-core age-depth profiles.

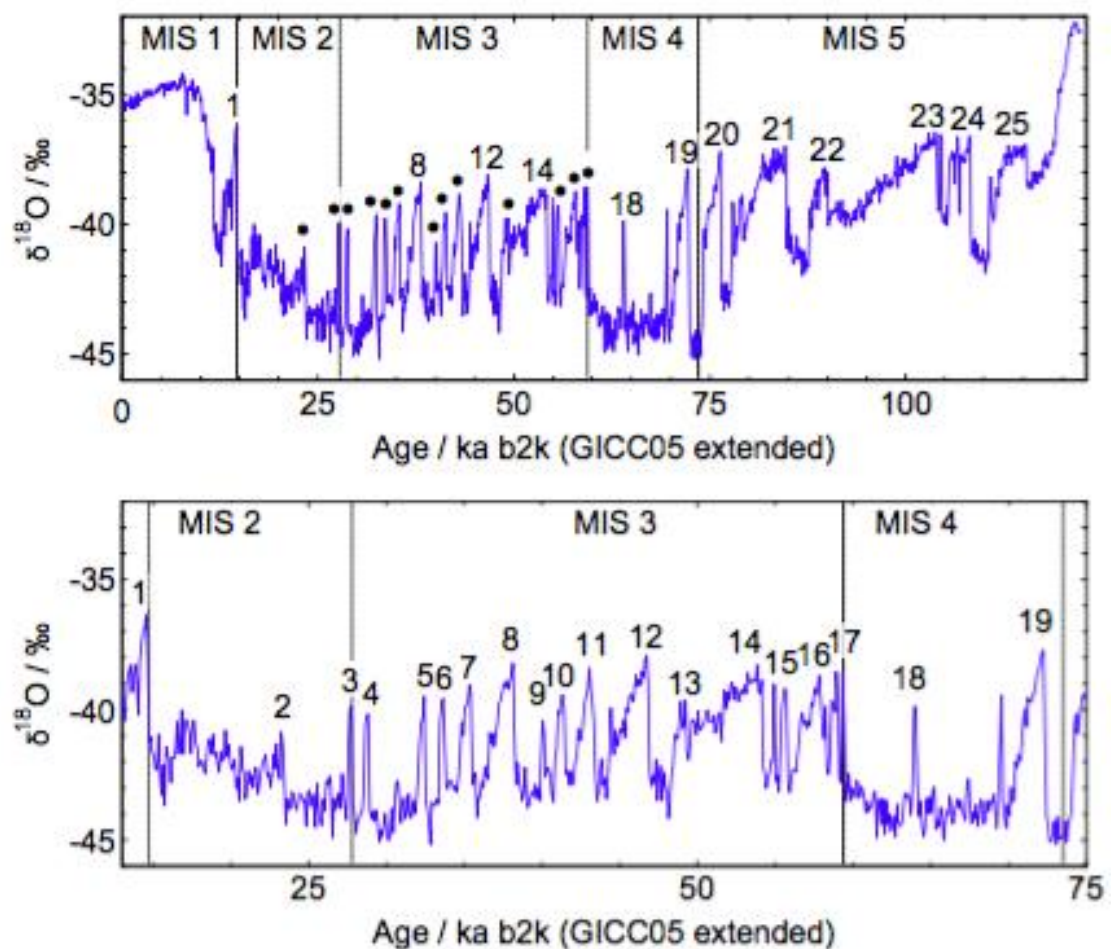


Figure 2.06: The figure is taken from Wolff et al. (2010) presents the Dansgaard-Oeschger events in the NGRIP ice core, Greenland. Top: From the present back to 123,000 years ago; bottom: Marine Isotope Stage (MIS) 2-4. The oxygen-isotope data (NGRIP Members, 2004) has been smoothed to 100-year average, and is presented here on the GICC05 age scale back to 60 ka BP (Svensson et al., 2008), and before that on the ss09sea modelled age scale (Johnsen et al., 2001) shifted (by -705 years) to

*match GICC05 at 60 ka. The numbers denote the standard notation for Greenland Interstadials (GI), with dots marking each intermediate numbered event in the top plot.*

The signatures are easily-identified in high-resolution stable water isotope profiles and can be corroborated with additional proxies including gas measurements. Therefore, AIM events are often used in ice-core age-depth profiles based on the observed timing of the events in published chronologies.

The long-term millennial-scale variability preserved in continuous records means that one can take a broad view of climate processes and the links between atmosphere, ocean and the climate. These records are important for understanding climate processes, and predicting future responses to climate variability. In order to understand the full record preserved within the ice core, on both a sub-annual and millennial scale, it is necessary to obtain the most accurate and high-resolution ice-core record.

#### 2.4 Analysis of Ice-Core Records

In order to understand the seasonal records in shallow cores, and the highly compressed records preserved in deep ice cores, analysis must be carried out at the highest resolution available. Sub-annual resolution in deep Antarctic ice cores is particularly rare due to the low mean accumulation rates across the continent and the thinning of ice layers at depth; thus it is usually not possible to obtain a seasonal view along the full depth of an ice core. Improvements to the analytical resolution have been achieved by two approaches, namely high-resolution discrete sampling over short sections, and continuous trace-element analysis over the full core. Measuring discretely-cut samples of ice is a useful technique, though it is often associated with ice loss by the cutting process. The future development of this technique is limited by the resolution of the cutting method, the potential for ice loss during cutting, and the development of suitable analytical instruments. The highest resolution achieved thus far by this method, developed at the British Antarctic Survey, addressed the issue of ice loss from discretely-cut samples by employing a microtome device to shave the ice sample at a finite resolution and collect the sample directly off the device. The method was employed on NGRIP ice to analyse the characteristics of the DO 8 event at ~38 ka BP at 2 mm depth resolution (Thomas, 2009). A full geochemical profile outlined the dominant and passive mechanisms for the transition into DO 8 at a sub-annual resolution. The

method, though effective for high-resolution analysis on deep ice, is labour-intensive and hence it is difficult to analyse more than small sections of an ice core.

Alternatively, methods using a continuous and direct method of trace-element analysis are less labour-intensive. Continuous melting of an ice section coupled with the *in situ* analysis of trace chemical species by spectrometric techniques has achieved a spatial resolution of ~10 mm (Sigg et al., 1994; Rothlisberger et al., 2000b). This type of analysis, hereafter referred to as continuous flow analysis (CFA), also has a major advantage in that it limits the risks of contamination; the melt system only measures the inner part of a core to remove the risk of contamination from sample handling. Another benefit of the continuous flow system is its ability to provide a high-resolution, continuous profile of multiple chemical species on a common depth scale. This allows – where possible – annual layer counting, and hence the determination of the age-depth relationship of a section or the full length of an ice core, as has been achieved for the deep ice cores from Greenland (Rasmussen et al., 2006; Vinther et al., 2006; Svensson et al., 2008), and sections of the James Ross Island, WAIS Divide, EDML and Dome Fuji ice cores (Mulvaney et al., 2012; Svensson et al., 2015; Sigl et al., 2015).

The limitations of CFA lie in the resolution necessary to achieve sub-annual profiles beyond the upper sections of ice cores. In order for it to be possible to retrieve a sub-annual profile by CFA beyond the upper depths, as has been achieved for the WAIS Divide ice core and Dome Fuji, mean annual accumulation at the time of deposition must be sufficient that the thickness of an annual layer at depth is greater than the standard CFA resolution of ~10 mm. Where sub-annual resolution is possible in high mean annual accumulation sites, seasonal profiles provide insight into the sub-annual mechanisms of a climate event.

For some time, ultra-violet laser-ablation inductively-coupled plasma mass spectrometry (hereafter referred to as LA ICP-MS) has been applied to geological samples in order to improve the spatial resolution of trace-element analysis in geochemical analyses (Arrowsmith 1987; Bea, 1996). More recently, this technique of ultra-high resolution direct trace-element analysis has been independently developed in ice-core laboratories. A prototype Excimer LA ICP-MS analysis of frozen ice cores has yielded sub-annual signals of multiple trace elements with minimal damage (Reinhardt et al., 2001; Müller et al., 2011). Recent implementation of this technique has obtained an ultra-high resolution view of the onset of the current interglacial period, *circa* 11.6 ka BP, at a depth of 1677.5 m, retrieved from the GISP2 ice core archive (Mayewski, 2014). Correlation of LA ICP-MS

results on Greenland and alpine ice with other records confirms the repeatability of the method for lower resolution records (Müller et al., 2011; Mayewski et al., 2014; Sneed et al., 2015; Della Lunga et al., 2016). Sneed et al. (2015) introduced the LA ICP-MS apparatus and calibration technique at the WM Keck Laser Ice Facility at the University of Maine and confirmed the reliability of the novel method by comparing ultra-high resolution LA ICP-MS results to the lower-resolution CFA profiles of the Colle Gnifetti alpine ice core (fig. 2.06).

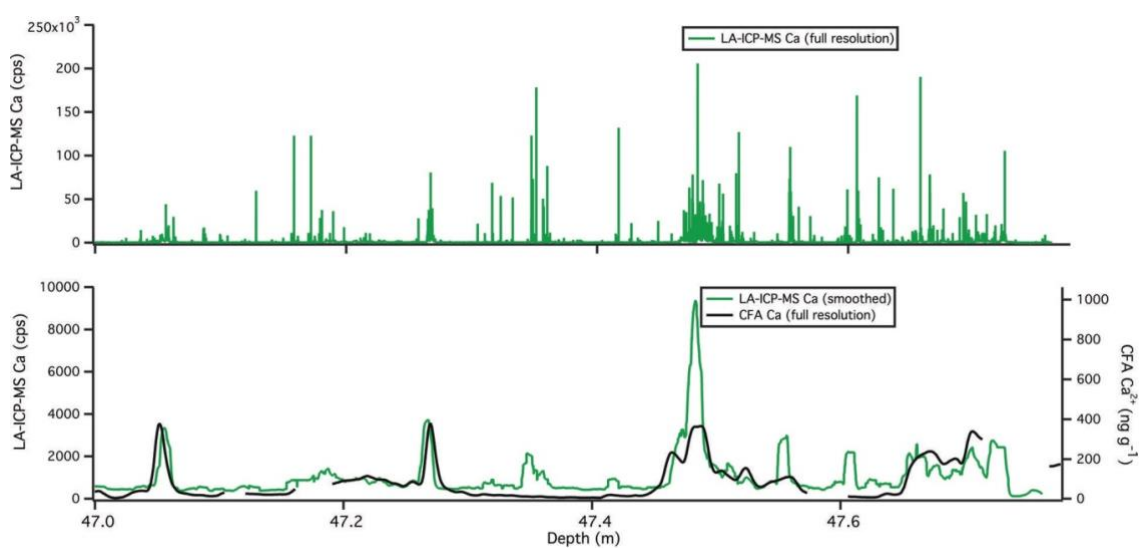


Figure 2.07: Colle Gnifetti ice core data; top: LA ICP-MS Ca full resolution record; bottom: the smoothed resolution LA ICP-MS Ca record and the CFA data for the same section of ice. Records show good agreement between the results from the two analytical techniques and confirm the reliability of LA ICP-MS (taken from Sneed 2015).

The major advantages of LA ICP-MS lie in the rapid analysis time and the non-destructive method of using an ultra-violet Excimer laser, which means the repeatability of analysis is easily afforded. Ultra-high resolution is achieved by individual line scans for each element, whilst the limited sample handling necessary before analysis limits the risk of contamination. LA ICP-MS has the potential to become a standard technique in the geochemical analysis of short sections of deep ice cores and greatly advance the interpretation of past climatic variability as well as improve ice core chronologies in the Antarctic region. However, the method has only recently been applied to Antarctic ice, and it produced variable seasonal profiles and annual layer thickness estimates that glaciological models failed to reconstruct (Haines et al., 2016).

For Antarctica, seasonal resolution ice-core analysis is often more difficult than in northern hemispheric ice cores. Low annual accumulation over the Antarctic ice sheets, and compaction and strain in the thick ice column, leads to small annual layer thicknesses in deep ice cores that are beyond the current resolution of standard laboratory methods. LA ICP-MS has not yet been applied to ice originating from earlier than the Last Glacial Maximum (LGM), or ice with predicted layer thicknesses smaller than  $3 \text{ mm yr}^{-1}$ . Further assessment of LA ICP-MS on deep Antarctic ice is therefore a useful step for the development of techniques used in the analysis of Antarctic deep ice core profiles.

### 2.5 Chronology of Ice-Core Records

Crucial to the analysis of ice core records is the construction of a precise chronology. Without accurate age-depth estimates along an ice core, it is difficult to interpret the records of past climate that are preserved in the ice, and the relationships between global processes that arise as a result of climatic variation. If the ice core drill site is in a location with limited material available for radiogenic dating, the most common practice in forming an accurate age-depth profile is to use a combination of four methods: (a) layer counting; (b) glaciological modelling; (c) identification of known-age reference markers, and (d) orbital tuning and comparison to insolation changes (Parrenin et al., 2001).

Fig. 2.08 is a flow chart that demonstrates how to construct an age-depth profile using atmospheric and ice-sheet reconstructions, and where the use of chemical profiles and observational data preserved within an ice core can constrain and improve an age-depth estimate. The chemical records preserved within ice sheets provide a continuous climate history that can be annual-layer counted when analysed at a sufficient resolution. For most Antarctic ice cores, sub-annual records do not continue deep into the ice sheet due to a low mean annual precipitation rate across the continent and the fact that standard analytical techniques only reach a maximum resolution of  $\sim 10 \text{ mm}$ . Where annual layer counting is no longer viable, a combination of the remaining three methods (b-d) must be implemented to estimate the age of ice. Typically, chemical profiles that can be interpreted from the chemical information preserved in the ice core are used as inputs to glaciological models in order to reconstruct the local atmospheric conditions and ice-sheet processes that control the reconstructions of the ice-core profile, such as past surface temperature, accumulation and ice flow.

Established methods for reconstructing temperature, accumulation and vertical thinning in an ice core are described below. Present-day mean values of parameters are noted by a superscript *theta*,  $\theta$ . In order to estimate the age-depth profile of an ice core for which the sub-annual record is beyond the resolution of current laboratory methods and precludes simple layer counting, reconstructions of past surface temperature, accumulation and vertical thinning history at the drill site, derived from the stable water isotope record, are combined to determine the vertical profile of annual layer thickness (Parrenin et al., 2007; Lemieux-Dudon et al., 2010; Bazin et al., 2012). Ultimately, the age of ice at a given depth is the sum of annual layers above it; this assumed relationship between annual layer thickness and age forms the basis of research throughout the thesis and will be described below.

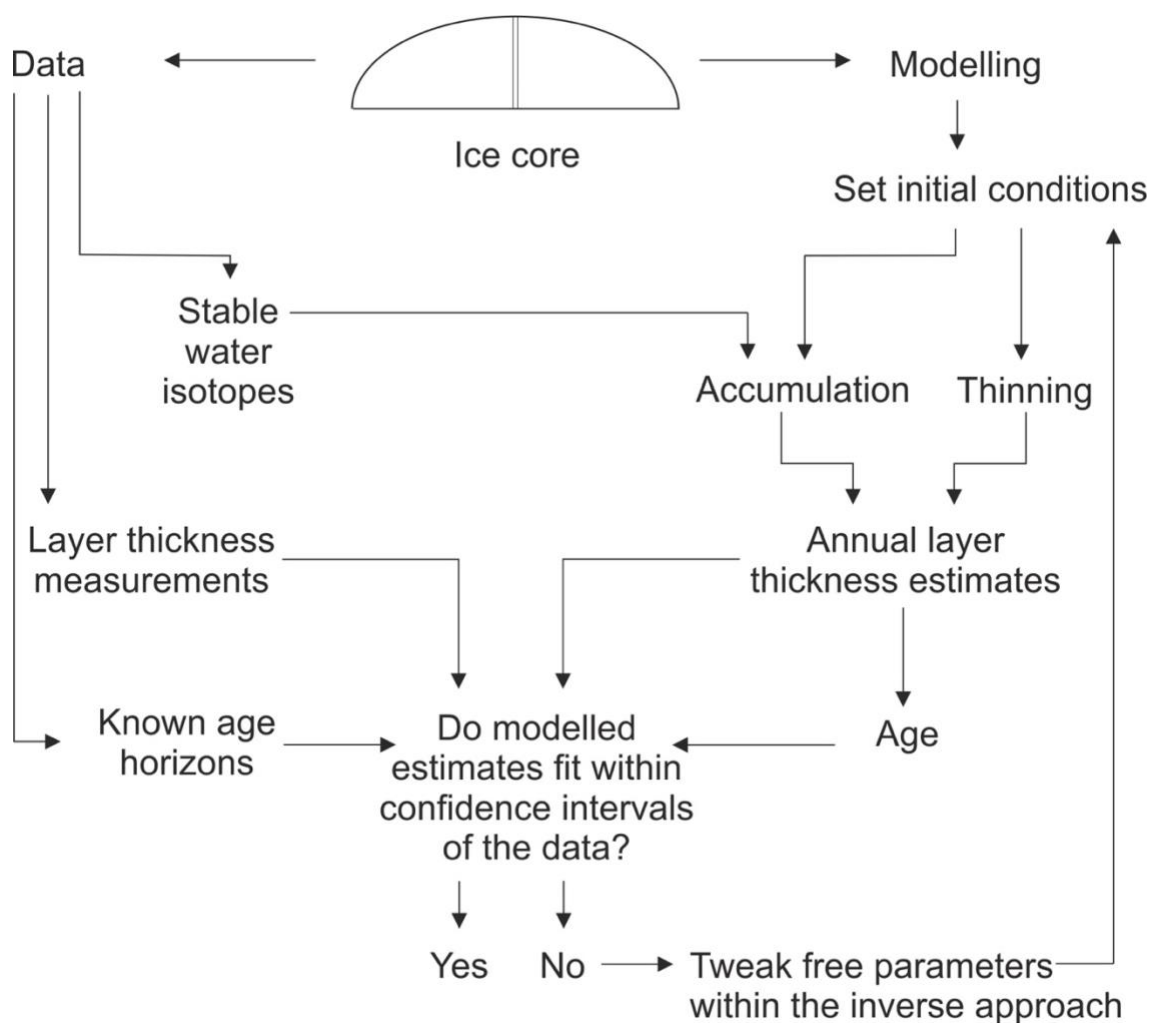


Figure 2.08: A flow chart outlining the construction of an age-depth profile and where each reconstruction or chemical measurement is incorporated.

The following section will present the mathematical relationships that have previously been used to reconstruct the past surface temperature, accumulation, thinning, annual layer thickness, and hence age-depth for an ice-core record. Following this, the section will introduce an alternative technique that can be used to reconstruct surface temperature using the temperature measurements retrieved from an ice core borehole, before introducing the inverse approaches that can be used to optimise initial profiles of accumulation and thinning.

### 2.5.1 Temperature

The MWL reflects the linear relationship between stable water isotopes (Dansgaard, 1964). Under the assumption that the concentration of stable water isotopes is principally controlled by temperature, the following approximation can be applied to isotopic datasets in order to determine an average surface temperature history, although it will be dependent on the sampling resolution of the ice core analysis.

$$T_S = T_S^{\theta} + \left[ \Delta\delta D \cdot \left( \frac{1}{-6.34} \right) \right] \quad (2.03)$$

The change in surface temperature,  $T_S$ , from present-day surface temperature,  $T_S^{\theta}$ , with depth can be deduced by analysing the deviation between present-day and measured isotopic concentrations along an ice core. For example,  $\Delta\delta D$ , the temporal difference in the deuterium/hydrogen ratio between present-day and the measured value, is multiplied by the isotope/temperature gradient of  $1/-6.34 \text{ K } \text{‰}^{-1}$  to estimate a depth-dependent anomaly in surface temperature. This gradient has been determined by linear regression of a database of values of  $\delta D$  and surface temperature from sites across Antarctica (Masson-Delmotte et al., 2008).

$T_I$ , the temperature at the inversion layer in the atmosphere, can be estimated from the reconstructed surface temperature history using eq. 2.04 (Connolley, 1996). The temperature at the inversion layer is important because one method of reconstructing past accumulation depends on this value (see section 2.5.2.2).

$$T_I = 0.63 \cdot T_S + 99.0 \quad (2.04)$$

### 2.5.2 Accumulation

The relationship between stable water isotope concentrations and surface temperature links the preserved ice core record with atmospheric processes including precipitation. Under the assumption that accumulation is controlled thermodynamically by the ability of warmer air to deliver moisture, palaeoaccumulation can be estimated by three main methods based on an exponential relationship with  $\Delta\delta D$ . As surface temperatures increase, the rate of precipitation over an ice sheet increases, and it similarly decreases with a corresponding drop in surface temperature. Using the stable water isotope profile to reconstruct a surface temperature history, past accumulation of snow at a site can be estimated using the following four relationships.

#### 2.5.2.1 Arrhenius

Kapsner et al. (1995) outlined the following method for palaeoaccumulation reconstruction, based on the thermodynamic control of accumulation by atmospheric circulation. They assumed an Arrhenius dependence where reaction rates (precipitation) are reliant on absolute temperature. In this case, the temperature profile is a reconstructed surface temperature history with respect to vertical depth of an ice core,  $T_s(z)$ .

$$A(z) \propto \exp\left(-\frac{Q}{RT_s(z)}\right) \quad (2.05)$$

Accumulation,  $A$ , is proportional to the exponential of the inverse of surface temperature, where  $Q$  is the activation energy for the reaction (estimated to be around  $60\text{kJ mol}^{-1}$ ), and  $R$  represents the gas molar constant ( $8.314\text{ J mol}^{-1}\text{ K}^{-1}$ ).

#### 2.5.2.2 Clausius-Clapeyron

A second method assumes that snow deposition is proportional to the derivative of the mean saturation vapour pressure at the inversion layer with respect to the temperature at the inversion layer in the atmosphere,  $T_i$  (K) (Parrenin et al., 2001; 2004; Schwander et al., 2001). Inversion temperature is determined through an empirical relationship (eq. 2.04) (Connolley, 1996) before accumulation is calculated using the following relationships:

$$A(x, T_i) = A^\theta \cdot \frac{f(T_i)}{f(T_i^\theta)} \quad (2.06)$$

This accounts for distance from the ice divide,  $x$ , and calculates accumulation as a function of  $T_i$ ,  $f(T_i)$ , calculated as:

$$f(T_i) = \frac{d}{dT} \left[ \frac{P_S(T)}{T_i} \right] \quad (2.07)$$

$P_S(T)$ , the saturation vapour pressure function of temperature, is calculated using an exponential relationship where  $A_S = 3.64149 \cdot 10^{12}$  Pa, and  $B_S = 6148.3$  K (two constants taken from Smithsonian tables that correspond to a best fit to the empirical curve of  $P_S$  over ice in the temperature range -60 to +20°C).

$$P_S(T) = A_S \cdot \exp^{-\frac{B_S}{T}} \quad (2.08)$$

### 2.5.2.3 Simple Exponential

The third method to be explored is based on a simple relationship that assumes an exponential dependence on the difference between the present-day deuterium value and the ice core deuterium profile, scaled by the modern accumulation rate (Ritz et al., 2001):

$$A(z) = A^0 \cdot \exp[\beta \Delta \delta D] \quad (2.09)$$

The relationship includes  $\beta$ , a parameter which represents the glacial-interglacial amplitude of accumulation changes. The parameter is calculated as part of an inverse model in existing chronologies, but can be calculated theoretically using the meteoric water line gradient for  $T_s/\delta D$ ,  $1/-6.34$  K‰<sup>-1</sup>, and the  $T_s/T_i$  relationship, 0.63 (Connolley, 1996; Parrenin et al., 2007a).

### 2.5.2.4 Global Circulation Model

A fourth technique used to estimate mean accumulation rates uses a global circulation model (GCM). A GCM is a climate model that estimates the circulation of the atmosphere and/or ocean on a planetary scale. A GCM can consider coupled atmosphere-ocean interactions (AOGCM) and can be used to estimate the evolution of sea ice and ice sheets. These models are typically used for local, regional and large-scale weather and climate

forecasting (IPCC, 2013). However, assuming that the relationships that control the circulation in the atmosphere and ocean are unchanged with time, a GCM can be constrained by observational data from ice cores in order to reconstruct the past climate on a millennial to million-year timescale (Pollard and DeConto, 2009; Sime et al., 2013; Holloway et al., 2016).

### 2.5.3 *Thinning functions*

An accumulation history can be used to estimate the mean rate of annual snowfall over a site; the total number of years recorded in an ice core profile is assumed to be the sum of annual layers preserved, however, these layers have been thinned due to the force exerted by subsequent snow deposition. Thus, the mean annual layer thickness that can be directly measured in the ice core record is a profile of the past accumulation that has decreased with depth due to increasing strain from subsequent years of annual snowfall (fig. 2.09). To estimate the impact of thinning on mean annual layer thickness, a thinning function,  $\eta(z)$ , also sometimes referred to as the shape function, must be derived and applied to an accumulation history. At a given depth, the thinning function is defined to be the ratio of the original layer thickness at the time of deposition,  $\lambda(t)$ , and the present-day layer thickness at depth  $z$ ,  $\lambda(z)$ .

Three empirical approaches to defining a thinning function – the ratio between the present-day and original annual layer thickness – are described below. A fourth approach makes use of a vertical velocity profile obtained by phase-sensitive radio-echo sounding, pRES. A thinning function is always calculated in ice equivalent depth units; this is the depth of an ice particle once the highly porous firn snow in the upper depths of a core has been converted into an ice-only volume (Herron and Langway, 1980).

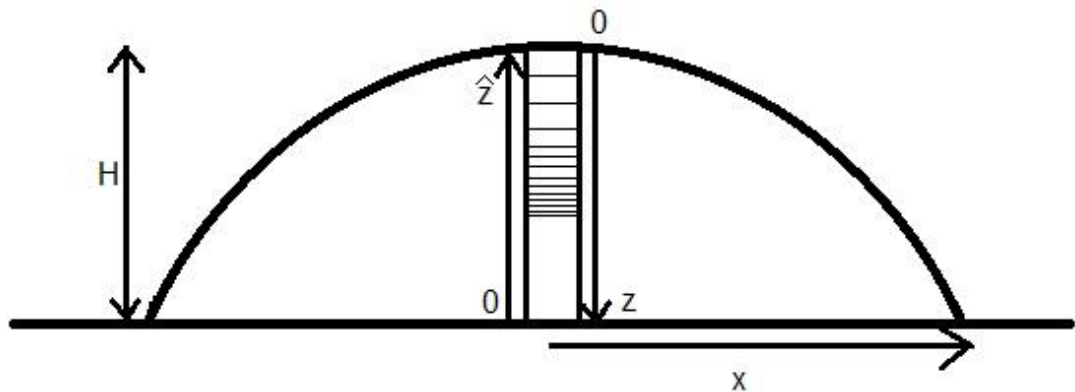


Figure 2.09: Schematic cross-section of an ice sheet showing how annual layer thickness decreases vertically at the ice divide, and the co-ordinates used in the thinning functions outlined below, where depth from the bedrock is defined as  $\hat{z}$ , whilst depth below the surface is defined as  $z$ .

### 2.5.3.1 Nye Model

The first model is based on the simplistic Nye estimation for vertical velocity (Nye, 1963). It assumes steady-state conditions for the original annual layer thickness at the time of deposition (accumulation), the annual layer thickness at depth  $z$ , and total ice sheet thickness,  $H$ , and it assumes that the ice sheet is frozen at bedrock. The relationship assumes a uniform vertical plastic strain at any given time, along any given vertical line in the ice. Thus, the model calculates a thinning ratio to be the annual layer thickness at depth from the bed,  $\lambda(\hat{z})$ , divided by original annual layer thickness,  $\lambda^0$ , known as *fractional depth*:

$$\frac{\lambda(\hat{z})}{\lambda^0} = \frac{z}{H} \quad (2.10)$$

### 2.5.3.2 Dansgaard-Johnsen two-step thinning function

The uniform plastic deformation modelled using the Nye relationship assumes only vertical velocity,  $w$ , and does not take into account any horizontal flow of ice. This becomes relevant to thinning models when analysing ice cores that have been extracted downstream from an ice divide. To account for horizontal advection of an ice particle, Dansgaard and Johnsen (1969) suggested two shape functions to estimate a strain ratio. The choice of which

method is used depends on whether the depth of an ice particle is greater than or less than a basal shear depth,  $h$ .

Dansgaard and Johnsen presented an age-depth model derived from the integral of the inverse of the vertical velocity of an ice particle,  $w$ , which incorporated a steady-state accumulation value to calculate annual layer thickness. The shape function of this model is (where  $\hat{z} = 0$  at bedrock):

$$\eta(\hat{z}) = \frac{2\hat{z} - h}{2H - h} \quad H \geq \hat{z} \geq h; \quad (2.11)$$

$$\eta(\hat{z}) = \frac{\hat{z}^2}{h(2H - h)} \quad h \geq \hat{z} \geq 0 \quad (2.12)$$

### 2.5.3.3 One-Dimensional Ice Flow Model

Vertical strain within an ice core is affected by ice-sheet processes dependent on drill location. Shape functions are often implemented under the assumption of steady-state conditions within an ice-sheet. This can be detrimental to the accurate modelling of the ice-sheet dynamics that are constantly varying due to external forcing (climate) variability. Ideally, ice cores will be extracted at the summit of an ice sheet (also referred to as the ice dome) from a location where there is no basal melting (temperature at bedrock,  $T_B < \text{pressure melting point}$ ). However, there is no guarantee that this location has always been the ice dome, or that total ice sheet thickness,  $H$ , and temperature at bedrock,  $T_B$ , have remained constant through time.

The one-dimensional shape function, outlined below, is calculated in terms of  $\zeta$ , a non-dimensional vertical coordinate defined as  $\zeta = \hat{z} / H$ . The model employs the Shallow Ice Approximation (SIA) and Glen's flow law to estimate the vertical velocity of an ice particle,  $w$ , as (Glen, 1958; Lliboutry, 1979; Parrenin et al., 2007a):

$$w(\hat{z}) = - \left[ m + \left( A^\theta - \frac{\partial H}{\partial t} - m \right) \eta(\zeta) \right] \quad (2.13)$$

This vertical velocity profile accounts for a basal melt rate,  $m$ , as well as temporal variations in ice sheet thickness – these parameters are estimated using three-dimensional ice-sheet models. The presence of a basal shear layer is not considered when calculating this shape

function. Instead, the formulation of the shape function,  $\eta(\zeta)$ , is continuous along an ice-core profile:

$$\eta(\zeta) = s \cdot \zeta + (1 - s) \cdot \eta_D(\zeta); \quad (2.14)$$

In the absence of temporal variations, it can be assumed that  $\eta(\zeta)$  is a one-dimensional thinning function, where  $s$  is the sliding ratio, and  $\eta_D(\zeta)$  is the vertical profile of deformation determined by Parrenin and Hindmarsh (2007):

$$\eta_D(\zeta) = 1 - \frac{p+2}{p+1} (1 - \zeta) + \frac{1}{p+1} (1 - \zeta)^{p+2}; \quad (2.15)$$

The  $p$ -parameter is an approximated rheological index used to calculate  $\eta_D(\zeta)$ ; it can be calculated from Lliboutry's approximation (Lliboutry, 1979), following Glen's flow law, by approximating the vertical temperature profile at the base of the ice sheet by a linear trend. The profile of vertical velocity is more non-linear for smaller values of  $p$ ; despite this, the parameter remains constant through time assuming that ice-flow conditions remain the same (Parrenin *et al.*, 2007a):

$$p = n - 1 + kG_0H; \quad (2.16)$$

Eq. 2.16 calculates the  $p$ -parameter;  $n$  is the Glen's Law exponent and it is assumed that  $n = 3$ ,  $G_0$  is an estimated vertical temperature gradient, and  $k$  is approximated assuming an Arrhenius dependence on the temperature at bedrock,  $T_B$ , for which  $Q = 60 \text{ kJmol}^{-1}$ .

$$k = \frac{Q}{RT_B^2} \quad (2.17)$$

Approximated values for the  $p$ -parameter are similar to the assumed value of Glen's index,  $n = 3$ . However, for several sites including EPICA Dome C, the rheological index is much higher (for EDC,  $p \cong 9$ ). There are several arguments that do not support the approximation for  $p$  (eq. 2.16). Firstly, the precise value for the activation energy required for eq. 2.17 remains uncertain, since an increase in the required energy is observable with higher temperatures at the bedrock. Secondly, the SIA is not applicable at the dome of an ice sheet, since isochrone layers will be perturbed beneath the ice divide due to the lack of horizontal ice flow stiffening the oldest ice frozen at the bedrock; these features are also known as Raymond stacks (Raymond, 1983; Parrenin *et al.*, 2007a). Finally, the adopted value of

Glen's flow law exponent is used widely in ice-sheet models, whilst values derived from field-based radar data suggest a range of values at the ice dome of 1-5 (Gillet-Chaulet *et al.*, 2011). As an alternative to the empirically-calculated parameter, the vertical deformation parameter,  $p$ , can be calculated within an inverse probability model, outlined later in this chapter.

#### 2.5.3.4 Phase-Sensitive Radio Echo Sounder (pRES)

A fourth technique that can be used to estimate a thinning function makes use of pRES measurements, collected over several seasons. These measurements provide an estimate of vertical velocity within an ice sheet, and thus could be used directly to infer the present-day conditions of an ice sheet including total strain, ice sheet thickness, rheology and basal melt rates (Corr *et al.*, 2002; Gillet-Chaulet *et al.*, 2011; Kingslake *et al.*, 2014).

Solving the age equation (eq. 2.18, for which age,  $\text{age}(t)$ , is assumed to be a function of both time,  $t$ , and depth,  $z$ ) dynamically allows us to interpret the pRES observational data,  $w$ , as vertical velocity through time, and it thus provides an estimate of age with relation to depth. However, the pRES observational data only provide an estimate of present-day vertical velocities, and the method assumes a steady state for both vertical velocity and accumulation, which may not hold in reality.

$$\frac{\partial \text{age}(t)}{\partial t} + w \cdot \frac{\partial \text{age}(t)}{\partial z} = 1 \quad (2.18)$$

Alternatively, a thinning function could be derived from the *in situ* vertical velocity measurements by adapting eq. 2.19, originally presented in Cuffey and Paterson (2010), into an iterative model. An iterative model would seek to optimise the accumulation profile, which has previously been assumed to be steady with time. As such, an iterative model would solve for a variable accumulation history,  $A(t)$ , by inverting an annual layer thickness,  $\lambda(t)$ , reconstruction that has been optimised using the derivative of *in situ* vertical velocity,  $w$ , with respect to depth,  $z$ :

$$\lambda(t) = A(t) \exp \int_{-\text{age}}^0 \frac{\partial w}{\partial z} dt \quad (2.19)$$

#### 2.5.4 Age-Depth Profile

As previously mentioned, the present-day annual layer thickness record is estimated in order to reconstruct the age-depth profile of the ice core. The age of an ice particle at depth  $z$  is

assumed to be the integral from the surface to depth  $z$ , of the inverse of modelled annual layer thickness,  $\lambda(z)$ :

$$\lambda(z) = A(z) \cdot \eta(z) \quad (2.20)$$

$$\text{age}(z) = \int_0^z \frac{dz'}{\lambda(z')} \quad (2.21)$$

where annual layer thickness is estimated to be the product of the accumulation history and the thinning function.

### 2.5.5 Borehole Temperature Profiles

Reconstruction of surface temperature history can be achieved by interpreting temperature measurements taken directly from the ice-core borehole. Borehole thermometry, the practice of measuring present-day temperatures along the depth of a borehole, can be used to infer recent surface temperature history and the geothermal heat transfer conducted through the subsurface of an ice sheet (Dahl-Jensen, 1986; Dahl-Jensen, 1998; Barrett, 2009). A one-dimensional version of the heat equation (eq. 2.22), in which properties only vary with depth, is given in eq. 2.23. In these equations,  $T$  is temperature,  $t_f$  is the length of the time period in question,  $C$  is the specific heat capacity of ice,  $\rho$  is the density profile of the ice,  $k$  is a profile of thermal conductivity,  $u$  is the ice velocity, and  $\varepsilon\sigma$  is a viscous heating term ( $\varepsilon$  is the strain rate tensor, and  $\sigma$  is the stress rate tensor) (Zagorodnov et al., 2012):

$$\rho C \frac{\partial T}{\partial t} = \nabla \cdot k \nabla T + \rho C u \cdot \nabla T + \varepsilon \sigma \quad (2.22)$$

$$\rho(z)C(z) \frac{\partial T(z, t)}{\partial t} = \frac{\partial}{\partial z} \left[ k(z) \frac{\partial T(z, t)}{\partial z} \right] - \rho(z)C(z)w(z) \frac{\partial T(z, t)}{\partial z} \quad (2.23)$$

In eq. 2.23, depth is given by  $z$ , where  $z = 0$  at the surface, and temperature is calculated from the surface to the bedrock,  $0 < z < H$ , where  $H$  is the total ice sheet thickness. Similarly for time,  $t = 0$  at the present day and the surface temperature is calculated with respect to the reference time,  $t_f$  as  $0 < t < t_f$ . At the surface,  $T(0, t) = U_0 + \mu(t)$ , where  $U_0$  is the present-day mean surface temperature and  $\mu$  is a parameter that accounts for the geothermal heat flux. The vertical velocity of the ice is calculated as  $w(z) = A(z) \cdot \eta(z)$  (where  $A$  is accumulation and  $\eta$  is a thinning function) (Cuffey and Paterson, 2010; Salamatin, 2000; Zagorodnov et al., 2012). Using an iterative approach, eq. 2.23 can be solved using eq. 2.24, which accounts for the deviation between present and past values of surface temperature,

accumulation rate, and geothermal heat flux. Other variables including  $k$ ,  $C$ , and  $\rho$  are calculated using eq. 2.25-2.27, and the density of ice is calculated as  $\rho_i = (916.8 - 0.14027T)$ . Eq. 2.27 includes two constants which are  $c_0 \approx 0.58$  and  $\gamma(z) \approx 0.021$ .

$$\frac{\partial}{\partial z} \left[ k(z) \frac{\partial U(z)}{\partial z} \right] - \rho(z)C(z)w(z) \frac{\partial U(z)}{\partial z} = 0 \quad (2.24)$$

$$k(z) = 9.828 \exp^{-0.0057(273.15+T(z))} \quad (2.25)$$

$$C(z) = 2098 + 7.122T(z) \quad (2.26)$$

$$\rho(z) = \rho_i(1 - c_0 \exp^{-\gamma(z)}) \quad (2.27)$$

Depending on the location of the borehole and the timeframe that the study spans, horizontal ice flow and temporal changes to ice sheet thickness should be considered. The resolution of the temperature profiles will be decadal, centennial or millennial, dependent on site-specific accumulation rates (Salamatin, 2000). Application of borehole temperature reconstructions in frozen contexts must consider vertical heat advection, basal melting, and the thinning of annual layers due to compaction (Lachenbruch & Marshall, 1986; Salamatin, 2000). Ultimately, diffusion of the temperature with depth decreases the resolution available for temperature reconstructions. To address this issue, an inverse model with *a priori*  $\delta^{18}\text{O}$  and  $\text{CH}_4$  information is often employed to constrain rapid climatic fluctuations within smoothed temperature profiles (Schwander *et al.*, 1997; Dahl-Jensen *et al.*, 1998; Salamatin, 2000).

### 2.5.6 Inverse Probabilistic Approach

As outlined at the start of the section, there are four main principles to the construction of an ice-core age-depth profile. Where annual layer counting is not possible, a combination of glaciological modelling must be employed, constrained using known-age horizons from reference markers preserved in the ice core. The age-depth profile estimated by eq. 2.21 can be constrained using an inverse technique that seeks to limit the deviation between known-age horizons and the modelled age at specific depths.

Reference ages commonly identified along the core are volcanic tephra markers or isotopic signatures that indicate well-dated and globally-synchronous events such as solar activity, Milankovitch cycles, and isotopic signatures linked with climatic events. Dependent on the age of the ice core, structured Beryllium-10 ( $^{10}\text{Be}$ ) peaks indicating the Laschamp and Brunhes-Matuyama geomagnetic events at  $40.4 \text{ ka BP} \pm 2.0 \text{ ka}$  and  $775 \text{ ka BP} \pm 10 \text{ ka BP}$ ,

respectively, provide reliable age constraints because independently-dated stratigraphic markers associated with these events are agreed to be globally synchronous (Bassinot *et al.*, 1994; Guillou *et al.*, 2004). For this research project, AIM events have been used as age horizons in constraining the ice-core age-depth profiles for three deep ice cores from the AP and Weddell Sea region. As outlined in section 2.3.4, AIM events are assumed synchronous across the Antarctic continent and are easily identifiable and replicated in ice-core records. The precise age of each AIM event and the prescribed uncertainty is taken from the AICC2012 EPICA Dome C chronology (Bazin *et al.*, 2012). This is the most current synchronised chronology available for Antarctic ice cores.

In a hypothetical situation, model output can be optimised by using an inverse approach to constrain the results using observational, *a priori*, information. Translated mathematically, an inverse method will calculate the poorly-known parameters while the model is iterated, with the aim of getting the output to fit a set of observational parameters on the model space. The inverse method tries to infer information from i) the estimated values of observational datapoints, or *a priori* information,  $\rho^D$ , ii) the estimated values extracted from the model,  $\rho^M$ , and iii) the relationship between  $\rho^D$  and  $\rho^M$  given by the model (Parrenin *et al.*, 2001). In the specific case of an ice-core age-depth model, the age-depth profile is calculated iteratively – changing the value of one or more free parameters with each iteration – in order to reconstruct a profile that agrees with age horizons.

An important step within the inverse approach is the assessment of the difference between the probability distributions,  $\rho$ , of the observed data,  $d$ , hereafter referred to as  $\rho^D(d)$ , and modelled estimates,  $m$ , hereafter referred to as  $\rho^M(m)$ . In the inverse method, this difference is calculated using a root mean square error (RMSE) approach (eq. 2.28);  $E(m)$  is calculated using the RMSE relationship, and quantifies the differences between the model output,  $\rho^M(m)$ , with respect to the observational parameters,  $\rho^D(d)$ ; low values suggest a good-fit of model parameters. Specific to the construction of age-depth profiles, the aim of the inverse approach is to examine the difference between an empirically-calculated age-depth model and an *a posteriori* age-depth profile. Any differences between the two profiles may reflect (i) simplifications adopted within the modelling process, or (ii) inadequacies in the distribution of the age constraints.

$$E(m) = \sqrt{\frac{\sum_{i=1}^n (\rho^D(d)_i - \rho^M(m)_i)^2}{n}} \quad (2.28)$$

For an ice-core age-depth model, a Monte Carlo Markov Chain (MCMC) sampling technique has previously been used to systematically explore the model parameter space (Parrenin et al., 2007a; 2007b). Referring to fig. 2.08, such a search is achieved here by iterating the model, setting new 'initial conditions' within set boundaries, and assessing the difference between observed and modelled age-depth estimates at depths corresponding to observational data horizons. This approach produces optimised values for the 'initial conditions' and more accurate profiles of thinning and/or accumulation, and hence age-depth.

### 2.5.7 Perturbation Theory

For some elements of ice core analysis, perturbing a profile as part of the inverse approach is necessary to find the optimal information (section 3.6.1). Perturbation theory can be used to find an approximate solution to a problem, by starting from the exact solution of a related problem. It was first used in the 19<sup>th</sup> century as a means to calculate astronomical relationships in the motion of planets in the solar system (Poincaré, 1892). For this study, perturbation theory is applied in order to reconstruct the optimal accumulation profile. This is completed in order to account for the potential uncertainty on the empirical accumulation reconstructions.

Within perturbation theory, a problem is broken down into solvable parts, and a small term,  $\varepsilon$ , is added to the exact solution of each of these parts. This leads to the following expressions, or perturbation series, given in terms of a formal power series. The term  $A_0$  is the exactly-solved solution to a problem, with further terms describing the deviation in the solution as a result of the perturbation term.  $A_n$  represents the higher-order terms which may be found iteratively; the perturbation series relationship can be approximated by truncating eq. 2.29 (eq. 2.30).

$$A = A_0 + \varepsilon^1 A_1 + \varepsilon^2 A_2 + \dots + \varepsilon^n A_n \quad (2.29)$$

$$A \approx A_0 + \varepsilon A_1 \quad (2.30)$$

## 2.6 Firn Compaction in the upper depths of an ice core

In order to compare model estimates with the observational data in the ice-phase of the core, the ice core density is assumed to be the equivalent of ice,  $\rho_i = 0.917 \text{ Mg m}^{-3}$ . This means that the profile of increasing density from snow to ice in the upper layers of the ice core must be accounted for. However, in order to interpret the gas-phase record in the ice

core, the changes in the density of ice with respect to depth must be fully understood. First introduced in section 2.3.3, the process of densification in the firn layer of the ice core, and the techniques that can be applied to interpret the gas-phase record, are outlined in this section in more detail.

### 2.6.1 *Densification of an ice core*

The density profile,  $\rho$ , of the highly porous firn snow reflects the fact that the density of snow deposited at the surface of an ice sheet increases as subsequent annual snowfall is deposited on top of it, eventually reaching the density of ice. This snow in the firn layer goes through a well-observed three-stage densification process:

$0 \leq \rho \leq 0.55 \text{ Mg m}^{-3}$  – The initial phase of compaction where gas particles are free to move throughout porous firn snow;

$0.55 \leq \rho \leq 0.83 \text{ Mg m}^{-3}$  – Compaction of firn snow has reached “critical density” at  $0.55 \text{ Mg m}^{-3}$  (Blunier and Schwander, 2000), with packing and grain settling the dominant mechanisms of the second stage. Density increases more slowly than in the first stage, with air passages closing off to form individual bubbles at a “close-off” density of  $0.83 \text{ Mg m}^{-3}$ ;

$0.83 \leq \rho \leq 0.917 \text{ Mg m}^{-3}$  – “Close-off” density has been reached and gas particles are no longer free to move within the ice matrix. Density continues to increase by further compression of the gas bubbles until the density of pure ice is reached.

The change in density is defined by Herron and Langway (1980) for these three stages, where  $C$  is a constant for each stage:

$$C = \frac{d \ln(\rho/(\rho_i - \rho))}{dz} \quad (2.31)$$

The measured density profile of an ice core contains imperfections. These imperfections could be chips, breaks, or particulates in the ice core. Hence, a least squares approach is applied to eq. 2.31 for the three stages of densification to estimate the slope of density with depth. In doing this, two pieces of information are obtained: (i) the close-off depth at which the gas bubbles are occluded in the ice matrix; and (ii) an idealised density profile that can be used to convert snow depth to a depth scale that assumes an ice-only volume.

### 2.6.2 Gas-phase age-depth profiles

In addition to the estimation of an ice-phase age-depth profile, a second age-depth profile is obtained from the gas-phase of an ice core. The gas-phase age-depth profile has the advantage that these records (particularly methane) can be synchronised between Greenland and Antarctica because of the rapid mixing of gases in the atmosphere. In any core, there is a fixed offset ( $\Delta\text{age}$ ) between the age of gas and ice at a particular depth ( $\Delta\text{depth}$  for the depth-difference between gas and ice of the same age). This offset exists because the age of the gas in an ice core is younger than the ice that encloses it, as air circulates in firn above the close-off depth, trapping the younger air.

Within the firn column, throughout the first two stages of the densification process, gravitational fractionation in the firn column will lead to heavy isotopes of a gas concentrating at the bottom of the fractionation column before the snowpack densifies to the “close-off” density at  $0.83 \text{ Mg m}^{-3}$ . Air bubbles will be occluded at a “lock-in depth” (LID) once the surrounding snow reaches the third stage of the densification process. The  $\Delta\text{age}$  is dependent on the accumulation rate and temperature, i.e.  $\Delta\text{age}$  and the height of the firn column should be assumed inversely proportional to the accumulation rate. Alternatively,  $\Delta\text{depth}$  – the depth difference between the gas and ice phases of the same age – is independent of the modelled age-depth profile and accumulation profile as there is a limited effect of the accumulation rate on both LID and the shape function (Parrenin et al., 2012).

In order to accurately estimate the LID,  $\Delta\text{age}$ , and  $\Delta\text{depth}$ , it is important to accurately reconstruct the past structure of the firn column. Firn densification models estimate the gas-phase age-depth profile of an ice core by assuming homogenous snow material in isothermal conditions, where the density profile of a firn column is assumed to be dependent on the accumulation rate, surface temperature and surface density (Herron and Langway, 1980; Pimienta et al., 1987; Barnola et al., 1991). For changing climatic conditions, a dynamical model can be interpreted from the Herron and Langway (H-L) and Pimienta-Barnola (P-B) models (Buizert et al., 2015).

Alternatively, firnification models estimate gravitational settling of the heavier unreactive gases in the firn column during the densification process to estimate the lock-in depth (LID) and  $\Delta\text{age}$  (Barnola et al., 1991; Schwander et al., 1997; Arnaud et al., 2000; Goujon et al., 2003; Landais *et al.*, 2006; Capron et al., 2013). Due to gravitational fractionation – the gravitational settling of heavier isotopes of unreactive gases, for example  $^{15}\text{N}/^{14}\text{N}$  or

$^{40}\text{Ar}/^{36}\text{Ar}$ , at the deeper end of the firn column – air at the base of the firn layer is enriched with heavier isotopes by an amount that is proportional to the diffusive column height (DCH). Gravitational fractionation,  $\delta_{\text{grav}}$ , follows the barometric equation, for which  $\Delta m$  is the mass difference between the heavy and light isotopes of the measured gas ( $\text{kg mol}^{-1}$ ),  $g$  is gravitational acceleration ( $\text{m s}^{-2}$ ),  $z = \text{DCH}$  (m),  $R$  is the gas molar constant of  $8.314 \text{ J K}^{-1} \text{ mol}^{-1}$ , and  $T$  is the firn temperature (K) (Capron et al., 2013).

$$\delta_{\text{grav}} = \left[ \exp\left(\frac{\Delta m g z}{RT}\right) - 1 \right] \quad (2.32)$$

Arnaud et al. (2000) adapted this relationship in order to develop a sophisticated firnification model, which considers two densification stages: pure sliding of snow grains where density  $\rho < 0.55 \text{ Mg m}^{-3}$ ; and pure deformation of grains where density  $\rho > 0.55 \text{ Mg m}^{-3}$ . Advancing from this work, Goujon et al. (2003) adapted the Arnaud model into a firn-densification-heat-transfer model, accounting for temporal variations in temperature and thermal fractionation.

Finally, the  $\Delta\text{age}$  can be calculated from a depth profile, where LID is estimated along the ice core from  $\Delta\text{depth}$  estimations from an ice flow model coupled with a firn densification model (Parrenin et al., 2012). The advantages of this method are twofold: (i) firstly its aforementioned weak dependence on the accumulation history, and (ii) the information this method can yield about the past flow of ice at the drilling site.

In addition to understanding firn processes to reconstruct the gas-phase age-depth profile, accurate reconstruction of firn compaction and densification is an important step in determining the age of the ice-phase of an ice core since a corrected density profile is required for conversion to water-equivalent depth. As explained in section 2.5.3, all thinning functions are assumed to relate to the compaction of ice, with no open spaces for gas transfer in the upper sections of the ice core. Furthermore, expanding on the principles of the densification process, a dynamical model can be used to reconstruct the  $\Delta\text{age}$  and  $\Delta\text{depth}$  profiles along the ice core by accounting for climatic changes that impact on the DCH.

## 2.7 Development of established ice-core chronologies

Published chronologies for established deep Antarctic ice cores have been constructed using the relationships for accumulation (eq. 2.05 – 2.09) and thinning (eq. 2.10 – 2.19) described

above, often invoking an inverse approach to solve for the optimal profiles (Schwander *et al.*, 2001; Parrenin *et al.*, 2004; Parrenin *et al.*, 2007a; 2007b; Bazin *et al.*, 2012; Parrenin *et al.*, 2015). In the following section the approaches used to develop an ice-core chronology are outlined using the example of the development of the age-depth profile for the EPICA Dome C ice core.

### 2.7.1 EPICA Dome C

In the original age-depth profile, accumulation and ice-flow were reconstructed using the Clausius-Clapeyron relationship and a one-dimensional ice flow model (eq. 2.05 – 2.08 and eq. 2.13 – 2.17), constrained using an MCMC algorithm by the process of ‘random walk’, optimising the ice-core reconstructions of accumulation and thinning by constraining the profiles to observational data. The observational data was interpreted from volcanic and geomagnetic age horizons. This approach achieved an extended climatic record to 800ka BP (Schwander *et al.*, 2001; EPICA members, 2004; Jouzel *et al.*, 2007; Parrenin *et al.*, 2007a). Later, Parrenin *et al.* (2007b) utilised the method of multi-parameter age constraints to refine the existing EDC chronology and construct “EDC3”; incorporating volcanic markers, gas markers, the Laschamp and Brunhes-Matuyama geomagnetic events, and  $^{14}\text{C}$  and  $^{10}\text{Be}$  trends marking solar activity. This updated chronology reconstructed an accumulation history using the simple exponential relationship (eq. 2.09). The approach used to reconstruct the EDC3 chronology was also used to construct the EPICA Dronning Maud Land “EDML1” chronology (Ruth *et al.*, 2007), spanning 150 ka BP. EDC3 and EDML1 were constructed using the same combination of inverse glaciological modelling and known-age markers. EDML1 is synchronised from present-day to 52 ka BP using common known-age markers such as volcanic ties, and presented on a common timescale to EDC3 (Severi *et al.*, 2007).

Most recently, Bazin *et al.* (2012) synchronised the age-depth profiles for EDC, EDML, Talos Dome, and Vostok, as well as the NGRIP record in Greenland, to produce the AICC2012 chronology (Lemieux-Dudon *et al.*, 2010; Bazin *et al.*, 2012; Veres *et al.*, 2012). This chronology, modelled using the “Datice” tool, is capable of synchronising ice-core profiles on a common timescale (Lemieux-Dudon *et al.*, 2010), using globally-synchronous known-age markers including  $\text{CH}_4$  concentrations as greenhouse gas signatures, stable water isotope signatures, volcanic stratigraphy, and geomagnetic  $^{10}\text{Be}$  structures.

Improvements to the “Datice” method are found in the “IceChrono” package – a freely-available model, written in Python, which is capable of estimating the age-depth profile for multiple ice-core datasets simultaneously using a non-linear least squares probabilistic approach (Parrenin et al., 2015). The “IceChrono” model is capable of calculating the optimal age-depth profile with limited data and constraints, but it can also take in *a priori* information on accumulation, thinning, firnification, density, layer thickness measurements and known-age horizons. The model approach is unchanged between “IceChrono” and “Datice”, only the length of the model scripts and efficiency of the code are different.

### 2.7.2 Other deep ice cores

Parallel to the development of EPICA ice core chronologies, other deep ice core chronologies have used similar methods to those outlined in this chapter. Prior to the AICC2012 synchronisation, the Vostok ice core was presented with an estimated climate time series extending to 150 ka BP (Lorius *et al.*, 1985). Just over a decade later, Petit et al. (1999) modelled the initial age-depth profile for the whole Vostok ice core, estimating an age-depth profile spanning 420 ka BP in 3310 m of ice. Later, this age-depth profile was further constrained by orbitally-tuned markers and later compared to the climatic variances of the EDC core (Lorius *et al.*, 1985; Parrenin *et al.*, 2001; 2004; EPICA members, 2004). Similarly, the Dome Fuji ice core drilling programme obtained an ice-core record spanning 400 ka BP; the age-depth profile was constrained using orbitally-forced precessional cycles – identified through the sensitivity of  $\delta^{18}\text{O}$  values to Milankovitch cycles (Watanabe *et al.*, 2003). The Dome Fuji chronology has been refined using a Bayesian approach that is similar to the method used for the EDC3 chronology (Parrenin et al., 2007; Kawamura et al., 2012; Nakano et al., 2016). In addition to a larger dataset of Uranium-Thorium (U-Th) dated speleothem records of insolation as age horizons,  $\text{O}_2/\text{N}_2$  records of orbital activity have been used to constrain an age-depth profile, which extends 720 ka BP (3035 m) (Dome Fuji Project Members, 2017).

Finally, the 3404 m-deep WAIS Divide ice core has been dated to 68 ka BP using a combination of annual layer counting and ice flow modelling (Buizert et al., 2015; Sigl et al., 2016). The high mean annual accumulation at the site, coupled with low thinning rates and high basal melt rates, has preserved an annual layer thickness along the ice core within the resolution of standard laboratory techniques, permitting annual layer counting to 2850 m at an age of  $\sim 31$  ka BP. CFA measurements of trace-element aerosols including  $\text{Na}^+$ , non-sea-salt sulphur (nss-S), and black carbon (BC), revealed a seasonal profile extending to 2850 m,

with a minimum annual layer thickness reaching 30 mm at 2850 m (Sigl et al., 2016). Beyond this depth, the remainder of the ice-core profile has been modelled using an inverse approach, for which accumulation is assumed to follow a Clausius-Clapeyron relationship with stable water isotopes at the site (eq. 2.05 – 2.08), and a thinning function has been estimated using the Dansgaard-Johnsen relationship (eq. 2.11 – 2.12). Free parameters estimated within the inverse approach include a basal stretching parameter and the ice-sheet thickness. Using this approach, the base of the WAIS Divide ice core is dated to ~68 ka BP (Buizert et al., 2015).

The development of ice-core chronologies has seen an increase in complexity, from the earlier models using steady-state assumptions to the most recent reconstructions for the deep ice cores that synchronise multiple ice core records (Dansgaard et al., 1969; Parrenin et al., 2015). The most accurate age-depth reconstructions incorporate an inverse approach and observational data on known-age horizons and annual layer thickness measurements along the core. As with all palaeoclimate analysis, an accurate chronology is important for the interpretation of the preserved climate record. Deep ice cores from coastal sites, such as the three ice core sites used in this thesis, pose a particular problem for the current leading ice-core age-depth model, “IceChrono”. The main assumptions used in the model to reconstruct past atmospheric and ice-sheet processes, such as steady mean annual accumulation during interglacial periods and the relationship between stable water isotopes, temperature and accumulation, are not as reliable at coastal sites during interglacial periods due to the high inter-annual climate variability, for which the source of water vapour and precipitation patterns can vary (Sime et al., 2009a; Fudge et al., 2016). As a consequence of the complexity of near-coastal ice core climate history, this thesis seeks to individually model the age-depth relationship for each ice core.

## 2.8 Summary

The progress of ice-core research over the last six decades has realised the potential of ice cores as a proxy for past climate and continuous records of climate spanning 800,000 years have been developed. This accomplishment has led to the development of sophisticated ice flow modelling approaches, in addition to the chemical analysis of preserved constituents of an ice core. However, the complexity of coastal climate processes during interglacial periods limits the effectiveness of age-depth models such as “IceChrono” when attempting to interpret ice cores from the AP and the Weddell Sea Embayment. There is wide agreement that the most robust age-depth relationships can be inferred from high-resolution, sub-

annual profiles that can be annual layer counted. Improvements to ice-core analysis through the development of techniques that can achieve ultra-high resolution provide an alternative to age-depth modelling by increasing the depth to which annual layers can be counted. Measurements of annual layer thickness at depths previously unattainable by standard laboratory resolution extend the depth to which annual layer thickness profiles can be obtained for mid-depth ice cores in regions of high mean annual accumulation. These profiles provide a better control on ice flow modelling as well as age-depth modelling. Through the validation of these relationships, and subsequent tests of glaciological reconstructions, all of the existing and novel options to construct the optimal age-depth profile for the three ice cores can be assessed.



## Chapter 3: Methodology

### 3.1 Introduction

This chapter outlines the methodologies used to address the research hypotheses identified in the thesis aims (Chapter 1). Section 3.2 describes the work carried out in the field to extract the ice cores studied in this thesis, and make borehole temperature measurements. The chemical profiles of these ice cores were obtained by a series of laboratory methods that are outlined in section 3.3 of this chapter. Further analysis of some sections of the ice cores required ultra-high resolution trace-element analysis; sampling and laboratory methods are outlined in sections 3.4 and 3.5. Established statistical techniques employed in reconstructing glaciological profiles are outlined in the review of literature in Chapter 2 (section 2.5; eq. 2.03 – 2.19), but novel techniques in modelling and statistical analysis are described in section 3.6.

### 3.2 Site Details

#### 3.2.1 *Sampling Locations and Drilling Process*

The focus of this study is on the Antarctic Peninsula (AP) and the Weddell Sea sector of Antarctica, where three deep ice cores have been drilled to bedrock (Mulvaney et al., 2007; 2014). Subsequent measurement of the stable water isotopes along the ice core provide a proxy for the temperature history of each site (section 2.5.5). The boreholes produced in drilling the ice cores remain open for some time, allowing access for further physical measurements. Precise measurements of the borehole temperature to the full depth ice sheet depth can be used to reconstruct an independent temperature proxy that can be compared with the empirically-calculated temperature profile used in the age-depth reconstructions (section 2.5.4), and may be used to calculate the geothermal heat flux from the earth's mantle (Chapter 8).

The locations of the three deep ice core drill sites, James Ross Island (JRI), Berkner Island (BI) and Fletcher Promontory (FP) are shown on fig. 3.01. In addition to the deep ice core sites, the locations of three short boreholes that are used in Chapter 8 are included in fig. 3.01. The precise site co-ordinates, as well as present-day ice-sheet conditions for mean surface temperature, snow accumulation, ice-sheet thickness, and distance from the ice divide are recorded for the three deep ice cores in table 3.01. The three deep ice cores were drilled over several Antarctic field seasons between 2003 and 2012 using a typical

electromechanical ice core drilling system based on previous European Project for Ice Coring in Antarctic (EPICA) drilling systems working in a fluid-filled borehole.

*Table 3.01: Information pertaining to site specifications at each ice core drill site.*

	<b>FP</b>	<b>BI</b>	<b>JRI</b>
<b>Latitude</b>	77°54.1'S	79°32.9'S	64°12.1'S
<b>Longitude</b>	82°36.3'W	45°40.7'W	57°41.1'W
<b>Altitude of present ice surface (metres above sea level (masl))</b>	873	890	1542
<b>Ice sheet thickness (m)</b>	654	947	364
<b>Distance from the ice divide (m)</b>	575	0	1000
<b>10 m-deep temperature (K)</b>	246.0	248.2	258.7
<b>10 m-deep temperature (°C)</b>	-27.1	-24.9	-14.4
<b>Measured Basal temperature (K)</b>	255.0	261.5	264.5
<b>Measured Basal temperature (°C)</b>	-18.1	-11.6	-8.6
<b>Mean Annual Accumulation (m yr<sup>-1</sup>)</b>	0.38	0.18	0.63



Figure 3.01: Map showing the site locations of deep ice cores and short boreholes in the Antarctic Peninsula and Weddell Sea region. Pale grey areas indicate grounded ice, with dark grey surfaces extending from the grounding lines to the calving front of the ice shelves.

Essentially, a winch and tower at the surface controls a cable carrying power to a drill sonde in the borehole that comprises a motor/gear section. A 190 V permanent magnet DC motor, producing 600 W at 2000 rpm through a gear reducing the rotation to 80 rpm, drives the rotation of a hollow shaft connected to a core barrel and drill head with cutters that cut an annulus in the ice, while an 'anti-torque' section at the upper end of the sonde prevents the drill spinning in the hole. The borehole is filled with a fluid Exxon/Mobil 'Exxsol', which has a density of  $0.79 \text{ Mg m}^{-3}$  at 288 K, to prevent natural ice flow narrowing the borehole during the drilling and to help transport ice chips. Chips from the cutting head are pumped away by a double-piston pump into the hollow shaft where they are caught by a sieve and the fluid returned to the borehole while the core itself passes into the core barrel. The drill captures about 2 m of ice core on each drilling run, then the drill is returned to the surface to recover the ice core, and clear the chips. The drill system and the field projects are described by Mulvaney et al. (2007, 2014).

### *3.2.2 Borehole Temperature Measurements*

Following the retrieval of the ice core, the borehole temperature profile for each ice core is measured. For the three ice core sites in this study, the process differs depending on the site location and logistics of the drilling. All borehole temperature measurements were obtained prior to this study. At JRI, the temperature measurement was made over two days, three days after the drilling of the core ended, in the fluid-filled borehole. Three calibrated glass bead thermistors in thin walled sealed probes were mounted on the lower end of the drill cable in a multi-wire arrangement that allowed the measurement of the cable resistance and the resistance across the cable plus each thermistor. Thermistors were each calibrated at BAS (in Cambridge) using a triple point cell reference and in a circulating bath of cooled salt water measured against a platinum resistance thermometer (independently calibrated by the National Physical Laboratory). At each depth, the thermistors were allowed to settle for around 20 minutes before measurements were carried out on each thermistor and cable resistance using a low current resistance meter, with the results compared to a standard resistance. Multiple measurements were taken at each depth, until the drift of temperature had been reduced to less than 1 mK per minute. Measurements in the field were made on a transit down the borehole, and on the return of the probe to the surface, with a depth resolution of 20 m, and the mean of the three temperature measurements at each depth was reported.

At FP, a similar scheme was used, with three calibrated (as above) thermistors arranged in a four-wire configuration on the drill cable, a low current resistance meter to measure the resistance across each thermistor, and the cable resistance, with all measurements referenced against an *in situ* standard resistor. At this site, the temperature at each level was logged automatically every second for at least 20 minutes, and the graph of the settling was used to determine when the thermistor drift had settled. Measurements were commenced four days after drilling ceased, after the borehole fluid had been removed. The transit of the probe to the base of the borehole and back to the surface took three days. A depth resolution of 2 m was achieved between the surface and 120 m depth, with a lower resolution of 5 m - 15 m to the greatest-measured depth.

At BI, the measurements were made one year after drilling was completed, in a fluid-filled borehole. Measurements were made every 2 m on a transit down the borehole only, with the thermistors allowed to settle for before the readings were taken. This measurement is considered to be the most precise of the three deep boreholes since any small transient change in the ice sheet temperature due to the drilling process will have equilibrated between drilling and measurement.

### 3.3 Initial ice-phase chemical profiles

This section, and the subsequent sections, outlined the analytical work that is completed on the three ice cores. Table 3.02 sets out the different types of chemical analysis that have been available to the three ice cores, and outlines the work completed on each.

*Table 3.02: Table outlining the application of different methods of chemical analysis to the three ice cores. Where stated 'Already available', the data was obtained prior to or separate to this project.*

	<b>FP</b>	<b>BI</b>	<b>JRI</b>
<b>Stable Water Isotopes</b>	Already available	Already available	Already available
<b>Continuous Flow Analysis (CFA)</b>	N/A	Already available	Already available
<b>LA ICP-MS</b>	N/A	Yes	N/A
<b>Discrete Sampling</b>	Yes	Yes	N/A

In particular, this section outlines the chemical analysis that was completed independently of this study, but for which the results are used. An ice core is analysed by several

techniques to build up a full chemical profile. The core is processed by band saw in a cold room so that half of the ice core is preserved for future analysis in two archive quarters, and the rest is used in the initial post-drilling analysis (fig. 3.02). Two main analytical techniques were used to build up the initial ice-phase chemical profile used in this thesis: continuous flow analysis (CFA), and the analysis of stable water isotopes. Subsequently, very high-resolution analysis of short sections was carried out using laser ablation mass spectrometry (section 3.4) and very high resolution discrete sampling (section 3.5).

### 3.3.1 *Continuous Flow Analysis (CFA)*

The JRI ice core has been analysed by a continuous flow analysis technique on two occasions: initially at BAS, and for a second time at the Desert Research Institute (DRI), Nevada, USA.

The BAS system generates a flow of liquid by continuously melting a section of the ice core on a heated melt-head in a cold room held at 248 K (-25 °C), and passing that liquid through to a warm lab where pumps and manifolds distribute the liquid amongst several instruments. The BAS CFA system has recently been updated to measure stable water isotope profiles: a cavity ring-down laser spectrometer measures the stable water isotopes, in addition to the existing system of a rapid ion chromatograph (IC) that measures a range of anions, and ultra-violet (UV)/Visible and fluorescence spectrometers that measure simple compounds and a low resolution inductively coupled plasma mass spectrometer measures a few light elements. However, the method to obtain the stable water isotope profiles used in this study for JRI is outlined in the next paragraph, and the profiles of FP and BI have been measured discretely using the methods outlined in the next section.

The DRI Ultra Trace Chemistry Laboratory continuous measurements at high depth resolution for the chemistry, dust, black carbon and water isotopes in ice cores using a similar source of sample stream as described above with the core melting on a melt-head in a cold room. A combination of CFA UV/Visible, fluorescence and laser spectrometers measure simple chemical compounds and the water isotopes, together with instruments for black carbon and dust. Critically for the dating of the JRI core described in Chapter 7, the DRI system incorporates two high mass resolution inductively coupled plasma mass spectrometers (ICP-MS) for trace elements. These two ICP-MS instruments are capable of measuring heavy metals and rare earth elements at ultra-trace levels, as well as some light elements such as sulphur that cannot be measured at BAS. The DRI system is referred to

here as the BC-TE-CFA (Black Carbon-Trace Element-Continuous Flow Analysis) system and is fully described by McConnell et al. (2002) and Sigl et al. (2015).

The continuous chemical and stable water isotope dataset used in this study for JRI pertains to the analysis at DRI. Analysis of the JRI ice core measured sea-salt and non-sea salt trace-element species, black carbon, and stable water isotopes. Using the BC-TE-CFA system, at a melt rate of  $\sim 50 \text{ mm min}^{-1}$ , an effective resolution of  $\sim 20 \text{ mm}$  was achieved (McConnell et al., 2002; McConnell, 2010; Pasteris et al., 2014a; 2014b). For this thesis, it is the additional ultra-trace elements and sulphur that are used to match the ages between the BAS JRI ice core, and a very well-dated deep core from the West Antarctic Ice Sheet (the United States WAIS Divide Ice Core).

### 3.3.2 *Stable Water Isotopes*

For BI and FP, the stable water isotope ( $\delta\text{D}$  and  $\delta^{18}\text{O}$ ) profiles were obtained prior to the commencement of this study by measuring discrete samples cut from the cores. Measurements were made using an Isotope Ratio Mass Spectrometer (IRMS) at the NERC Isotope Geochemistry Laboratory (NIGL, courtesy of Carol Arrowsmith) and using two cavity ring down laser spectrometers at BAS. The water isotope data for the two institutes were compiled by R. Mulvaney (pers comm). Discrete samples were cut from the original cores at a range of resolutions: initially at  $\sim 550 \text{ mm}$  (the 'bag average') to give a rapid overview of the shape of the isotope profile and likely age range along the full core depth, and subsequently at  $110 \text{ mm}$  near the surface and decreasing in sample size down to  $10 \text{ mm}$  at full depth to improve the resolution of the isotope/climate record. A parallel study completed during the course of this research project by Masters Student, Amy Pike, took very high-resolution samples of the FP ice core in the upper depths of the ice core record and measured stable water isotope content. The highest resolution data available were used in this thesis.

### 3.4 Laser Ablation Inductively-Coupled Plasma Mass Spectrometry

The following chemical analysis has been carried out by myself for the purpose of this study. In this thesis, the age-depth profile for BI is constructed using glaciological models (section 2.5), and will be assessed against ice chemistry measurements made using a novel method in ultra-high resolution trace-element analysis. The work described in this section contributes to the second objective outlined in section 1.2.1, and it involves making measurements of annual layer thickness which may be compared with accumulation

reconstructions developed as part of the first objective. To observe seasonal cycles in chemistry in the glacial period, where the layer thickness is very small, ice chemistry was measured at a sub-millimetre resolution using laser ablation ICP-MS (LA ICP-MS). The analysis of BI ice using LA ICP-MS was completed at the W.M. Keck Laser Ice Facility, part of the Climate Change Institute (CCI), University of Maine, USA, in collaboration with Dr. Sharon Sneed and Professor Paul A. Mayewski. Annual layer thicknesses were measured at depths where seasonal cycles could not be retrieved using standard laboratory methods. The LA ICP-MS methodology is a novel method for Antarctic ice (Muller et al., 2011; Mayewski et al., 2014; Sneed et al., 2015). The measurements for BI ice represent the first test of LA ICP-MS on Antarctic ice from the last glacial period; this is significant because annual layers from this period of low mean annual accumulation will have a mean thickness of less than 5 mm, which is beyond the means of standard laboratory methods. The following section outlines the methodology used in obtaining ultra-high resolution measurements using LA ICP-MS.

#### *3.4.1 Sampling Strategy for LA ICP-MS*

In order to validate the modelled estimates for annual layer thickness, samples of ice were taken at several depths along the BI ice core. The large variations in surface temperature that occur over glacial-interglacial cycles lead to large differences in the stable water isotope record. Therefore, it is relatively easy to identify which sections of the ice core record were originally deposited during an interglacial or a glacial period, by comparing stable water isotope records with published Greenland and Antarctic ice core records (Rasmussen et al., 2014; Sigl et al., 2016). In this study, samples have been taken from sections of the BI core identified as the mid-Holocene period and the last glacial period.

Sample depths are listed below; within each ice core bag (table 3.03), sample depths were chosen based on the condition of the archive material and so the ice sample has not been taken from the same place in each ice core bag. The inconsistency in the sampling strategy from the depth point in each ice core bag yields no significant difference to the analytical results as all of the ice samples are treated for potential contamination from the drilling process (this process is outlined in section 3.5.4). Table 3.03 lists the bottom depth of the ice core bag as well as the depth range of analysed ice and the approximate age of the ice, based on its position in the isotopic record.

Table 3.03: BI sample depths for LA ICP-MS. The assumed time-origin of deposition and an estimated age using a simple age-depth model are also included.

Core Number	Bag	Bottom depth of ice core bag (m below the surface)	Analysed ice (m below the surface)	Assumed origin in time (based on the isotope record)	Estimated age using a simple age-depth model (ka BP)
03/T2/826		454.31	454.11 – 454.15	Mid-Holocene	5.5
03/T2/830		456.51	456.31 – 456.35	Mid-Holocene	5.6
03/T2/834		458.71	458.51 – 458.59	Mid-Holocene	5.6
AQ/T2/1263		694.65	694.45 – 694.53	Last Glacial Period	27.1
AQ/T2/1265		695.75	695.55 – 695.67	Last Glacial Period	27.4
AQ/T2/1267		696.85	696.65 – 696.73	Last Glacial Period	27.7
AQ/T2/1278		702.9	702.35 – 702.43	Last Glacial Period	29.7
AQ/T2/1281		704.55	704.51 – 704.55	Last Glacial Period	30.4
AQ/T2/1285		706.75	706.20 – 706.40	Last Glacial Period	31.1

### 3.4.2 Cutting Process

Ice samples were cut in cold room conditions at around 253 K. During the cutting process, ice loss from the band saw was accounted for to ensure the ice samples were cut at 30 mm x 15 mm dimensions. After cutting, sticks of ice were placed in plastic lay-flat bags with the ice core bag number and top of the core clearly indicated. The ice samples were cut from the inner section of the archive material to avoid potential contamination by the drilling fluid residue on the exterior of the ice core; this is demonstrated in fig. 3.02 below.

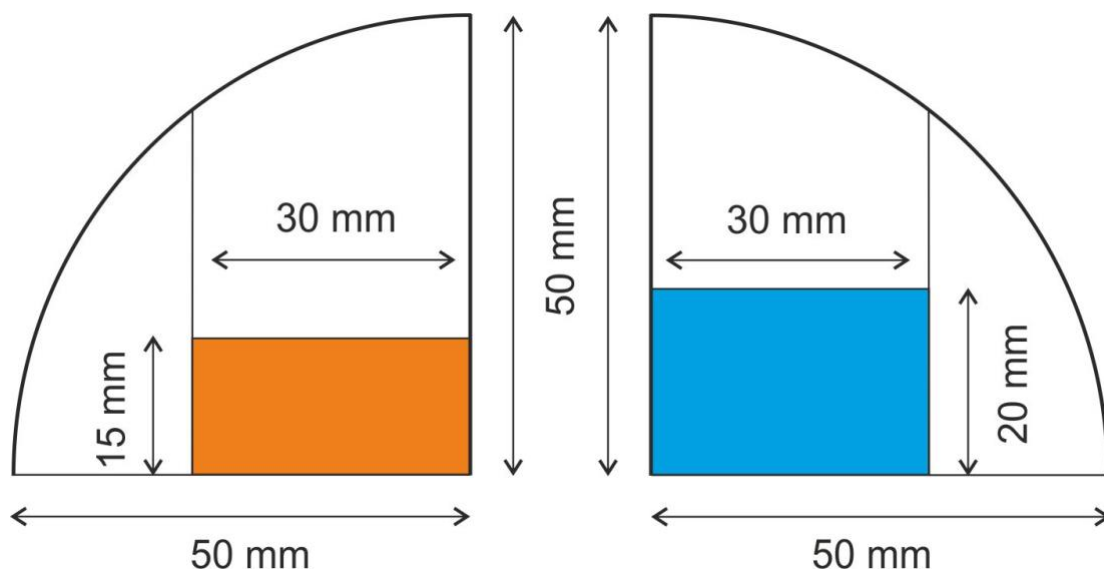


Figure 3.02: Diagram of ice sampling from the archive material; left: the orange shaded section shows sampled ice for LA ICP-MS; right: the blue section shows sampled ice for discrete sampling (see section 3.5).

### 3.4.3 Chemical Analysis using LA ICP-MS

For the analysis completed at the CCI, the ice samples were stored in a polystyrene box along with several eutectic gel packs to prevent melting en route from Cambridge to the US. From previous work (Mulvaney, unpublished) using temperature loggers, this method guaranteed minimal warming in the box for up to 24 hours. In transit to CCI, the ice was in the polystyrene box for 17 hours.

LA ICP-MS profiles were generated using the Sayre Cell™ cryocell, developed at the University of Maine, which is capable of holding up to 1 m of ice at 248 K and has a small volume (~20 cm<sup>3</sup>) open-design ablation chamber. The cryocell system is held underneath a New Wave UP-213 laser which is connected to a Thermo Element 2 ICP-MS with Teflon tubing; the engineering of the Sayre Cell™ cryocell is described by Sneed *et al.* (2015).

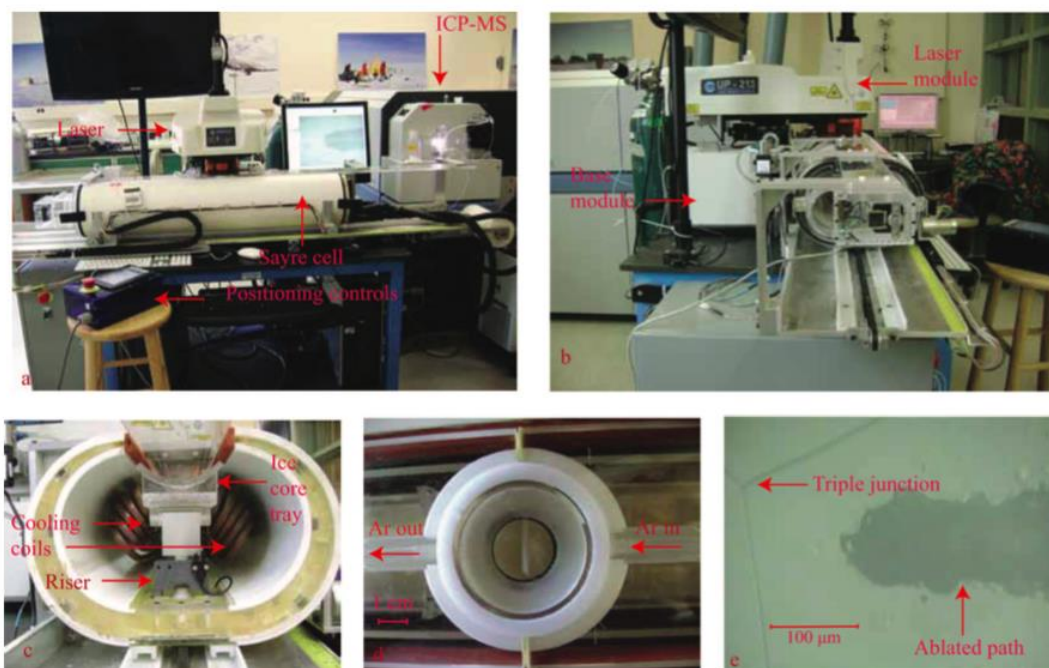


Figure 3.03: Images taken from Sneed et al. (2015): (a) Complete Sayre Cell™ system with labels; (b) Side view of the LA system, with modules labelled. (c) End view into the cryocell; (d) Top view of ablation chamber positioned in centre of fixed upper rail of cryocell; (e) Image of ablated pass on an ice sample. Triple junction can be seen in the surface.

Before analysis, the ice sample was cleaned by removing the outer 1 mm layer using a ceramic scraper. After this, the ice was placed in the cryocell and the Argon (Ar) gas flow was purged for 2 minutes. To obtain ultra-high resolution (sub-millimetre) chemical profiles, the ice is analysed using an individual line scan per element (fig. 3.03e). LA profiles are measured using a 100  $\mu\text{m}$ -diameter laser spot and are continuous for 40 mm. Once a line scan has been completed, the cryocell can be moved automatically to either continue the analysis for a further 40 mm, or to begin a new analysis parallel to the previous line scan. Line scans are separated by 200  $\mu\text{m}$  to prevent any overlap. Sampling resolution is 121.25  $\mu\text{m}$  per sample, but can vary depending on the laser spot diameter, firing rate, scan speed and the ICP-MS sampling rate (Sneed et al., 2015).

The BI ice samples were analysed for seasonal cycles of sodium (Na) only, with results available in counts per second ( $\text{counts s}^{-1}$  or cps). The relative intensity of element concentrations can be converted to concentrations (ppb) using calibration curves constructed by lasing frozen standards (Sneed et al., 2015).

Daily calibration of the ICP-MS is facilitated using a combination of liquid standards and frozen reference materials in a two-step process. Firstly, liquid standards of known concentrations were measured; the results of these initial analyses were used to construct the calibration curves for posterior analysis (the relative standard deviations of the liquid standards are shown below in table 3.04). The second step analysed frozen reference material, SLRS-5. SLRS-5 is frozen river water from the National Research Council, Canada, and was ablated by the LA ICP-MS system to establish the conversion factor between the liquid standards and ablated reference material.

*Table 3.04: Relative Standard Deviations ( $\sigma$ ) of liquid standard measurements for the CCI ICP-MS calibration.*

<b>Liquid Standard</b>	<b>Relative Standard Deviation of liquid standard measurements (%)</b>
Sodium (Na)	1.4
Calcium (Ca)	3.3
Iron (Fe)	2.9

#### 3.4.4 Mitigation of Sampling Errors

To ensure accurate results using the Sayre Cell™ cryocell, the base of the open cell must have an airtight seal with the ice sample (fig. 3.03d displays a top-view of the LA system and the cell that is sealed against the ice sample). Soundness of the seal is tested in two ways: (i) a flowmeter is built into the cryocell system and (ii) the ICP-MS is tuned with the ice in place so that a small leak would be observable in the ice chemistry signal (Sneed et al., 2015).

Secondly, the daily calibration of the Sayre Cell™ LA ICP-MS system could affect the consistency of the ice-core analysis if inhomogeneities were present in the frozen reference material used in the calibration process. To counter this potential limitation, a stepwise process is employed to minimise inhomogeneities in frozen ionic solutions. A 75 mm petri dish is partially filled with SLRS-5 standard and allowed to freeze at ~239 K in a class-100 clean room facility. The process is repeated two times, adding more SLRS-5 to the initial petri dish and allowing the solution to freeze. Finally, a layer of ~1 mm is added and allowed to freeze. Three 10 mm ablated lines are lased in the frozen SLRS-5 and the mean counts s<sup>-1</sup>

for each element is used to account for any inhomogeneities. The results of this stepwise process are discussed in Sneed *et al.* (2015).

### 3.5 Discrete Sampling at a high resolution

A second technique used in obtaining high-resolution chemical profiles from an ice core measures ion concentrations of the bulk content of small, discrete samples. This technique, hereafter referred to as the 'discrete sampling' technique, differs from the LA ICP-MS and CFA techniques in that a section of ice is not measured continuously on one instrument. However, it is similar to LA ICP-MS and CFA techniques in that, where the sampling resolution is sufficient, annual layers can be identified and hence the annual layer thickness can be measured along the ice core. By developing methods of high-resolution sampling, discrete sampling can obtain annual layer thickness measurements at a higher standard laboratory resolution than is currently available using a CFA system (~10 mm).

As outlined in section 1.2.1, the second objective of this study is to obtain measurements of annual layer thickness in the three deep ice cores in order to assess the accuracy of accumulation reconstructions developed through the first objective. In addition to the LA ICP-MS analysis that has been carried out on BI ice (as described in section 3.4), discrete sampling at a high resolution has been used to analyse ice samples from the BI and FP ice cores. To assess the reliability of LA ICP-MS at ultra-high resolution, a comparison study was required. For this comparison study, discrete samples were cut on parallel sections of the ice (fig. 3.02), and measured using IC. For the upper depth ranges analysed (454 – 459 m), three 200 mm sections of ice were analysed, with each section being discretely subsampled at a spatial resolution of 5 mm resolution using a band saw. The 200 mm sections of ice expand the LA ICP-MS records covering parallel sections of ice, where 40 – 80 mm of ice was analysed. At the greatest depths analysed (702 – 705 m), two 80 mm sections of ice were analysed, with each being cut into discrete samples at a spatial resolution of 0.32 mm; this higher resolution was achieved using a microtome device.

In addition to the discrete sampling on BI, used to compare with – and expand upon – LA ICP-MS analysis, sections of the FP ice core have been analysed using the discrete sampling technique. This was done in conjunction with the analysis of BI, in order to fulfil the second objective of this study and assess the accumulation reconstructions developed through the first objective (section 1.2.1). The sampling strategy for the FP analysis differs from BI, as sections of ice were chosen for analysis using the model estimates for layer thickness

(results of the model that was used to estimate mean annual layer thickness are presented in Chapter 4). Depths were initially chosen for the FP ice core where the modelled annual layer thickness was ~20 mm. This is at a depth in the ice core profile where ice, according to the stable water isotope profile, is considered to have originally been deposited during the Mid-Holocene. Subsequent sample depths were chosen when the modelled annual layer thickness had halved, continuing until the annual layer thickness estimate was ~5 mm. At the greatest depth analysed, the stable water isotope profile suggests that the ice was deposited during the transition into the Early Holocene. Sections of ice were cut at 80 mm, and sampled using the microtome device at a spatial resolution of 0.32 mm.

The remaining subsections of this chapter section outline the sample depth ranges for each core, and describe in detail the cutting processes for high- and low-resolution discrete sampling (using a band saw and the microtome device), and subsequent analysis using IC. The measures taken to mitigate potential errors in the sampling and analytical process are also outlined.

### 3.5.1 *Sampling Strategy for Discrete Methods*

The following section describes the sampling strategies used for the two ice cores. Sampling strategies differ for the FP and BI ice cores, due to the ongoing development of the sampling process throughout the study.

#### 3.5.1.1 *Berkner Island*

Five sections of ice were analysed using a discrete sampling method for comparison with LA ICP-MS cation results. The sections of ice were cut using a band saw into dimensions of 30 mm x 20 mm (see fig. 3.02), with the length of sampled ice ranging between 80 mm and 200 mm of ice before they were cut into discrete samples. After this sampling process, sticks of ice were placed in plastic lay-flat bags with the ice core bag number and top of the core clearly indicated.

The sections of ice originating from the Mid-Holocene period were sampled at a resolution of 5 mm (table 3.05), and were cut using a band saw. Deeper sections of ice originating from the last glacial period were sampled at a resolution of 0.32 mm, and have been cut using the microtome device. The sections of ice sampled, the depth range in the ice core, the sampling resolution, and the assumed time of deposition are outlined in table 3.05.

Table 3.05: BI sample depths for discrete sampling. The assumed original of deposition and an estimated age using a simple age-depth model are also included.

Core Bag Number	Bottom depth (m)	Analysed ice (m)	Sampling Resolution (mm)	Assumed origin in time (based on the isotope record)	Estimated age using a simple age-depth model (ka BP)
03/T2/828	455.41	455.21 – 455.41	5.00	Mid-Holocene	5.5
03/T2/830	456.51	456.31 – 456.51	5.00	Mid-Holocene	5.6
03/T2/834	458.71	458.51 – 458.71	5.00	Mid-Holocene	5.6
AQ/T2/1278	702.9	702.35 – 702.43	0.32	Last Glacial Period	29.7
AQ/T2/1285	706.75	706.3 – 706.38	0.32	Last Glacial Period	31.1

### 3.5.1.2 Fletcher Promontory

As with BI, FP ice was sampled at dimensions 30 mm x 20 mm. Originally, the sections of ice were cut to 80 mm in length but some ice at the bottom of each section was lost due to the sample fracturing in the vice system of the microtome. All of the samples from FP were cut using a microtome device at a sampling resolution of 0.32 mm. Table 3.06 outlines the sample characteristics including the depth range, sampling resolution, and the assumed period of deposition.

Table 3.06: FP sample depths for discrete sampling. The assumed original of deposition and an estimated age using a simple age-depth model are also included.

Core Bag Number	Bottom depth (m)	Analysed ice (m)	Sampling Resolution (mm)	Assumed origin in time	Estimated age using a simple age-depth model (ka BP)
11/FP/532	425.6	425.419 – 425.600	0.32	Mid-Holocene	4.9
11/FP/605	484.2	484.086 – 484.157	0.32	Mid-Holocene	7.5
11/FP/654	523.2	523.121 – 523.2	0.32	Early Holocene	10.9

### 3.5.2 Cutting Process

Using the prepared sticks of ice for each ice core, one of two techniques of discrete sampling was used, depending on the resolution required. The lower resolution technique involved using a band saw, this was sufficient for a 5 mm resolution. For ice originating from deeper in the ice core, a microtome technique was employed to achieve sub-millimetre resolution, but it should be noted that this method is time- and labour-expensive. The methods for each technique are described below. Fig. 3.04 shows the cold room set-up for the band saw and microtome techniques.

#### 3.5.2.1 Band Saw Cutting

Discrete samples were cut at 5 mm resolution using a band saw in the cold room. The band saw has a blade of 1mm thickness which causes ice loss between samples and is accounted for in the resolution calculation.

#### 3.5.2.2 Microtome Cutting

The microtome is able to hold a section of ice in a mantle system (fig. 3.04b; 3.04c). Once mounted, the ice was passed under the blade; with every forward stroke under the blade, the mantle automatically raises 40µm, thus the exact sample size could be determined by

the number of times the ice is passed under the blade and collected in the same vial. As this method shaves the ice at a high resolution and the sample remains on the microtome blade until it is manually brushed into the vial, no ice loss is recorded.



*Figure 3.04: Photos taken of the cold room sampling set-up. From top left: (a) the band saw; (b) a front profile of the microtome system; (c) a section of ice held in the mantle system of the microtome during sampling; (d) Collecting a discretely-cut sample on the microtome blade using a sterile pipette tip.*

### 3.5.3 *Chemical Analysis using Discrete Methods*

Ion profiles were measured on a Dionex IC 4000 IC system in a class-100 clean room, which has less than 100 particles of  $0.5 \mu\text{m ft}^{-3}$ . Use of an injection volume of only 10  $\mu\text{L}$  into the IC separator column increased the spatial resolution from 100  $\mu\text{L}$  used in earlier discrete sampling studies carried out at BAS due to the lower volume of sample required for IC injection. Two channels measure a full ion profile: for the cations, sodium ( $\text{Na}^+$ ), potassium ( $\text{K}^+$ ), magnesium ( $\text{Mg}^{2+}$ ) and calcium ( $\text{Ca}^{2+}$ ), whilst for the anions, chloride ( $\text{Cl}^-$ ), nitrate ( $\text{NO}_3^-$ ), methanesulfonic acid ( $\text{MSA}^-$ ), fluoride ( $\text{F}^-$ ), and sulphate ( $\text{SO}_4^{2-}$ ) were measured.

### 3.5.4 *Mitigation of Sampling Errors*

To ensure the discrete samples were cut cleanly, several precautions were designed and included in the methodology to minimise the risk of contamination to the low-volume samples. The methodology aims to limit the apparatus with which the sample comes into contact, and to minimise outer surface contamination. Specifically, two additional procedures were included to confirm the continued cleanliness of the sample throughout the process.

#### 3.5.4.1 *Ensuring clean apparatus*

In order to prevent contamination of the sample, protective clothing and powder-free nitrile gloves were worn throughout the sampling process. All of the apparatus was cleaned before and after the cutting process using isopropanol, including the tongs, a scalpel and the band saw and the microtome device. The ice sample was only handled with tongs and the outer millimetre of the ice sample was scraped away using a scalpel to remove any contaminants from the surface of the sample.

In addition to cleaning the microtome blade using isopropanol prior to a cutting session, a pre-frozen section of ultra-high purity (UHP) water was passed under the blade to ensure it had been cleaned thoroughly. Five 0.32 mm samples of UHP shavings were collected for use as a background standard for the cold room method during the chemical analysis of the Antarctic ice samples. After each section of Antarctic ice was sampled, the work surface and surroundings were cleaned to remove snow powder generated by the cutting process, to avoid contamination.

#### 3.5.4.2 *Potential contamination in the sampling process using the microtome*

The initial procedure used a paintbrush to collect the sample ice shavings from the microtome blade into 10 ml vials, before transferring the melted sample to smaller 2 ml vials by a pipette. Measurement of procedural blanks of frozen UHP water that had been in contact with each piece of apparatus showed negligible concentrations except for the samples that had been in contact with the paintbrush and the tongs (see table 3.07). As a result, the paintbrush was removed from the methodology and instead a plastic pipette tip was used to collect ice shavings directly into 2 ml vials to limit the total pieces of apparatus used. Extra care was taken to clean the metal tongs before sample preparation, with the UHP samples used as a calibration for any remaining contamination from the tongs and the microtome blade.

Table 3.07 outlines the various experiments carried out to identify potential sources of contamination to the sample collection. For the results, “N/D” indicates where the concentration of the chemical species is lower than detection limits and negligible. Five samples were taken for each experiment and stored in their various conditions for 24 hours: “CL/x” is a UHP water sample in an unsealed vial that was stored in clean room conditions; “CL/Lx” is a UHP water sample in a sealed vial that was stored in clean room conditions; “T/x” is UHP water that has been in contact with the tongs; “PB/x” is a UHP water sample that has been in contact with the paintbrush; “CR/x” is a UHP water sample in an unsealed vial that was stored in cold room conditions (and melted in clean room conditions prior to analysis); “CR/Lx” is a UHP water sample in a sealed vial that was stored in cold room conditions; “LF/x” is UHP water that was frozen in a plastic lay-flat bag and sampled from the centre of the UHP ice core.

Table 3.07: Table of anion results for all instruments that come into contact with ice samples as part of the discrete sampling method. In the sample ID names, UHP water is referred to as MilliQ (MQ) water. N/D signifies 'not determined' (below the detection limit). Precision of the ion chromatography is estimated at 4-10% on measurements; the precision is lower for measurements close to the detection limit.

Sample ID	Contamination test	F (ppb)	MSA (ppb)	Cl (ppb)	NO <sub>3</sub> (ppb)	SO <sub>4</sub> (ppb)
<b>Detection limit (ppb)</b>		0.4	0.1	0.5	1.45	1.7
MQ/CL/1	UHP water samples in that have been stored in unsealed vials in clean room conditions for 24 hours	N/D	N/D	N/D	N/D	N/D
MQ/CL/2		N/D	N/D	N/D	N/D	N/D
MQ/CL/3		N/D	N/D	N/D	N/D	N/D
MQ/CL/4		N/D	N/D	N/D	N/D	N/D
MQ/CL/5		N/D	N/D	N/D	N/D	N/D
MQ/CL/L1	UHP water samples that have been stored in sealed vials in clean room conditions for 24 hours	N/D	N/D	N/D	0.5	N/D
MQ/CL/L2		N/D	N/D	N/D	N/D	N/D
MQ/CL/L3		N/D	N/D	N/D	N/D	N/D
MQ/CL/L4		N/D	N/D	N/D	N/D	N/D
MQ/CL/L5		N/D	N/D	N/D	N/D	N/D
MQ/T/1	UHP water samples that have been in contact with the tongs used in the sampling process	N/D	N/D	N/D	3.0	N/D
MQ/T/2		N/D	N/D	N/D	3.9	N/D
MQ/T/3		N/D	N/D	N/D	3.2	N/D
MQ/T/4		N/D	N/D	N/D	6.4	N/D
MQ/T/5		N/D	N/D	N/D	3.0	N/D
MQ/PB/1	UHP water	N/D	N/D	43.5	185.2	12.9

MQ/PB/2	samples that have been in contact with a paint brush used in the sampling process	N/D	N/D	31.4	40.7	7.6
MQ/PB/3		N/D	N/D	30.6	21.7	7.2
MQ/PB/4		N/D	N/D	29.3	17.2	6.8
MQ/PB/5		N/D	N/D	30.5	18.0	6.7
MQ/CR/1	UHP water samples that have been stored in unsealed vials in cold room conditions for 24 hours	N/D	N/D	N/D	N/D	N/D
MQ/CR/2		N/D	N/D	N/D	N/D	N/D
MQ/CR/3		N/D	N/D	N/D	N/D	N/D
MQ/CR/4		N/D	N/D	N/D	N/D	N/D
MQ/CR/5		N/D	N/D	N/D	N/D	N/D
MQ/CR/L1	UHP water samples that have been stored in sealed vials in cold room conditions for 24 hours	N/D	N/D	N/D	N/D	N/D
MQ/CR/L2		N/D	N/D	N/D	N/D	N/D
MQ/CR/L3		N/D	N/D	N/D	N/D	N/D
MQ/CR/L4		N/D	N/D	N/D	N/D	N/D
MQ/CR/L5		N/D	N/D	N/D	N/D	N/D
MQ/LF/1	UHP water samples that have been frozen in a plastic lay-flat bag	N/D	N/D	N/D	N/D	N/D
MQ/LF/2		N/D	N/D	N/D	N/D	N/D
MQ/LF/3		N/D	N/D	N/D	N/D	N/D
MQ/LF/4		N/D	N/D	N/D	N/D	N/D
MQ/LF/5		N/D	N/D	N/D	N/D	N/D

#### 3.5.4.3 Testing for contamination of outer core section

Thomas (2006) found that it was necessary to remove as much as 10mm from the outer edges of the ice core to remove contamination from handling. As part of that study, a full section of the GRIP ice core, 50 mm in length, was cut using a band saw and cleaned using a

scalpel to remove the outer millimetre of ice. The convex area of the cut section was then removed and sampled to test the hypothesis that drilling fluid contamination from the outer surface of the ice core permeates into the ice core section. Using a band saw, this convex section of ice was cut into 4 mm sections of ice from the outside edge to the inside edge until no ice remained (fig. 3.05). The ice sections were then melted and analysed via ion chromatography.

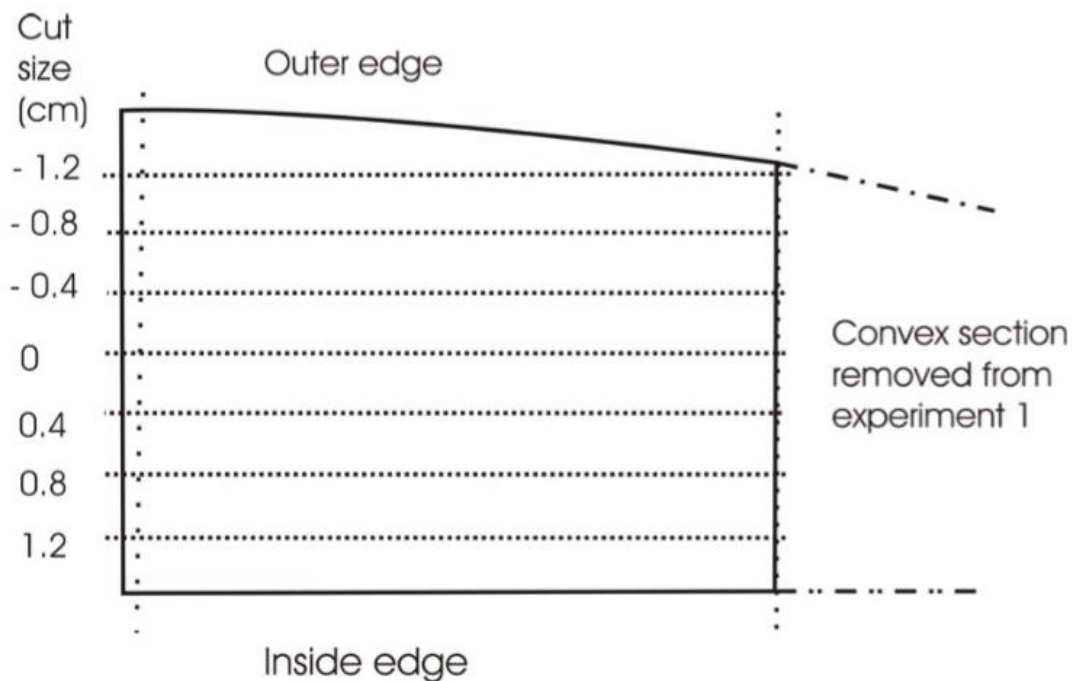


Figure 3.05: Diagram of the convex section of ice sampled in an experiment to test the hypothesis that contaminants from the drilling process permeate into the ice core (Thomas, 2006). Figure taken from Thomas (2006).

The ion concentrations measured from the cut sections were presented in relation to the distance from the centre of the ice core. The outer edges have the highest concentrations of all the ions measured whilst the lowest concentrations were found at the centre (fig. 3.06) (Thomas, 2006). This suggests that the outermost sections of ice are contaminated through the drilling process, and that the innermost section of the ice core should be analysed separately to yield an uncontaminated chemical profile. The maximum amount of ice that should be removed in order to eliminate the risk of contamination from the outer section of the ice core was determined to be 10 mm. Therefore, in this study the sampled ice was taken from the middle section of the archive ice in order to avoid the most contaminated

outer surface, and we can be confident that by scraping the outer millimetre at the start of every cutting session we will remove any remaining contamination from the ice sample.

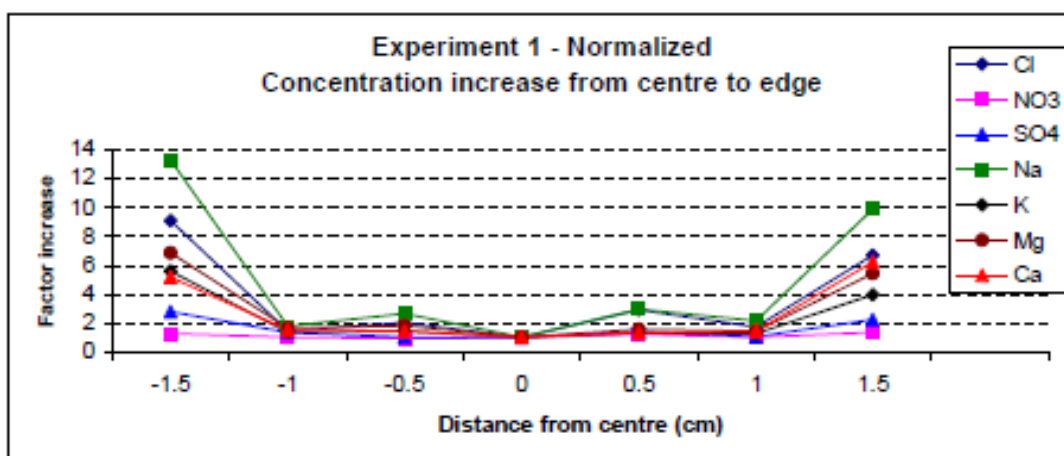


Figure 3.06: Factor increase of ion concentrations emanating from the centre of a section of the GRIP ice core. Results show concentrations decrease from the outside towards the centre of the core, suggesting that the outer 1 cm of ice contains contaminants from the drilling process. Figure taken from Thomas (2006).

### 3.5.5 Potential uses of high-resolution analysis on ice cores

By developing techniques that improve the spatial resolution at which ice cores can be sampled, measurements now have the potential to yield sub-annual profiles originating from periods of time currently not available using standard laboratory techniques. Sub-annual profiles can be an important tool for assessing the accuracy of accumulation reconstructions and thinning profiles. The comparison of modelled annual layer thickness with measured values can also be used as a constraint within an inverse approach. The following section outlines how such a technique has been used to improve a standalone age-depth model. Annual layer thickness has been used as an observational constraint within an inverse approach for all three age-depth profiles constructed during this study.

### 3.6 Development of ice-core modelling techniques

Working from a platform based on published techniques in ice core reconstructions, this study seeks to develop and improve age-depth modelling techniques by accounting for several factors that are important for dating high accumulation coastal ice cores. The techniques developed here employ free parameters that are solved for within the inverse

approach; these free parameters have been used to optimise either accumulation or thinning profiles and are constrained using observational data measured either *in situ* on the ice sheet, or in the ice-core record.

The following sections will outline the mathematical approaches that have been used in this study, from the established inverse approaches to the methodological approach particularly developed for this study.

### 3.6.1 *Inverse Probabilistic Approach*

Using the mathematical approach explained in section 2.5.6 (eq. 2.28 – 2.30), several inverse approaches have been developed in this study. These approaches use age horizons to anchor the modelled age-depth profile at specific depths using a variety of techniques. The general purpose of an inverse approach is to explore options within a defined model space and calculate optimal values for poorly-constrained parameters that are associated with either the accumulation reconstruction or thinning function. This permits the optimisation of the reconstructed profiles and leads to a better fit between age estimates and known-age horizons at shared depths.

In addition to the known-age horizons, the deep ice cores studied here can also be constrained using physical data, such as annual layer thickness measurements, obtained from the ice-phase of the ice core by both LA ICP-MS and the discrete sampling technique (sections 3.4 and 3.5). In the following section, two statistical techniques that can be applied to a forward model to iteratively search the model space and optimise age-depth profiles are described.

#### 3.6.1.1 *Monte Carlo Markov Chain (MCMC) algorithm*

The most simplistic inverse approach involves the use of an iterative MCMC model, where a single parameter is constrained using the observational data. Translated from mathematical notation, eq. 2.28 – 2.30 explore the model space using eq. 2.28 to quantify the misfit between the model estimates and the observational data, and hence constrain the  $p$ -parameter (Chapter 2; section 2.5).

This  $p$ -parameter controls the shape of the thinning function (section 2.5.3.3; eq. 2.13 – 2.17). By starting with *a priori* information (in the case of this model it is the empirically-calculated  $p$ -parameter; eq. 2.16), the model space is explored by increasing or decreasing the  $p$ -parameter value, and then re-solving for the thinning function, the annual-layer

thickness, and the age-depth profile. Comparison of these profiles with the observational data determines the direction of the next iteration by the assessment of the root mean square error (RMSE) value with the previous iteration. This approach seeks to minimise the RMSE value in order to find the  $p$ -parameter value which reduces the deviation between observed and modelled profiles the most. Convergence on a stable solution is assumed once RMSE values from the previous and present iterations differ by less than 0.005%.

The *a posteriori* information provides a new value for the  $p$ -parameter, which controls the shape of the vertical deformation and the thinning function; this also allows the recalculation of an *a posteriori* value for Glen's flow law exponent,  $n$ .

### 3.6.1.2 Directed Search Algorithm

The MCMC approach used in the ice-core age-depth model is ideal when assessing a large model space. Alternatively, when the boundaries of a model are well understood and can be constrained, one or more free parameters can be optimised using a 'pattern search' approach. This approach is part of the 'Directed Search' methods, and was first used by Fermi and Metropolis on the Los Alamos MANIAC (Lewis et al., 2000).

A 5-dimensional model, explained in detail later in this chapter, optimises the geothermal heat flux (GHF), surface temperature, and mean annual accumulation, whilst accounting for potential error in depth and borehole temperature measurements. The model uses a Directed Search algorithm to optimise the five variables, which are tightly bounded by small error margins. These tight boundaries mean that a random search approach, such as the MCMC algorithm, is not required. Instead, the Directed Search method is more useful in this scenario as it can efficiently and systematically calculate optimal values by working through every potential solution quickly.

### 3.6.1.3 Perturbed Accumulation Profile

In Chapter 2, the general principles behind perturbation theory were introduced (section 2.5.6). Perturbation theory has been used in this study to develop an inverse approach where the results are evaluated in a two-step model: in the first step, a perturbed accumulation profile is constructed by adding a smooth perturbation profile,  $\varepsilon(z)$ , to the empirically-derived initial accumulation profile,  $A_m$  (estimated using any of the three empirical accumulation relationships outlined in eq. 2.05 – 2.09).

The perturbation profile is a randomly-generated, spatially-variable array that varies with respect to the depth below the surface (mweq). The number of points in the perturbation profile is determined on an ice-core specific basis; observational constraints are located between two perturbation points and this controls the length of an ice-core profile that is perturbed by the same value. The perturbation profile is applied to  $A_{in}$  to calculate a randomly-perturbed accumulation estimate (eq. 3.01). The randomly-perturbed accumulation profile is then used in the second step of this inverse approach.

$$A(z) = A_{in} \cdot [1 + \varepsilon(z)] \quad (3.01)$$

The second step uses the Directed Search approach to solve for the optimal thinning function, as explained in section 3.6.1.2. To solve for the optimal shape function, the  $p$ -parameter used in the One-Dimensional thinning function was adjusted during the second step of the iterated model. The  $p$ -parameter is used in the optimisation process as the empirical estimate is uncertain; as outlined in the introduction of the One-Dimensional ice-flow model (section 2.5.3.3), the estimated value of the  $p$ -parameter is based on several assumptions. In addition, the One-Dimensional ice-flow model is based on the Shallow Ice Approximation (SIA) (Lliboutry, 1979) that does not necessarily hold true at the ice divide (Parrenin et al., 2007a). In the case of the deep ice cores drilled at Berkner Island and Fletcher Promontory, the Shallow Ice Approximation (SIA) does not hold due to the presence of Raymond stacks at the bed (Raymond, 1983). The plugs of ice forming stiff arches (a Raymond stack) at the bed lead to increased thinning towards the bed and a build-up of older ice. Empirical estimations of ice flow that do not consider this scenario would underestimate the age of the ice at the bed.

A profile that fits the boundary conditions and the observational data will 'pass' and be kept as a potential age-depth profile. For this technique, the boundary conditions are set as a range of values in the  $p$ -parameter of the thinning function. The boundaries for the  $p$ -parameter are set as  $0.5 \leq p \leq 5.5$  (Raymond, 1983; Wolff and Doake, 1986; Gillet-Chaulet et al., 2011).

Following the two-step approach, optimised profiles of accumulation and thinning yield profiles of annual layer thickness and age-depth. The optimised profiles of accumulation and thinning are assessed based on the annual layer thickness and age-depth profiles that they yield, by comparing the differences between the estimated age and annual layer thicknesses at depths corresponding to observed values using a root mean square error

analysis (RMSE, eq. 2.28). The final profiles of accumulation, thinning, annual layer thickness and age-depth were chosen based on the fit within the observational data confidence intervals.

### 3.6.2 Phase-Sensitive Radio Echo Sounding (pRES) Thinning Function

Two techniques have been developed in this study to estimate age-depth profiles using pRES data. The principles of pRES and its potential to be used to calculate an independent thinning function is explained in section 2.5.3.4. pRES measurements have been provided by Jonathan Kingslake (*pers. comm.*) The two techniques differ: the first technique is steady-state and assumes that the mean annual accumulation rate is unchanged with time. The second technique is a dynamic model that optimises the annual layer thickness profile in order to reconstruct a variable past accumulation rate.

#### 3.6.2.1 Steady-state Age-Depth Profile

A steady-state age-depth profile is estimated by assuming that mean annual accumulation is unchanged with respect to time,  $t$ , and depth,  $z$ . Vertical velocity,  $w$ , is interpreted from the pRES measurements,  $u(z)$ , applied to the mean present-day annual accumulation rate,  $b$ :

$$w(z) = \frac{\partial u}{\partial z} \cdot b \quad (3.02)$$

The age-depth profile of the ice core is calculated using a finite difference approach, using eq. 3.03. For this approach,  $i$  and  $j$  are indexes on a grid defined by the time- and depth-steps,  $dt$  and  $dz$ .

$$\text{age}_j^i = \text{age}_j^{i-1} + dt \cdot [1 - w(z)] \cdot \left( \frac{\text{age}_j^{i-1} - \text{age}_{j-1}^{i-1}}{dz} \right) \quad (3.03)$$

#### 3.6.2.2 Variable Accumulation History and pRES

The second model derives an annual layer thickness estimate using the pRES measurements as an independent thinning function. Age-depth is then estimated using eq. 2.21. An initial profile of annual layer thickness is derived in a forward model using eq. 2.19. Eq. 2.19 uses the difference of the pRES measurements with respect to depth as a vertical velocity profile, and requires initial estimates of accumulation and age (the integral of the inverse of vertical velocity,  $1/w$ , can be used to reconstruct an initial steady-state age-depth estimate).

Fig. 3.07 outlines the pRES model. Following the calculation of the initial estimates, the age-depth profile has been updated using an annual layer thickness profile that is calculated using a perturbed accumulation history. Eq. 2.19 can be repeated, using an updated age-depth profile and a perturbed accumulation history with each iteration. The initial accumulation profile is perturbed using eq. 3.01.

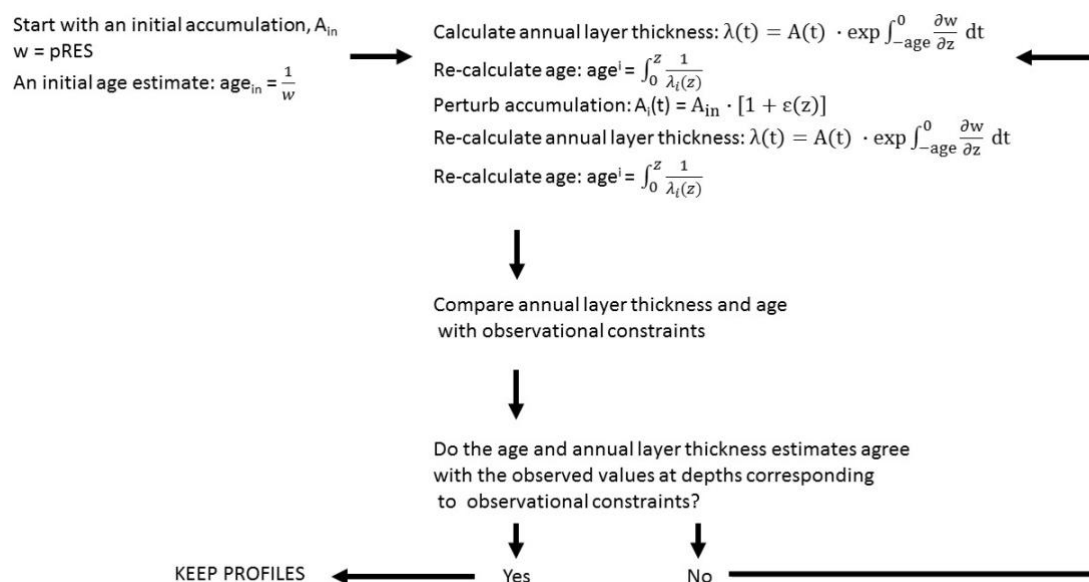


Figure 3.07: A flow diagram outlining an approach to reconstruct the accumulation, annual layer thickness, and age-depth profile using pRES measurements.

The model uses an MCMC algorithm to iterate the perturbation profile until the optimal profiles of accumulation, age, and annual layer thickness are found. Mean annual layer thicknesses and the age-depth profiles are compared with observational data. The approach is optimised by iterating eq. 2.19 until the model converges on the optimal profiles of age-depth, accumulation, and annual layer thickness; the optimal profiles are determined by comparison of the age-depth and annual layer thickness estimates with observational data. This process is repeated until 1000 possible profiles of accumulation, age, and annual layer thickness scenarios are outputted. The range of the 1000 profiles form the uncertainty in the model results.

Finally, the steps above are computed in snow-equivalent units because the vertical velocity measurements reflect densification of the firn layers in the upper 100 m of the ice core. Final modelled profiles are corrected for the firnification process using the density profile

(section 2.6.1). A thinning function,  $\eta$ , can be interpreted from the relationship between annual layer thickness and accumulation, after correction for density (for which the measured density profile is  $\rho(z)$ , and the density of ice is  $\rho_i$ ), with all profiles in snow-equivalent units:

$$\eta(z) = \frac{\lambda(z)}{A(z)} \bigg/ \frac{\rho(z)}{\rho_i} \quad (3.04)$$

### 3.6.3 Borehole Thermometry Profiles

In order to fulfil the fourth objective outlined in section 1.2.1, and to assess the degree to which *in situ* temperature measurements along the ice-core borehole can be used to reconstruct an independent surface temperature history, a second type of model has been developed. Based on the principles of heat advection, the advection from the surface of the ice sheet to the bedrock has been reconstructed using an MCMC Direct Search algorithm in order to minimise the error propagated from the observed depth measurements along the borehole. The model uses the equations outlined in section 2.5.5 (eq. 2.22 – 2.27), leaving the boundary conditions of GHF, mean annual accumulation,  $b$ , and surface temperature,  $T_s$ , open in order to solve for the optimal values by comparison with measured borehole temperature profiles. The model is outlined in the flow chart (fig. 3.08).

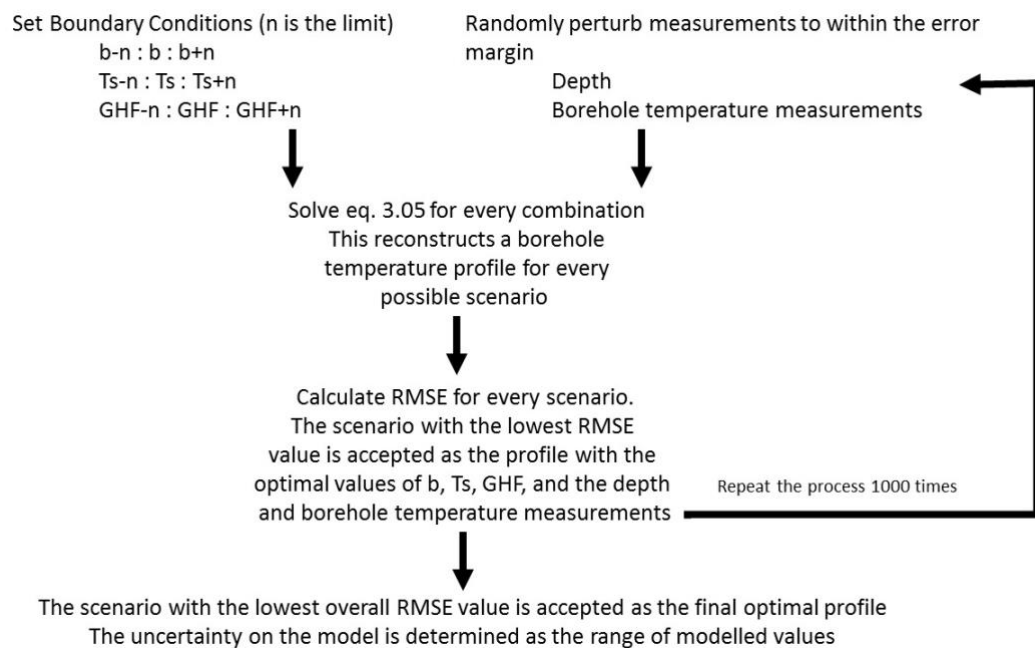


Figure 3.08: Flow chart outlining the methodological approach of the borehole temperature model.

Using the relationship for the advection of heat, three assumptions are made in this study, pursuant to similar studies by Nagornov et al. (2006) and Zagorodnov et al. (2012): (i) that the viscous heating term is negligible; (ii) that past variations in the ice velocity,  $u$ , have had little effect on the temperature field and accumulation rate due to the stability of the ice sheet thickness and location of the ice divide, and (iii) that the horizontal thermal gradient is negligible relative to the vertical gradient. As a result, we can assume that the temperature distribution can be completely described by solving the one-dimensional heat equation:

$$\alpha_D \frac{\partial^2 T}{\partial z^2} - w(z) \frac{\partial T}{\partial z} = 0 \quad (3.05)$$

Where  $\alpha_D$  is the term for thermal diffusivity, defined as  $\alpha_D = \alpha_C / \rho C$ . In this relationship,  $\rho$  is the density of pure ice,  $0.917 \text{ Mg m}^{-3}$ ,  $\alpha_C$  is the thermal conductivity ( $2.1 \text{ W m}^{-1} \text{ K}^{-1}$ ), and the specific heat capacity of ice ( $C$ ) is  $2097 \text{ J kg}^{-1} \text{ K}^{-1}$ . The density-corrected vertical velocity profile,  $w$ , is the product of the steady-state accumulation rate,  $b$ , and the Dansgaard-Johnsen thinning profile (Dansgaard and Johnsen, 1969). As part of the forward model,  $b$  and  $T_s$  (taken as the borehole temperature measurement at the surface of the ice sheet) are prescribed using present-day mean values in order to estimate GHF. These are the same values as used in the ice-core age-depth reconstructions for the three locations (table 3.01).

In order to limit potential error from the assumed present-day values and the depth and temperature measurements in GHF calculations,  $b$  and  $T_s$  are optimised as free parameters in an inverse approach. Using a 'pattern search' algorithm as part of a direct search method (section 3.6.1.2), the inverse model iterates the eq. 3.05, changing the value of the present-day accumulation rate, surface temperature and GHF. As a result, the optimal values of  $b$ ,  $T_s$ , and GHF are determined as the values that produce the best-fit reconstruction of the borehole temperature profile. Confidence intervals are estimated by solving for 1000 optimal values for each parameter; each unique parameter solution is optimised using a unique set of boundary conditions defined by perturbing the depth and temperature measurements within the prescribed error margin of the measured profiles (0.1 K for temperature measurement).

### 3.7 Summary

For this study into the most accurate techniques used to reconstruct the age-depth and past temperature profiles of three deep ice cores from the Antarctic Peninsula and Weddell Sea region, a combination of realistic ice flow modelling, observational data and novel

techniques in annual layer counting are required. Application of ultra-high resolution trace-element analysis will improve our interpretation of the accumulation rate in the deepest ice within the ice cores, where sub-annual profiles are not obtainable through regular techniques, due to small annual layer thicknesses. In order to be confident of the age-depth reconstructions presented in this study, novel applications of geophysical data have been introduced as a new option in estimating the thinning function at an ice divide, as well as reconstructing past surface temperature with a view to assessing the reliability of accumulation reconstructions from the stable water isotope profile. The following chapters will present the results of both these novel and published techniques in ice core modelling, and assess the results using an improved ice core chemical profile in order to best interpret the ice core records.



## Chapter 4: Results – Construction and analysis of age-depth models applied to the Fletcher Promontory deep ice core.

### 4.1 Introduction

Objective 1 of this project (section 1.2.1) is to quantify the variation in age-depth modelling techniques by comparing the relationships that are used to reconstruct accumulation and ice-sheet processes in order to model the age scale of an ice core. Quantification and assessment of these techniques is imperative in order to ensure that we apply the most robust modelling techniques to the Fletcher Promontory (FP), Berkner Island (BI), and James Ross Island (JRI) ice-cores. Within this chapter, multiple methods used in the reconstruction of ice sheet and atmospheric processes (sections 2.5, 2.6, and 3.6) have been synthesised and applied to the FP ice core profile in order to assess the variation between methods. In addition to using established techniques, this chapter also presents ice core profiles that have been reconstructed using novel techniques, combinations of techniques, and *in situ* measurements that can provide an independent validation of the modelling. The results are analysed with a view to understanding the impact that the use of each method can have on the age-depth profiles. The chapter only presents results for the FP ice core, since this is the only site at which all reconstruction techniques can be applied, due to the availability of *in situ* vertical velocity measurements at this site. Where applicable, each modelling technique has also been applied to the JRI and BI ice core records and results can be found in Appendix 1.

### 4.2 Ice-Core Reconstructions

As previously explained, the age of an ice particle at a particular depth is the sum of the annual layers above it. Following this principle, the most important properties that must be reconstructed are the local accumulation history and the rate of thinning of each annual layer subsequent to deposition. This allows us to estimate present-day annual layer thicknesses throughout the ice core, the integral of which yields an age-depth record. Accumulation and thinning profiles can be estimated using empirical reconstructions, and optimised using an inverse approach. This chapter will present empirical reconstructions for water-equivalent depth (mweq), surface temperature ( $T_s$ ), accumulation (A), and thinning ( $\eta$ ), before assessing the annual layer thickness ( $\lambda$ ) and age-depth profiles that are generated

via the application of thinning functions to each accumulation history. Accumulation is reconstructed using three empirical techniques, and three different thinning functions are applied to each accumulation reconstruction. In addition, an unconstrained age-depth reconstruction using phase-sensitive radio echo sounding (pRES) measurements is presented. Overall, ten unconstrained age-depth scenarios will be produced. The results of the inverse modelling techniques are presented as ‘constrained’ profiles later in the chapter.

In order to assess the techniques that are used in constructing the unconstrained age scales, inverse modelling approaches are used to constrain the ice-core reconstructions to observational data. This final step is carried out using four different modelling approaches, and the results are compared with an independent estimate of accumulation from a global circulation model (GCM). Different approaches in age-depth modelling can use different initial profiles of accumulation and thinning, resulting in multiple age-depth model scenarios from the same approach. Section 4.4 presents the ‘constrained’ profiles of accumulation, thinning, and age-depth, and is divided depending on the modelling approach used. The total number of model scenarios are outlined at the beginning of each subsection, detailing the *a priori* information that has been used.

#### 4.2.1 Observational Data

An inverse method requires *a priori* information to calculate an optimal age-depth profile; for this chapter the only observational data used to anchor the age-depth profiles are the age horizons identified throughout the ice core. These age horizons have been selected by matching clear features in the EPICA Dome C (EDC) stable water isotope profile with similar features observed in FP. Generally, these features are prominent warming events known as Antarctic Isotopic Maxima (AIM) observed in all Antarctic deep ice cores that span at least the last glacial cycle. This is with the exception of the youngest age horizon, which is identified as the peak in the stable water isotope signal at the transition from the LGM to the Holocene. The EDC age scale used is the Antarctic Ice Core Chronology 2012 (AICC2012), taken from Veres et al. (2013). Table 4.01 lists the age horizons, depth (snow, m, and water equivalent, mweq) and associated uncertainty on the age estimate. The associated uncertainty on each age constraint is taken from the uncertainty on the age from the AICC2012 (Bazin et al., 2013; Veres et al., 2013). Throughout this chapter, all accumulation, thinning, and age-depth profiles are presented in water equivalent depth units. The total thickness of the FP ice core is 599 mweq.

Table 4.01: List of age horizons used to constrain the FP ice core age-depth profile. Age horizons have been derived by Rob Mulvaney (pers. comm.) by matching FP stable water isotope signatures with EDC stable water isotope signatures of assumed-synchronous AIM events (Bazin et al., 2013; Veres et al., 2013).

Depth below the surface (m)	Depth below the surface (mweq)	Observed Age (ka BP)	Uncertainty (ka BP)	Observed feature
540.59	495.73	14.60	0.25	AIM 1
562.40	515.72	38.25	0.80	AIM 8
573.98	526.34	46.48	0.80	AIM 12
589.00	540.11	53.70	0.80	AIM 14
592.40	543.24	59.57	0.80	AIM 17

### 4.3 Empirical Reconstructions

The relationships for temperature, accumulation, and thinning functions, described in section 2.5 (eq. 2.03 – 2.19) and 3.6 (eq. 3.01 – 3.04), have been applied to the FP ice core. The relationships all assume a water-equivalent volume and depth scale, which is calculated using the Herron and Langway model (section 2.6). Age-depth profiles are estimated using an initial profile for accumulation and thinning. Three accumulation techniques, referred to as the Arrhenius (Arr, eq. 2.05; section 2.5.2.1), Clausius-Clapeyron (CC, eq. 2.06 – 2.08; section 2.5.2.2), and Simple Exponential (SE, eq. 2.09; section 2.5.2.3) relationships, are applied to the stable water isotope profile to reconstruct an empirical accumulation history. In order to estimate a present-day annual layer thickness, three thinning functions following the Nye (eq. 2.10; section 2.5.3.1), Dansgaard-Johnsen (D-J, eq. 2.11-2.12; section 2.5.3.2), and One-Dimensional Ice Flow (1-D, eq. 2.13-2.17; section 2.5.3.3) relationships are applied to the accumulation history. It has already been stated that in Polar Regions, where the mean annual surface temperature is below the freezing point and hence the annual snow deposition is preserved, the age of a particle of ice at a particular depth in the ice sheet is assumed to be the sum of the annual layers of snowfall above it. This is estimated using eq. 2.21. In addition to these techniques, a steady-state age-depth profile is interpreted from pRES *in situ* measurements of vertical velocity (eq. 2.19; eq. 3.03-3.04). This approach assumes accumulation has been steady through time.

Site-specific variables for the FP ice core are listed in table 4.02, including the present-day ice sheet thickness, mean annual present-day values for temperature (at the surface ( $T_s$ ), bed ( $T_b$ ), and inversion layer ( $T_i$ )), accumulation, and the stable water isotope ratio.

*Table 4.02: Site specific variables for the FP ice core. Information has been obtained from Mulvaney et al. (2014); the inversion temperature has been calculated using eq. 2.04.*

<b>Variables</b>	<b>FP</b>
Mean Annual Present-Day Accumulation Rate ( $\text{m yr}^{-1}$ )	0.38
Mean Annual Present-Day Deuterium Ratio, $\delta D^{\theta}$ (‰)	-258.64
Present-Day Ice-sheet thickness, H (m)	654.00
Mean Annual Present-Day Surface Temperature, $T_s^{\theta}$ (K)	246.00
Mean Annual Present-Day Surface Temperature, $T_s^{\theta}$ ( $^{\circ}\text{C}$ )	-27.10
Mean Annual Present-Day Temperature at the bed, $T_b$ (K)	255.00
Mean Annual Present-Day Temperature at the bed, $T_b$ ( $^{\circ}\text{C}$ )	-18.10
Mean Annual Present-Day Temperature at the inversion layer, $T_i^{\theta}$ (K)	254.01
Mean Annual Present-Day Temperature at the inversion layer, $T_i^{\theta}$ ( $^{\circ}\text{C}$ )	-19.14

#### 4.3.1 Water-Equivalent Depth Conversion

The ice core density profile is reconstructed using the Herron and Langway relationship (section 2.6). The density profile (fig. 4.01) is reconstructed in three stages, and a least squares regression analysis accounts for potential inconsistencies in the ice core (such as fractures and chips missing from the core). Using the density profile, the snow depth of the ice core is converted into a water equivalent depth by accounting for the lower density values in the shallow depths of the ice core.

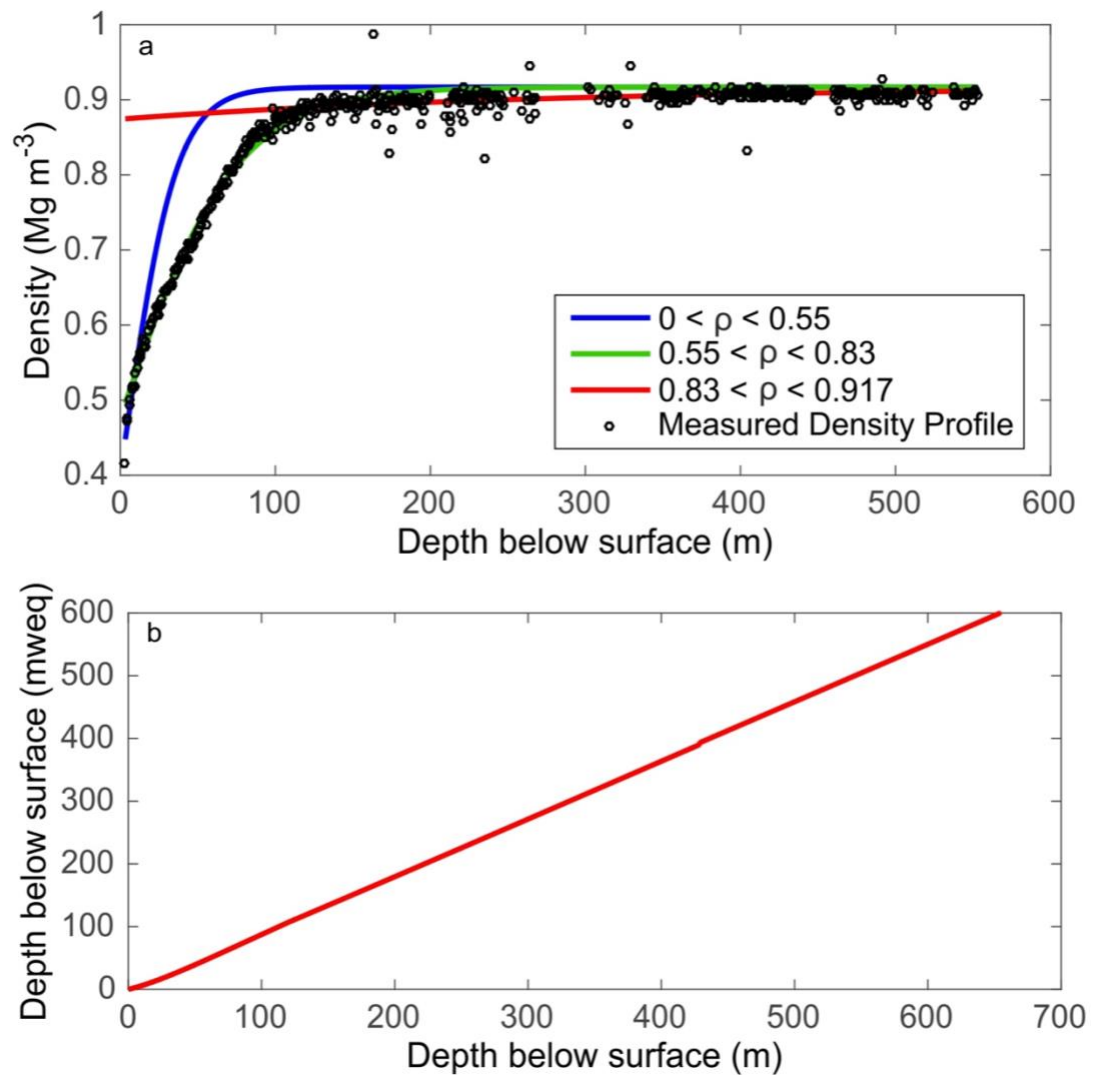


Figure 4.01: (a) Density Reconstruction for the FP ice core plotted against snow depth. The three different colours refer to the three stages of densification; parameters describing these three stages are optimised by least squares approach (section 2.6). The raw density profile is shown as black circles and was measured prior to this research project. Raw density was not measured for the full length of the ice core, and hence the reconstructions only go to the same depth. Density is extrapolated to the bed using the third stage equation fitted to the data; (b) Water-equivalent depth with respect to snow depth.

#### 4.3.2 Temperature Reconstruction

The techniques for reconstructing the surface temperature and inversion layer temperature history are presented in section 2.5.1 (eq. 2.03-2.04); the temperature profiles are plotted

against depth below surface in fig. 4.02. Temperature profiles are reconstructed using the stable water isotope profiles already available prior to this project.

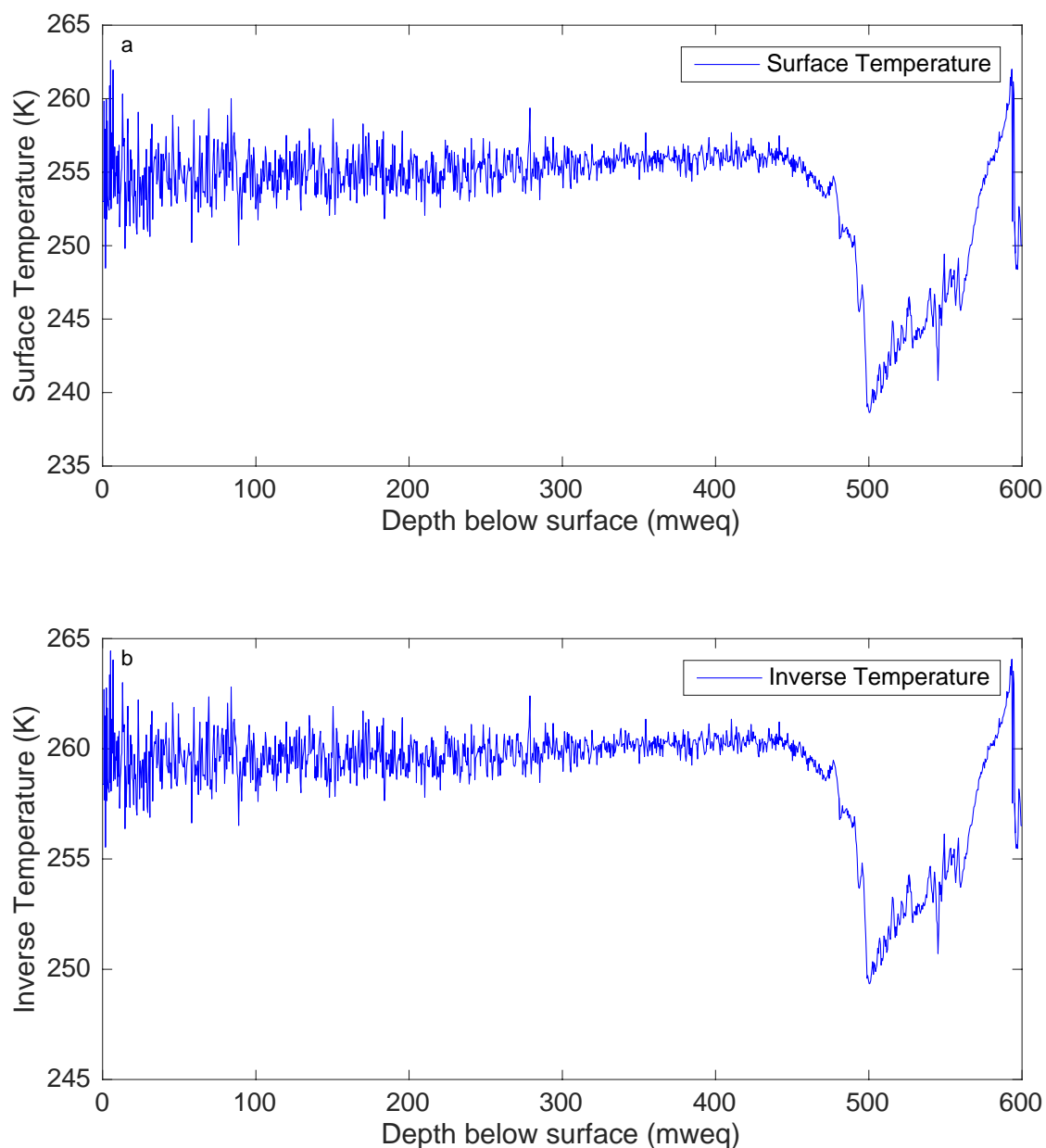


Figure 4.02: (a) Reconstructed surface temperature using eq. 2.03 using the stable water isotope profile obtained prior to this research project (section 2.5.1); (b) Reconstructed temperature at the inversion layer with respect to depth below the surface (mweq) using eq. 2.04 using the stable water isotope profile obtained prior to this research project (section 2.5.1). In both plots, a higher temperature at ~580 mweq that steadily decreases towards 500 mweq likely relates to the cooling from the last interglacial to the last glacial period. Furthermore, a sharp increase in temperature from ~500 mweq to 400 mweq is likely to be the transition from the Last Glacial Maximum (LGM) to the Holocene.

### 4.3.3 Accumulation Reconstructions

Three methods in accumulation reconstruction – that use the CC, SE and Arr relationships (section 2.5.2, eq. 2.05-2.09) – all assume that accumulation is proportional to the stable water isotope profile obtained from the ice cores. This is due to the shared assumption between the three empirical relationships that accumulation rates are partially dependent on the transport of moisture from warmer regions. The transportation is temperature-dependent, and hence there are obvious similarities between the three accumulation reconstructions and the surface temperature reconstruction, which is derived from the stable water isotope profile (fig. 4.02 and 4.03). Fig. 4.03 presents three empirical accumulation reconstructions, plotted against depth below surface, where the surface of the ice sheet is at 0 mweq. When converted to age, this depth corresponds to the year the ice core was drilled. The age of the ice increases with depth below surface.

The three accumulation reconstructions follow a similar shape due to the shared relationship based on stable water isotopes or temperature derived from the stable water isotope record. Between 500 mweq – 450 mweq, each accumulation reconstruction increases sharply. Based on the increases in stable water isotopes and temperature also observed in the FP record at this depth range, it has been hypothesised earlier in this chapter to be the transition from the LGM to the Holocene. Across this depth range, the temperature profile increases sharply by 15 K (fig. 4.02); the sensitivity of each technique is discussed in section 4.5.1.

The Simple Exponential (blue), Arrhenius (red), and Clausius-Clapeyron (purple) accumulation reconstructions are estimated as a difference in accumulation in comparison to the present-day mean annual accumulation rate, and hence estimate a mean annual accumulation rate throughout the upper 450 mweq close to the present-day value of  $0.38 \text{ m yr}^{-1}$ .

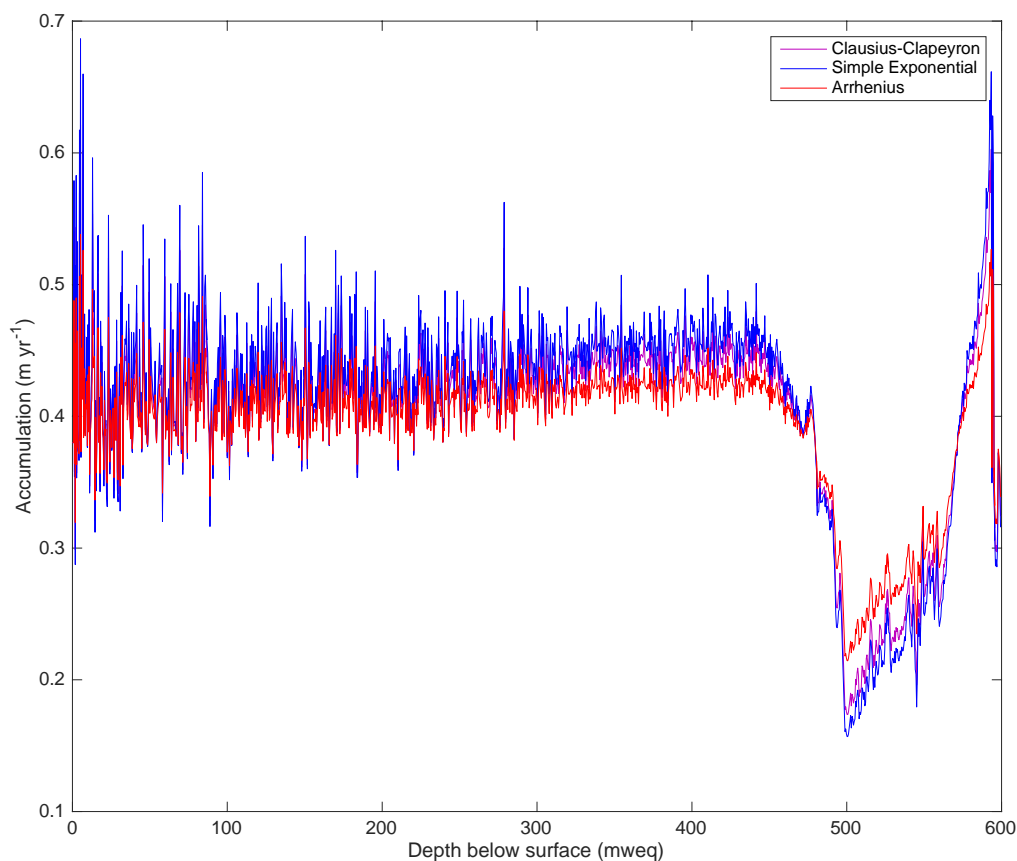


Figure 4.03: Accumulation reconstructions using empirical relationships using the stable water isotope profile obtained prior to this research project.

#### 4.3.4 Thinning Functions

Estimation of the compaction of annual layers due to total strain, and the effect on original layer thickness, is the second step in the age-depth reconstruction. The results of three methods – Nye, Dansgaard-Johnsen, and a One-Dimensional model (eq. 2.10 – 2.17; section 2.5.3) – that can estimate the rate of thinning of an original annual layer to its present-day thickness are presented (fig. 4.04). Unlike the accumulation reconstructions, these three techniques do not use any chemical or geophysical data obtained from the ice core or ice sheet. These methods provide only a depth-dependent view of the thinning function, and cannot account for any temporal variations in vertical velocity or ice flow. The thinning function is a non-dimensional ratio of the original annual layer thickness to the present-day annual layer thickness and varies with depth (in mweq), where 1 indicates no thinning at the surface, and 0 is total thinning at the bedrock. Mathematically translated, a thinning function with a value of 0 at the bed means that the age-depth profile will tend towards

infinity; the infinite value represents the high total strain that limits the precision of annual layer thickness estimates at the bed. As a result, the age scales presented in this chapter cover 99% of the ice core record, but do not yield an age at the bed, in order to prevent the age scale tending towards infinity.

The notable difference between the three thinning functions is the linearity of each profile. A steep gradient, where the thinning function decreases rapidly in the ice core profile, is interpreted as reflecting a high rate of thinning. The Nye relationship is a simple linear calculation; the linearity of the Dansgaard-Johnsen thinning function is determined by the prescribed basal shear depth ( $h$  – in this study I have used a value of 30% of the total ice sheet thickness,  $[0.3*H]$ ), whilst the shape of the One-Dimensional thinning function is determined by the value of the  $p$ -parameter (eq. 2.16). In an empirical reconstruction, the  $p$ -parameter directly controls the shape of the deformation profile that in turn controls the shape of the thinning function, presented in fig. 4.04. It is calculated by assuming a value for Glen's flow exponent of  $n = 3$ , and that the temperature gradient between the surface of an ice sheet and the bedrock is linear.

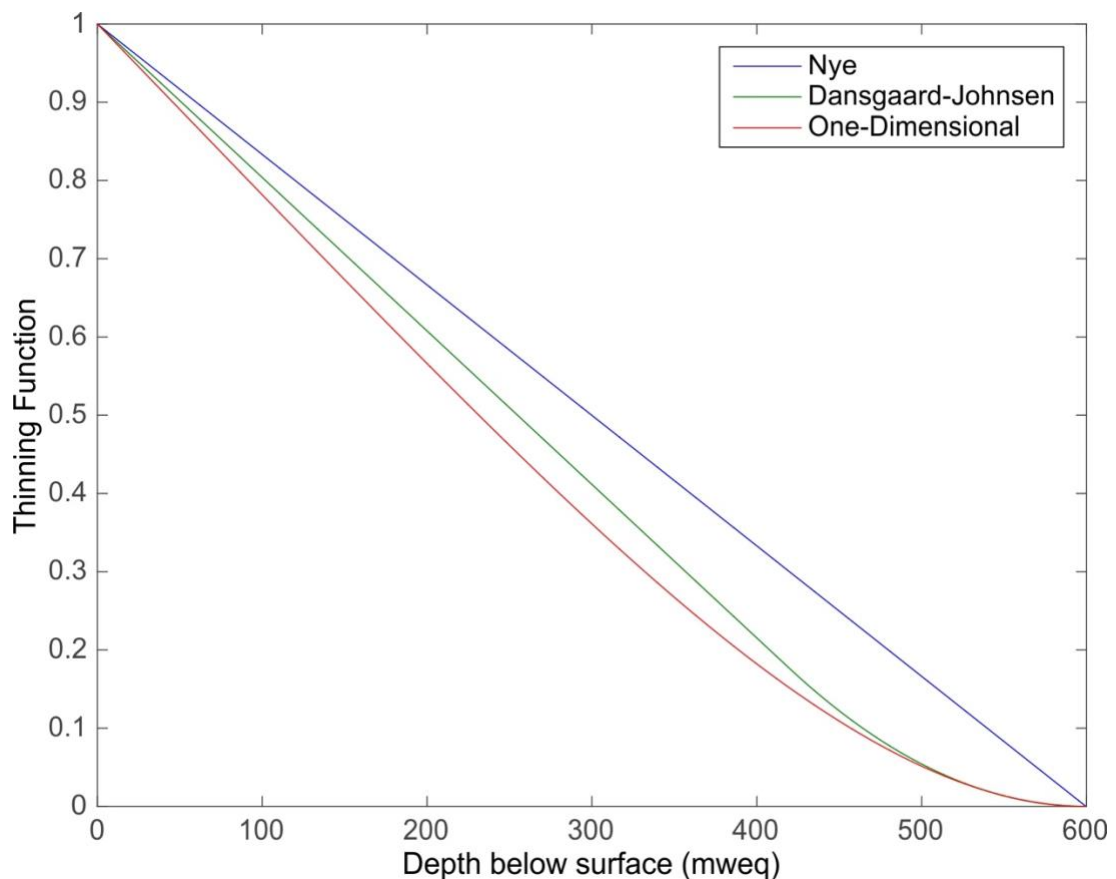
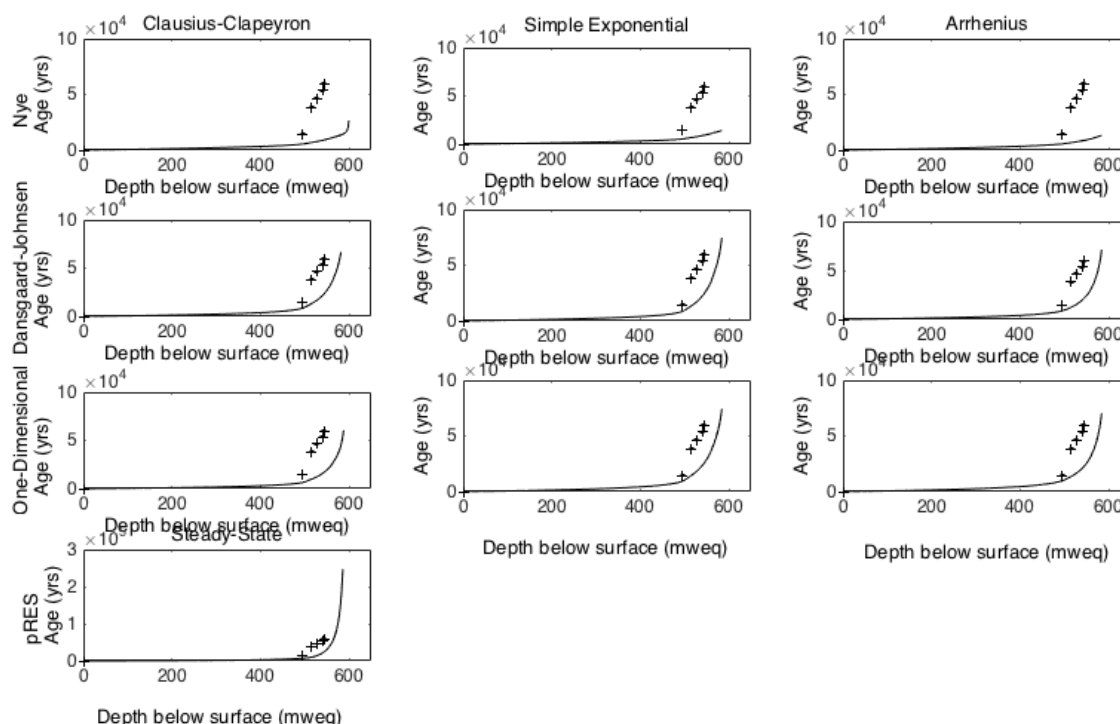


Figure 4.04: Unconstrained thinning functions – blue: Nye; green: Dansgaard-Johnsen; red: One-dimensional ice flow.

### 4.3.5 Age-Depth Profiles

Fig. 4.05 presents the age-depth profiles that are calculated by integrating annual layer thickness, which is calculated as the product of each of the accumulation and thinning function combinations. Results are presented in a table format: each column uses an accumulation estimate, combined with a thinning function that changes with each row, i.e. the first column presents the results of the Clausius-Clapeyron-derived accumulation history with each thinning function applied.

A tenth plot is presented at the bottom-left of fig. 4.05; in this particular case, using *in situ* measurements of vertical velocity from pRES and assuming a steady state rate of accumulation through time, an additional empirical age-depth profile can be reconstructed (section 2.5.3; eq. 2.18). For reference, the age horizons are marked on each plot by crosses so that the results can be compared with observational data, but this information has not been used to constrain the age-depth reconstructions. For further comparison, table 4.03 presents the age estimates at depths corresponding to age horizons for the ten empirical age-depth profiles.



*Figure 4.05: Age-depth profiles calculated by a combination of accumulation and thinning functions (grey) with respect to water equivalent depth below the surface of the ice sheet; age horizons plotted as black crosses with their associated age uncertainty. The uncertainty associated with each age constraint is represented as the height of the black cross marking each horizon, but this is too small to be visible in the figure. Each row applies a different thinning function; each column applies a different accumulation technique. This is with the exception of the bottom-left plot which assumes a steady-state rate of accumulation and uses in situ vertical velocity measurements to estimate an age-depth profile. All results present age with respect to the depth below the surface (mweq). None of the age-depth profiles agree with the age horizons, with the profiles using the Nye thinning technique reconstructing the youngest ages towards the bed (~20 ka BP) and One-Dimensional, Dansgaard-Johnsen, and pRES thinning profiles estimating an age close to the bed of 60-90 ka BP.*

*Table 4.03: Age estimates (yrs BP) at depths corresponding to age horizons in the FP ice core. Nine combinations of age-depth profiles using different empirical reconstructions of accumulation (Clausius-Clapeyron (CC), Simple Exponential (SE), and Arrhenius (Arr)), and different thinning functions (Nye, Dansgaard-Johnsen (DJ), and One-Dimensional (1-D)). A tenth set of age estimates are calculated using the empirical pRES model.*

		Age estimate (yrs BP)		
Chapter 4	Observed age and uncertainty (yrs)	Nye	DJ	1-D
<b>CC</b>	14600 ± 250	5474	8673	9590
	38250 ± 800	6866	13231	14347
	46480 ± 800	7629	16202	17390
	53700 ± 800	8753	21398	22630
	59570 ± 800	9028	22850	24079
		<b>Age estimate (yrs BP)</b>		
	Observed age and uncertainty (yrs)	Nye	DJ	1-D
<b>SE</b>	14600 ± 250	5389	8576	9477
	38250 ± 800	6908	13551	14669
	46480 ± 800	7729	16744	17940
	53700 ± 800	8929	22295	23538
	59570 ± 800	9221	23835	25075
		<b>Age estimate (yrs BP)</b>		
	Observed age and uncertainty (yrs)	Nye	DJ	1-D
<b>Arr</b>	14600 ± 250	5611	8828	9770
	38250 ± 800	6779	12656	13765
	46480 ± 800	7446	15252	16424
	53700 ± 800	8437	19838	21048
	59570 ± 800	8684	21141	22348
		<b>Age estimate (yrs BP)</b>		
	Observed age and uncertainty (yrs)	pRES		
<b>pRES</b>	14600 ± 250	7061		
	38250 ± 800	9979		
	46480 ± 800	13373		
	53700 ± 800	21337		
	59570 ± 800	23915		

#### 4.4 Constrained Profiles

The age-depth profiles constructed using the forward relationships in section 4.3.5 do not use age horizons to constrain the final age-depth profile. The results shown in fig. 4.05 do not fit the age constraints plotted for reference, and are referred to as unconstrained profiles. Optimised, or 'best-fit', profiles can be estimated by searching for optimal values of free parameters. The free parameter can be a single value, or a set of values, that is poorly constrained in the empirical model. It is notable that, through the development of the inverse approaches, the optimised parameters must balance the interplay between the accumulation and thinning profiles; i.e. a high mean annual accumulation rate must be balanced with a high rate of strain in order to reconstruct an annual layer thickness that

drives the age-depth profile through age constraints. In the previous chapters, a number of inverse methods have been outlined; further explanation of the approaches is given with the results. The accumulation and thinning relationships described in sections 4.3.3 and 4.3.4 are therefore used as *a priori* information for the IceChrono, Direct Search (DS), pRES, and Optimised Accumulation and Thinning (OptAcc) inverse approaches, which anchor the *a posteriori* profiles to age horizons (table 4.01). The following section presents the results of five approaches that explore the model space in order to estimate the optimal profiles of accumulation, thinning and age-depth.

#### 4.4.1 *IceChrono*

The IceChrono toolbox is introduced in section 2.7.1, as well as in Parrenin et al. (2015). Using the IceChrono model approach, seven scenarios, using different *a priori* information, reconstruct the optimal accumulation and thinning profiles, with an estimated uncertainty for the optimal profiles. In all cases the age horizons (table 4.01) are used as *a priori* information. Of the seven scenarios, three scenarios also use the three empirical accumulation profiles (section 4.3.3), where it is assumed that each accumulation estimate has a 95% confidence interval as *a priori* information; three use the three empirical thinning profiles (section 4.3.4) set with a 95% confidence interval as *a priori* information, and the final scenario uses the stable water isotope profile (obtained prior to this research project) in combination with the age horizons as *a priori* information (this model scenario will hereafter be referred to as the freely-calculated profile). The 95% confidence interval on *a priori* accumulation or thinning profiles is used to limit the degree to which these profiles are allowed to vary from their original values. In these scenarios, a good fit to the age horizons must therefore be achieved by perturbing the remaining profiles, or other free parameters in the calculation.

The IceChrono age-depth profiles differ greatly towards the bed; age-depth profiles reach a maximum age varying between 60 and 100 ka BP (fig. 4.06). The age estimate and uncertainty at the depths corresponding to observational constraints are presented in table 4.04. Model scenarios that use a Dansgaard-Johnsen and One-Dimensional thinning function yield similar age estimates and uncertainty at these 'known-age' depths despite the differences between reconstructed accumulation and thinning profiles (fig. 4.07). These two model scenarios do not estimate ages to within the age uncertainty of the observational data in the oldest two constraints. For the remaining scenarios, the age-depth profiles produced by IceChrono consistently reach the age horizon of ~14 ka BP one mweq earlier

than the corresponding depth at 496 mweq, but they nevertheless agree with the observed age horizon to within the modelled uncertainty (fig. 4.06; table 4.04). The modelled age estimates at 496 mweq, the depth corresponding to the first age constraint, are 156 - 220 years older than the age horizon, with the exception of the age estimate using the Nye thinning function which estimates an age at the corresponding depth 30 years younger than the age constraint.

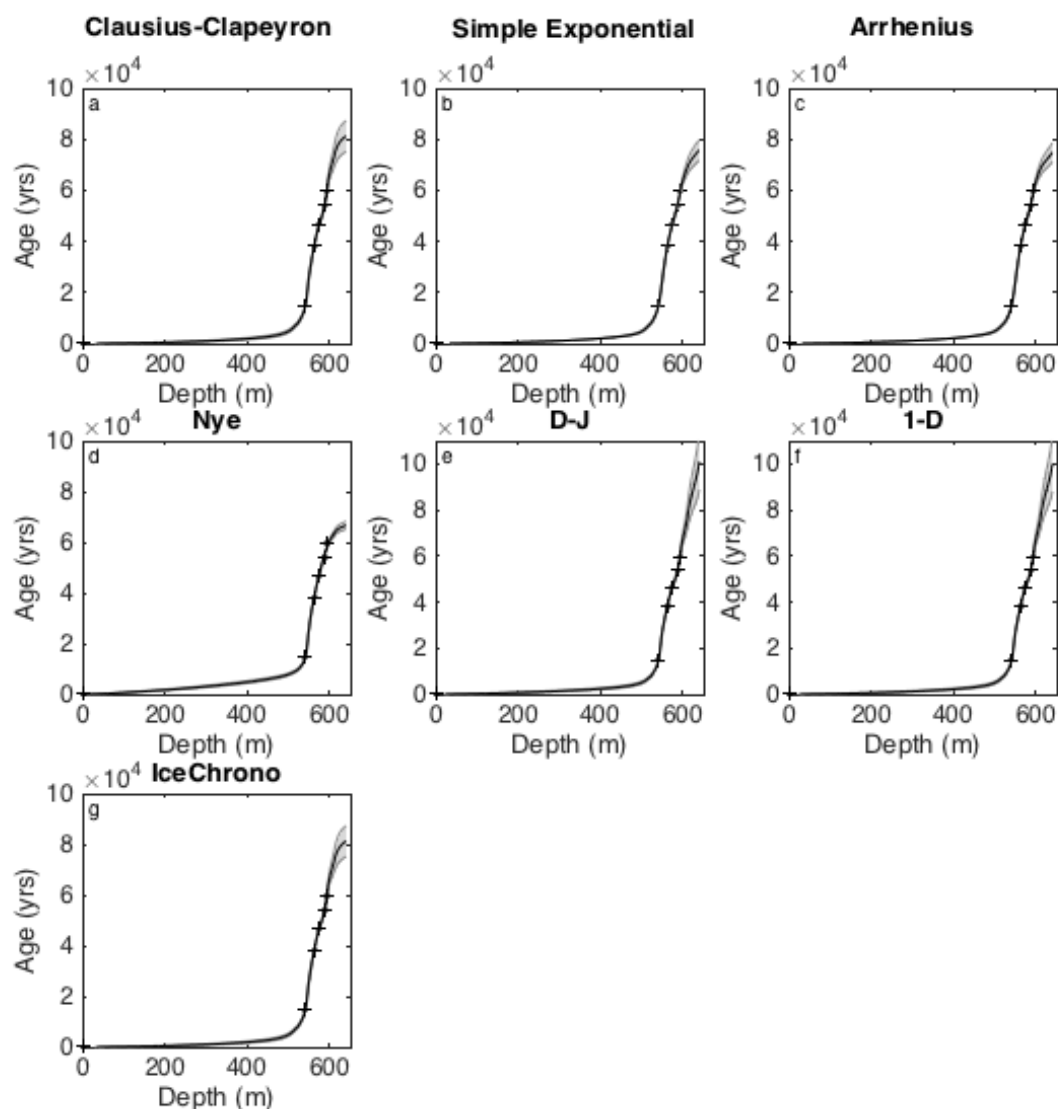


Figure 4.06: Age-depth profiles constructed using the IceChrono model. Top row (a-c): age-depth profiles with prior information on the accumulation profile; middle row (d-f): age-depth profiles with prior information on the thinning profile; bottom left (g): no prior information on either reconstruction. Uncertainty (grey) and age horizons with their associated uncertainty (black crosses) are included with each figure.

Table 4.03: Age estimate and uncertainty at the corresponding depth for the age constraints used in each scenario in the IceChrono model.

Depth (mweq)	Observed age and uncertainty (yrs BP)	Modelled age (yrs BP) and uncertainty (yrs BP)						
		CC	EXP	Arr	Nye	D-J	1-D	Free
495.73	14600 ± 250	14781 ± 943	14780 ± 273	14820 ± 273	14570 ± 265	14756 ± 273	14758 ± 275	14770 ± 277
515.72	38250 ± 800	38366 ± 977	38068 ± 448	38003 ± 449	38406 ± 418	38364 ± 459	38363 ± 461	38361 ± 467
526.34	46480 ± 800	46263 ± 995	46318 ± 434	46342 ± 434	46736 ± 379	46172 ± 450	46195 ± 452	46259 ± 459
540.11	53700 ± 800	55239 ± 1018	55582 ± 366	55589 ± 366	55870 ± 327	55254 ± 401	55237 ± 404	55238 ± 409
543.24	59570 ± 800	58732 ± 1023	58272 ± 429	58271 ± 429	57413 ± 378	58729 ± 456	58738 ± 458	58713 ± 462

The accumulation and thinning reconstructions that are produced when one of three empirical accumulation histories is set as boundary conditions with a 95% confidence interval are presented here (fig. 4.07 – 4.08). The empirical and optimised profiles of accumulation do not differ greatly in these scenarios. This is expected as a high confidence interval was assigned to each empirical profile. The freely-calculated scenario calculates an accumulation profile that suggests a similar mean accumulation rate throughout the Holocene (upper 520 m snow), but is more sensitive to changes in the stable water isotope ratio, as indicated by its variability (fig. 4.07a, grey line). The greatest deviations in *a posteriori* profiles occur during the last glacial period (~540 m; fig. 4.07a). The freely-calculated accumulation profile reaches similar minimum rates of accumulation ( $0.05 \text{ m yr}^{-1}$ ) as the Clausius-Clapeyron *a posteriori* profile. Unlike the empirical reconstructions of accumulation, the IceChrono scenario that uses a Simple Exponential relationship as *a priori* information predicts accumulation rates that are in the middle of the range of glacial accumulation rates; the Arrhenius relationship continues to estimate higher accumulation rates in comparison with the other techniques during glacial conditions (540 m). The higher rates of accumulation across 500 – 600 m result in a ‘kink’ feature in the thinning profiles for

the Arrhenius and Simple Exponential model scenarios (fig. 4.07b, red and blue lines); this feature is not replicated in model scenarios where mean accumulation rates reach a minimum value of  $0.05 \text{ m yr}^{-1}$  at 540 m.

In addition, the IceChrono model scenarios that use prescribed thinning functions at a 95% confidence interval to reconstruct accumulation and thinning profiles are presented in fig. 4.08. The thinning profiles display differing amounts of curvature. The differences between these thinning profiles are clear when comparing the modelled accumulation profiles for each *a priori* thinning profile; the freely-calculated, One-Dimensional, and Dansgaard-Johnsen reconstructions of accumulation demonstrate higher mean annual rates of accumulation in comparison to the Nye reconstruction of accumulation. The high rates of thinning are balanced by high accumulation rates to compensate for rapidly decreasing annual layer thickness (fig. 4.08). In contrast, the low rates of thinning from the Nye model leads to low rates of mean annual accumulation (fig. 4.08, green lines).

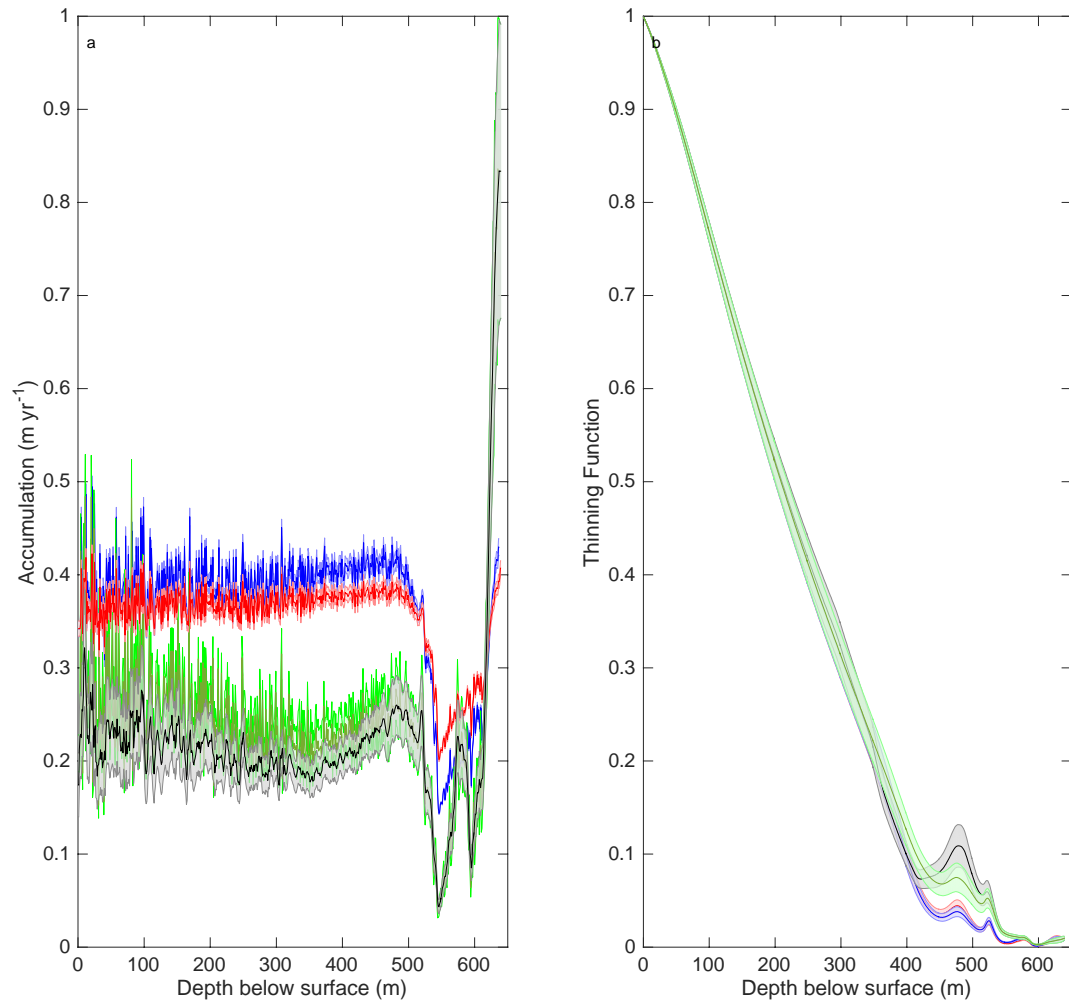


Figure 4.07: (a) Four accumulation reconstructions that have been optimised using the IceChrono toolbox, and (b) the associated thinning profiles for each model scenario. In these model scenarios, boundary accumulation profiles were fixed with 95% confidence to assess how this constraint would affect the thinning profile. Optimised profiles are colour-coded for each model scenario. Black: freely-calculated; green: Clausius-Clapeyron; blue: Simple Exponential; red: Arrhenius, with the associated uncertainty for each profile marked by a lighter shade of the main profile colour. The freely-calculated and Clausius-Clapeyron reconstructions are so similar that the freely-calculated reconstructions are presented as a 5-point moving average in order to smooth the profile and ensure that all profiles are visible.

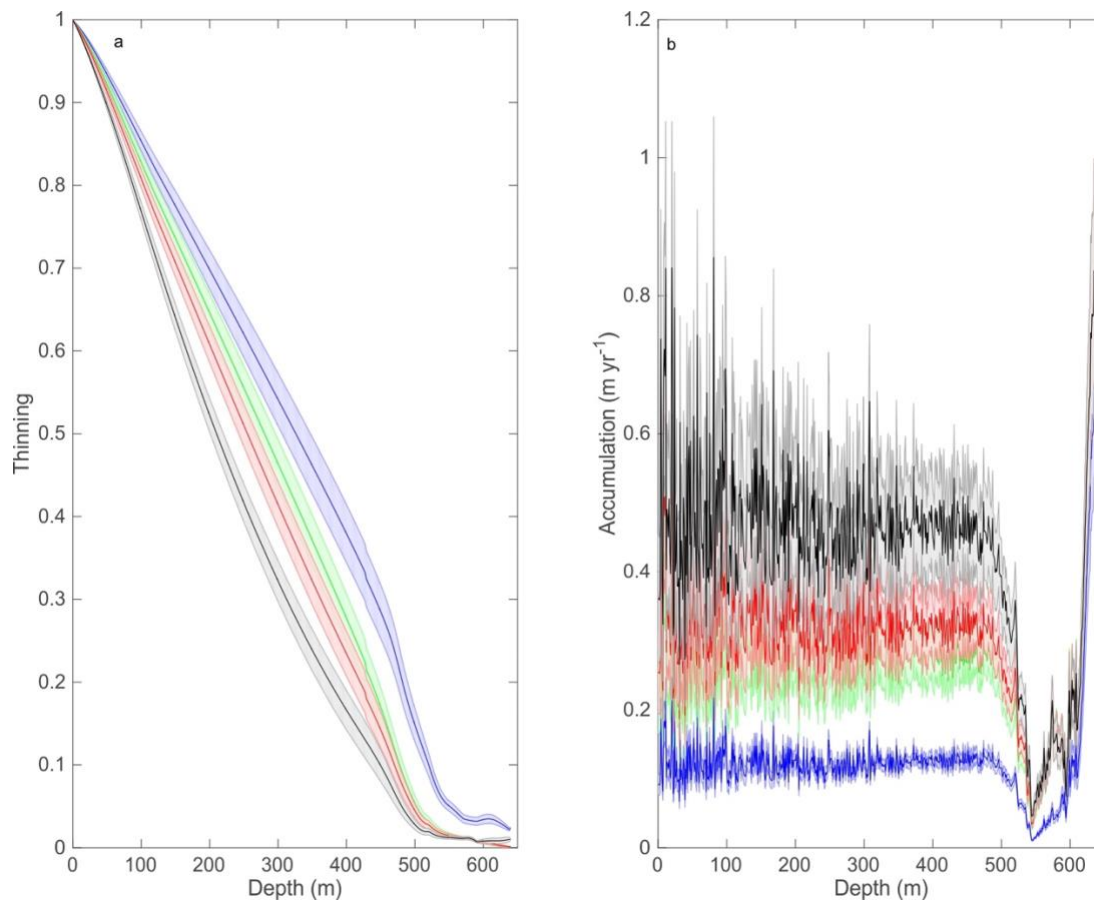


Figure 4.08: (a) Four thinning reconstructions that have been optimised using the IceChrono toolbox, and (b) the associated accumulation profiles for each model scenario. In these model scenarios, boundary thinning functions were fixed with 95% confidence to assess how this constraint would affect the accumulation profile. Optimised profiles are colour-coded for each model scenario. Black: freely-calculated; Blue: Nye; Green: Dansgaard-Johnsen; Red: One-Dimensional, with the associated uncertainty for each profile marked by a lighter shade of the main profile colour.

#### 4.4.2 GCM

A global circulation model (GCM) simulates climate and can yield information to a 250 km<sup>2</sup> resolution, including past accumulation rates over the Antarctic continent through time. The methodology is outlined in section 2.5.2.4. Accumulation is calculated using a Clausius-Clapeyron approach as explained in Gregory & Morris (1996). For this study, the HadCM3 GCM uses 200-year simulations for each millennium, spanning back to 21 kyr, and it provides a temporally dependent accumulation estimate for 250 km<sup>2</sup> grid cells (GCM results were provided by Dr Max Holloway, British Antarctic Survey). Each simulation runs for 200 years in order to reach an equilibrium state and is constrained by orbital parameters and

atmospheric gas markers. As a result, an independent estimate of accumulation and  $\delta^{18}\text{O}$  is available for comparison with the ice core chemistry and modelled accumulation profiles.

Table 4.05 outlines the results of each GCM simulation. The GCM simulations estimate a monthly mean precipitation rate, which is extrapolated to an annual rate of accumulation for direct comparison with other models. The mean accumulation per month (and extrapolated to per year) at the present day is significantly lower than the observed present-day mean accumulation rate of  $0.38 \text{ m yr}^{-1}$ . Additionally, accumulation estimates covering the LGM period are not consistent with accumulation estimates from the empirical methods of reconstruction nor the accumulation profile derived from some inverse approaches but they do agree with the freely calculated estimates in the IceChrono model. A comparison of accumulation estimates from each model scenario with the GCM estimates will be presented later in this chapter (4.5.2.1).

*Table 4.04: GCM results of mean monthly and annual precipitation and stable water isotope values for each 200-year simulation per millennium.*

Age (kyr)	Monthly Precipitation (mm)	Annual Precipitation (mm)	$\delta^{18}\text{O}$ (‰)
0	$18.5 \pm 3.4$	$222.0 \pm 41.1$	$-29.0 \pm 1.5$
1	$18.0 \pm 3.6$	$216.0 \pm 43.0$	$-29.5 \pm 1.7$
2	$17.6 \pm 3.3$	$221.2 \pm 40.2$	$-29.5 \pm 1.8$
3	$19.4 \pm 3.3$	$232.8 \pm 39.8$	$-28.7 \pm 1.8$
4	$19.3 \pm 3.0$	$231.6 \pm 35.5$	$-29.4 \pm 1.8$
5	$16.8 \pm 2.8$	$201.6 \pm 33.8$	$-29.9 \pm 1.8$
6	$16.3 \pm 2.6$	$195.6 \pm 31.2$	$-30.3 \pm 1.4$
7	$17.0 \pm 3.1$	$204.0 \pm 37.3$	$-30.1 \pm 1.6$
8	$17.0 \pm 3.1$	$204.0 \pm 44.2$	$-30.5 \pm 2.2$
9	$14.8 \pm 3.9$	$177.6 \pm 35.2$	$-31.2 \pm 2.0$
10	$15.7 \pm 3.0$	$188.4 \pm 34.9$	$-31.1 \pm 1.9$
11	$14.7 \pm 3.0$	$176.4 \pm 35.2$	$-29.1 \pm 1.7$
12	$10.2 \pm 2.7$	$122.4 \pm 35.0$	$-32.8 \pm 1.7$
13	$10.2 \pm 3.2$	$122.4 \pm 32.8$	$-33.3 \pm 1.7$
14	$9.6 \pm 3.0$	$115.2 \pm 38.1$	$-33.6 \pm 1.7$
15	$8.2 \pm 2.6$	$98.4 \pm 35.3$	$-33.3 \pm 2.1$

16	$7.7 \pm 2.1$	$92.4 \pm 30.8$	$-34.3 \pm 2.0$
17	$7.5 \pm 2.2$	$90.0 \pm 24.8$	$-34.8 \pm 1.6$
18	$7.9 \pm 2.2$	$94.8 \pm 26.3$	$-34.3 \pm 2.0$
19	$8.0 \pm 2.0$	$96.0 \pm 26.5$	$-34.9 \pm 2.4$
20	$9.0 \pm 1.4$	$108.0 \pm 24.5$	$-35.7 \pm 2.4$
21	$7.4 \pm 1.9$	$88.8 \pm 16.9$	$-34.6 \pm 2.5$

#### 4.4.3 Direct Search

The Direct Search method seeks to optimise the One-Dimensional thinning profile (section 4.3.4) by iterating within the model to find the optimal value of the  $p$ -parameter (eq. 2.16) using a Monte Carlo Markov Chain (MCMC) algorithm. The accumulation history is not changed through this method. The model starts with an initial age-depth profile calculated as the integral of the inverse of annual layer thickness, estimated as the product of an accumulation reconstruction and the empirical One-Dimensional thinning profile. Following this, it calculates a root mean square error (RMSE) value (eq. 2.28), which reflects the misfit between the modelled age estimate and age horizons. The value of the  $p$ -parameter is then changed, before the thinning function, and hence the annual layer thickness and age-depth profile, is recalculated. The RMSE value for the difference between modelled and observed constraints is calculated again, and compared with the previous iteration's RMSE value. Comparison of the RMSE value with the previous RMSE value controls the direction of the search for the optimal value of the  $p$ -parameter; the value of the  $p$ -parameter will be increased or decreased depending on whether the RMSE value has increased or decreased in line with the direction of the search. This leads to a direct search of the model space that converges on the optimal age-depth profile when the RMSE value is within 0.005% of the previous RMSE value.

Uncertainty bounds are determined through this method by adding a small perturbation to each age value within the associated age uncertainty for each constraint. The model is iterated to find 1000 possible age-depth scenarios; each iteration is constrained by the age constraints that have been perturbed randomly within the age uncertainty. The range of possible values of thinning and age-depth profiles across 1000 optimal profiles yields an uncertainty on the optimised profiles. The model run for 1000 iterations for the FP ice core typically requires 100 seconds.

Four alternative age-depth and thinning profiles are calculated using the Direct Search method: three using the empirical accumulation estimates from section 4.3.3 and one using the optimised accumulation history from the IceChrono model (the seventh model scenario). The age horizons are plotted as black crosses on each plot; the height of the cross indicates the uncertainty on the age horizon but the width of each cross is not associated with any uncertainty. As there is no uncertainty on the depth measurement for the age horizon, the width of the cross is specified by the software programming when the plot is constructed.

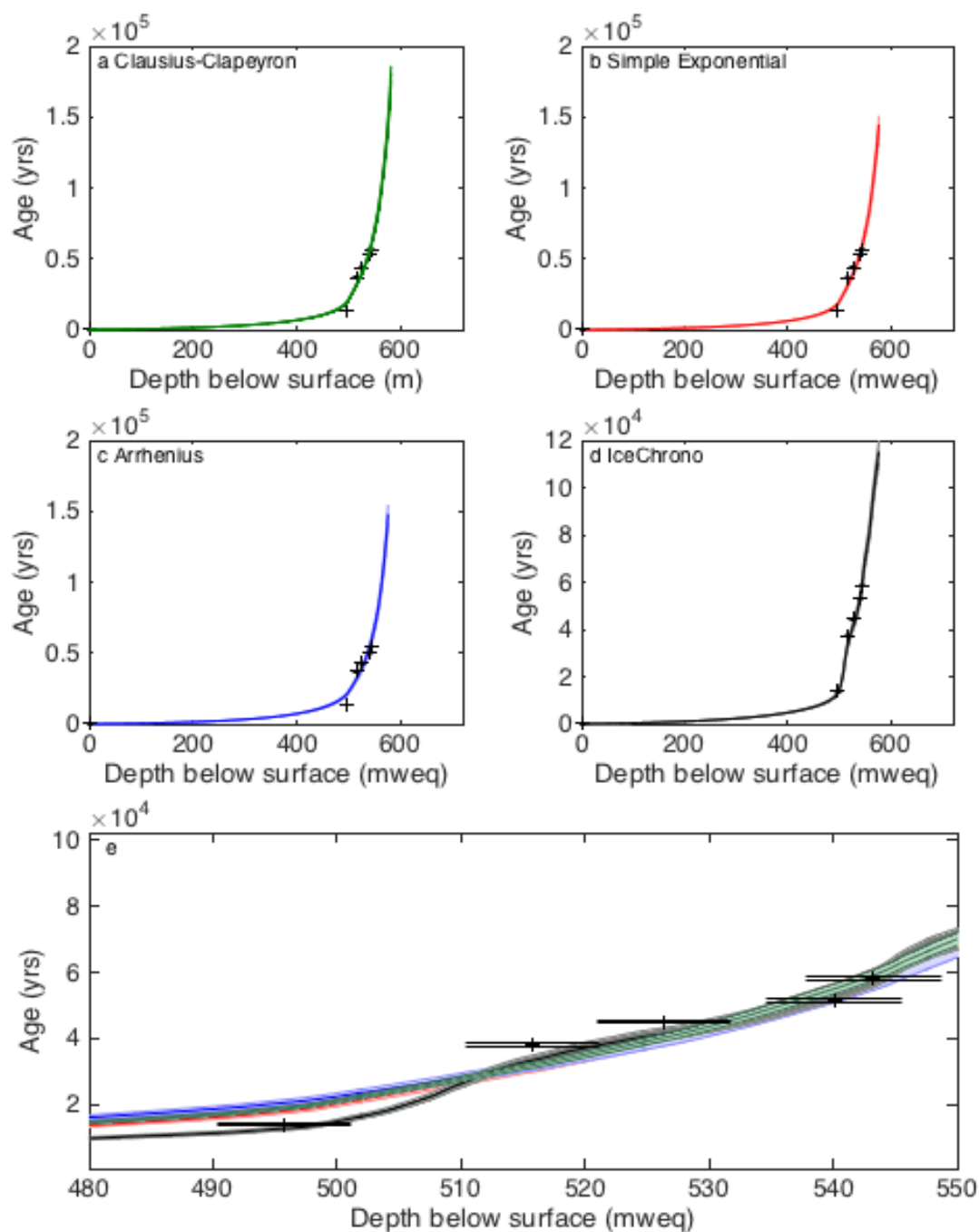


Figure 4.09: Age-depth profiles using the Direct Search approach as calculated using four different accumulation history profiles. Plot a-d: individual age-depth estimates (coloured line) and age horizons (black crosses; height of cross indicates age uncertainty but the differences are not visible); plot e: four age-depth estimates zoomed into the depth range 480 – 550 mweq to focus on fit with age horizons (black crosses). Each model scenario uses a different profile of accumulation and can be identified as: (a) Clausius-Clapeyron (green); (b) Simple Exponential (red); (c) Arrhenius (blue); (d) IceChrono (black). The zoom-in on plot (e) shows the four age-depth profiles; the Simple Exponential profile (red) is not easily visible in the figure due to its similarity with Clausius-Clapeyron profile (green).

Table 4.05: Age estimates and uncertainty for depths with corresponding age constraints used in the Direct Search method. Results are given for four different accumulation reconstructions. The colours used in the profiles presented in fig. 4.09 and 4.10 are listed after each initial accumulation to aid comparison with figures.

Depth (mweq)	Observed age and uncertainty (yrs BP)	Modelled age (yrs BP) and uncertainty (yrs BP)			
		CC (green profile)	EXP (red profile)	Arr (blue profile)	Free (black profile)
495.73	14600 ± 250	19033 ± 679	18264 ± 776	21085 ± 564	12820 ± 395
515.72	38250 ± 800	31548 ± 1150	31409 ± 1375	32635 ± 892	33481 ± 1112
526.34	46480 ± 800	39829 ± 1463	39947 ± 1767	40573 ± 1118	41515 ± 1394
540.11	53700 ± 800	54485 ± 2020	54938 ± 2458	54753 ± 1523	53945 ± 1834
543.24	59570 ± 800	58612 ± 2177	59125 ± 2652	58809 ± 1640	58430 ± 1993

The Direct Search method stops when the RMSE between observed and modelled profiles improves by less than 0.005% per iteration. This does not guarantee age-depth and thinning profiles that match the observed data, as outlined in table 4.06 and demonstrated in fig. 4.09e. The method leads to large uncertainties on the modelled age estimates and yet these values still do not agree to within the age uncertainty for the majority of the horizons.

The fourth model scenario used the freely-calculated IceChrono profile to prescribe the accumulation history (section 4.4.1; fig. 4.09d). The final age-depth profile fits the age constraints better than the age-depth estimates determined using the empirical accumulation profiles, and leads to a less negative  $p$ -parameter value (fig. 4.09e; table 4.07). This suggests that in order to improve the fit to the age constraints, it is useful to use an algorithm that can optimise the value of more than one free parameter within the inverse approach.

This inverse approach estimates the optimal value for the  $p$ -parameter that controls the profile of deformation in the One-Dimensional thinning function. Fig. 4.10 presents the thinning profiles estimated using the Direct Search model when different empirical

accumulation histories are used. As previously stated, four accumulation profiles have been used in the age-depth model: three empirical reconstructions following Arrhenius, Clausius-Clapeyron and Simple Exponential relationships and the freely-calculated accumulation history reconstructed using the IceChrono model. The differences in the accumulation reconstructions appear to have a significant impact on the resulting thinning and age-depth profiles.

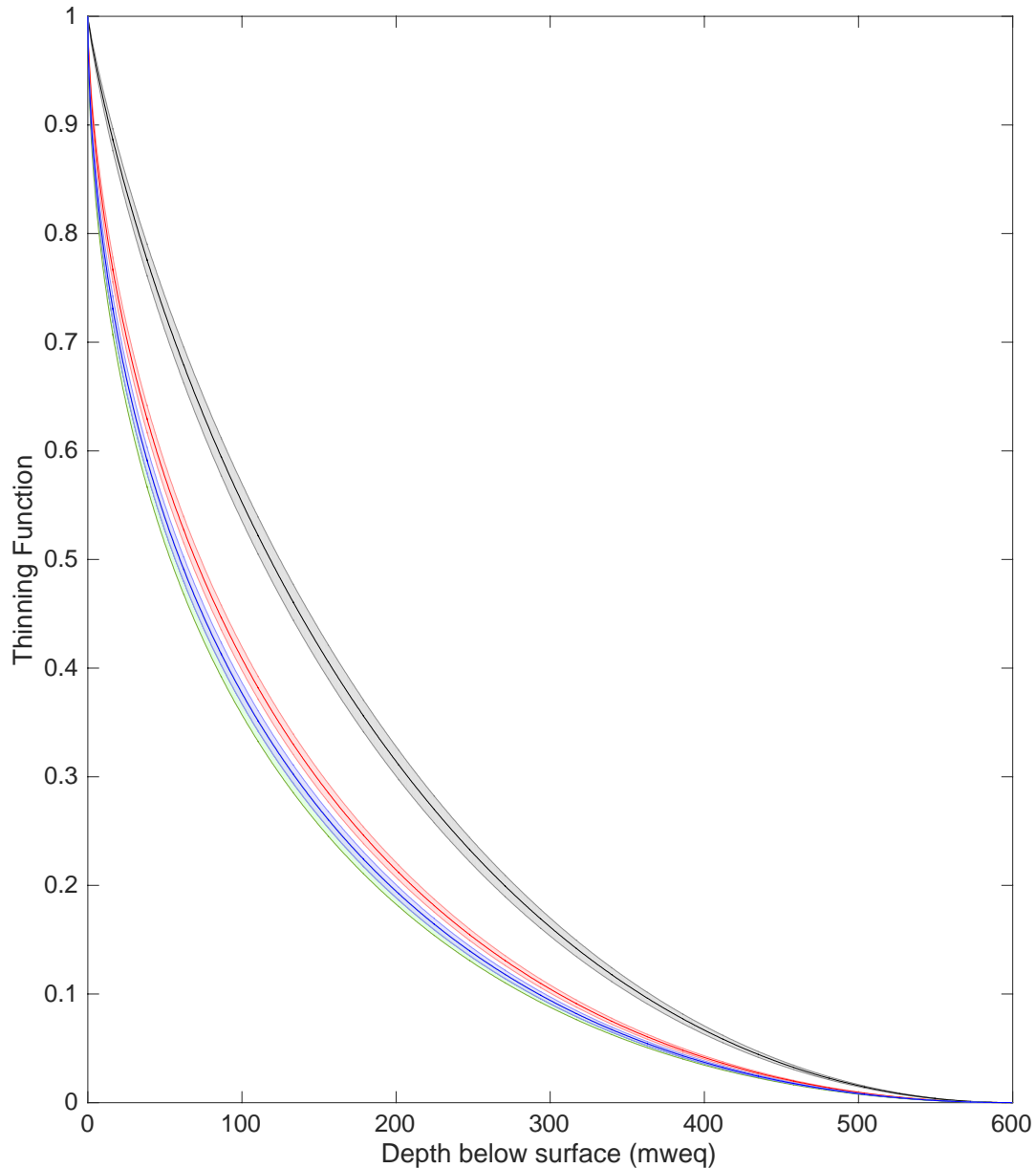


Figure 4.10: Posterior thinning functions and associated uncertainty constrained using the Direct Search method: four model scenarios using prescribed empirical accumulation. Green: Clausius-Clapeyron; Red: Simple Exponential; Blue: Arrhenius; Black: IceChrono.

The Direct Search model uses the One-Dimensional thinning function to optimise the age-depth profile, by estimating the optimal value of the  $p$ -parameter. This value can be empirically estimated using eq. 2.16, following the assumptions that the temperature gradient throughout the ice core is linear, the value of Glen's exponent,  $n$ , is 3, and the ice-sheet thickness, temperature at the bed, and activation energy are constant and accurate. The assumptions are numerous and so the  $p$ -parameter is an ideal parameter to optimise. However, by inverting eq. 2.16 using the optimised value of the  $p$ -parameter from the inverse approach, and an understanding of the assumptions made in the empirical relationship, an alternative estimate of Glen's exponent can be calculated. Although this estimate should not be assumed to be the correct value of Glen's exponent, it can yield information on the reliability of the optimised thinning function.

Table 4.07 lists the optimised values of the  $p$ -parameter for each *a priori* profile and solves for Glen's flow law exponent,  $n$ . The empirical estimate of the  $p$ -parameter in table 4.07 is calculated using eq. 2.16 and assumes  $n = 3$ ; for the remainder of the rows in table 4.07, the  $p$ -parameter is estimated using the Direct Search approach, and the value of  $n$  is calculated by inverting eq. 2.16. The optimised values of the  $p$ -parameter lead to consistently negative values of Glen's exponent. Negative values of  $n$  (table 4.07) suggest a deformation profile that is not consistent with current understanding of ice rheology, since a negative value would cause the rate of strain to decrease from the surface to the bed and the amount that annual layer thickness decreases from the original layer thickness with increasing depth from the surface would decrease. This profile of strain, estimated by the modelled thinning functions, cannot be replicated in any direct measurements of the ice core, and hence the modelled thinning functions using the Direct Search approach should not be considered a robust reconstruction.

The negative value of Glen's exponent calculated using the Direct Search model could be affected by the assumptions made in eq. 2.16. The temperature gradient from the surface of the ice sheet to the bed is not linear due to the diffusion of heat through an ice column (this will be further discussed in Chapter 8); furthermore, the value of the activation energy,  $Q$ , is not well-constrained but assumed to be  $\sim 60 \text{ kJ mol}^{-1}$  (Parrenin et al., 2007a). These assumptions could lead to an under-estimation of the  $n$  exponent. However, it is apparent that in order to minimise the deviation between the observed and modelled age estimates using the Direct Search approach, a non-linear profile of thinning is required and thus a low value of the  $p$ -parameter is required. The value is increased for the age-depth profile

estimated using the fourth scenario (the optimised accumulation profile estimated using the IceChrono approach). The fourth scenario – the freely-calculated scenario – yields a more accurate age-depth reconstruction through the reduction of the differences between observed and modelled age estimates. This reduces the non-linearity in the thinning function, and yields a  $p$ -parameter closer to the range of reasonable values of 1-5 (Wolff and Doake, 1986; Petitt et al., 2003; Gillet-Chaulet et al., 2011). Therefore, by comparing the age-depth and thinning reconstructions using empirical accumulation estimates with the equivalent results using the IceChrono optimised accumulation reconstruction, this study suggests that an additional approach is required to account for the remaining uncertainties and natural variability preserved in the ice core record.

*Table 4.06: Glen Exponent value for the Direct Search model. The first row lists the empirical estimate of the  $p$ -parameter using eq. 2.16, assuming a value of  $n = 3$  for Glen's exponent. The following rows present the  $p$ -parameter values optimised using the Direct Search model and different initial accumulation profiles. The value of Glen's exponent is calculated by inverting eq. 2.16.*

<b>Accumulation Method</b>	<b>Profile of deformation, <math>p</math>, and uncertainty</b>	<b>Glen's Exponent, <math>n</math>, and uncertainty</b>
Empirical estimate (eq. 2.16)	2.2220	3.000
Clausius-Clapeyron	$-1.46 \pm 0.02$	$-0.67 \pm 0.02$
Simple Exponential	$-1.31 \pm 0.03$	$-0.53 \pm 0.03$
Arrhenius	$-1.43 \pm 0.03$	$-0.65 \pm 0.03$
IceChrono	$-0.91 \pm 0.07$	$-0.17 \pm 0.07$

#### 4.4.4 OptAcc

The OptAcc model is outlined fully in section 3.6.1. This model searches for the optimal values for two variables: (i) a smooth perturbation profile, and (ii) the  $p$ -parameter. The smooth perturbation profile, developed within this project and introduced through eq. 3.02, perturbs an initial accumulation history before the model solves for an optimised one-dimensional thinning function (as used in the Direct Search model). The RMSE does not control the direction of the search for the optimised accumulation profile, but it is again used to solve for the optimal  $p$ -value associated with each accumulation profile. The model searches for optimised perturbation profiles using an MCMC random search direction algorithm. Like the Direct Search model, the model iterates until it finds 1000 possible optimal perturbation profiles for accumulation and corresponding  $p$ -parameter values. The

range of possible values of accumulation, thinning, and age-depth profiles across 1000 optimal profiles yields an uncertainty on the optimised profiles.

Each model scenario requires an initial accumulation history. Three separate profiles of accumulation, thinning, and age-depth have been reconstructed using a different initial accumulation profile from the three empirical techniques available. Table 4.08 outlines the age estimates and uncertainty for the depths that correspond to the age horizons in the FP ice core. The optimised age-depth profiles agree with the age constraints, with the exception of the fourth constraint. The OptAcc models consistently estimate the ice age 25 mweq above the bedrock to be 120 – 140 ka BP, depending on the *a priori* accumulation history prescribed (fig. 4.11). This age estimate close to the bed agrees with the hypothesis that the surface temperature and accumulation reconstructions derived from the stable water isotope demonstrate a climate signal preserved from the last interglacial period (LIG).

*Table 4.07: Age estimates and uncertainty for depths with corresponding age constraints used in the OptAcc method.*

Depth (mweq)	Observed age and uncertainty (yrs BP)	Modelled age (yrs BP) and uncertainty (yrs BP)		
		CC	EXP	Arr
495.73	14682 ± 250	14681 ± 349	14749 ± 194	14462 ± 323
515.72	38250 ± 800	38456 ± 568	38628 ± 959	38526 ± 304
526.34	46480 ± 800	45891 ± 134	45972 ± 1054	45945 ± 239
540.11	53700 ± 800	55668 ± 280	55603 ± 613	55637 ± 961
543.24	59570 ± 800	58405 ± 495	58278 ± 1001	58393 ± 1578

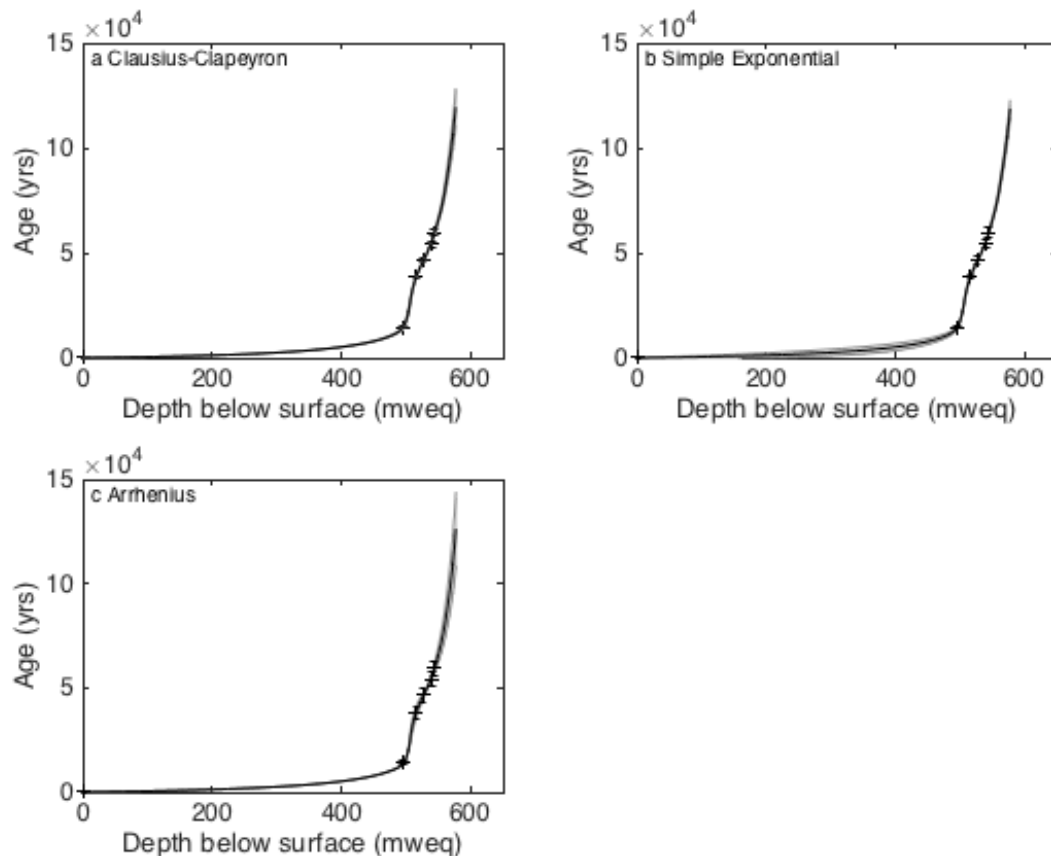


Figure 4.11: Age-depth profiles using the Optimised Accumulation models with uncertainty (grey) and age horizons (black crosses). Clockwise from top left: (a) Clausius-Clapeyron, (b) Simple Exponential, and (c) Arrhenius relationships were used as initial accumulation profiles prior to optimisation.

In fig. 4.12, three optimised accumulation records are presented (blue); these have been derived using the (a) Clausius-Clapeyron, (b) Simple Exponential, and (c) Arrhenius relationships to prescribe the initial accumulation history. Also shown is the optimal annual layer thickness (red), with the associated uncertainty on the annual layer thickness profile, and *a priori* accumulation profile (grey). Fig. 4.13 presents the perturbation profiles used in the reconstruction of the three optimised accumulation histories in the same order as fig. 4.12. Results are similar for accumulation, thinning and age-depth when the initial accumulation history is estimated using any of the three empirical relationships, with only the size of the perturbation to the initial profile changing. Table 4.09 presents the  $p$ -parameter values and Glen's flow law exponent for each inputted accumulation history. As previously explained, Glen's exponent,  $n$ , can be calculated by inverting eq. 2.16. Although, this interpretation of  $n$  is not robust, it does yield information on the optimisation process.

The OptAcc model yields more reasonable estimates for the  $p$ -parameter and Glen's exponent than estimated using the Direct Search approach (table 4.07) but are still lower than typical values of Glen's exponent that are within an appropriate range measured using *in situ* techniques (Gillet-Chaulet et al., 2011). Further discussion of the shape of the deformation profile is included later in this study, when the optimised accumulation, thinning, and age-depth profiles are presented for the FP, BI, and JRI ice cores.

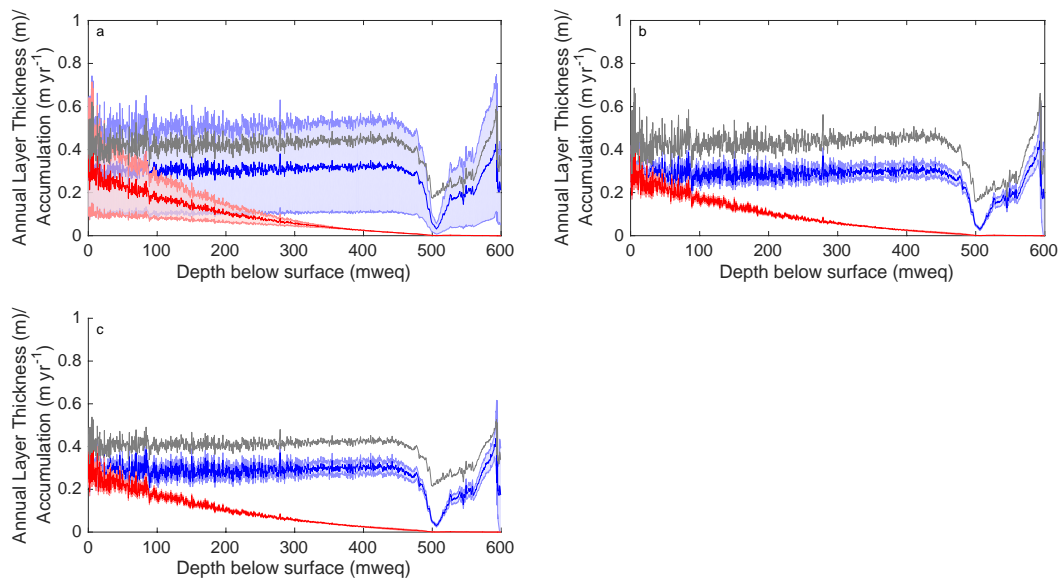


Figure 4.12: Annual layer thickness profiles and accumulation estimated for FP ice core. *A priori* accumulation profiles: (a) Clausius-Clapeyron; (b) Simple Exponential; (c) Arrhenius. Dark blue: optimal accumulation profile modelled using the optimisation model; pale blue: uncertainty on the optimal accumulation profile; grey: the *a priori* accumulation profile (one of three empirical reconstructions); red: optimal annual layer thickness profile; pale red: uncertainty on annual layer thickness profile.

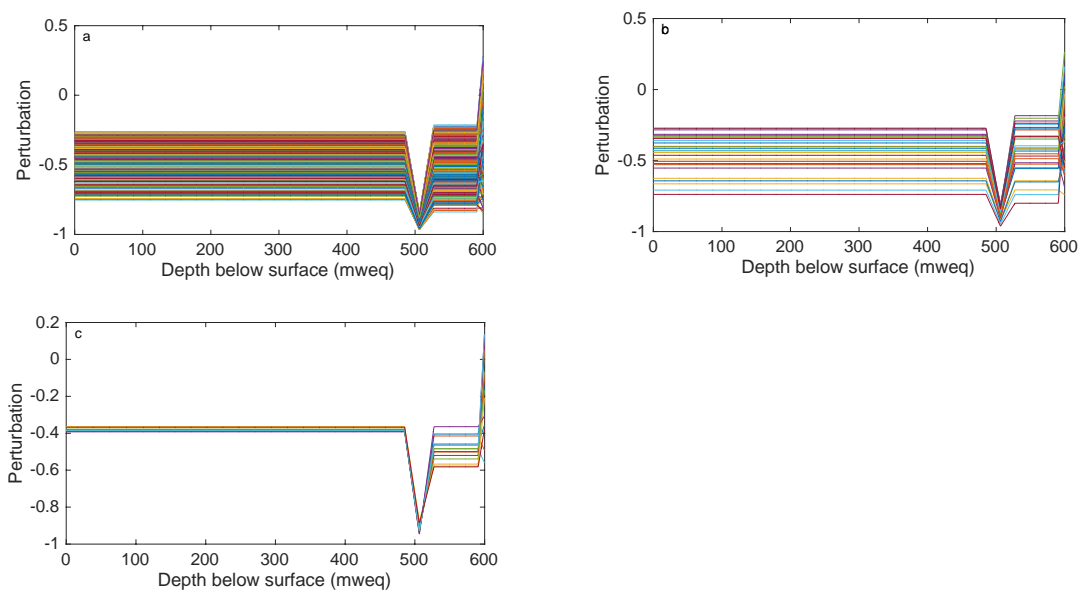


Figure 4.13: Perturbation profiles for each possible optimal profile (1000 profiles) for the FP ice core using an initial accumulation profile derived from the (a) Clausius-Clapeyron relationship; (b) Simple Exponential relationship; (c) Arrhenius relationship.

Table 4.08: Glen Exponent value for the OptAcc model. The following rows present the  $p$ -parameter values optimised using the Direct Search model and different initial accumulation profiles. The value of Glen's exponent is calculated by inverting eq. 2.16.

Accumulation Method	Profile of deformation, $p$ and uncertainty	Glen's Exponent, $n$ and uncertainty
Clausius-Clapeyron	$-0.75 \pm 5.2$	$0.03 \pm 5.2$
Simple Exponential	$-0.51 \pm 0.01$	$0.12 \pm 0.01$
Arrhenius	$-0.68 \pm 0.15$	$0.10 \pm 0.15$

#### 4.4.5 pRES

The fifth inverse approach still relies on the assumption that the age of ice at a particular depth is the sum of annual layers above it. However, the pRES inverse model seeks to reconstruct the optimal annual layer thickness profile, and hence age, using eq. 2.19 (section 2.5.3.4). The full model approach is explained in section 3.6.2.2. To estimate annual layer thickness this way requires an accumulation history as input as well as *in situ* measurements of vertical velocity (obtained from Jonathan Kingslake (*pers. comm.*)). This model seeks to perturb and optimise the accumulation history, using the same approach in the OptAcc

model (eq. 3.01). One model scenario, using an initial accumulation history derived using the Simple Exponential relationship (eq. 2.09) and pRES measurements, is used to determine an optimal accumulation, annual layer thickness and age-depth profile (eq. 3.04). For the FP ice core, the upper 80% of the record is modelled using this approach, where there are continuous pRES observations. Beyond this, the thinning function is extrapolated to reach 0 (total thinning) at the bedrock.

Table 4.10 presents the modelled age estimates at the depths corresponding to the age constraints, with the age-depth profile presented in fig. 4.14. The modelled age estimates agree with the constraints with the exception of the second and third age estimates, which are 5 – 10 kyr younger than the age horizon. Annual accumulation decreases rapidly into the LGM from the last interglacial but remains higher than the empirical reconstruction until 500 mweq (fig. 4.15); this is a large difference between the empirical and optimised accumulation profiles and would result in a higher mean annual layer thickness that would lead to an age-depth profile where age increases more slowly with depth across this range. The pRES age-depth profile (fig. 4.14) estimates an age close the bed (570 mweq) greater than 140 ka BP. This is likely due to the high thinning rates estimated in the deepest part of the core (pRES observations do not extend to bedrock and so vertical velocity has been extrapolated to 0). Mathematically, this would cause age-depth estimations to tend toward infinity and estimate annual layer thickness to be sub-mm.

*Table 4.9: Age estimate and uncertainty for the depths that correspond to an age horizon using the pRES model.*

<b>Depth (mweq)</b>	<b>Observed age and uncertainty (yrs BP)</b>	<b>pRES age estimate and uncertainty (yrs BP)</b>
495.73	14600 ± 250	14027 ± 579
515.72	38250 ± 800	29758 ± 899
526.34	46480 ± 800	42829 ± 1861
540.11	53700 ± 800	56223 ± 2649
543.24	59570 ± 800	59887 ± 3459

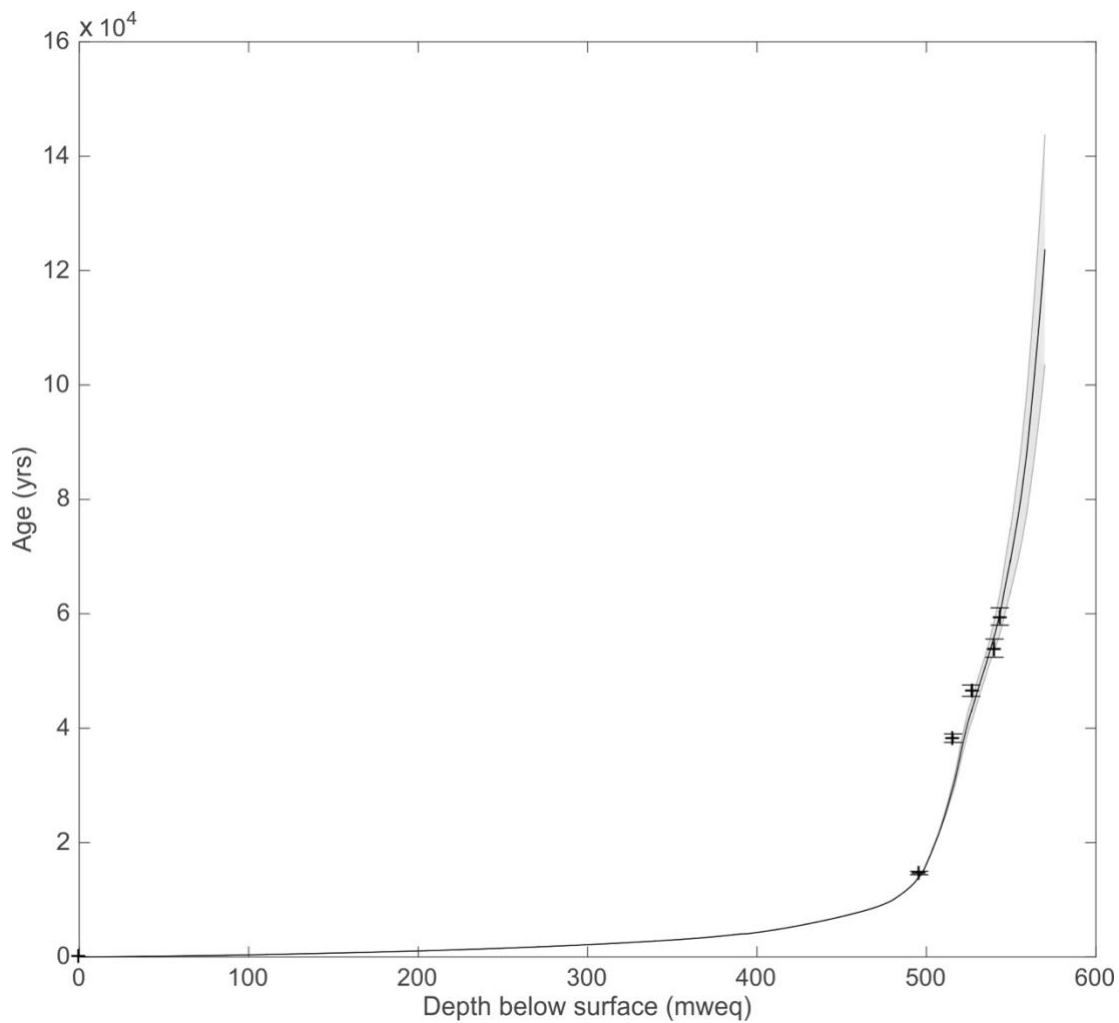


Figure 4.14: Age-depth profile using an empirical age-depth model based on pRES data with uncertainty (grey) and age horizons (black crosses).

Similar to fig. 4.12, fig. 4.15 presents the *a posteriori* accumulation (blue) and annual layer thickness (red) profiles. The accumulation history strongly resembles the Simple Exponential empirical profile (grey) throughout the Holocene, but with a large uncertainty estimate of  $\pm 10\%$  throughout the period. Despite solving for the compaction of snow in the upper sections of the ice core (eq. 3.04), the model reproduces a non-linear and rapid rate of thinning in the upper 100 m of the ice core.

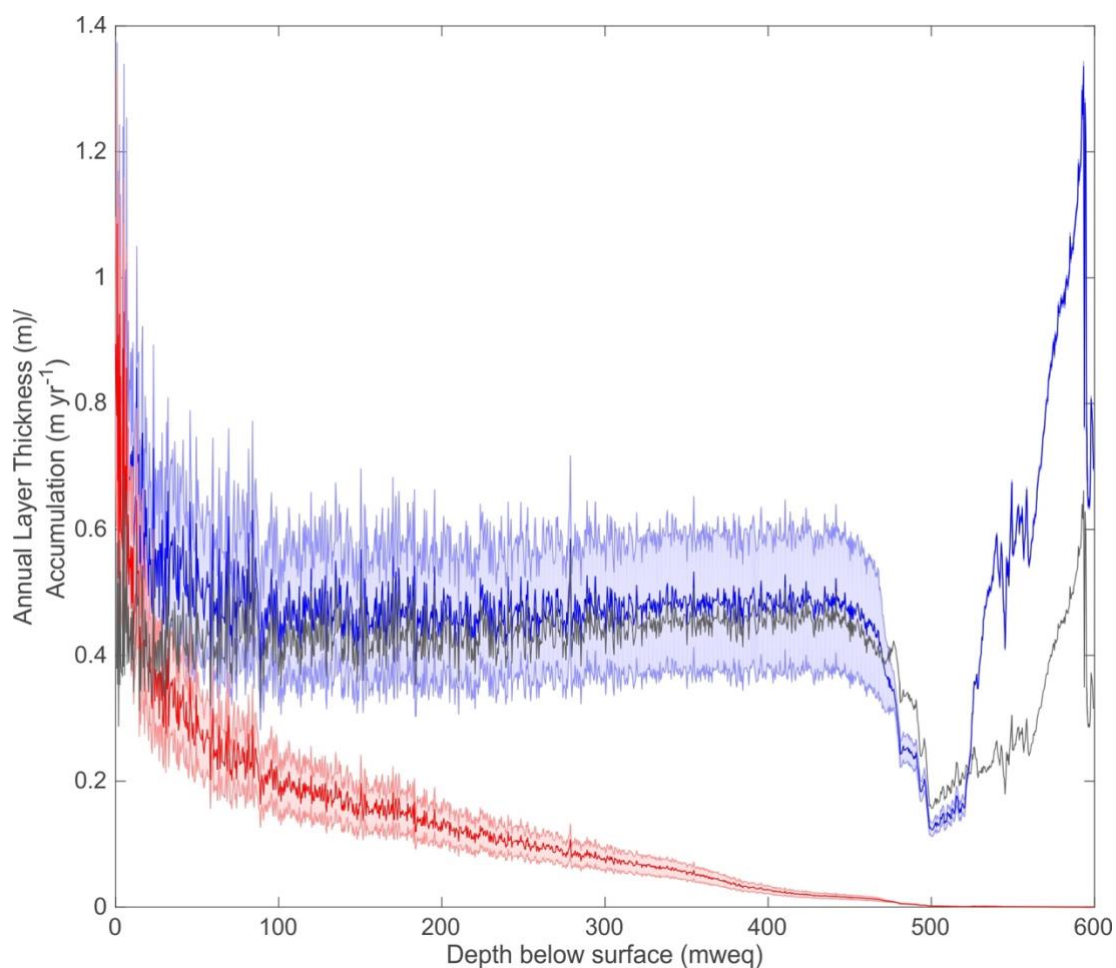


Figure 4.15: As calculated by pRES model: accumulation (original annual layer thickness) profile (blue) with uncertainty (pale blue); present-day annual layer thickness (red) with uncertainty (pale red). An initial accumulation history calculated using the Simple Exponential empirical relationship is shown in grey.

#### 4.5 Discussion

In order to date these ice core records accurately, an assessment of the multiple techniques that are used to reconstruct the accumulation, thinning and age-depth profiles of an ice core was required. As part of this study, a synthesis of these techniques is presented and analysed in this chapter for the FP core (similar results for BI and JRI are included in the Appendix) before the optimal age-depth strategy is applied to the FP, BI, and JRI ice cores in chapter 6 and 7. Differences between profiles are evident for each technique, and the reasons for the differences must be understood in order to decide which set of techniques are the most reliable for reconstructing the most accurate accumulation, thinning and age-depth histories in the three ice cores. The following section will discuss the differences

between empirical and constrained approaches to reconstructing accumulation, thinning, and age-depth profiles of the FP ice core, with a view to determining the reliability of each technique in order to address the first objective of this study.

#### 4.5.1 Empirical Reconstructions

Accumulation reconstructions are all based on an exponential relationship with the surface temperature or the stable water isotope profile. However, the underlying principles of each method lead to differences in accumulation that are most evident when compared with changes in surface temperature. Fig. 4.16 demonstrates the sensitivity of accumulation to changes in temperature. It is clear that the sensitivity of accumulation is more linear in the Arrhenius reconstruction (fig. 4.16, red line), whilst the Simple Exponential and Clausius-Clapeyron relationships are more sensitive to changes in temperature (blue and purple lines), leading to the largest changes in annual accumulation during the LGM and glacial-interglacial transition. There is no method to statistically quantify which is the most accurate accumulation reconstruction without laboratory analysis, despite the deviations between profiles. The atmospheric processes that are invoked in the reconstructions must be considered in addition to an analysis of the thinning, annual layer thickness, and age-depth profiles determined by the inverse approaches.

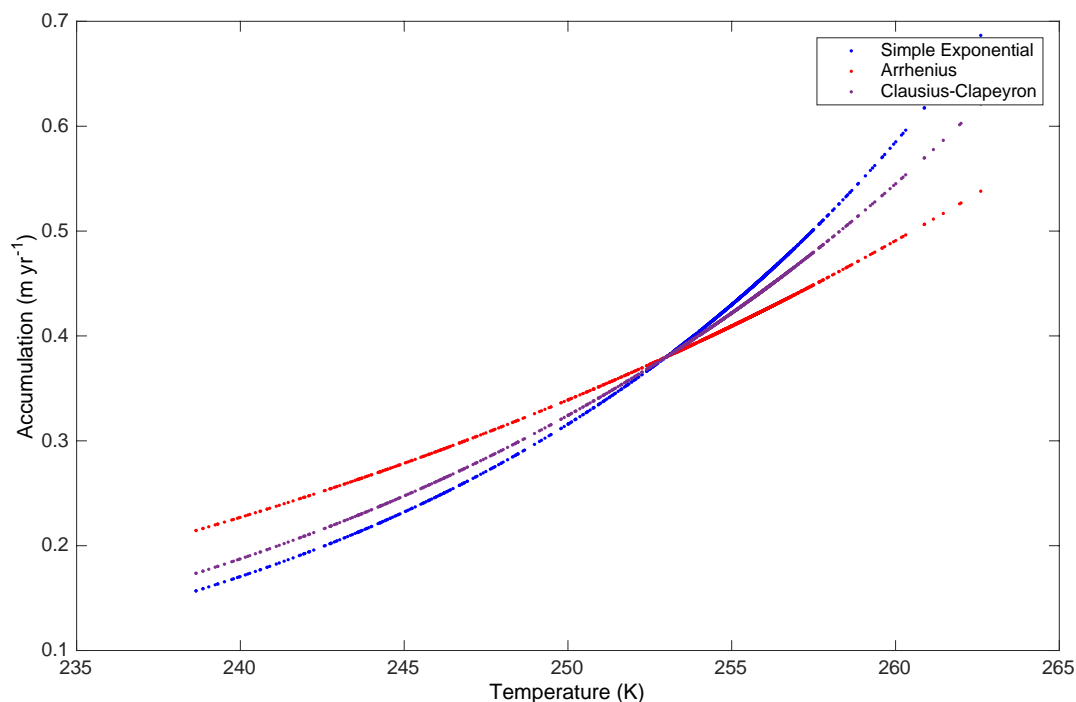


Figure 4.16: Sensitivity change of accumulation reconstructions with respect to temperature.

Unlike the empirical estimations of accumulation, the differences in the thinning functions are more apparent. In the empirical age-depth estimations (fig. 4.05), the use of a different accumulation reconstruction does not alter the age-depth profile as significantly as the use of a different thinning function. The historical development of these thinning functions has had the greatest effect on the accuracy of deformation profiles. Most notably, it is the progression from steady-state assumptions and uniform plastic deformation (Nye, 1963), to understanding the nonlinear deformation of an ice column (Dansgaard and Johnsen, 1969; Lliboutry, 1979; Parrenin and Hindmarsh, 2007) which determines the improvement in age-depth estimates as demonstrated in table 4.03. As a result, the forward age-depth estimates that apply the One-Dimensional thinning function (eq. 2.13 - 2.17) provide the best fit to the age horizons, although it should be noted that none of the methods fit the age constraints within the observational uncertainty.

#### 4.5.2 *Constrained Models*

Accumulation and thinning profiles of ice cores can be improved through the application of one of several inverse approaches. This study has synthesised five approaches; the IceChrono, Direct Search, pRES, a GCM, and OptAcc models. These techniques provide alternative solutions for accumulation and thinning, which differ and ultimately affect the age-depth solutions.

##### 4.5.2.1 *Accumulation Reconstructions*

The perturbed profiles from the OptAcc model, IceChrono, pRES, and the precipitation estimates from the HadCM3 GCM can yield information on the reliability of each reconstruction. The perturbation profile revises the assumed relationship between stable water isotopes and surface temperature and accumulation. Assessment of the accumulation reconstructions provides insight into whether these profiles are realistic and, if they are realistic, what impact these reconstructions have on the assumed surface temperature – accumulation relationship.

- a) IceChrono: the accumulation reconstructions do not differ greatly during the current interglacial record until 450 mweq, with the greatest deviation occurring during the last glacial/interglacial transition. This is due to the 95% confidence interval prescribed for the empirical accumulation reconstructions that were used as boundary conditions for each scenario, and hence the thinning function must account for any variability in the annual layer thickness profile. A ‘kink’ at ~600 m in

the thinning profiles are more significant for profiles outputted from model scenarios that used *a priori* accumulation reconstructions based on the Simple Exponential and Arrhenius relationships (fig. 4.07b). One reason for this is that the model scenarios using the Arrhenius accumulation history estimate higher rates of accumulation during the last glacial period, and hence the model needs to reduce the annual layer thickness to drive the profiles through age horizons around this depth.

- b) GCM: The HadCM3 GCM under-estimates observed present-day mean annual accumulation, which the empirical relationships are based on. As a result, accumulation estimates during the present interglacial are lower than the accumulation profiles reconstructed using the IceChrono and pRES models, though not much lower than the accumulation profile derived using no prior information in the IceChrono toolbox. Table 4.11 compares accumulation rates estimated using a number of different approaches with millennial-scale GCM estimates for accumulation (see also fig. 4.17). Changes in GCM-derived accumulation with respect to changes in surface temperature follow a similar relationship to that displayed by the IceChrono-derived accumulation profile (fig. 4.18). For comparison with the empirical reconstructions, the GCM accumulation rates are estimated using a method based on the Clausius-Clapeyron relationship (Gregory and Morris, 1996), and therefore they follow a similar rate of change in accumulation with respect to surface temperature as this corresponding technique.
- c) pRES: The perturbed accumulation history that has been reconstructed from the pRES data does not differ greatly from the initial accumulation profile prescribed in the pRES model, but the mean annual accumulation rate does drop to  $\sim 0.1 \text{ m yr}^{-1}$  during the LGM (fig. 4.15). Apart from during the LGM, the accumulation rate is consistently higher than other optimised profiles, due to the high rates of thinning calculated from the *in situ* vertical velocity measurements. The accumulation rates estimated by the pRES model during the LGM are higher than the rates of the OptAcc model, and increase sharply from glacial conditions to interglacial conditions to a mean annual accumulation closer to the present-day mean annual accumulation rate (fig. 4.17).
- d) OptAcc: The optimal profiles reconstructed using these models yield an age-depth profile that is capable of fitting the age horizons, with a minimum accumulation rate of  $\sim 0.03 \text{ m yr}^{-1}$  at the LGM. This is similar to results obtained using the IceChrono

model. The accumulation reconstructions are consistent, despite varying *a priori* accumulation histories, due to the role of the perturbation profile (fig. 4.13). The accumulation reconstruction using the Clausius-Clapeyron relationship yields a larger uncertainty than the reconstructions using the Simple Exponential and Arrhenius techniques, as demonstrated in fig. 4.12 and 4.13.

In order to reconstruct age-depth and thinning profiles accurately to fit the age constraints, optimal accumulation profiles suggest a mean interglacial accumulation rate lower than estimated through the empirical techniques. The large uncertainty of the OptAcc CC-derived accumulation profile is evident when compared to the other model scenarios. The large uncertainty across 0 – 14 ka BP is due to the lack of constraints across this time period in the FP ice core. Unlike other modelling approaches that use the same constraints, the OptAcc profile requires more information to constrain the potential perturbation range.

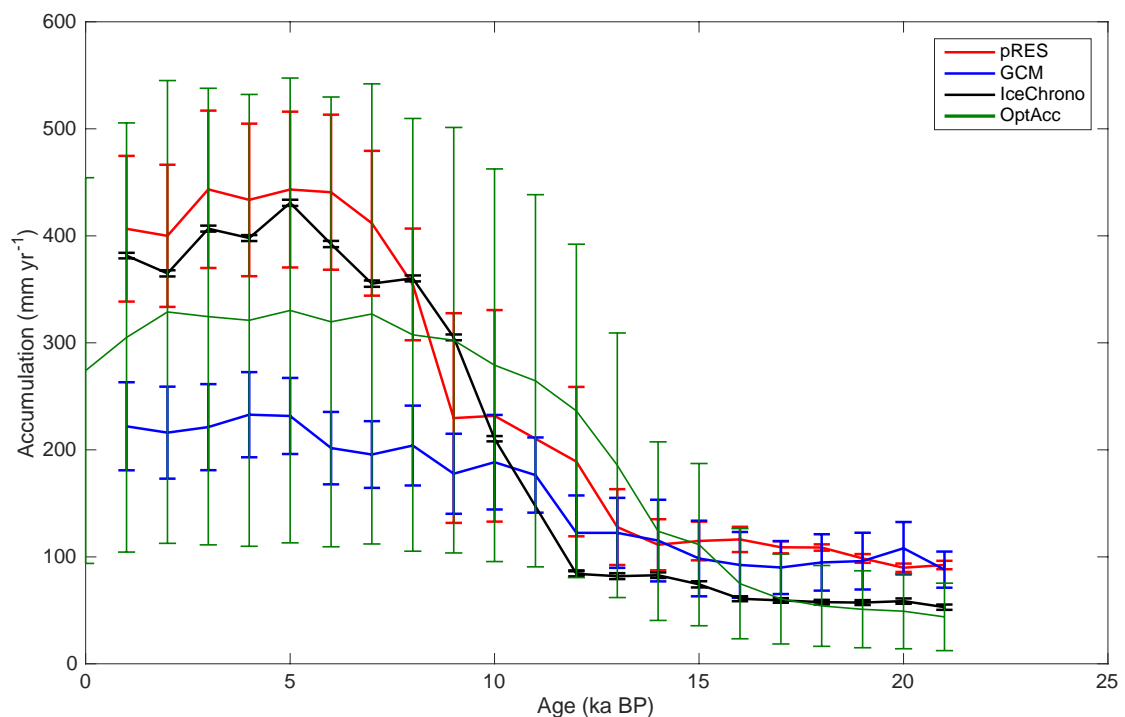


Figure 4.17: Accumulation estimates for each millennium for comparison with GCM estimates. Crosses at each modelled data point represent the associated uncertainty for each estimate. The results present the freely-calculated IceChrono and the Clausius-Clapeyron-derived OptAcc approaches.

The most realistic profiles are chosen based on the goodness-of-fit between the observed and modelled ages at depths corresponding to age constraints. The most realistic accumulation reconstructions, coupled with realistic rates of thinning and a good fit to the age constraints, reach a mean annual accumulation rate of  $0.05 \text{ m yr}^{-1}$  during the LGM (the IceChrono and OptAcc reconstructions that are derived using the Clausius-Clapeyron relationship; fig. 4.07a green and fig. 4.12). The accumulation reconstructions that use an initial accumulation estimate derived from the Clausius-Clapeyron relationship do not show a significant 'kink' in the modelled thinning functions as they are not perturbed in order for the modelled profiles of annual layer thickness and age-depth to agree with observational data.

The pRES reconstruction does not require a large perturbation on the initial accumulation estimate in order to agree with the age horizons, with the exception of the second youngest constraint. The pRES model is able to develop pRES observations of vertical velocity into an ice core thinning function for the FP ice core. The thinning function is dependent on *in situ* observations only, and cannot account for any temporal ice-sheet thickness changes at Fletcher Promontory. Although the other inverse approaches also do not consider temporal changes in the ice sheet thickness, the free parameter within the thinning functions could account for some of the uncertainty in the ice flow history. Furthermore, the OptAcc and IceChrono accumulation reconstructions estimate a mean present-day accumulation rate lower than the present-day mean annual value. Despite this, the IceChrono and OptAcc models appear to be the most accurate and reliable age-depth reconstructions for the FP ice core (table 4.04; table 4.08; table 4.12).

Table 4.10: Precipitation estimates for each millennium, estimated by each inverse accumulation approach for comparison with GCM estimates ( $\text{mm yr}^{-1}$ ). Uncertainty in the modelled estimates is included. The OptAcc and IceChrono reconstructions use an initial accumulation profile estimated using the Clausius-Clapeyron relationship.

Age (kyr)	GCM (mm)	OptAcc (mm)	IceChrono (mm)	pRES (mm)
0	222.0 ± 41.1	274.0 ± 180.2	274.5 ± 6.7	374.8 ± 1.3
1	216.0 ± 43.0	305.0 ± 200.6	381.5 ± 6.5	406.6 ± 68.0
2	221.2 ± 40.2	328.9 ± 216.3	364.9 ± 5.6	399.9 ± 73.4
3	232.8 ± 39.8	324.5 ± 213.4	406.7 ± 5.4	443.4 ± 71.2
4	231.6 ± 35.5	321.0 ± 211.1	397.9 ± 5.6	433.5 ± 71.2
5	201.6 ± 33.8	330.3 ± 217.2	430.8 ± 5.9	443.2 ± 72.8
6	195.6 ± 31.2	319.6 ± 210.2	392.3 ± 5.2	440.7 ± 72.4
7	204.0 ± 37.3	326.9 ± 215.0	355.3 ± 5.0	411.8 ± 67.6
8	204.0 ± 44.2	307.5 ± 202.2	360.2 ± 5.6	354.6 ± 52.1
9	177.6 ± 35.2	302.4 ± 198.8	305.1 ± 4.5	229.7 ± 97.9
10	188.4 ± 34.9	279.1 ± 183.5	210.4 ± 3.4	231.7 ± 98.8
11	176.4 ± 35.2	264.5 ± 174.0	202.3 ± 3.0	240.0 ± 40.0
12	122.4 ± 35.0	236.4 ± 155.7	84.1 ± 1.4	189.0 ± 69.8
13	122.4 ± 32.8	185.6 ± 123.6	81.9 ± 1.3	127.8 ± 35.4
14	115.2 ± 38.1	123.9 ± 83.4	82.8 ± 1.4	111.2 ± 23.9
15	98.4 ± 35.3	111.4 ± 75.8	74.3 ± 1.3	114.8 ± 18.1
16	92.4 ± 30.8	74.9 ± 51.5	60.8 ± 1.0	116.2 ± 11.8
17	90.0 ± 24.8	60.6 ± 42.0	59.2 ± 1.0	108.9 ± 5.6
18	94.8 ± 26.3	54.1 ± 37.8	57.6 ± 1.0	108.7 ± 2.9
19	96.0 ± 26.5	50.9 ± 35.9	57.2 ± 0.9	98.5 ± 4.1
20	108.0 ± 24.5	49.1 ± 34.9	47.3 ± 0.9	120.0 ± 5.0
21	88.8 ± 16.9	43.8 ± 31.6	52.9 ± 0.8	92.3 ± 3.9

Fig. 4.18 suggests that the relationship between surface temperature and accumulation is not robust when accumulation is reconstructed using an inverse approach. In contrast to fig. 4.16, in which the surface temperature – accumulation relationship is well-defined for the empirical techniques (section 4.3.3), the relationship is weakened by the perturbation profile on each of the optimised accumulation records. Most notably, fig. 4.18 demonstrates that

the assumed role of the surface temperature – accumulation relationship differs for each inverse approach.

Fig 4.18a presents the surface temperature – accumulation relationships for the seven IceChrono model scenarios used in this study. The figure does not show visibly correlating profiles of accumulation with respect to a change in surface temperature. When accumulation is reconstructed using IceChrono, bounded by a thinning function, a change in accumulation with respect to a change in surface temperature shows no correlation with an  $r^2$  coefficient of 0.159 – 0.223. For the IceChrono scenarios that are bounded by an initial accumulation history, the  $r^2$  coefficient improves to 0.255 – 0.622 but still suggests that there is little correlation between surface temperature and accumulation. Finally, the freely-calculated IceChrono scenario yields a  $r^2$  value of 0.621 but still suggests weak correlation. This demonstrates the independence of the IceChrono accumulation reconstruction with respect to the changes in surface temperature.

Fig. 4.18b presents the surface temperature – accumulation relationship for the three accumulation reconstructions using the OptAcc model. This plot is easier to read in comparison with fig. 4.18a, suggesting strong correlation between surface temperature and accumulation despite the perturbed accumulation profiles. For the accumulation reconstruction using a Clausius-Clapeyron relationship as an initial accumulation estimate, an  $r^2$  coefficient of 0.964 determines that the assumed relationship between stable water isotopes – surface temperature – accumulation is robust. This is replicated in the Simple Exponential model scenario, with an  $r^2$  coefficient of 0.956, and the Arrhenius model scenario with an  $r^2$  coefficient of 0.906. Despite the high coefficient values, two distinct surface temperature – accumulation relationships are visible in the OptAcc profiles on fig. 4.18b. Although the full initial accumulation profile is perturbed throughout the ice-core record, the perturbation profile is steady for the majority of the record with a significant perturbation between 450 mweq and 500 mweq. The combination of a steadily perturbed accumulation profile until the greatest perturbation at 450 mweq leads to these two distinct surface temperature – accumulation profiles in fig. 4.18b (the perturbation profiles are shown in fig. 4.13). This perturbation coincides with the suggested transition from the last glacial period to the present-day interglacial. The shift in the surface temperature – accumulation relationship using the OptAcc model suggests a change in the relationship between these time periods and will be further investigated later in this study.

Finally, fig. 4.18c presents the surface temperature – accumulation relationships for the HadCM3 estimates and the pRES estimates, and the freely-calculated IceChrono scenario and the Clausius-Clapeyron-derived OptAcc scenario for comparison. The Clausius-Clapeyron-derived accumulation estimate using the HadCM3 GCM strongly correlates a change in accumulation with a change in surface temperature. The pRES model suggests the perturbation profile impacts on the surface temperature – accumulation relationship with an  $r^2$  coefficient of 0.551. Overall, the OptAcc model preserves the relationship between surface temperature and accumulation, and can yield information on potential changes in this relationship as interpreted from the perturbation profiles.

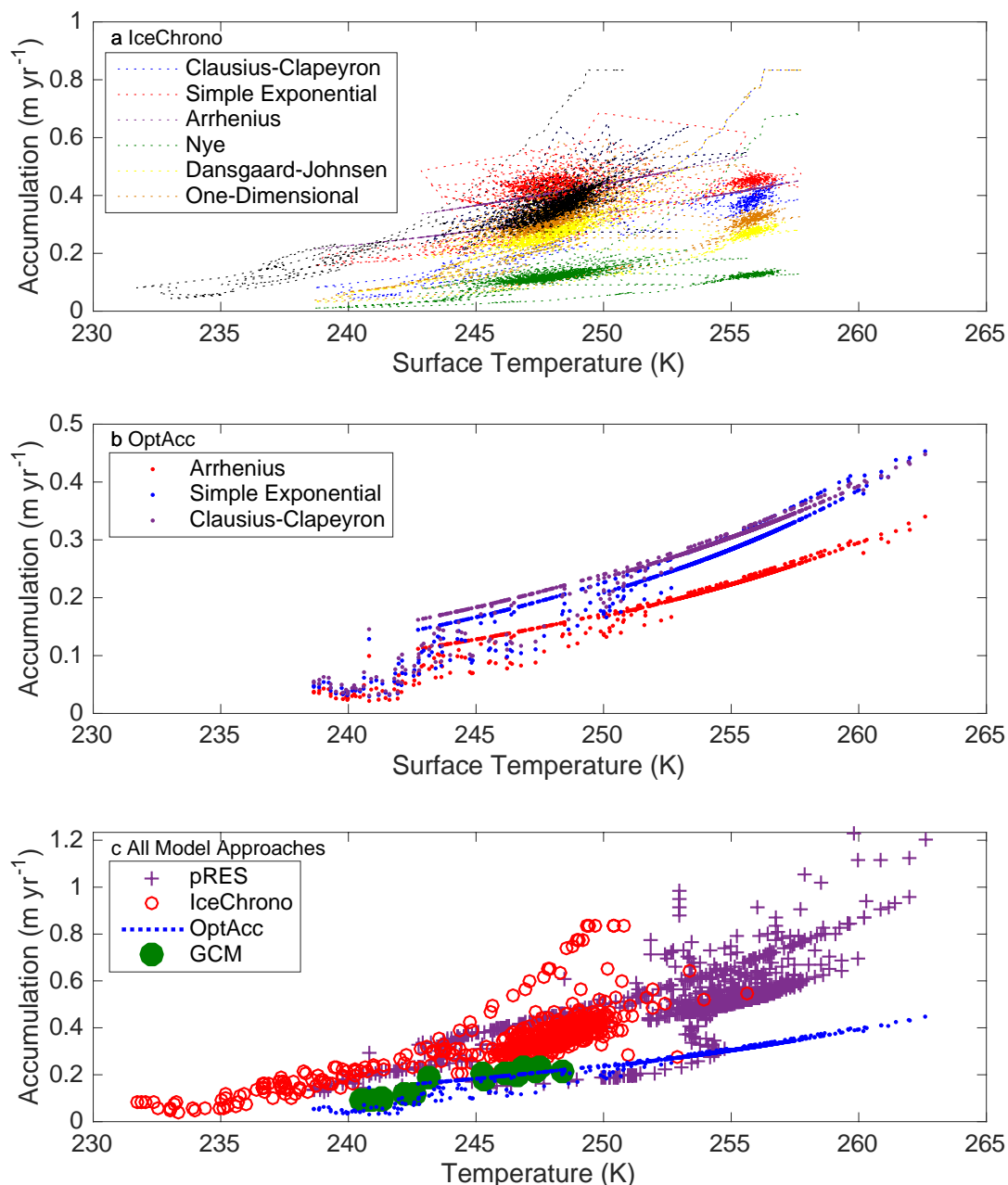


Figure 4.18: Changes in accumulation reconstructed using inverse methods with respect to changes in surface temperature (K) for (a) IceChrono model scenarios; (b) OptAcc model scenarios; (c) all model approaches for comparison.

#### 4.5.2.2 Thinning Reconstructions

The more realistic assumptions underpinning the One-Dimensional thinning function is the reason why, when developing a more complex age-depth model using an inverse approach, this relationship alone was used to determine the optimum profile of deformation along the

ice core. Three inverse approaches have been used to reconstruct the profile of deformation at the drilling location from an initial profile. The IceChrono, Direct Search and OptAcc models optimise a free parameter in the thinning function. The following section will discuss the implications of the differences between the thinning functions optimised using these inverse approaches.

- a) IceChrono: In order to assess the empirical thinning techniques, three scenarios used in the IceChrono study had thinning functions prescribed (Nye, Dansgaard-Johnsen, and One-Dimensional Thinning functions), and a fourth (as used in the accumulation reconstructions) used no *a priori* information. The results (fig. 4.08) demonstrate the significance of the assumptions used in these empirical thinning functions when assessing the range of accumulation reconstructions. Most notably, the low rates of thinning estimated by the linear Nye method (resulting in consistently young age-depth estimates on an empirical age-depth profile (fig. 4.05)), force the accumulation reconstruction to be ~30% of the present-day mean accumulation rate throughout the Holocene. As already suggested in this chapter, this is to keep the annual layer thickness values sufficiently low to ensure that the age horizons fit throughout the ice core. Therefore, this thinning function must be considered an unreliable reconstruction of the ice core record due to the age-depth underestimations. Similarly, by limiting the variability in the *a priori* Dansgaard-Johnsen and One-Dimensional thinning profiles, the accumulation reconstructions display lower present-day rates of accumulation than the observed present-day mean rate of accumulation. During glacial conditions where accumulation rates are much lower, the accumulation reconstructions using *a priori* thinning information match the profile reconstructed using no prior information.
- b) Direct Search: Thinning functions estimated using the Direct Search method are dependent on the *a priori* accumulation history that is unchanged through the inverse model. For the FP ice core, a high rate of deformation is predicted in the model. This is reflected in the value for the  $p$ -parameter and the  $n$ -exponent in Glen's Flow law ( $n$  is calculated by inverting eq. 2.16; presented in table 4.07). High rates of thinning – particularly in the upper 200 m of the FP ice core – are evident in all model simulations irrespective of accumulation input. This is despite a correction for the densification of snow in the upper 100 m of the ice core. The  $p$ -parameter that controls the shape of deformation is a single value, and cannot always fit the age constraints throughout the ice core record if there is a step-change in the

thinning profile. This is the case for FP; when the thinning function is reconstructed through the Direct Search method using an accumulation history optimised through the IceChrono model, the fit of constraints is improved. Through this experiment, it is evident that it is not sufficient to optimise just a single parameter when calculating the age-depth profile of the FP ice core. An already-optimised accumulation profile is required to account for further uncertainties, such as the natural variability in the accumulation history, and improve the accuracy of the age-depth reconstructions produced using this model.

- c) OptAcc: Following the development of the Direct Search inverse approach, an additional optimisation process is included in the inverse approach in order to improve the accumulation reconstructions in addition to the thinning function. Fig. 4.11 and 4.12 present the results of this model with three different *a priori* accumulation reconstructions. The results are all similar as the final age-depth profile is mostly controlled by the perturbation that is applied to the accumulation history. Table 4.09 presents the  $p$ -parameter and  $n$ -exponent values determined using this optimisation technique. Results yield a higher  $p$ -parameter for all reconstructions than the Direct Search approach, and hence a value for Glen's exponent that is positive but these values remain low. This suggests that the reconstructed values of the  $p$ -parameter are improved using the OptAcc model, in comparison to the Direct Search model.

#### 4.5.3 Optimal Dating Strategy

Through the synthesis of these models, it is evident that the choice of techniques used to reconstruct the accumulation and thinning profiles impacts on the accuracy of the age-depth profile. Throughout this chapter, the age estimates at the depths corresponding to age horizons are presented with the modelled age uncertainty; table 4.12 concatenates these results to present the RMSE value for each scenario, in order to directly assess the accuracy of each simulation. The final section of this chapter will discuss the results of each model approach with a view to suggesting the optimal dating strategy for the FP ice core. This will be completed by first assessing the different model approaches, before discussing the most accurate independent reconstructions of accumulation and thinning.

#### 4.5.3.1 Assessment of the Modelling Approaches

The results presented throughout this chapter consistently suggest that optimising a single parameter is not sufficient to reconstruct the most accurate profiles of accumulation and thinning. Assessment of the RMSE values confirms this statement; the optimisation of a single profile, using the pRES or the Direct Search methods, leads to the age-depth reconstruction with the largest RMSE value (table 4.12). Without a method to account for uncertainty in both the accumulation and thinning profiles, the final age-depth profile will incur error. To test this, an additional scenario for the Direct Search method used the optimised accumulation profile from the freely-calculated IceChrono scenario (fig. 4.07; 4.08; table 4.04 (final column)). This model scenario appears to fit the constraints better (fig. 4.09 and table 4.04), despite the fact that the resulting RMSE value for the IceChrono-derived Direct Search model scenario is higher than the other model scenarios (table 4.12). The improvement in the accuracy of the age scales (when compared with age horizons) is assumed to be because of the additional solution to accumulation. Therefore, IceChrono and OptAcc models yield smaller RMSE values than the pRES and Direct Search methods by incorporating additional free parameters and multiple constraints (table 4.12). As a result, the model scenarios from the IceChrono and OptAcc approaches present the most accurate age-depth profiles with RMSE values up to 25 times smaller than the corresponding values for the Direct Search and pRES approaches.

*Table 4.11: RMSE values quantify the misfit between observed age constraints and the modelled estimates at corresponding depths for the optimised age-depth profile in every scenario presented in this chapter. The row across the top of the table establishes the model boundary conditions (initial profiles) for each modelling technique. All RMSE values are in years. For the Direct Search and OptAcc models, the results are presented based on the scenarios using different initial accumulation profiles, despite an a priori thinning function is prescribed using the One-Dimensional approach in all cases.*

<b>Model</b>	<b>CC</b>	<b>SE</b>	<b>Arr</b>	<b>Nye</b>	<b>D-J</b>	<b>1-D</b>	<b>Free</b>
<b>IceChrono</b>	195	188	190	176	301	309	331
<b>Direct Search</b>	3712	3604	1937	N/A	N/A	N/A	5066
<b>OptAcc</b>	204	257	148	N/A	N/A	N/A	N/A
<b>pRES</b>	N/A	4031	N/A	N/A	N/A	N/A	N/A

Following the assessment of the models, it is apparent that the IceChrono and OptAcc techniques yield age-depth profiles of higher accuracy than the other approaches. However, further assessment is required to compare these two approaches. The RMSE values for the OptAcc scenarios of 148-204 years are similar to those calculated for the IceChrono model scenarios. The differences between these RMSE values are minor as they are all derived from age-depth profiles that agree with the age constraints. Furthermore, the profiles of accumulation and thinning reconstructed using the accumulation-derived IceChrono scenarios are similar to the equivalent reconstructions by the OptAcc approach (fig. 4.07 and 4.12). However, the two approaches differ when one compares the age-depth estimations close to the bed. The IceChrono model consistently estimates an age at bedrock of 60-100 ka BP, regardless of the initial profiles bounding the seven different IceChrono scenarios. In the optimised simulation with no prior information, the age at bedrock is estimated as  $85.5 \pm 7.4$  ka BP. The OptAcc model estimates an age close to the bedrock of 120-140 ka BP. Without age constraints in the final 100 m of the FP ice core, we must seek independent evidence to determine the age of ice at the base of this ice core.

Assessing the stable water isotope record of the FP ice core, the values indicate that ice from the end of the LIG is preserved in the record. By comparing the FP stable water isotope record with annual-layer counted Greenland records that are known to contain LIG ice (NEEM, 2013), the LIG is present in the deepest 50 mweq of the FP ice core. Annual-layer counted ice core records indicate that the globally synchronous Eemian interglacial ended at 115 ka BP (NEEM, 2013). As a result, the IceChrono age-depth profiles that consistently estimate an age at the bed of 60 – 100 ka BP are not accurate and it must be assumed that the OptAcc model reconstructs the most reliable age-depth profile, producing an age at the bedrock consistent with independent evidence (NEEM, 2013).

#### 4.5.3.2 Assessment of the Reconstructions of Accumulation and Thinning

The *a priori* empirical accumulation profiles, calculated in section 4.3.3 and used as initial profiles in the constrained approaches, lead to differences in the final age-depth estimates. This is due to the differences in each empirical relationship – particularly the sensitivity of the rate of accumulation to changes in surface temperature (fig. 4.16 and fig. 4.18). Assessment of the optimised accumulation profiles should determine which of the empirical accumulation relationships could be the most reliable for reconstructing the FP accumulation record.

The Arrhenius approach yields the smallest RMSE value in all of the constrained approaches, followed by the Clausius-Clapeyron technique and Simple Exponential for the OptAcc approach. Using the IceChrono method, the RMSE values for each accumulation reconstruction agree to within seven years. Despite the relatively similar RMSE values across the OptAcc and IceChrono approaches, the Arrhenius and Simple Exponential relationships do not provide the most reliable constructions of accumulation. In the IceChrono approach, the Arrhenius and Simple Exponential-derived thinning functions present 'kinks' (fig. 4.07). Furthermore, using the OptAcc and Direct Search approaches, Simple Exponential and Arrhenius initial accumulation profiles result in more negative and lower values of the  $p$ -parameter and Glen's exponent. This is because of the differences in the surface temperature – accumulation relationship for each technique, that controls the sensitivity of accumulation with respect to a change in surface temperature. For Arrhenius and the Simple Exponential, there is a less significant change in accumulation with respect to a change in surface temperature (as derived from the relationship assumed with stable water isotopes) (fig. 4.16 and 4.18). Therefore, the Arrhenius and Simple Exponential accumulation profiles do not estimate a mean annual accumulation rate during glacial conditions that is sufficiently low to ensure a stable reconstruction of strain throughout the ice core; instead a change in the profile of thinning at 600 m in these scenarios suggest a change in the ice flow at the site. This suggestion is not reasonable for the FP ice core, as previously explained (section 4.5.2.1).

Therefore, this study suggests that despite the slightly higher RMSE value, the Clausius-Clapeyron accumulation relationship yields a more reliable reconstruction of accumulation. Clausius-Clapeyron-derived RMSE values remain smaller than the smallest uncertainty on the age constraints and should therefore be considered reliable. IceChrono scenarios that use a Clausius-Clapeyron initial accumulation profile yield similar profiles of thinning (fig. 4.07) as other accumulation-derived scenarios, but do not require an adjustment to the ice flow in order to attain a low annual layer thickness at 600 m in the FP ice core. Furthermore, comparison of the initial accumulation reconstructions with the final modelled profile using the OptAcc approach suggests that the initial Clausius-Clapeyron relationship yields a more accurate profile and requires less perturbation throughout the ice core record.

This chapter has already concluded that the OptAcc model approach reconstructs the most reliable FP ice core record. The OptAcc model optimises the  $p$ -parameter that is used in the calculation of the One-Dimensional thinning function. In table 4.03, the age estimates at

depths corresponding to age horizons are similar for age scales estimated using either a Dansgaard-Johnsen and or the One-Dimensional thinning function. However, the One-Dimensional thinning function contains a parameter that can be optimised, and therefore this relationship was used in the development of constrained approaches. However, one can still discuss the accuracy of each thinning function by assessing the accumulation reconstructions from thinning function-derived IceChrono model scenarios. It has already been discussed that the accumulation and age-depth profiles reconstructed from IceChrono scenarios using the Nye thinning is not realistic for long ice core records (section 4.5.2.2). The Nye thinning function is satisfactory for short ice-core records, but longer ice-core records that experience substantial annual layer thinning are not accurately reconstructed using this approach (fig. 4.08). The aforementioned balance of interplay between accumulation and thinning profiles is demonstrated here: as a result of low rates of strain using an *a priori* Nye and Dansgaard-Johnsen thinning profiles in the IceChrono approach, the modelled accumulation reconstructions remain low throughout the record to maintain a sufficiently low annual layer thickness (fig. 4.08). The freely-calculated and One-Dimensional thinning functions result in a steeper deformation profile, like the profiles estimated through the OptAcc model, and an accumulation history throughout the current interglacial period that is closer to the present-day mean annual accumulation rate.

Additional assessment on the accumulation reconstruction throughout the ice core record must be completed to confirm the most reliable initial accumulation estimate. However, the results of this chapter suggest that the most accurate reconstruction of the FP ice core is achieved using by optimising free parameters in the Clausius-Clapeyron accumulation relationship and the One-Dimensional thinning profile, using the OptAcc model approach.

#### 4.6 Summary

A synthesis of all the modelling techniques that are used to reconstruct the accumulation history and thinning profile of an ice core was required before this study progresses. The age-depth profile of the FP ice core has been reconstructed using three different empirical accumulation techniques, and three different thinning techniques, with an additional four inverse approaches employed to optimise either accumulation, thinning, or both. In addition to these four inverse approaches, a GCM provides an independent technique to estimate the mean annual accumulation on a millennial-scale resolution. The differences between age-depth profiles produced using different model combinations have been assessed in order to determine the impact alternative dating strategies have on age-depth

profiles. Differences in the thinning profile have a greater impact on the final age-depth profile than differences in the accumulation history, but the accumulation reconstruction must also be improved through an inverse approach to account for any inconsistencies in the ice core record that are not reconstructed using a forward model. Further assessment of the results demonstrates that the most accurate empirical reconstructions of accumulation and thinning profiles for this ice core are the Clausius-Clapeyron and One-Dimensional relationships, respectively. To evaluate these techniques, and the inverse approaches, critical assessment of the stable water isotope record is required. Despite having a reasonable, stable accumulation rate throughout the Holocene, and fitting all age constraints, the IceChrono age-depth estimation at bedrock is too young to explain the stable water isotope record that is preserved in the ice core. Moving forward with this study, the FP, BI, and JRI ice core age-depth profiles have been reconstructed using the OptAcc model, with *a priori* accumulation information estimated using the Clausius-Clapeyron relationship. This combination is capable of reconstructing the higher, more variable annual accumulation at coastal sites that is preserved in high resolution in the FP, BI, and JRI ice cores.

Before the FP, BI, and JRI ice cores can be accurately reconstructed, additional information must be gathered and assessed as part of the first objective of this project (section 1.2.1). Annual layer thickness measurements can assess the accuracy of the model estimates, or constrain the annual layer thickness estimates. In the following chapter, novel techniques of chemical analysis are used to retrieve sub-annual records from sections of the Berkner Island ice core, and used to assess the various inverse approaches more comprehensively.



## **Chapter 5: A comparison of annual layer thickness model estimates with observational measurements using the Berkner Island ice core, Antarctica**

A. Massam, S.B. Sneed, G.P. Lee, R.R. Tuckwell, R. Mulvaney, P.A. Mayewski, P.L. Whitehouse. 2017. A comparison of annual layer thickness model estimates with observational measurements using the Berkner Island ice core, Antarctica. *Antarctic Science*, doi: doi:10.1017/S0954102017000025.

### **5.1 Summary**

Reconstructions of ice-sheet and atmospheric processes yield varying annual layer thickness and age-depth profiles (Chapter 4). In order to assess the accuracy of the reconstructed age-depth models, comparison with observational data is needed. The following chapter is the manuscript of a peer-reviewed paper that presents annual layer thickness measurements. The text in the manuscript is unchanged; only the layout has been reformatted for this thesis. The annual layer thickness measurements have been obtained by three different analytical techniques at varying analytical resolution, taken from three depth ranges along the Berkner Island ice core. The principal motivation behind this paper was to apply a novel technique in ultra-high resolution trace-element analysis and assess the reliability of the resulting profiles in identifying annual layers at a resolution currently beyond standard laboratory techniques. In doing this, the identified annual layers contribute to the second and third objective of this study (section 1.2.1), in which the measured thicknesses are compared with the modelled estimates of annual layer thickness at corresponding depths.

Supplementary to this manuscript (section 5.8 onwards), this chapter explains the choice of the most accurate and reliable age-depth model constructed in Chapter 4 and Appendix 1. This is done by comparison of all modelled annual layer thickness estimates from the approaches described in Chapter 4. In addition, the chapter provides a brief statistical analysis of the LA ICP-MS analytical data that was not included in the final manuscript.

## 5.2 Abstract

A model to estimate the annual layer thickness of deposited snowfall at a deep ice core site, compacted by vertical strain with respect to depth, is assessed using ultra-high resolution laboratory analytical techniques. A recently established technique of high-resolution direct chemical analysis of ice, using ultra-violet laser ablation inductively-coupled plasma mass spectrometry (LA ICP-MS) has been applied to ice from the Berkner Island ice core, and compared with results from lower-resolution techniques conducted on parallel sections of ice. The results from both techniques have been analysed statistically in order to assess the capability of each technique to recover seasonal cycles on deep Antarctic ice where annual layer thickness is beyond the current standard laboratory resolution of ~10 mm. Results do not agree with the annual layer thickness estimates from the age–depth model for individual samples < 1 m long as the model cannot reconstruct the natural variability present in annual accumulation. However, when compared with sections >4 m long, the deviation between the modelled and observational layer thicknesses is minimized to within two standard deviations. This confirms that the model is capable of successfully estimating mean annual layer thicknesses around analysed sections. Furthermore, our results confirm that the LA ICP-MS technique can reliably recover seasonal chemical profiles beyond standard analytical resolution.

Keywords: ice core; ultra-high resolution; chemistry; Berkner Island; mass spectrometry; age-depth model

### 5.3 Introduction

The deposition of snow across Antarctica results in a record spanning millennia and capable of recording seasonal cycles of several different climatic proxies, revealing past climatic conditions on local, regional and global scales, on both short- and long-term timescales. Preservation of temporal variations in stable water isotopes and chemistry as the deposited snow turns to ice creates an isotope-chemistry series that can provide seasonal to glacial/interglacial reconstructions of past climate (Dansgaard 1953, 1964).

Unreactive gases trapped within the ice matrix offer continuous records of atmospheric conditions on a global scale due to rapid rates of atmospheric mixing. In order to reconstruct large-scale climatic events on an inter-hemispheric scale, climate proxies from multiple sources must be integrated and tied to a single chronology, which requires a continuous, high-resolution record. Accurate synchronisation of ice core records with climate proxy records from marine, polar and terrestrial sites gives the best view of global climate responses during glacial/interglacial periods, and high-resolution profiles are vital to the full interpretation of the timing and characteristics of underlying mechanisms and to understanding the relationship between the Polar Regions and the rest of the Earth.

The dating of deep Antarctic ice cores still relies primarily on modelled accumulation derived from seasonal cycles in the stable water isotopes and chemistry. Therefore, improvements to existing chronologies depend on further developments of the analytical techniques. The low mean annual accumulation characterizing much of Antarctica makes it difficult to obtain sub-annually resolved proxy records in ice cores beyond certain depths. Therefore, the construction of Antarctic ice-core chronologies – and the subsequent interpretation of palaeoclimate records – typically relies on glaciological modelling techniques that are constrained using observational data, e.g. known-age horizons preserved in the ice or chemical records. Increasing the resolution of palaeoclimate records improves the information that can feed into climate or chronological models. The models applied to ice-core profiles rely on the resolution of the stable water isotope profile as well as a number of glaciological assumptions on ice-sheet stability and thus have larger age-uncertainty compared to annual layer counted ice core chronologies.

As water isotopes tend to diffuse in ice and the seasonal cycles may be lost, improvements to analytical resolution have been progressing following two main approaches, continuous and discrete trace-element analysis. A direct, continuous method (continuous flow analysis

– CFA) takes measurements continuously along the length of the ice core. CFA methods are less labour-intensive, although they usually result in the destruction of the ice core by melting. Continuous melting of an ice section coupled with the *in situ* analysis of trace-chemical species by ICP-MS and UV/visible spectroscopy improves the resolution of continuous records and achieves a spatial resolution of ~10 mm (Sigg et al. 1994, Rothlisberger et al. 2000). A great advantage of CFA systems relies on their relatively low contamination levels, ensured by removing the meltwater produced by the outermost part of the ice core. A disadvantage of CFA systems is the dispersion in the melting and liquid transport that limits the sub-annual resolution of deep Antarctic ice cores and consequently, the information available on long timescales that can be accurately synchronised with other climate proxy archives.

Developments to direct trace-element analysis improve the depth-resolution by the application of ultra-violet laser sampling coupled with an ICP-MS. For some time, LA ICP-MS has been applied to geological samples in order to optimise the resolution and accuracy of trace-element analysis in geochemical contexts (Arrowsmith 1987, Bea et al. 1996). More recently, this technique in ultra-high resolution direct trace-element analysis has been independently developed in ice-core laboratories (Reinhardt et al. 2001, Müller et al. 2011, Sneed et al. 2015). Previous studies have demonstrated that the ultra-violet LA ICP-MS apparatus and calibration technique developed at the WM Keck Laser Ice Facility at the Climate Change Institute (University of Maine) yields data that are similar in the shape and trends of the ice-core profile to those produced using CFA profiles, but at orders of magnitude higher resolution (Sneed et al. 2015). Correlation of LA ICP-MS results with existing chemical records on alpine ice-core chemistry profiles confirms the reproducibility of the results (Sneed et al. 2015). Further to this, LA ICP-MS can be utilized as a basis of comparison for previous studies; a recent study dramatically increased the resolution of the record comprising the end of the Younger Dryas and the onset of the Holocene as preserved in the GISP2 ice core. This ultra-high resolution record offered a novel view of abrupt climate change over this period and suggested a decrease in storm frequency and an increase in the length of the Arctic summer season at this transition (Mayewski et al. 2014). Most recently, LA ICP-MS has been applied to West Antarctic ice originating from the last glacial period at Siple Dome-A. Successful analysis of sub-seasonal profiles demonstrated the variability in the annual layer thickness measurements that had not been identified earlier in glaciological models or ice core chemistry (Haines et al. 2016).

In addition to increased resolution of climate records, major advantages of the LA ICP-MS technique include the rapid analysis time and the fact that the ultra-violet laser results in negligible ice loss, allowing repeated analyses to be carried out (Müller et al. 2011). In repeating the analysis, individual line scans can be used to measure single- and multi-element arrays, increase the spatial resolution available, and provide an alternative technique to acquire ultra-high resolution profiles of climatic proxies in ice cores.

An alternate discrete high-resolution technique, developed by R. Mulvaney and E. Wolff (pers. comm, 2016) at the British Antarctic Survey, cuts samples at a higher resolution than standard discrete techniques of ~10 mm by employing a microtome device to shave the ice sample at a sub-millimetre resolution (Thomas et al. 2009). Seasonal cycles in chemistry recovered in glacial ice from the North Greenland Ice Core Project (NGRIP) ice core allowed an absolute measurement of annual layer thickness and insight into the phasing of chemical signals and characteristics of the DO 8 event at *circa* 38 ka BP at 2 mm depth-resolution (Thomas et al. 2009). A full geochemical profile outlined the dominant and recessive mechanisms for the duration of the climatic transition into DO 8 at sub-annual resolution. The method, though effective for high-resolution analysis on deep ice, is labour-intensive and it is difficult to cover more than small sections of an ice core. Improvements to the ion chromatography system at the British Antarctic Survey – principally a new Dionex 4000 IC system – allow a reduced sample volume and therefore improve the spatial resolution of each measurement.

Despite these advances in direct ice-core analysis, LA ICP-MS is yet to be employed on ice originating from the Weddell Sea, Antarctica, where traditional discrete and CFA methods fail to recover seasonal chemical cycles at great depths. The aim of this study is to compare the different analytical techniques, and then use the results to test the accuracy of the modelling of the annual layer thickness of the Berkner Island ice core. The Berkner Island ice core was drilled over three field seasons 2003-2006 (Mulvaney et al. 2007), reaching the ice sheet base at a depth of 948 m, at the south dome of the island which is embedded within the Ronne and Filchner ice shelves in the Weddell Sea, Antarctica. In this study, we reconstruct annual layer thickness from the stable water isotope profiles and glaciological modelling and, following a study to assess the reliability of the records, we compare these model estimates with the observational annual layer thickness measurements obtained by LA ICP-MS.

## 5.4 Methodology

High-resolution analysis, completed on parallel sections of ice from three depth ranges along the Berkner Island ice core, was achieved by indirect and direct trace-element methods. For comparison and confirmation of the record obtained by LA ICP-MS on Antarctic frozen samples, discrete sampling has been completed on parallel sections of ice to obtain a second geochemical profile. Where the annual layer thickness is estimated to be greater than 20 mm, the discrete samples were not cut using the microtome technique, but instead using a band saw for which an associated ice loss is calculated. The ion profiles generated by each method have been compared by identifying annual peaks in each profile and calculating the mean annual layer thickness for each section. For assistance in the identification of annual layer peaks, a long section of CFA data is presented for the Berkner Island ice core at a depth where sub-annual resolution is still attainable by this lower-resolution technique.

Successively, comparison of annual layer thickness measurements with the annual layer thickness estimated from the model is the final assessment in this work. The methodology for the annual layer thickness model is included in the supplementary material, accompanied with a list of the parameters and known-age horizons used in the estimation of annual layer thickness at Berkner Island.

### 5.4.1 *Continuous Flow Analysis*

A full ice core can be continuously melted in core sections with the dimensions of 30 x 30 mm, with only the inner part of the ice section measured to eliminate the risk of contamination. The remainder of the ice section melted runs off the melt-head as waste. Analysis of the Berkner Island ice core by CFA was completed at BAS, on a system that is capable of measuring a full ion profile among other chemical species, at a continuous rate with a maximum resolution of 10 mm.

### 5.4.2 *LA ICP-MS and Discrete Sample Details*

The ice core retrieved from Berkner Island was selected for this study for its low mean annual accumulation at the surface, with an overall thickness of 948 m. Present-day mean annual accumulation at the core site is 0.185 m yr<sup>-1</sup> in water equivalent, with an age-depth profile reaching the last interglacial period. As a result, the annual layer thickness model estimates that the depth at which thinned annual layers are beyond the standard laboratory resolution of ~10 mm is ~560 m. This leaves 40% of the total ice core profile beyond the reach of sub-annual profiles using standard methods.

Parallel sticks of ice, cut from the archived ice core material, have been analysed by two methods including high and ultra-high resolution measurements. Sticks of ice were cut from the inner section of the ice core to avoid potential contamination by the drilling fluid residue on the exterior of the ice core. Sticks of ice were placed in plastic lay-flat bags with the ice core bag number and top of the core section clearly indicated.

#### 5.4.3 LA ICP-MS

The analysis of Berkner Island ice using LA ICP-MS was completed at the WM Keck Laser Ice Facility, at the Climate Change Institute (CCI), University of Maine. The laser-ablated ICP-MS methodology is largely described in Sneed et al. (2015) and only a brief summary of the key features is mentioned here. Profiles were acquired using the Sayre Cell™ cryocell, developed at CCI, which is capable of holding up to one metre of ice at 248 K and has a small volume (~20 cm<sup>3</sup>) open-design ablation chamber. The cryocell system is positioned underneath a New Wave UP-213 laser, connected to a Thermo Element 2 ICP-MS with Teflon tubing (Sneed et al. 2015).

Prior to analysis, the ice sample was cleaned by removing the outer millimetre of ice using a ceramic scraper to limit the contamination risk. The ice is held in the cryocell whilst the gas flow was purged for two minutes in order to remove impurities in the system. Individual line scans, measured using a laser spot size of 100 µm in diameter, yield the ultra-high spatial resolution of LA profiles. LA ICP-MS profiles are continuous for 40 mm; once finished, the ice is automatically moved to begin the next 40 mm segment to start at the end of the previous ablation pass. Adjacent line scans, used for multi-element analysis, are separated by 200 µm to prevent overlapping scans. Sampling resolution is 121 µm sample<sup>-1</sup>; this resolution is dependent on the laser spot diameter, firing rate, scan speed and the ICP-MS sampling rate (Sneed et al. 2015).

Ice samples, up to 200 mm in length, were analysed for sodium (Na), which has been shown to have a clear annual cycle (Sommer et al. 2000). The LA ICP-MS generates results available in counts per second (cps). The relative intensity of element concentrations in cps were converted to concentrations (µg/L) using calibration curves constructed from liquid samples and lasing frozen standard reference material (Sneed et al. 2015).

A dual-cyclonic spray chamber with entrance ports for liquid samples and laser aerosols is fitted to the ICP-MS system. A low-flow nebuliser (20 µL min<sup>-1</sup> from Elemental Scientific) aims to reduce the amount of liquid aspirated and to enable higher gas flow in the laser

ablation chamber. This facilitates daily calibration of the ICP-MS, which is completed using a combination of liquid standards and frozen reference materials in a two-step process outlined by Sneed et al. (2015). To ensure accurate results using the Sayre Cell™ cryocell, the base of the open cell must have an airtight seal with the ice sample. Soundness of the seal is tested in two ways: (i) a flowmeter built into the cryocell system, and (ii) the ICP-MS is tuned with the ice in place so that a small leak would be observable in the ice chemistry signal (Sneed et al. 2015).

#### 5.4.4 Discrete Samples

For the deepest sections investigated by LA ICP-MS, we obtained discrete samples from a parallel cut of the same ice core, to be measured in solution mode. This method has been used successfully to analyse the warming transition of Dansgaard-Oeschger 8 (DO8), at *circa* 38kyr in Greenland ice (Thomas 2006, Thomas et al. 2009).

Unlike the ice sampled by the other techniques in this study, sections of ice for the discrete method were limited to 80 mm in length. The reason for this was to limit the bending moment exerted on the stick of ice as it passed under the blade whilst being held in the microtome vice system. The depth ranges of discretely cut samples are included in table 5.01.

Prior to cutting the discrete samples, any dust or residue was removed from the instruments by cleaning the microtome blade and mantle using isopropanol. A pre-frozen section of ultra-high purity (UHP) water was passed under the blade to clean it thoroughly; after this process, five samples of UHP water were collected for use as a background standard for the cold room procedure during the chemical analysis.

A clean microtome blade removed the outer millimetre of ice in order to avoid contamination from the outer layers. The ice was then placed in the mantle of the microtome and passed under the blade. The mantle automatically raises 40 µm with every forward stroke so the exact sample size can be determined by the number of times the ice has passed under the blade.

#### 5.4.5 Lower Resolution Discrete Sampling

A lower-resolution discrete sampling method was employed on sections of ice for which annual layer thickness is estimated to be greater than 20 mm. For these sections, the high-resolution microtome technique would not be necessary and instead 5 mm discrete samples

were cut using a band saw and measured using the same method as samples obtained from the microtome device. An associated ice loss of a millimetre was accounted for in the depth profile, as calculated by the width of the band saw blade.

For all discrete samples, a full ion profile was obtained in sterile conditions by ion chromatography (IC), except for the ice section at 703.2 – 703.22 m where due to low sampling volume, only a cation profile was measured. In order to prevent contamination during the discrete sampling process, protective clothing and powder-free nitrile gloves were worn throughout both the sampling and analysis procedures. The ice sample was only handled with pre-cleaned tongs and the outer millimetre of the ice sample was scraped away using a scalpel or microtome blade to remove any contaminants from the surface of the sample. Ion profiles were measured on a Dionex IC 4000 ion chromatography system in a class-100 clean room, which has less than 100 particles of  $0.5 \mu\text{m}$   $\text{foot}^{-3}$ .

## 5.5 Results

We begin by presenting the estimated age and layer thickness of the analysed samples, as derived using the glaciological model. Subsequent sections contain the LA ICP-MS and discrete sampling results, respectively. Annual cycles are identified in the IC and LA ICP-MS records based on the prominence of the Na and Mg peaks from the baseline, and the return of the peak to the baseline between the seasons. Peaks that do not return to the baseline are characterised as discrete events within one annual cycle.

### 5.5.1 *Model Estimates*

Specific sampled depths were chosen based on the estimated period of original deposition, as interpreted from the isotopic record (see figure 5.01), the modelled annual layer thickness (equation S5.01-S5.03), and ultimately the condition of the archive material at BAS (presented in table 5.01).

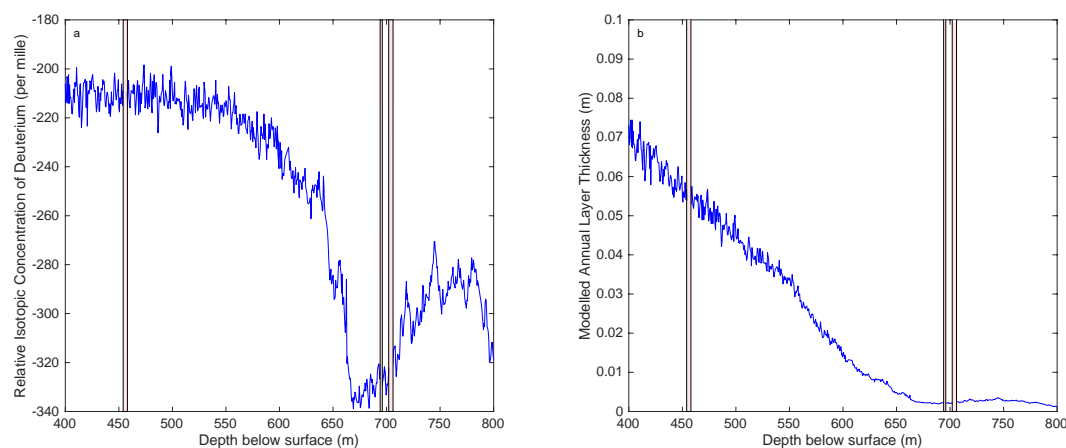


Figure 5.01: Berkner Island ice core sampled sections of ice (pink bands) across the (a) isotopic and (b) modelled annual layer thickness profiles. See supplementary information for model description.

### 5.5.2 CFA Results

As a method of comparison, and to aid the analysis of annual layer identification, a four-metre section of the Berkner Island ice core at 447 m, analysed by CFA, is presented with the correlating dielectric profiling (DEP) data (fig. 5.02). The section shows a mean annual layer thickness of  $\sim 57$  mm, and highlights the variable annual layer thickness and values of Na.

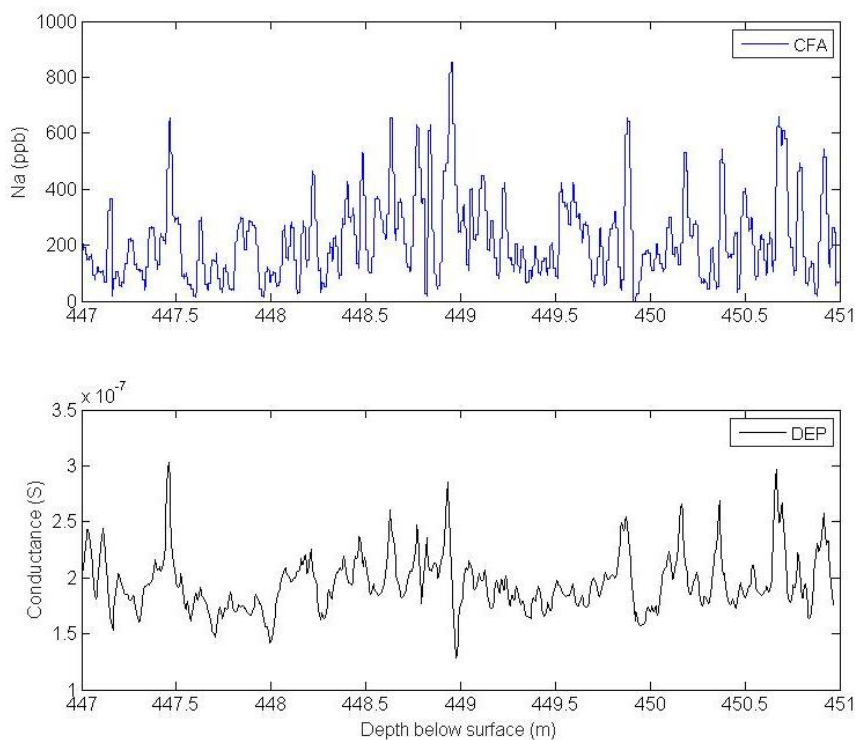


Figure 5.02: Four-metre section analysed by CFA and DEP. Top: CFA Na; bottom: DEP.

### 5.5.3 LA ICP-MS results

#### 5.5.3.1 Mid-Holocene Ice from 5.5 ka BP (454 – 459 m)

Fig. 5.03 shows the sections of ice analysed by LA ICP-MS originating from the mid-Holocene period. Three sections were taken from the depth range 454 – 459 m, where the model predicts the annual layer thickness model to be ~57 mm (table 5.01). Results are presented on semi-logarithmic plots. Red dashed lines delineate peaks that could represent either an annual or sub-seasonal deposition increase in Na. Between these sections, we are not as confident that the seasonal peak can be seen unequivocally. Examination of the results suggests that the seasonal cycles within these sections of ice are not uniform, rather they vary in layer thickness.

*Table 5.01: Annual layer thickness determined as the mean thickness value of all layers identified in each analysed section, and the standard deviation of each set of annual layers. Modelled annual layer thickness given with model error attached. For depths that have not been analysed by a particular technique, the table reads "N/A". The estimated age for each sample depth is presented, as estimated by the age-depth model.*

Depth Analysed (m)	LA ICP-MS +/- std dev (mm)	Discrete Sampling +/- std dev (mm)	CFA +/- std dev (mm)	Model +/- error (mm)	Estimated age (ka BP)
447-451	N/A	N/A	57.0 ± 8.8	56.7 ± 1.5	3.6
454	Variable	57.0 ± 10.0	N/A	56.7 ± 1.5	3.7
456	6.7 ± 0.6	55.0 ± 1.3	N/A	54.9 ± 1.4	3.7
458	26.1 ± 2.3	70.0 ± 2.8	N/A	52.9 ± 1.4	3.8
694	2.9 ± 0.1	N/A	N/A	2.1 ± 0.3	28.5
695	3.6 ± 0.1	N/A	N/A	2.3 ± 0.3	29.0
696	4.0 ± 0.2	N/A	N/A	2.1 ± 0.2	29.4
702	3.1 ± 0.1	2.6 ± 0.1	N/A	2.3 ± 0.2	31.2
704	6.1 ± 0.2	N/A	N/A	2.3 ± 0.1	32.8
706	5.1 ± 0.2	6.0 ± 2.3	N/A	2.3 ± 0.1	33.6

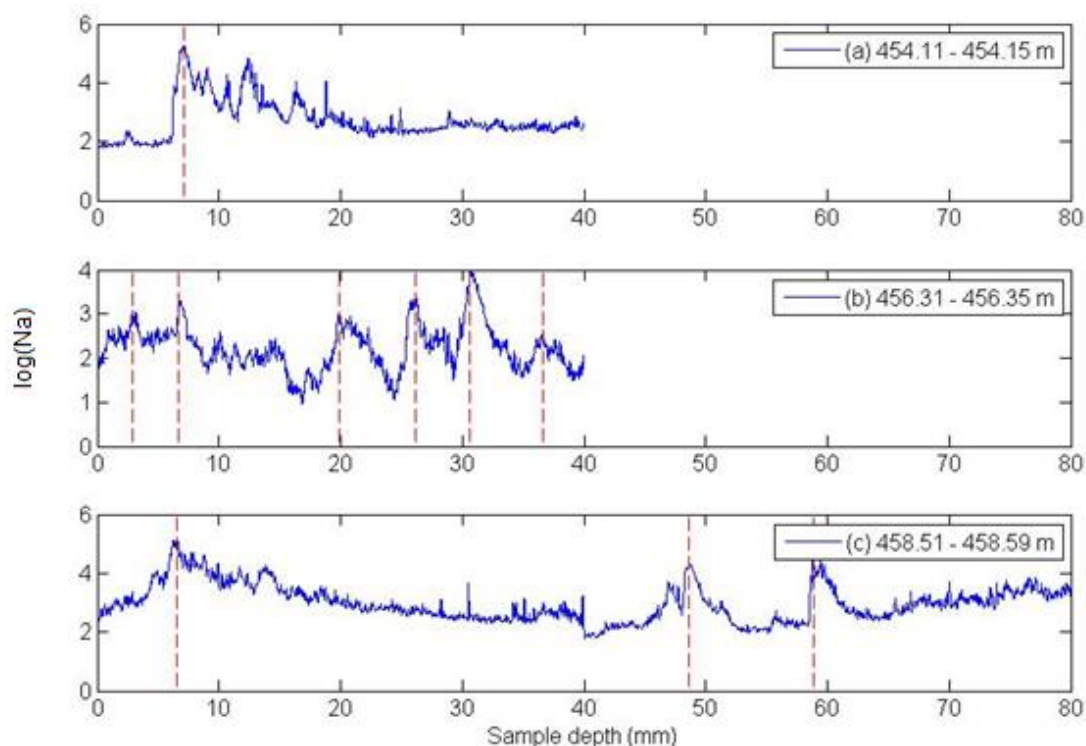


Figure 5.03a – c: LA ICP-MS profiles for three sections of sample from 454 – 459 m; semi logarithmic plots show the  $\log(\text{Na}^+)$  on a common depth scale with red dashed lines delineating a seasonal peak.

### 5.5.3.2 Glacial Ice from 27.1 – 27.7 ka BP (694 – 697 m)

Over the second depth range of 694 – 697 m, the mean annual layer thickness is estimated by disregarding sections of ice where the chemical signal is not resolvable ( $\sim 19 - 38$  mm and  $\sim 50 - 70$  mm). An increase in the periodicity per sampled section of ice, as determined by the seasonal fluctuations in Na, is due to the compaction of annual layers. In fig. 5.04c, a drop in concentration at 40 mm is likely due to the recommencement of a line scan.

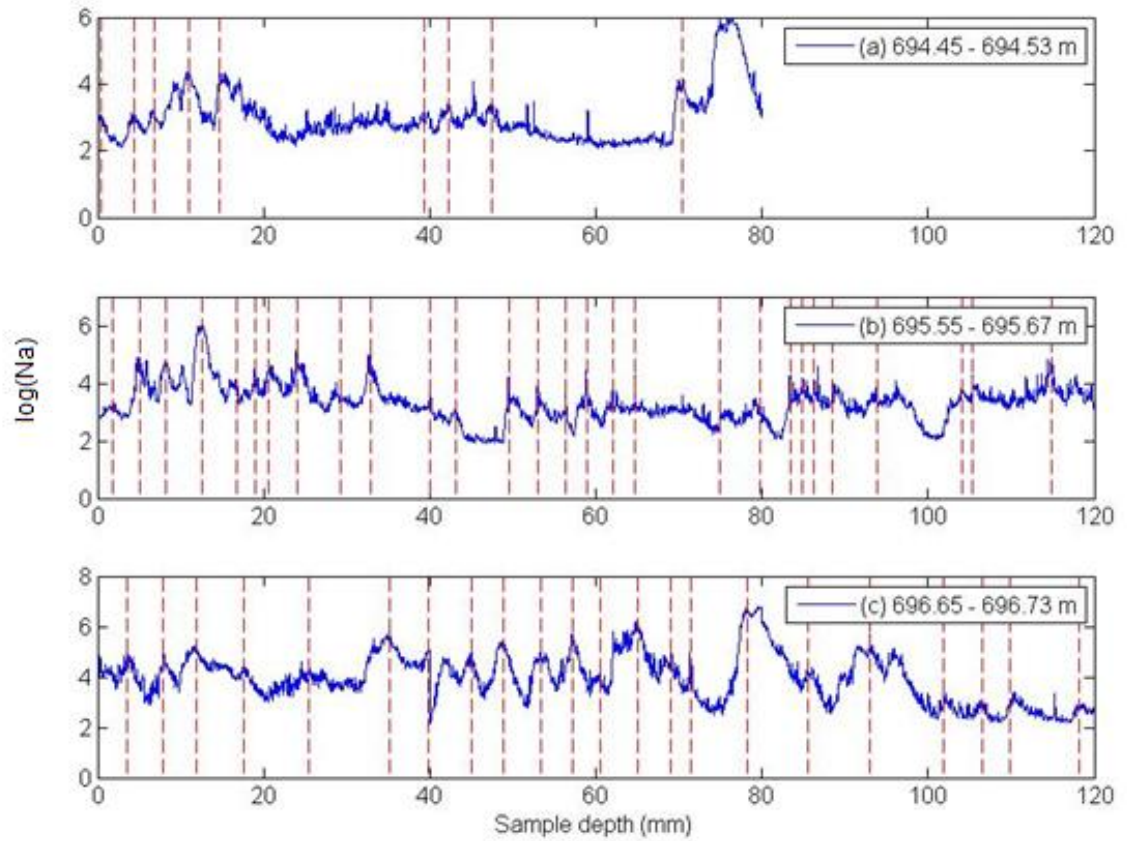


Figure 5.04a – c: LA ICP-MS profiles for three sections of ice from 694-697 m; semi logarithmic plots show the  $\log(\text{Na}^+)$  on a common depth scale with red dashed lines delineating a seasonal peak.

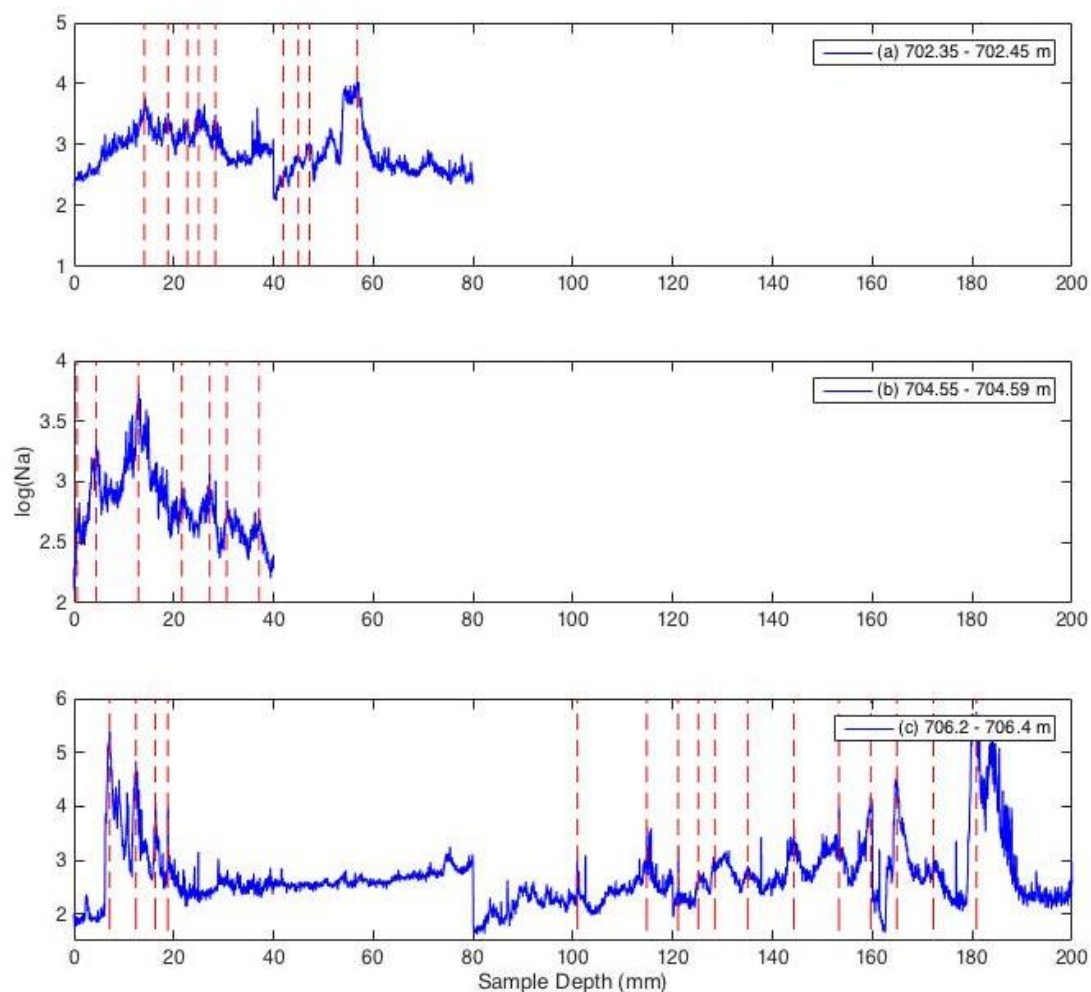


Figure 5.05a – c: LA ICP-MS profiles for three sections of ice from 702 - 707 m; semi logarithmic plots show the  $\log(\text{Na})$  on a common depth scale with red dashed lines delineating a seasonal peak.

### 5.5.3.3 Glacial Ice from 29.7 – 31.2 ka BP (702 – 707 m)

Similar to the sections of ice analysed from 694 – 697 m, there is a drop in concentration values at 40 mm in fig. 5.05a, and 80 mm in fig. 5.05c, due to the recommencement of line scans. Additionally, as with the observed layer thickness estimations from 694 – 697 m, observed layer thickness has been estimated only for sections of ice where a seasonal signal is resolvable in the ice. Layer thickness is counted between  $\sim 10 - 25$  mm and  $\sim 45 - 60$  mm in fig. 5.04a, meaning an average thickness of 3.1 mm. Across the ice sections analysed between 702 and 707 m, the chemical signal appears to be a smoothed signal where annual layers are no longer resolvable either in the ice-core record or through the analytical

technique. Where identifiable in these profiles, the peaks appear to increase from ~3 mm in fig. 5.05b to 5-6 mm in fig. 5.05c.

Initial observations on the geochemical profiles confirm that fluctuations in the Na signal are visible in the Berkner Island ice-core record. These layers do not show a clear seasonal pattern in many places, with variations in strength, thickness and signature common throughout the profiles. This is most visible between the Holocene sections at 454 – 459 m and the late glacial sections at 695 – 697 m where the number of layers over a common depth range increases by up to a factor of 10.

Focussing on the LA ICP-MS profiles within the depths of 454 and 459 m it is not possible to identify a uniform annual layer thickness, despite a relatively stable isotopic record for this depth range (fig. 5.01a, 5.03a – c). The layers identifiable in these sections range in thickness between 5 and 30 mm, compared with the 57 mm estimated in the annual layer thickness model.

Within the profiles analysed from a depth 694 m and deeper, sections of ice appear to have little seasonality in the analysed profiles (fig. 5.04a and 5.05c). These results raise the following questions regarding the reliability of LA ICP-MS at greater depths: firstly, is the method capable of obtaining sub-annual cycles in the ice originating from the last glacial period, preserved in the Berkner Island ice core? Secondly, has the chemical signal diffused at these depths, leading to a smoothed record in the ice? The answers to these questions will partly be addressed by determining the repeatability of the ultra-high resolution results using the alternative, established methods.

In the deepest analysed sections of the ice core, the observed mean annual layer thickness doubles between 695 m and 704 m, suggesting a significant increase in annual accumulation at the time of original deposition. This is contrary to what has been predicted by the model that is unable to identify natural variability not preserved in the stable water isotope profile.

#### 5.5.4 *Discrete Sampling*

The results presented have been obtained using both lower- and high-resolution discrete sampling methods. Results are presented as semi logarithmic plots of chemical profiles against the sample length, mm.

5.5.4.1 *Mid-Holocene Ice from 5.5 ka BP (454 – 459 m)*

Discrete samples were cut roughly at a 5 mm spatial resolution on sections of ice parallel to ice analysed by LA ICP-MS. In addition, the dataset has been expanded by sampling an additional 100 – 150 mm of ice per metre of ice in each depth range. Fig. 5.06 displays the results from this study, and the expanded profiles for sections of ice sampled from 455 – 459 m, with red dashed lines indicating the point at which a peak is visible. An immediate observation of the three expanded profiles is that seasonality appears smoothed throughout each profile, with a variable annual layer thickness of 50-70 mm that agrees with the CFA profiles and annual layer thickness model. Additional chemistry and the DEP datasets for the corresponding depths have been included for a thorough comparison of the between the LA ICP-MS Na and the lower-resolution datasets (fig. 5.07-5.08). The LA ICP-MS Na signal is presented a semi logarithmic in two ways: (i) the original dataset high-resolution dataset; (ii) smoothed to the lower-resolution used in the discrete sampling. Sub-seasonal discrete events are visible in the sodium and chloride profiles but are not identifiable in the non-sea salt Sulphur (nss-S) and DEP datasets. Annual layers are delineated with grey bands in each figure, in comparison to the red dashed lines in previous plots where chemical peaks could have been interpreted as an annual signal.

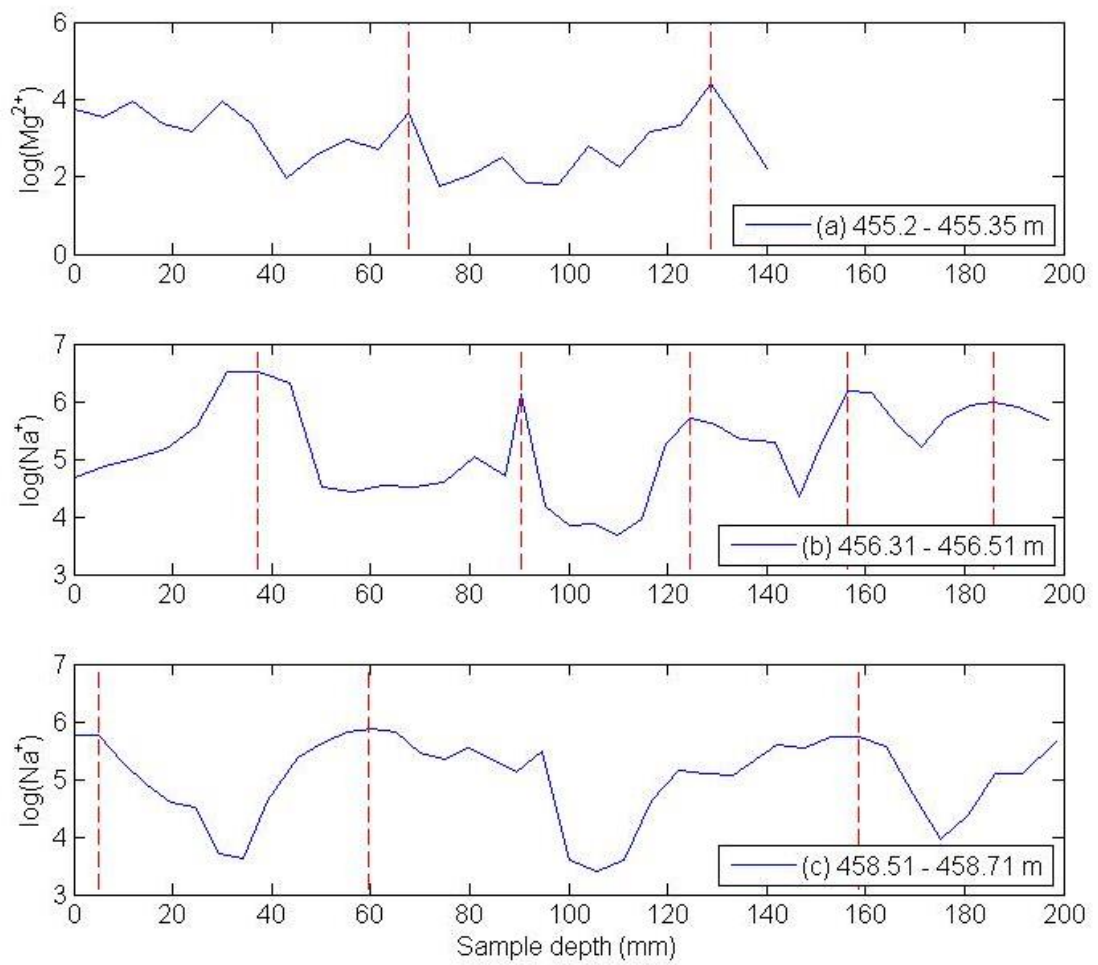


Figure 5.06a – c: Three sections of ice originating from 455 – 459 m analysed by ion chromatography and displayed as semi logarithmic plots of element concentration with red dashed lines indicating annual peaks.

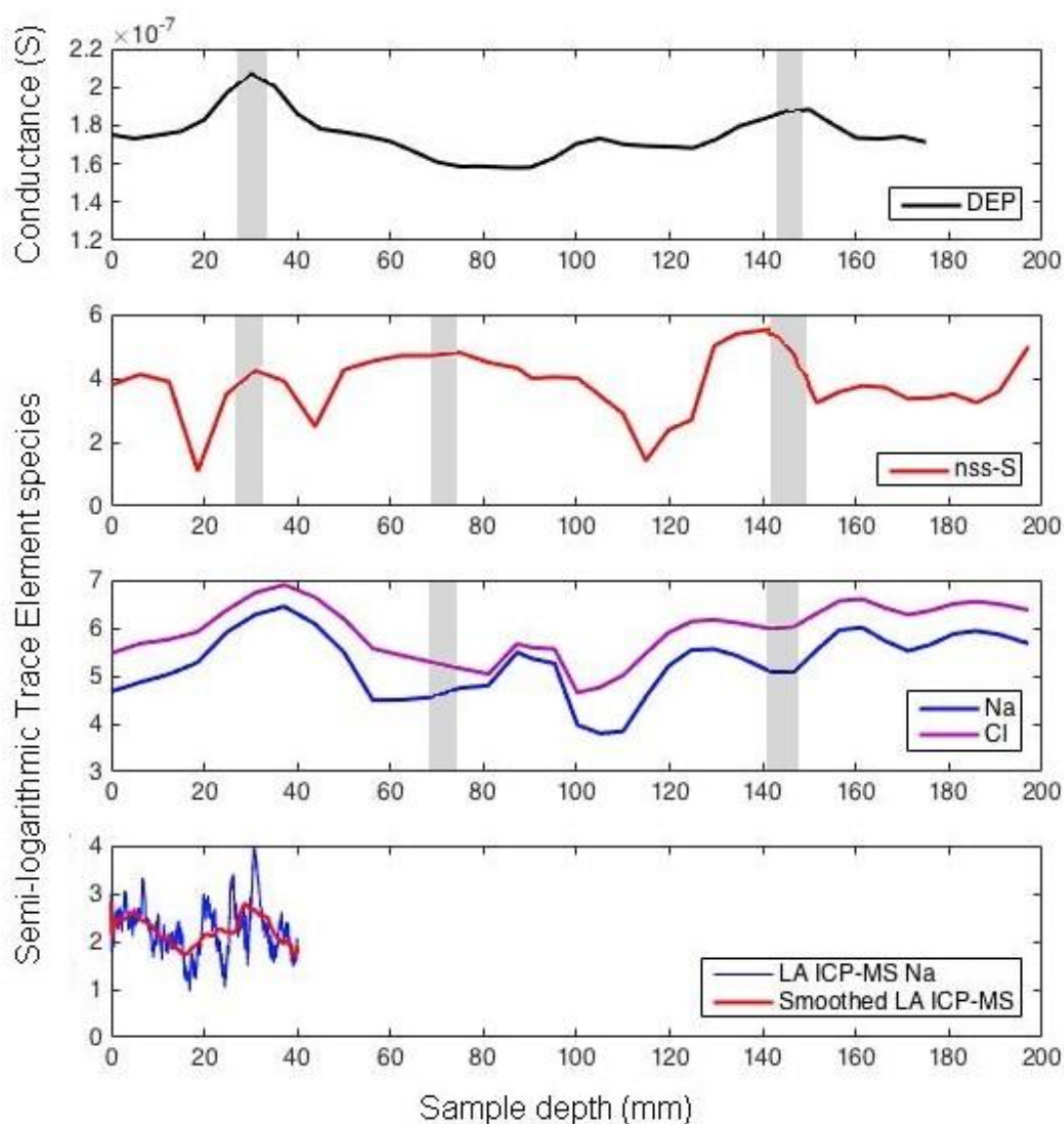


Figure 5.07: Comparison of parallel sections of ice from 456.31 m – 456.51 m from top to bottom: the DEP data; nss-S profile analysed by discrete sampling; sodium and chloride profiles analysed by discrete sampling; ice analysed by LA ICP-MS with the profile smoothed to the same resolution used in the discrete sampling technique, with annual layers indicated by grey lines.

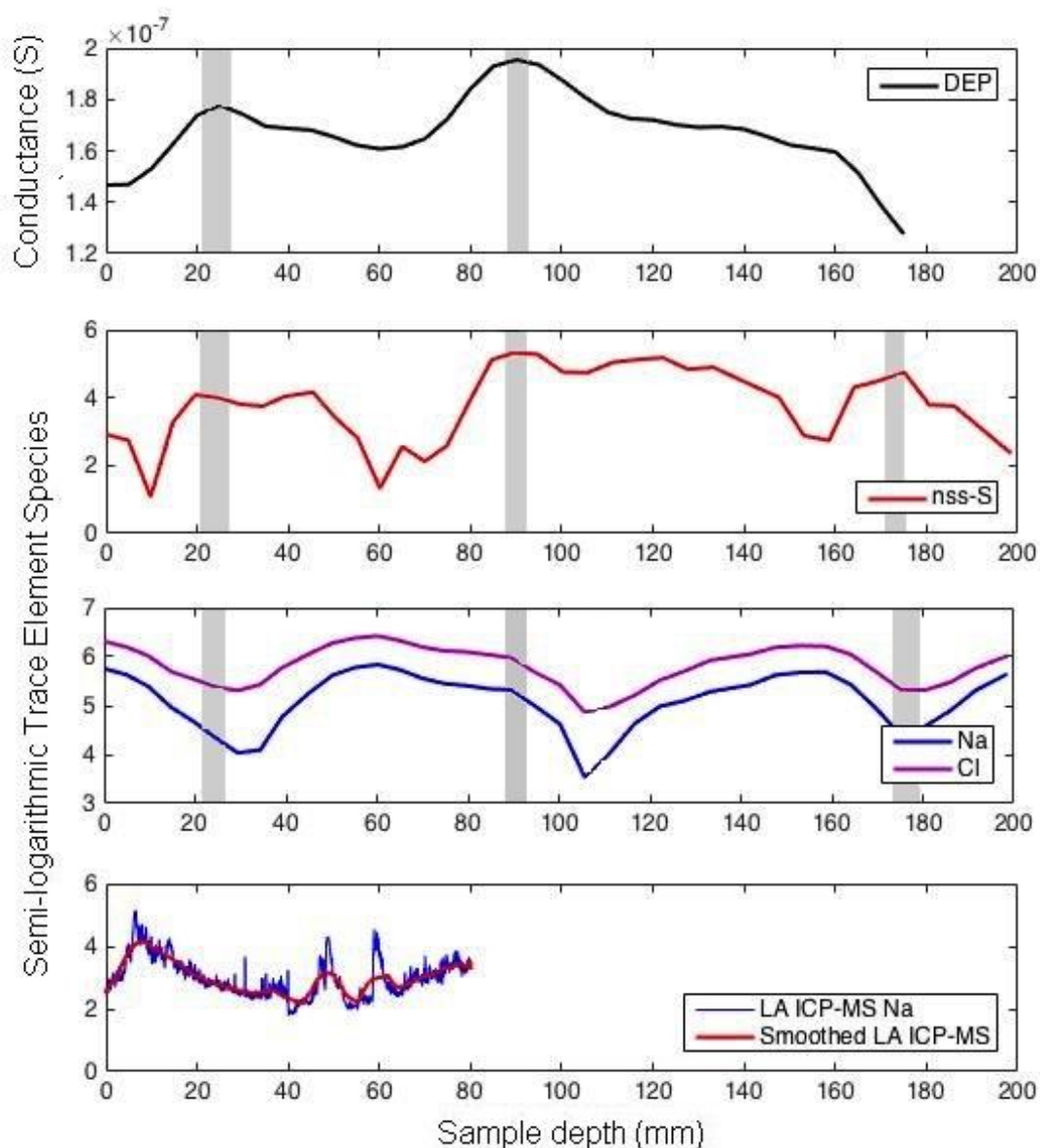


Figure 5.08: Comparison of parallel sections of ice from 458.51 – 458.71 m from top to bottom: the DEP data; nss-S profile analysed by discrete sampling (red); sodium and chloride profiles analysed by discrete sampling; ice analysed by LA ICP-MS with the profile smoothed to the same resolution used in the discrete sampling technique (red), with annual layers indicated by grey lines.

#### 5.5.4.2 Glacial Ice from 29.7 – 31.2 ka BP (702 – 707 m)

A microtome blade was used to discretely cut samples for two sections of ice, originating from the last glacial period, at a spatial resolution of 320 – 480  $\mu\text{m}$ . The results of these analyses are displayed in fig. 5.09-5.10, against the LA ICP-MS results. The IC profiles are displayed as semi logarithmic plots of trace-element sodium, ( $\text{Na}^+$ ), magnesium ( $\text{Mg}^{2+}$ ), and

calcium ( $\text{Ca}^{2+}$ ) against sampled depth (mm). Only a cation profile is available for ice at 703.2 – 703.22 m due to low sampling volume, meaning there is a sulphate signal only available at 706.3 – 706.38 m in this depth range.

Additional annual layers are identified in the lower-resolution profile, suggesting that the loss of an annual signal during the LA ICP-MS analysis is due to the capability of the technique and that the seasonal record of the Berkner Island ice core is resolvable and preserved.

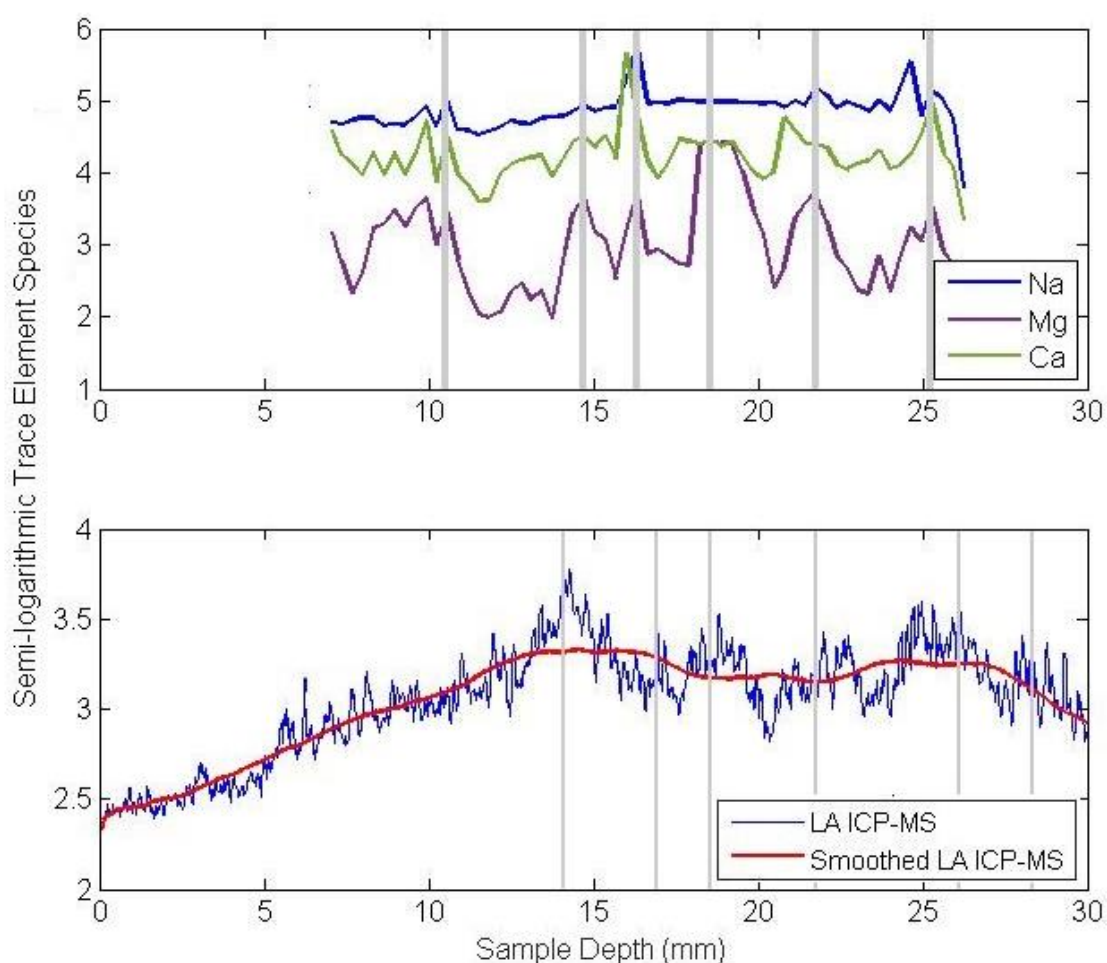


Figure 5.09: Comparison of parallel sections of ice from 703.2 - 703.22 m from top to bottom: ice analysed by discrete sampling technique; ice analysed via LA ICP-MS with a smoothed profile (red).

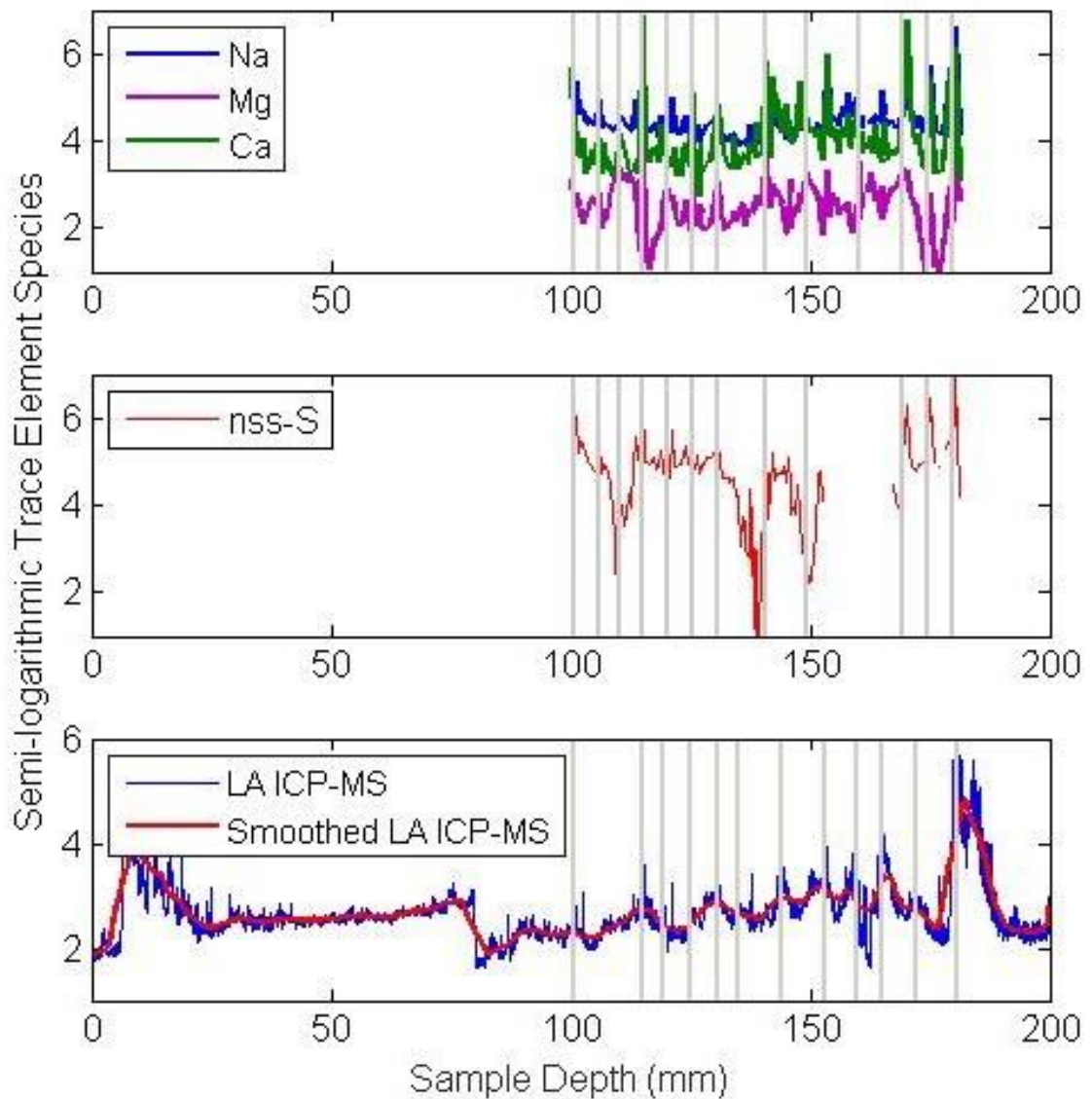


Figure 5.10: Comparison of parallel sections of ice from 706.3 - 706.38 m from top to bottom: ice analysed by discrete sampling technique; the nss-S profile from the discrete sampling technique; ice analysed via LA ICP-MS with a smoothed profile (red).

## 5.6 Discussion

The methods employed in this study have all used a sample resolution where seasonal variability should be visible in the resulting profile based on the estimated annual layer thicknesses at each analysed depth. As a result, the detection of annual layers is dependent on three factors: (i) the preservation of a seasonal cycle in the ice-core record, (ii) the

reliability of the method to extract the seasonality, and (iii) whether the sampling resolution was sufficient. The following section will discuss the feasibility of each analytical approach to obtain a seasonal profile on the ice used as part of this study.

Analysis of ice at depths 454 – 459 m using the lower-resolution discrete technique was not successful in repeating the trends in the high-resolution profile due to the high sampling volume required (fig. 5.07-5.08). This opened the line of inquiry into the small-scale variations resolved in the high-resolution analysis that suggest the LA ICP-MS technique was able to measure sub-annual discrete events within an annual layer. In addition to this sub-seasonal variability, the profile shows the changes in annual accumulation in short timeframes. The Holocene period shows no consensus of a mean annual accumulation rate consistent over the timeframe analysed, suggesting a highly variable annual accumulation. Both of these unresolved questions can be answered by comparison of the high-resolution datasets with longer time series of annual layers from the Berkner Island ice core. Wagenbach et al. (1994) presented a high-resolution profile for the upper depths of ice at two domes (north and south) on Berkner Island. The annually resolved profiles demonstrated significant variability in annual layer thickness over a depth range of 11 m; CFA and the corresponding DEP profile replicates this variable profile (fig. 5.02). Results show a mean annual layer thickness that matches the modelled estimate for its depth range, but the measured profile demonstrates great variability over a couple of metres, suggesting a natural variability in annual accumulation at the site.

This study has assessed the preservation of annual layers in ice originating from the last glacial period by comparing with lower-resolution techniques. Good correlation can be seen between LA ICP-MS profiles and profiles derived using lower-resolution techniques on ice from the last glacial period, as well as comparison of each sampling technique with the modelled estimates (fig. 5.09-5.10; table 5.01). The trend, magnitude and frequency of Na cycles suggests that annual layers are visible and that these methods can be applied to deep Antarctic ice cores with confidence that the technique is capable of a sub-annual resolution where annual layers are at least as small as 3 mm.

In the deeper section, continuous seasonal profiles are not always visible in the record despite the fact that annual layer thickness is estimated to be greater than the resolution of all the techniques used. This implies a potential loss of signal within the ice core record, resulting in a smoothed profile with limited seasonal fluctuations. However, this loss of seasonality in the record is not repeated in the lower-resolution discretely cut ice core

profile at 702 – 707 m (fig. 5.09-5.10) when presented as semi logarithmic, suggesting the annual record is still resolvable at this depth. In the glacial ice analysed, annual layer thickness appeared to increase dramatically; this increase in annual layer thickness from ~3 mm at 704 m to ~6 mm at 706 m indicates significant natural variability not previously identified through modelling techniques.

#### 5.6.1 Annual Layer Visibility in the LA ICP-MS Record

The cycles visible in the laser-ablated profiles follow the pattern expected of ice core annual layers. The greatest annual layer thicknesses are visible in the upper depths of the ice core, with the number of seasonal cycles visible increasing with depth due to the compaction of annual layers in the ice core. The patterns that emerge as the analysed depth increases indicate that the ultra-high resolution method at shallower depths results in a “noisy” signal. The low sampling volume required makes the LA ICP-MS profiles more sensitive to small-scale variations; as the frequency of the cycles increase with depth, the number of small-scale variations decreases, suggesting that the main cause for this “noise” in the signal is the analytical resolution.

The seasonal layers visible in the Berkner Island ice, retrieved at a depth in the ice sheet previously unattainable by standard laboratory resolution, confirm that our results are in line with other studies suggesting that LA ICP-MS is a valuable technique for high-resolution ice core analysis (Müller et al. 2011, Mayewski et al. 2014, Sneed et al. 2015). Since the initial development of LA ICP-MS on frozen samples, the technique has been established through successful application to Greenland and alpine ice. Most notably, LA ICP-MS demonstrated a clear sub-annual view of abrupt climate events including the onset of the Holocene in the GISP2 record as well as the assessment of the capability to identify sea ice and dust markers in the GRIP ice core record (Reinhardt et al. 2001, Mayewski et al. 2014). In particular, the ultra-high resolution records that can be produced using LA ICP-MS have the potential to enhance the information available to constrain age-depth models. The profiles presented as part of this study show that the method is capable of inferring climatic variability not recorded in the stable isotopic history of the ice core such as rapid changes in mean annual accumulation.

In addition to the ultra-high spatial resolution achieved when using LA ICP-MS on frozen samples, the contribution of LA ICP-MS to ice-core analyses is significant. The rapid analysis time, permitted by the balance between the laser spot diameter and high spatial resolution,

means it is possible to measure a 40 mm profile in several minutes. Furthermore, the methodology and implementation of an ultra-violet laser is non-destructive to the frozen samples unlike both discretely-cut and IR LA ICP-MS. These features of ultra-violet LA ICP-MS add support to the recommendation that this technique should be applied to frozen samples where possible in order to improve the resolution of an ice core profile, and the subsequent chronology and palaeoclimate analysis.

#### *5.6.2 Annual Layer Visibility in Discrete Sampling Record*

The lower-resolution sampling technique used to analyse the sections of ice originating from the Holocene does not reproduce similar results to the laser-ablated profiles. Seasonal variations in the high-resolution LA ICP-MS results were beyond the 5 mm sampling resolution of the lower-resolution technique. Similarities in the broad shape of the lower-resolution profiles suggest a smoothed record that is comparable to the shape and trends in the high-resolution LA ICP-MS record. These results agree with the comparison study on the Colle Gnifetti ice core, which found that lower-resolution CFA was unable to detect seasonal variability but showed a profile resembling a smoothed version of the ones acquired by LA ICP-MS (Sneed et al. 2015).

In ice originating from the last glacial period, a higher and variable spatial resolution of 320 – 480  $\mu\text{m}$  was necessary. The results presented in fig. 5.09-5.10 correlate well with the corresponding ultra-high resolution records, and help confirm the potential of LA ICP-MS on Antarctic ice from the last glacial. Annual layers identified throughout each analysed profile correspond well, though discrepancies are apparent between the discretely sampled and laser-ablated profiles, with more annual layers identifiable in the lower-resolution profile.

#### *5.6.3 Assessment of the Annual Layer Thickness Model*

As part of this study, a model was used primarily to estimate the annual layer thickness along the ice core to assist the initial sampling observations (see the supplementary information to this article). The confirmation that seasonal profiles are visible in the glacial ice permits a second comparison study; the observational data with the modelled layer thickness estimates. By comparing these two profiles, the model can be independently validated and give insight into the empirical relationships that contribute to age-depth determinations.

Table 5.01 outlines the depths (m, to the nearest integer) that have been sampled and analysed by LA ICP-MS and the discrete sampling techniques, the observed annual layer

thickness (if available), and the modelled annual layer thickness estimate and standard deviation ( $2\sigma$ , mm). The results of the ultra-high resolution analysis, in comparison with the modelled annual layer thickness approximations, demonstrate that the model is successful in estimating the annual layer thickness along the ice core at each depth section except for the depth range 704 – 707 m.

The Holocene record produced by both techniques does not agree with the modelled estimates, suggesting a highly variable accumulation profile that cannot be accurately modelled to account for small-scale accumulation rates over several years. Looking at a broader view, the mean annual layer thickness over the four metres analysed by CFA is  $57.0 \pm 8.8$  mm, and  $51.75 \pm 3.51$  mm for the discretely measured profiles. The confidence intervals of the mean annual layer thickness values agree to within the confidence interval of the mean modelled estimate of  $54.8 \pm 1.4$  mm.

The small uncertainties attached to the annual layer thickness retrieval and estimations are also close to corroboration between high and low sampling resolutions and the model estimates on ice originating from the last glacial period. Estimates agree to within 2 mm, but not the prescribed error margin for ice analysed at a depth of 694-704 m. For the full 10 m section analysed, the mean annual layer thickness measured by LA ICP-MS is  $3.4 \pm 0.2$  mm, which does not corroborate with the mean modelled annual layer thickness estimate of  $2.2 \pm 0.3$  mm.

The inter annual mean annual layer thickness measurements agree with the modelled estimates for upper depth section analysed, suggesting that the model is reliable for estimating annual layer thickness for sections of the ice-core on a metre resolution or greater, but cannot accurately reconstruct natural, local variability in the accumulation profile. This is unsurprising as the resolution of this model is 0.55 m, based on the resolution of the stable water isotope data in the accumulation reconstruction (eq. S5.01).

At 704 m, the layer thickness observations deviate from the estimated profile due to an increase in annual layer thickness despite continued compaction along the ice core and no evidence in the record to suggest a deviation from the ice-core physics of strain and layer compaction. The age estimate at 706 m ( $\sim 34$  ka BP) coincides with a large increase in stable nitrogen isotopes ( $\delta^{15}\text{N}$ ) identified in the gas-phase of Berkner Island (Mani 2010). From 37 ka BP, a large, positive excursion in  $\delta^{15}\text{N}$  begins and does not return to start-values for  $\sim 10$  ka. One suggestion for this excursion in  $\delta^{15}\text{N}$  records is a rapid and significant increase in the

accumulation rate that increased the firm diffusive height, and the gravitational fractionation. This accumulation increase would have been rapid in order to leave little-to-no trace in the isotopic record. It is highly probable that the deepest section of ice analysed by LA ICP-MS corresponds to this signature preserved in the gas-phase record, and that the observed increase in annual layer thickness within this section strengthens the hypothesis of a rapid increase in annual accumulation. However, the employment of further analysis by ultra-high resolution techniques could explore the potential of these results. The increase in annual layer thickness is likely due to a significant increase in mean annual precipitation at the time of original deposition, and warrants further investigation.

Ultra-high resolution records are paramount to the assessment and improvement of ice-core chronologies. With respect to the annual layer thickness model and the application of high-resolution trace-element analysis, the results of this study suggest that a combination of glaciological modelling and reliable annual layer thickness observations, derived using ultra-high resolution measurement techniques, would improve the estimation of annual layer thickness and consequently the age-depth profile of Antarctic ice cores.

### 5.7 Conclusions

LA ICP-MS on ice has the potential to retrieve continuous, seasonal signals from ice core records at depths currently beyond the range of standard laboratory methods. The application of two techniques in high-resolution trace element analysis on frozen ice samples from the Berkner Island ice core agree in measurements of annual layer thickness at three depth ranges, providing a detailed snapshot of the Na and Mg seasonal record of the last glacial period. The results of this analysis have been compared with results from a lower-resolution technique applied to parallel sections of ice; trends, depositional peaks in Na and Mg, and absolute values of calibrated concentration in the IC and LA ICP-MS profiles agree – particularly well in the ice originating from the last glacial period. The low sample volume required for LA ICP-MS yields additional information and small-scale variability is resolved in the Holocene profiles. Care and extra assessment of LA ICP-MS profiles should be taken to ensure annual layers are not misappropriated during the analysis of ice cores.

Assessment of a simple one-dimensional model to estimate the annual layer thicknesses along an ice core confirms that the model is effective at estimating annual layer thicknesses for Holocene and glacial ice on a low resolution. Modelled annual layer thickness for each individual ice section do not compare well with the observed measurements; the model is

unable to reconstruct the natural variability on a local scale without a higher resolution stable water isotope profile and better observational data. The optimal annual layer thickness estimates should be constructed using a combination of the glaciological techniques used in the paper, and ultra-high resolution analytical techniques to constrain the compaction rates such as LA ICP-MS and the discrete sampling technique.

## 5.8 Supplementary Material to the Paper

### 5.8.1 Annual Layer Thickness Model Variables

*Table S5.01: List of parameters and the values used in calculating the annual layer thickness in the Berkner Island ice core, Weddell Sea.*

Variable	Value
Present-Day Mean Annual Accumulation, $A^{\theta}$	0.185 m yr <sup>-1</sup>
Ice-Sheet Thickness, H	948 m
Temperature at the bed, $T_B$	262 K
Surface Temperature, $T_S$	248.2 K
Glen's Exponent, n	3
Activation Energy, Q	60 kJ mol <sup>-1</sup>

*Table S5.02: Known-age horizons along the Berkner Island ice core with associated error. Age horizons have been derived by Rob Mulvaney (pers. comm.) by matching BI stable water isotope signatures with EDC stable water isotope signatures of assumed-synchronous AIM events (Bazin et al., 2013; Veres et al., 2013).*

Depth below the surface (mweq)	Age (ka BP)	Error (ka BP)
579.341	13.50	0.3
584.843	14.75	0.5
596.351	17.60	0.5
641.788	38.10	0.5
666.712	46.50	1.0

693.700	57.16	1.0
709.591	64.75	1.0

### 5.8.2 Statistical Analysis of LA ICP-MS data

In addition to the work reported in the published paper and its accompanying supplementary information, I present here a statistical analysis of the LA ICP-MS Na data. As an alternative method of identifying annual signals in the LA profiles, fast fourier transform (FFT) analysis was applied to the data. Fourier transforms are tools for processing discrete data that is presented as a function of time or space. Data is fragmented into frequency components with a view to identifying a periodicity or frequency of a profile. In the case of the LA profiles, FFT analysis was applied in order to identify a periodicity of peaks in Na deposition.

The results show that regardless of the modelled annual layer thickness, and the details of the layers identified in the semi-logarithmic plots (fig. 5.03 – 5.05), power density spectrums yield similar results for all nine sections of ice analysed. The greatest power is seen at the shortest wavelength, with additional frequencies occurring with decreasing strength with respect to increasing annual layer thickness, suggests that there are numerous layer thicknesses identified in each measured series (fig. S5.01). This is particularly surprising as one would expect the results to change dependent on the analysed ice; i.e. one would expect the annual layer thickness in ice originating from the Holocene to be greater than annual layer thickness in ice originating from the last glacial period.

The reason these datasets do not show different results at different depths is that the analysis has been completed with respect to a depth series that is not linear with time. As such, the FFT analysis is able to pick out power spectra at any wavelength.

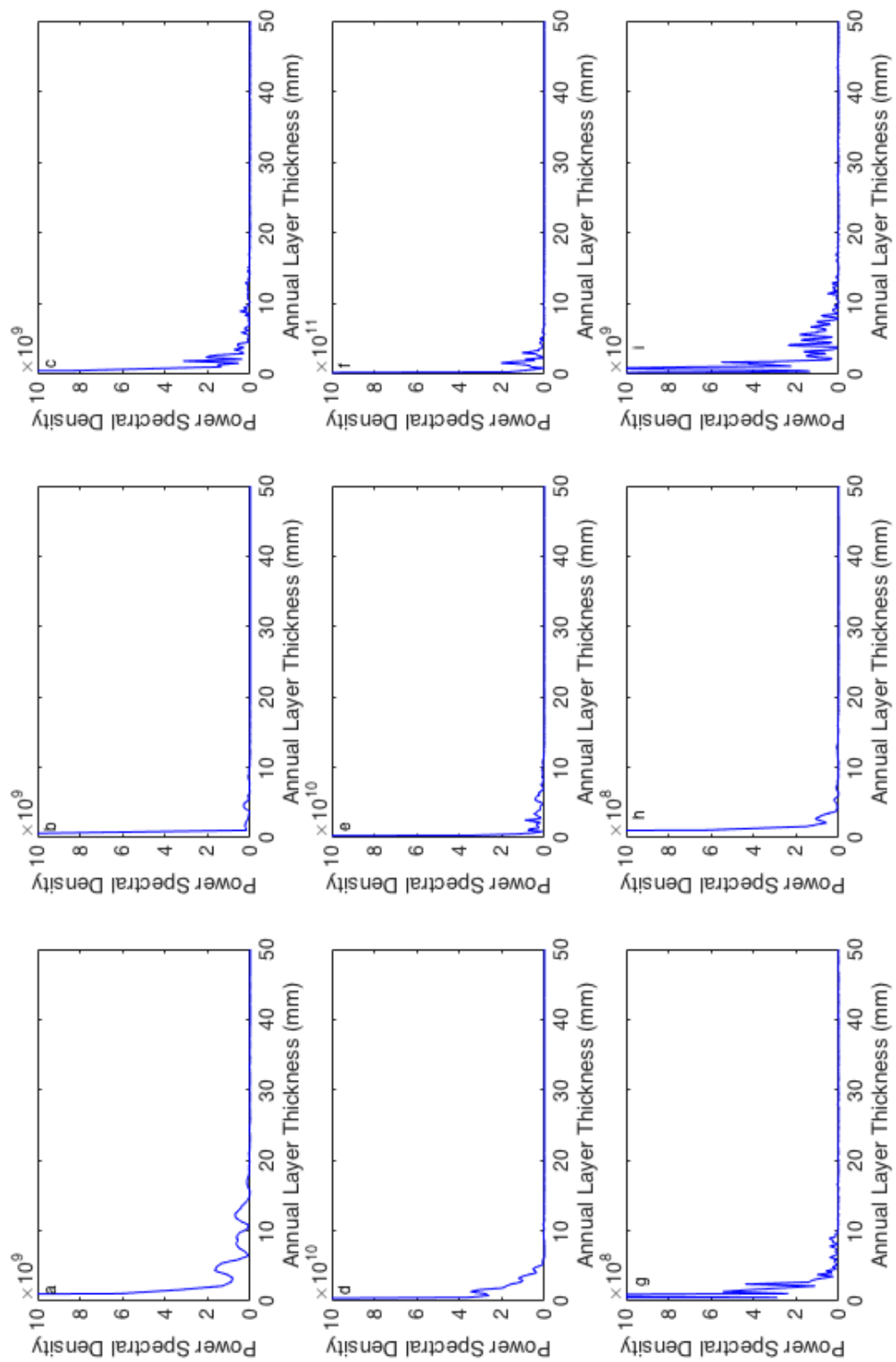


Figure S5.01(a-i): FFT power spectrum density plots for each section of ice analysed. Results are presented for sections of ice in increasing depth order, and the plots read left to right, starting with the top row. Each plot suggests multiple peaks of potential annual layer thicknesses.

### 5.8.3 Modelled Annual Layer Thickness

The peer-reviewed publication focussed on validating the LA ICP-MS Na results by comparison with alternative trace-element profiles. In addition to this, the LA ICP-MS Na record was used to measure annual layer thickness for comparison with the modelled estimates of annual layer thickness. The paper presents annual layer thicknesses estimated using the Optimised Accumulation and Thinning (OptAcc) model, with an *a priori* accumulation history that was derived using the Clausius-Clapeyron relationship (section 4.2.2(b)). However, the LA ICP-MS Na results and annual layer thickness measurements were also compared with the estimated thicknesses from all of the inverse approaches presented in Chapter 4. Similar to the results of Chapter 4, which found that the OptAcc model yielded the most accurate reconstruction of accumulation, thinning, and age-depth for the FP ice core, table S5.03 suggests that the OptAcc model is most accurate in reconstructing annual layer thickness for the BI ice core. For the BI ice core, the OptAcc model is able to produce optimised profiles for accumulation as well as thinning, unlike the Direct Search method. Both models use an initial accumulation history estimated using a Clausius-Clapeyron relationship, but the OptAcc model perturbs this initial accumulation profile in order to estimate the optimal profile. This relationship assumes a direct relationship between water vapour sources and the rate of precipitation.

As explained earlier, the optimised annual layer thickness estimates do not correlate with measured layer thicknesses at a resolution of one metre (section 5.5.3). This includes the ice analysed that does not show a significant increase in accumulation at 694-704 m. The OptAcc model is no more accurate at estimating annual layer thicknesses than IceChrono when compared with the observational data (shown in table S5.03). Both the IceChrono and OptAcc approaches estimate annual layer thickness outside of the measured standard deviation at a metre-resolution, particularly when comparing sections from a depth greater than 694 m. Comparison of model estimates with annual layer thickness measurements provides no additional evidence towards the most robust modelling approach. Therefore, this study chose to continue with the OptAcc approach, using a Clausius-Clapeyron accumulation relationship.

Table S5.03: Annual Layer Thickness estimates from every model combination, using a Clausius-Clapeyron accumulation reconstruction

Depth (m)	Forward model (mm)			Inverse model (mm)			Measured Annual Layer Thickness (mm)
	Nye	Dansgaard-Johnsen	One-dimensional	Direct Search	IceChrono	OptAcc	
447	103.2	86.4	83.1	35.1 ± 4.2	66.0 ± 0.7	56.7 ± 1.5	57.0 ± 8.8
454	103.1	85.7	82.4	34.4 ± 4.2	57.6 ± 0.7	56.7 ± 1.5	57.0 ± 10.0
456	100.1	83.1	79.8	33.2 ± 4.1	57.6 ± 0.7	54.9 ± 1.4	6.7 ± 0.6
458	96.7	80.1	77.0	31.9 ± 3.9	57.6 ± 0.7	52.9 ± 1.4	26.1 ± 2.3
694	16.0	7.9	8.4	2.4 ± 0.5	2.4 ± 0.06	2.1 ± 0.3	2.9 ± 0.1
695	17.0	8.4	8.9	2.5 ± 0.5	2.4 ± 0.06	2.3 ± 0.3	3.6 ± 0.1
696	15.5	7.6	8.1	2.3 ± 0.5	2.4 ± 0.06	2.1 ± 0.2	4.0 ± 0.2
702	16.2	7.8	8.3	2.3 ± 0.5	3.0 ± 0.07	2.3 ± 0.2	3.1 ± 0.1
704	16.0	7.6	8.2	2.3 ± 0.5	3.5 ± 0.07	2.3 ± 0.1	6.1 ± 0.2
706	17.2	8.1	8.7	2.4 ± 0.5	2.8 ± 0.07	2.3 ± 0.1	5.1 ± 0.2



# Chapter 6: The optimal age-depth profiles for the Berkner Island and Fletcher Promontory ice cores

## 6.1 Introduction

The overall rationale of this study is to develop the optimal dating strategy for three deep ice cores from the Antarctic Peninsula (AP) and Weddell Sea region. The third specific objective of this study, as outlined in section 1.2.1, aims to use the results of the model development and chemical analysis of the ice cores (the previous two objectives) and develop and apply the most robust approach to reconstruct the accumulation, thinning, and hence annual layer thickness and age-depth profiles for the ice cores from Fletcher Promontory (FP), Berkner Island (BI), and James Ross Island (JRI).

Through previous chapters, the optimal dating strategy has been developed by applying an inverse approach to empirical accumulation and thinning functions. The model calculates the optimal values of two functions: (i) the first function controls the sensitivity of accumulation change with respect to temperature, and (ii) the second function controls the shape of deformation in the thinning function. This model is referred to as the Optimised Accumulation and Thinning (OptAcc) model. The optimal profiles of annual layer thickness and age-depth are constrained using observational data; age horizons identified throughout the ice core record and measured annual layer thicknesses at sub-millimetre resolution. The additional observational data improves on the constraints used in the FP reconstructions presented in Chapter 4, by incorporating the annual layer thickness measurements yielded through three techniques of high-resolution trace-element analysis along the ice core records, applied to ice from multiple depths of the FP and BI ice core records (Chapter 5). Constraining the mean annual layer thickness in this way, using observed measurements throughout the ice core, further refines the optimised age-depth profile as the age of an ice particle at a particular depth is ultimately the sum of annual layers above it.

In this chapter, the age-depth profiles of the FP and BI deep ice cores are reconstructed using the OptAcc model. The JRI ice core age-depth profile is presented separately to this chapter, due to the additional work and collaboration required in reconstructing the accumulation and annual layer thickness profiles.

## 6.2 Methods

The techniques used in reconstructing the FP and BI accumulation and annual layer thickness records are outlined in previous chapters. In order to reconstruct the most accurate climate record, the profiles of accumulation and thinning are optimised using the dating strategy that produces the most accurate ice core record (Chapter 4).

The profiles of accumulation, thinning, and hence annual layer thickness and age-depth are constructed using the OptAcc model presented in Chapter 4 (section 4.4.4). An initial accumulation history is estimated following the Clausius-Clapeyron relationship (eq. 2.06-2.08; section 2.5.2.2) and is optimised through an inverse approach by estimating a smooth perturbation profile (eq. 3.01). Annual layer thickness is estimated by reconstructing the thinning function using the One-Dimensional relationship (eq. 2.13-2.17; section 2.5.3.3) and applying this to the optimised accumulation profile. Finally, the estimated annual layer thickness and age-depth profiles (eq. 2.20-2.21; section 2.5.4) are compared with observational data for the optimisation of the parameters that control the accumulation and thinning profiles, which feed into the annual layer thickness profile. Final profiles of accumulation, thinning, annual layer thickness, and age-depth are the output from the model iteration that yields the smallest root mean square error (RMSE) value.

Age horizons are commonly identified in ice cores by globally- or regionally-synchronous signatures preserved in the stable water isotope and gas records, as well as the sulphate and tephra peaks from volcanic eruptions. Detailed chemical and gas records are not available along the length of the FP and BI ice cores, but a small number of age horizons have been selected by matching climate features in the water isotope records of these two cores with similar features in the EPICA Dome C (EDC) ice core. Novel techniques for very high resolution chemistry measurements across short sections of the cores yield annual layer thickness measurements that can be used to further constrain the BI and FP ice core records. For BI, low-resolution discrete sampling and continuous flow analysis (CFA) analysis yield layer thickness measurements for middle depths of the ice core, and ultra-high resolution LA ICP-MS data is used to determine layer thickness on ice originating from the last glacial period at greater depths. The annual layer thickness measurements are presented in Chapter 5, with the assessment of each technique and its ability to obtain sub-annual profiles at great depths in the ice sheet. Additional chemical profiles are presented in this chapter for FP, for which sub-annual profiles were collected by discrete sampling using the microtome technique and analysed by ion chromatography (IC) (section 3.5). Five

depth ranges were analysed for the FP ice core. For the two uppermost depth ranges,  $\delta^{18}\text{O}$  concentrations were measured at a spatial resolution of 10 mm and 3 mm, respectively. These results are from a parallel study, as explained in section 3.3.2. The remaining three depth ranges have been sampled and analysed using the discrete sampling approach as used on BI ice in Chapter 5 at a spatial resolution of 0.32 mm.

## 6.3 Results

The analysis of the BI and FP ice cores at a high resolution yields observational data that can constrain the annual layer thickness and age-depth profile. The following section presents the measured annual layer thickness and age horizons from the laboratory analysis, section 6.3.2 presents modelled profiles of accumulation, thinning and annual layer thickness, and section 6.3.3 presents age-depth profiles for the BI and FP ice cores.

### 6.3.1 Observational Constraints

#### 6.3.1.1 Berkner Island

The observational data used to constrain the optimisation model are presented as table 6.01 and 6.02 for age constraints and observed annual layer thickness, respectively. Annual layer thickness measurements are presented in millimetres, with the associated standard deviation to  $2\sigma$ .

Age horizons only exist for depths greater than 650 m of the 947 m ice core; the BI reconstructions of accumulation and annual layer thickness throughout the uppermost 650 m of the ice-core record therefore predominantly rely on the accuracy of the empirical relationships. The age horizons are identified in the stable water isotope record, and tuned to the AICC2012 ice-core chronology. The uncertainty in the age horizons is based on the AICC2012 model uncertainty (Bazin et al., 2013; Veres et al., 2013).

Some additional constraints in the form of observed annual layer thickness measurements are obtained from depths shallower than 650 m to provide a balanced distribution of observational data throughout the ice core record. Depths are presented in snow (m) and ice equivalent (mweq) units; the snow depth is converted into ice equivalent units by accounting for the increase in density with depth (section 4.3.1). Model results are presented solely in ice-equivalent units.

*Table 6.01: BI age constraints and uncertainty. Age horizons have been derived by Rob Mulvaney (pers. comm.) by matching BI stable water isotope signatures with EDC stable water isotope signatures of assumed-synchronous AIM events (Bazin et al., 2013; Veres et al., 2013).*

<b>Depth below the surface (m)</b>	<b>Depth below the surface (mweq)</b>	<b>Observed Age (yr since drill date)</b>	<b>Uncertainty (yrs)</b>	<b>Observed feature</b>
650.80	596.78	13050.0	250.0	Coldest part of the Antarctic Cold Reversal (ACR), tuned to AICC2012
656.80	602.28	14600.0	250.0	AIM 1
669.35	613.79	18390.0	1000.0	Start of warming
718.90	659.23	38250.0	800.0	AIM 8
745.08	683.24	46480.0	800.0	AIM 12
775.51	711.11	56890.0	800.0	Coldest part of stadial, tuned to AICC2012
792.84	726.59	64750.0	2200.0	AIM 18

*Table 6.02: Observed annual layer thickness and standard deviation used as constraints in the BI age-depth profile, with method of analysis used to obtain the sub-annual record and the analytical resolution used during the sampling in Chapter 5.*

<b>Depth below the surface (m)</b>	<b>Depth below the surface (mweq)</b>	<b>Observed layer thickness (mm)</b>	<b>Standard deviation (mm)</b>	<b>Method of analysis</b>	<b>Sample Resolution (mm)</b>
447 – 451	409 – 413	57.0	8.8	CFA	5.0
454 – 458	416 – 419	51.7	3.5	LA ICP-MS	0.1
694 – 704	636 – 645	3.2	1.0	LA ICP-MS	0.1

### 6.3.1.2 *Fletcher Promontory*

Similar to the BI ice core, two forms of observational data are used to constrain the model. The age horizons, with their corresponding depth and uncertainty were presented in Chapter 4, section 4.2.1 (table 4.01). In addition to the age constraints, annual layer thickness measurements derived from the discrete sampling methods are presented in fig. 6.01. The mean annual layer thickness measurements and the respective standard deviation ( $2\sigma$ ) are presented in table 6.03; additional information on the method of analysis and snow and ice-equivalent depth is included. For the uppermost two depth ranges, between 299 – 390 m,  $\delta^{18}\text{O}$  concentrations are measured at a depth resolution of 3 – 10 mm (table 6.03), these are results from a parallel study (Pike, unpublished). Annual layers were identified in the same manner as in Chapter 5 for the BI ice core: by identifying the minimum value over a presumed seasonal cycle of trace-element or stable water isotope deposition (section 5.4.3).

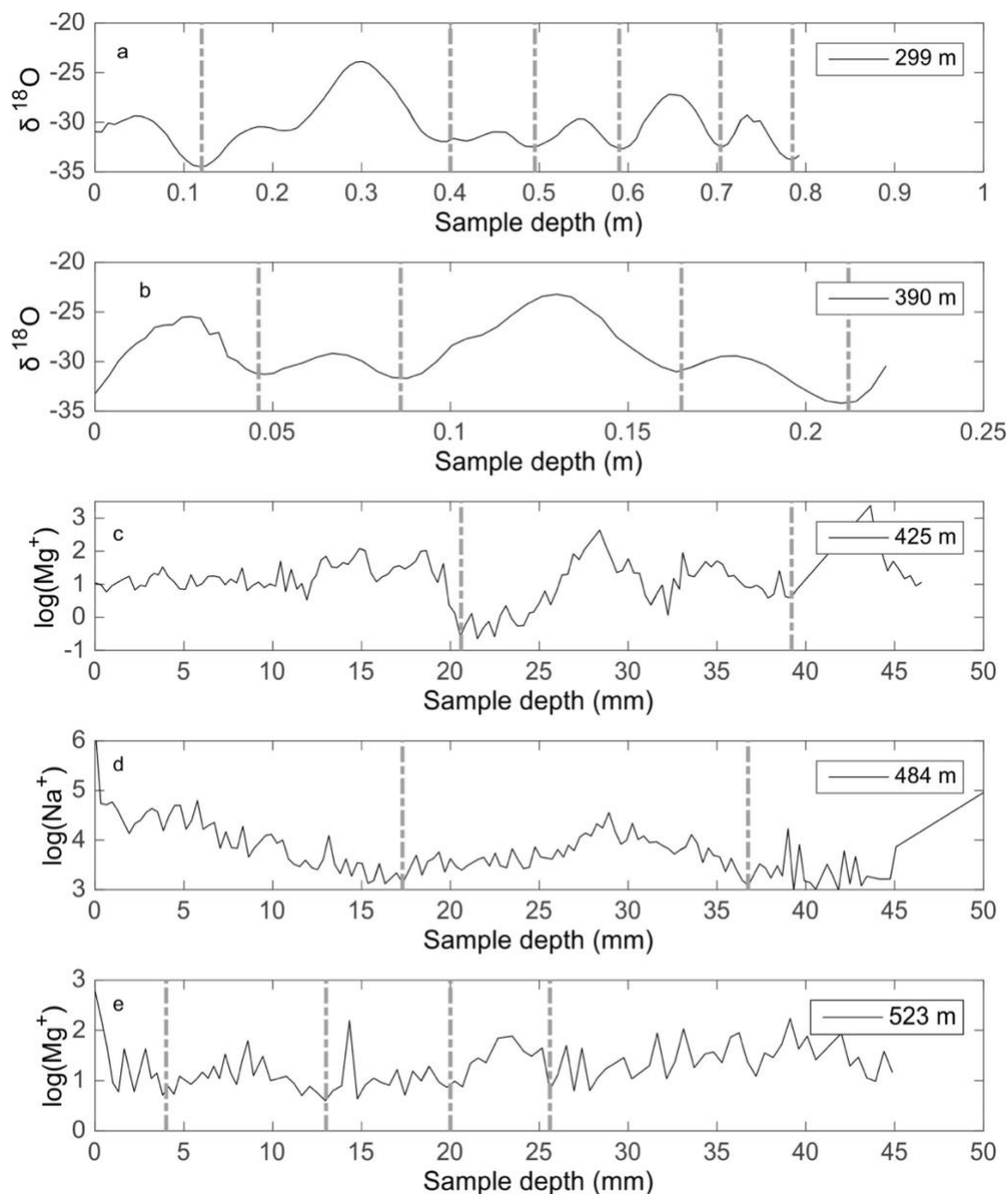


Figure 6.01: Sub-annual measurements on the Fletcher Promontory ice core. A-B: stable water isotope measurements with respect to depth in metres (snow); C-E: ion profiles with respect to depth in millimetres (snow). Dashed lines delineate assumed annual peaks in deposition. Measurements in plots (a-b) were obtained separate to this study by Amy Pike. Measurements in plots (c-e) were obtained by this study using discrete sampling techniques.

Table 6.03: Observed annual layer thickness and standard deviation used as constraints in the FP age-depth profile, with method of analysis used to obtain the sub-annual record and the analytical resolution used during the sampling for measurements presented in fig. 6.01.

Depth below the surface (m)	Depth below the surface (mweq)	Observed layer thickness (mm)	Standard deviation (mm)	Method of analysis	Sample Resolution (mm)
299	270	98.0	30.0	$\delta^{18}\text{O}$ profile	10.00
390	354	52.0	17.0	$\delta^{18}\text{O}$ profile	3.00
425	387	18.0	0.0	Discrete Sampling (microtome)	0.32
484	444	15.9	0.0	Discrete Sampling (microtome)	0.32
523	480	7.7	2.6	Discrete Sampling (microtome)	0.32

### 6.3.2 Accumulation and Annual Layer Thickness

The OptAcc Model estimates 1000 possible profiles of accumulation and thinning that are perturbed in order to agree with the observational data, at least to within the associated uncertainty on the observational data. The observational data used to constrain the optimised profiles includes age horizons and measured annual layer thicknesses. The reconstructions are presented with their confidence interval – the spread of possible values for each profile found through 1000 iterations.

#### 6.3.2.1 Berkner Island

Fig. 6.02 presents the present-day (blue) and original annual layer thickness (accumulation) (red) profiles, as derived using the OptAcc approach; the empirical accumulation history is in grey. The range of perturbation profiles on the initial Clausius-Clapeyron accumulation

history is across the Holocene period (-5% – +35% than the initial profile; fig. 6.03a). The only constraints throughout this period are measured annual layer thicknesses at 409 – 413 mweq and 416 – 419 mweq, and hence the range of potential mean annual accumulation rates is large. At the perceived Last Glacial Maximum (LGM) in the isotope record (~600 mweq), the greatest perturbation of -50% is applied to the empirical estimate; this coincides with the start of age horizons at 579 mweq. The accumulation profile is perturbed at 720 – 800 mweq by around +7%, before dropping to -6% close to the bedrock (fig. 6.03a).

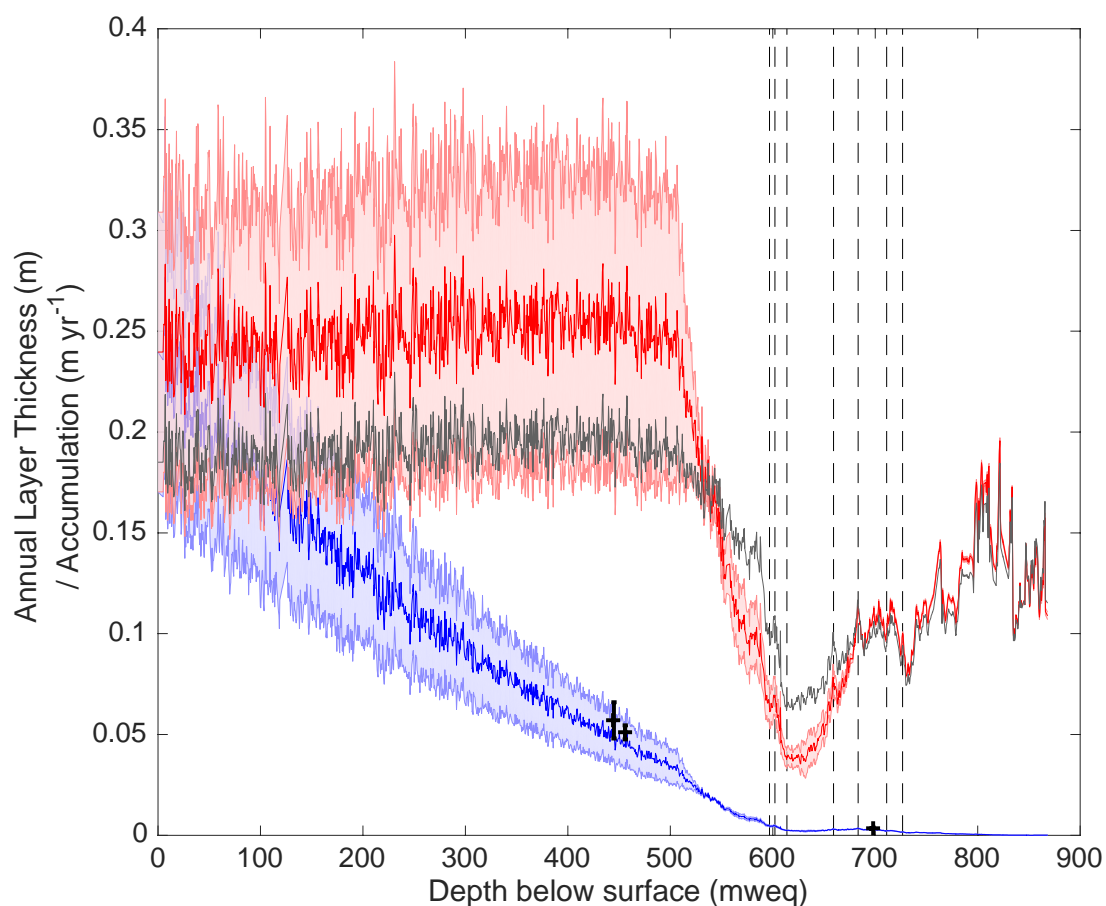


Figure 6.02: Present-day (blue) and original annual layer thickness (red) for the BI ice core. Present-day annual layer thickness is assumed to be the product of the final accumulation and thinning profiles. Black crosses show the observed annual layer thickness measurements. The initial Clausius-Clapeyron accumulation history is presented in grey. The depths corresponding to age horizons are delineated by black dashed lines.

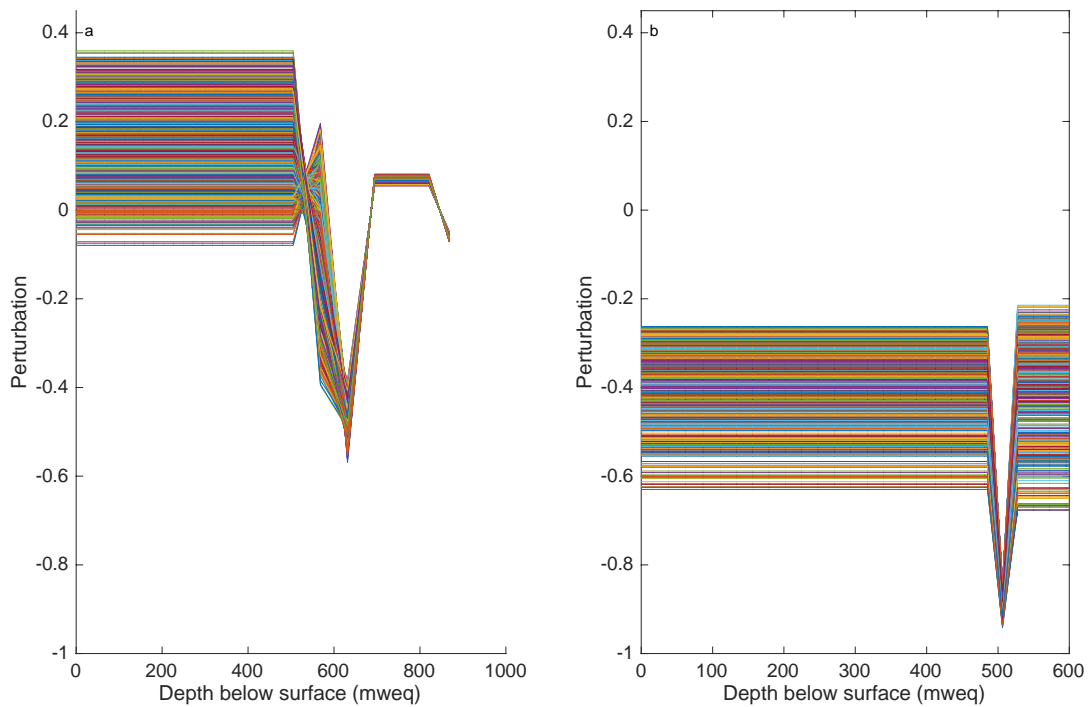


Figure 6.03: Perturbation profiles for each ice core reconstruction: (a) 1000 perturbation profiles for BI; (b) 1000 perturbation profiles for FP. Each coloured line is an individual perturbation profile.

Annual layer thickness replicates the sharp decrease in accumulation at around 500 mweq (fig. 6.02). The observed annual layer thickness measurements throughout the ice core constrain the modelled annual layer thickness and are represented in fig. 6.02 as black crosses. Fig. 6.04 presents the range of modelled annual layer thicknesses at the depths corresponding to measured values, with a normal density function fitted (red line), with the modelled values from the annual layer thickness values and RMSE values presented in table 6.04. The modelled annual layer thicknesses distributions agree to within the standard deviation of the measured values.

The profile of deformation is controlled by the  $p$ -parameter, which is solved for within the inverse approach (fig. 6.05). The optimal thinning function is presented on the normalised depth scale used in the One-Dimensional thinning function (section 2.5.3.3), where 1 is the surface and 0 is the normalised depth at the bed. The thinning function yields a value of the  $p$ -parameter of  $-0.54 \pm 0.18$  (also presented in table 6.05 with the calculated value of Glen's Flow Law exponent,  $n$ , which is estimated by inverting eq. 2.16 in section 2.5.3.3). This initially appears to be a large range in the uncertainty, but it isn't reflected in the confidence

interval of the annual layer thickness profile where the confidence interval is presented as pale blue band surrounding the mean annual layer thickness profile (fig. 6.02).

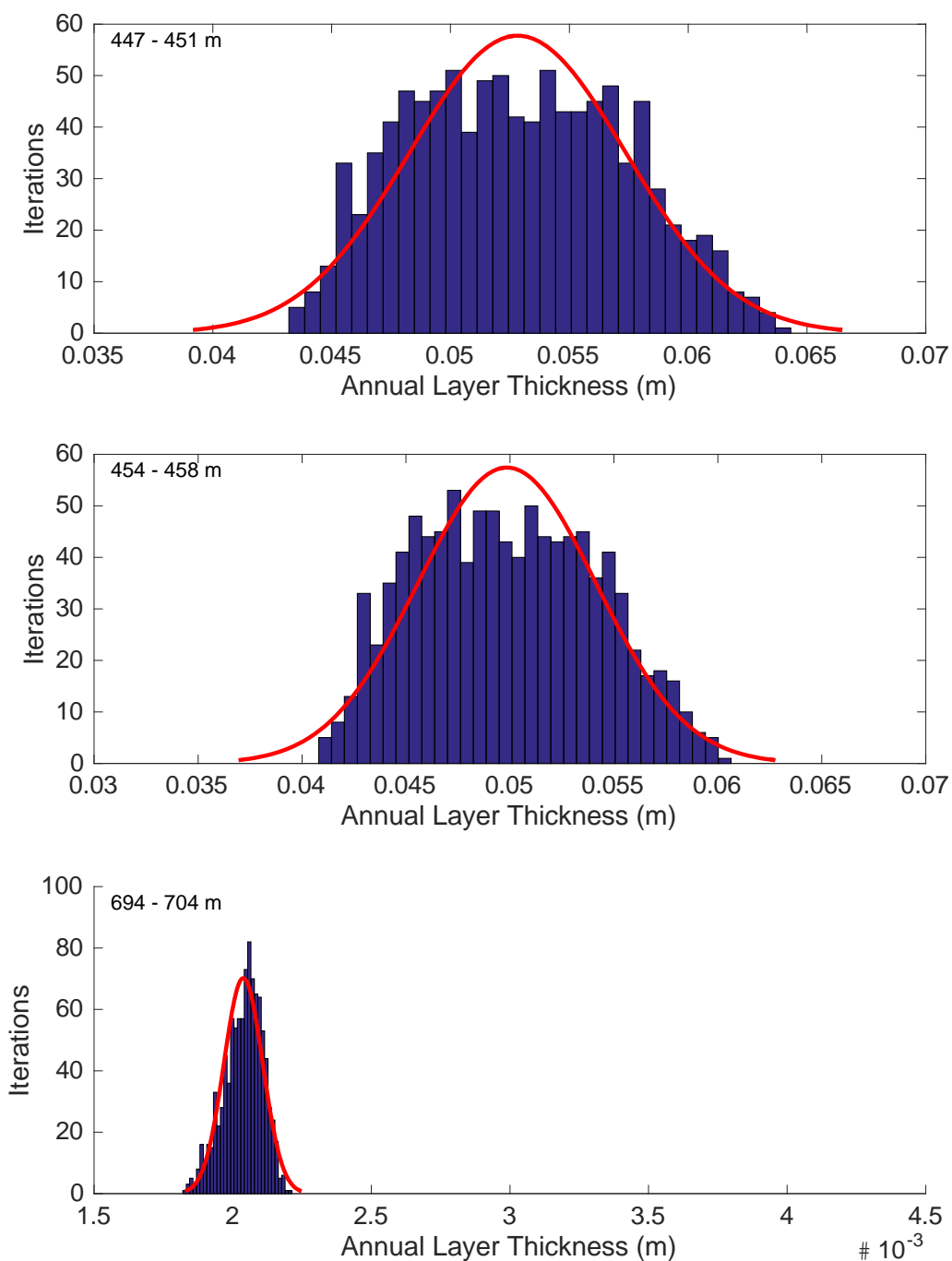


Figure 6.04: Density distribution of the modelled annual layer thickness at depths corresponding to measured values in the BI ice core, with a normal density distribution fitted (red line). The depth at which the annual layer thickness is measured and compared is shown in the top-left corner. The standard deviation of the measured annual layer thickness is shown as a grey box.

Table 6.04: Estimated annual layer thicknesses at depths corresponding to the depths of annual layer thickness measurements and the respective RMSE value for BI.

Depth below the surface (m)	Depth (mweq below the surface)	Layer Thickness Constraint (mm)	Modelled Layer Thickness (mm)
447 – 451	409 – 413	$57.0 \pm 8.8$	$56.9 \pm 1.4$
454 – 458	416 – 419	$51.7 \pm 3.5$	$55.3 \pm 1.4$
694 – 704	636 – 645	$3.2 \pm 1.0$	$2.2 \pm 0.2$
<b>RMSE (mm)</b>			<b>1.4</b>

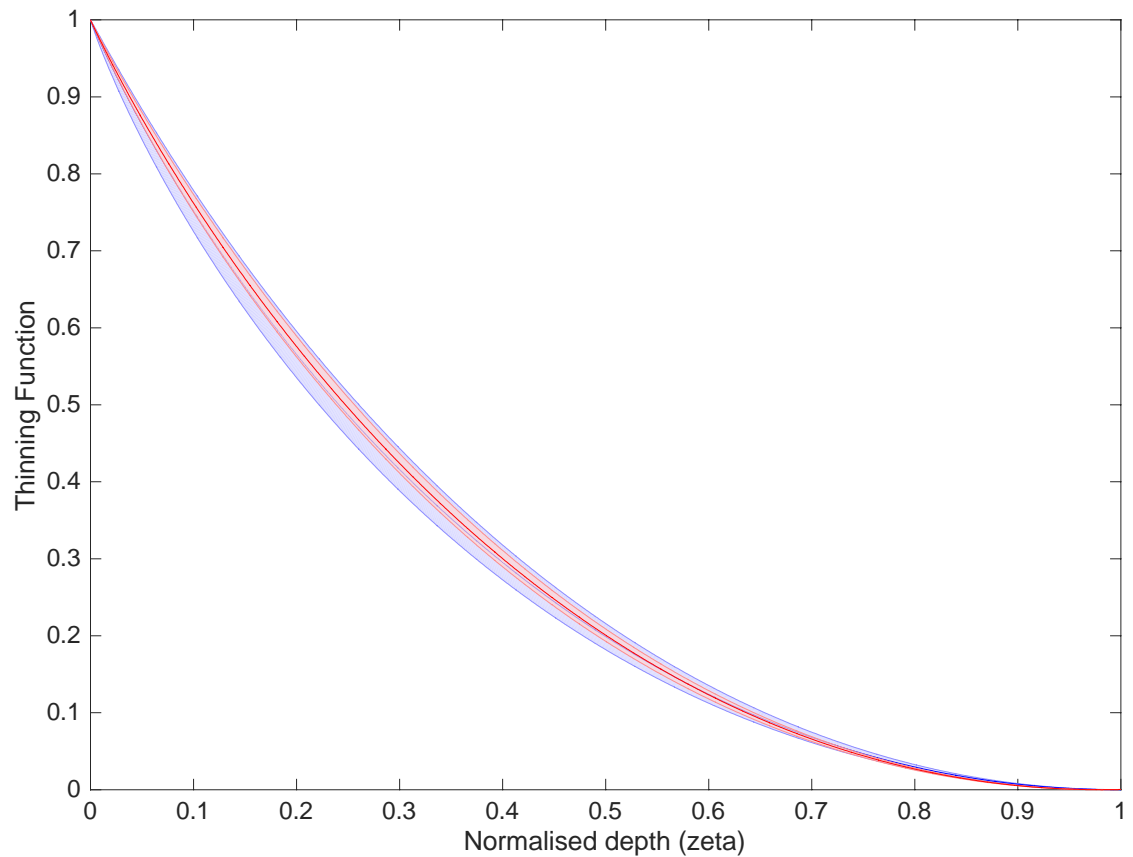


Figure 6.05: Thinning functions reconstructed through the model for each ice core (FP is blue; BI is red) with the associated uncertainty, presented on a normalised depth scale where the depth is 1 at the surface of the ice sheet and 0 at the bed.

Table 6.05: Optimised values of the  $p$ -parameter and Glen's Flow Law exponent,  $n$ , with associated error for the BI and FP ice core. Glen's Flow Law exponent has been estimated by inverting eq. 2.16 in section 2.5.3.3.

Ice Core	$p$ -value $\pm$ error	$n$ -value $\pm$ error
BI	$-0.54 \pm 0.18$	$-1.12 \pm 0.18$
FP	$-0.73 \pm 1.93$	$0.06 \pm 1.93$

### 6.3.2.2 Fletcher Promontory

Immediate observations for the FP ice core reconstructions are that the accumulation and thinning profiles yield a large uncertainty throughout the Holocene period due to the lack of constraints. As such, the uncertainty is carried forward to the annual layer thickness profile. As a result of the large uncertainty, the empirical accumulation profile estimated using the Clausius-Clapeyron relationship is within the uncertainty of the optimised accumulation reconstruction. However, the modelled accumulation history over the LGM to the Holocene suggests a different relationship between accumulation with respect to a change in surface temperature to that assumed in the Clausius-Clapeyron relationship. For the optimised FP reconstruction, the accumulation profile (red) is perturbed to be consistently lower in comparison to the initial accumulation history (grey, fig. 6.06). The perturbations to the initial accumulation profile result in a lower mean annual accumulation rate throughout the Holocene by  $\sim 34\%$ , decreasing to  $86\%$  during the LGM (fig. 6.03b). However, the large uncertainty on the accumulation reconstruction during the Holocene period suggests that the mean annual accumulation rate could have been up to  $63\%$  less than the present-day accumulation rate. The perturbation doesn't change the apparent timings of the response to the transition between glacial and interglacial cycles.

Fig. 6.07 presents the range of modelled annual layer thicknesses at the depths corresponding to measured values, with a normal density function fitted (red line), with the modelled values from the annual layer thickness values and RMSE values presented in table 6.06. The modelled annual layer thicknesses distributions agree to within the standard deviation of the measured values, with the exception of the third annual layer thickness measurement at 387 mweq (425 m snow). The third measured value is  $18.0 \text{ mm} \pm 0.0 \text{ mm}$ ; the standard deviation is  $0.0 \text{ mm}$  as only one annual layer is identified in this analysed section of ice. Without expanding the analysis of this section of ice to the surrounding ice in

order to identify further annual layer thicknesses, this constraint should not be considered robust.

The thinning function reconstructs a high rate of thinning in the upper part of the FP ice core (fig. 6.05). The optimised value of the  $p$ -parameter, that controls the shape of deformation, is  $-0.73 \pm 1.93$  (table 6.05 with the calculated value of Glen's Flow Law exponent,  $n$ ). The low value controls the high rate of thinning (the highly non-linear profile) that continues from 100 mweq to the bed (corresponding to 0.16 in the normalised depth units on fig. 6.05). When this thinning function is combined with the lowered mean annual accumulation throughout the ice core record, the annual layer thickness reconstruction fits to within the standard deviation of the observed annual layer thickness measurements, with the exception of the constraint at 387 mweq.

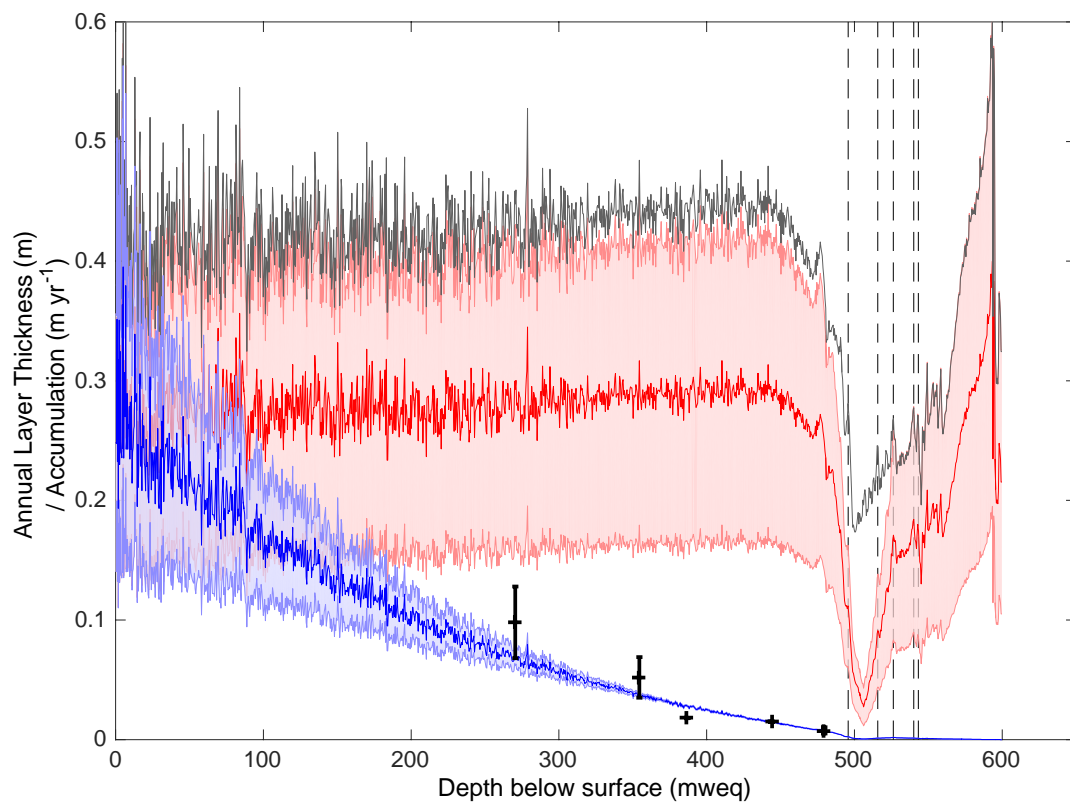


Figure 6.06: Present-day and original annual layer thickness for the FP ice core. Present-day annual layer thickness is assumed to be the product of the final accumulation and thinning profiles. Black crosses show the observed annual layer thickness measurements. The initial Clausius-Clapeyron accumulation history is presented in grey. The depths corresponding to age horizons are delineated by grey dashed lines.

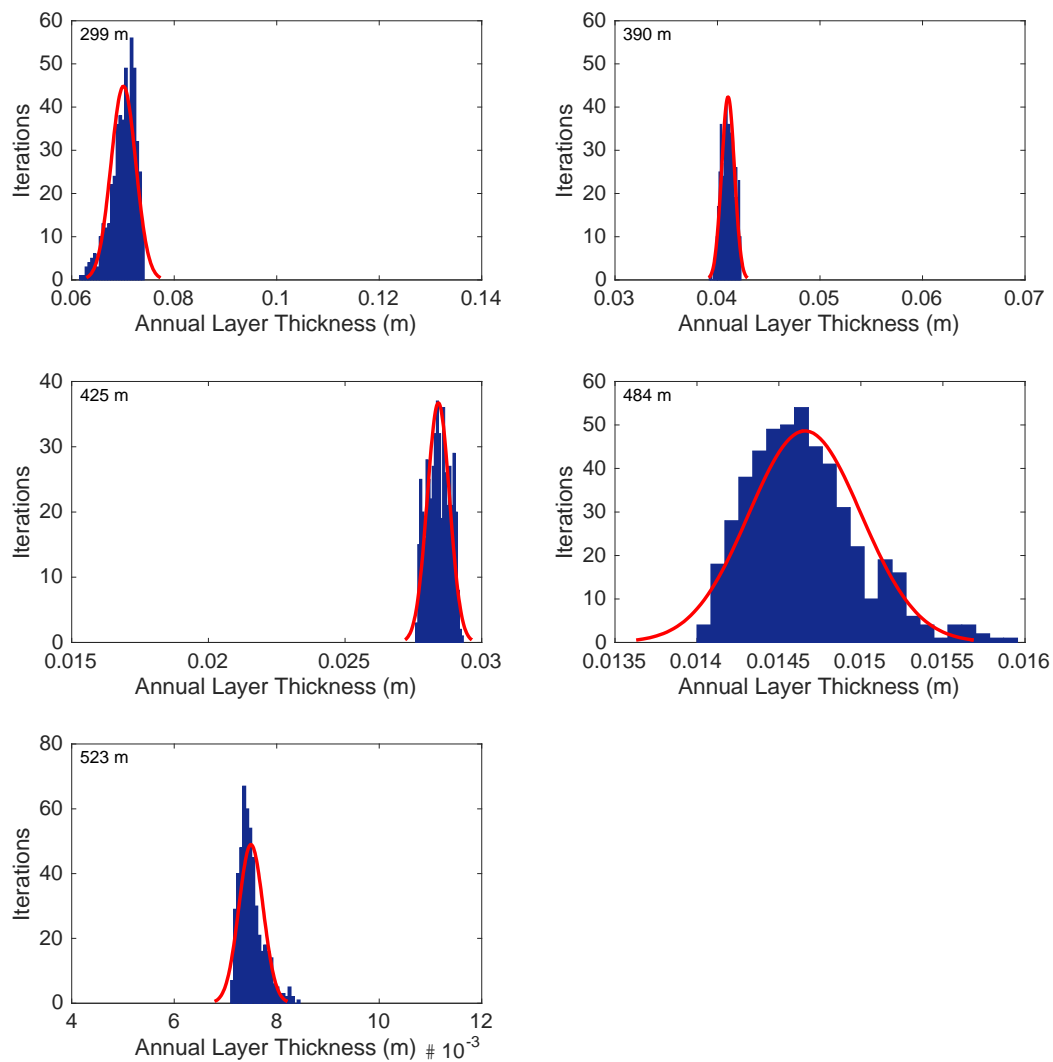


Figure 6.07: Density distribution of the modelled annual layer thickness at depths corresponding to measured values in the FP ice core, with a normal density distribution fitted (red line). The depth at which the annual layer thickness is measured and compared is shown in the top-left corner. The standard deviation of the measured annual layer thickness is shown as a grey box.

Table 6.06: Estimated annual layer thicknesses at depths corresponding to the depths of annual layer thickness measurements and the respective RMSE value for FP.

Depth below the surface (m)	Depth (mweq below the surface)	Layer Thickness Constraint (mm)	Modelled Layer Thickness (mm)
299	270	98.0 ± 30.0	71.2 ± 9.4
390	354	52.0 ± 17.0	41.1 ± 1.9
425	387	18.0 ± 0.0	28.3 ± 0.7
484	444	15.9 ± 0.0	14.5 ± 0.4
523	480	7.7 ± 2.6	7.4 ± 0.3
<b>RMSE (mm)</b>			<b>5.8</b>

### 6.3.3 Age-depth profiles

The age of an ice particle at a particular depth is assumed to be the sum of annual layers above it (eq. 2.21). The age-depth profiles are presented below, with the age horizons and their associated age uncertainty marked in black crosses.

#### 6.3.3.1 Berkner Island

The optimal age-depth profile is constrained using seven age horizons and three observed mean annual layer thickness measurements. The modelled age estimations agree with the observed age constraints to within 97.5% of the value and within the absolute age uncertainty (fig. 6.08). The distributions of modelled ages at depths corresponding to the age constraints demonstrate this (fig. 6.09; table 6.07), with the largest range of modelled ages in the deepest three age constraints. The uncertainty of 0.25-2.20 kyr on the age estimates allows a greater independence in modelled profiles, leading to larger uncertainty on the optimal profiles. Despite this, the age 50 m (snow equivalent) above the bed is estimated to be  $250 \pm 16$  ka BP.

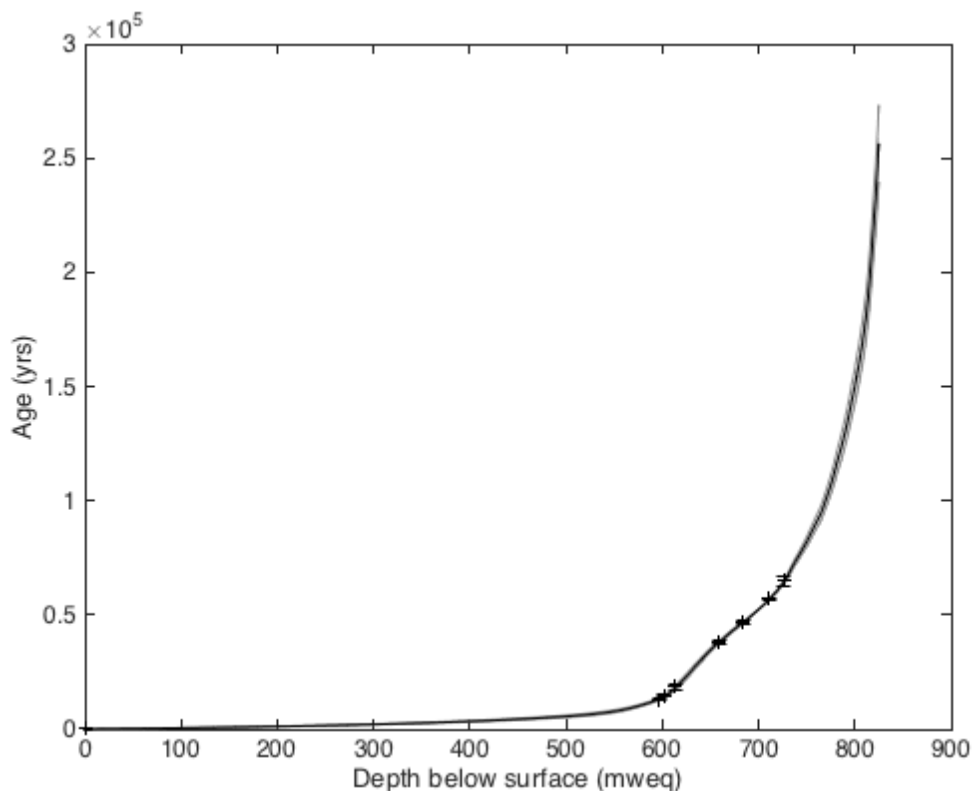


Figure 6.08: Age-depth profile of the BI ice core (black line) with associated error margin (grey). Age constraints are represented by black crosses with the associated age uncertainty.

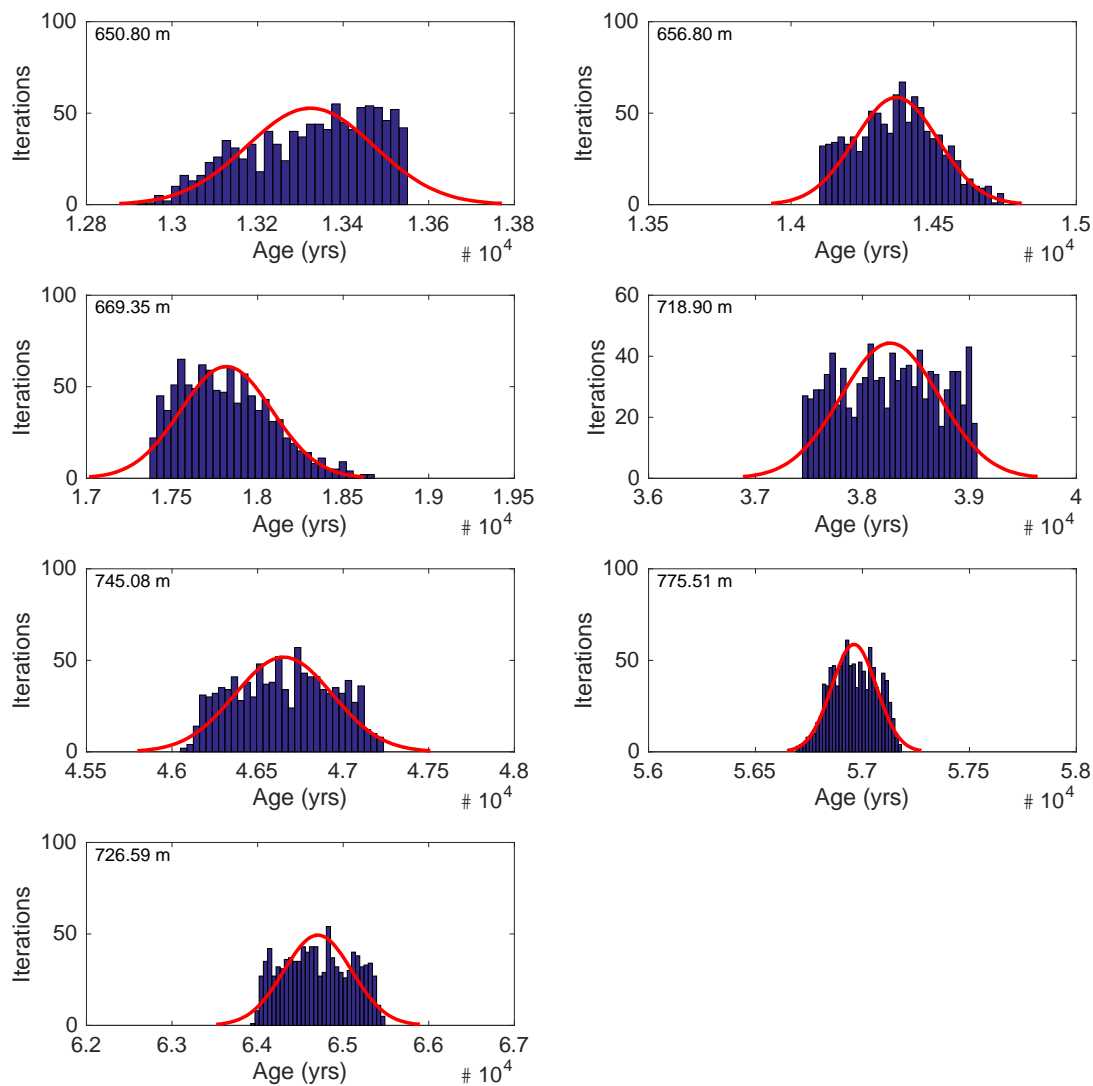


Figure 6.09: Probability distribution with the normal density function fitted (red line) of all age estimates at the depths corresponding to age constraints for BI. The depth corresponding to the age constraint is shown in the top-left corner. The age constraint and associated uncertainty is shown as a grey box.

Table 6.07: Estimated ages at depths corresponding to the depths of age horizons and the respective RMSE value of the modelled age-depth profile for BI.

Depth below the surface (m)	Depth (mweq below the surface)	Observed Age (kyr since drill date) and uncertainty (kyr)	Modelled Age Estimate (kyr since drill date) and uncertainty (kyr)
650.80	596.78	13.05 ± 0.25	13.37 ± 0.44
656.80	602.28	14.60 ± 0.25	14.52 ± 0.42
669.35	613.79	18.40 ± 1.00	18.17 ± 0.78
718.90	659.23	38.25 ± 0.80	38.16 ± 0.71
745.08	683.24	46.48 ± 0.80	46.52 ± 0.45
775.51	711.11	56.90 ± 0.80	56.93 ± 0.23
792.84	726.59	64.75 ± 0.80	64.75 ± 0.80
<b>RMSE (kyr)</b>			0.01 ± 0.30

### 6.3.3.2 Fletcher Promontory

The FP ice core record is constrained using five age constraints and five additional observed annual layer thickness measurements. This is an increase in the number and type of observational constraints than what has been used in the candidate FP age scales constructed in Chapter 4. The age-depth profile has a much smaller confidence interval (fig. 6.10) despite fewer age constraints than the BI ice core; this is due to the balanced distribution of the observational data throughout the ice core record. The distributions of modelled ages, at depths corresponding to the age constraints demonstrate the good fit of the optimised profiles to the observational data (fig. 6.11; table 6.08). The age 25 m (snow equivalent) above the bed is estimated to be  $120 \pm 5.5$  ka BP.

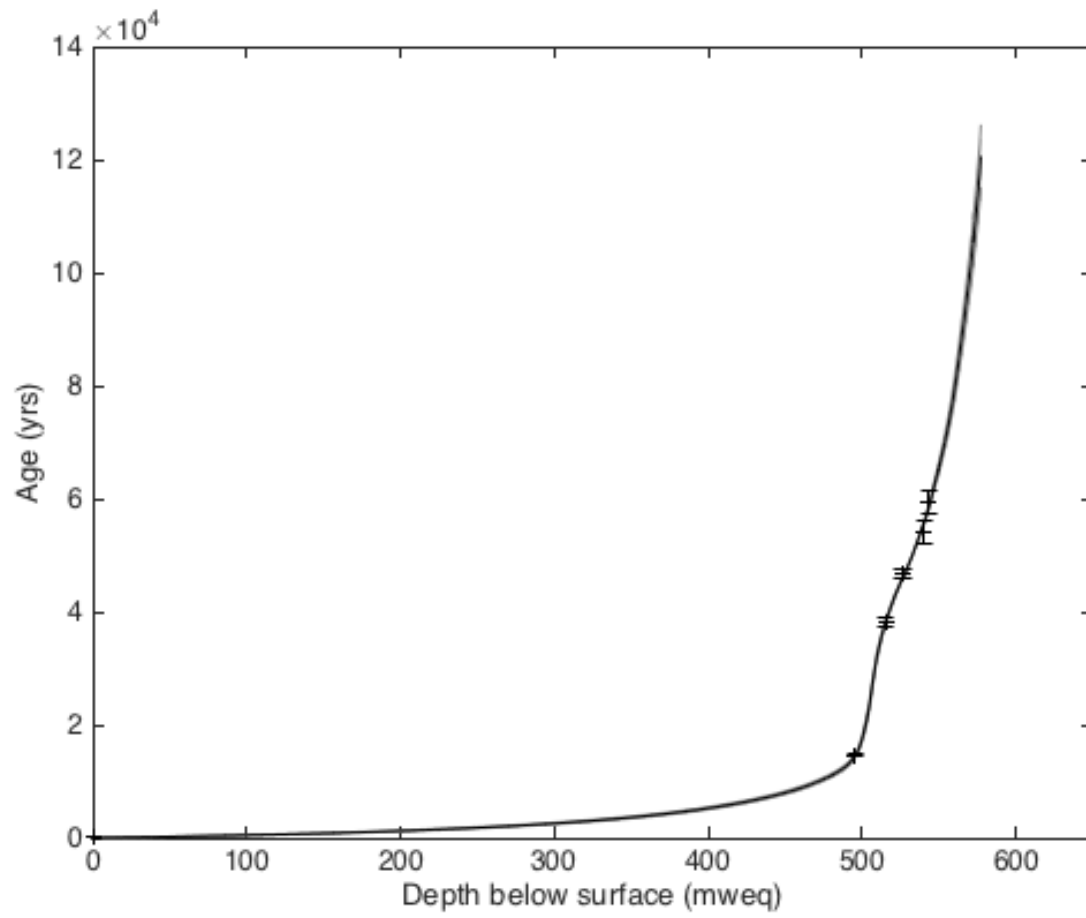


Figure 6.10: Age-depth profile of the FP ice core (black line) with associated error margin (grey). Age constraints are represented by black crosses with the associated age uncertainty.

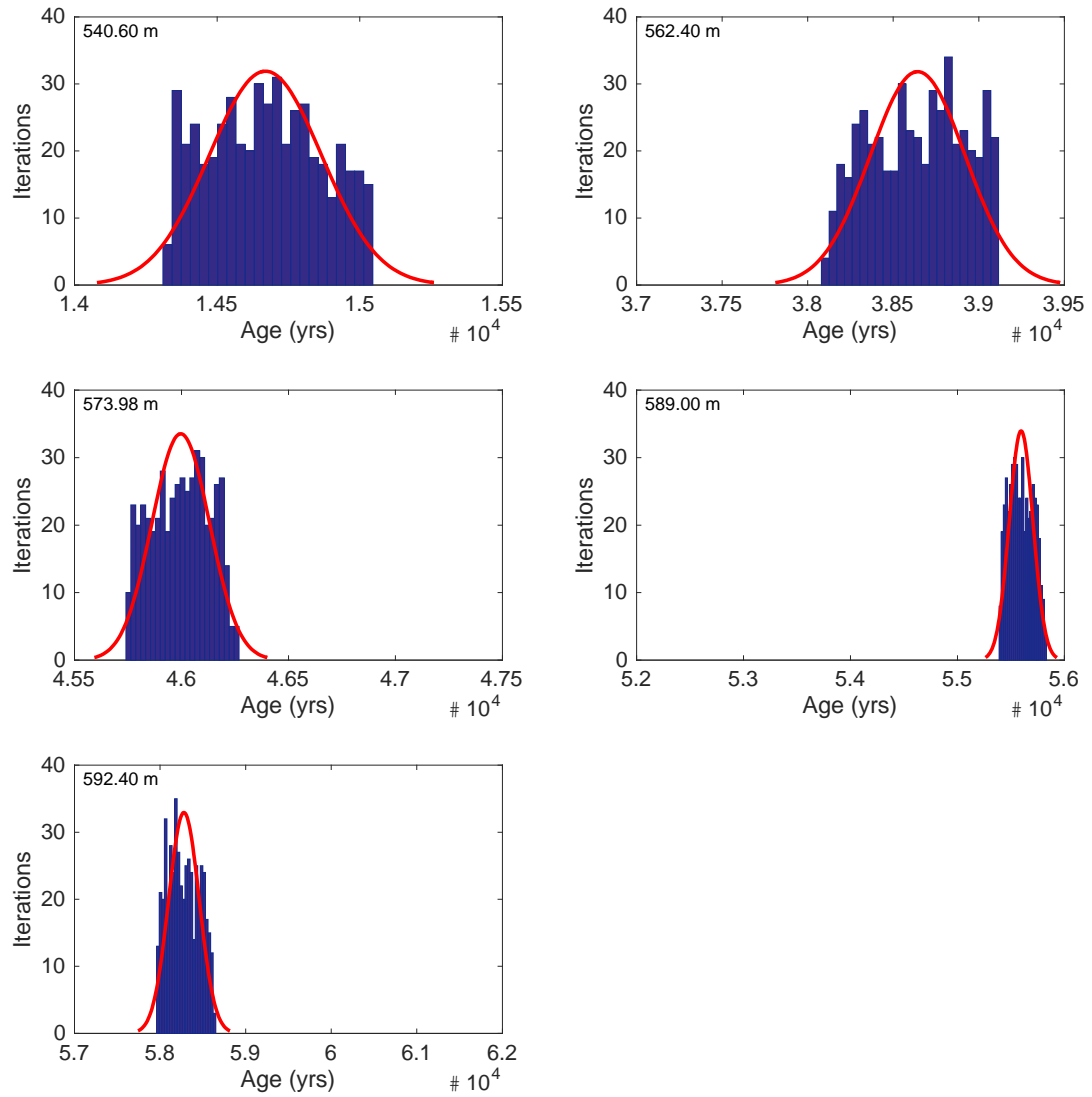


Figure 6.11: Probability distribution with the normal density function fitted (red line) of all age estimates at the depths corresponding to age constraints for FP. The depth corresponding to the age constraint is shown in the top-left corner. The age constraint and associated uncertainty is shown as a grey box.

Table 6.08: Estimated ages at depths corresponding to the depths of age horizons and the respective RMSE value of the modelled age-depth profile for FP.

Depth below the surface (m)	Depth (mweq below the surface)	Observed Age (kyr since drill date) and uncertainty (kyr)	Modelled Age Estimate (kyr since drill date) and uncertainty (kyr)
540.59	495.73	14.60 ± 0.25	14.69 ± 0.36
562.40	515.72	38.25 ± 0.80	38.49 ± 0.40
573.98	526.39	46.48 ± 0.80	45.91 ± 0.16
589.00	540.11	53.70 ± 0.80	55.66 ± 0.26
592.40	543.25	59.57 ± 2.20	58.38 ± 0.41
<b>RMSE (kyr)</b>			0.05 ± 0.71

#### 6.4 Discussion

Through the course of this study, multiple combinations of modelling techniques have been assessed in order to determine the optimal dating strategy (Chapter 4). The OptAcc model, using an initial accumulation history calculated using a Clausius-Clapeyron relationship and an initial thinning profile derived using the One-Dimensional thinning function, produced the most accurate annual layer thickness and age-depth profile (Chapter 4 and 5). Therefore, this model has been further developed for the FP and BI ice core chronology, making use of additional observational layer thickness data retrieved through techniques outlined in Chapter 5.

##### 6.4.1 Inclusion of Annual Layer Thickness Measurements as Model Constraints

Before the ice core chronologies can be discussed, the two separate FP ice core age scales must be assessed. In Chapter 4, candidate FP age scales were constructed using several approaches in order to assess the accuracy of each method in comparison with age horizons. Following this, Chapter 5 develops three analytical chemistry techniques to measure annual layer thickness in the ice core. The success in measuring actual annual layer thickness deep in the cores provides additional observational constraints for the inverse approach, leading to an improvement on the accumulation, thinning, and age-depth reconstructions initially presented in Chapter 4. The inclusion of measured annual layer thicknesses constrains the FP ice core chronology at more depth ranges along the profile. Fig. 6.12 presents the accumulation and layer thickness reconstructions presented in Chapter 4 (without annual

layer thickness constraints), and the reconstructions presented here (with annual layer thickness constraints).

The reconstructions presented in Chapter 4 and Chapter 6 both yield large uncertainty in the unconstrained sections of the accumulation and annual layer thickness profiles. The age constraints cover a 50 mweq section of ice that preserves the climate record during the last glacial period and transition into the Holocene. The inclusion of additional observational data throughout the ice core reconstruction leads to a shift in the final optimised profile of accumulation at all depths, as well as improving on the precision of the modelled accumulation profiles by limiting the uncertainty associated to the modelled chronology (as shown in fig. 6.12).

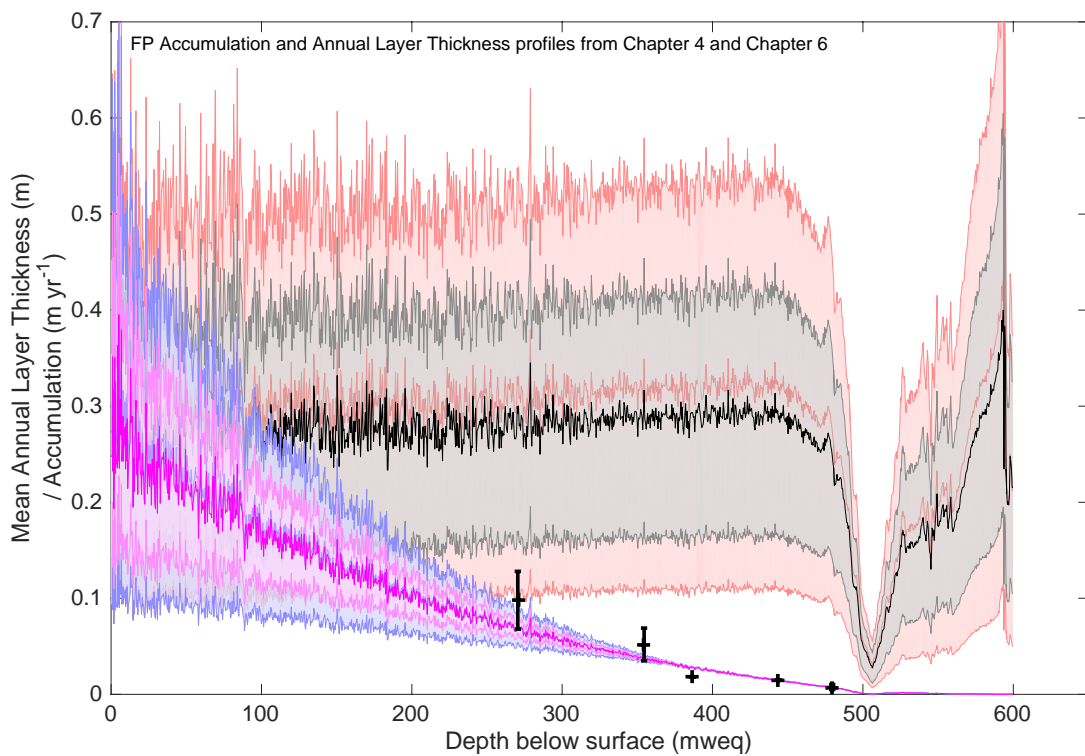


Figure 6.12: The optimised accumulation and present-day annual layer thickness profiles of FP, estimated using the OptAcc model. The 10-point averaged accumulation profiles and associated uncertainty for the model scenarios that are constrained by either only age horizons (red), or constrained by age horizons and measured annual layer thickness (black). Also shown are the 10-point averaged layer thickness profiles and associated uncertainty for the model scenarios that are constrained by only age horizons (blue), or constrained by age horizons and measured annual layer thickness (purple). Annual layer thickness constraints are also shown as black crosses on the figure.

The annual layer thickness measurements provide additional constraints on the ice-core age-depth model, and test the layer thickness output of the model. By choosing the depths to analyse, the inclusion of annual layer thicknesses as a constraint means that the distribution of the constraints along the ice core profile can be spread more evenly and add confidence to the reconstructed profiles. The FP and BI ice core reconstructions are constrained by annual layer thickness measurements. The results for each annual layer thickness profile agree to within the standard deviation of the measured values, with the exception of the annual layer thickness measurement at 387 mweq in the FP ice core, where only one annual layer is identified in each of the sections of ice analysed.

#### 6.4.2 Age-Depth Profiles

The constrained OptAcc chronology for the FP ice core implies an age of  $120 \pm 5.5$  ka BP at 25 m from the bed. The same model predicts that the BI ice core reaches an age of  $250 \pm 16$  ka BP 50 m from the bed. Fig. 6.13 presents the surface temperature and accumulation reconstructions for FP and BI on a common age scale. The 11.3 ka BP boundary delineating the start of the Holocene is marked on each of the plots by a grey dashed line (Walker et al., 2009). Beyond this line, the timing of globally-synchronous events across the LGM and last glacial period are synchronised between the ice cores, due to the identification of synchronous AIM events. The age scales correlate from 15 – 53 ka BP (after 53 ka BP, the FP age scale does not estimate an age to within the uncertainty of an age horizon at  $\sim 56$  ka BP). The age scales agree again at 59 ka BP as FP is constrained to AIM 17 ( $\sim 59$  ka BP) and BI is constrained to AIM 18 ( $\sim 65$  ka BP). Beyond this age, the age scales no longer correlate as they are no longer constrained to AIM events.

There are two notable observations in the BI reconstruction: firstly, the BI accumulation record is slower to increase from the LGM (21 ka BP) to Early Holocene (11 ka BP) accumulation values when compared with the FP ice core. Secondly, a signature in the BI surface temperature and accumulation reconstructions at  $\sim 150$  ka BP can be identified through comparison with other records as the last interglacial (LIG) (Bazin et al., 2013; Veres et al. 2013). This suggests that the BI ice core is not correctly dated as the LIG is assumed to be synchronous at 115 – 126 ka BP. Therefore, the accuracy of the accumulation for BI throughout the Holocene will be considered later in this chapter.

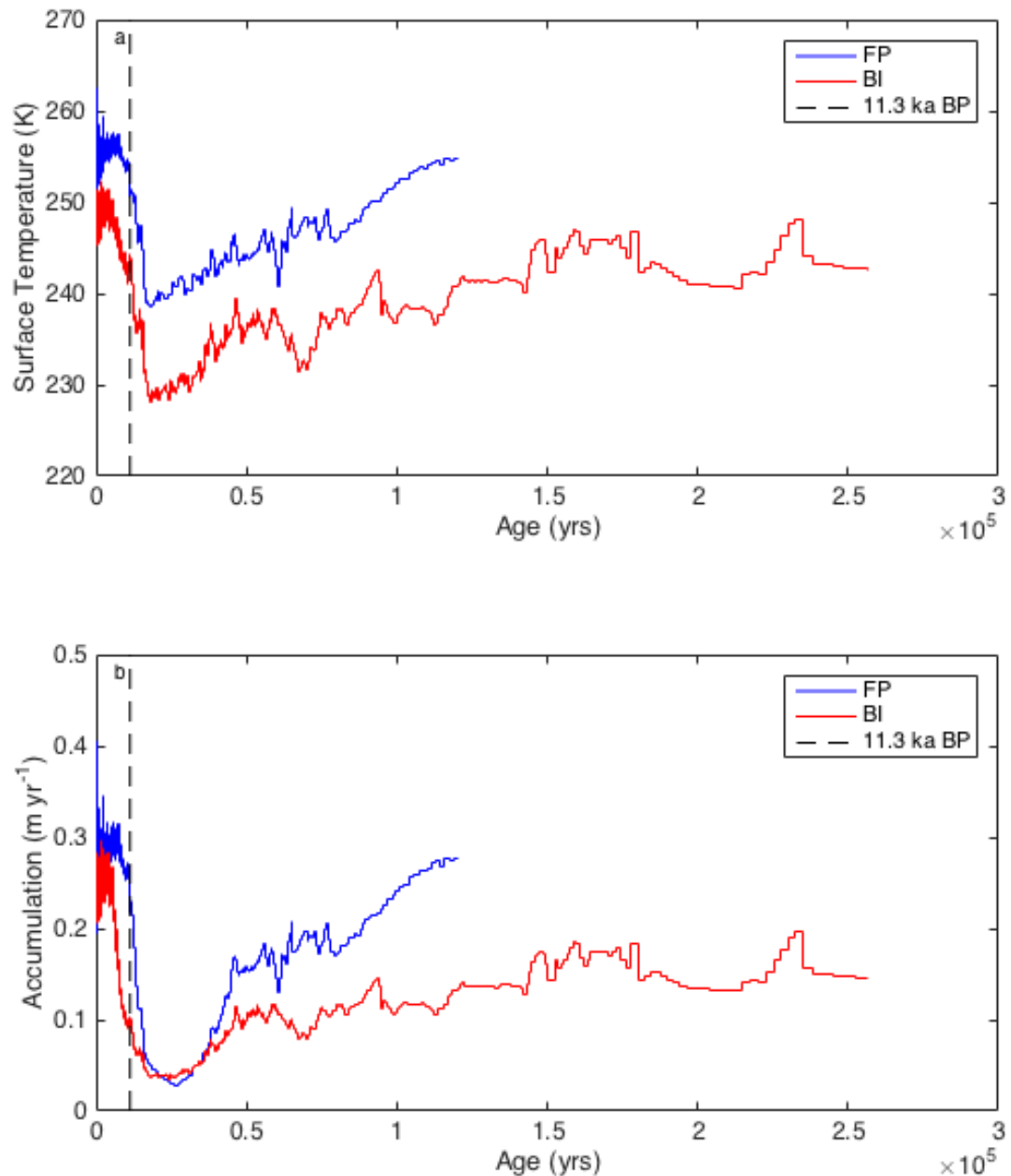


Figure 6.13: (a) Temperature reconstructions, and (b) Accumulation reconstructions for FP and BI ice cores. Blue: FP records; Red: BI ice core reconstruction. The 11.3 ka BP initiation of the Holocene period is marked by the grey dashed line.

#### 6.4.3 Thinning Profiles

The FP thinning profile decreases steadily until 500 mweq (0.19 in normalised depth units; fig. 6.05); below 500 mweq the thinning profile continues to decrease but less steeply than the rates above. This suggests that there is a decrease in the vertical velocity 100 mweq above the bed. This feature is not replicated in the empirical estimates of thinning (section

4.3.2; fig. 4.04). Our understanding of the ice rheology and topography of the bedrock at Fletcher Promontory is that the ice core was drilled at a Raymond arch. A Raymond arch (Raymond, 1983) develops due to the low deviatoric stress and hence slow vertical flow of ice beneath the ice divide, which ultimately leads to the accumulation of stiff ice at the bed. The stiff plug of ice then further decreases the vertical velocity towards the bed. Using phase-sensitive radio echo sounding (pRES), the internal structure of radar reflecting layers within the ice sheet can be identified. Measurements at a single site by pRES made over several years can identify distinct radar reflections and their vertical displacement between observations can be used to interpret the velocity by measuring the rate of the downwards trajectory with respect to time (Hindmarsh et al., 2011). The FP and BI ice cores were both drilled at ice divides; continuous over-snow radar data collected using a travelling radar system pulled by skidoo around the two ice core sites show the internal layering and the prominent elevation of the Raymond arch at both sites, which at FP was at least 100 m (snow equivalent units) from the bed (Hindmarsh et al., 2011; Kingslake et al., 2014; 2016).

The *in situ* measurements of vertical velocity at the FP ice core site using the pRES radar permits a test of the accuracy of the thinning function reconstructed using the OptAcc model. In order to be compared with the thinning function, the *in situ* vertical velocity profiles are normalised. Fig. 6.14 presents (a) the vertical velocity measurements, and (b) the reconstructed thinning function (red) and the normalised vertical velocity measurements (blue) (data is courtesy of J. Kingslake and is only available for the FP ice core). Uncertainty on the vertical velocity measurements increases substantially close to the bed due to the extrapolation of data. Vertical velocity measured over several field seasons at the FP site suggests a decrease in velocity with depth, reaching zero at 550 m below the surface (100 m above the bed). This agrees with the expected profile of vertical velocity in the presence of a Raymond arch, where the stiff plug of ice at the bed leads to slow vertical flow of ice. At around 400 m (fig. 6.14b), the pRES measurements suggest a lower vertical velocity than the modelled thinning function. This change in the gradient of the pRES measurements suggests that the *in situ* pRES measurements identify the sudden change in vertical velocity associated with the Raymond arch in a way that the modelled thinning profile cannot. Despite this, these measurements of *in situ* vertical velocity agree fairly well with the thinning profile reconstructed using the OptAcc model (fig. 6.14b). Comparison of the normalised profiles show similarities in the rate of thinning throughout the ice core profile, with the thinning profile and normalised vertical velocity reaching less than 0.1 by 420 m.

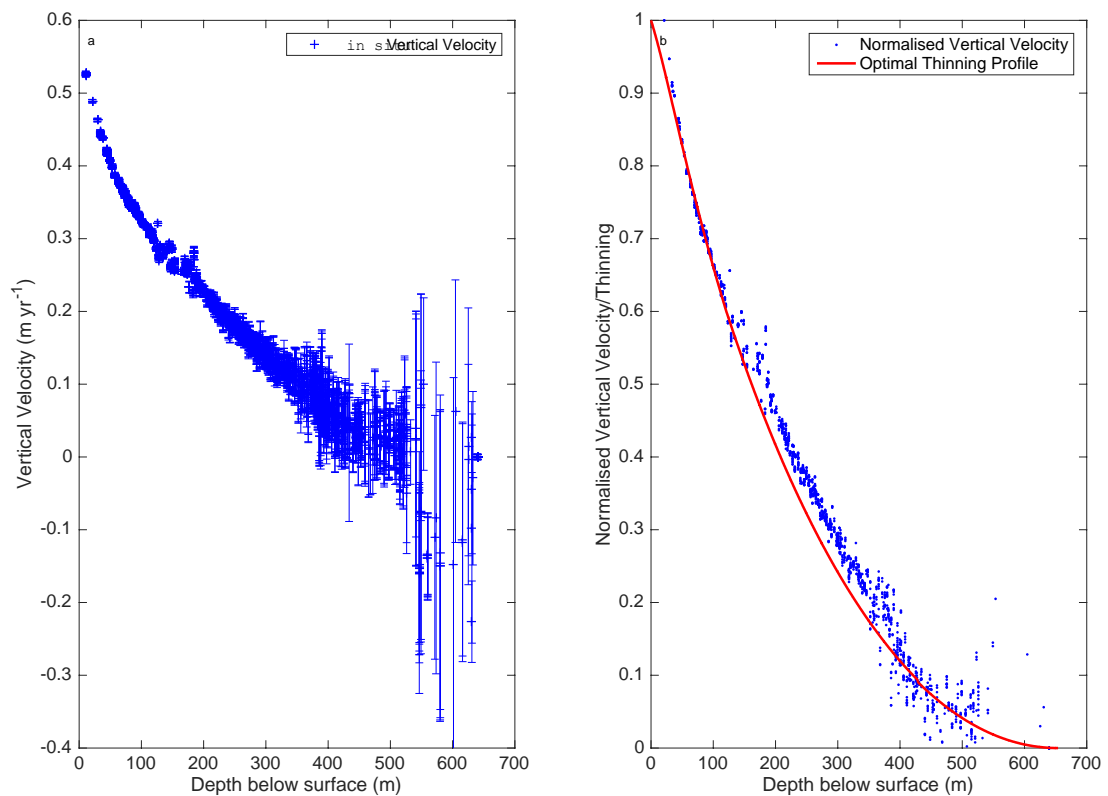


Figure 6.14: (a) Vertical velocity measurements with the associated error margin using pRES at the FP ice core site. Data courtesy of J. Kingslake; (b) Normalised pRES measurements (blue) and the optimal thinning profile calculated using the OptAcc model (red).

In order to account for the Raymond arches at the ice divide, the optimised thinning functions must rapidly decrease with depth in the upper depths of the ice core in order to accurately reconstruct the low stresses towards the bed. As a result, the optimised  $p$ -parameter in the thinning function of the OptAcc model is low for the FP and BI ice cores (table 6.05). Low values of the  $p$ -parameter suggest a highly non-linear deformation profile within the ice sheet that agrees with the expected effect of a Raymond arch. High rates of thinning through the majority of the ice sheet could reflect either a large ice sheet thickness or high mean annual accumulation rates. Accumulation rates at both BI and FP are an order of magnitude higher than in East Antarctica (EPICA, 2004; Mulvaney et al., 2007; 2014), but this study concludes that the presence of the Raymond arch is the most likely reason for the high stress on the ice flow in the upper part of the ice core, as implied by both the modelled thinning function at both sites and the additional pRES data on FP.

The estimated value of Glen's exponent,  $n$ , is still lower than any values inferred from direct measurements in the ice sheet. For this analysis, the value of  $n$  has been interpreted by inverting eq. 2.16 (section 2.5.3.3). This estimate of  $n$  should only be considered a 'best guess' approximation due to the assumptions made in eq. 2.16. It is generally understood that the temperature profile through the ice column is not linear (as assumed in eq. 2.16), and the activation energy,  $Q$ , necessary for the approximation of  $k$  (calculated in eq. 2.17, also a parameter required in eq. 2.16), could differ greatly from the assumed value of 60 kJ mol<sup>-1</sup> (Parrenin et al., 2007a).

Furthermore, laboratory experiments consistently calculate the value of Glen's exponent to be  $\sim 3$  (Glen, 1958), although *in situ* ice sheet calculations suggest the value could be between 1 and 5 (Raymond, 1983; Martin et al., 2006; Gillet-Chaulet et al., 2011). Therefore, despite the unusually low estimates for the parameters used to calculate the thinning profile, there is sufficient evidence to suggest that non-linear thinning functions are necessary to accurately estimate the ice flow at the divide where a Raymond arch is present, such as at FP and BI.

#### 6.4.4 Accumulation Profiles

The most likely accumulation scenarios for FP and BI ice cores are compared in fig. 6.13b. The accumulation scenarios have been perturbed by the OptAcc model, and yield information on the accumulation history for each site. The following section will discuss the final accumulation scenarios and compare past precipitation rates with other ice core sites from the West Antarctic Ice Sheet (WAIS) and AP regions, in order to assess the accuracy and reliability of the ice-core reconstructions through the OptAcc model.

##### 6.4.4.1 Industrial Era (1850 – Present-Day)

As already stated, the perturbed FP accumulation rate is lower than the empirically-estimated accumulation rate. The Clausius-Clapeyron relationship (eq. 2.06-2.08, section 2.5.2.2), used for the initial accumulation profile, assumes a steady present-day rate of accumulation, and it estimates the accumulation history as a deviation from the present-day rate. For the FP ice core, this steady present-day rate of accumulation is 0.38 m yr<sup>-1</sup> as interpreted directly from annual layers observed in the ice core over the most recent decade, yet the modelled mean accumulation rate is  $\sim 0.28$  m yr<sup>-1</sup>. One explanation for the discrepancy between empirical and reconstructed accumulation profiles at FP could be that there has been an increase in accumulation coinciding with rapid regional warming across

the AP and Weddell Sea regions over the most recent 150 years (Rignot et al., 2004; Turner et al., 2005; Steig et al., 2009). Other sites across the AP and WAIS, such as Gomez, record accumulation increases by up to 100% in the last 300 years (Thomas et al., 2008; 2015). Thomas et al. (2008) presented the mean annual and decadal snowfall at sites in the AP and WAIS, for which present-day mean annual accumulation was consistently greater than the 30-year average annual accumulation rate. A warmer surface temperature brings a warmer moisture source that leads to increased accumulation (Krinner et al., 2007; Bracegirdle et al., 2008; Frieler et al., 2015); the current rapid regional warming across the AP and Weddell Sea region may suggest a higher mean annual accumulation rate than is true for a long-term mean annual rate.

A steady increase in accumulation is visible in the FP ice core record, particularly over the most recent 150 years; this agrees with an increase in surface temperature (fig. 6.15). Using a linear regression model, an increase in the rate of mean annual accumulation of 10 mm century<sup>-1</sup> is calculated, with a total 15 mm increase in mean annual accumulation since the onset of Industrial Era warming at 1850 AD. In contrast to the FP record, the BI accumulation record does not show any change in the most recent 150 years. However, absence of evidence is not evidence of absence. The BI ice core was retrieved in 2004, and does not include the upper 8 m of the firn (the modelled reconstructions assume a steady stable water isotope concentration equivalent to the present-day value, and a mean annual accumulation rate equivalent to the present-day rate, for the top 8 m of the ice core). Assuming a mean annual accumulation rate of 0.18 m yr<sup>-1</sup> from the ice core model and including the 13 years since the retrieval, more than 50 years of accumulation history could be missing from the record. The short ice core retrieved from Berkner Island in 1994, ahead of the deep ice core used throughout this study, would not shed light on the most recent 23 years of accumulation at BI (Wagenbach et al., 1994), but the 1000-year record retrieved from this short ice core does agree with the deep ice core record (Mulvaney et al., 2002). However, early indications from the information preserved in this short ice core suggested that BI is influenced by large-scale air mass regimes and hence could be susceptible to changes in the surface temperature across the region (Wagenbach et al., 1994). Analysis of alternative ice core and ice sheet proxies should be completed before confirming the response of Berkner Island to rapid regional warming across the Weddell Sea sector. In particular, proxies that reflect the extent of annual sea ice (Sodium - Na) or the proximity of open ocean conditions (methanesulfonic acid - MSA) yield information on the region

surrounding an ice core site that could be used to interpret the sensitivity of the region to temperature changes (which are reconstructed from the stable water isotope record).

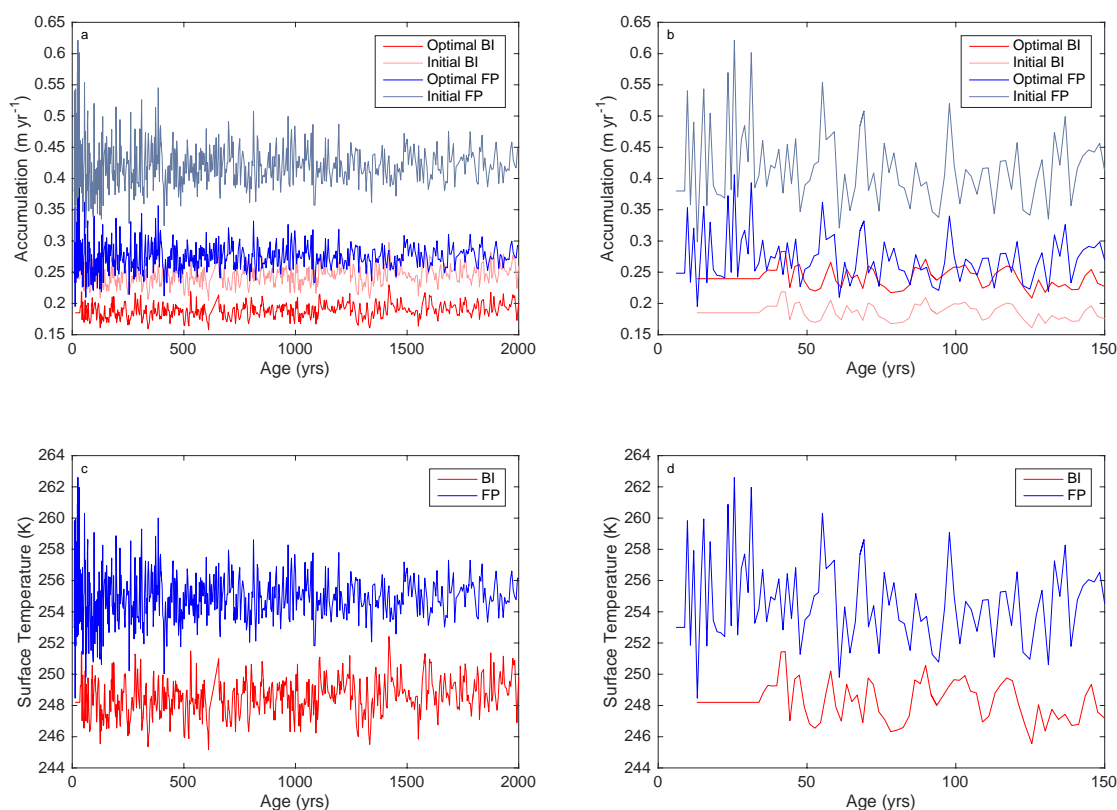


Figure 6.15: Accumulation reconstructions over the last 2000 years; a) accumulation spanning 2000 years; b) accumulation over the last 150 years. Red: BI accumulation with the initial profile in pale red; Blue: FP accumulation profile with the initial profile in pale blue. Underneath, the surface temperature reconstructions of the BI and FP ice cores spanning (c) 2000 years, and (d) the last 150 years.

#### 6.4.4.2 Holocene

Throughout the Holocene period, the modelled BI accumulation history is significantly perturbed. Using cubic interpolation, between 9 ka BP and 2.5 ka BP, the accumulation increases by 160% from  $\sim 0.10 \text{ m yr}^{-1}$  to  $0.26 \text{ m yr}^{-1}$  (fig. 6.16). The sharpest increase in the modelled accumulation rate is observed between 9 ka BP and 5.5 ka BP at a rate of  $30 \text{ mm millennium}^{-1}$ . At 5.5 ka BP, the accumulation rate increases more slowly until 2 ka BP, from  $0.24 \text{ m yr}^{-1}$  to  $0.26 \text{ m yr}^{-1}$  at a rate of  $5 \text{ mm millennium}^{-1}$ . The rapid increase in accumulation is constructed using a perturbation profile as part of the OptAcc model; in the empirical reconstruction of accumulation, the increase is observed more gradually from the onset of the Holocene. This change in accumulation is not replicated in the FP ice core record (fig.

6.16). The optimised accumulation in the FP ice core increases by 7% from 9 ka to 5 ka BP before decreasing for the remainder of the ice core record to the present day (fig. 6.16).

An increase in accumulation from 9 ka BP is recognised in other Antarctic ice core records which experience a later Holocene Thermal Maximum (HTM) (Koutnik et al., 2016). A highly variable accumulation record is recorded in the Taylor Dome ice core record, which does not resemble the stable water isotope record (Monnin et al., 2004). This is similar to the modelled accumulation record at BI, as the increase in accumulation over 9 – 5.5 ka BP is not as abrupt in the empirical accumulation estimate, which estimates a 28% increase over the equivalent time period. Similarly, an increase in accumulation from 9 ka to 2.3 ka BP has been retrieved in the WAIS Divide ice core (Koutnik et al., 2016). The 40% increase in accumulation at WAIS Divide during this period is significantly less than the increase reconstructed at BI, but it is greater than the increase inferred by the empirical BI accumulation history.

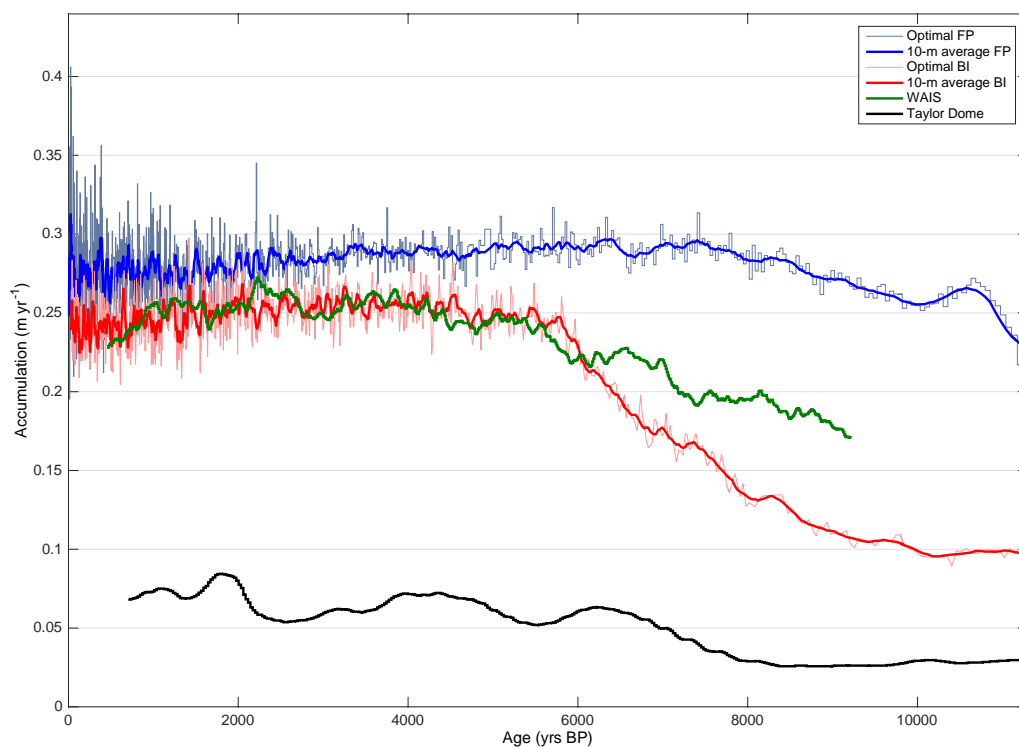


Figure 6.16: Accumulation in-depth view of 11.3 ka BP to 2 ka BP. Blue: FP 10-metre average accumulation records with the metre-average accumulation history in pale blue; Red: BI 10-metre average accumulation records with the metre-average accumulation history in pale red. In addition, the WAIS (green) and Taylor Dome (black) accumulation records are presented for comparison.

The 112% increase in accumulation over 9 – 5.5 ka BP is reconstructed in the ice core between the 450 – 550 mweq. In this section, there are no observational constraints on annual layer thickness or age. The annual layer thickness measurement at 409 mweq, and the youngest age constraint at 596 mweq sandwich this section of the ice core, and therefore, it is likely that the OptAcc model reacts slowly to an increase in accumulation from glacial conditions at the ACR to the Holocene conditions as there are no additional constraints across this period of time. Therefore, the accuracy of the BI accumulation and age-depth reconstruction throughout this depth range should be treated with caution, before the shape of the perturbation profile is assessed against the stable water isotope profile.

#### 6.4.4.3 LGM

The FP and BI age scales correlate throughout the last glacial period insofar as they are constrained to age constraints that correspond to synchronous AIM events. At ages greater than 60 ka BP, where the FP stable water isotope profile is no longer at a sufficient resolution to observe and identify age constraints, the accumulation and surface temperature profiles do not agree in fig. 6.13. The oldest constraint used in the construction of the BI age scale is at ~64 ka BP. As such, it is difficult to ascertain the accuracy of either age scale beyond this point without additional constraints at greater depths in the ice-core profile.

Unlike the FP and BI ice core records covering 14 – 60 ka BP, the FP and BI ice core records spanning 0 – 14 ka BP are poorly-constrained and unsynchronised. Over the transition from the ACR to the Early Holocene (14 – 11 ka BP), there is only one age horizon younger than the ACR in the FP and BI ice core records. The discussion of the FP and BI accumulation records for this time period is derived from the OptAcc approach alone. The modelled BI accumulation is slower to respond to changes in temperature due to the modelled perturbation to the accumulation record. This slower response to warming temperatures continues into the Holocene and feeds into the delayed increase in accumulation over 9 – 5.5 ka BP. Therefore, there is additional reason to be cautious when assessing the perturbed accumulation profile during this period. Following the end of the LGM, the BI accumulation record rapidly increases to Holocene conditions but this response occurs over 1 kyr later than at FP (fig. 6.13b). This is not replicated in the temperature record, which gradually increases to interglacial conditions (fig. 6.13a). When compared with surface temperature history, the magnitude of the change in the accumulation records is greater because of the

perturbation of empirical accumulation reconstructions. The optimal ice-core reconstruction is determined by the agreement of the annual layer thickness and age scale with observational constraints, of which the success of the fit of these profiles to observational constraints is demonstrated in fig. 6.08. As already stated, during the Holocene only the BI accumulation record increases whilst the FP accumulation record shows little change throughout this period. The delayed response to accumulation change during the LGM/Holocene transition at BI should raise doubts in the efficacy of the perturbed accumulation profile for BI (fig. 6.13; 6.16). The perturbation profiles should be compared and assessed with the stable water isotope profiles and the climate history of the AP and Weddell Sea region.

#### 6.4.5 *Stable Water Isotopes and Accumulation*

The questions remaining over the accuracy of the BI and FP accumulation reconstructions can be investigated further by analysing the modelled perturbation profiles against the surface temperature reconstructions. Surface temperature profiles are reconstructed directly from the measured stable water isotope profiles (eq. 2.03). It is assumed that changes in precipitation rates are proportional to changes in the surface temperature due to the atmosphere's ability to hold moisture (Bracegirdle et al., 2008; Palerme et al., 2017). Therefore, the following section will analyse the relationship between stable water isotopes, surface temperature, and the modelled accumulation profiles for the BI and FP ice cores in order to thoroughly investigate the reliability of the perturbation algorithm developed in the OptAcc model.

##### 6.4.5.1 *Berkner Island*

As already mentioned in this chapter (section 6.4.4.2), the BI accumulation, annual layer thickness, and age-depth profiles are presented in this study with low confidence. The perturbation profile has a large range throughout the Holocene, with tighter control on the perturbation profile deeper in the core. Despite the large range, the possible perturbation profiles of the BI ice core are stable in the Late Holocene (0 – 4 ka BP) and from the ACR to the end of the age-depth profile (14 – 250 ka BP). The stability throughout these periods results in a surface temperature – accumulation sensitivity of 4 % K<sup>-1</sup>; in line with published estimates of sensitivity rates of 4 – 6 % K<sup>-1</sup> (Palerme et al., 2017).

The surface temperature – accumulation sensitivity rate increases from 4 % K<sup>-1</sup> to 18 % K<sup>-1</sup> over the period 4 – 14 ka BP. This change in the sensitivity rate suggests a deviation from

the understood relationship between stable water isotopes – surface temperature – accumulation. This change is due to one of two possible reasons: (i) the lack of age and annual layer thickness constraints in the 400 – 600 mweq of the BI ice core, or (ii) the 9 – 5.5 ka BP accumulation profile reflects a later surface temperature warming from ACR conditions to the Early Holocene than is recorded at FP. The BI and FP ice core records both identify an isotopic signature in the ice-core record that reflects the ACR, and hence each record should be readily tuneable to each other. However, the BI ice-core record at 400 – 600 mweq, preceding the ACR constraint, is not constrained to any age horizons. Therefore, this study cannot rule out that the lack of constraints throughout this depth range is a vulnerability to the BI accumulation reconstruction.

The alternative explanation for the change in the surface temperature – accumulation sensitivity, and the late temperature warming and accumulation increase into the Early Holocene, is that there are asynchronous climate conditions at the BI and FP site locations. To investigate this, it is necessary to assess the BI ice core record in a regional context for the time period 0 – 21 ka BP. It was suggested earlier that the BI ice core location is susceptible to regional climate and that the accumulation record is dominated by regional air masses rather than local climate (Wagenbach et al., 1994). Therefore, the accumulation history preserves a record of continental accumulation change across the WAIS.

Following the LGM maximum ice-sheet elevation and extent, research indicates that the deglaciation of the AP and Weddell Sea did not reveal BI as a standalone ice rise in the Weddell Sea at the same time as FP and JRI. The BI ice core is drilled on an ice rise within the Filchner and Ronne ice shelves, and the dynamics of this ice rise will be affected by changes in the extent of the surrounding ice shelves. During the last glacial period, it is assumed that the grounding line of the Antarctic Ice Sheet (AIS) reached approximately 450 km north of Berkner Island, with an ice sheet thickness up to three times greater than the current ice sheet thickness (Ritz et al., 2001; Huybrechts et al., 2002; Pollard and DeConto, 2009; Le Brocq et al., 2011; RAISED Consortium, 2014). This means that the present-day BI drilling site was an inland, continental location at a high altitude at the LGM ice-sheet extent. Following the LGM, the AIS did not retreat across the AP and Weddell Sea region uniformly. Research suggests that whilst the AP was undergoing significant deglaciation 21-15 ka BP, the Weddell Sea remained mostly ice-covered (Siegert et al., 2013; RAISED Consortium, 2014). By 10 ka BP, the AIS grounding line was north of BI, leaving the southern region of the Weddell Sea still ice-covered (RAISED Consortium, 2014). The AIS did not retreat to the

present-day grounding line south of BI until  $\sim 4$  ka BP (Siegert et al., 2013; RAISED Consortium, 2014), despite research indicating that the location of FP – at a similar latitude to BI – was already an exposed ice rise (RAISED Consortium, 2014; Hein et al., 2016).

The geometry of the deglaciation could explain the different accumulation profiles reconstructed using the OptAcc model. A site in the Weddell Sea during the deglaciation would transition from a continental to coastal location and decrease in altitude, affecting the mean annual rates of precipitation and surface temperature. In particular, based on recent research into the AIS deglaciation, as BI emerged as a standalone island more recently than FP, one would expect a later, gradual increase from surface temperature and mean annual accumulation rates at both sites, occurring later at BI than at FP. This is evident in the modelled reconstructions of accumulation, where a longer deglaciation at BI would extend into the Holocene period and yield a later HTM, as expressed in fig. 6.13 and 6.16.

This study suggests that the delayed onset of the Early Holocene conditions and later HTM should not be considered surprising. However, the post-LGM change in ice sheet thickness history and the migration of the ice divide through time could have had a significant impact on the ice core record. By addressing the additional factors that may influence the modelled estimates of annual layer thickness, such as temporal changes in ice sheet thickness and the migration of the ice divide, the BI accumulation reconstruction might change from the profile that is presented in this chapter. The perturbation to the stable water isotope – surface temperature – accumulation relationship from the LGM to the Early Holocene likely accounts for the differences not reconstructed as part of the OptAcc approach as well as the delayed HTM.

#### 6.4.5.2 *Fletcher Promontory*

As previously stated, the reconstructed FP accumulation profile was consistently perturbed – 34% throughout the Holocene in accordance with the initial accumulation history and therefore the stable water isotope profile and final accumulation profiles preserve the same trends. In addition to the uncertainties in the  $T_s/A$  relationship, the OptAcc model assumes the observed present-day mean annual accumulation rate is correct. Despite the increases in accumulation due to rapid regional warming seen in other West Antarctic and AP ice cores (Thomas et al., 2008; 2015), the mean annual accumulation rate has been measured here from ice core records over only the previous decade. A wrongly-estimated present-day

mean annual accumulation rate, calculated as a decadal mean value during a period in which the annual accumulation is increasing, may explain the reason for the high rate of perturbation in the OptAcc accumulation reconstruction throughout the Holocene at this ice core site.

The significant perturbation over the Holocene period required by the OptAcc model could also be explained by the rapid regional warming across the AP region, and the record of warming and increased accumulation preserved in the FP ice core. The Gomez and Ferrigno ice core sites have experienced an increase in mean annual accumulation of up to 100% in the late 20<sup>th</sup> century to present-day (Thomas et al., 2015). The FP accumulation reconstruction shows a small increase in accumulation over the last 125 years (fig. 6.15b). This increase is replicated in the stable water isotope and hence the surface temperature reconstructions (fig. 6.15d), as the relationship between the three processes is unchanged by the perturbation profile during the last 125 years. We should consider that the rapid regional warming, leading to an increase in the present-day mean annual accumulation, could be responsible for an incorrect value for present day mean accumulation that underpins the empirical accumulation estimate.

The supposition of an overestimated present-day accumulation rate is supported by the OptAcc model and data observations. Over the Holocene period, the mean annual rate of accumulation, estimated using the GCM, IceChrono, and OptAcc model approaches, is  $0.22 \pm 0.04 \text{ m yr}^{-1}$  (section 4.3.2; table 4.02). The agreement between the IceChrono, GCM, and OptAcc model reconstructions, which reconstruct accumulation through different methods, support the theory that the measured present-day rate of annual accumulation is inaccurate. If this is true for the FP ice core, the optimised accumulation profile might not sufficiently reconstruct the amplitude of the change in accumulation with respect to rapid regional warming, as the perturbed accumulation profile never reaches the measured annual layer thickness of  $0.38 \text{ m yr}^{-1}$ , which is used in the empirical estimates. Therefore, the discrepancies between the initial and final accumulation reconstructions for the FP ice core could be explained by a wrongly-estimated present-day mean annual accumulation rate.

## 6.5 Summary

This chapter presents results that directly contribute to achieving the third objective of this thesis (section 1.2.1). The BI and FP ice core records have been reconstructed using the

OptAcc model. Annual layer thickness observations, retrieved by techniques used in Chapter 5, have constrained accumulation, thinning, annual layer thickness and hence age-depth profiles. Optimised profiles of annual layer thickness and age-depth profiles have been constrained using measured annual layer thickness, accounting for associated uncertainties on the observations. The new annual layer thickness observations provide a more balanced range of constraints across the FP ice core profile to counter the pre-Holocene cluster of known ages, but more analysis is required to balance the BI ice-core record. The accumulation records over the current interglacial period at each site indicate variability that is replicated in ice cores from across the WAIS and AP regions, including Taylor Dome and WAIS Divide (fig. 6.16). Similarly, due to the stiff ice causing Raymond arches at ice divides, the thinning functions agree with both measured vertical velocity and theoretical explanations for a highly non-linear thinning function causing slow vertical velocity towards the bed. The FP and BI ice core records extend beyond the last glacial period, preserving a record that covers at least 120 kyr at FP and 250 kyr at BI.

This work confirms that these two ice caps did not undergo retreat or collapse during the LIG but may preserve a record of proxies indicating open ocean (MSA) and hence the potential collapse or retreat of the WAIS during this period, or the continued presence of WAIS sea ice (Na). The FP optimised profiles provide reliable reconstructions that can be used to interpret the climate history of the site in the wider context of the AP and Weddell Sea region, Antarctica, and the rest of the world. Following this work, the inclusion of additional information at BI is necessary to investigate the BI ice core record further, in particular the response of the BI ice core to periods of warming. The lack of evidence of a recent accumulation increase or present-day regional warming at BI disagrees with other records from the WAIS, yet the region should respond to regional changes in climate more than local changes. Furthermore, the ACR transition into the Holocene occurs later at BI than at other ice cores, with a rapid increase in accumulation occurring 1 kyr after FP. Following this, the Holocene record shows a response to regional warming with a steady increase in the accumulation record. Additional research must be completed in order to better interpret the BI ice core record and constrain the accumulation and surface temperature record.



# Chapter 7: A revised chronology for the James Ross Island ice core

## 7.1 Introduction

The previous chapter presented model results for the Berkner Island (BI) and Fletcher Promontory (FP) ice core records. In this chapter, the James Ross Island (JRI) ice core age-depth profile is reconstructed following similar techniques to those used in Chapter 6. The JRI ice core already has a published chronology (Mulvaney et al., 2012); initial analysis was carried out at the British Antarctic Survey (BAS), with a primary chronology (JRI1) published by Mulvaney et al. (2012), suggesting an age at the base of the core of ~50 ka BP. Recent chemical analysis of the JRI ice core by colleagues at the Desert Research Institute (DRI) by high-resolution continuous-flow analysis (CFA) highlighted some inaccuracies in the observed age horizons that had previously been used in the chronology. The upper section of the ice core has now been annual layer counted to a greater depth than the earlier JRI chronology. Following this, the past accumulation and thinning have been reconstructed using the Optimised Accumulation and Thinning (OptAcc) model (section 4.4.4). In this chapter, revised age horizons are tied to the annual layer-counted West Antarctic Ice Sheet (WAIS) Divide ice core; these additional constraints are considered to be robust, and increase the confidence in the age-depth estimate for JRI. This chapter presents a revised chronology for JRI, hereafter referred to as the JRI2 chronology.

James Ross Island is located in one of the most rapidly warming regions on Earth, where ice mass loss has been particularly significant following the break-up of the Prince Gustav Channel and Larsen B ice shelves (Pudsey and Evans, 2001; Vaughan et al., 2003, Mulvaney et al., 2012). Marine sediment core records suggest the extent of the local ice shelves has changed markedly through the Holocene (Domack et al., 2005; Pudsey and Evans, 2006; Hjort et al., 1997). Geomorphological records suggest that a warming event and period of deglaciation and loss of ice shelves in the north-eastern Antarctic Peninsula (AP) at approximately 7.4 – 4.6 ka BP was followed by a period of glacier and ice-shelf advance to present-day limits (Hjort et al., 1997; 2001). If the current AP ice shelves are not remainders of the ice sheet extent during the Last Glacial Maximum (LGM), this raises questions about the processes and climate thresholds controlling the presence of ice shelves in the region.

Principally, if the ice sheet did retreat behind its present-day extent at some point during the mid-Holocene, what were the climate conditions during this retreat? To answer this, the James Ross Island ice core was drilled to 363.9 m in 2008, on the north-eastern tip of the AP (Mulvaney et al., 2012; 2014). The JRI ice cap is perhaps the best site in the northern AP to recover an ice core record of local climate as it sits on a discrete ice dome with almost radial ice flow. Around 80% of JRI is covered by the Mount Haddington ice cap and its outlet glaciers (fig. 7.01) (Hjort et al., 1997).

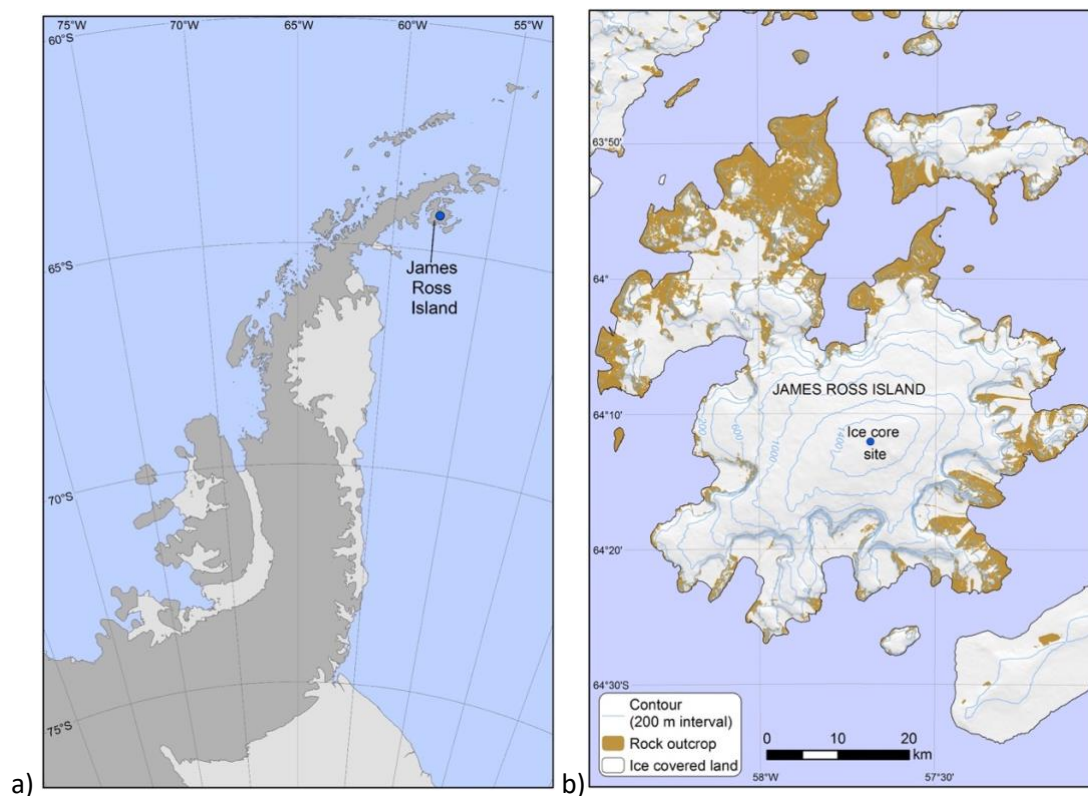


Figure 7.01: (a) JRI in the AP region; (b) a zoom-in to JRI showing the drill site in the context of the Mt. Haddington ice cap that covers the majority of the island.

## 7.2 Methods

The construction of the JRI2 chronology makes use of a number of additional techniques compared with those used to reconstruct the FP and BI ice core records. As such, the JRI2 chronology is presented in this chapter, separate to the FP and BI ice cores. The high-resolution chemistry profile for this core enables annual layer counting of the upper layers, as well as the identification of a set of precisely-dated age horizons. The chemical profile and precisely-dated age horizons tightly constrain the ice-core reconstructions of accumulation and thinning. The OptAcc age-depth reconstruction must agree to within the uncertainty of the age horizons. The numerous age horizons over a short ice-core range

poses a problem for the OptAcc model: the increase in age with depth is not linear under the assumption that the accumulation rate is stable throughout the Holocene. This was the first indication that the past accumulation rate is highly variable over the ice core. The OptAcc model reconstructs the mean annual accumulation at a 50 cm-resolution. In the shallowest 100 m of the JRI ice core, annual layer thickness fluctuates between 40 cm – 70 cm. The OptAcc model is not capable of the necessary resolution in the upper part of the JRI ice core to reconstruct the variable accumulation history, and hence additional techniques must be applied. The following section introduces the methods used in the re-analysis, annual layer interpretation, and modelling of the JRI ice core record.

### 7.2.1 Continuous Flow Analysis

The DRI Ultra Trace Chemistry Laboratory is capable of continuous measurements at high resolution for the chemistry, dust, black carbon and water isotopes in ice cores. These measurements are made using a combination of CFA Ultra Violet (UV)/Visible, fluorescence and laser spectrometers for simple compounds and water isotopes, together with instruments for black carbon and dust and two high resolution inductively coupled plasma mass spectrometers (ICP-MS) for trace elements (McConnell et al. 2002; Sigl et al. 2015). This system, hereafter referred to as black carbon trace element continuous flow analysis (BC-TE-CFA) system, was used to reanalyse the JRI ice core at a melt rate of  $\sim 50 \text{ mm min}^{-1}$ , and an effective resolution of  $\sim 20 \text{ mm}$  is achieved (McConnell et al., 2002; McConnell, 2010; Pasteris et al., 2014a; 2014b). The BC-TE-CFA system is introduced in the methodology (section 3.3.1) with a full explanation in McConnell et al. (2002); the chemicals measured on the BC-TE-CFA system are listed in table 7.01.

*Table 7.01: List of chemicals measured using the BC-TE-CFA system at DRI.*

<b>Measurement</b>	<b>Used in this study</b>
Stable Water Isotopes	Primary marker of winter/summer seasonality – signal dampens with depth
Hydrogen Peroxide	Primary marker of summer layer – signal dampens with depth
Ammonia	Secondary marker of summer layer
Total sulphur	Non sea salt sulphur (nss-S) calculated from sea salt sodium (ss-Na) – primary marker either as nss-S or as the ratio nss-S/ss-Na

	Also used as volcanic origin reference horizons to tie with WAIS core
Sea salt elements sodium, calcium, magnesium, potassium	Sodium – primary marker; Calcium – secondary marker
Chlorine	From sea salt – signal similar to sodium. Not used
Nitrate	Secondary marker of summer layer
Liquid conductivity	Not used
Particle counts (dust), binned into four size ranges	Medium size bin particles occasionally used as secondary markers
Black carbon	Not used
Trace elements – heavy metals and rare earth elements	Used as markers of volcanic origin reference horizons as tie with WAIS core

### 7.2.2 Age-Depth Profile

The JRI2 ice core age-depth profile is constructed in two parts: (i) annual layer counting in the upper sections; and (ii) the OptAcc model (section 4.4.4) reconstructs the accumulation, thinning, and annual layer thickness profiles from the surface to the bed, but only uses the reconstructed profiles from the base of the layer-counted section to the bed. Unlike the reconstruction of the FP and BI ice core records, the present-day annual layer thickness in the JRI ice core has been counted to 246 water equivalent metres (mweq) (290 m) by multiple observers using the *Matchmaker* tool. *Matchmaker* is a Matlab-based tool, primarily used to synchronise multiple ice core age-depth records based on the chemical signatures preserved in the ice (Rasmussen et al., 2013). Annual layer counting was completed at three institutions (BAS, DRI, and the Australian National University, ANU) and corroborated.

For the remaining age-depth profile, the OptAcc model has been employed. The model uses an initial accumulation profile following the Clausius-Clapeyron relationship, based on the stable water isotope profile measured at DRI (eq. 2.06 – 2.08), and optimises the profile through an inverse approach by estimating a smooth perturbation profile (eq. 3.01; eq. 2.28-2.30). A thinning profile is reconstructed using the One-Dimensional relationship, which does not account for any temporal variation in ice thickness (eq. 2.13-2.17). Combining the

optimised accumulation and thinning profiles allows one to calculate annual layer thickness and age-depth profiles (eq. 2.20 – 2.21); an iterative approach to determining the perturbation profile and the thinning function is used in order to provide the best fit with observed age horizons.

The ice-core age-depth model is constrained using observational data throughout the ice core. For JRI2, unlike the FP and BI reconstructions which used additional observed annual layer thickness data, this reconstruction used only age horizons. The OptAcc model seeks 1000 possible scenarios for accumulation, thinning, annual layer thickness, and age-depth profiles that agree to within the uncertainty of the observed constraints. The range of values for each profile determines the uncertainty in the modelled reconstructions. The JRI1 chronology used age horizons in the upper part of the ice core that can now be improved upon by using a higher-resolution chemical dataset to identify age horizons tied to the WAIS Divide ice core. Revised age horizons are identified by synchronising the JRI CFA profile with the WAIS Divide ice core that is annual layer counted to 38 ka BP (Sigl et al., 2016). The OptAcc model reconstructs the accumulation, thinning, annual layer thickness, and age-depth profiles for the whole of the JRI ice core. At shallow depths (ice younger than 662 years), age uncertainties associated with the layer counting method are less than 2 years, but there is large variability in the annual layer thickness which makes it difficult for the OptAcc model to precisely reproduce the layer-counted age-depth profile. Annual layer counted constraints older than 662 years have an uncertainty of 5 years. Despite the limitations of the OptAcc model, it is used to produce the full ice core reconstructions of accumulation, annual layer thickness, and age-depth, which can be compared with the more accurate annual layer counted profiles. This is a useful test for the reliability of the OptAcc model.

In greater depths of the JRI ice core, four age horizons correctly identified in the JRI1 chronology can be used to constrain the deepest 50 m of the ice core. These constraints are a tephra horizon and three stable water isotope globally-synchronised signatures, with ages tuned to the EPICA Dome C (EDC) ice core. The stable water isotope signatures correspond to the Antarctic Cold Reversal (ACR) event, which interrupted the deglaciation at *circa* 14.5 ka BP following the release of Melt Water Pulse 1A (MWP1A) (Blunier et al., 1997; Mulvaney et al., 2012; Pedro et al., 2016). The given ages of these horizons have been updated since the JRI1 publication, following more recent studies on the geochronological constraints

across the Antarctic continent (Bazin et al., 2012; Roberts et al., 2017). The tephra at 349.53 m below the surface has been geochemically identified in sediment records from James Ross Island and radiocarbon dates associated with this event are constrained to 5,330 – 5,645 yr BP (Roberts et al., 2017). The three stable water isotope age constraints (which were tied to the EDC3 chronology in JRI1) have been updated in line with the latest EDC chronology, AICC2012, and are presented in the next section of this chapter (Bazin et al., 2012).

### 7.3 Results

Prior to the presentation of the JRI2 reconstructions, the re-analysis of the JRI ice core is presented here with seasonal profiles that can be used to annual layer count the ice-core record and identify a new set of constraints that are synchronised with the WAIS Divide ice core. Following this, the JRI2 reconstructions of accumulation, annual layer thickness and age-depth profile are presented.

#### 7.3.1 *Seasonality*

The reanalysis of the JRI ice core by colleagues at the high resolution achievable by CFA permitted annual layer counting using the *Matchmaker* tool to a depth of 246 mweq (290 m), and an age of 899 years. A strong seasonal profile is visible in several trace-element aerosols that are believed to be deposited seasonally (fig. 7.02). The annual layer-counted record was agreed between three separate observers. Fig. 7.02 presents four trace-element aerosols deposited at 120 – 130 m; in the figure, the annual layers are delineated by a grey dashed line during the winter season. The volcanic signal from the Tambora eruption in AD 1817 can be identified in the figure at ~ 126 m.

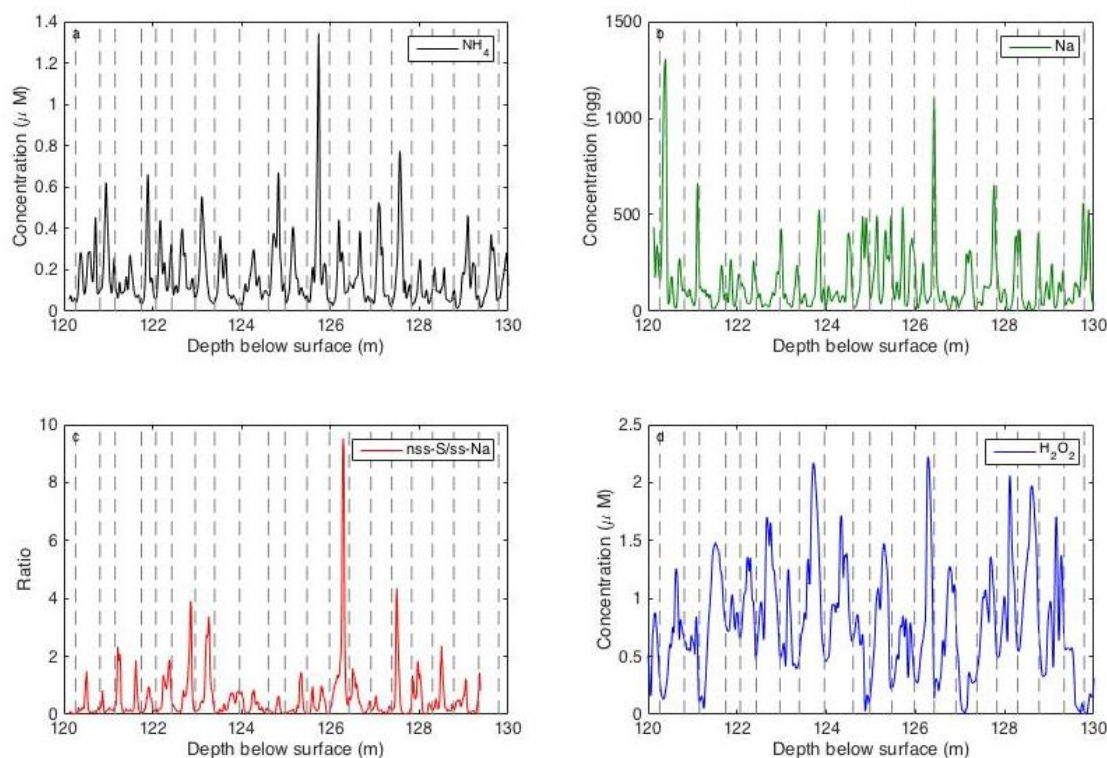


Figure 7.02: Seasonal cycles across a 10 m section of the JRI ice core (120 – 130 m) analysed by colleagues at DRI; a) Ammonium b) Sodium; c) the ratio of non-sea salt Sulphur and sea-salt Sodium; d) Hydrogen Peroxide. Grey dashed lines indicate annual layers identified using the Matchmaker tool.

### 7.3.2 WAIS Divide tie points

The high-resolution analysis of JRI has permitted the identification of chemical signatures that are also identifiable in the WAIS core and so can supplement the deeper constraints used in the new age-depth model (table 7.02). The WAIS Divide tie points are reported as having a small error associated with each constraint for two reasons: (i) due to the type of age horizon that is identifiable in the chemical profile measured on the high-resolution DRI BC-TE-CFA system, such as the annually-mixed and annually-deposited chemicals that directly relate to bomb exposure in the atmosphere of a known historical date, and (ii) because the annual-layer counted WAIS Divide age-depth profile has a small uncertainty for the Holocene period of a maximum 11 years (Sigl et al., 2016).

In addition to the WAIS Divide-derived tie points, four horizons of tephra and globally-synchronous climate events constrain the greatest depths in the JRI ice core. These constraints had previously been used to constrain the JRI1 chronology, and are included in table 7.02. More recent publications have updated the original age estimates (Bazin et al.,

2012; Roberts et al., 2017). For the tephra at 349.53 m (300.62 mweq), the JRI1 chronology suggested that the tephra was originally deposited at ~5000 years before the drilling but with a large uncertainty (Mulvaney et al., 2012), but an updated James Ross Island volcanic history has tightened the uncertainty around this constraint (Roberts et al., 2017). Furthermore, the most up-to-date chronologies for the deep Antarctic ice cores have been synchronised onto a single chronology using the Datice modelling tool (Lemieux-Dudon et al., 2010). This chronology, hereafter referred to as the AICC2012 chronology, updates the timing of continent-wide climate events, which are preserved in the isotopic profile of all ice cores and can be used as age constraints (Bazin et al., 2012). As a result, the oldest two age horizons used in the JRI2 chronology are carried forward from the JRI1 chronology but updated to agree with the most up-to-date ice-core chronologies.

*Table 7.02: Age constraints tied to the annual layer counted WAIS Divide ice core to 299 m below surface (provided by Joe McConnell (pers. comm.), and then to tephra or stable water isotope features below this point (see text for details).*

<b>Depth below the surface (m)</b>	<b>Depth below the surface (mweq)</b>	<b>Observed Age (yr since drill date)</b>	<b>Uncertainty (yrs)</b>	<b>Observed feature</b>
0.00	0.00	0.00	0	Top
18.72	10.14	16.5	2	Pinatubo volcanic signal (Sigl et al., 2013)
50.98	32.94	52.5	2	1955 Bomb test
68.01	46.76	78.5	2	Raikoke volcanic signal (Sigl et al., 2013)
87.81	63.78	113.5	2	Additional volcanic horizon seen in JRI
112.81	86.06	160.0	2	Additional volcanic horizon seen in JRI
126.88	98.76	191.5	2	Tambora volcanic signal (Sigl et al., 2013)
152.15	121.60	248.0	2	Unknown volcanic signal (Sigl et al., 2013)
177.62	144.63	313.0	2	Ruiz volcanic signal
263.70	222.62	662.0	5	Unknown volcanic signal

				(Sigl et al., 2013)
273.40	231.43	737.0	5	Unknown volcanic signal (Sigl et al., 2013)
275.02	232.90	748.0	5	1259 CE volcanic signal
284.10	241.14	836.0	5	Unknown volcanic signal (Sigl et al., 2013)
289.96	246.46	899.0	5	Hekla volcanic signal (Sigl et al., 2013)
295.92	251.88	968.0	11	Unknown volcanic signal (Sigl et al., 2013)
298.96	254.64	1014.0	11	Unknown volcanic signal (Sigl et al., 2013)
349.53	300.62	5478.0	500	Tephra (Roberts et al., 2017)
358.50	308.78	12024.0	550	ACR tuned to AICC2012
358.78	309.04	12771.0	550	ACR tuned to AICC2012
359.00	309.24	14664.0	550	Optimum temperature of ACR, tuned to AICC2012

The JRI2 reconstructions are capped at the depth of the oldest age constraint (359.00 m). The final constraint used in the JRI1 chronology of  $17,480 \pm 500$  yr BP, at a depth of 359.07 m, signifying the start of the deglaciation and tuned to the EDC3 chronology, is not used in the JRI2 chronology because of a potential hiatus in the ice-core record. Fig. 7.03a presents the JRI stable water isotope profile at 357-363 m, with dotted lines indicating the depths of the isotopic constraints that are tuned to other deep ice core records. Between the depths of the bottommost two constraints in the JRI1 chronology, a mean annual layer thickness of 0.02 mm is required, as the age constraints suggest that the 70 mm of ice between the constraints covers  $> 3$  kyr. For comparison to JRI, fig. 7.03b presents the transition from the LGM to the Early Holocene in the EPICA Dome C ice core, with the dotted lines delineating the same age horizons. The age horizons at 14.7 ka BP and 17.5 ka BP do not occur in rapid succession in the EPICA Dome C ice core, as is seen in the JRI record. Further examination of the mean annual layer thickness profile from the JRI2 reconstruction will determine whether some of the JRI ice core record is missing.

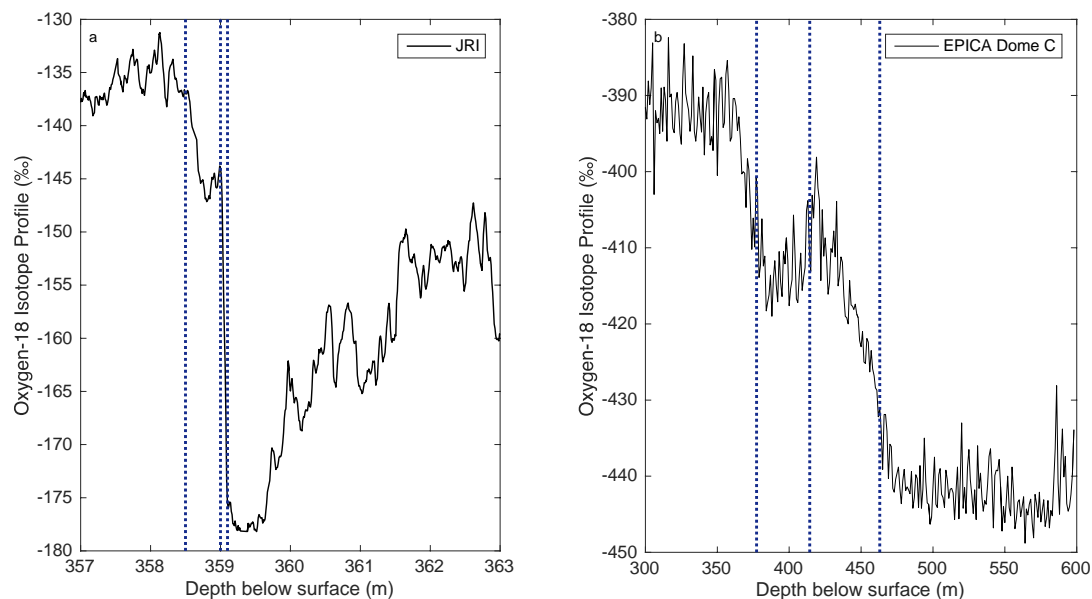


Figure 7.03: (a) The JRI stable water isotope profile at 357 - 363 m (black line) (measured separate to this study); (b) The EPICA Dome C stable water isotope profile at 300 - 600 m (black line) (measured separate to this study). Age constraints at circa 12.8 ka BP, 14.7 ka BP, and 17.5 ka BP are identified by blue dotted lines in each figure.

### 7.3.3 Accumulation and Annual Layer Thickness

Figure 7.04a presents the accumulation history (black) and annual layer thickness (green) profile for the JRI2 chronology. As previously explained, the JRI2 ice core has been annual layer counted to 246 mweq (290 m), marked in fig. 7.04a as the dashed line. The annual layer measurements (green; fig. 7.04a) have been used to reconstruct accumulation above this depth by using the modelled thinning function to invert the compression of annual accumulation into annual layer thickness. Below 246 mweq (290 m) (to the right of the dashed line in fig. 7.04a), the annual layer thickness and accumulation is estimated from the results of the OptAcc model.

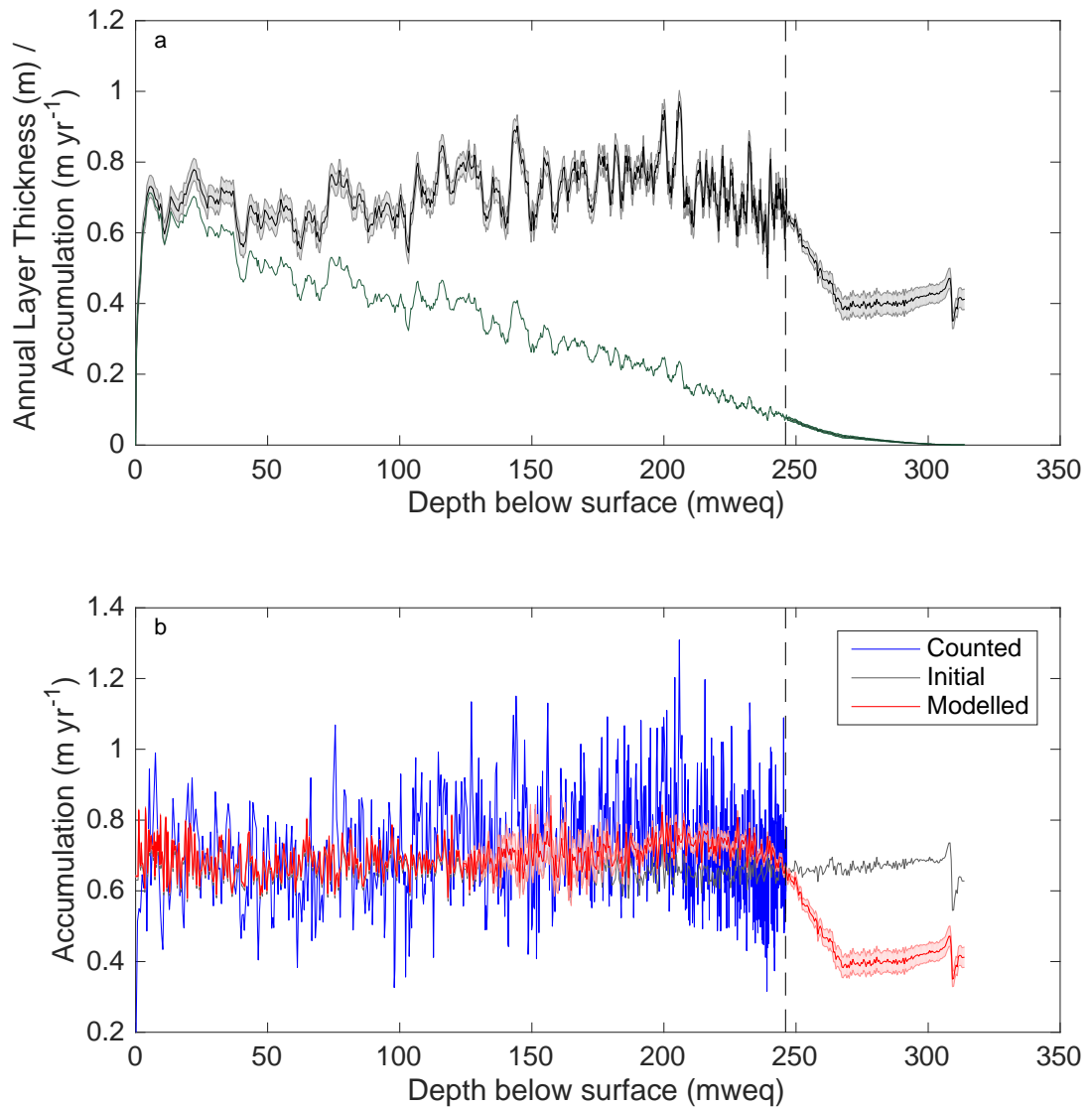
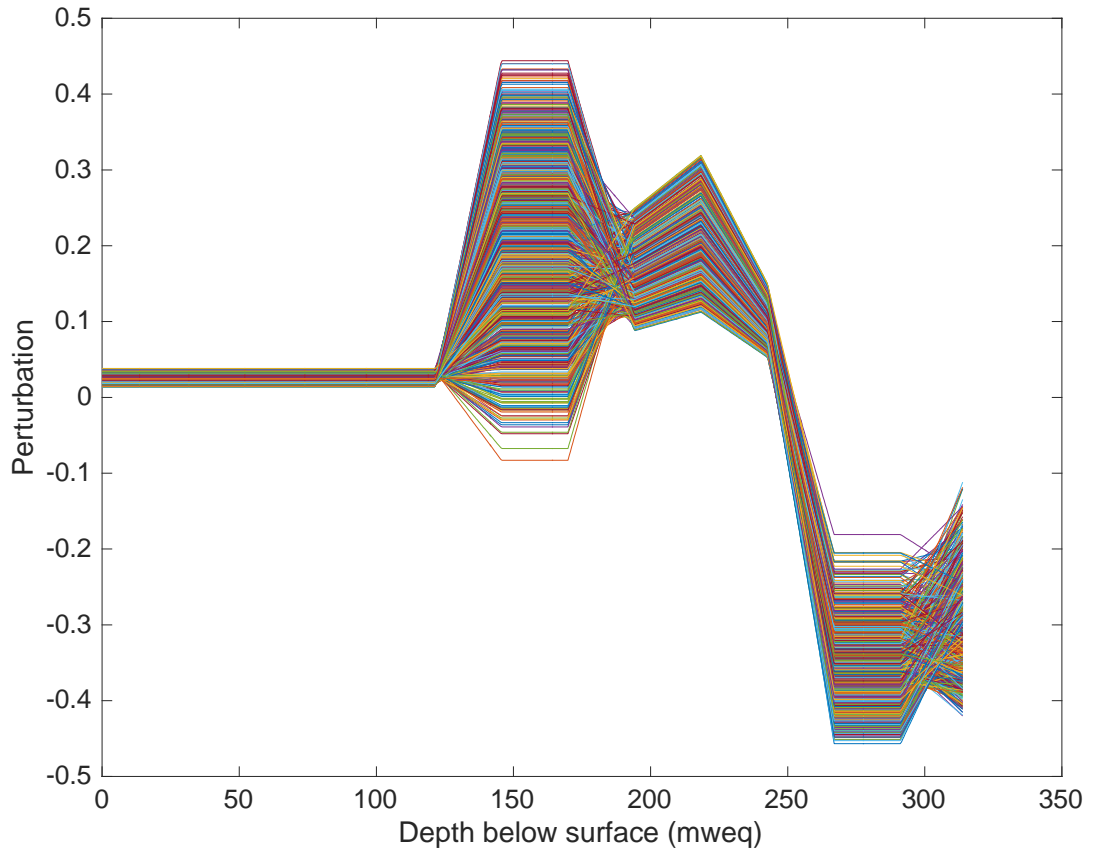


Figure 7.04: The final accumulation and annual layer thickness profiles, and the accumulation reconstructions that contribute to the final accumulation reconstruction. Plot (a) Dark green: present-day annual layer thickness; black: the final accumulation profile. The final accumulation profile is constructed by combining the ten-year mean of the annual layer measurements (left of the grey dashed line), and the OptAcc model reconstruction (right of the grey dashed line). Figure (b) presents the three alternative accumulation profiles. Grey: the initial accumulation profile, reconstructed empirically from the stable water isotope record using the Clausius-Clapeyron relationship; red: the full modelled accumulation reconstruction using the OptAcc model; blue: the annual layer-measured accumulation reconstruction. In each plot, uncertainty on the profiles is presented in the pale shade of the optimised profile. The annual layer measured accumulation reconstruction is estimated by inverting the annual layer thickness measurements (green profile; plot a) using the optimised thinning function.

Fig. 7.04b presents the three different accumulation histories that have been reconstructed for the JRI2 chronology. The Clausius-Clapeyron-derived accumulation profile, used as an initial accumulation input for the OptAcc model, is shown in grey (fig. 7.04b). The OptAcc-modelled accumulation history for the full length of the JRI ice core is shown in red, and the inverted annual layer thickness measurements that are used for the mean annual accumulation profile in the upper 246 mweq (290 m) are shown in blue. The three accumulation profiles demonstrate the significant differences between the OptAcc-modelled accumulation (red) and the initial accumulation profile (grey). In the modelled accumulation profile, there is an increase in the mean annual accumulation rate from  $0.69 \text{ m yr}^{-1}$  by up to 7% between 150 – 200 mweq, before an equivalent decrease over the next 50 mweq. The modelled accumulation decreases by 40% from the empirical accumulation reconstruction, leading to a mean annual accumulation rate lower in the final reconstruction during the transition from the LGM to the Early Holocene (the deepest 50 m) than the empirical accumulation reconstruction.

Presenting the three accumulation profiles provides the opportunity to compare and assess the individual reconstructions. The modelled and measurement-derived accumulation profiles can be compared to assess the validity of using a perturbation profile in the OptAcc model. The perturbation profile used in the OptAcc model suggests a lot of adjustment to the initial accumulation profile is required to replicate the observed natural variability (fig. 7.05). However, the modelled accumulation profile does reconstruct the trends in variability along the ice core. Despite this, it is apparent that the resolution of the OptAcc model is not sufficient to reconstruct the high variability observed in the recent accumulation history at JRI.

Initial observations between the final accumulation profile and the empirical profile are that the final profile shows variability over a longer depth range. These longer variations are not evident in the stable water isotope record. Instead, the annual layer measurements, and (for deeper sections of the JRI ice core) the perturbation profile used in the OptAcc model, present a variability not captured in the stable water isotope record, suggesting that the assumed relationship between isotopes – temperature – accumulation is inaccurate on the JRI ice core.



*Figure 7.05: 1000 perturbation profiles for the JRI2 accumulation reconstruction. All of the possible scenarios of the perturbed accumulation profile that are presented here can be combined with a thinning function to produce an annual layer thickness profile, and hence an age-depth profile that agrees (within uncertainty) with the observational data.*

Fig. 7.06 presents the thinning function for the JRI2 chronology; this thinning function is applied throughout the ice core. At ice core depths shallower than 246 mweq (290 m), the thinning function is used to ‘decompress’ the measured annual layer thicknesses and interpret past rates of annual accumulation. At depths greater than 246 mweq (290 m), the thinning function is applied to the modelled accumulation reconstruction to estimate annual layer thicknesses.

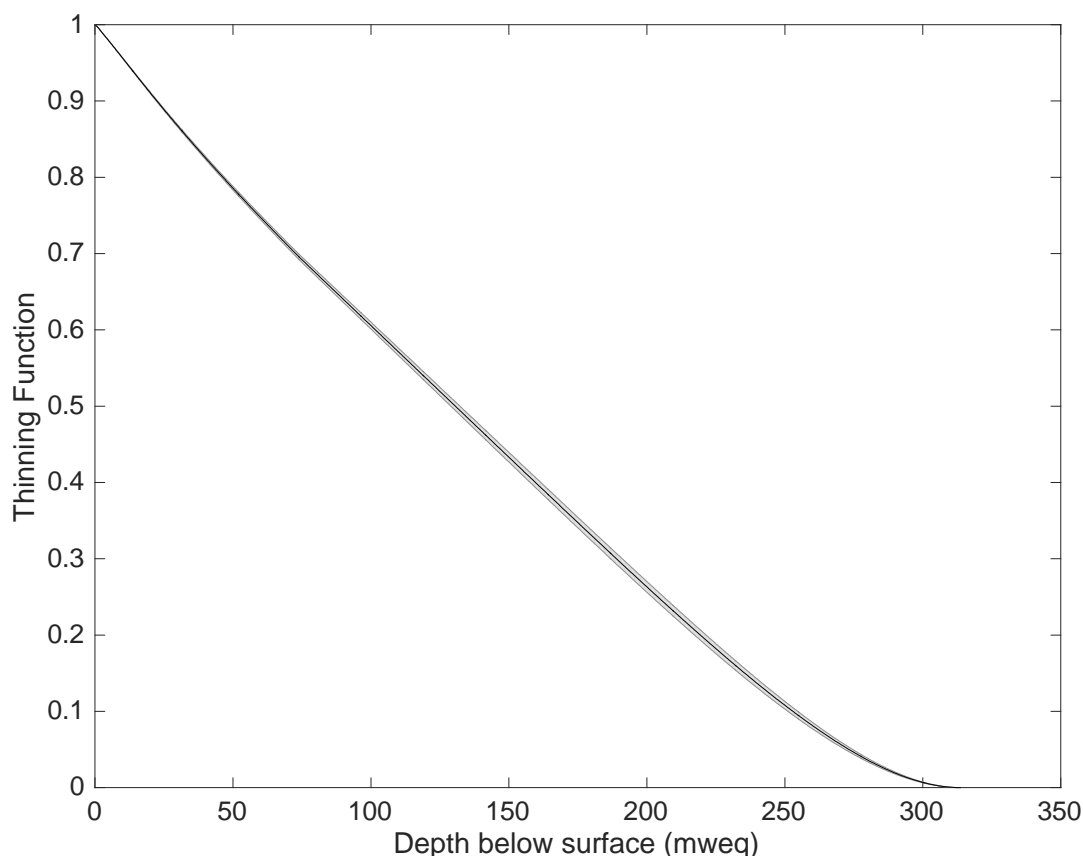


Figure 7.06: Thinning function for the JRI ice core with associated uncertainty in grey.

#### 7.3.4 Age-Depth Profile

The age-depth profile and associated uncertainty is presented with the age horizons and their associated uncertainty in fig. 7.07. The age-depth profile extends beyond the Holocene to reach the end of the Last Glacial Maximum (LGM) at *circa* 18 ka BP, and the stable water isotope profile suggests the record continues to > 40 ka BP (Mulvaney et al., 2012; 2014). However, the JRI2 chronology is only presented until *c.* 14.7 ka BP (~310 mweq) due to the suspected hiatus in the ice-core record beyond this age. As a result, there are no differences to the JRI1 chronology due to the common age constraints used in the deepest 50 mweq of the ice core.

The high mean annual accumulation at the site means that much of the upper 300 mweq of the ice core covers the last two millennia at a high resolution, and this provides much insight into the region's sensitivity to climate events. This means that the rest of the 40 kyr climate record is preserved in the deepest ~10 mweq of the ice core. Despite the long record

preserved in the ice, a high rate of strain towards the bed has compacted much of this record to a resolution beyond any laboratory analysis of seasonal cycles.

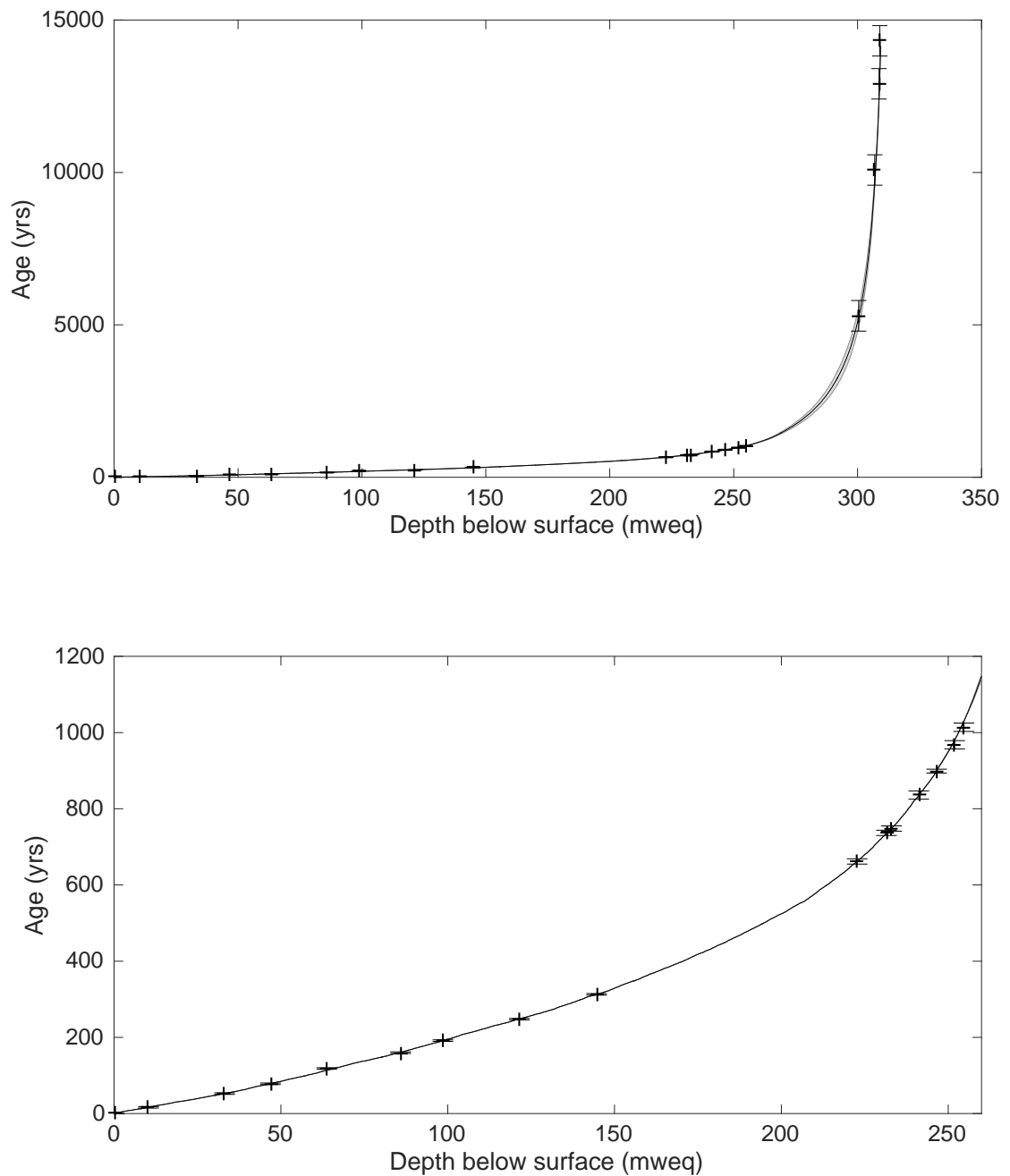


Figure 7.07: (a) Age-depth profile with confidence interval (grey). Black crosses show age horizons (table 7.02) and the associated error of the observational constraints used in the model; (b) A zoom-in of plot (a) to show the most recent 1100 years.

A condition of the OptAcc model is that no possible age-depth profile is accepted unless it agrees with the age horizons to within the confidence interval. Therefore, the distribution of modelled ages for each age horizon all demonstrate good fit for all observational data beyond the depth to which the chronology was layer counted (see fig. 7.08). Fig. 7.08 presents the modelled distribution of ages for the full length of the ice core. The model does not always agree to within the uncertainty of the age horizons above 246 mweq (290 m), but the age-depth profile in the upper depth section is constructed by layer counting. However, the results in fig. 7.08 demonstrate the goodness-of-fit for the modelled age-depth profile despite the small uncertainty on each age horizon and the high variability in the accumulation profile that could not be accurately reconstructed using empirical methods. Table 7.03 presents the modelled age estimates and uncertainty at depths corresponding to the age horizons used throughout the ice-core profile. This provides a useful comparison of the modelled and measured profiles, with a root mean square error (RMSE) value of  $199.3 \pm 143.5$  years across 20 age horizons. The high RMSE value is due to the large uncertainty on the older age constraints used in the greatest depths of the JRI ice core.

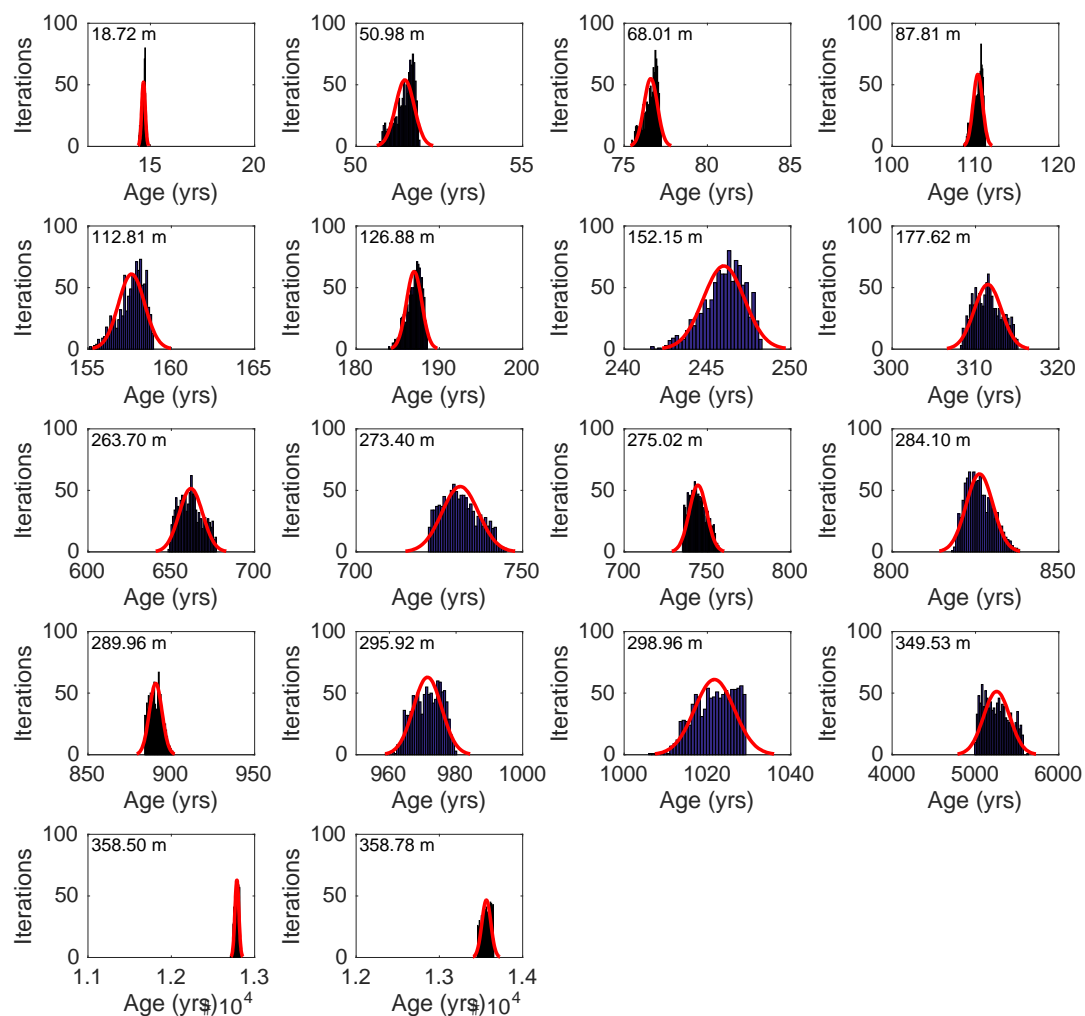


Figure 7.08: Histogram distributions of modelled age estimates at depths corresponding to age horizons with a normal distribution function fitted. A grey box corresponds to the age horizon and uncertainty. The depth in snow-equivalent metres is in the top-left corner.

Table 7.03: Estimated ages at depths corresponding to the depths of age horizons and the respective RMSE value of the modelled age-depth profile for JRI.

Depth below the surface (m)	Depth below the surface (mweq)	Observed Age (yr since drill date) and uncertainty (yr)	Age Estimate for JRI1 (yr since drill date)	Modelled Age Estimate for JRI2 (yr since drill date) and uncertainty (yr)
0.00	0.00	0.00 ± 0.0	0.0	0.00 ± 0.0
18.72	10.14	16.5 ± 2.0	16.8	14.7 ± 0.1
50.98	32.94	52.5 ± 2.0	55.9	51.7 ± 0.3
68.01	46.76	78.5 ± 2.0	81.9	76.8 ± 0.4

87.81	63.78	113.5 ± 2.0	116.3	110.5 ± 0.7
112.81	86.06	160.0 ± 2.0	166.9	157.7 ± 1.2
126.88	98.76	191.5 ± 2.0	198.8	187.0 ± 1.5
152.15	121.60	248.0 ± 2.0	263.4	245.7 ± 2.6
177.62	144.63	313.0 ± 2.0	340.9	314.4 ± 0.7
263.70	222.62	662.0 ± 5.0	806.6	676.5 ± 0.5
273.40	231.43	737.0 ± 5.0	903.1	744.9 ± 2.0
275.02	232.90	748.0 ± 5.0	920.9	757.7 ± 0.8
284.10	241.14	836.0 ± 5.0	1032.9	837.5 ± 0.5
289.96	246.46	899.0 ± 5.0	1118.0	900.1 ± 1.4
295.92	251.88	968.0 ± 11.0	1217.8	979.2 ± 1.0
298.96	254.64	1014.0 ± 11.0	1275.0	1028.8 ± 0.2
349.53	300.62	5478.0 ± 500	5306.6	5323.0 ± 310.3
358.50	308.78	12024.0 ± 550.0	13429.0	12778.0 ± 46.3
358.78	309.04	12771.0 ± 550.0	14134.0	13540.9 ± 111.5
359.00	309.24	14664.0 ± 550.0	14744.0	14141.0 ± 162.7
<b>RMSE (yrs)</b>			4161.7	199.3 ± 143.5

## 7.4 Discussion

Reanalysis of the JRI ice core highlighted the need for an updated chronology. High-resolution analysis, carried out by colleagues at DRI and presented in this study, permitted the development of an annual layer counted record that extends beyond the initial chronology (Mulvaney et al., 2012). In addition, the new high-resolution analysis presented in this thesis identified a new set of age horizons that can be used to constrain a revised chronology; these age constraints are tied to the annual-layer counted WAIS Divide ice core chronology with a maximum uncertainty of  $\pm 11$  years for the Holocene period. Hence, the JRI2 chronology is a tightly-constrained age-depth profile and it has a small confidence interval for the upper 300 mweq due to the number of WAIS-derived constraints.

### 7.4.1 Age-Depth Profile

The JRI2 chronology is constructed in two parts: (i) the record in the shallowest 246 mweq (290 m) is at a resolution sufficient to count annual layers, and (ii) the remainder of the ice

core at a depth greater than 246 mweq (290 m) is reconstructed using the OptAcc model. Therefore, there is much information that can be interpreted due to the accuracy of the reconstruction, the differences between the JRI1 and JRI2 reconstructions, and thus the JRI climate history.

For the JRI2 record at depths shallower than 246 mweq (290 m), the record is annual layer counted to 899 years. The constraints up to this depth have an uncertainty of less than 2 – 5 years, where the chemicals that can be preserved in the ice originate from a globally synchronous event such as volcanic eruptions, which rapidly mixes in the atmosphere. The original JRI1 age-depth profile was also annual layer counted in the upper section of the ice core; comparison of the original annual layer record with the revised record used in the JRI2 chronology (fig. 7.09) shows divergence throughout the upper 260 mweq. In the uppermost 50 mweq, there is a 3.5 year age discrepancy between annual layer counted profiles, increasing to a 7-year difference by 100 mweq. The largest differences in the JRI1 and JRI2 chronologies occur in the greater depths which are still annual layer counted in the JRI2 chronology. Comparison of the JRI1 chronology to the modelled JRI2 age estimates show differences of 139.20 years at 222.62 mweq, increasing to 270.50 years at 254.64 mweq. By this latter depth, the JRI1 age-depth profile estimates an age of 1275 years in comparison to 1004 years in the JRI2 chronology, for which the age constraint at 254 mweq is 1014 years (since the drill date in 2008) (table 7.03).

Below 246 mweq (290 m) the JRI2 chronology is modelled using the OptAcc model (section 4.4.4) which reconstructs the accumulation and thinning profiles to the bed. The number of constraints in the upper 300 mweq of the ice core heavily constrains the age-depth profile so that by this depth, the JRI2 chronology deviates from the JRI1 chronology by 310 years (fig. 7.09). The tight error margins on the age horizons in the upper 300 mweq in the ice core originate from the confidence interval on the WAIS Divide ice core. The WAIS Divide ice core has been annual layer counted to 31.2 ka BP with a confidence interval of up to 5 years for the upper sections of the ice core and 11 years for the remainder of the Holocene (Sigl et al., 2016).

The deviations between the original and revised age-depth profiles for JRI are stark in fig. 7.09, but the divergence does not continue in the deepest 50 mweq of the ice core as the updates to the age horizons only improve the precision of the modelling process. The

modelled age-depth profile (JRI2) agrees with the observations to within the uncertainty of the revised age constraints, and yields a more precise age-depth record in the deepest 50 mweq of the ice core. However, beyond the depth of the oldest age constraint used in the JRI2 chronology (359 m), this study does not seek to update the JRI ice core chronology. The omission of the final constraint used in JRI1, alongside the decision to cap the JRI2 chronology at the constraint indicating the ACR ( $14,664 \pm 500$  yrs since 2008 at 309.24 mweq), yields an age-depth profile that does not disagree with the assertion that the JRI ice core preserves a climate record originating from  $> 40$  ka BP, as implied by the presence of several Antarctic Isotopic Maxima (AIM) events in the stable water isotope record, which are assumed to be synchronous with dated events in the EDC record (Mulvaney et al., 2012; 2014). The updated annual layer thickness record from the JRI2 reconstructions of age-depth and layer thickness is evidence of the hypothesis that there is a hiatus in the preserved ice-core record. The modelled annual layer thickness, supported by annual layer counting in the upper 246 mweq (290 m) of the record, yields a thickness value of  $2.6 \pm 0.3$  mm yr<sup>-1</sup> at the depth of the ACR-derived constraint (309.24 mweq). This is in contrast with the estimated thickness value of 0.02 mm that would be required in order to increase the age-depth profile  $\sim 3$  kyr in the 70 mm of ice-core record between the 14.7 and 17.5 ka BP age horizons (Mulvaney et al., 2012).

The JRI2 chronology is an improvement on the original chronology due to the use of observational data derived from the highly-resolved and precise WAIS Divide age-depth profile. As a result, interpretations based on the initial age-depth profile must be corrected for this new JRI2 chronology.

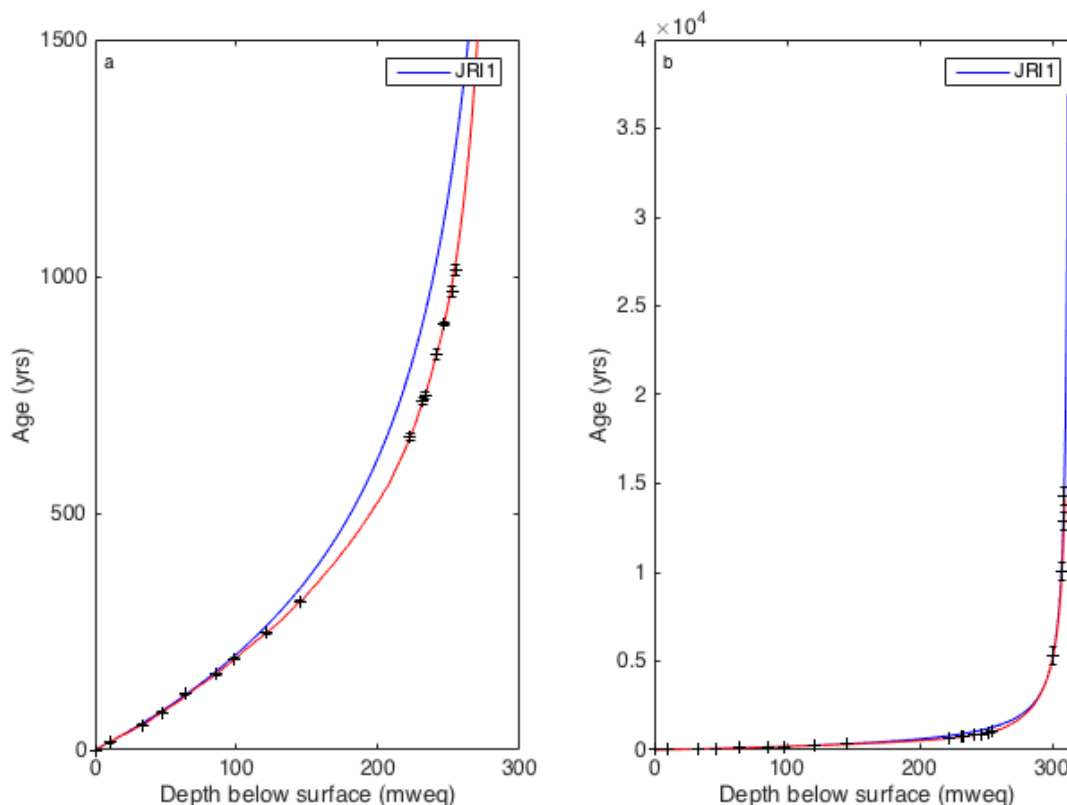


Figure 7.09: (a) Comparison of the JRI1 age-depth profile (blue) with the JRI2 chronology (red) and age horizons (black crosses) for the last 1500 years; (b) Comparison of the initial JRI age-depth profile (blue) with the JRI2 chronology (red) and JRI2 age horizons (black crosses).

#### 7.4.2 Thinning Profile

A thinning function can be used in two ways on the JRI2 profiles: firstly, it can be used to invert the annual layer thickness measurements to produce an accumulation history. Layer thicknesses in the upper section of the JRI ice core record are highly resolved due to the high mean annual accumulation at the site, which permits annual layer counting. Hence, where annual layers can be measured, an accumulation history is interpreted by ‘decompressing’ the measured profile. Secondly, the thinning function can be used to ‘compress’ the modelled accumulation (for example, as derived using the Clausius-Clapeyron relationship) into a present day annual layer thickness in the core, which can then be used to construct an age-depth profile. The thinning function is used to compress the accumulation history in the JRI2 chronology where annual layer thickness is beyond the analytical resolution and hence can no longer be identified and measured in the ice core record. For the JRI ice core, at depths greater than 246 mweq (290 m), the ice is highly thinned and its age rapidly increases

with depth as annual layer thickness is reduced (to sub-centimetre) in comparison with the annual layer thickness above this depth.

In the OptAcc model, the One-Dimensional relationship is used to reconstruct the thinning function. Using the One-Dimensional thinning function, a vertical profile for deformation is controlled by one parameter,  $p$ . The JRI2 thinning function required a  $p$ -value of 5.4. The  $p$ -parameter depends on the exponent in Glen's flow law,  $n$ , which directly influences the rate at which ice sheets respond to external stress (Glen, 1958; Gillet-Chaulet et al., 2011). Assuming linear relationships for the other parameters in the calculation of  $p$ , as explained in chapter 2 (section 2.5.3.3), a value of  $n = 6.1$  is inferred for the flow of ice at the JRI ice core location.

Laboratory experiments on ice to determine strain rates suggest a mean value for Glen's exponent of  $n = 3$  (Glen, 1958); *in situ* measurements of Glen's exponent in the ice sheets suggest that the value could range between 1 and 5 (Wolff and Doake, 1986; Petit et al., 2003; Gillet-Chaulet et al., 2011). A value of  $n$  greater than 3 is suitable for ice sheets with high mean surface temperatures, high rates of annual accumulation and thus higher stress on the ice sheet (Glen, 1958). The high, present-day mean annual accumulation of  $0.63 \text{ m yr}^{-1}$  could explain the high value of Glen's exponent at JRI. In addition, the JRI ice divide is frozen to the bedrock with a temperature at the bed of  $-8^\circ\text{C}$ ; since the low ice sheet thickness results in the ice at the bed being below the 'pressure melting point' (Chapter 8). Values of  $n$  greater than 4 have been reported at ice divides where the ice is frozen to the bed, forming Raymond stacks that affect the vertical strain rate profiles at the greatest depths in the ice sheet (Raymond, 1983; Martin et al., 2006; Gillet-Chaulet et al., 2011).

#### 7.4.3 Accumulation Profile

The JRI2 reconstruction of accumulation is highly resolved for the most recent 2000 years. In this time frame, the accumulation profile (fig. 7.04, black) contains five oscillations that are visible in fig. 7.11a. Four of the oscillations are on a frequency of  $\sim 100$  years, with one large oscillation spanning  $\sim 900 - 1600$  AD. The longest recorded event coincides with two major northern hemispheric climate events, discussed below. Finally, this section will discuss the accumulation reconstruction for the Industrial Era warming between  $\sim 1850$  AD and the present-day, in relation to recent studies on West Antarctic surface mass balance (Thomas et al., 2008; 2015).

#### 7.4.3.1 *Early Holocene Accumulation Record*

Fig. 7.10 presents two reconstructions from the JRI ice core spanning 15 – 0 ka BP: (a) the final accumulation reconstruction that is derived from annual layer measurements (the most recent 900 years) and modelling, with the associated uncertainty presented in grey; (b) the mean annual surface temperature. For each plot, the oldest age constraint at  $14.7 \pm 550$  ka BP is delineated using a dotted line. This age constraint corresponds to the initiation of the ACR, a climate event identified in the stable water isotope profile and tuned to the AICC2012 ice-core chronology (Bazin et al., 2012). The annual layer counted accumulation profile is presented in full resolution, and appears in fig. 7.10a as a noisy, highly variable accumulation profile. The remainder of the ice core accumulation profile is reconstructed using the OptAcc model at a depth resolution of 0.5 m, and is therefore less variable. The surface temperature profile is reconstructed using the empirical relationship outlined in section 2.5.1 (eq. 2.03). This is also reconstructed at a depth resolution of 0.5 m. The profiles agree in the stepped increase in accumulation and surface temperature over 15 – 11.3 ka BP, coinciding with the timing of the oldest age constraint corresponding to the ACR. Following 11.3 ka BP, accumulation and surface temperature remain stable until 1.5 ka BP. This profile of accumulation is similar to the FP ice core, but it does not agree with the Early Holocene accumulation profile reconstructed for the BI ice core (Chapter 6). The accumulation and surface temperature profiles spanning the most recent 1,500 years will be discussed in detail in the following section.

#### 7.4.3.2 *Climate of the Common Era*

The most recent 2000 years, hereafter referred to as the Common Era (CE), is a useful time period to study as an analogue to present-day environment and climate systems. The climate is similar to the present day and proxy records often yield highly-resolved profiles that permit the collation of proxies and interpretation of northern and southern hemispheric climate (PAGES 2k Consortium, 2013; 2017). The annually-resolved JRI profile can be compared with the findings of the PAGES 2k Consortium. Fig. 7.11 presents the 900-year annually-resolved accumulation and uncertainty, and surface temperature records. Two coloured boxes on each plot indicate the supposed timings of the Medieval Warm Period (MWP; red box) and Little Ice Age (LIA; blue box) in the southern hemisphere (PAGES 2k Consortium, 2013).

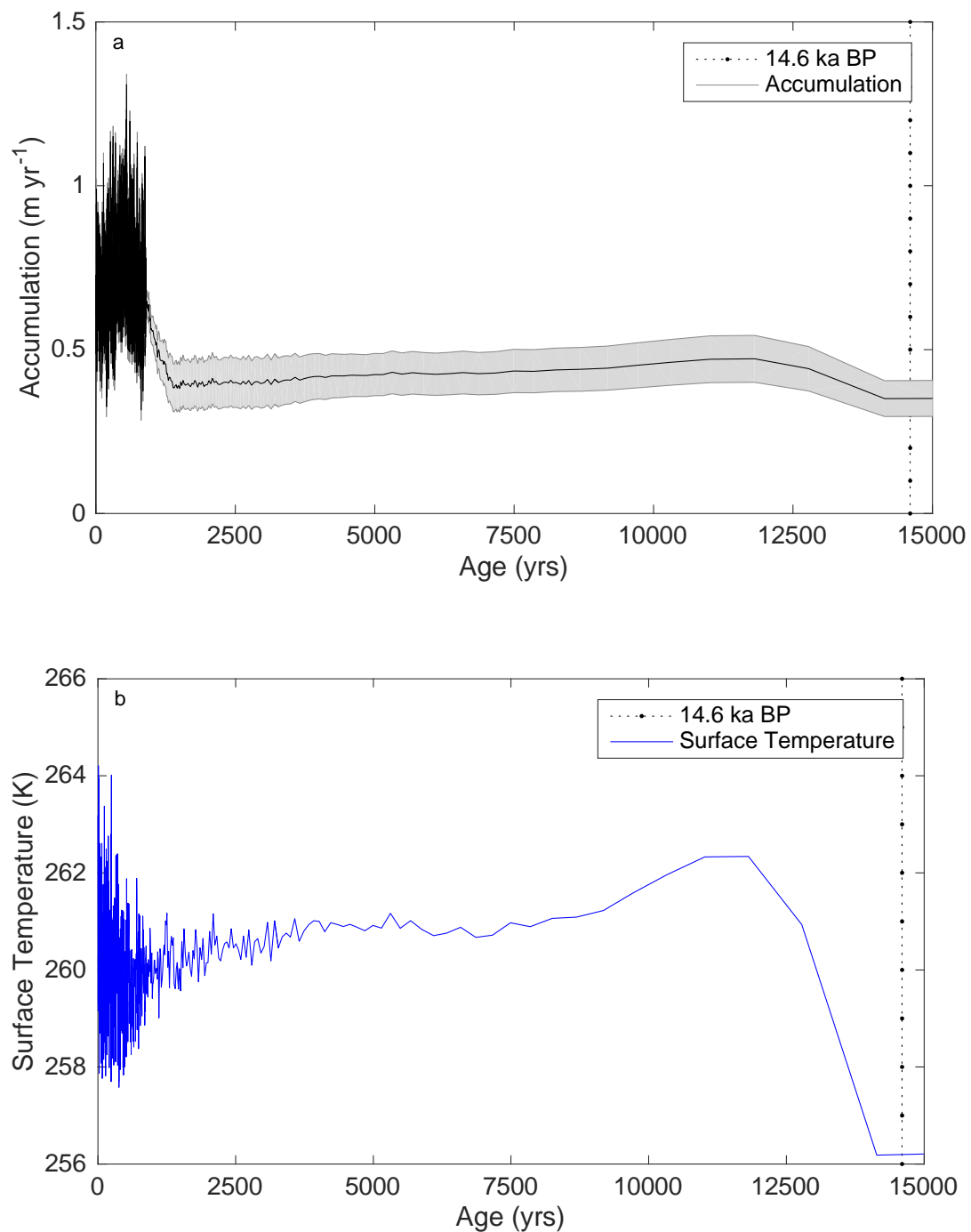


Figure 7.10: (a) Full-resolution accumulation reconstruction from 15-0 ka BP with the uncertainty (grey), and the 14.6 ka BP constraint presented as a dotted line; (b) Mean annual surface temperature spanning 15 - 0 ka BP, with the 14.6 ka BP constraint presented as a dotted line.

The MWP and LIA events are no longer thought to be geographically confined to the Northern Hemisphere (Neukom et al., 2011; Guglielmin et al., 2015). The PAGES 2k Consortium discuss in detail the spatial and temporal homogeneity of centennial-to-millennial warming and cooling periods. Recent research suggests that a warming period is

not identifiable in southern hemispheric ice core and glacial records (PAGES 2k Consortium, 2013; Neukom et al., 2014). The JRI accumulation and surface temperature reconstructions corroborate with the PAGES 2k research conclusions, as the reconstructions yield no evidence of an MWP-like warming period. Despite a positive temperature anomaly throughout AD 1200-1450, there is no evidence of a prolonged period of increasing surface temperature and accumulation (fig. 7.11). Throughout the last 900 years, there are oscillations visible in the annually-resolved accumulation profile smoothed to a decadal resolution. The variability in the accumulation record is not matched by the variability in the surface temperature over the same period; the change in accumulation in comparison to the change in surface temperature is not on the same magnitude. Elsewhere in Antarctica, the EDC record corroborates the JRI ice core record: evidence of an increase in accumulation and wind processes from AD 1300 -1500 at EDC is not supported by the surface temperature record (Castellano et al., 2005).

Following the proposed timing of the MWP, a subsequent cooling period is evident in the palaeoclimate records lasting AD 1580-1880 (Neukom et al., 2011; PAGES 2k Consortium, 2013). The only agreement between the seven continental-scale regions analysed as part of the PAGES 2k Consortium (2013) is that the climate during this period was generally cooling until the late nineteenth century. On a decadal-centennial scale, the general cooling trend is variable, and dominated by solar irradiance and volcanic activity (PAGES 2k Consortium, 2013). Antarctic ice core records are punctuated by decadal-scale variability that is out of phase with Northern Hemispheric ice-core records (Kreutz et al., 1997; Goosse et al., 2004; Rhodes et al., 2012). In the JRI2 accumulation reconstruction, oscillations in accumulation are evident on a multi-decadal to centennial scale throughout the annual layer counted record, particularly over the period AD 1450-1850 (fig. 7.11a and fig. 7.12a). These events follow a pattern of a sharp increase in accumulation over 10-15 years, with a subsequent decrease over a similar period before an even greater increase in accumulation over 20-30 years; accumulation returns to the original baseline accumulation value within 50 years. This pattern is replicated in the sea-salt Sodium (ss-Na) and Calcium (Ca) proxies of the ice core, until the oscillations in accumulation continue into the Industrial Era (AD 1850 onwards) (fig. 7.12).

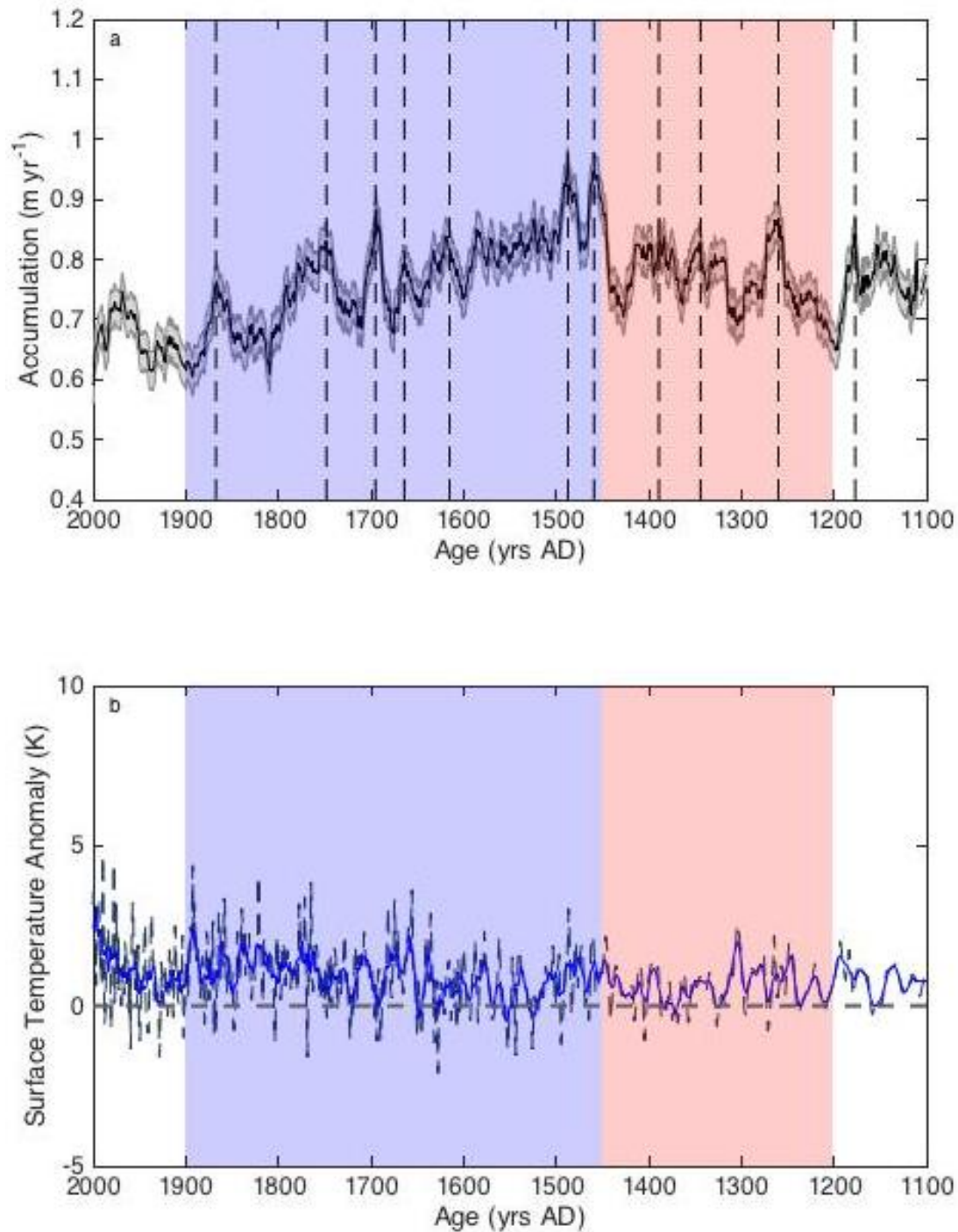


Figure 7.11: (a) Optimised Accumulation reconstruction for the most recent 900 years with the Medieval Warm Period (red) and Little Ice Age (blue) highlighted. Dashed lines indicate oscillations in accumulation identified throughout the annual layer counted JRI2 record; (b) Reconstructed surface temperature anomaly (K) from the stable water isotope record; mean decadal surface temperature (continuous blue line) and mean annual surface temperature (blue dashed); present-day (0 K) is delineated as a grey dashed line for comparison; the LIA and MWP events are highlighted in blue and red, as perceived by the accumulation reconstruction.

The occurrence, timing, and magnitude of the accumulation oscillations are very similar to the patterns seen in the accumulation record of an ice core obtained from Mt. Erebus, Saddle (Rhodes et al., 2012). The Mt. Erebus ice core preserves a surface temperature and ion chemistry record that demonstrates three 12-30 year intervals of cooler temperatures over AD 1690 – 1840 (fig. 7.12d). Fig. 7.12 presents the JRI measurements of two proxies (ss-Na and Ca) and accumulation, along with two proxies measured in the Mt. Erebus ice core (Na and Mg). Dashed lines indicate the decadal-centennial variability identifiable in the Common Era records. There is a noticeable shift in both JRI and Mt. Erebus ice cores from centennial to decadal variability from AD 1700 to the present day, corroborating the climate records at each site with PAGES 2k results.

Variability in the decadal surface temperature agrees with the variability in the accumulation profile over the LIA period, but does not show the general trend of increase and decline as seen in the accumulation record over the time period AD 1100-2000 (fig. 7.11). The surface temperature variability translates to variability in precipitation due to the role that the atmospheric water masses have in controlling the rate of snowfall over the continent, but the magnitude of change in accumulation with respect to surface temperature shows no correlation despite the presumed relationship (fig. 7.11). In modelled reconstructions of precipitation, the variability in surface temperature should affect the rate of accumulation by  $\sim 5\% K^{-1}$  (Frieler et al., 2015), but analysis of our JRI2 accumulation reconstruction suggests this relationship does not hold true. Assessment of the rate of change in accumulation with respect to a change in surface temperature suggests that there is no correlation between the reconstructed surface temperature record and the accumulation record derived from annual layer measurements. Deviation from the modelled rate of change of  $\sim 5\% K^{-1}$  is evident in other coastal sites in West Antarctica. The annual layer counted WAIS Divide ice core demonstrates a  $17\% K^{-1}$  accumulation sensitivity between 0-8 ka BP (Fudge et al., 2016). The WAIS Divide ice core chronology is similar to the JRI2 chronology in that the annual layer counted ice-core record allows accumulation to be reconstructed by ‘decompressing’ the observed annual layer thickness observed in the detailed chemistry record by inverting the role of the thinning function. Although the JRI2 accumulation sensitivity rate does not agree with the WAIS Divide rate, it does highlight that precipitation at coastal sites does not follow the presumed surface temperature – accumulation relationship that proves more accurate and reliable on longer – and lower resolution – ice core records from inland sites. It is the natural variability in the precipitation record over

West Antarctica and the Antarctic Peninsula, coupled with the high-resolution record of the last millennia in the JRI ice core, that makes it difficult for

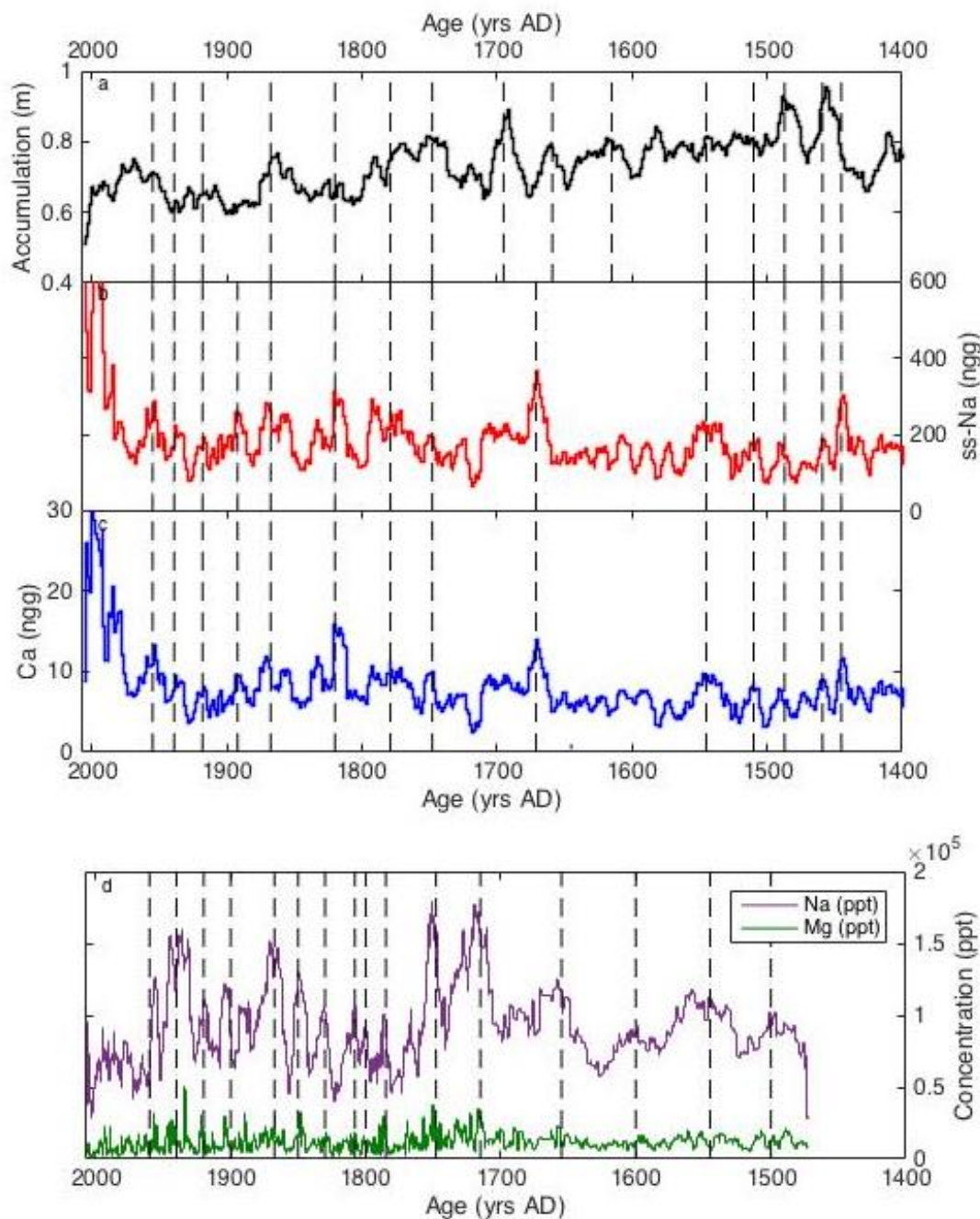


Figure 7.12: LIA signatures in the JRI ice core from 1400 AD – 2000 AD. From top to bottom, a: accumulation ( $\text{m yr}^{-1}$ ); b: sea-salt Sodium ( $\text{ngg}$ ); c: Calcium ( $\text{ngg}$ ). All profiles were measured separate to this research project at DRI. Profiles are presented on a decadal-mean to show trends. Plot d: Mt Erebus ice core data presented as a smoothed decadal mean record in parts per trillion (ppt) (data available courtesy of Rhodes et al. from <https://www.ncdc.noaa.gov/paleo-search/study/13175>). Purple: Sodium; green: Magnesium. Dashed lines indicate decadal to centennial variability in the records.

the age-depth model to accurately reconstruct accumulation, and hence the age-depth profile, for the upper section of the ice core. Furthermore, it is the natural variability and unreliable surface temperature-accumulation relationship at these sites that should be considered in future PAGES 2k research.

#### 7.4.3.3 *Rapid Regional Warming*

The Antarctic Peninsula is one of the most rapidly warming regions on Earth, with increasing atmospheric surface temperatures contributing to significant ice mass loss across the region (Vaughan et al., 2003; Rignot et al., 2008). General circulation model (GCM) predictions suggest that, despite an increase in ice mass loss in line with an increase in surface temperature, the potential contribution of ice mass loss from the AP to global mean sea level (GMSL) could be partly offset by an increase in surface mass balance in line with an increase in surface temperature (Bracegirdle et al., 2008; Frieler et al., 2015; Palerme et al., 2017). Recent studies on the surface mass balance across the WAIS and the AP suggest accumulation has increased since 1850 AD by up to 100%, with an average accumulation increase across WAIS of 30% (Thomas et al., 2008; 2015). Whilst accumulation has doubled since 1850 AD at Gomez, which is located in the south-western AP, no change in accumulation is observed in the WAIS Divide ice core over the same period (Thomas et al., 2008; 2015). For the JRI site, accumulation has increased by 10% between 1900 and 1975, based on cubic interpolation (fig. 7.13), with a peak in accumulation at  $0.91 \text{ m yr}^{-1}$  and a decadal mean deposition of  $0.78 \pm 0.01 \text{ m yr}^{-1}$  (fig. 7.13). Between 1975 and 1994, a rapid decrease in accumulation is observed; this decrease in snowfall is replicated in records from Bryan Coast and Ferrigno (Thomas et al., 2015). During the twentieth century, the decadal mean surface temperature record at JRI increased by 3 K, as reconstructed from the stable water isotope profile (fig. 7.11b). This increase in surface temperature, coupled with a 10% increase in mean accumulation, suggests a present-day accumulation-surface temperature relationship of  $4.4\% \text{ K}^{-1}$ . This value is close to the stable water isotope – accumulation relationship used in both empirical reconstructions of accumulation and GCM estimates (Frieler et al., 2015; Palerme et al., 2017). The high rate of recent warming at James Ross Island has been discussed in previous publications using the earlier JRI chronology, and this still holds true for the most recent annual-layer counted section of the record (Mulvaney et al., 2012; Abram et al., 2011; 2013).

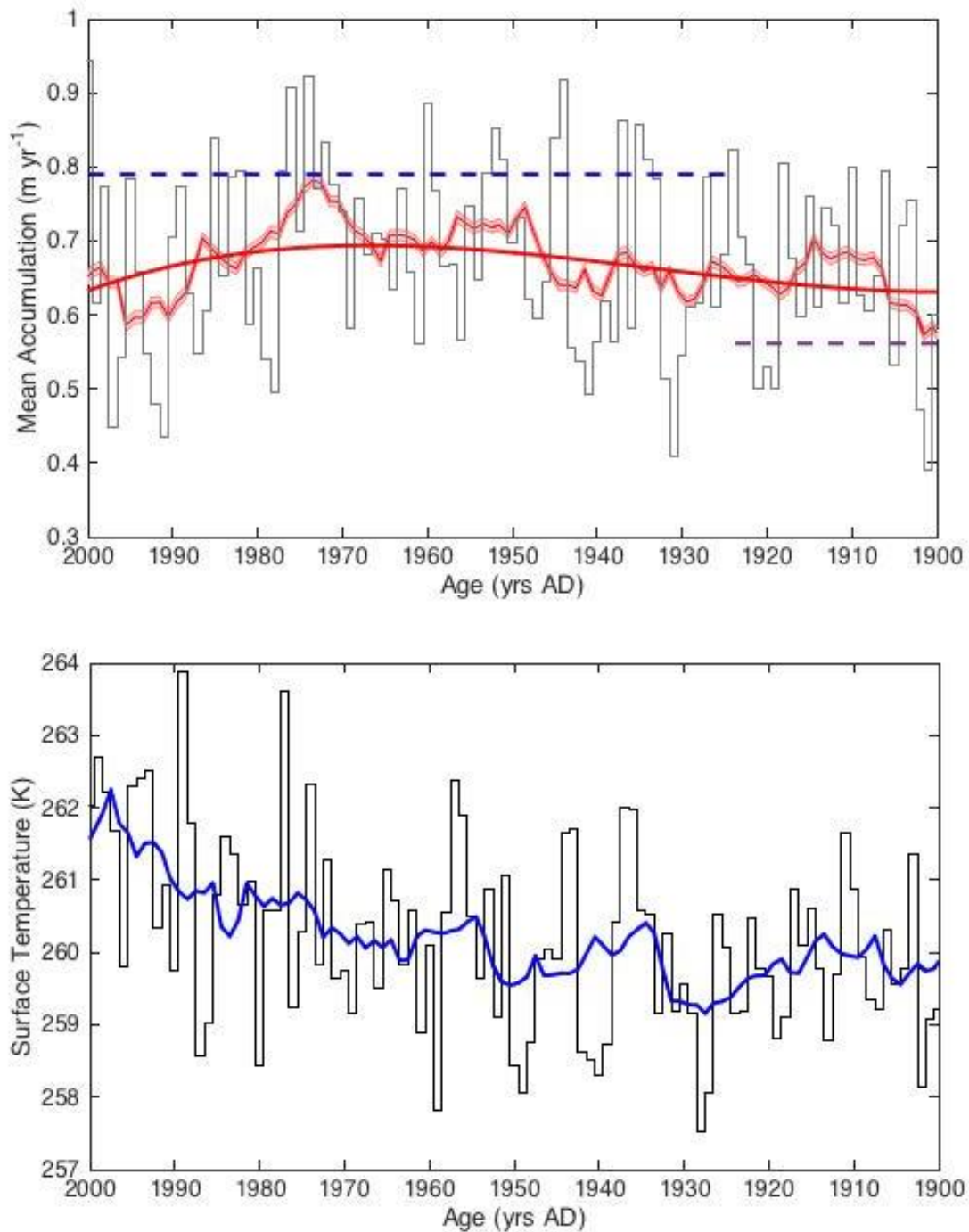


Figure 7.13: (a) Mean Decadal Accumulation for James Ross Island and std dev (red); annual accumulation (black); minimum mean accumulation at 1890 – 1910 AD of  $0.56 \text{ m yr}^{-1}$  (purple dash) and maximum mean accumulation at 1970 – 1990 of  $0.79 \text{ m yr}^{-1}$  (blue dash). Data fitting using cubic interpolation is presented as the bold red line. (b) Mean annual surface temperature (K) (black line) with a smoothed decadal average (blue).

#### 7.4.4 *Stable Water Isotopes and Accumulation*

The JRI measured accumulation record is highly variable through the most recent 2000 years. The high variability in the measured annual accumulation, coupled with the small uncertainty on the age constraints, means that the OptAcc model could not reconstruct the accumulation and hence age-depth profile at a high-enough resolution to agree with the age constraints and corresponding uncertainty. As discussed in Chapter 6 (section 6.4.5) for the FP and BI ice cores, the JRI accumulation variability suggests that the stable water isotope – accumulation relationship is not robust.

Fig. 7.04 shows the natural variability in the JRI ice core record, as the final accumulation record (black line in fig. 7.04a) before 264 mweq is taken from the measured accumulation rate (blue line in fig. 7.04b). The natural variability is particularly significant when compared with the initial accumulation history estimated from the Clausius-Clapeyron relationship with temperature (grey line in fig. 7.04b). The regional position of JRI and the local climate are the likely causes of the high variability that is seen in the empirically-reconstructed accumulation record, but not recorded in the stable water isotope profile.

The JRI ice core was retrieved from an island at the northernmost tip of the AP. The island is particularly exposed to the climate variability described by the Southern Annular Mode (SAM) index, which is defined as the difference in the normalised monthly zonal mean sea level pressure (SLP) between 40°S and 70°S (Nan and Li, 2003). James Ross Island, at 64°S, is subjected to the climate variability across this latitudinal zone. A positive SAM index is an indicator of a higher storm frequency, which may lead to a variable mean annual accumulation record. However, the mean annual SAM index from 1957 to 2012 does not correlate with the annual accumulation at JRI, with an  $r^2$  coefficient of less than 0.3 (fig. 7.14), suggesting that the high variability in accumulation at this site is not dominated by the SAM index and the storm frequency. Fig. 7.14a is a comparison of the mean annual (bar) and smoothed (line) five-year mean SAM index (data from Marshall et al., 2003); a distinct increase in the positivity of the SAM index from 1990 onwards coincides with a steady increase in accumulation, but this change in accumulation is preceded by a significant decrease from the mean annual accumulation throughout 1950-1970, a period where the SAM index was steadily negative. Instead, the accumulation variability at JRI must be controlled by additional forcing to lead to strong inter-annual variability that decouples the surface temperature-accumulation relationship at coastal locations (Fudge et al., 2016; Turner et al., 2016).

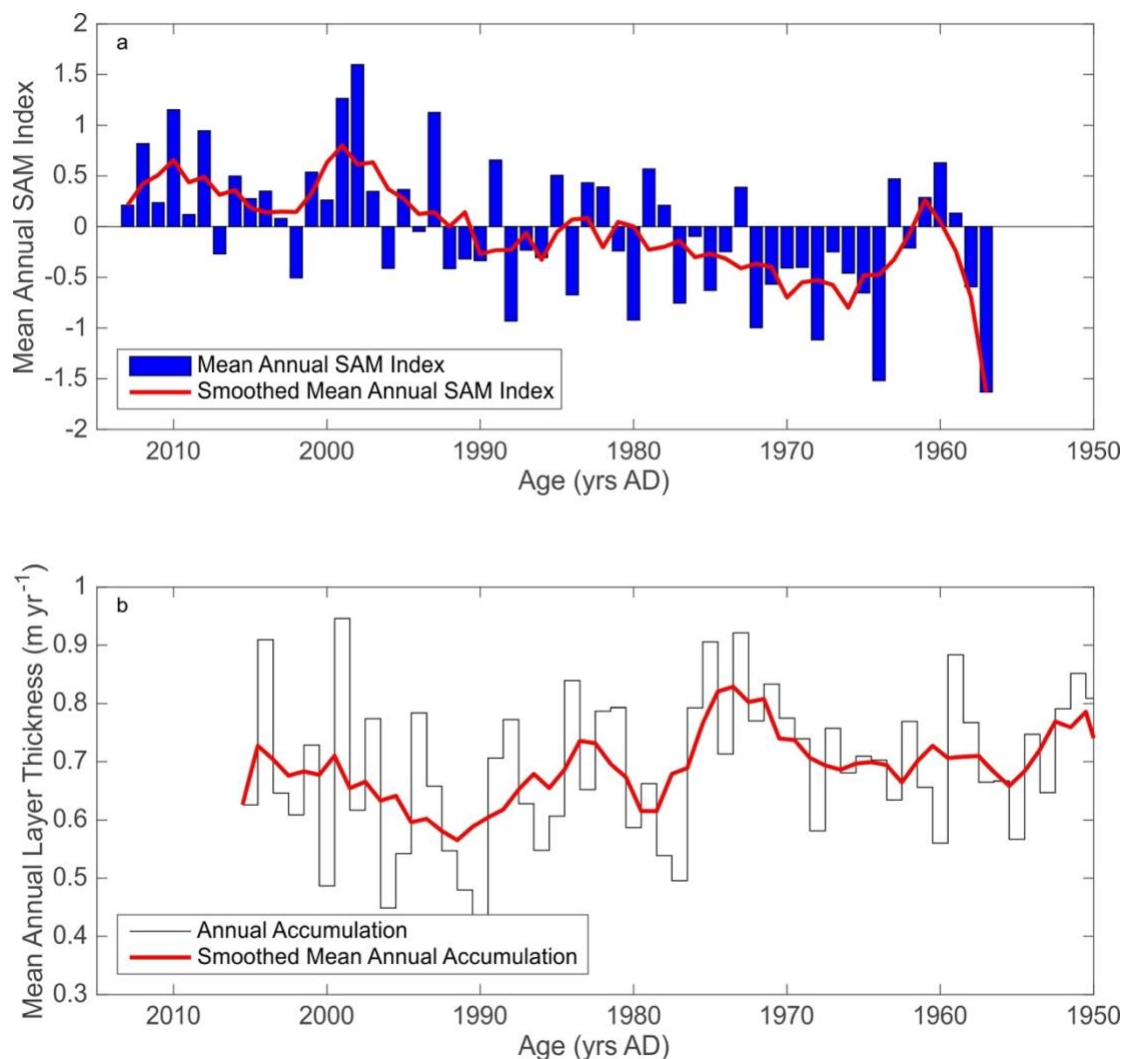


Figure 7.14: (a) the Mean Annual SAM index for the period 1957 – 2012, for comparison with (b) annual accumulation at JRI between 1955 and 2005. Comparison of the annual records in plot (a) and plot (b) give an  $r^2$  coefficient of 0.3, suggesting there is additional forcing on the high variability in annual accumulation at JRI.

Initial assessment of the accumulation profile for the JRI ice core suggested that significant perturbation was required in order to reconstruct an accumulation history that can fit observational constraints. Hence, it was suggested that the empirical relationships used to estimate an accumulation history relied on assumptions that did not account for all necessary factors that impact on the rate of precipitation. The deviation between the initial and optimal accumulation profiles for each ice core, particularly in the changes in accumulation during transitional periods or periods of rapid regional warming, could be

evidence of a decoupling between the surface temperature and accumulation relationship, as is evident in the WAIS Divide ice core (Fudge et al., 2016).

### 7.5. Summary

The JRI2 chronology is presented in order to address the third objective outlined in section 1.2.1. High-resolution sub-annual CFA measurements are used to identify seasonal signals, and improve upon the existing JRI1 chronology. The JRI2 chronology has been constructed using a combination of annual layer counting and inverse modelling; the annual layer counted profile reaches a greater depth in the ice core than was achieved in the JRI1 chronology, and has a maximum error margin of 2 – 5 years. The remainder of the ice core has been reconstructed using the OptAcc model, constrained to fit new observational tie points identified in the annual-layer counted WAIS Divide ice core. An increase in the uncertainty on the modelled portion of the age-depth profile is evidenced, but uncertainties are limited to 11 years in the most recent 1200 years due to the use of well-dated volcanic age horizons observed in the annual-layer counted WAIS Divide ice core and the high level of confidence on their identification. JRI2 deviates from the original chronology by up to 270 years in the most recent two millennia of the record. The highly-resolved ice-core profiles present a new, optimised accumulation history for a site that demonstrates significant natural variability in precipitation over the last 1500 years, recording the MWP and the variability in accumulation and surface temperature punctuating the LIA. Finally, an increase in accumulation of up to 10% during the twentieth century correlates with other ice core records from the Antarctic Peninsula and West Antarctica.

At greater depths in the JRI ice core, the final age at the bed does not change between the chronologies but the age horizons at depths greater than 300 m have been updated according to the AICC2012 EDC chronology. Furthermore, the JRI2 chronology is capped at the depth of the oldest constraint used, *circa* 14.7 ka BP, and evidence is found to suggest that ice is missing from the JRI record between 14.7 – 17.5 ka BP.

The JRI2 chronology is the third ice-core reconstruction presented in this thesis using the OptAcc model, and it yields further information on the climate history of the AP and Weddell Sea region. Following this, further investigation of the region will be completed in order to understand the present-day climate dynamics before addressing the results of this study in a wider context.



# Chapter 8: Determination of geothermal heat flux from borehole temperature measurements in the Weddell Sea sector of Antarctica

## 8.1 Introduction

This chapter will present the geothermal heat flux (GHF), present-day surface temperature ( $T_s$ ), and a steady-state mean annual accumulation rate ( $b$ ) for three boreholes, drilled to retrieve the James Ross Island (JRI), Fletcher Promontory (FP), and Berkner Island (BI) ice cores. In addition to the three ice-core sites,  $b$  and  $T_s$  values are reconstructed for comparison with measured values at two additional borehole sites, Dolleman and Dyer Plateau. The values are calculated using a model that was developed to reconstruct the transport of heat through an ice column using *in situ* measured temperatures in the borehole with a view to estimating the surface temperature history at each site, as outlined in section 2.5.5 and 3.6.3. A surface temperature history reconstructed from the borehole temperature profiles would provide an independent temperature history for comparison to the profiles estimated using the stable water isotope profile, and fulfil the fourth objective set by this study (section 1.2.1). The model did not reconstruct a surface temperature history using this method; however, the borehole model has been used to calculate the GHF information at each borehole site.

Borehole temperature profiles that are measured to the bedrock can provide information on the transport of heat through an ice column. In turn, this can be inverted to yield information on the site location characteristics such as the GHF,  $T_s$ ,  $b$  through the ice column. In this chapter, an inverse model is developed and applied to borehole temperature profiles from JRI, FP, and BI, to calculate the GHF values, present-day  $T_s$ , and  $b$ .

GHF has a great influence on ice-sheet dynamics, particularly via its influence on subglacial conditions (predominantly the basal temperature and hydrology) (Winsborrow et al., 2010). Although the surface conditions of an ice sheet are well understood, studied and documented, the subglacial conditions are less easy to observe and thus less well-constrained in ice-sheet studies.

Understanding such conditions is critical; the mean GHF is estimated to be  $\sim 65 \text{ mW m}^{-2}$  for much of West Antarctica and the Antarctic Peninsula (AP), and between  $\sim 20\text{-}40 \text{ mW m}^{-2}$

across East Antarctica (Shapiro and Ritzwoller, 2004; Fox Maule et al., 2005). Basal melting underneath a glacier can occur for two reasons: (i) GHF beneath the bed provides heat to the underneath of a glacier; and (ii) the temperature at which the ice will start to melt increases as the pressure in the ice sheet increases from the weight of the ice sheet above. This is referred to as the 'pressure melting point'. The large ice sheet thickness of the East Antarctic Ice Sheet (EAIS), coupled with low mean annual accumulation can lead to basal melting where GHF is  $\sim 40 \text{ mW m}^{-2}$  (Pattyn, 2010). Consequently, up to 55% of the grounded Antarctic Ice Sheet (AIS) is currently at pressure melting point (Pattyn, 2010). In addition to this, high heat flux anomalies beneath the WAIS of up to  $\sim 285 \text{ mW m}^{-2}$  provide an explanation for the high abundance of ice streams and subglacial lakes in this region (Wright and Siegert, 2012; Fisher et al., 2015).

A better understanding of the subglacial conditions is necessary to model processes within and underneath the ice sheet that can be used to infer more accurate information on Polar Regions, at a higher resolution than is currently available (Winsborrow et al., 2010). In particular, a better understanding of the subglacial conditions can lead to better-informed decisions on where one should aim to retrieve an ice core (Winsborrow et al., 2010). The oldest climate records preserved within the ice sheet will be found in areas with a large ice sheet thickness, and a low mean annual accumulation. High GHF values promote basal melting which will affect the stability of an ice sheet (Fisher et al., 2015). Basal melting will also destroy the oldest part of the record and restrict the length of the climate history that can be recovered, as has happened at the current oldest ice-core site at Dome Concordia (EPICA, 2004). For the longest ice-core records, optimal sites would have a low mean annual accumulation, an ice sheet thickness greater than 2000 m, and horizontal flow velocity of less than  $2 \text{ m yr}^{-1}$ , with a basal temperature estimated to be below freezing so the oldest ice is not lost to basal melting (Pattyn, 2010; van Liefferinge and Pattyn, 2013). Recent studies propose potential locations of records spanning over a million years of ice (van Liefferinge and Pattyn, 2013). These possible sites avoid subglacial lakes and areas of basal melting underneath the AIS. Without prior knowledge of the subglacial conditions, ice core sites at Vostok, EPICA DML, Dome C and Dome Fuji were later found to be above a subglacial lake, or in an area of basal melting (Salamatin et al., 1994; Augustin et al., 2007, Pattyn, 2010).

Despite the influence of GHF on ice dynamics, there are few measured values across Antarctica. Three continent-wide studies have estimated GHF values (Shapiro and Ritzwoller, 2004; Fox Maule et al., 2005; Purucker, 2016). The first study used a global

seismic model of the crust and upper mantle to extrapolate existing heat-flow measurements (Shapiro and Ritzwoller, 2004); the second set of GHF estimates was derived from satellite magnetic measurements (Fox Maule et al., 2005). A third set of GHF estimates is based on low-resolution satellite magnetic measurements and follows the method used in Fox Maule et al. (2005) and Purucker (2016). Discrepancies between these estimates are evident in spatial patterns across the continent, with the later sets of modelled values suggesting GHF values that are greater than those predicted by Shapiro and Ritzwoller (2004) across the EAIS and the WAIS. The resolution of these datasets varies between 150 and 300 km<sup>2</sup>. This can be a problem for ice-sheet models; higher-resolution directly-measured GHF datasets suggest that GHF varies on a spatial resolution of 50 – 100 km<sup>2</sup> (Dahl-Jensen et al., 2003; Näslund et al., 2005).

Directly measuring GHF at a particular site remains the optimal method for testing modelled GHF values across Antarctica. These directly measured values are sparse across the continent, as they mostly rely on the presence of a borehole drilled to bedrock and temperature measurements from within the borehole. Using borehole temperature measurements, simple GHF estimates can be calculated using a linear thermal gradient and an estimate for the thermal conductivity,  $\alpha_c$  (Fisher et al., 2015). Alternatively, an inverse approach can be used to estimate the optimal GHF value by solving the standard equation for heat transport (Pattyn, 2010; Zagorodnov et al., 2012). Both of these approaches do not account for temporal changes in surface temperature in relation to changes to the transport of heat through an ice column. A novel third technique was developed using airborne radar sounding coupled with a subglacial water routing model over Thwaites Glacier in order to estimate the distribution of basal melting and GHF (Schroeder et al., 2014). These techniques do not yield direct measurements of GHF but can provide alternative estimates to those produced by the continent-wide studies of Shapiro and Ritzwoller (2004) and Fox Maule et al. (2005). GHF values calculated by borehole temperature measurements across the WAIS demonstrate a high variability that has not been detected by low resolution modelling (Schroeder et al., 2014; Fisher et al., 2015). It is also apparent that the globally-modelled GHF values appear to be underestimated when compared with the direct temperature measurements.

The differences in GHF estimates add to the argument that better coverage of Antarctica by robust site-specific observations is necessary. Three deep ice cores originating from the AP and Weddell Sea region have been drilled to bedrock at JRI, FP, and BI. Following

completion of the drilling at each site, temperature measurements were made throughout the borehole to bedrock. This study uses an inverse approach that solves the heat transport equation along the borehole, to calculate the optimal values for GHF,  $T_s$ , and  $b$ , for comparison with the observed present-day surface temperature and the mean annual accumulation rate. Alongside this inverse method, GHF values have been separately calculated from the thermal gradient of the bottom 25% of the borehole temperature profile in order to compare with the GHF values derived using the inverse model. The results provide three GHF values for the AP and Weddell Sea region, adding to the current Antarctic-wide database of modelled and calculated GHF values.

## 8.2 Methods

GHF,  $T_s$ , and  $b$  are estimated in this study by reconstructing the diffusion and advection of heat within an ice sheet. Using an iterative model, the reconstructions are compared with temperature observations from the borehole column; the optimum solution is assumed to be the one where there is minimum deviation between the observed and modelled temperature profiles. Tests on the robustness of this method are carried out by comparing the model results with GHF calculations from a second method that uses the temperature gradient in the lower 25% of the ice sheet.

### 8.2.1 *Site Description and Drilling*

Measurements of the *in situ* temperature profiles of the boreholes for the three ice cores used throughout this study have been used for this research. The site description and drilling process is outlined in Chapter 3 (section 3.2.1).

### 8.2.2 *Temperature Measurements*

The method used to measure the borehole temperature profiles differs slightly at each site, but all followed a scheme of measuring the resistance across calibrated glass bead thermistors with a low current device to reduce self-heating to a negligible amount. Resistances were converted to temperature using the Steinhart-Hart equation, and the three parameters A, B and C used in the equation were derived by calibration in the laboratory for each thermistor (Steinhart and Hart, 1968). The methodology used to measure the temperature profiles for each borehole is outlined in Chapter 3 (section 3.2.2).

### 8.2.3 *The Inverse Model Approach*

The iterative model used to calculate the GHF,  $T_s$ , and  $b$ , uses the relationship explained in section 2.5.5 (eq. 2.22 – 2.27). Following this relationship, the borehole temperature model is designed to calculate GHF,  $T_s$ , and  $b$ , using eq. 3.05 (section 3.6.3). As mentioned in section 8.1, this approach does not account for temporal changes in surface temperature in relation to changes to the transport of heat through an ice column.

The assumed error on the accuracy of thermistor measurements of 0.1 K is principally accrued from errors in the calibration and from the influence of heat carried from a particular depth measurement to the next by the thermal mass of the cable. The error on the depth measurement along the borehole is assumed to be 0.5% of the depth measurement, this error is cumulative with depth throughout the borehole. In order to account for potential error on each of these measurements, 1000 different realisations of the temperature-depth profile are calculated. These are assessed against the measured temperature-depth profiles that have been randomly perturbed to within the uncertainty of both temperature and depth. The temperature-depth reconstruction that yields the smallest root mean square error (RMSE) deviation from the perturbed measured temperature-depth profile is presented as the final temperature profile and provides the values for GHF,  $T_s$ , and  $b$ .

### 8.2.4 *The Temperature Gradient Approach*

A second method, implemented to calculate an alternative GHF value at each deep ice-core site, uses the thermal gradient of the observed temperature profile from the deepest 25% of the borehole and the thermal conductivity of ice:  $GHF = -\alpha_c \cdot \partial T / \partial z$ . In this relationship,  $T$  is the measured temperature profile in the borehole, and  $z$  is depth. This is a simple form of Fourier's Law for heat flow, and it assumes a linear and stable thermal gradient. The depth at which the top of the deepest 25% begins corresponds to a significantly different age at each deep borehole site, but it is a fixed point in each temperature profile where the thermal gradient is relatively stable down to bedrock. The thermal gradient is estimated as the mean change in temperature with depth in the deepest 25% of the borehole, and the error on each GHF estimate is determined as  $GHF = -\alpha_c \cdot \sigma_{\partial T / \partial z}$ , where  $\sigma_{\partial T / \partial z}$  is the standard deviation of the temperature profile.

### 8.3 Results

Values of GHF,  $T_s$  and  $b$  have been calculated using an inverse approach to solve the equation for the transport of heat in an ice sheet. In addition, a second ‘temperature gradient’ method, which accounts for uncertainties in the temperature measurements, is used to determine alternative values of GHF. The following sections present the results of each of these approaches.

#### 8.3.1 Optimal Values from the Inverse Model Approach

The optimal values for GHF,  $T_s$  and  $b$  are presented in table 8.01 for each deep borehole site, and compared to the present day measured values. GHF values that satisfy the constraints provided by the temperature profile are shown for each borehole site in fig. 8.01. Dashed lines in each plot indicate the modelled estimate of GHF using published datasets and the temperature gradient approach used in this study (Shapiro and Ritzwoller, 2004; Fox Maule et al., 2005; Purucker, 2016). In addition, the distribution of  $T_s$  and  $b$  are presented in fig. 8.02 and fig. 8.03. In each figure, the present-day measured mean values of  $T_s$  and  $b$  are indicated (these values are the same as were used in the ice-core age-depth models in chapter 6 and 7).

*Table 8.01: Values for GHF, surface temperature, and mean accumulation using the inverse approach for deep borehole sites at James Ross Island, Fletcher Promontory and Berkner Island, compared to the present day observed values of  $T_s$  and  $b$  taken from Mulvaney (2014).*

	<b>JRI</b>	<b>FP</b>	<b>BI</b>
<b>Mean Observed <math>T_s</math> (°C)</b>	-14.40	-27.10	-24.95
<b>Mean Observed <math>T_s</math> (K)</b>	258.75	246.05	248.20
<b>Observed <math>b</math> (m yr<sup>-1</sup>)</b>	0.63	0.38	0.18
<b>Modelled GHF (mW m<sup>-2</sup>)</b>	62.50 ± 4.40	46.80 ± 1.12	47.00 ± 0.90
<b>Modelled <math>T_s</math> (°C)</b>	-14.80 ± 0.25	-28.00 ± 0.20	-26.15 ± 0.25
<b>Modelled <math>T_s</math> (K)</b>	258.50 ± 0.25	245.15 ± 0.20	247.00 ± 0.25
<b>Modelled <math>b</math> (m yr<sup>-1</sup>)</b>	0.58 ± 0.11	0.18 ± 0.01	0.11 ± 0.01

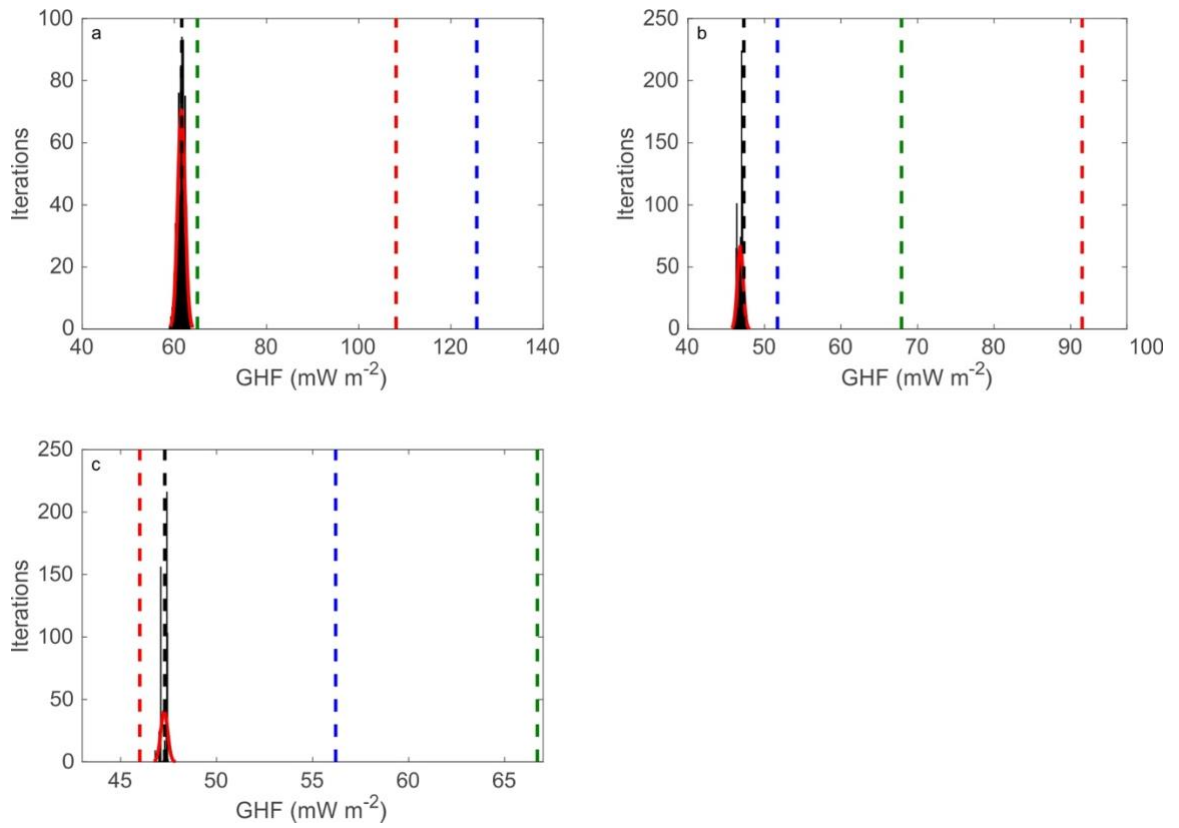


Figure 8.01: Distribution of GHF values with a probability density function fitted (solid red line) for (a) JRI; (b) FP; (c) BI. Dashed lines indicate the modelled GHF estimates: black: the alternative 'temperature gradient' method in this study (section 8.2.4); red: Shapiro and Ritzwoller (2004); green: Fox Maule et al. (2005); blue: Purucker (2016).

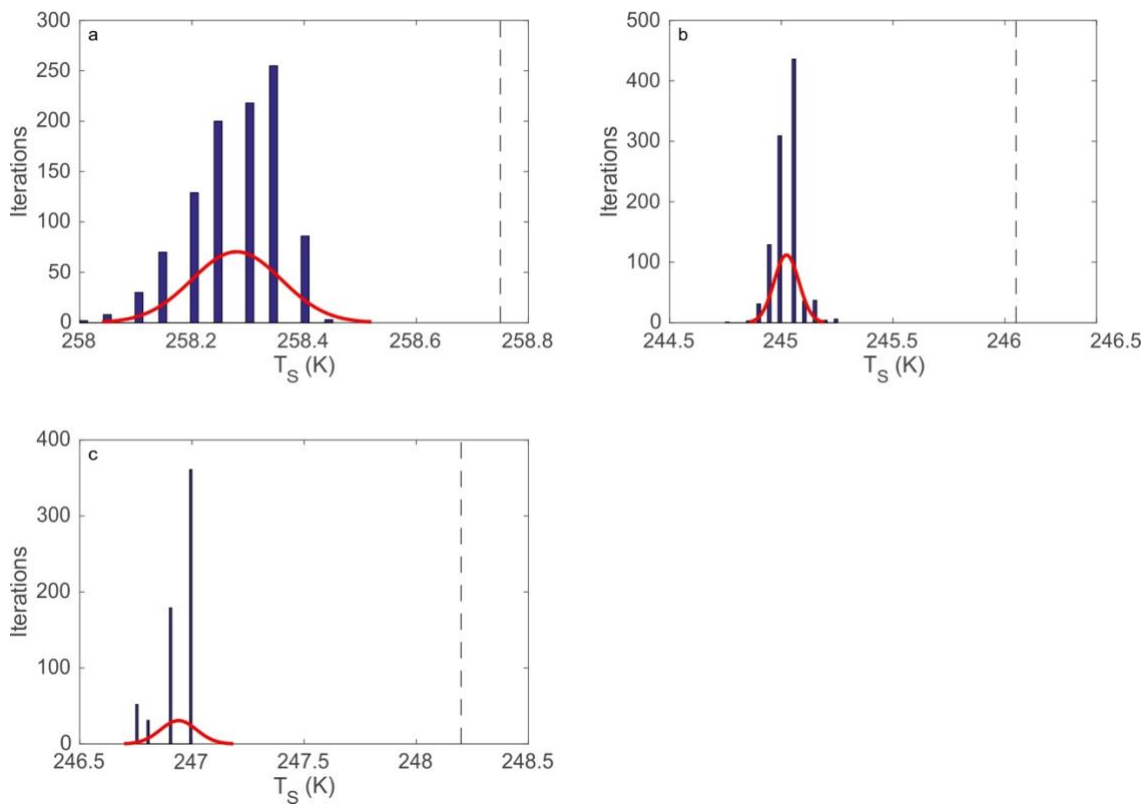


Figure 8.02: Distribution of  $T_S$  values with a probability density function fitted (solid red line) for (a) JRI; (b) FP; (c) BI. Present-day mean  $T_S$  is indicated by a black dashed line.

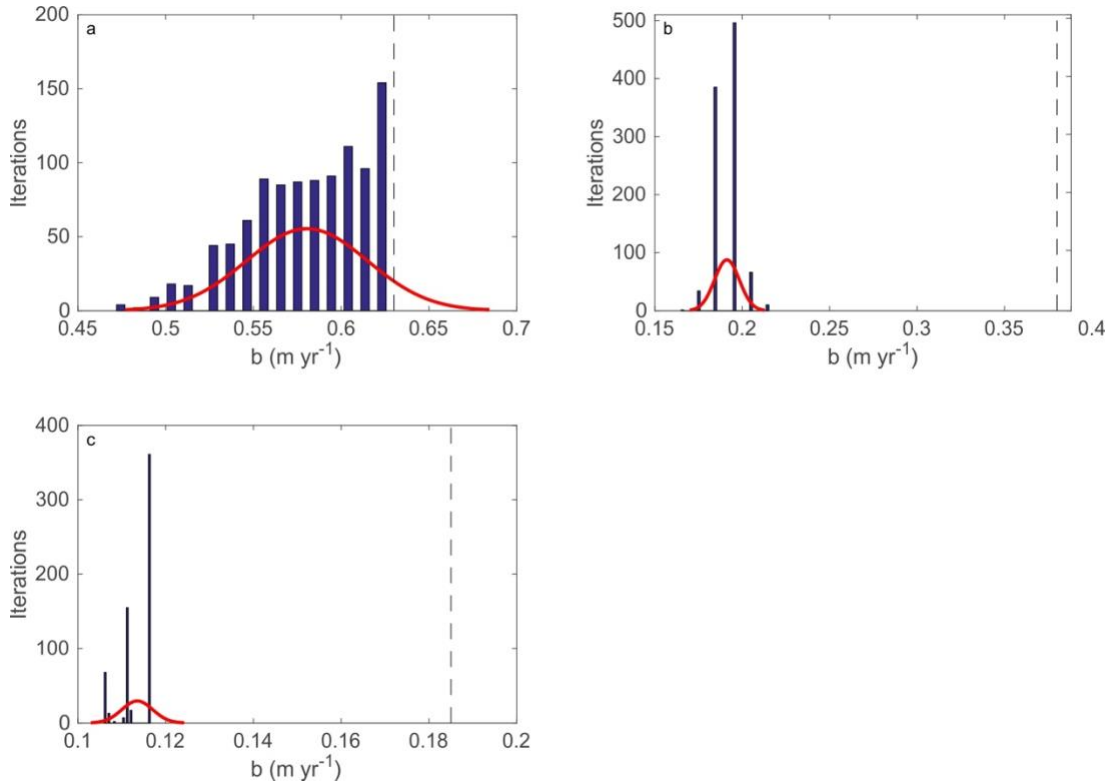
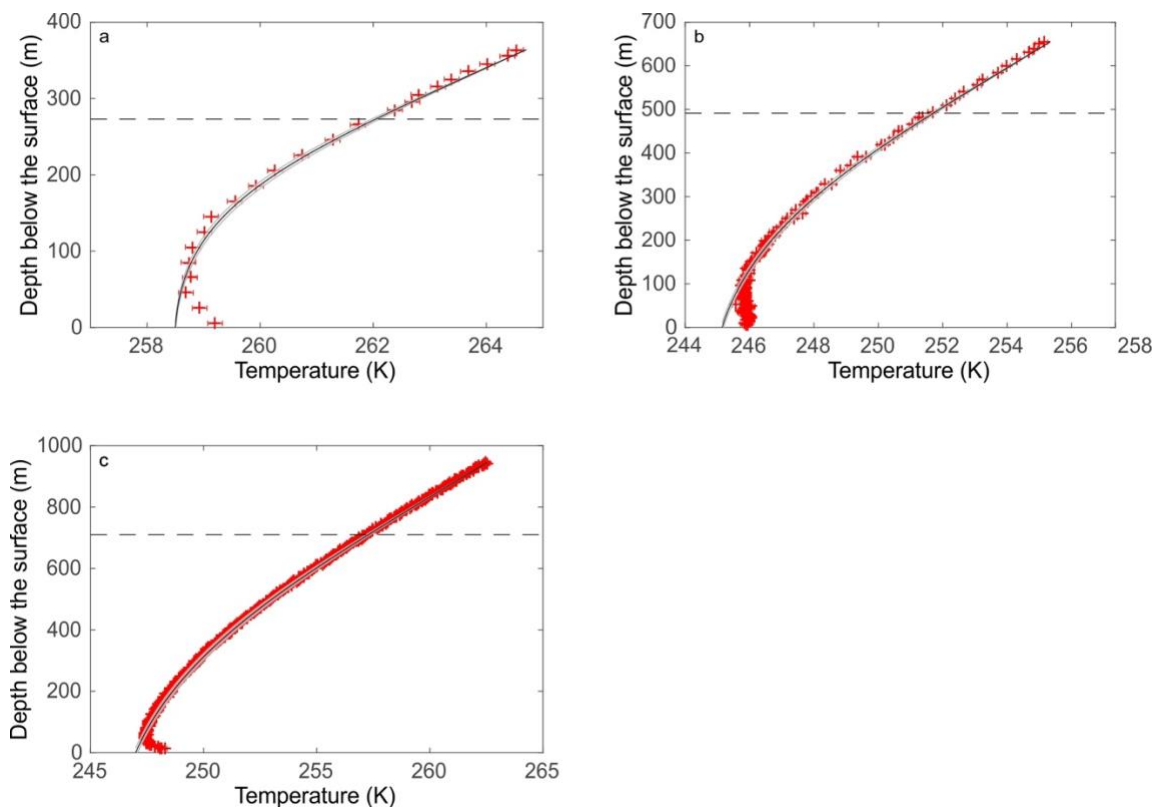


Figure 8.03: Distribution of  $b$  values with a probability density function fitted (solid red line) for (a) JRI; (b) FP; (c) BI. The present-day mean annual accumulation rate is indicated by a black dashed line.

Fig. 8.04 shows the modelled temperature profiles and the borehole temperature measurements for each deep borehole site. These figures demonstrate the good fit between all the modelled profiles and the observational data, with the exception of the upper 15% of the borehole profile (where depth is 0 at the surface). The modelled  $T_S$  values (table 8.01; fig. 8.02; fig. 8.04) for each deep borehole site differ very slightly from the present-day mean  $T_S$  values of 258.75 K, 246.05 K, and 248.20 K (-14.40 °C, -27.10 °C, and -24.95 °C) for the JRI, FP, and BI sites respectively (taken from Mulvaney, 2014). Deviation between modelled surface temperature values and observed temperature values of up to 1.5 K is apparent in the upper 5-16% of each of the three borehole temperature profiles. There is an inflection in the measured temperature profiles towards the surface. The modelled temperature profiles do not reconstruct this, suggesting a period of rapid warming is preserved in the upper 5-15% of the borehole temperature profile that the model is not capable of reconstructing.

Modelled mean accumulation values differ dramatically from present-day mean values of 0.63 m yr<sup>-1</sup>, 0.38 m yr<sup>-1</sup>, and 0.18 m yr<sup>-1</sup> for JRI, FP, and BI. The reconstructed values for FP and BI are 40-50% lower than the present-day values, and the reconstructed accumulation rate for JRI is 8% lower than the present-day rate. This is because the rate of accumulation reconstructed using this model assumes the same rate of accumulation for the entire ice column. The deepest 80-90% of the ice cores from BI, FP, and JRI consists of ice from the last glacial period, during which accumulation was lower (see the accumulation reconstructions in Chapters 6 and 7; fig. 6.13 and fig. 7.04). The reconstructed values presented in this chapter reflect a mean accumulation rate throughout a glacial and interglacial period, and therefore are both lower than the mean annual accumulation rate during the interglacial and greater than the mean rate during the last glacial period. A smaller difference in observed and modelled mean annual accumulation at the JRI site is probably due to the fact that this shorter record contains mostly interglacial (Holocene) ice.



Figures 8.04: Red crosses: Observed temperature measurements with the associated error on depth and temperature measurements (measurements provided by Rob Mulvaney (pers. comm.); black line: modelled temperature profiles with associated uncertainty in grey; (a) James Ross Island; (b) Fletcher Promontory; (c) Berkner Island. A dashed line across each plot represents the depth below which the temperature gradient is used in the alternative GHF calculation (section 8.2.4). All of the ice-core profiles are presented with respect to the depth from the surface (m).

### 8.3.2 The Temperature Gradient Approach

An alternative method described in section 8.3.4 uses the thermal gradient of the deepest 25% of each borehole and results in GHF values of  $61.6 \pm 1.7 \text{ mW m}^{-2}$  for JRI,  $45.3 \pm 1.3 \text{ mW m}^{-2}$  for FP, and  $47.3 \pm 2.8 \text{ mW m}^{-2}$  for BI. The range of GHF values for each borehole site determined using the temperature gradient approach is in close agreement with the values calculated using the inverse approach (table 8.01). This is understandable as the measured temperature gradient in the deepest 25% of each borehole does not deviate from the modelled temperature gradient in the deepest 60 - 70% of the profile that is used in the inverse approach.

## 8.4 Discussion

The current database of GHF values across Antarctica contains few direct measurements from boreholes, despite the significance of the values for glaciology studies and ice-sheet models. This study has presented GHF values for three sites across the Weddell Sea sector, to expand the dataset into the AP and Weddell Sea region. The following section will discuss the GHF,  $T_s$ , and  $b$  values reconstructed using the inverse approach and the alternative temperature gradient approach, and compare the results with the values estimated from other studies.

### 8.4.1 *Comparison of GHF values estimated by the two approaches*

The thermal gradients of  $0.029\text{ °C m}^{-1}$  for JRI, and  $0.019\text{ °C m}^{-1}$  for FP, and  $0.022\text{ °C m}^{-1}$  for BI, when combined with a thermal conductivity constant estimated at  $2.10\text{ W m}^{-1}\text{ K}^{-1}$ , indicate GHF values within the confidence intervals of the optimised GHF value for each borehole site (fig. 8.01). The estimates using Fourier's Law use the thermal gradient from the bottom 25% of the borehole. In the case of BI and FP, this covers the last glacial period only. However, the JRI borehole record spans mostly the current interglacial period and the LGM, extending into the LGM in the deepest 3 m of the ice sheet (Chapter 7; see fig. 7.03). The corroboration of the values derived using the simple form of Fourier's Law with the GHF values estimated by the inverse model suggests stability and robustness in the estimated values. This indicates that the simple Fourier's Law relationship would have been sufficient as a standalone method for estimating GHF at these sites (if the sole objective was to estimate the GHF) as the verification of results implies that the steady-state assumptions in this relationship hold true in the deepest 25% of each borehole site.

### 8.4.2 *Probability range of optimal values*

The potential error accrued from the thermistor measurements can be used to determine a probability range for the optimal values at each borehole site. In every iteration of the borehole model, temperature measurement uncertainty is accounted for by perturbing the temperature profile to within the assumed potential error of 0.1 K for every temperature measurement. Every borehole temperature profile is randomly perturbed and therefore provides alternative targets for the inverse method, which could impact on GHF,  $T_s$ , and  $b$  values. The limited distributions for the values of GHF,  $T_s$ , and  $b$  at each borehole site suggest that the error on thermistor measurements has little significance on GHF estimations (fig. 8.01). Despite this, the accumulation and surface temperature estimates do

not match the present-day mean values for each site (table 8.01). It has already been stated in this chapter that the age of the ice at the bedrock of each site originates from the last glacial period, and hence the accumulation rates suggested for the mean annual accumulation will be lower than the present-day accumulation rates but greater than the mean annual accumulation during the last glacial period (interpreted from the accumulation reconstructions in chapters 6 and 7).

The temperature value measured at a 10 m-depth in the borehole is commonly assumed to be the mean present-day surface temperature. However, the surface temperature estimated through the inverse model is consistently colder. Surface temperature and GHF act as boundary conditions on the temperature profile, and thus past glacial periods should not affect the estimation of these values. Instead, the colder values estimated using the inverse model than the measured surface temperature suggest that the influence of a period of rapid recent warming has not yet diffused beyond the upper section of the borehole. Potential proof of rapid regional warming in the AP could be evident by the inflection in the temperature profile in the uppermost depths of the boreholes, where the temperature profiles have warmed rapidly (fig. 8.04). Further investigation of the inflection in measured profiles is necessary to understand the significance of these results and their potential as a proxy for the rapid regional warming.

As the basal temperatures are 264.65 K, 261.55 K, and 255.15 K (-8.5 °C, -11.6 °C, and -18.0 °C) for the JRI, FP, and BI borehole sites respectively, one can assume that the high mean annual accumulation and low ice sheet thickness at each site cools the ice mass and prevents basal melting despite the relatively high GHF values. As previously mentioned in this chapter, the pressure from the weight of the ice sheet can increase the temperature threshold that leads to basal melting. Therefore, the weight of a large ice-sheet thickness can induce pressure melting with little input from GHF. However, as the basal temperatures are several degrees from melting, it should be suggested that the ice sheet thickness and mean annual accumulation rate across the AP region has a greater effect on the basal temperatures. In conjunction, a thinner ice sheet thickness and high mean annual accumulation rates lead to a lower “insulating effect” on the ice sheet, in comparison to the greater ice sheet thickness and lower accumulation rates across the EAIS. For an ice sheet thickness and mean annual accumulation similar to those found at the BI drill site, it is estimated that a GHF of  $\sim 140 \text{ mW m}^{-2}$  would be required to reach the pressure-melting point at the bedrock (van Liefferinge and Pattyn, 2013). Extrapolating these GHF estimates,

for a site of high mean annual accumulation and low ice sheet thickness similar to JRI, a GHF value upwards of  $\sim 200 \text{ mW m}^{-2}$  would be required to melt ice at the bed. This is in contrast with conditions across East Antarctica where sites with GHF values as low as  $40 \text{ mW m}^{-2}$  experience basal melting due to the extremely low mean annual accumulation and the large ice sheet thickness (Pattyn, 2010). Therefore, it is with confidence that this study suggests that the ice sheet in the region of the three borehole sites studied here does not experience pressure melting at the bed.

#### 8.4.3 Comparison with existing datasets

The GHF values for JRI, FP, and BI, as estimated from existing global and continent-wide models (Shapiro and Ritzwoller, 2004; Fox Maule et al., 2005; Purucker, 2016), are presented in table 8.02. Comparison of the values from this study and the previously published values demonstrates a lack of agreement between several of the modelled estimates and GHF values calculated from borehole thermometry profiles (table 8.02). Modelled estimates from Shapiro and Ritzwoller's model (2004), Purucker (2016), and Fox Maule et al. (2005) are similar to the values for BI, FP, and JRI, respectively. However, the remainder of the estimates by the three published methods overestimate GHF values considerably in comparison to the derived values. Fig. 8.05 shows the range of GHF values across the continent according to the mean value from the three datasets.

*Table 8.02: A list of GHF values estimated by methods outlined in this paper, and earlier studies for the three sites. Values are presented in  $\text{mW m}^{-2}$ .*

	<b>JRI</b>	<b>BI</b>	<b>FP</b>
<b>Inverse Model (this study)</b>	62.50	46.80	47.00
<b>Thermal Gradient approach (this study)</b>	61.6	47.3	45.3
<b>Shapiro and Ritzwoller (2004)</b>	108.1	46.0	91.5
<b>Fox Maule et al. (2005)</b>	65.0	66.7	67.9
<b>Purucker (2016)</b>	125.6	56.2	51.7

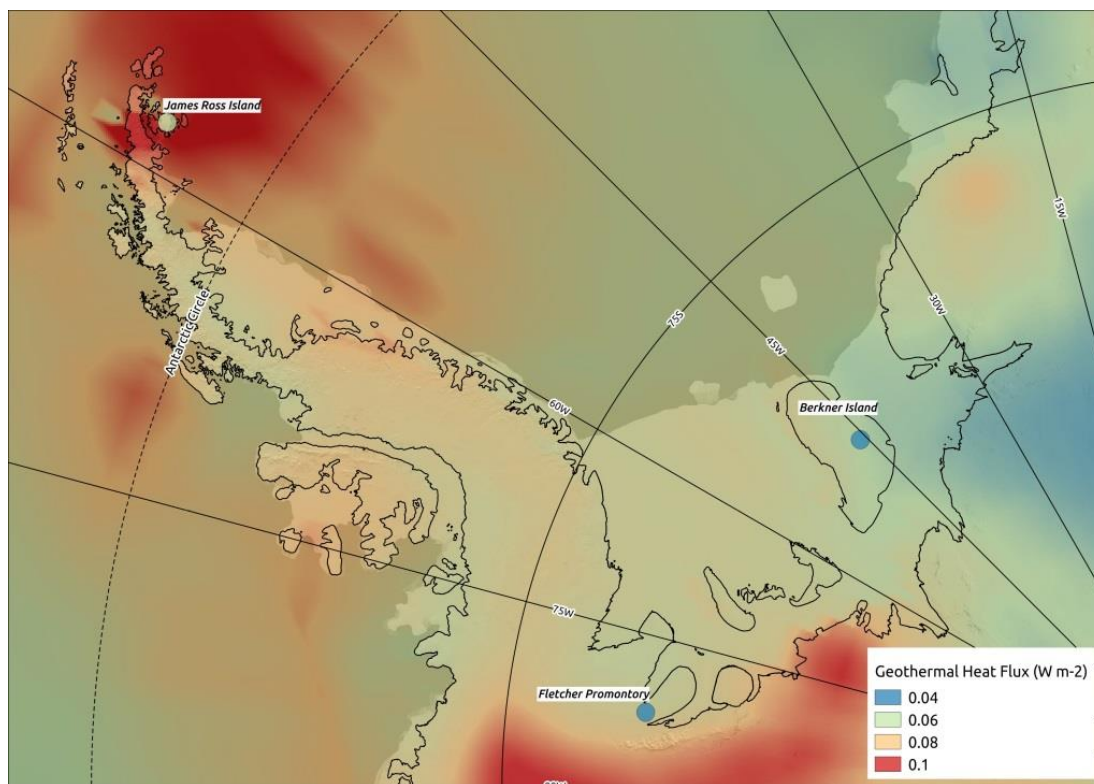


Figure 8.05: Mean GHF values calculated from three sources compared with the measured GHF values at each ice-core site with the locations of the three deep boreholes overlaid, demonstrating the contrast between modelled and derived GHF values. Site locations are denoted using the same colour scheme as used in the map.

The precision of borehole-derived GHF values are specific to location but more reliable than the continent-wide model estimates due to the direct interpretation of the temperature gradient. One reason for the apparent mismatch between the borehole-derived values and the previously-published estimates is the low resolution at which the seismic and magnetic-derived heat flow estimates are calculated. The modelled GHF values from published studies are all estimated on a  $5^\circ \times 5^\circ$  grid resolution, which translates to  $156.25 \text{ km}^2$  grid squares. Although the results are presented at a resolution of  $156.25 \text{ km}^2$ , these values are in fact extrapolated from a much lower resolution of between  $500$  and  $1000 \text{ km}^2$  (Shapiro and Ritzwoller, 2004; Fox Maule et al., 2005). GHF values can vary on a resolution of  $50 - 100 \text{ km}^2$  (Pattyn, 2010). Hence, the GHF values calculated for specific locations, directly from borehole temperature profiles, yield information that cannot be accurately interpreted on a continent-wide model scale.

Another potential reason for the wrongly-estimated GHF values by previously-published models is the influence of the crustal heat production, mantle heat flow and tectonic history of a location. Past volcanism around the Weddell Sea sector – particularly at the volcanic James Ross Island – would be expected to influence the geothermal energy in the region. This is a similar case to Iceland, where active volcanism and geothermal energy leads to an average GHF value of  $175 \text{ mW m}^{-2}$  (Hjartarson, 2015). The GHF estimates for JRI using the Shapiro and Ritzwoller (2004) and Purucker (2016) datasets are  $108.1 - 125.6 \text{ mW m}^{-2}$ , as to the model approaches have inferred information from past volcanism, whilst GHF estimates derived from satellite magnetic data correlate with the borehole-derived value of  $62.50 \pm 4.40$  at JRI (Fox Maule et al., 2005).

Overall, comparison of the GHF estimates from the three models with the borehole-derived GHF values suggests a lack of consistency between all model approaches for the AP and Weddell Sea region. The borehole-derived heat flux measurements should be considered as accurate in calculating the GHF values. However, they are only pertinent for the individual location, as GHF can vary relatively short distances (Pattyn, 2010). Therefore, the borehole-derived GHF values should be considered a useful tool to calibrate existing and future model estimates of the GHF, and this study can be used to enhance the modelled databases (Fisher et al., 2010).

#### 8.4.4 *Surface Temperature Warming and Borehole Modelling*

##### 8.4.4.1 *Extending the Borehole Model to other Sites*

In addition to estimating the GHF at each ice core location, the borehole temperature model showed that there was a substantial deviation between modelled and measured present-day mean annual surface temperature at each of the sites. An inflection in the upper 5 – 20% of the measured curve, tending towards warmer temperatures in comparison to the modelled curve, suggests a recent increase in local surface temperature. This contrasts the steady-state profile of the transport of heat through an ice column, that suggests the borehole temperature profile should cool throughout the column from the surface to the bed, as demonstrated in the modelled profile in the figures (fig. 8.04). The modelled borehole temperature profile would be expected to intersect the surface at the present-day mean annual temperature; that the AP and Weddell Sea region borehole profiles do not do this suggests an inaccuracy in the present-day mean annual surface temperature estimation. Consequently, borehole temperature profiles may be used to interpret information on the

present-day mean surface temperature and estimate regional warming (Barrett et al., 2009; Zagorodnov et al., 2012).

The initial hypothesis on why these near-surface values deviate from the steady state model solution is that the borehole temperature profiles record the rapid regional warming experienced across the AP and Weddell Sea regions over the most recent 150 years (Steig et al., 2009; Vaughan et al., 2003). To investigate this, the borehole model was applied to each of the five borehole temperature profiles to replicate the observed borehole temperature profile to determine the optimum values for surface temperature. The methods used are briefly described below.

The methods used to drill into the ice sheet, and to measure the temperature profile within the ice sheet for the two additional sites were similar to those outlined in section 3.2.2. The same modelling approach as used to produce the GHF,  $b$ , and  $T_s$  reconstructions is used for the five borehole temperature profiles. Additionally, a simple age-depth model using the modelled mean present-day annual accumulation rate,  $b$ , and the Nye thinning function (eq. 2.10; eq. 2.20-2.21) is used to identify the time at which the measured borehole temperature profile begins to curve away from the model profile. The deviation in the measured and modelled borehole temperature profiles occurs in the upper 5 – 20% of each borehole. The Nye thinning function can be assumed correct for the upper depths of the ice sheet, where the strain at an ice divide is assumed to increase linearly with depth (Nye, 1963). As a result, the present-day surface temperature is calculated along with an age at the depth that the modelled and measured borehole temperature profiles deviate, yielding an age from which the borehole temperature profiles are assumed to begin warming significantly.

Two additional borehole temperature profiles from shallow boreholes on the Dyer Plateau and Dolleman Island suggest similar trends in surface temperature warming as observed in the BI, JRI and FP borehole temperature profiles (a map showing the location of these boreholes is found in Chapter 3; fig. 3.01). These additional boreholes were not used in the main study of this chapter as the temperature profiles do not reach the bed and hence cannot be used to calculate the GHF. However, in each of the five boreholes, the measured upper temperature profile can be compared to the modelled temperature profile and used to estimate regional surface warming (fig. 8.06).

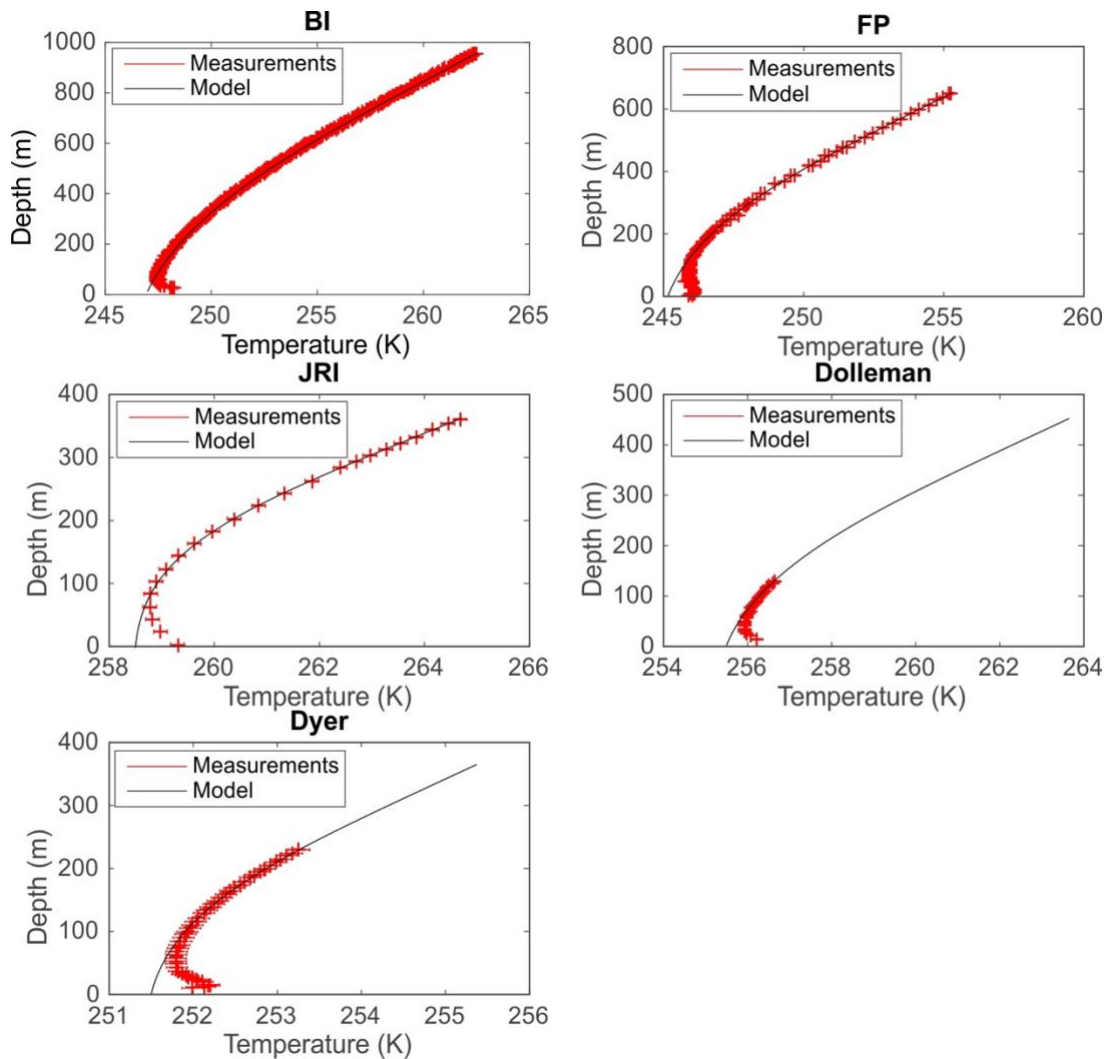


Figure 8.06: Borehole temperature reconstructions (black line) for each borehole site, with measured borehole profiles in red crosses. Measured borehole temperature profiles provided by Rob Mulvaney (pers. comm.).

Table 8.03: Borehole results for each site.  $T_s^D$  is the measured surface temperature (K), and  $T_s^M$  is the modelled surface temperature value (K).

Borehole site	$b^D$ (m yr <sup>-1</sup> )	$b^M$ (m yr <sup>-1</sup> )	$T_s^D$ (K)	$T_s^M$ (K)	Date of start of warming	Warming rate (K century <sup>-1</sup> )	Latitude	Longitude
JRI	0.63	0.58	259.30	258.50	1890 AD	0.70	64°12.1'S	57°41.1'W
Dolleman	0.43	0.27	256.20	255.50	1912 AD	0.76	70°37.0'S	60°45.0'W
Dyer	0.44	0.42	252.20	251.50	1864 AD	0.38	70°60.0'S	65°00'W
FP	0.38	0.18	246.10	245.15	1858 AD	0.59	77°54.1'S	82°36.3'W
BI	0.18	0.11	248.30	246.90	1717 AD	0.44	79°32.9'S	45°40.7'W

By applying a simple age-depth model to these boreholes and estimating the age of the deviation, it is established that the warming in the ice column consistently originates from the Industrial Era (AD 1850 – present day). The mean present-day observed surface temperature,  $T_s^D$ , the mean modelled present-day surface temperature,  $T_s^M$ , and the rate of warming are calculated for each borehole site (table 8.03).

#### 8.4.4.2 *Assessment of the Surface Temperature Records*

It is accepted here that the surface temperature warming study is an over-simplification as it neglects vertical diffusion of the temperature signal. However, it provides a first approximation of the time scale of the warming signal. The calculated rates of warming (table 8.03) suggest a north-south trend, indicating that the northernmost tip of the AP is warming at a faster rate than the inland, southern sites such as the Dyer Plateau. The north-south trend in warming agrees with automatic weather station (AWS) data across the region. Between 1950 and 2000, there has been an increase in the number of positive degree days (PDD; a PDD event is when the maximum daily surface temperature is great enough to cause surface melting) occurring each year across the AP region, with the Faraday/Vernadsky AWS demonstrating a 74% increase in PDD events over the same period (Vaughan, 2006). AWS data from the AP region shows that the occurrence of PDD events also follow the north-south trend, with the northernmost tip of the AP experiencing more PDD events than the inland or southern AP AWS sites between 1999 and 2009 (Barrand et al., 2013). Turner et al. (2005) quantified the AP warming between 1951-2000 to be  $+0.56 \text{ K decade}^{-1}$  at the northern AP AWS at Faraday/Vernadsky, as opposed to a  $+0.2 \text{ K decade}^{-1}$  warming rate at the AWS at Orcadas, southern AP. Despite the agreement in geographical trends, the AWS rates of warming are greater than the borehole-derived rates by an order of magnitude.

The geographic trends of the rate of warming derived from borehole measurements agree with AWS data (Turner et al., 2005; Barrand et al., 2013) but the rates are not consistent, which may be a result of the over-simplification of the estimate on commencement of warming. Furthermore, the rates of warming per century do not agree with the surface temperature profile interpreted from the stable water isotope measurements from the ice cores. The JRI isotope-derived surface temperature record suggests an increase of 3 K over the last century, whilst the borehole-derived rate of warming estimates  $+0.7 \text{ K century}^{-1}$ . This study suggests that these trends in the borehole temperature profiles could be further interpreted as a proxy for rapid regional warming and warrant further investigation. The

results of this study could be more robust by improving the modelling approach. Following improvements to the method, the results of this study would provide an independent assessment of the records for the AP and Weddell Sea region. The following section will discuss potential improvements to the modelling approach.

#### 8.4.4.3 *Potential Improvements to the Method*

As already stated, the borehole-derived surface temperature warming rates agree with the AWS trends. The difference in the rates of warming between the direct AWS observations and borehole measurements could be due to the over-simplification of the modelling approach. The forward model successfully calculates a GHF value, but assumes that the mean present-day accumulation rate and mean present-day surface temperature are steady state. This is because the model does not account for vertical diffusion through the ice column, as the only objective of the forward model is to determine present-day conditions. To improve the estimates of recent warming in surface temperature, it is recommended that the forward model is inverted to reconstruct the past surface temperature history. To do this, one must start with initial conditions on the ice sheet and solve the heat equation (eq. 3.05) backwards in time (MacAyeal et al., 1991). Following other studies, there are three techniques that could be applied to the existing borehole model to improve upon the reconstructions of surface temperature history:

- i) Monte Carlo Markov Chain: the forward heat equation used in the borehole temperature model (eq. 3.05) could be inverted to estimate a temporal surface temperature history using a Monte Carlo Markov Chain (MCMC) algorithm (Dahl-Jensen et al., 1998; 1999; Barrett et al., 2009). Dahl-Jensen et al. (1999) used this method to reconstruct the surface temperature history at Law Dome, Antarctica. The borehole temperature profile was discretized into depth steps of 20 m using a Crank-Nicholson finite-difference scheme, and the forward model was iterated within set boundaries. An MCMC algorithm can be used to randomly explore a model space to construct an infinite number of temperature profiles. However, a drawback of this approach is that the reconstructed surface temperature history must satisfy a strict set of mathematical conditions set in the forward model, which is not always possible (MacAyeal et al., 1991).
- ii) Least Squares Approach: MacAyeal et al. (1991) argued that using a least squares approach to reconstruct the past surface temperature history does not require the optimal surface temperature to conform to the stringent

mathematical conditions required in an MCMC approach. This technique presents the 'best-fit' surface temperature history by approximating a borehole temperature profile that closely resembles but is not equal to the measured borehole temperature profile. A surface temperature history has been reconstructed using a least squares approach in Greenland and Antarctica, for the Dye 3 borehole, and the WAIS Divide borehole, respectively (MacAyeal et al., 1991; Orsi et al., 2012).

- iii) **Stable Water Isotopes:** The third technique inverts the borehole temperature model for a surface temperature history by including constraints to an inverse model. Cuffey and Clow (1997) constrained a temporal surface temperature profile by iterating the heat equation and constraining the reconstructed temperature profiles using the stable water isotope profiles for the GISP2 borehole. The temporal surface temperature profile was achieved by calibrating a profile derived from the stable water isotope profile so that it matched changes in the borehole temperature profile.

In order to pursue the analysis of surface temperature warming rates from borehole temperature profiles, the existing borehole model should be optimised using one of the approaches outlined. In doing this, a robust rate of surface temperature warming could be reconstructed and assessed against direct AWS observations. The benefit of this analysis is that the borehole temperature profiles could yield a temporally-longer and spatially-variable record of surface temperature warming than available from AWS.

## 8.5 Conclusions

The fourth objective of this study is to reconstruct a surface temperature history from borehole temperature profiles to provide an independent temperature history, for comparison to the profiles estimated using the stable water isotope profile (section 1.2.1). The model has not been used to reconstruct a surface temperature history using this method; however, the borehole model has been used to calculate the GHF information at each borehole site.

GHF estimations are an important tool for geological and glaciological reconstructions. Across Antarctica, GHF values are important for accurate ice flow modelling and the identification of prospective deep ice-core drilling sites (Pattyn, 2010; van Liefferinge and

Pattyn, 2013). Measurements of the borehole temperature profiles, at three deep ice core sites at James Ross Island, Fletcher Promontory and Berkner Island, have been used to derive GHF values. The reconstructed present-day mean annual accumulation values reflect conditions throughout the borehole, and therefore are consistently lower than the observed present-day mean annual accumulation values. A second, empirical method of GHF estimation using the thermal gradient agrees with the inversely-calculated GHF values, suggesting a stable thermal gradient for the bottom 25% of the borehole.

Key findings of this study include the observation that the GHF values determined from the borehole temperature profiles, when compared with modelled estimates from previous studies, are significantly lower. This is likely due to the low resolution of the previous models, the extrapolation of the estimated values across the continent, and the influence of past volcanism on the region, interfering with modelled estimates. Secondly, the model is capable of estimating an independent mean present-day surface temperature at each site. The modelled surface temperature for all three sites is consistently lower than present-day values used in ice-core age-depth modelling. The assumption that the temperature gradient is unchanged with time is not true, and this is evident in the upper 5 – 15 % of each borehole temperature profile (fig. 8.04). The results show that there is a discrepancy between the present-day observed mean surface temperature and the modelled surface temperature value. These results could be used as an additional measure to understand the recent surface temperature warming across the AP and Weddell Sea region.



# Chapter 9: Climate Records from the Antarctic Peninsula and their Wider Context

## 9.1 Introduction

Following the presentation and discussion of results in Chapters 4-8 with a view to addressing the five main objectives outlined in Chapter 1 (section 1.2.1), this chapter presents the climate and age-depth records of James Ross Island (JRI), Fletcher Promontory (FP), and Berkner Island (BI) in the wider context of the climate of the Antarctic Peninsula (AP) and Weddell Sea region.

The three ice cores are all situated in locations of dynamic and profound environmental change in response to the current climate warming (Vaughan et al., 2003; Steig et al., 2009). Ice cores from these three locations provide the long-term climate context that underpins research on the rate of ice mass loss from the AP and Weddell Sea, as well as the West Antarctic Ice Sheet (WAIS), as the region continues to experience rapid regional warming. The three ice cores from the AP and Weddell Sea region can directly contribute to the understanding of four topics: firstly, the ice mass loss in these regions is not unique to the present day; marine records from the AP suggest that the ice shelves have not been stable throughout the Holocene but instead have undergone periodic growth and retreat over the last 11 ka BP (Domack et al., 2005; Pudsey et al., 2006). Secondly, going further back into the climate record, multi-disciplinary studies reconstructing sea-surface temperatures (SST) and global mean sea level (GMSL) during the last interglacial (LIG), at 129 ka BP – 116 ka BP, suggest that the Antarctic Ice Sheet (AIS) (principally the WAIS) may have contributed up to 6 m of a 6 – 9 m increase to GMSL (Dutton et al., 2015; Hoffman et al., 2017), during a period that was 3 – 6 K warmer than the present interglacial (Sime et al, 2009b). Thirdly, these ice cores from the AP and Weddell Sea region can inform us of the climate during periods when the region experienced growth and retreat of ice shelves, and may hold clues as to the extent of the WAIS during the last interglacial. Finally, analysis of the results presented in Chapters 4-8 will contribute to our understanding of the surface temperature – accumulation sensitivity that is used in modelling ice-core records. However, to understand the record preserved in these ice cores, it is necessary to construct an accurate and highly-resolved age-depth profile. This chapter will seek to place the results of this study in the wider context, in particular it will discuss the JRI, FP, and BI ice core reconstructions and how they contribute to our understanding of the three main research questions in the AP and Weddell Sea region.

## 9.2 Integration of Results from Chapters 4-8

Throughout Chapters 4-8, this study has addressed the first four objectives outlined in section 1.2.1. Following these individual lines of study, a compilation of the results can be used to assess the implications of the climate history on the AP and Weddell Sea region from the last interglacial to the present day.

The optimal age-depth profiles of the FP, BI, and JRI ice cores are presented in Chapters 6 and 7. Here, these three ice cores will be compared with other records from the region or with each other. Fig. 9.01 presents the temperature and accumulation history for each site on a common timescale (semi-logarithmic). Comparison of the accumulation and temperature reconstructions with respect to time yields a number of key observations about the three ice cores in Chapters 4-8:

1. JRI and FP surface temperature profiles record an increase from 1850 – present day (Industrial Era);
2. A highly-resolved accumulation record in JRI shows significant variability in the accumulation record throughout the Holocene;
3. FP extends into the LIG period and may yield information on the potential collapse or retreat of the WAIS during the LIG;
4. JRI and FP accumulation reconstructions are markedly dissimilar with the BI deglacial increase in accumulation, which takes place later than at JRI and FP with the main increase in accumulation at BI taking place during the period 9 – 2 ka BP;
5. BI and FP accumulation and surface temperature reconstructions do not correlate beyond ~60 ka BP.

In Chapter 6 (section 6.4.5.1), the accuracy of the BI accumulation reconstruction was questioned due to discrepancies between the BI record and other ice cores. This is evident in fig. 9.01, when comparing BI surface temperature and accumulation reconstructions with the JRI and FP reconstructions. One particular discrepancy between the BI, JRI, and FP accumulation profiles is the delayed onset to the Early Holocene period in the BI record. The glacial-interglacial transition in the BI accumulation record does not coincide with the timing of the transition in the FP and JRI accumulation records (fig. 9.01). This transition is expected to be synchronous across the whole ice sheet, and therefore the transition into the Holocene should line up in all of the ice cores. The JRI, FP, and BI ice core age horizons all use the

Antarctic Cold Reversal (ACR) at 14.6 ka BP as a constraint. Despite this common age constraint, the transition from the ACR to the warmer conditions in the Early Holocene is not synchronous. In Chapter 6, it was suggested that the discrepancies in the BI accumulation record are caused by a combination of the characteristics of the deglaciation of drill location from the Last Glacial Maximum (LGM) and deficiencies in the modelling approach. BI is embedded in the Filchner and Ronne ice shelves; the Weddell Sea embayment, containing the Filchner and Ronne ice shelves. The BI record could have been disturbed by changes in the ice flow around Berkner Island, as is hypothesized to have occurred at the Bungenstock Ice Rise south of BI (Bradley et al., 2015).

As the AIS deglaciation occurred following the LGM (~21 ka BP), the AIS grounding line retreated across the Weddell Sea and the AP and the region changed from a high-altitude, continental site to a low-altitude, coastal location. This change from continental to coastal location would lead to an increase in mean annual surface temperature and accumulation. The location of BI was one of the most recent sites to deglaciate and become a coastal site, which explain a slower increase in surface temperature and accumulation from the ACR to the Early Holocene in comparison to FP and JRI. Additional parameters to account for changes in the horizontal ice flow, the migration of the ice divide, and changes in the ice-sheet thickness should be incorporated in any future revision to the OptAcc model.

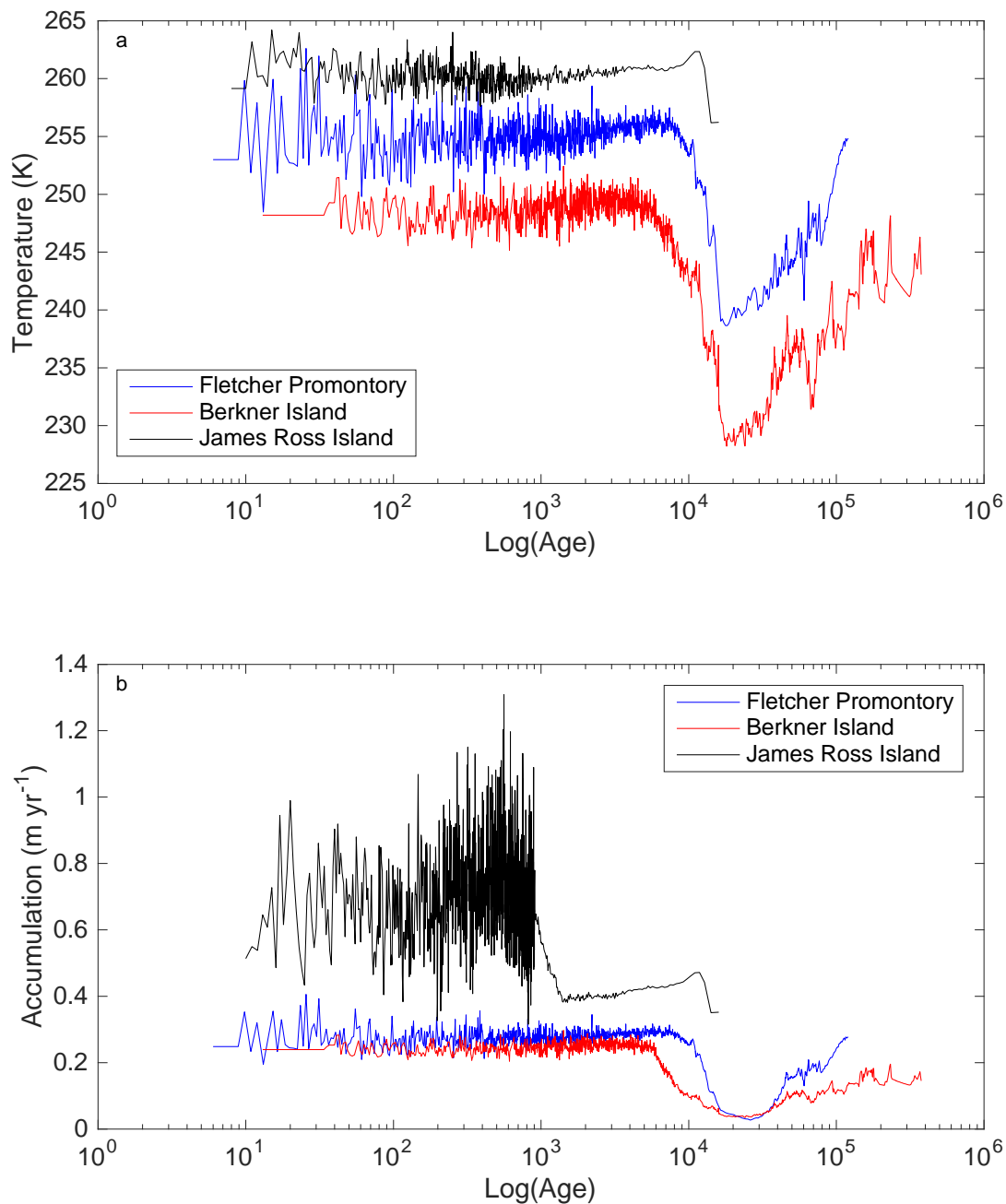


Figure 9.01: (a) Temperature Reconstructions, and (b) Accumulation Reconstructions for James Ross Island (black), Berkner Island (red), and Fletcher Promontory (blue). The JRI profile is capped at the depth of the greatest age constraint used.

A second discrepancy between the BI ice-core reconstructions and the FP and JRI ice-core reconstructions is the mismatch in the timing of Antarctic Isotopic Maxima (AIM) events beyond 60 ka BP (fig. 9.01). These AIM events are thought to be synchronous across the continent, and are identifiable in the stable water isotope-derived surface temperature profile. The difference between the BI profile and the FP and JRI ice cores is caused by the

large uncertainty on the BI age scale. Beyond 700 mweq, there are no age constraints in the BI ice core. Beyond 700 mweq towards the bed, the BI ice-core record preserves the signature of AIM events that are not only preserved, but are better constrained in the FP.

Following the presentation of results in Chapters 4-8, it was necessary to compare the reconstructions of the three ice cores. The results have been presented for comparison (fig. 9.01), and will be discussed in the context of the wider climate of the AP and Weddell Sea region.

### 9.3 Wider Context

By collating all of the ice-core reconstructions from BI, FP, and JRI from Chapters 6 and 7, the accumulation, surface temperature, and age-depth profiles should be discussed in a wider context. In particular, this study will assess how the FP, BI, and JRI ice-core reconstructions contribute to five key research topics: (i) the stable water isotopes – surface temperature – accumulation relationship; (ii) the potential changes in surface mass balance (SMB) of the AP region in the near-future (2005-2050); (iii) the mid-Holocene ice-sheet evolution; (iv) the last interglacial global mean sea level (GMSL) and the potential contribution from the WAIS; (v) the OptAcc ice-core model and its contribution to ice-core chronologies.

#### 9.3.1 *Stable Water Isotopes and Accumulation*

Throughout the development of an ice-core age-depth model, the relationship between surface temperature and accumulation rates have formed the basis of accumulation reconstructions. The optimal dating strategy presented by this study perturbs the accumulation history from the empirically-estimated initial profile to more accurately reconstruct thinning and age-depth profiles. In Chapter 4 and 5, the Clausius-Clapeyron relationship (section 2.5.2.2; eq. 2.06-2.08) was determined as the most accurate accumulation reconstruction. However, following this study, further investigations on the optimal dating strategy are warranted to further evaluate the reliability of reconstructions and the assumptions that underpin the processes incorporated into the model.

By comparing the empirical and optimised accumulation reconstructions, the relationship between stable water isotopes and surface temperature, and the subsequent relationships assumed between surface temperature and accumulation that form the crux of these

empirical accumulation relationships (section 2.5.2), could be assessed. One method to investigate the strength of the  $T_s/A$  relationship at FP, BI, and JRI, could be to use an isotope-enabled regional climate model to assess the position of each site in the region and the regional climate. Another method to investigate the relationship is by assessing the final accumulation profiles reconstructed using the OptAcc approach. The OptAcc model includes a perturbation approach,  $\varepsilon(z)$ , in order to account for uncertainties in the accumulation record. As the OptAcc model uses only a spatially-dependent gradient for the stable water isotope – surface temperature relationship, the perturbation profile can account for uncertainties in wind erosion at the surface, rapid changes in temperature at the surface, and a potential temporal change in the assumed  $T_s/A$  relationship of 4-6 %K<sup>-1</sup> that affects the amplitude of accumulation change with respect to a change in surface temperature.

Section 6.4.5 (Chapter 6) and 7.4.4 (Chapter 7) analysed the stable water isotope – accumulation relationship for the BI, FP, and JRI ice cores. The JRI ice core record demonstrates such high annual variability in measured accumulation that the OptAcc model couldn't accurately reconstruct the accumulation history for the upper 264 mweq. This is because the high-resolution chemical analysis and high mean annual layer thickness permit a sub-annual profile to be directly determined for most of the ice-core record. When compared, the Clausius-Clapeyron-derived accumulation history bore little resemblance to the optimised profile (fig. 9.02c).

Section 7.4.4 compared the JRI accumulation variability with the mean annual Southern Annular Mode (SAM) index. A positive mean annual SAM index is indicative of increased storm frequency, which can lead to variable and wind-scoured accumulation rates. Analysis of the relationship between JRI accumulation variability and the SAM index suggested that the site is dominated by external climate forcing but not entirely by the SAM.

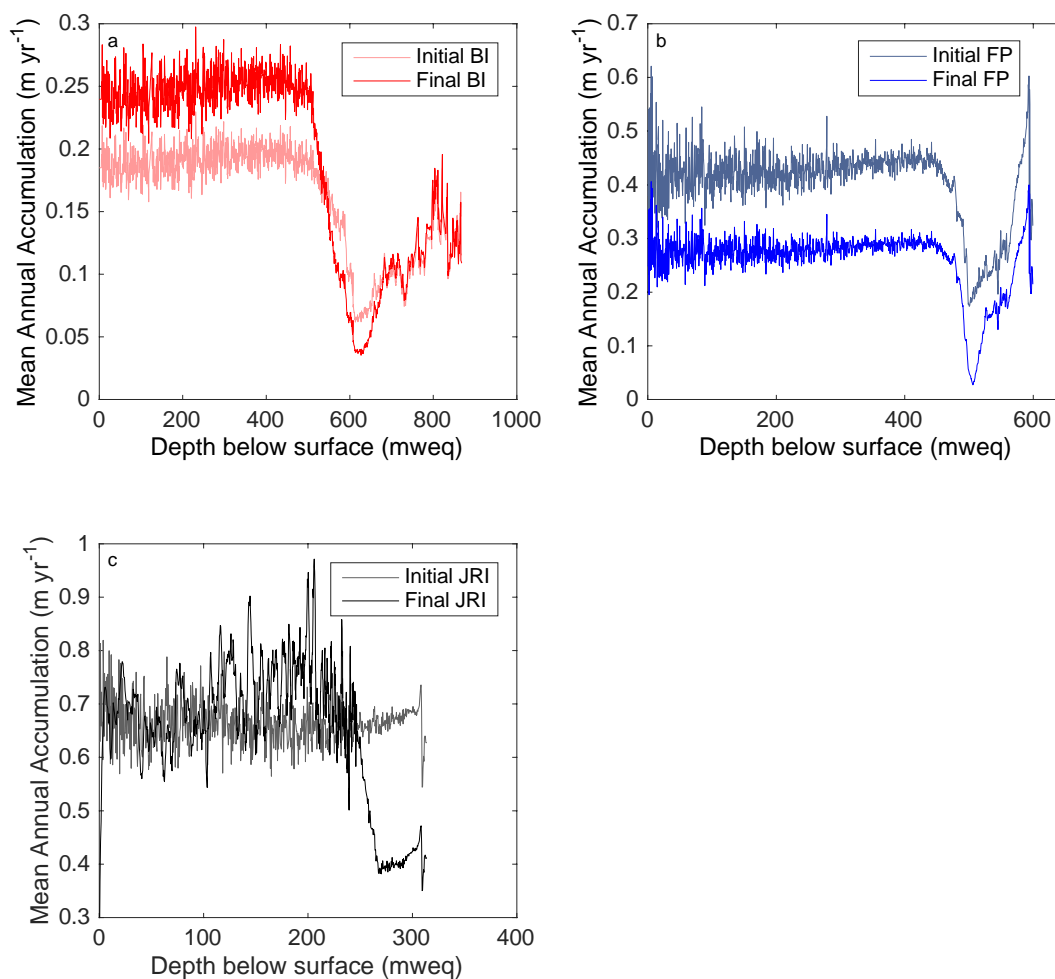


Figure 9.02: Initial and optimised accumulation profiles for the (a) BI; (b) FP; and (c) JRI ice cores. Initial accumulation profiles are estimated using the Clausius-Clapeyron relationship and presented in a pale shade of the colour used to present the optimised reconstruction.

It could also be suggested that the FP and BI ice-core sites also have a high inter-annual variability but this has not yet been confirmed largely due to limitations in the routine analytical resolution. The BI ice core accumulation reconstruction derived using the OptAcc model is consistently perturbed from the empirical accumulation reconstruction throughout the Holocene by up to 32% (fig. 9.02a). The perturbation is consistent throughout the ice-core profile, with the exception of the ACR-Early Holocene transition, and a greater perturbation was required to decrease the empirical accumulation rates to a low mean annual rate throughout the last glacial period. The FP ice core mean annual accumulation reconstruction derived using the OptAcc model is consistently ~34% lower than the empirically-calculated accumulation history (fig. 9.02b). The FP ice core is perturbed

consistently throughout the Holocene period, with a greater perturbation required to reduce accumulation rates during the last glacial period. Each accumulation profile needs to be perturbed significantly throughout the ice core record in order to reconstruct the most accurate profiles of accumulation, thinning, and age-depth, further adding doubt to the assumed relationship between accumulation and surface temperature. Overall, the analysis of the stable water isotope – accumulation relationship, conducted in Chapters 6 and 7, determined that throughout specific depth and time ranges in the ice cores, the coastal location of the ice core sites leads to variable accumulation rates that do not conform to the assumed accumulation rate sensitivity of 4-6% K<sup>-1</sup>.

For ice core sites located in the interior of the Antarctic ice sheets, the mean annual precipitation rate is closely tied to the saturation vapour pressure used in the Clausius-Clapeyron relationship (eq. 2.06 – 2.08). By following this method, continuous accumulation histories in the low-resolution, long ice-core records demonstrate a 4-6 %K<sup>-1</sup> change in accumulation with respect to a change in surface temperature (Palerme et al., 2014; 2017). This is similar to the 6-8% K<sup>-1</sup> change seen in GCM accumulation estimates, which are also based on a Clausius-Clapeyron relationship (Gregory & Morris, 1996; Frieler et al., 2016; Palerme et al., 2017). However, the stability of the relationship between isotopic fractionation, surface temperature, and mean rate of precipitation over the West Antarctic continent should be questioned (Sime et al., 2009; Schlosser et al., 2017; Steiger et al., 2017).

For coastal sites with a high seasonal variability in surface temperature and climate, surface temperature and accumulation are not as tightly coupled as they are at sites on the East Antarctic Ice Sheet (EAIS) (Sime et al., 2009). Evidence of this is found at AP ice cores from Dyer, Gomez, and JRI (Sime et al., 2009), and the WAIS Divide ice core, where both modern and early Holocene accumulation records are unresponsive to rising temperatures (Fudge et al., 2016). Furthermore, any temporal variability of the stable water isotope – surface temperature – accumulation relationship will lead to inaccuracies in the accumulation reconstruction derived from an ice core (Masson-Delmotte et al., 2008; Sime et al., 2009). Therefore, the stable water isotope – surface temperature relationship that defines the shape of the empirical accumulation reconstruction should not be considered robust for coastal sites.

### 9.3.2 *Future Changes to the Surface Mass Balance of the Antarctic Peninsula*

Extending further back in time than the AWS records in the region, ice core records provide context to the changes in the present-day climate that are recorded at AWS stations. The BI, JRI, and FP ice cores were retrieved in 2005, 2008, and 2012, respectively, and hence record a modern history of the climate. It is well observed across the AP that the region has been undergoing rapid regional warming (Vaughan et al., 2003; Turner et al., 2005; Steig et al., 2009). The warming surface temperatures across the region have led to increased ice mass loss from the ice shelves, which in turn speeds up the feedback responses from tributary glaciers (Weertman, 1974; Rignot et al., 2004).

Two of the three ice core records (FP and JRI) in this study show an increase in surface temperature over the most recent 150 years. This leads to an increase in mean annual accumulation over the last century. A mean increase in accumulation of 10% is recorded at FP and JRI ice core sites over this period. This occurs at the same time as the surface temperature at the FP and JRI sites increases by 1-3 K. Using a linear regression model, a sensitivity rate of  $3.3 - 10\% \text{ K}^{-1}$  for accumulation with respect to a change in surface temperature is interpreted at these sites. This sensitivity rate is similar to the rate of  $5\% \text{ K}^{-1}$  determined when accumulation is derived from an empirical relationship (Frieler et al., 2015), and the value of  $6 - 8\% \text{ K}^{-1}$  that is seen when accumulation rates are derived from a GCM (Palerme et al., 2017).

In addition to the ice core data, borehole temperature profiles provide a secondary dataset and reveal the extent and commencement of the regional warming at FP and JRI. Parallel to the ice core records, a recent warming of  $0.6 - 0.7 \text{ K}$  is deduced by comparing reconstructions of the present-day surface temperature with measured values of present-day surface temperature at FP and JRI (Chapter 8). An increase in accumulation and surface temperature in borehole records may date to the Industrial Era (1850 – present), similar to the ice core records at FP and JRI as well as the accumulation record at other sites not used in this study, such as the Gomez ice core (Thomas et al., 2008).

Model simulations of the surface mass balance (SMB) of the AIS predict an increase that began in the twentieth century to continue in the twenty-first century (Ohmura et al., 1996; Krinner et al., 2007; IPCC, 2013; Palerme et al., 2017). Model simulations of an increase in the SMB across Antarctica are corroborated by ice core evidence from West and East Antarctica. The mean annual accumulation has doubled at the West Antarctic site of Gomez since 1850 AD

(Thomas et al., 2008). The high inter-annual accumulation variability at Gomez strongly correlates with the SAM index, suggesting that the increasingly positive index value is a primary cause for an increase in accumulation over the last 150 years. Parallel to this, two short ice cores at Ferrigno and the Bryan Coast also demonstrate an increase in mean annual accumulation of 30% over the same time period (Thomas et al., 2015). From 1850 AD, highly resolved short ice cores from the Derwael ice rise and the Fimbul ice shelf, Dronning Maud Land, East Antarctica, show the first evidence of an increase in SMB in East Antarctica (Phillippe et al., 2016; Vega et al., 2016). An increase in the SMB over the AIS can have a significant impact on rising sea levels predicted by increased land ice mass loss (Ohmura et al., 1996; Bracegirdle et al., 2008; Palerme et al., 2017). An increase in precipitation over the continent could help to negate the ice mass loss that contributes to a rise in GMSL from other sources, including the thermal expansion of ocean waters and changes in the mass of ice sheets (IPCC, 2013).

Finally, the poor accumulation history from the deep BI ice core does not initially rule out evidence of recent regional warming at the site. Two short ice cores obtained at BI, before the retrieval of the deep ice core, presented an accumulation profile that is influenced by large-scale air mass regimes, suggesting that the BI record could be susceptible to surface temperature changes (Wagenbach et al., 1994). In section 6.4.4 of Chapter 6, it was suggested that the BI ice core record should be compared with other temperature records from the region to determine whether the full ice core record reflects changes to the local surface temperature. Despite rapid warming leading to an increase in accumulation across the AP and WAIS over the most recent 150 years (Turner et al., 2005; Bracegirdle et al., 2008; Steig et al., 2009), some coastal sites do not show any change in the accumulation trends. For example, annually-resolved short ice cores from the central WAIS and *in situ* radar measurements across Thwaites Glacier show no change in accumulation over the period 1975 – 2010 (Burgener et al., 2013; Medley et al., 2013). Between 1975 and 1995, the FP, BI, and JRI ice core records also show no increase in accumulation or a hiatus in the increases evident on a century-scale (Chapter 6 and 7). However, extending beyond 1975, the BI ice core shows no century-scale changes in the accumulation history unlike the FP and JRI sites (Chapter 6; fig. 6.15).

The BI record is corroborated by ice cores retrieved from coastal sites in the northern EAIS. A short core spanning 60 years from Adélie Land in East Antarctica agrees with the BI record,

that the surface temperature has not increased from 1975 to the present day unlike FP and JRI. The unchanged surface temperature record demonstrates the complexity of determining accumulation reconstructions based on a direct relationship with surface temperature in coastal locations (Goursand et al., 2017). A hiatus in changes to the accumulation record demonstrates the complexity of coastal locations, which are subjected to a complicated seasonal climate with a high inter-annual variability in surface temperature and high wind speeds due to the zonal winds that circumnavigate the Antarctic continent. This variability is evidence of the potential periodic decoupling of the relationship between surface temperature and accumulation and hence, results in an accumulation record across WAIS and the AP that does not consistently correlate with the sensitivity rate of modelled accumulation (Krinner et al., 2007; Frieler et al., 2015; Palerme et al., 2017). The rates of warming calculated using borehole temperature profiles at five sites across the AP, established that the warming is consistent with the warming trends recorded at AWS stations. However, despite the evidence of continued warming across the continent, the projected increase in SMB across the AP and Weddell Sea region cannot be predicted by the analysis of the ice core and borehole temperature profiles.

### 9.3.3 *Mid-Holocene Ice Sheet Evolution*

The three ice cores from the AP and Weddell Sea region were obtained to fulfil specific motivations outlined in Chapter 1 (section 1.2.1). One particular motive was to assess the temperature thresholds on the stability of the ice masses on the AP. The AP region has undergone severe ice mass loss following the disintegration of the Larsen A and B ice shelves in 1995 and 2002, triggering an increase in glacier and ice stream velocity across the region (Rignot et al., 2004). The retreat or collapse of the ice shelves across the region is not unique to the present-day, with terrestrial and marine evidence of ice sheet retreat during the Holocene period (Clapperton and Sugden, 1982; Ingolfsson et al., 1992; Hjort et al., 1997; Pudsey and Evans, 2001; Pudsey et al., 2006). A significant deglaciation at JRI between 7.4 – 4.6 ka BP is recorded (Ingolfsson et al., 1992; Hjort et al., 1997) that correlates with the disintegration of the George VI ice shelf at ~6.5 ka BP (Clapperton and Sugden, 1982; Hjort et al., 2001). Marine sediment records suggest the AP region had open oceans between 5 – 2 ka BP at five sites which are currently small ice shelves (Pudsey and Evans, 2001). The present-day ice mass loss is influenced by warming surface temperatures across the AP and Weddell Sea region (Vaughan and Doake, 1996) and thus ice cores provide an insight into the

thresholds on climate warming that could rapidly increase the current deglaciation across the AP region and lead to open waters.

The reconstruction of the JRI, FP, and BI Holocene age-depth profiles using the OptAcc model permits the analysis of the three AP and Weddell Sea ice core surface temperature records during this time period. Fig. 9.03 shows the difference between the present-day surface temperature value and the surface temperature reconstruction (section 2.5.1; eq. 2.09), spanning the time period 11 – 0 ka BP (fig. 9.03a) and 8 – 4 ka BP (fig. 9.03b). The JRI2 record is poorly-resolved beyond the most recent 2000 years due to the high mean annual accumulation and the high rate of strain in the shallowest depths of the ice core record. As a result, there are few surface temperature estimates throughout the age range 8 – 4 ka BP for this ice core. Despite this, a surface temperature reconstruction using the high-resolution reanalysis at DRI demonstrates no significant change in mean surface temperature across the 8 m section of the ice core that covers this time period, but it does suggest a mean temperature anomaly of +2 K compared to present day temperature (fig. 9.03b).

The FP surface temperature record is at a higher resolution than the JRI2 record, and demonstrates a variable surface temperature history. The mean surface temperature across the period of 8 – 4 ka BP is 3 K higher than the present-day mean surface temperature at FP (fig. 9.03b). Using a cubic interpolation data fitting on the surface temperature record, an increase in surface temperature is evident in the BI ice core record, with a rise in 4 K over 8 – 4 ka BP. At BI, the surface temperature increases to 1 K higher than the present-day surface temperature, but this period of time is covered by 9 – 2 ka BP period in question in the BI age scale.

Current rates of warming indicated by AWS observations suggest that average surface temperatures are increasing by  $3.5 \text{ K century}^{-1}$  (Mulvaney et al., 2012). IPCC projections range from 0.6 – 4 K warming by 2100 (IPCC, 2013), with Antarctic surface temperature warming estimated to occur at  $0.34 \text{ K decade}^{-1}$  (Bracegirdle et al., 2008). If these projections are robust, as they are expected to since the IPCC 'best-case' scenario still predicts 0.6 – 1 K warming (IPCC, 2013), the warming will reach a surface temperature similar to the mid-Holocene when the AP suffered high mass loss. By combining the AWS data, model projections of climate warming and the ice core records, the observations concur with the modelling studies that

suggest that the WAIS and AP regions have already reached this surface temperature threshold (Vaughan, 2006; Steig et al., 2009).

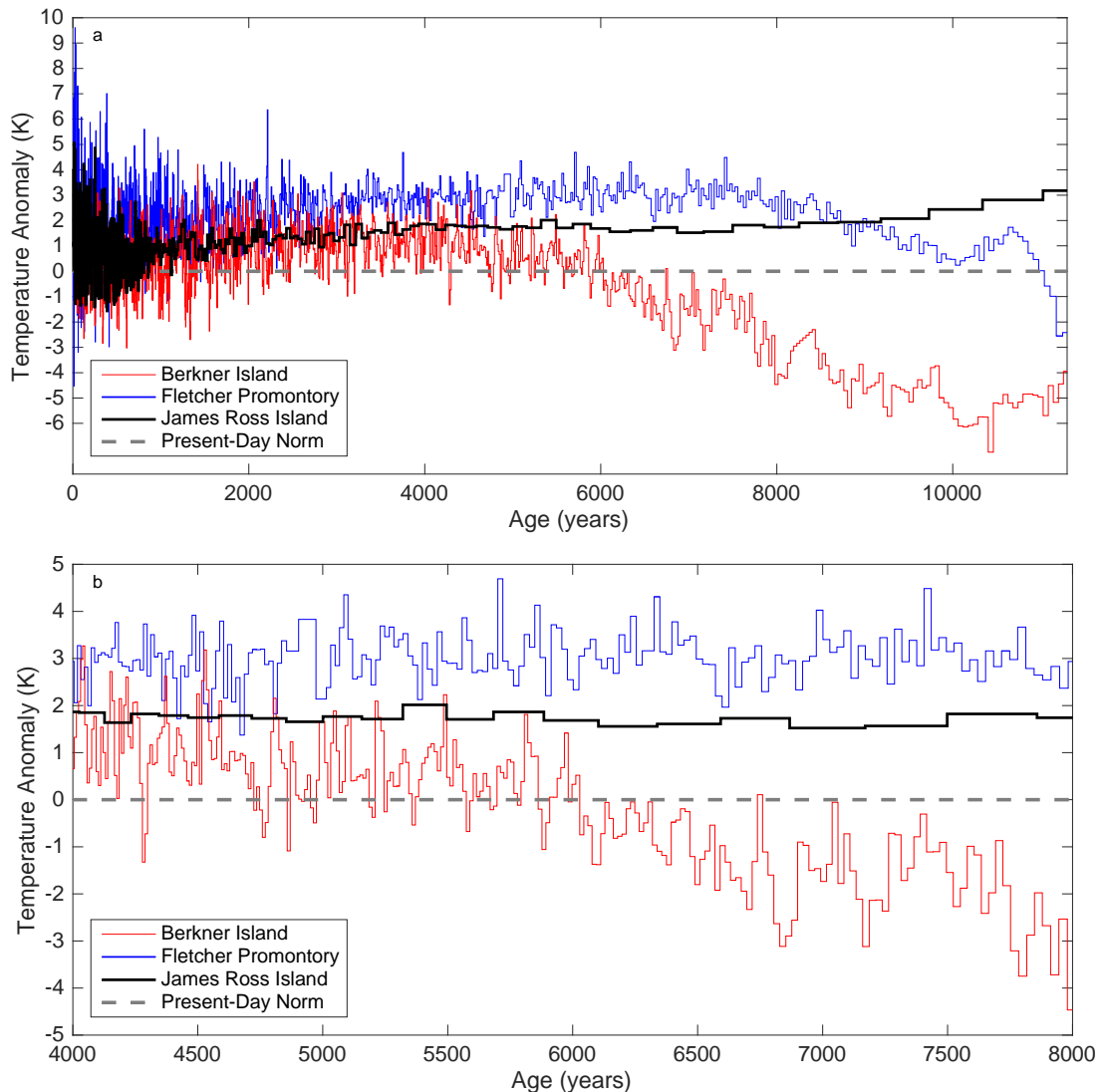


Figure 9.03: (a) Reconstructed surface temperature anomaly covering the Holocene (11.3 - 0 ka BP) for JRI (black), FP (blue), and BI (red). The grey dashed line is a normalised present-day surface temperature; (b) a zoom-in of plot (a) on the period 8-4 ka BP when marine and geomorphological records indicate the AP had more open ocean.

#### 9.3.4 Last Interglacial GMSL and the WAIS Contribution

Another motivation behind the retrieval of the FP and BI ice cores is to obtain a climate history that extends beyond the last interglacial (Mulvaney et al., 2014). The LIG (129 – 116 ka BP) is preserved in records as a warmer interglacial than the present, with ice core records

suggesting a mean surface temperature up to 5 K higher than the present interglacial (NGRIP members, 2004). A warmer interglacial contributed to a significant reduction in the glacial coverage across Antarctica, leading to a higher GMSL of 6 – 9 m (Dutton et al., 2015; Hoffman et al., 2017). Modelling studies suggest that the AIS contributed 3.3 – 6 m of this GMSL rise, with a significant input from the WAIS (Dutton et al., 2015). If the WAIS retreated significantly or collapsed during the LIG, the FP and BI ice core records would preserve a climate history that could reveal the climatic thresholds required for a WAIS collapse. The FP and BI ice core records extend into the last interglacial, confirming that neither ice cap retreated or disappeared during the warmer interglacial. Therefore, the FP and BI ice cores should be analysed further to interpret the climate record preserved during the LIG period, when the WAIS possibly diminished.

### 9.3.5 *The OptAcc ice core model*

The optimal dating strategy has been developed, assessed, and the results have been widely discussed. The OptAcc model is capable of reconstructing the records preserved in the BI, FP, and JRI ice cores, which have been successfully tested against observational data. The JRI2 record is annual layer counted to 290 m, with the remainder of the ice-core record reconstructed using the OptAcc model. The principle motivation of this study was to develop an ice-core age-depth model that was capable of modelling an accurate accumulation, thinning, and hence age-depth profile of three mid-depth, coastal ice cores. Despite the publication of IceChrono during the course of this study, the OptAcc model contributes to the interpretation of ice cores from the AP and Weddell Sea region. To discuss this contribution, two main questions must be addressed:

- i. Can this model be applied to other ice-core records?

The success of the ice-core reconstructions at FP and JRI support the use of this model for the construction of accumulation, thinning, and age-depth profiles. As such, it should be assumed that the OptAcc model could be applied to other ice core records successfully. For FP and JRI, the records preserve mostly the present interglacial climate history, but the transition from the last glacial period to the present-day climate is also successfully reconstructed at the FP site. For JRI, the age-depth reconstruction, and as such the accumulation and thinning reconstructions, are capped at the depth of the greatest constraint used. This is because of

the hypothesized hiatus of unknown start, end, or duration, observed in the ice core record between two age constraints identified at  $\sim 14.6 - \sim 17.5$  ka BP.

Unlike the FP and JRI ice cores, the BI ice-core reconstructions have been presented with high uncertainty. Prior to applying it to other ice core records, the OptAcc model should be improved by incorporating additional parameters and variables. As already discussed in this chapter (section 9.2), the location of BI, embedded in the Filchner and Ronne ice shelves, threatens the preservation of a clear climate history. Additional ice-sheet processes, that have the potential to impact the preservation of the climate profile, may have disturbed this record. To account for changes in the horizontal ice flow, the migration of the ice divide, and changes in the ice-sheet thickness, parameters to reconstruct these processes must be incorporated as a second dimension to the OptAcc model.

Further, for sites where the temperature at the bed is at ‘pressure melting point’, the melting of the ice – and hence the climate record – must be considered. For example, the EPICA ice cores reach ‘pressure melting point’ and thus the ice record at the bed is constantly being destroyed, affecting the ultimate age of the ice at the bed and drawing down ice layers from above. Melting at the bed is incorporated into the IceChrono toolbox, as a ratio in an equation for strain that can be interpreted as a thinning function (section 2.5.3.3; eq. 2.13). Adaptation of the OptAcc model is therefore necessary in order to apply the method to other cores.

- ii. Why should this model be developed when the IceChrono model is freely-available?

The IceChrono model has been developed separately to this study in conjunction with the development of the Vostok and EPICA ice core chronologies (Parrenin et al., 2001; 2004; 2007a; 2007b; 2012; 2015). The FP, JRI, and BI ice core records were reconstructed using the IceChrono model and it was determined that this method would not be the most suitable technique to sufficiently reconstruct the records preserved in these three ice cores for several reasons. Principally, the IceChrono age scales did not suggest that the FP ice core records the LIG, which does not agree with the information preserved in the stable water isotope profile. Secondly, the IceChrono model uses the Simple Exponential technique to reconstruct accumulation; this technique assumes a  $5\% K^{-1}$  amplification of accumulation with respect to a change in temperature (Parrenin et al., 2007; 2015). The surface temperature – accumulation amplification relationship is assumed not to change with time as the ice-core

records reconstructed using IceChrono typically extend across multiple glacial cycles. For example, the EPICA Dome C (EDC) ice core is taken from the EAIS inland plateau, and it preserves the climate history of eight glacial cycles; only a small fraction of the ice-core record relates to interglacial climates. The surface temperature – accumulation relationship is less stable during interglacial periods, as warmer periods increase the transport of moisture in the atmosphere and impact on the rate of precipitation (Bracegirdle et al., 2008). Therefore, the accumulation reconstruction using the IceChrono approach does not reconstruct the natural variability in accumulation during interglacial periods, which are the predominant climate period preserved in coastal, mid-depth ice cores. The OptAcc model is capable of reconstructing interglacial accumulation, by perturbing the accumulation and assuming that the assumed sensitivity of accumulation with respect to a change in surface temperature could change with time during interglacial – glacial transitions.

#### 9.4 Summary

Over the course of this study, four objectives were outlined in order to assess the techniques currently used to reconstruct ice-core profiles of accumulation, thinning, annual layer thickness, and age-depth. The fifth objective aimed to assess the results of the study and how the results fit into the wider context of research in the region. This chapter has collated the results of Chapters 4-8 and placed the ice-core climate and age-depth profiles within the existing record. In doing this, the study provides evidence that the stable water isotope – accumulation relationship is not robust at coastal locations, and that the JRI, FP, and BI ice core records are useful analogues for present-day climate warming. The ice core temperature reconstructions suggest that the increasing present-day surface temperature will reach a threshold temperature which could trigger mass ice loss across the AP region. Concurrently, the surface temperature increase yields an increase in mean annual accumulation which could offset some rise in the GMSL. The following chapter will conclude this study by summarising the main objectives of the study, the outcomes of the study and the interpretation of the results in a wider context, and will outline how future research could continue following from this study.

## 10.0 Conclusions

### 10.1 Introduction

This study set out to synthesise and consider all of the relationships that can be used to reconstruct past accumulation, thinning, and hence annual layer thickness and age-depth of an ice core, with a view to assessing the strengths and weaknesses of each technique and developing the optimal dating for three deep ice cores from the Antarctic Peninsula (AP) and Weddell Sea region. The three deep ice cores that this study uses have been retrieved from James Ross Island (JRI), Fletcher Promontory (FP), and Berkner Island (BI). To fulfil the rationale of this study, five objectives were outlined (section 1.2.1) that aimed to develop and assess the relationships that can be used to reconstruct age-depth profiles, in order to apply the most reliable approach to an ice core and reconstruct the past accumulation, thinning, annual layer thickness, and age-depth profiles.

### 10.2 Achievement of Study Objectives

To address the five objectives set out at the beginning of the study, the results can be divided into two sections: (i) mathematical modelling, and (ii) chemical analysis. The following paragraphs summarise and highlight the main results from each section of the study.

#### 10.2.1 *Mathematical Modelling*

The mathematical modelling branch of this study had three independent objectives (objectives i, iii, and iv). The first objective sought to collate and compare the relationships that are used to reconstruct mean annual accumulation, thinning, annual layer thickness, and age-depth with one another. As well as comparing the established relationships and techniques, this objective allowed the development of new techniques and approaches to reconstruct these profiles. In total, 25 alternative age-depth combinations were applied to the FP ice core (Chapter 4). These modelling approaches develop in complexity, provide alternative solutions for poorly-defined parameters and yield multiple optimised profiles of accumulation, thinning, annual layer thickness and age-depth. Novel developments include constructing a thinning function using the vertical velocity profile within an ice sheet from *in*

*situ* phase-sensitive radio echo sounding (pRES) measurements. Vertical velocity measurements using pRES provide a direct measurement that can be interpreted as a thinning function, but only as a present-day snapshot.

Aside from the novel developments, there were similarities in the established unconstrained approaches used to reconstruct accumulation and thinning due to the assumed relationships in the ice sheet. Differences between approaches occurred in the way each technique was applied to an ice core. To minimise the inaccuracy of the age-depth profile, constrained approaches used inverse modelling to optimise one or more parameters or variables in the ice-core reconstructions. The accuracy of each constrained modelling approach was assessed by comparing the estimated ages at depths corresponding to a known-age horizon with the observed age, using a root mean square error (RMSE) value. The RMSE comparison suggested that the OptAcc and IceChrono approaches yielded the most accurate age-depth reconstructions by assessment of the RMSE values. Further assessment of the model approaches considered the age estimate at the bed for the FP ice core; the stable water isotope profile suggests a record extending into the last interglacial (LIG), at ~126 – 115 ka BP. The IceChrono approach consistently estimated an age at the bed of 80-100 ka BP, whereas the OptAcc model estimated an age at the bed of ~150 ka BP, agreeing with the interpretation of the stable water isotope record.

Therefore, the results of Chapter 4 suggested that the OptAcc model is the most reliable approach to reconstruct the past accumulation, thinning and age-depth profile of a coastal ice core. In order to address the second model-based objective (objective (iii) in section 1.2.1) – to develop the optimal strategy for reconstructing the ice-core records preserved at the JRI, FP, and BI ice-core sites – additional assessment of the modelling synthesis was required (objective (ii) of the study). The outcome of objective (ii) will be discussed in section 10.2.2, before discussing the results of objective (iii) in section 10.3.1.

The aim of the final objective that required mathematical modelling (objective (iv) in section 1.2.1) was to reconstruct the past surface temperature using the borehole temperature measurements (Chapter 8). Instead, an independent borehole model (section 3.6.3) was used to calculate the mean annual accumulation rate, mean annual surface temperature, and geothermal heat flux (GHF) values for the BI, FP, and JRI ice core sites. Although not directly applicable to the main objectives of this study, GHF values are important to

accurately reconstructing ice-sheet processes by constraining the basal conditions. The calculated GHF values were different to the modelled estimates published by other studies (Shapiro and Ritzwoller, 2004; Fox Maule et al., 2005; Purucker, 2016), and should be used to calibrate future continent-wide modelling studies.

An additional observation of the borehole temperature study suggested that the difference between the measured and modelled mean annual surface temperature could be evidence of the recent rapid regional warming across the AP and Weddell Sea region that is not yet preserved in the ice-core and borehole temperature record. The surface temperature reconstruction was applied to other short borehole temperature profiles from the region. By combining this additional work with a simple age-depth profile, further evidence was found to support the suggestion that the inflection in borehole temperatures towards the surface of the ice sheet was evidence of the rapid regional warming. The warming trends interpreted from the differences between the modelled and measured surface temperatures are consistent with the warming trends identified in automatic weather stations (AWS) and the trend of the number of positive degree days (PDD) across the AP (Turner et al., 2005; Vaughan, 2006; Barrand et al., 2013). However, the rates of warming on a decadal- and centennial-scale do not agree with the AWS-derived rates of warming or the ice-core derived rates of warming. Whether the borehole temperature records of warming suggest a gradual rate of warming that extends further than the AWS records, or are a proxy of the surface warming, must be further investigated.

#### 10.2.2 *Chemical Analysis of BI, FP, and JRI*

The analysis and interpretation of the ice-phase chemistry in the FP and BI ice cores was required to supplement the modelling work in this study. The principle motivation for this research was to obtain sub-annual profiles at depths along the ice core where the mean annual layer thickness is beyond the current standard laboratory resolution (objective (ii) of the study). Real annual layer thickness measurements were used for comparison with the corresponding modelled profiles as two techniques in ultra-high resolution chemical analysis were developed and applied for the first time to Antarctic ice deposited during the last glacial period. The annual layer thickness measurements provided an additional assessment to the modelling synthesis that was carried out.

## Conclusions

By developing and assessing ultra-high resolution analytical techniques of discrete sampling and LA ICP-MS techniques, sub-annual profiles of sodium deposition during the mid-Holocene, *circa* 5 ka BP, and the last glacial period, *circa* 30 ka BP, were obtained from the BI ice core. The annual layer thickness measurements ranged from  $\sim 57.0 \text{ mm yr}^{-1}$  in the youngest sampled section (*c.* 5 ka BP at  $\sim 447 - 456 \text{ m}$ ) to  $\sim 3.0 \text{ mm yr}^{-1}$  at *c.* 30 ka BP (694 – 697 m). An interesting observation was the increase in layer thickness from  $3.0 \text{ mm yr}^{-1}$  at *c.* 27 ka BP to  $\sim 6.0 \text{ mm yr}^{-1}$  at *c.* 31 ka BP. This doubling in annual layer thickness over a depth range of  $<10 \text{ m}$  in the ice core suggests a significant accumulation event in the climate record.

Discrete sampling also yielded chemical measurements at a sub-annual resolution at three depth ranges along the FP ice core, providing annual layer thickness measurements between 2 – 11 ka BP. These results were supplemented with two mean annual layer thickness measurements identified by the stable water isotope signal, taken from shallower depths in the FP ice core. For the FP ice core, the annual layer thickness measurements range from  $\sim 98.0 \text{ mm yr}^{-1}$  in the youngest sampled section ( $\sim 2.1 \text{ ka BP}$  at 299 m), to  $7.7 \text{ mm yr}^{-1}$  at  $\sim 11 \text{ ka BP}$  (523 m). The second objective of this study was to make laboratory measurements of annual layer thickness for the BI and FP ice cores to test the accumulation reconstructions derived under objective (i). The annual layer thickness measurements were initially used to assess the accuracy of the layer thickness estimates derived from the modelling synthesis (section 5.8.3). Following comparison and assessment of the annual layer thickness estimates, the OptAcc model was confirmed as optimal modelling approach for the FP, BI, and JRI ice cores, thus fulfilling objective (iii) of the study. The annual layer thickness measurements were later used to provide constraints for the OptAcc model for the ice-core reconstructions at FP, BI, and JRI. As a result, the distribution of the observational data available to constrain an ice-core model along the depth of an ice core can be controlled and improved.

### 10.3 Summary of the Results in a Wider Context

In addition to the results already summarised from the modelling and chemical analysis completed for this study, the final objectives developed and applied the optimal dating strategy to the FP, BI, and JRI ice cores, with a view to interpreting the climate records preserved in these ice cores.

### 10.3.1 *The Optimal Dating Strategy*

By combining both modelling and chemical techniques, this study has developed the optimal strategy for reconstructing the past accumulation, thinning, annual layer thickness, and age-depth profiles. In order to account for the high inter-annual variability in accumulation at coastal ice-core sites, a Clausius-Clapeyron relationship should be applied to the stable water isotope profile to derive an accumulation history (section 2.5.2.2). This accumulation reconstruction was optimised by developing a perturbation profile,  $\varepsilon(z)$  (section 3.6.1.3). A second variable has been optimised as part of the One-Dimensional thinning function (section 2.5.3.3 and section 3.6.1.1).

The modelling approach, referred to as the OptAcc model, has been applied to the FP and BI ice cores (Chapter 6) and the JRI ice core (Chapter 7). The JRI ice core has been annual layer counted to 246 mweq (290 m); the remainder of the ice-core profile is reconstructed using the OptAcc model, which has been constrained to age horizons. The full length of the FP ice core has been modelled using the OptAcc approach and has been constrained to age horizons and annual layer thickness measurements. The BI ice core has been reconstructed using the same approach as used on the FP ice core, constrained using annual layer thickness measurements and age horizons. However, the timing of some Antarctic Isotopic Maxima (AIM) events beyond 60 ka BP identified in the BI accumulation history do not agree with the same events identified in Antarctic ice cores despite the assumed synchronicity across the continent (section 9.2). The differences between the BI accumulation history and the reconstructed accumulation from other Antarctic ice cores (both FP and JRI, and records not reconstructed in this study including the WAIS Divide and EPICA Dome C (EDC) ice cores) led this study to suggest that the BI ice core requires the reconstruction of additional processes such as ice sheet thickness history to accurately reconstruct the accumulation, thinning, annual layer thickness and age-depth profiles. Additional improvements that could be made to the OptAcc model, such as the incorporation of parameters that would account for temporal changes to the ice-sheet thickness and ice divide, would also enable the OptAcc model to be applied to other ice core records.

### 10.3.2 *Climate Information Interpreted from the BI, FP, and JRI ice cores*

Although this study has raised doubts on the accuracy of the reconstructions for BI, the FP and JRI ice-core reconstructions are presented with confidence. This study has

reconstructed profiles of past accumulation, thinning, annual layer thickness, and age-depth using the observational data and modelling approaches available, and it yields information on the past climate preserved in the ice records. Principally, these records show the warmer conditions during both the Holocene and the LIG; climatic conditions that resulted in ice mass loss across the AP and West Antarctic Ice Sheet (WAIS). Ice cores from JRI, BI, and FP preserve information on the climate ‘thresholds’ of surface temperature warming with regards to ice mass loss, suggesting that an increase in surface temperature of 1-3 K across the region is sufficient to cause open ocean conditions across the AP and Weddell Sea region. Finally, further analysis and assessment of the ice core records from BI and FP are required to fully understand the relationship between the climate and the stability of the WAIS during the last interglacial period.

### 10.4 Future Research

Models consistently improve our understanding of processes that we cannot directly measure. For an ice core, these processes have occurred in the past. Precipitation is deposited in the past and has been subsequently altered through time, as the original accumulation is compacted to the present-day annual layer thickness. A model is an invaluable tool for enhancing our knowledge and understanding of records preserved in the ice sheet. By addressing the objectives of this study, there are several branches of research that could be further explored in order to develop the initial results.

#### 10.4.1 *Model Development*

The ice-core age-depth model development, outlined in Chapter 4, sees a gradual improvement to the accumulation and thinning reconstructions. Ultimately, the OptAcc model reconstructs the most reliable profiles of accumulation and thinning for the FP, JRI, and BI ice core records. The OptAcc approach is sufficient for the records preserved at the FP and JRI sites, where it is understood that the ice sheet and basal conditions have been stable for the duration of the record preserved in the ice core. In order for the age-depth model to be applied to other ice core records and BI, additional parameters should be included to account for potential uncertainties that do not pose a problem in the FP and JRI ice core records.

As discussed in Chapter 9, the OptAcc approach must be developed to account for additional processes that occur to, within, and at the bed of the ice sheet. Therefore, this study summarises here the suggestions to develop the OptAcc approach. Changes in the ice sheet

can influence the final age-depth estimate; the migration of the ice divide, and changes to ice-sheet thickness through time. Furthermore, the preservation of the record at the bed can be affected if the temperature at the bed reaches the 'pressure melting point' and leads to basal melt and sliding. Towards the end of this research study, early attempts were made to introduce a second dimension to the model and incorporate temporal changes to the ice-sheet thickness. Unfortunately, time constraints on the study hindered this work, but the basic hypothesis is that an ice-sheet thickness history could be interpreted from preserved proxies and an initial age-depth profile.

The OptAcc model only reconstructs the ice-phase processes in the ice core record. A second alternative to improving the efficacy of the OptAcc model is to incorporate a firn densification model, and estimate two parallel age-depth profiles: the ice-phase of the ice core that is currently modelled using the OptAcc model, and a second profile for the gas-phase of the ice core. As introduced in Chapter 2 (section 2.6), the compaction of snow into ice in the upper section of the ice core leads to an offset in the timing of the occlusion of gas bubbles and ice-phase chemicals deposited synchronously. As a result, two age-depth profiles present simultaneous climate records at different depths in the ice-core record. By including a firnification model to the OptAcc approach, the age-depth model can open an alternative line of enquiry by assessing the depth difference between the same age in each phase of the ice core. The depth difference can yield information on the diffusive column height, any rapid changes in accumulation history, and it would make use of the gas-phase records that are also preserved in the ice core on a synchronized age-depth profile.

#### *10.4.2 High-resolution Analysis*

The resolution of standard laboratory ice-core analysis is constantly being improved. Ultra-high resolution analysis of an ice core is labour-intensive without the adoption of novel techniques such as LA ICP-MS. LA ICP-MS can analyse 1 m of ice in  $\sim 3$  hours, whilst the standard laboratory techniques such as CFA operate at 30 mm per minute, or 1.8 m per hour, but at a resolution 100 times lower. Discrete measurements, such as those used in this study or previous analysis of the NGRIP ice core (Thomas, 2006; Thomas et al., 2009), require weeks of laboratory hours in order to cover up to 1 m of an ice core. As a result, the depth to which a sub-annual record can be retrieved in a deep ice core is substantially greater when using a continuous ultra-high resolution technique such as LA ICP-MS, and it enables a longer annual layer counted profile to be produced. The longest annual layer

counted record of Antarctic climate extends to 38 ka BP in the WAIS Divide ice core (Sigl et al., 2016), retrieved by CFA due to the high mean annual accumulation and low strain rates at the site. Sub-annual records from the WAIS Divide record do not yield only observational data along an ice core to constrain an age-depth model, but provide a high-resolution, sub-annual account of climate processes and interactions (WAIS Divide Project members, 2014). In other Antarctic ice-core records, where the present-day ice-sheet conditions yield a mean annual layer thickness that is smaller than the standard analytical resolution of 10 mm, sub-annual profiles and hence an annual layer counted ice-core record are not available using traditional techniques. Therefore, the application of more ultra-high resolution techniques could improve our understanding of the processes and feedbacks associated with climatic events. For future research and analysis of a deep ice core from Antarctica, application of techniques capable of ultra-high resolution analysis, should be considered in order to enhance the length of a sub-annual profile available for interpretation and therefore the quality of the interpreted record.

### 10.4.3 WAIS Collapse Analysis

As the FP and BI ice core records extend beyond the last glacial period, additional analysis should be completed to further interpret the record preserved during the LIG in these ice cores. The potential collapse or retreat of the WAIS can be interpreted from the ice core record by the presence of proxies that indicate open ocean or sea-ice during the warmer interglacial. The success of the ultra-high resolution analysis on the FP and BI ice cores (section 3.4 and 3.5 in Chapter 3) could enable the determination of whether the FP and BI ice cores were surrounded by open ocean during the last interglacial. The depths in the FP and BI ice cores that correspond to the last interglacial are ~580 mweq and ~750 mweq, respectively. At this depth, the OptAcc model estimates a mean annual layer thickness of 0.3 mm yr<sup>-1</sup> and 0.15 mm yr<sup>-1</sup>, respectively. A sub-annual record cannot be resolved at this thickness using the ultra-high resolution techniques developed in this study, but a sub-annual record is not fundamental to understanding WAIS dynamics during the whole of the LIG. These techniques should be applied to deeper sections of the ice core records in order to obtain a high-resolution record of the sea-ice proxies during the last interglacial. During this study, the greatest depth at which the discrete sampling technique was applied was 523 m (480 mweq) (section 3.5). At this depth, the FP ice was brittle and thus prone to breaking. Therefore, this study suggests that the LA ICP-MS technique should be applied to a deeper section of ice rather than the discrete sampling technique.

#### 10.4.4 Borehole Thermometry Modelling

The fourth objective of this study was to develop an independent temperature record that could be compared with the temperature reconstruction derived from the stable water isotope profile preserved in the ice core. As already stated, the borehole temperature record was not at a sufficient resolution to yield any significant surface temperature profiles, but the borehole model that was supposed to reconstruct a surface temperature history was still applied to yield present-day conditions for GHF, surface temperature and the mean accumulation rate throughout the ice core record (Chapter 8). Although this work does not have a direct impact on the rest of this study, ice core boreholes provide a temperature profile that could improve the GHF coverage of the continent. Following from this work, initial interrogation of the deviation between modelled and measured surface temperature led to the suggestion that the rapid regional warming occurring across the AP has perturbed the temperature profile in the ice sheet, and the temperature profile has not yet stabilised throughout the ice column (section 8.4.4). Further investigation of the borehole temperature profiles as a proxy for rapid regional warming in the AP could be substantial, and hence analysis of borehole temperature profiles should be considered for future work in the region. The key questions raised by these interesting results are:

- i. Do the results reflect long-term warming across the AP and Weddell Sea region?

The results of the initial study in this thesis are only suggestions and have not been thoroughly investigated to confirm whether they reflect warming since the Industrial Era or the recent increased surface temperatures diffusing through the ice column.

- ii. Could these results be interpreted as a proxy for warming?

If the results of the borehole model indicate warming in the ice sheet, but are not directly comparable with the rates of warming estimated from AWS data, are the results a proxy for contemporary warming, or do they suggest a long-term period of warming that is not recorded in AWS data? Further investigation of the results, and additional modelling would be required to answer this question.

- iii. Is this study transferrable to other glaciated regions?

Principally, could this technique reproduce similar results in regions that experience seasonal melting, such as the Greenland ice sheet (GrIS) and non-polar glaciated regions?

## Conclusions

Past surface temperatures can be reconstructed using borehole temperature profiles in the GrIS (Dahl-Jensen and Johnsen, 1986; Dahl-Jensen et al., 1998; Tarasov and Peltier, 2003). In long-term records, the diffusion of heat through an ice column does not mask climate events such as the Little Ice Age (LIA) in the GrIS (Tarasov and Peltier, 2003). These records do not appear to be affected in the long-term by warmer summer seasons, and they preserve the record of rapid climate events in the northern hemisphere (Dahl-Jensen and Johnsen, 1986; Dahl-Jensen et al., 1998; Tarasov and Peltier, 2003). Is the recent rapid regional warming, that is having a detrimental impact on the GrIS and leading to an average mass loss of  $269 \text{ Gt yr}^{-1}$  (MacMillan et al., 2016), visible in the temperature structure of the GrIS?

- iv. What could we learn of the propagation of heat into an ice sheet?

Finally, succeeding these initial questions, if this technique is able to provide a reliable interpretation of warming in glaciated regions, an interesting study could be to assess the propagation of heat into an ice sheet such as WAIS or GrIS to assess the role of surface temperature on ice sheet retreat in comparison to the role of the ocean and meltwater crevasses. These questions remain pertinent to the wider context of the warming climate across Earth, and should be developed and applied in regions where the impact of the warming climate on large ice masses is not fully understood.

## 10.5 Summary

From synthesising all of the relationships used to reconstruct past accumulation, thinning, annual layer thickness, and age-depth, this study has developed the OptAcc model. In addition, chemical analysis of the ice cores provides constraints that can be used to improve on the modelled reconstructions of accumulation and annual layer thickness. The OptAcc model is presented as the optimal dating strategy for the FP, BI, and JRI ice cores from the AP and Weddell Sea regions, constrained using annual layer thickness measurements and age constraints. Using this model, the accumulation history, thinning, annual layer thickness and age-depth profiles are presented for the three ice cores. These records have been presented and compared with each other, and yield information on the past climate across the region.

## Appendix 1: Supplementary model results to Chapter 4

This appendix supplements the results presented in Chapter 4 with the same techniques and modelling approaches applied to the ice core records from James Ross Island (JRI) and Berkner Island (BI).

### A1.0 Observational Data

*Table A1.01: List of known-age horizons used to constrain the BI ice core age-depth model. Age horizons have been derived by Rob Mulvaney (pers. comm.) by matching BI stable water isotope signatures with EDC stable water isotope signatures of assumed-synchronous AIM events (Bazin et al., 2013; Veres et al., 2013).*

Depth below the surface (m)	Depth below the surface (mweq)	Observed Age (yr since date)	Age (yrs)	Uncertainty (yrs)	Observed feature
650.80	596.85	13050.0		250.0	Coldest part of the ACR, tuned to AICC2012
656.80	602.10	14600.0		250.0	AIM 1
669.35	613.79	18390.0		1000.0	Start of warming
718.90	659.35	38250.0		800.0	AIM 8
745.08	683.39	46480.0		800.0	AIM 12
775.51	711.11	56890.0		800.0	Coldest part of stadial, tuned to AICC2012
792.84	726.59	64750.0		2200.0	AIM 18

*Table A1.01: List of known-age horizons used to constrain the JRI ice core age-depth model. Age horizons have been derived by Joe McConnell (pers. comm.) and Rob Mulvaney (pers. comm.) by matching JRI stable water isotope signatures with WAIS Divide stable water isotope signatures of assumed-synchronous events and tephra layers.*

<b>Depth below the surface (m)</b>	<b>Depth below the surface (mweq)</b>	<b>Observed Age (yr since drill date)</b>	<b>Uncertainty (yrs)</b>	<b>Observed feature</b>
0.00	0.00	0.00	0	Top
18.72	10.14	16.5	2	Volcanic
50.98	32.94	52.5	2	Pu
68.01	46.76	78.5	2	Volcanic
87.81	63.78	113.5	2	Volcanic
112.81	86.06	160.0	2	Volcanic
126.88	98.76	191.5	2	Volcanic
152.15	121.60	248.0	2	Volcanic
177.62	144.63	313.0	2	Volcanic
263.70	222.62	662.0	5	Volcanic
273.40	231.43	737.0	5	Volcanic
275.02	232.90	748.0	5	Volcanic
284.10	241.14	836.0	5	Volcanic
289.96	246.46	899.0	5	Volcanic
295.92	251.88	968.0	11	Volcanic
298.96	254.64	1014.0	11	Volcanic
349.53	300.62	5478.0	500	Volcanic
358.50	308.78	12024.0	500	Volcanic
358.78	309.04	12771.0	500	ACR tuned to AICC2012
359.00	309.24	14664.0	500	Optimum temperature of ACR, tuned to AICC2012

Table A1.02: List of ice-sheet variables used in the ice-core age-depth model for BI and JRI (Mulvaney et al., 2007; 2014).

Parameter	Value for each ice core	
	BI	JRI
Mean Annual Present-Day Accumulation Rate, $A^{\theta}$ (m yr <sup>-1</sup> )	0.18	0.63
Mean Annual Present-Day, $\delta D^{\theta}$ (‰)	-218.14	-154.36
Ice-sheet thickness, H (m)	947.00	364.00
Mean Annual Present-Day Surface Temperature, $T_S^{\theta}$ (K)	248.20	259.15
Mean Annual Present-Day Surface Temperature, $T_S^{\theta}$ (°C)	-24.95	-14.00
Mean Annual Present-Day Temperature at the bed, $T_B$ (K)	262.00	262.00
Mean Annual Present-Day Temperature at the bed, $T_B$ (°C)	-11.00	-11.00
Mean Annual Present-Day Temperature at the inversion layer, $T_{inv}^{\theta}$ (K)	255.37	262.26
Mean Annual Present-Day Temperature at the inversion layer, $T_{inv}^{\theta}$ (°C)	-17.78	-10.89

A1.1 Empirical Profiles

The chapter explores the multiple techniques that can be used to reconstruct atmospheric and ice sheet processes without an inverse approach.

A1.1.1 Water-Equivalent Depth Conversion

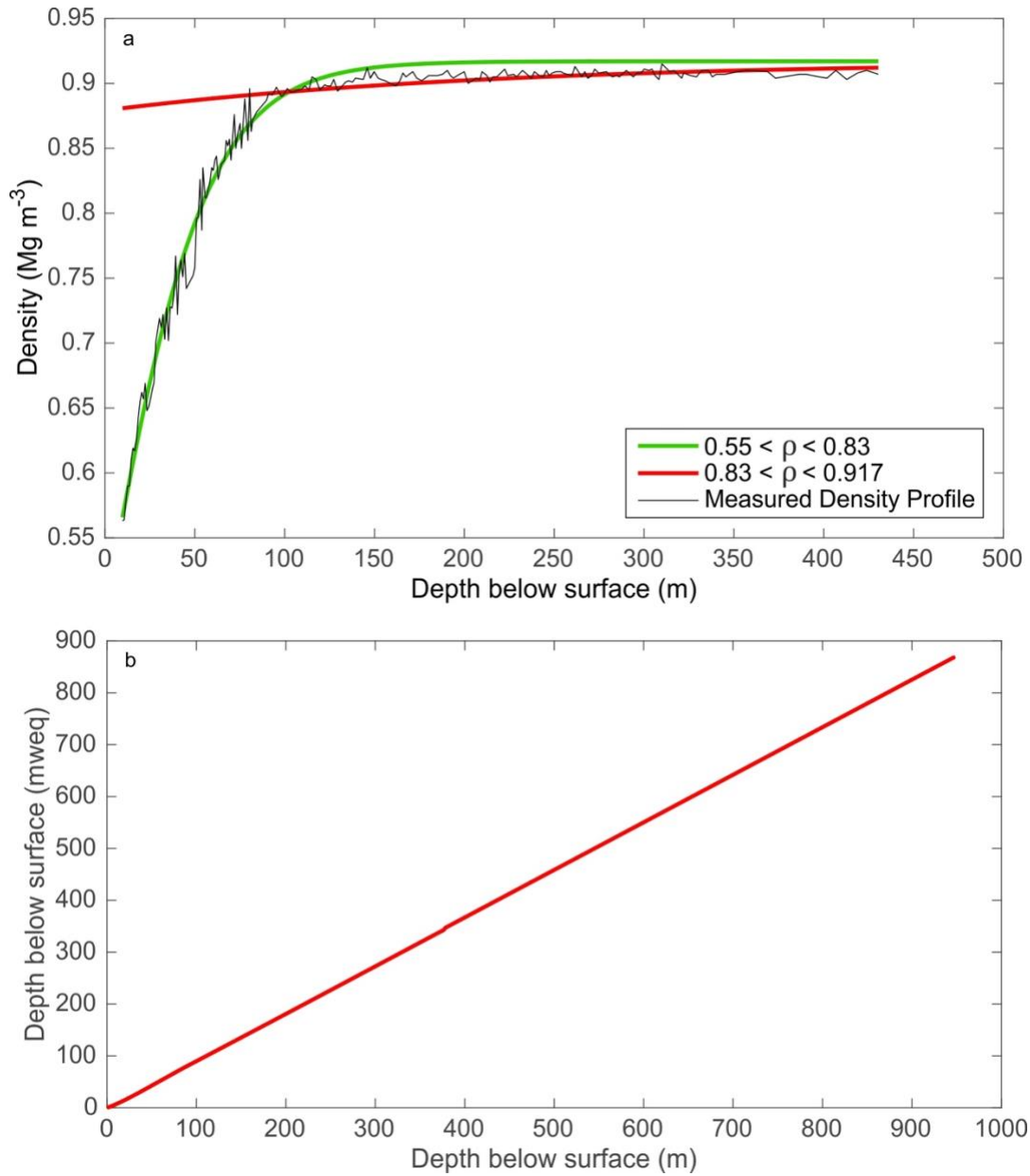


Figure A1.01: (a) Density Reconstruction for the upper 450 m of the BI ice core; (b) Depth below the surface in snow and water-equivalent units. Raw density (black line) measured prior to this research project).

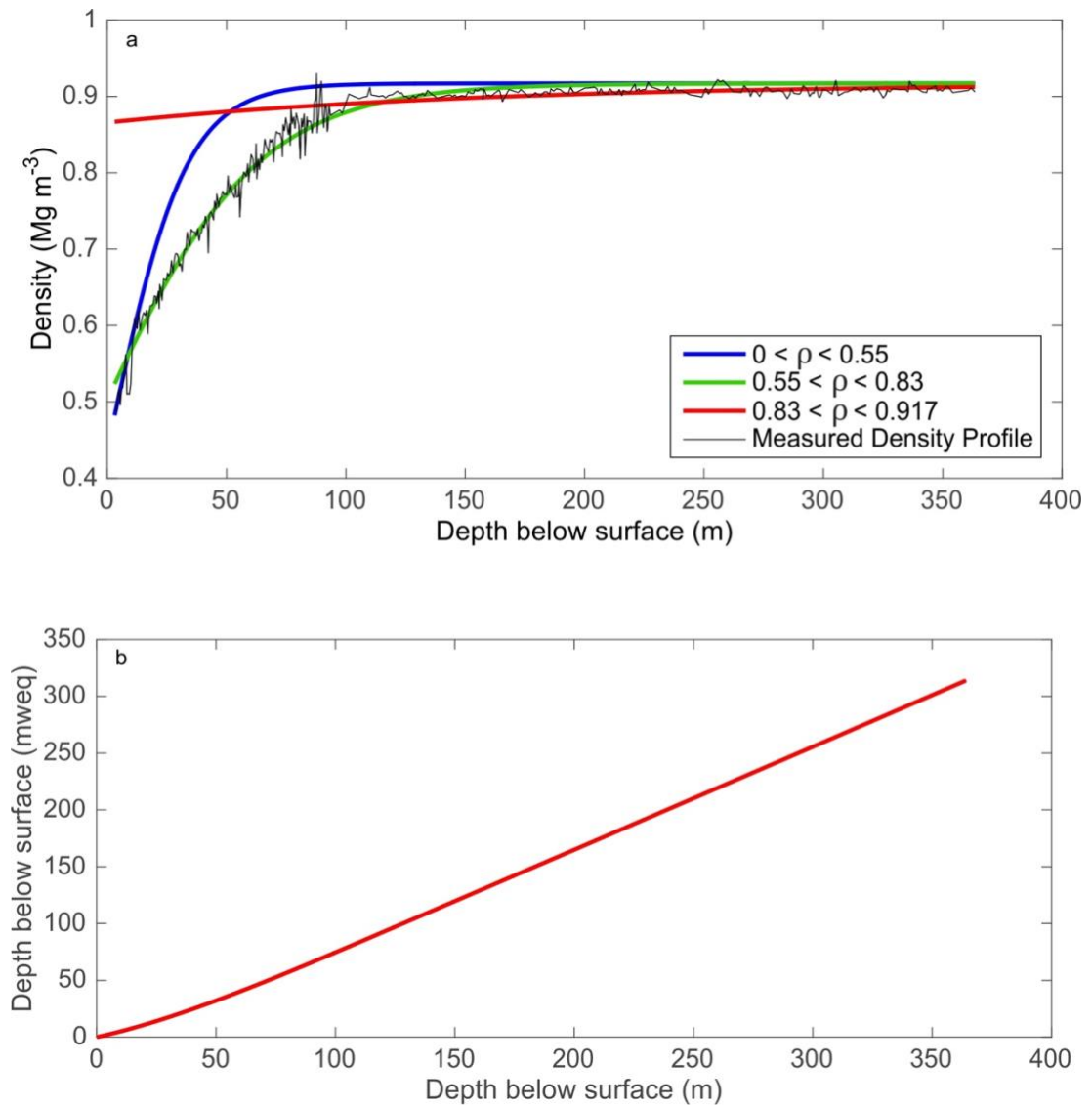


Figure A1.02: (a) Density Reconstruction for the JRI ice core; (b) Depth below the surface in snow and water-equivalent units. Raw density (black line) measured prior to this research project.

A1.1.2 Temperature Reconstructions

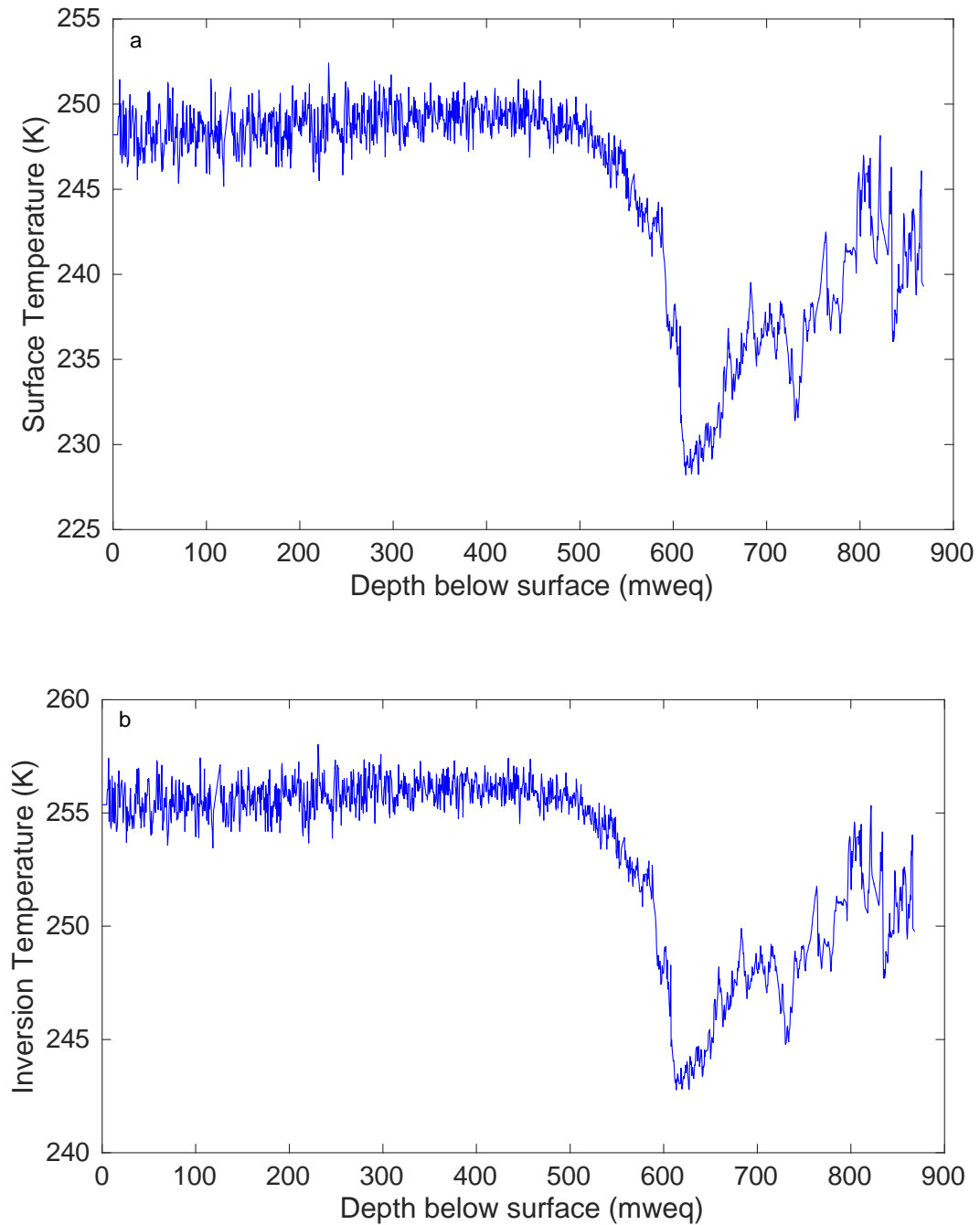


Figure A1.03: (a) Surface Temperature reconstruction using eq. 2.03 (stable water isotope profile measured prior to this project); (b) Inversion Temperature for the BI ice core reconstruction using eq. 2.04 (stable water isotope profile measured prior to this project).

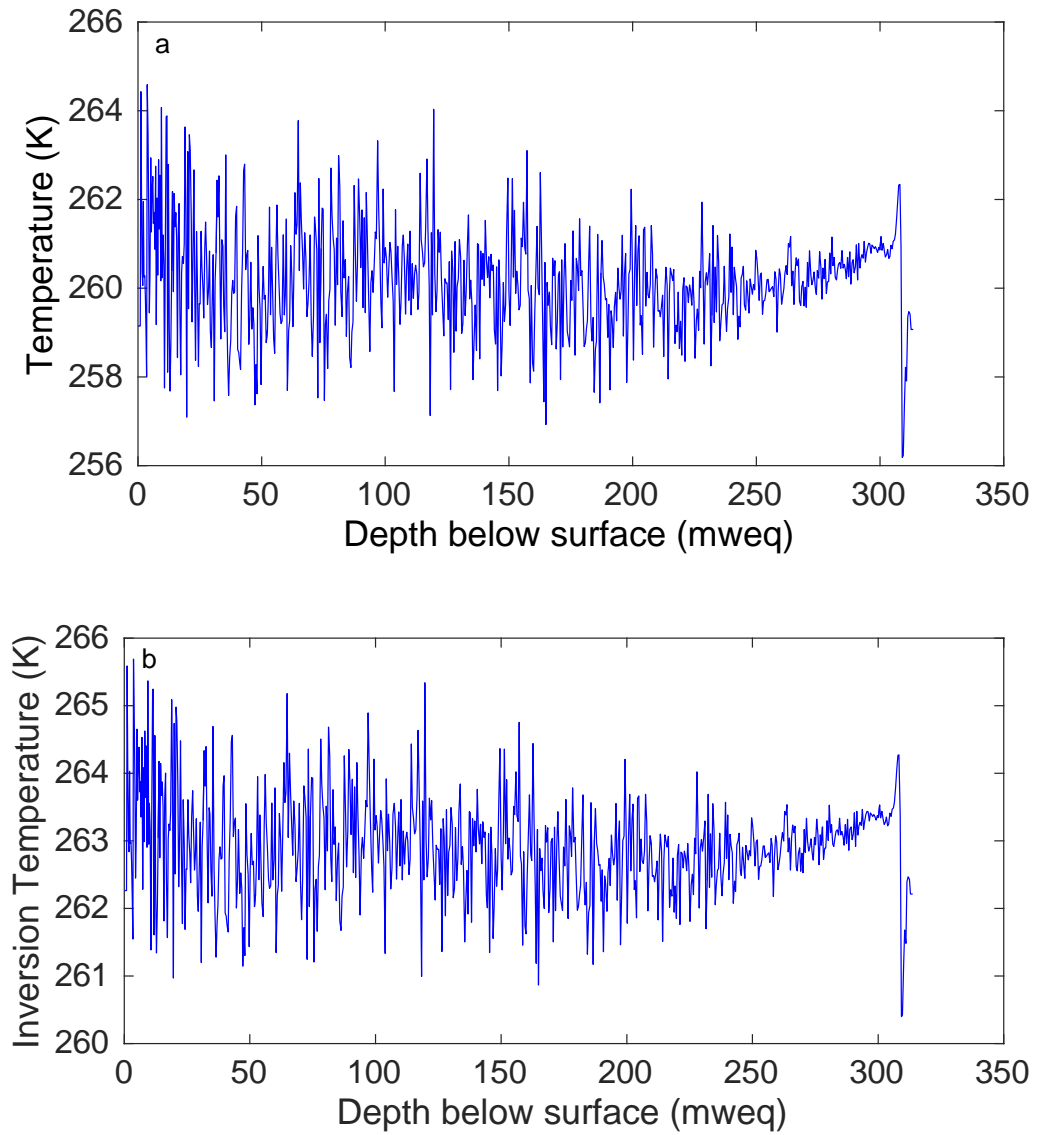


Figure A1.04(a) Surface Temperature reconstruction using eq. 2.03 (stable water isotope profile measured prior to this project); (b) Inversion Temperature for the JRI ice core reconstruction using eq. 2.04 (stable water isotope profile measured prior to this project).

## A1.1.3 Accumulation

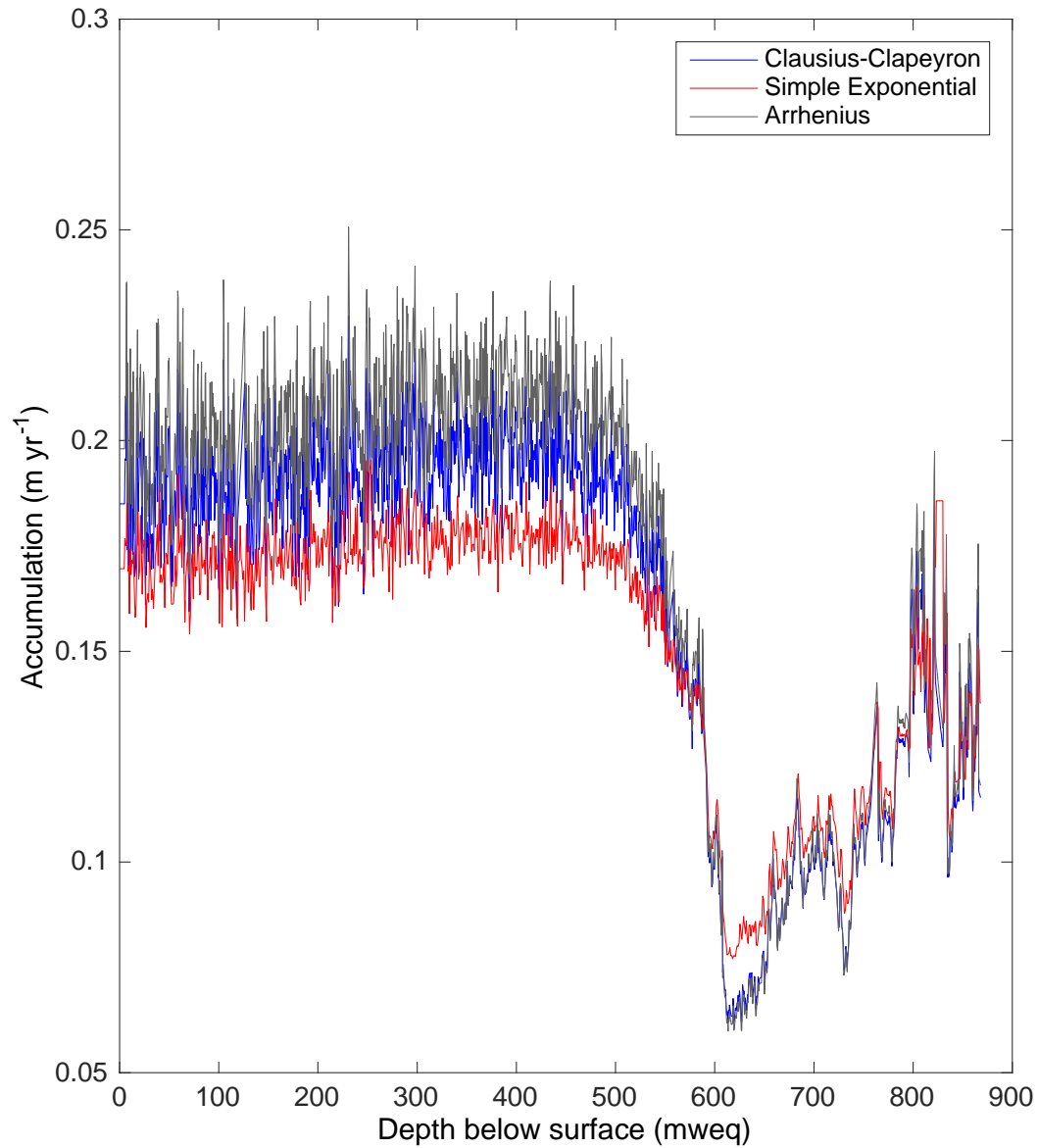


Figure A1.05: Accumulation reconstructions for the BI ice core. Accumulation reconstructions use stable water isotope profiles obtained separate to this research project.

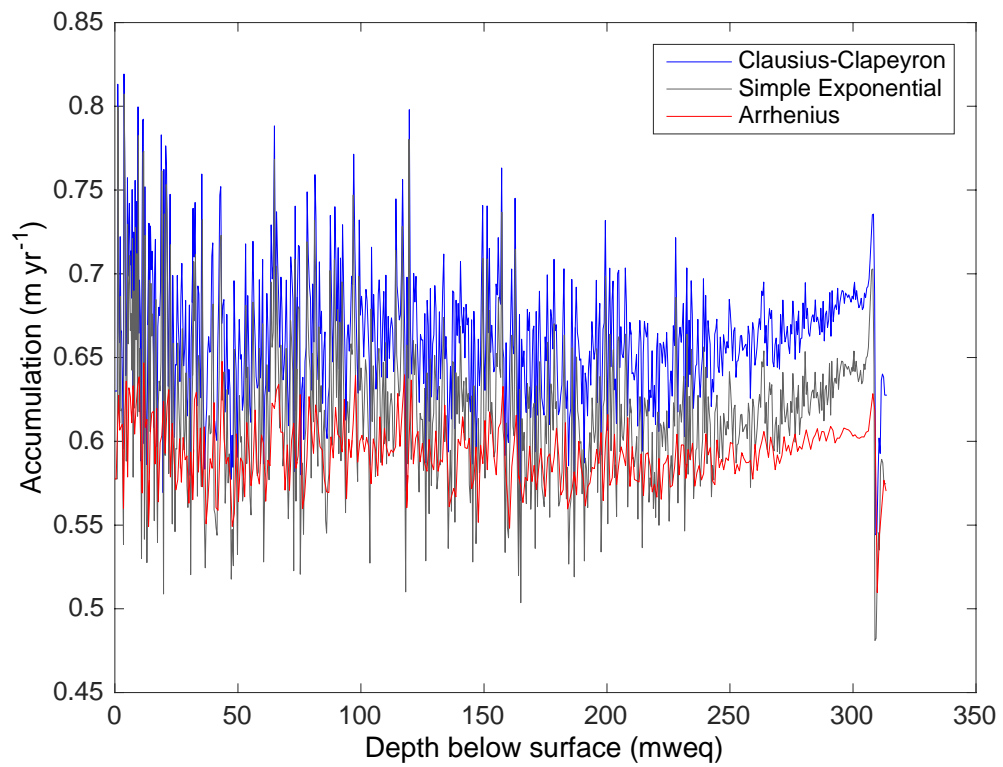


Figure A1.06: Accumulation reconstructions for the JRI ice core. Accumulation reconstructions use stable water isotope profiles obtained separate to this research project.

A1.1.4 Thinning Functions

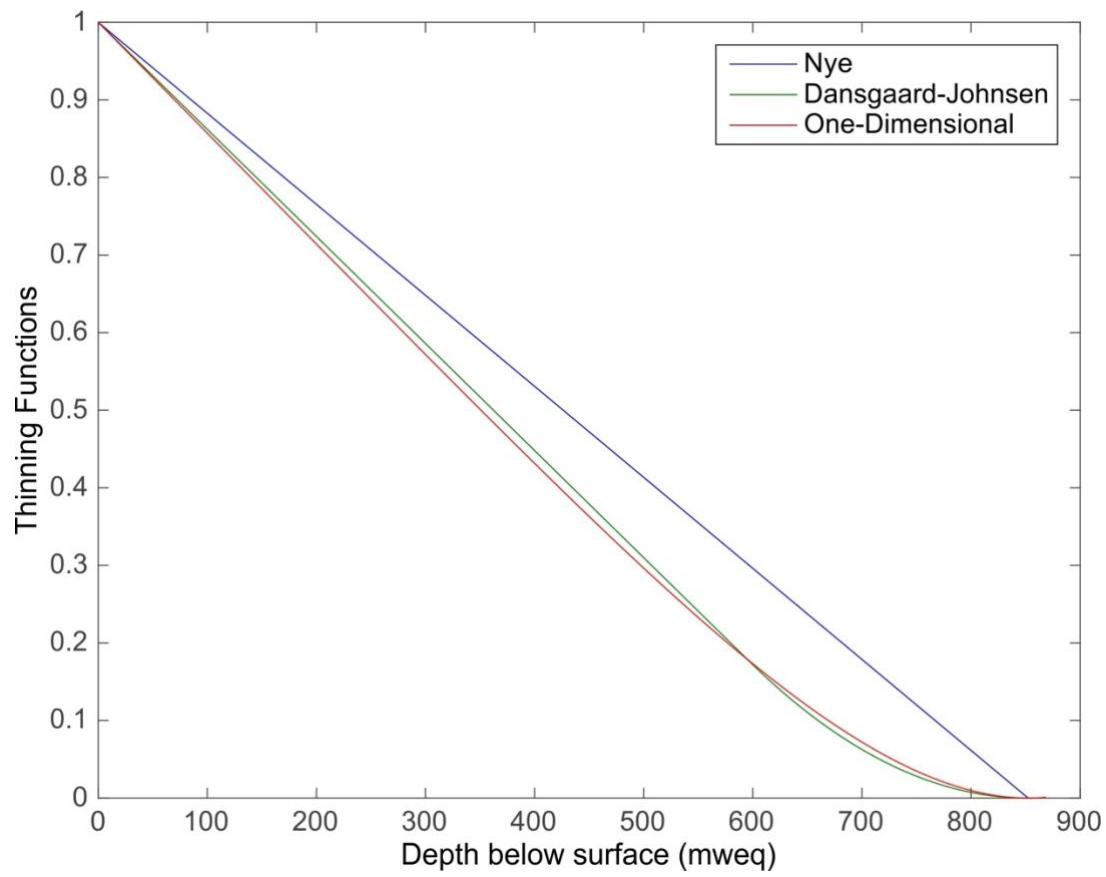


Figure A1.07: Thinning Functions for the BI ice core.

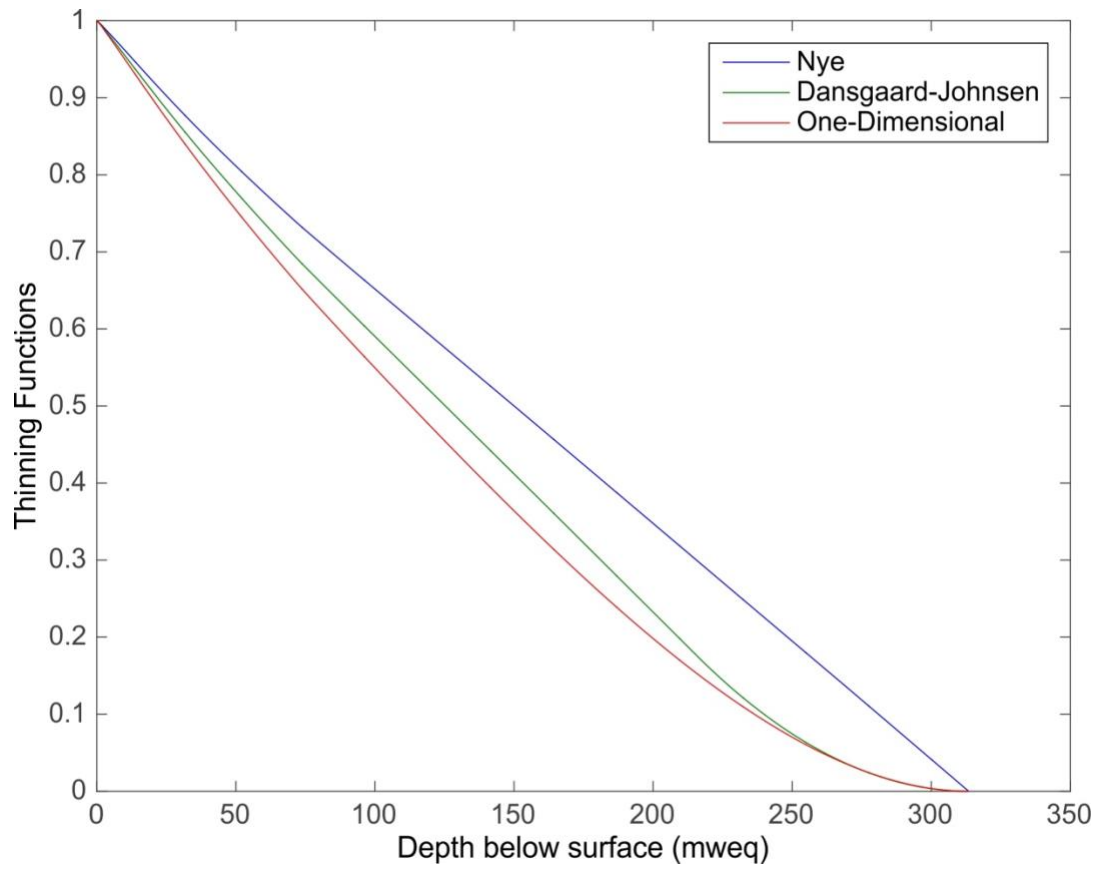


Figure A1.08: Thinning Functions for the JRI ice core.

A1.1.5 Age-Depth Profiles

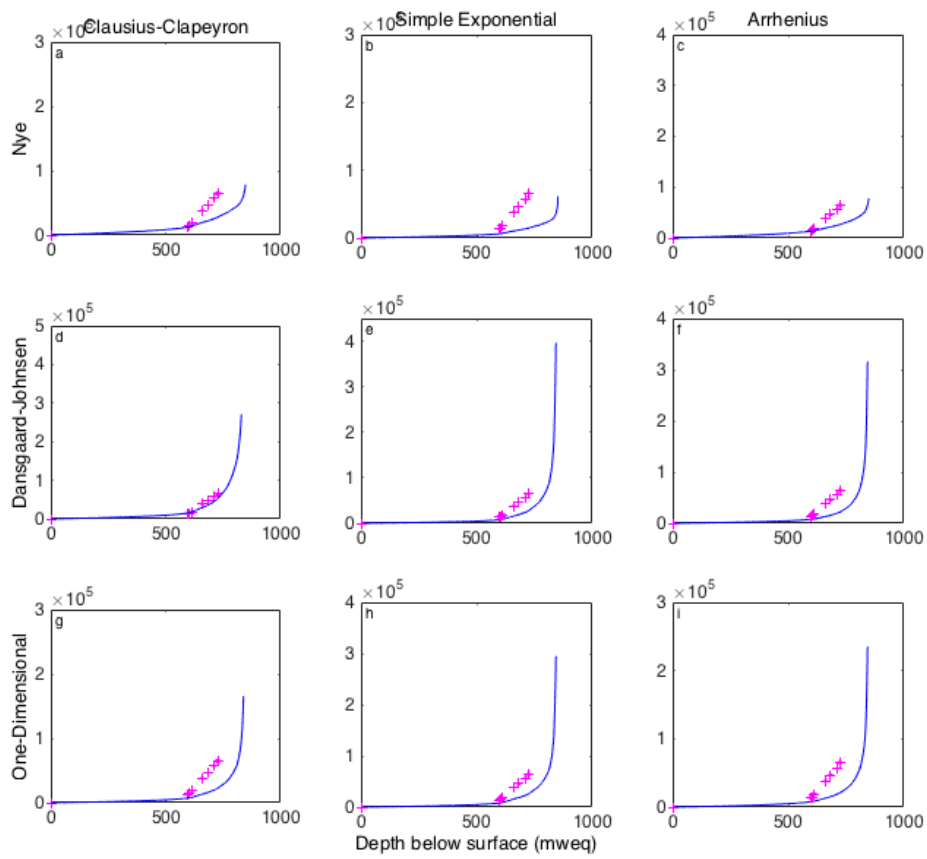


Figure A1.09: Age-Depth Combinations using all forward accumulation and thinning reconstructions for the BI ice core. Figure laid out as a table.

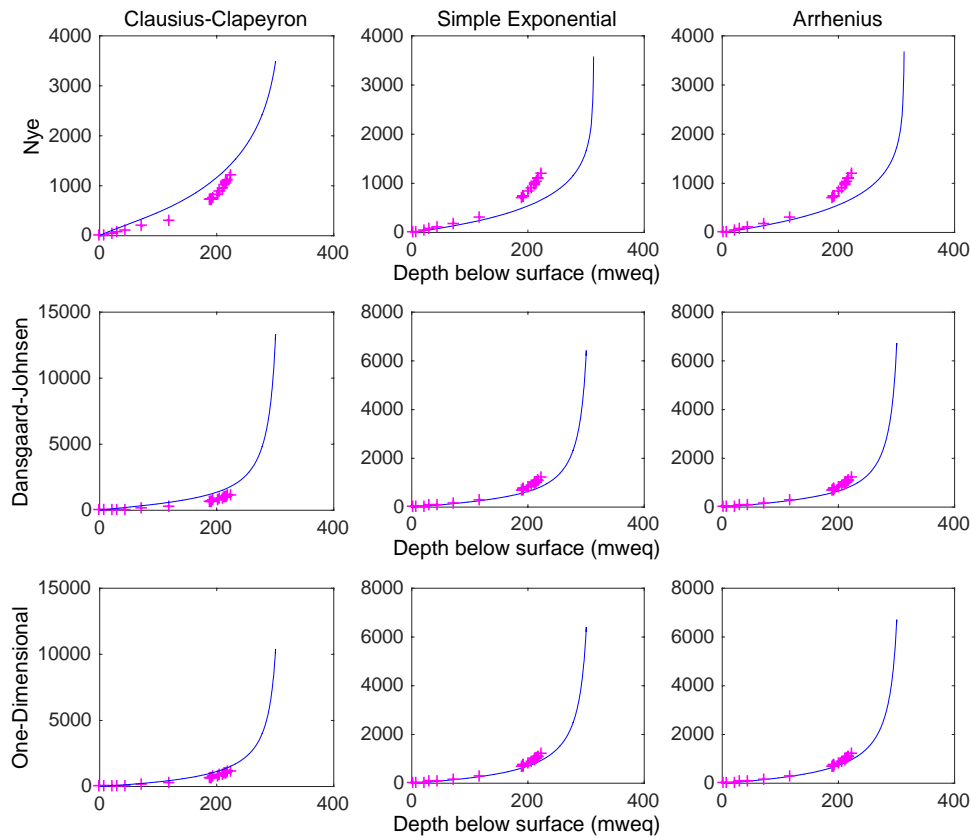


Figure A1.10: Age-Depth Combinations using all forward accumulation and thinning reconstructions for the JRI ice core. Figure laid out as a table.

### A1.2 Constrained Profiles

Following the forward model combinations, the JRI and BI ice core records have been reconstructed using three inverse approaches. Two additional accumulation and age-depth reconstructions employed a GCM and *in situ* pRES measurements, and have been included in the chapter. However, this data is only available for the FP site, and is not presented in the appendix for BI and JRI.

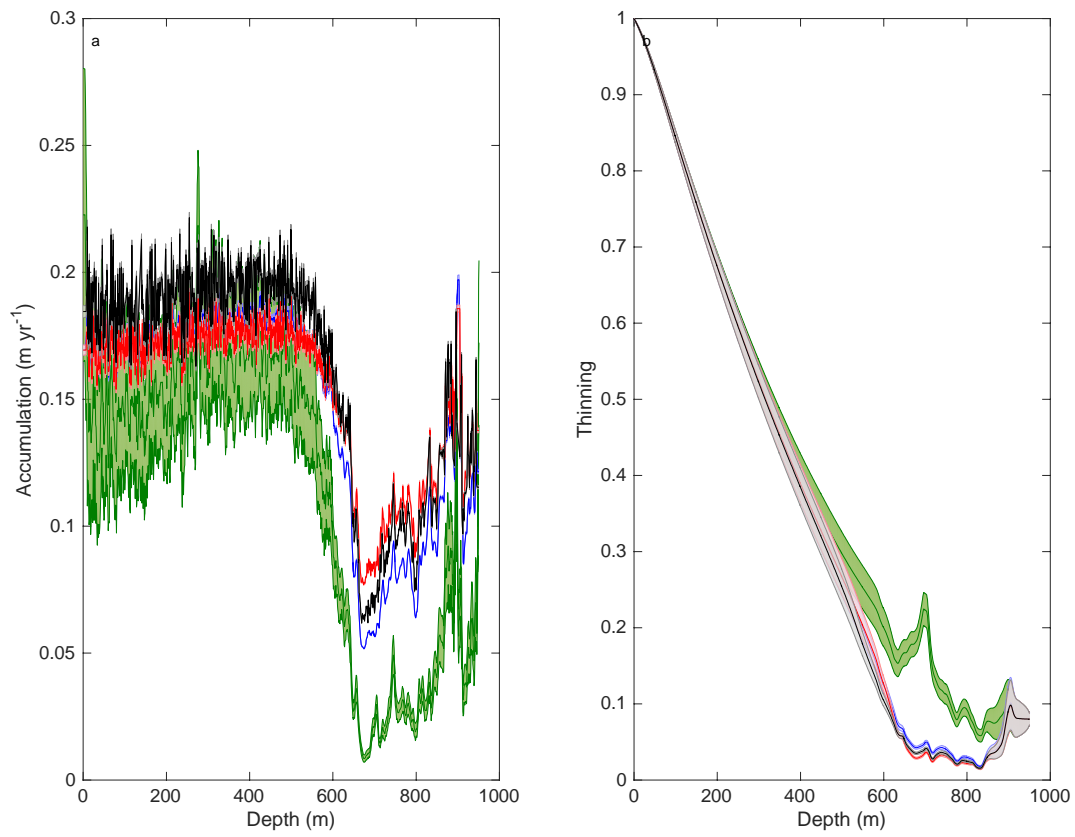
A1.2.1 *IceChrono*

Figure A1.11: Accumulation and thinning reconstructions using the *IceChrono* model and prescribed accumulation functions at 95% confidence interval for BI. Different initial accumulation profiles have been used as an input for this figure and are colour-coordinated as black: *Clausius-Clapeyron*; blue: *Simple Exponential*; red: *Arrhenius*; green: *IceChrono*.

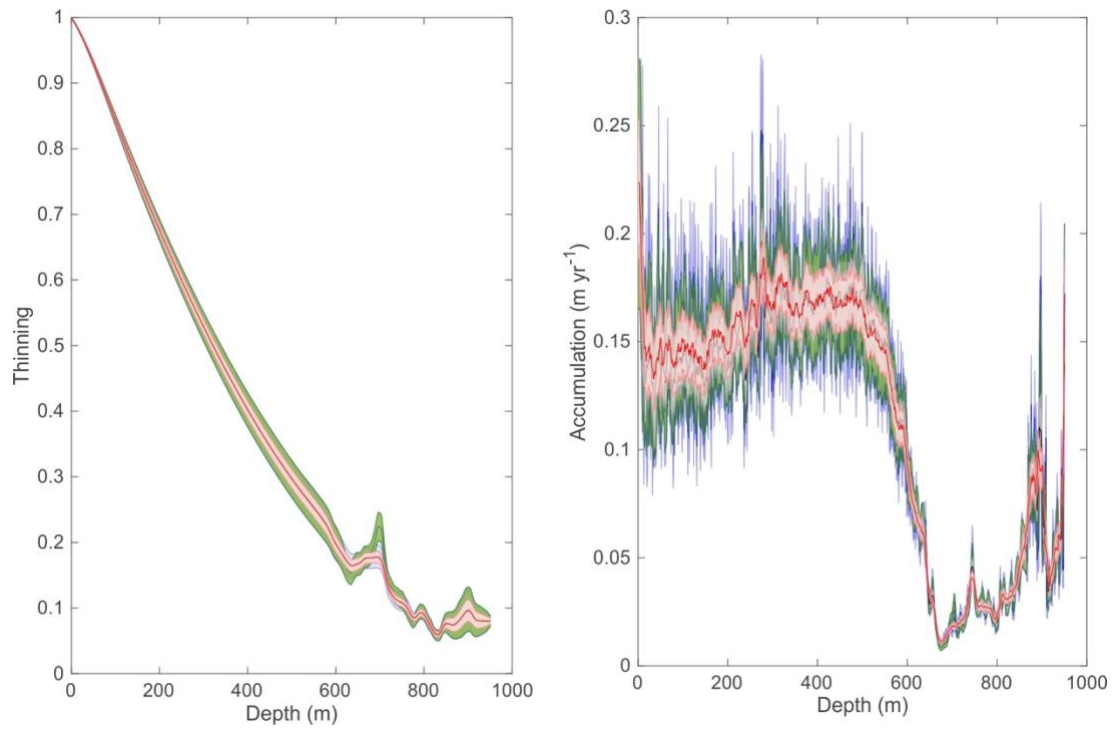


Figure A1.12: Thinning and accumulation reconstructions using the IceChrono model with prescribed thinning functions at 95% confidence interval for the BI ice core. Different initial thinning profiles have been used as an input for this figure and are colour-coordinated as red: Nye; blue: Dansgaard-Johnsen; black: One-Dimensional; green: IceChrono.

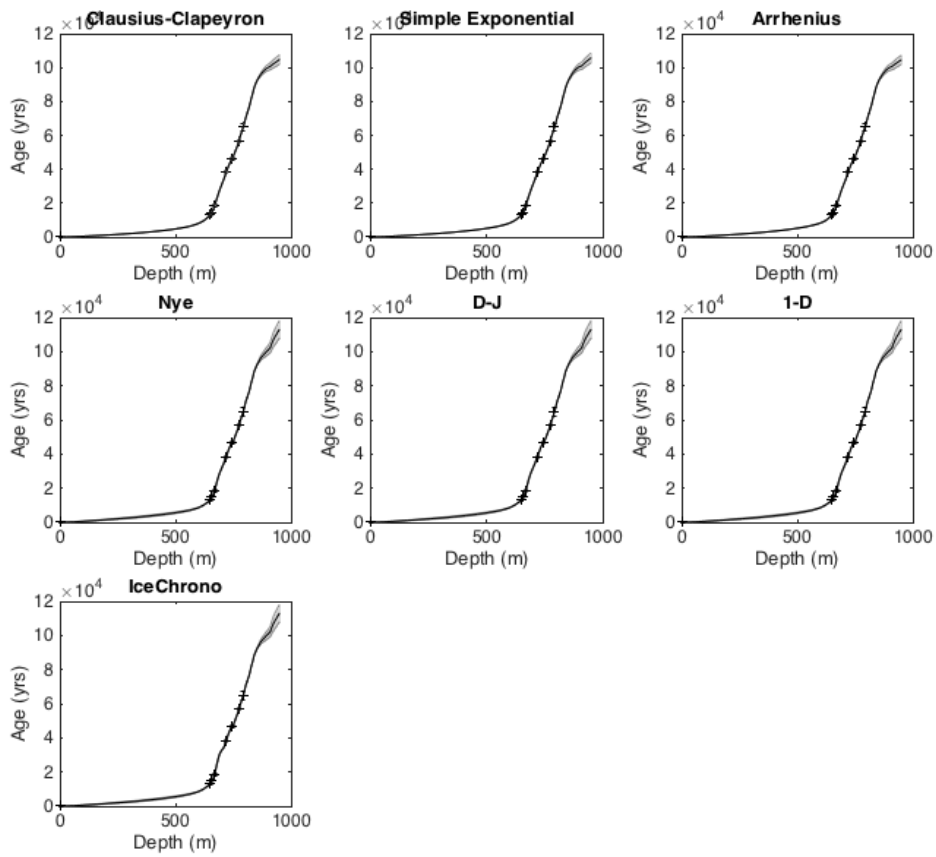


Figure A1.13: Age-depth profiles with the uncertainty (pale shade) and age horizons marked (black crosses) for the BI ice core.

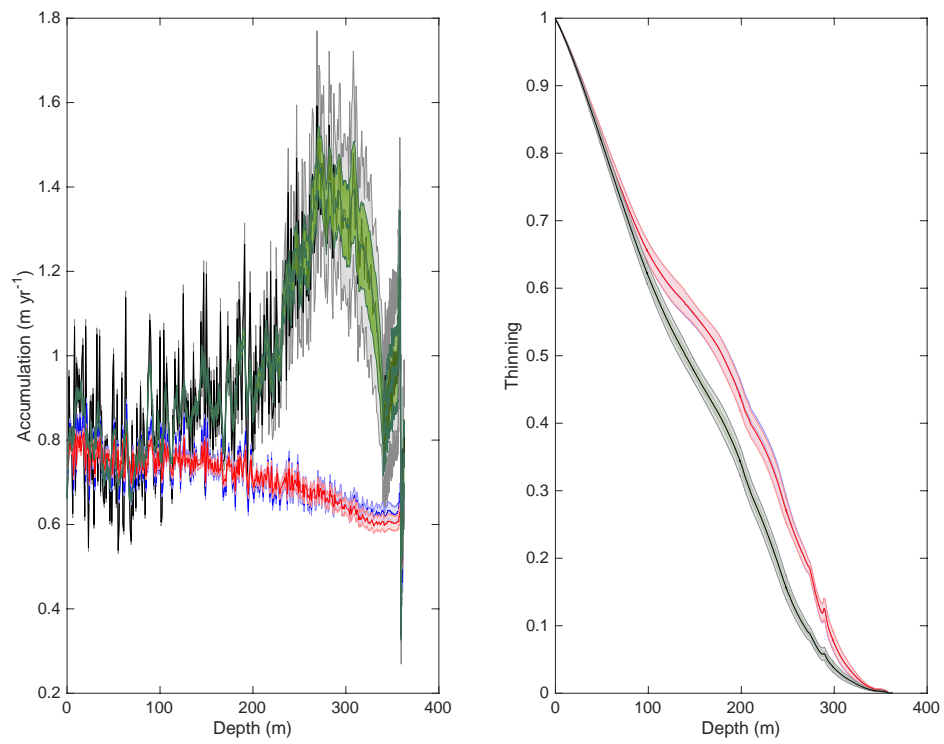
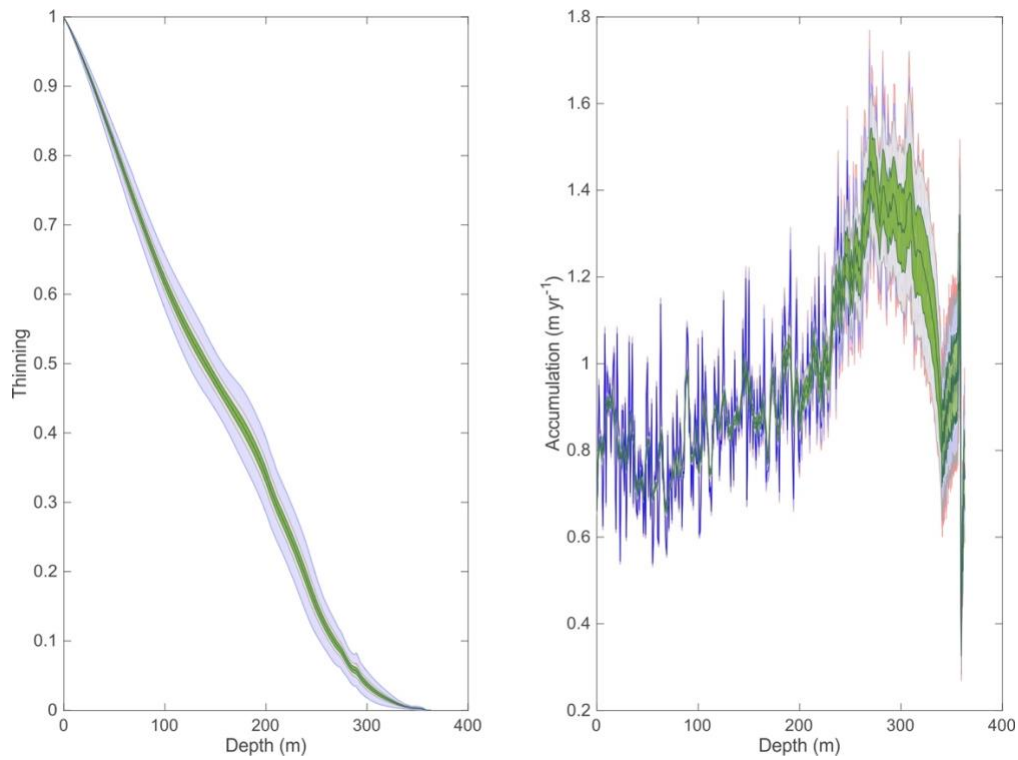


Figure A1.14: Accumulation and thinning reconstructions using the IceChrono model and prescribed accumulation functions at 95% confidence interval for JRI. Different initial accumulation profiles have been used as an input for this figure and are colour-coordinated as black: Clausius-Clapeyron; blue: Simple Exponential; red: Arrhenius; green: IceChrono.

## Appendix 1



*Figure A1.15: Thinning and accumulation reconstructions using the IceChrono model and a prescribed thinning function at 95% confidence interval for the JRI ice core. Different initial profiles have been used as an input for this figure and are colour-coordinated as red: Nye; blue: Dansgaard-Johnsen; black: One-Dimensional; green: IceChrono.*

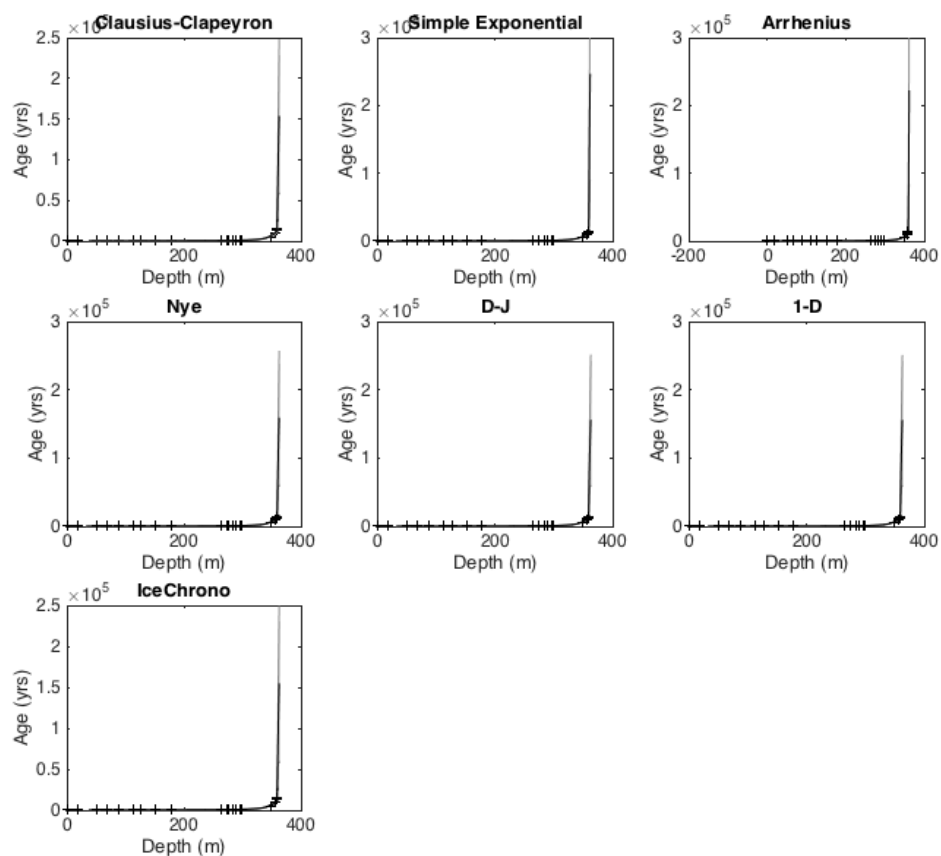
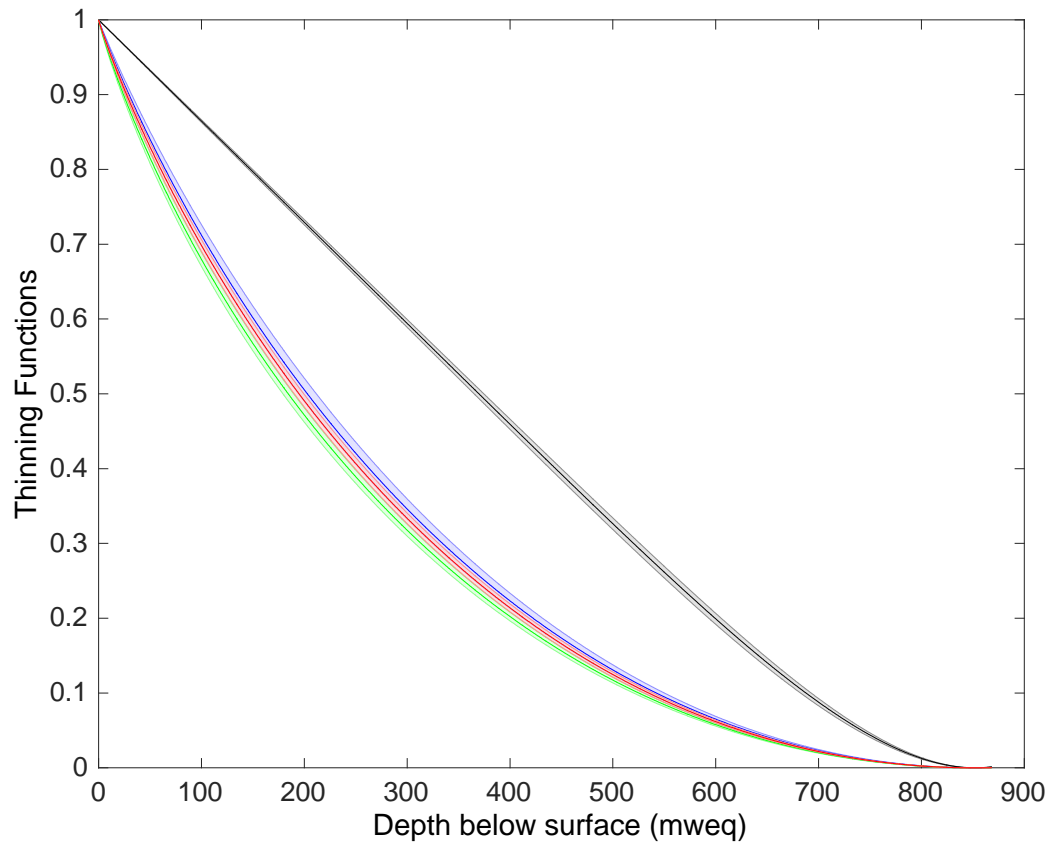


Figure A1.16: Age-depth profiles with the uncertainty (pale shade) and age horizons marked (black crosses) for the JRI ice core.

### A1.2.2 Directed Search

Table A1.03: Values of the  $p$ -parameter and the subsequent calculation of Glen's exponent using the Direct Search model for BI.

Accumulation	$p$ -value	$n$ -value
Clausius-Clapeyron	-0.69	-1.23
Simple Exponential	-0.61	-1.19
Arrhenius	-0.79	-1.37
IceChrono	5.53	4.95



*Figure A1.17: Reconstructed thinning functions for the BI ice core using the Direct Search model. Each scenario uses a different initial accumulation profile: red: Clausius-Clapeyron; blue: Simple Exponential; green: Arrhenius; black: IceChrono. Each scenario has an associated uncertainty presented in a pale shade of the presented colour.*

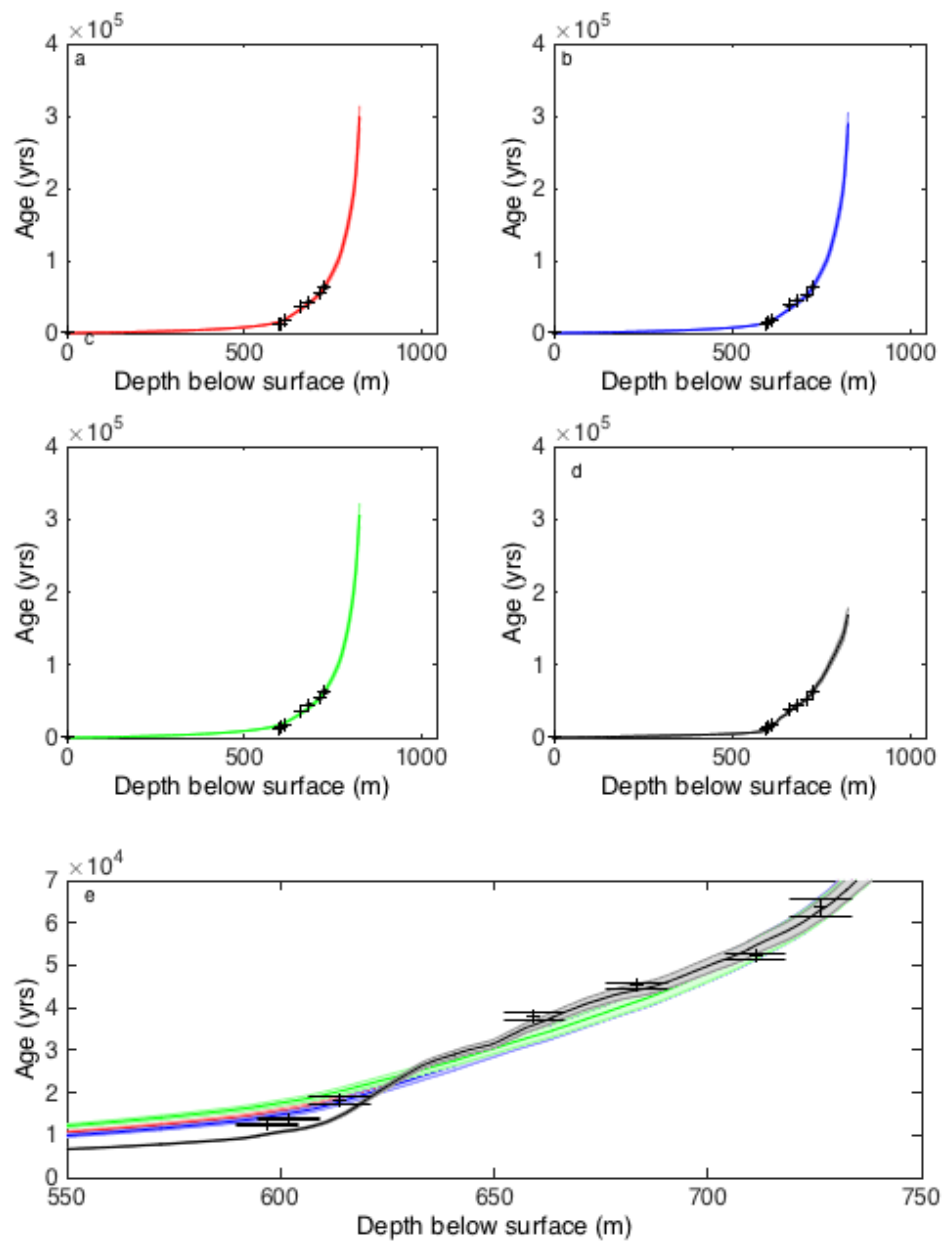


Figure A1.18: Age-Depth reconstructions for the BI ice core using the Direct Search model. Each scenario uses a different initial accumulation profile: red: Clausius-Clapeyron; blue: Simple Exponential; green: Arrhenius; black: IceChrono. Each scenario has an associated uncertainty presented in a pale shade of the presented colour; known-age horizons and the associated uncertainty are presented as black crosses.

Table A1.04: Values of the  $p$ -parameter and the subsequent calculation of Glen's exponent using the Direct Search model for JRI.

Accumulation	$p$ -value	$n$ -value
Clausius-Clapeyron	8.58	9.28
Simple Exponential	3.36	4.06
Arrhenius	4.32	5.02
IceChrono	1.78	2.47

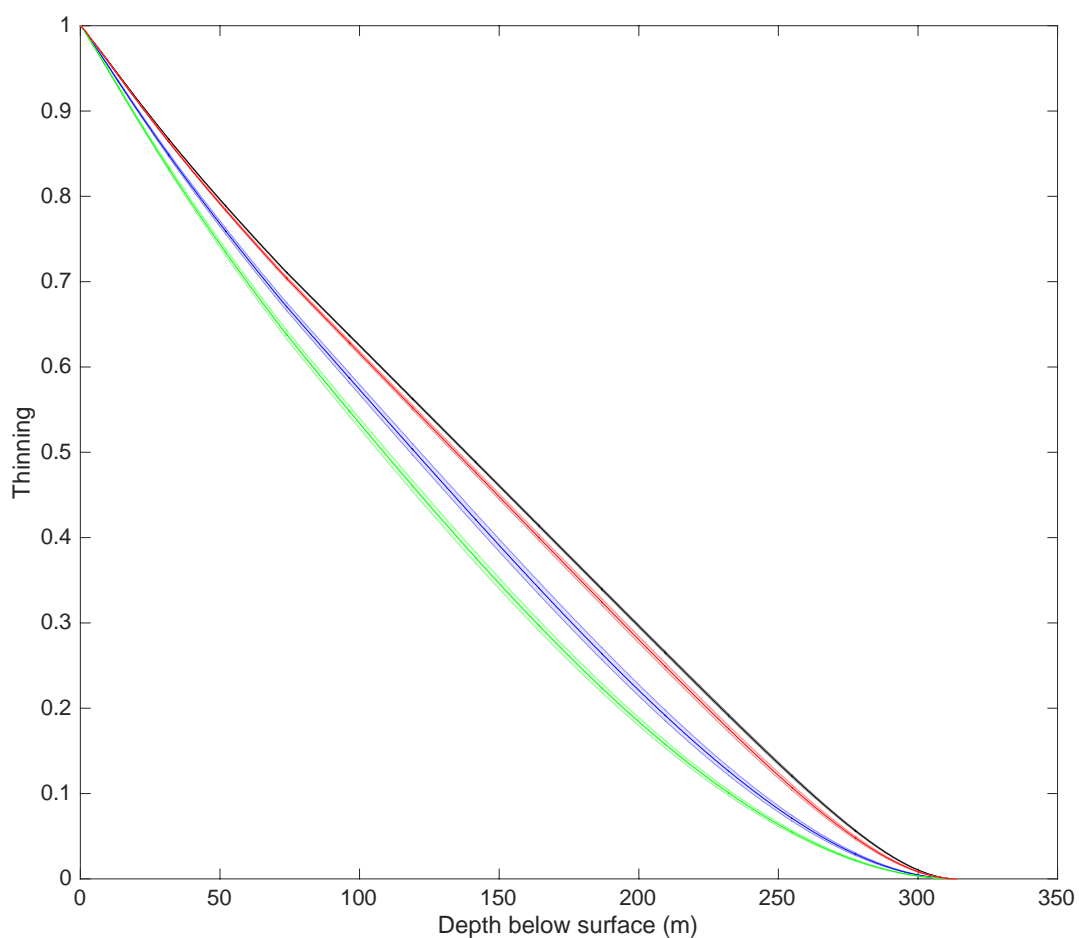


Figure A1.19: Reconstructed thinning functions for the JRI ice core using the Direct Search model. Each scenario uses a different initial accumulation profile: red: Clausius-Clapeyron; blue: Simple Exponential; green: Arrhenius; black: IceChrono. Each scenario has an associated uncertainty presented in a pale shade of the presented colour.

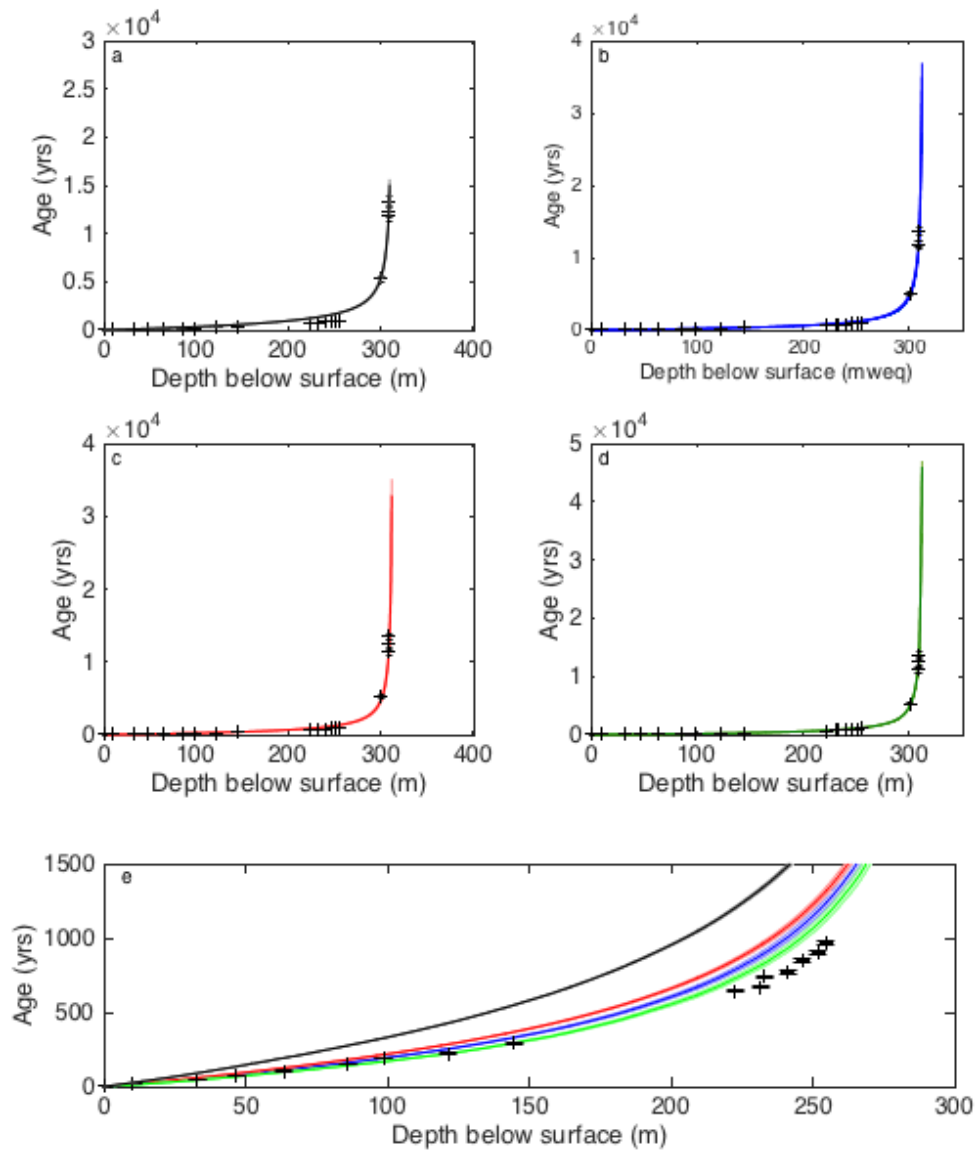


Figure A1.20: Age-Depth reconstructions for the JRI ice core using the Direct Search model. Each scenario uses a different initial accumulation profile: black: Clausius-Clapeyron; blue: Simple Exponential; red: Arrhenius; green: IceChrono. Each scenario has an associated uncertainty presented in a pale shade of the presented colour; known-age horizons and the associated uncertainty are presented as black crosses.

## A1.2.3 Optimised Accumulation and Thinning

Table A1.05: Optimised values for the  $p$ -parameter and  $n$  values using different initial accumulation reconstructions on the Optimised Accumulation and Thinning model for Berkner Island.

Accumulation	$p$ -value	$n$ -value
Clausius-Clapeyron	$-0.57 \pm 0.18$	$-1.12 \pm 0.18$
Simple Exponential	$-0.04 \pm 0.30$	$-0.97 \pm 0.30$
Arrhenius	$-0.53 \pm 0.13$	$-1.10 \pm 0.13$

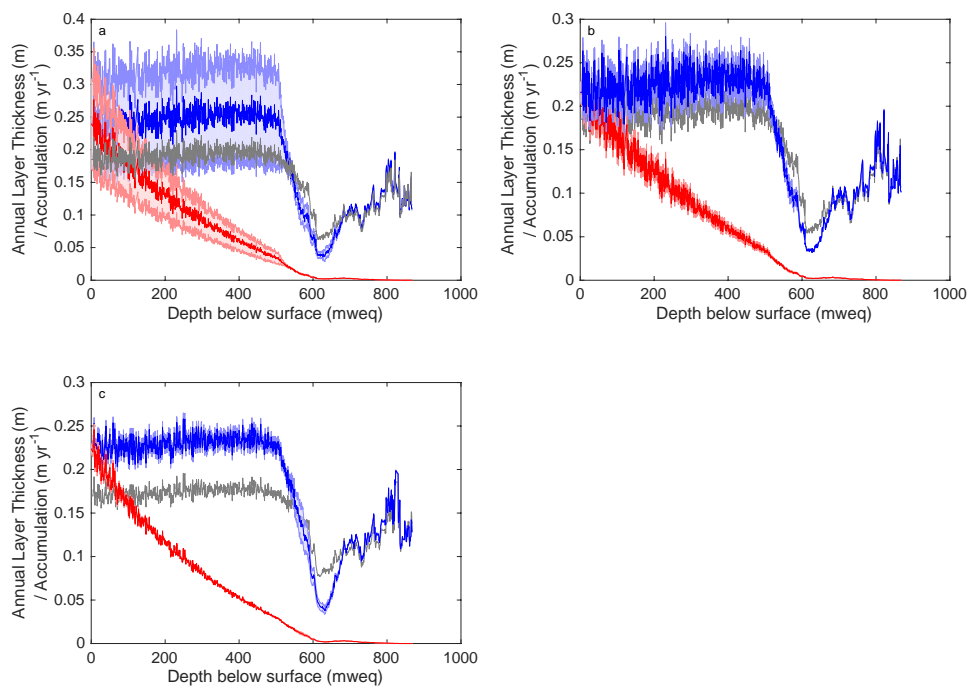


Figure A1.21: Original (red with the confidence interval in pale red) and present-day annual layer thickness (blue with the confidence interval in pale blue) reconstructions using different initial accumulation profiles and perturbed using the Optimised Accumulation and Thinning model for BI. Initial accumulation history (grey) from top left: (a) Clausius-Clapeyron, (b) Simple Exponential, and (c) Arrhenius.

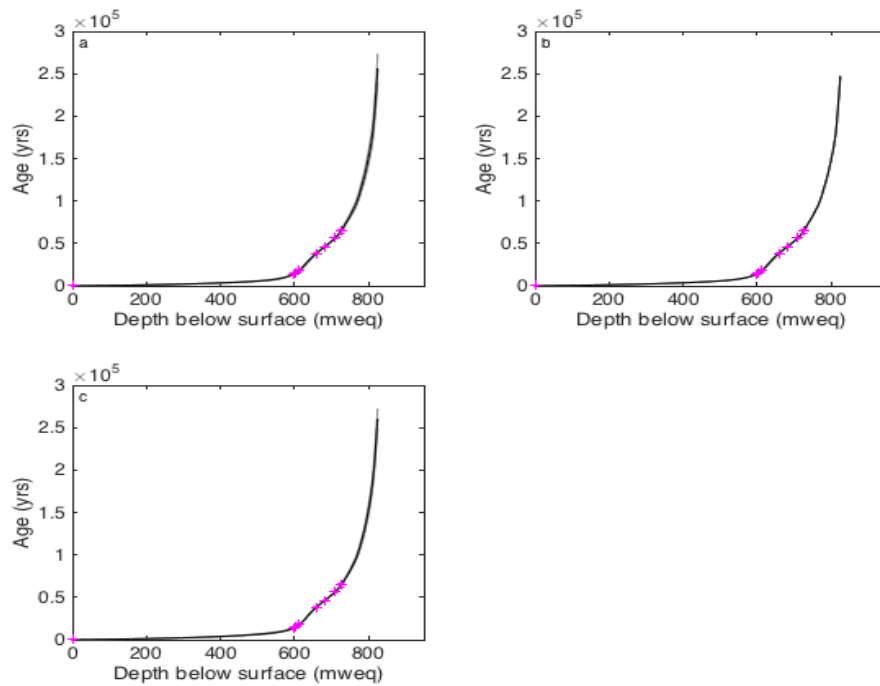


Figure A1.22: Age-depth reconstructions using different initial accumulation profiles and optimised using the Optimised Accumulation and Thinning model for BI, with known-age horizons in pink crosses. Initial accumulation history from top left: (a) Clausius-Clapeyron, (b) Simple Exponential, and (c) Arrhenius.

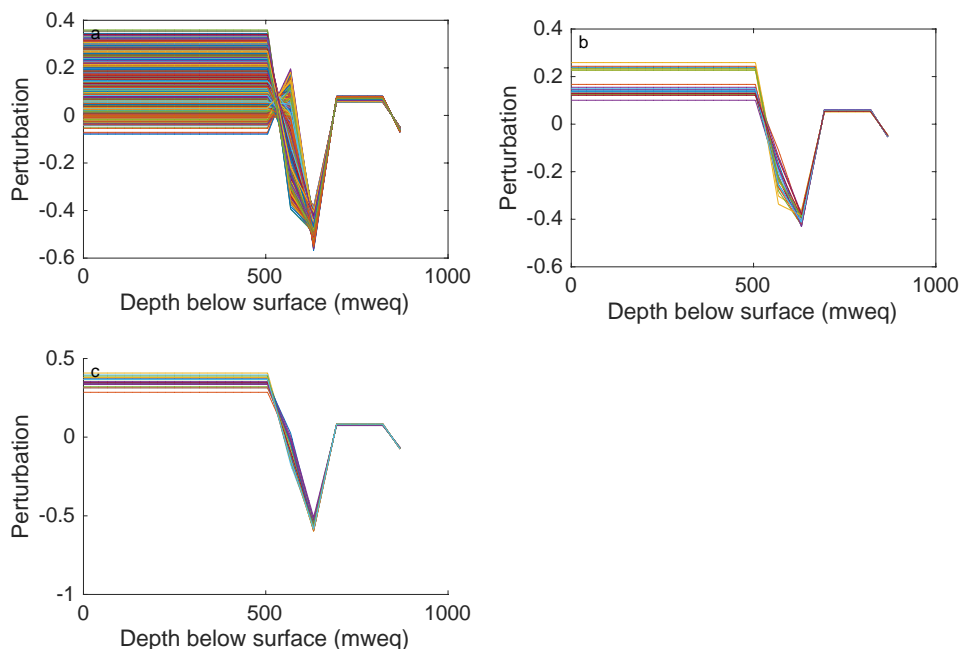


Figure A1.23: Perturbation profiles for 100 possible scenarios for the BI ice core using the Optimised Accumulation and Thinning model. Model scenarios use an initial accumulation profile using (a) Clausius-Clapeyron; (b) Simple Exponential; (c) Arrhenius relationships.

Table A1.06: Optimised values for the  $p$ -parameter and  $n$  value using different initial accumulation reconstructions on the Optimised Accumulation and Thinning model for James Ross Island.

Accumulation	$p$ -value	$n$ -value
Clausius-Clapeyron	$2.30 \pm 4.20$	$3.00 \pm 4.20$
Simple Exponential	$4.48 \pm 0.70$	$5.19 \pm 0.70$
Arrhenius	$4.77 \pm 0.99$	$5.47 \pm 0.99$

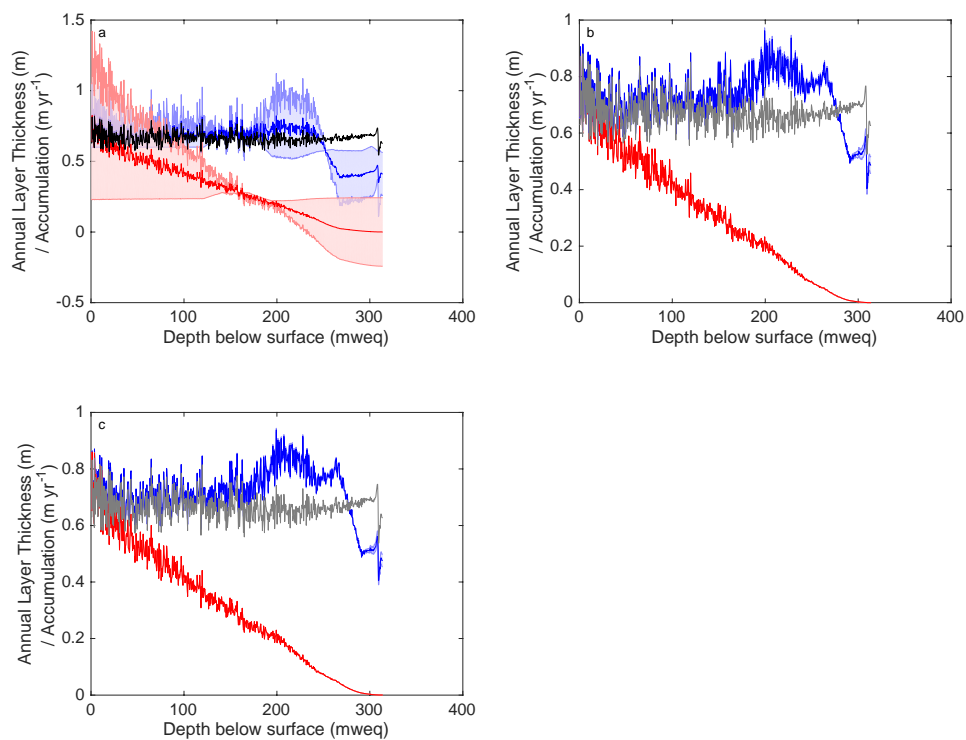


Figure A1.24: Original (red with the confidence interval in pale red) and present-day annual layer thickness (blue with the confidence interval in pale blue) reconstructions using different initial accumulation profiles and perturbed using the Optimised Accumulation and Thinning model for JRI. Initial accumulation history (grey) from top left: (a) Clausius-Clapeyron, (b) Simple Exponential, and (c) Arrhenius.

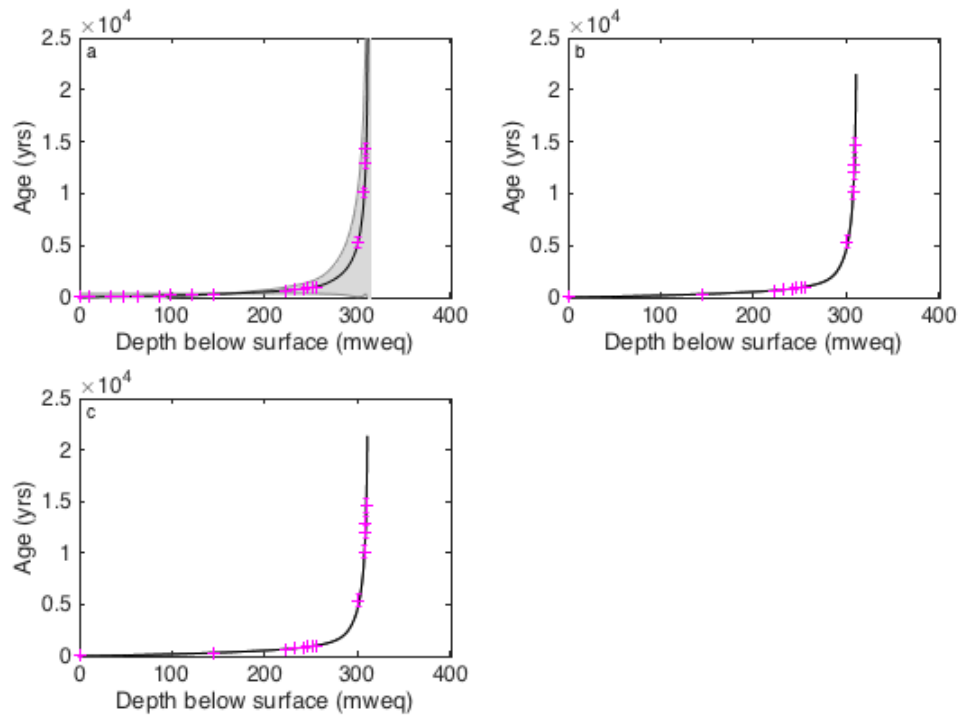


Figure A1.25: Age-depth reconstructions using different initial accumulation profiles and optimised using the Optimised Accumulation and Thinning model for JRI, with known-age horizons in pink crosses. Initial accumulation history from top left: (a) Clausius-Clapeyron; (b) Simple Exponential; (c) Arrhenius relationships.

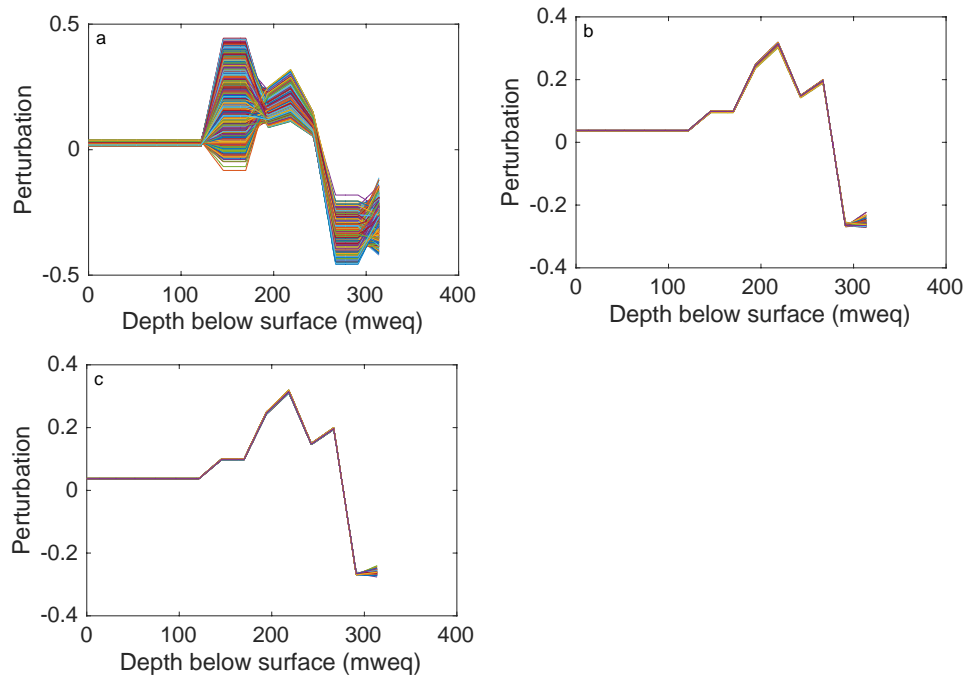


Figure A1.26: Perturbation profiles for 100 possible scenarios for the JRI ice core using the Optimised Accumulation and Thinning model. Model scenarios use an initial accumulation profile using (a) Clausius-Clapeyron; (b) Simple Exponential; (c) Arrhenius relationships.

## References

- Abram, N.J., Mulvaney, R., Arrowsmith, C. 2011. Environmental signals in a highly resolved ice core from James Ross Island, Antarctica. *Journal of Geophysical Research – Atmospheres*, **116**, doi: 10.1029/2011JD16147.
- Abram, N.J., Wolff, E.W., Curran, M.A.J. 2013. A review of sea ice proxy information from polar ice cores. *Quaternary Science Reviews*, **79**, pp. 168-183.
- Ahn, J., Wahlen M., Deck, B. 2003. Atmospheric CO<sub>2</sub> Trapped in the Ice Core from Siple Dome, Antarctica. Boulder, CO: National Snow and Ice Data Center. <http://dx.doi.org/10.7265/N5N877Q9> (last accessed 6/12/16).
- Alley, R.B., 1987. Firn Densification by Grain-Boundary Sliding: A First Model. *Journal de Physique*, **48**, 249-256.
- Arnaud, L., Barnola, J-M., and Duval, P., 2000. Physical modelling of the densification of snow/firn and ice in the upper part of the polar ice sheets. In Hondoh, T (ed.) *Physics of Ice Core Records*, Saporro, Hokkaido University Press, pp. 285-305.
- Arrowsmith, P. 1987. Laser Ablation of Solids for Elemental Analysis by Inductively Coupled Plasma Mass Spectrometry. *Anal. Chem.*, **59**, pp. 1437-1444.
- ASOC, 2013. Update: The Future of the West Antarctic Ice Sheet. *XXXVI Antarctic Treat Consultative Meeting*, Brussels.
- Augustin, L., Motoyama, H., Willhelms, F., Johnsen, S., Hansen, S., Talalay, P., Vasiliev, N., 2007. Drilling comparison in 'warm ice' and drill design comparison. *Ann. Glaciol.* **47**, 73-78.
- Bamber, J.L., Riva, R.E.M., Vermeersen, B.L.A., Le Brocq, A. 2009 Reassessment of the Potential Sea-Level Rise from a Collapse of the West Antarctic Ice Sheet. *Science*, **324**, pp. 901-903.
- Barnola, J.M., Raynaud, D., Korotkevich, Y.S., Lorius, C. 1987. Vostok ice core provides a 160,000-year record of atmospheric CO<sub>2</sub>. *Nature*, **329**, pp. 408-414.
- Barnola, J-M., Pimienta, P., Raynaud, D., and Korotkevich, Y.S., 1991. CO<sub>2</sub>-climate relationship as deduced from the Vostok ice core: a re-examination based on new measurements and on a re-evaluation of the air dating. *Tellus*, **43B**, pp. 83-90.
- Barrand, N.E., Vaughan, D.G., Steiner, N., Tedesco, M., Kuipers Munneke, P., van den Broeke, M.R., Hosking, J.S. 2013. Trends in Antarctic Peninsula surface melting conditions from observations and regional climate modelling. *Journal of Geophysical Research: Earth Surface*, **118**, pp. 315-330.

## References

- Barrett, B.E., Nicholls, K.W., Murray, T., Smith, A.M., Vaughan, D.G., 2009. Rapid recent warming on Rutford Ice Stream, West Antarctica, from borehole thermometry. *Geophysical Research Letters*, **36**, DOI: 10.1029/2008GL036369.
- Bazin, L., Landais, A., Lemieux-Dudon, B., Toye Mahamadou Kele, H., Veres, D., Parrenin, F., Martinerie, P., Ritz, C., Capron, E., Lipenkov, V., Loutre, M.-F., Raynaud, D., Vinther, B., Svensson, A., Rasmussen, S.O., Severi, M., Blunier, T., Leuenberger, M., Fischer, H., Masson-Delmotte, V., Chappellaz, J., Wolff, E. 2012. An optimized multi-proxy, multi-site Antarctic ice and gas orbital chronology (AICC2012): 120-800ka. *Clim. Past*, **9**, pp. 1715-1731.
- Bea, F., Montero, P., Stroh, A., Baasner, J. 1996. Microanalysis of minerals by an Excimer UV-LA-ICP-MS system. *Chemical Geology*, **133**, pp. 145-156.
- Bentley, M.J., Fogwill, C.J., Le Brocq, A.M., Hubbard, A.L., Sugden, D.E., Dunai, T.J., Freeman, S.P.H.T. 2010. Deglacial history of the West Antarctic ice sheet in the Weddell Sea embayment: constraints on past ice volume change. *Geology*, **5**, pp. 411-414.
- Björck, S., Walker, M.J.C., Cwynar, L.C., Johnsen, S., Knudsen, K.-L., Lowe, J.J., Wohlfarth, B. and INTIMATE members. 1998. An event stratigraphy for the Last Termination in the North Atlantic region based on the Greenland ice core record: a proposal by the INTIMATE group. *Journal of Quaternary Science*, **13**, 283-292.
- Blaauw, M. 2010. Methods and code for 'classical' age-modelling of radiocarbon sequences. *Quaternary Geochronology*, **5**, pp. 512-518.
- Blockley, S.P.E., Lane, C.S., Hardiman, M., Rasmussen, S.O., Seierstad, I.K., Steffensen, J.P., Svensson, A., Lotter, A.F., Turney, C.S.M., Bronk Ramsey, C., INTIMATE members. 2012. Synchronisation of palaeoenvironmental records over the last 60,000 years, and an extended INTIMATE event stratigraphy to 48,000 b2k. *Quaternary Science Reviews*, **36**, 2-10.
- Blunier, T., Schwander, J., Stauffer, B., Stocker, T., Dällenbach, A., Indermühle, A., Tschumi, J. 1997. Timing of the Antarctic Cold Reversal and the atmospheric CO<sub>2</sub> increase with respect to the Younger Dryas event. *Geophysical Research Letters*, **24**, pp. 2683-2686.
- Blunier, T. and Schwander, J. 2000. Gas enclosure in ice: age difference and fractionation. In Hondoh, T. (ed.) *Physics of Ice Core Records*, Hokkaido University Press, Sapporo.
- Bracegirdle, T.J., Connolley, W.M., Turner, J. 2008. Antarctic climate change over the twenty first century. *Journal of Geophysical Research*, **113**, doi: 10.1029/2007JD008933.

- Bradley, S.L., Hindmarsh, R.C.A., Whitehouse, P.L., Bentley, M.J., King, M.A. 2015. Low post-glacial rebound rates in the Weddell Sea due to Late Holocene ice-sheet readvance. *Earth and Planetary Science Letters*, **413**, pp. 79-89.
- Broecker, W.S. 1998. Paleoccean circulation during the last deglaciation: a bipolar seesaw? *Palaeoceanography*, **13**, 119-121.
- Bronk Ramsey, C. 1995. Radiocarbon calibration and analysis of stratigraphy: the OxCal program. *Radiocarbon*, **37**, pp. 425-430.
- Buizert, C., Cuffey, K.M., Severinghaus, J.P., Baggenstos, D., Fudge, T.J., Steig, E.J., Markle, B.R., Winstrup, M., Rhodes, R.H., Brook, E.J., Sowers, T.A., Clow, G.D., Cheng, H., Edwards, R.L., Sigl, M., McConnell, J.R., Taylor, K.C. 2015. The WAIS Divide deep ice core WD2014 chronology – Part 1: Methane synchronization (68-31 ka BP) and the gas age-ice age difference. *Clim. Past*, **11**, pp. 153-173.
- Burgener, L., Rupper, S., Koenig, L., Forster, R., Christensen, W.F., Williams, J., Koutnik, M., Miege, C., Steig, E.J., Tingey, D., Keeler, D., Riley, L. 2013. An observed negative trend in West Antarctic accumulation rates from 1975 to 2010: Evidence from new observed and simulated records. *Journal of Geophysical Research*, **118**, pp. 4205-4216.
- Capron, E., Landais, A., Buiron, D., Cauquoin, A., Chappellaz, J., Debret, M., Jouzel, J., Leuenberger, M., Martinerie, P., Masson-Delmotte, V., Mulvaney, R., Parrenin, F., Prie, F., 2013. Glacial-interglacial dynamics of Antarctic firn columns: comparison between simulations and ice core air- $\delta^{15}\text{N}$  measurements. *Clim. Past*, **9**, pp. 983-999.
- Capron, E., Govin, A., Stone, E.J., Masson-Delmotte, V., Mulitza, S., Otto-Bleisner, B., Rasmussen, T.L., Sime, L.C., Waelbroeck, C., Wolff, E.W. 2014. Temporal and spatial structure of multi-millennial temperature changes at high latitudes during the Last Interglacial. *Quaternary Science Reviews*, **103**, pp. 116-133.
- Castellano, E., Becagli, S., Hansson, M., Hutterli, M., Petit, J.R., Rampino, M.R., Severi, M., Steffensen, J.P., Traversi, R., Udisti, R. 2005. Holocene volcanic history as recorded in the sulfate stratigraphy of the European Project for Ice Coring in Antarctic Dome C (EDC96) ice core. *Journal of Geophysical Research*, **110**, doi: 10.1029/2004JD005259.
- Cheng, H., Edwards, R.L., Broecker, W.S., Denton, G.H., Kong, X.G., Wang, Y.J., Zhang, R., Wang, X.F., 2009. Ice Age Terminations. *Science*, **326**, pp. 248-252.
- Clapperton, C. M. and Sugden, D. E. 1982. Late Quaternary glacial history of the George VI Sound area, West Antarctica. *Quaternary Research*, **18**, pp. 243-267.
- Connolley, W.M. 1996. The Antarctic temperature inversion. *Int. J. Climatol.*, **16**, pp. 1333-1342.

## References

- Cook, A.J., Fox, A.J., Vaughan, D.G., Ferrigno, J.G. 2005. Retreating glacier fronts on the Antarctic Peninsula during the Holocene epoch. *Science*, **308**, pp. 541-544.
- Cook, A.J., Fox, A.J., Vaughan, D.G., Ferrigno, J.G. 2005. Retreating glacier fronts on the Antarctic Peninsula during the Holocene epoch. *Science*, **308**, pp. 541-544.
- Cook, A.J., Holland, P.R., Meredith, M.P., Murray, T., Luckman, A., Vaughan, D.G. 2016. Ocean forcing of glacier retreat in the western Antarctic Peninsula. *Science*, **353**, pp. 283-286.
- Corr, H.F.J., Jenkins, A., Nicholls, K.W., Doake, C.S.M. 2002. Precise measurement of changes in ice-shelf thickness by phase-sensitive radar to determine basal melt rates. *Geophysical Research Letters*, **29**, doi: 10.1029/2001GL014618.
- Craig, H., 1961. Isotopic variations in Meteoric Waters. *Science*, **133**, pp. 1702-1703.
- Cuffey, K., & Clow, G. 1997. Temperature, accumulation, and ice sheet elevation in central Greenland through the last deglacial transition. *Journal of Geophysical Research*, **102**, pp. 26383-26396.
- Cuffey, K.M. and Paterson, W.S.B. 2010. *The Physics of Glaciers (4<sup>th</sup> edition)*. Elsevier.
- Curran, M.A.J., van Ommen, T.D., Morgan, V.I., Phillips, K.L., Palmer, A.S. 2003. Ice Core Evidence for Antarctic Sea Ice Decline since the 1950s. *Science*, **302**, doi: 10.1126/science.1087888
- Dahl-Jensen, D. & Johnsen, S.J. 1986. Palaeotemperatures still exist in the Greenland ice sheet. *Nature*, **320**, pp. 250-252.
- Dahl-Jensen, D., Mosegaard, K., Gundestrup, N., Clow, G.D., Johnsen, S.J., Hansen, A.W., Balling, N., 1998. Past temperatures directly from the Greenland Ice Sheet. *Science*, **282**, pp. 268-271.
- Dahl-Jensen, D., Morgan, V.I., Elcheikh, A. 1999. Monte Carlo inverse modelling of the Law Dome (Antarctica) temperature profile. *Annals of Glaciology*, **29**, pp. 145-150.
- Dahl-Jensen, D., Gundestrup, N., Gogineni, P., Miller, H., 2003. Basal melt at NorthGRIP modelled from borehole, ice-core and radio-echo sounder observations. *Annals of Glaciology*, **37**, 207-212.
- Dansgaard, W., 1953. The abundance of <sup>18</sup>O in atmospheric water and water vapour. *Tellus*, **5**, pp. 461-469.
- Dansgaard, W., 1964. Stable Isotopes in Precipitation. *Tellus*, **16**, pp. 436-468.
- Dansgaard, W. and Johnsen, S.J. 1969. A flow model and a time scale for the ice core from Camp Century, Greenland. *J. Glacio.*, **53**, pp. 215-223.
- Dansgaard, W., Johnsen, S.J., Moller, J., and Langway, C.C.J. 1969. One thousand centuries of climatic record from Camp Century on the Greenland ice sheet. *Science*, **166**, pp. 377-381.

- Dansgaard, W., Clausen, H.B., Gundestrup, N., Hammer, C.U., Johnsen, S.J., Krinstindottir, P., Reeh, N., 1982. A new Greenland deep ice core, *Science*, **218**, pp. 1273-1277.
- Dansgaard, W., Johnsen, S.J., Clausen, H.B., Dahl-Jensen, D., Gundestrup, N.S., Hammer, C.U., Hvidberg, C.S., Steffensen, J.P., Sveinbjörnsdottir, A.E., Jouzel, J., Bond, G. 1993. Evidence for general instability of past climate from a 250-kyr ice-core record. *Nature*, **364**, 218-220.
- Delaygue, G., Jouzel, J., Masson, V., Koster, R.D., Bard, E., 2000. Validity of the isotopic thermometer in central Antarctica: limited impact of glacial precipitation seasonality and moisture origin. *Geophysical Research Letters*, **27**, pp. 2677-2680.
- Della Lunga, D., Müller, W., Rasmussen, S.O., Svensson, A., Vallelonga, P. 2016. Calibrated cryo-cell UV-LA ICPMS elemental concentrations from NGRIP ice core reveal abrupt, sub-annual variability in dust across the interstadial period GI-21.2. *The Cryosphere*, doi:10.5194/tc-2016-244.
- Domack, E., Duran, D., Leventer, A., Ishman, S., Doane, S., McCallum, S., Amblas, D., Ring, J., Gilbert, R., Prentice, M. 2005. Stability of the Larsen B ice shelf on the Antarctic Peninsula during the Holocene epoch. *Nature*, **436**, pp. 681-685.
- Dome Fuji Project Members, 2017. State dependence of climatic instability over the past 720,000 years from Antarctic ice cores and climate modelling. *Science Advances*, **3**, DOI: 10.1126/sciadv.1600446.
- Dutton, A., and Lambeck, K. 2012. Ice volume and sea level during the last interglacial. *Science*, **337**, pp. 216-219.
- Dutton, A., Carlson, A.E., Long, A.J., Milne, G.A., Clark, P.U., DeConto, R., Horton, B.P., Rahmstorf, S., Raymo, M.E. 2015. Sea-level rise due to polar ice-sheet mass loss during past warm periods. *Science*, **349 (6244)**, doi: 10.1126/science.aaa4019.
- Etheridge, D.M., Steele, L.P., Langenfelds, R.L., Francey, R.J., Barnola, J.-M., Morgan, V.I. 1998. Historical CO<sub>2</sub> records from the Law Dome DE08, DE08-2, and DSS ice cores. In Trends: A Compendium of Data on Global Change. Carbon Dioxide Information Analysis Center, Oak Ridge National Laboratory, U.S. Department of Energy, Oak Ridge, Tenn., U.S.A. (<http://cdiac.ornl.gov/trends/co2/lawdome.html>) (last accessed 6/12/16).
- EPICA Community Members, 2004. Eight glacial cycles from an Antarctic ice core. *Nature*, **429**, pp. 623-628.
- EPICA Community Members, 2006. One-to-one coupling of glacial climate variability in Greenland and Antarctica. *Nature*, **444**, doi: 10.1038/nature05301.

## References

- Fischer, H., Werner, M., Wagenbach, D., Schwager, M., Thorsteinsson, T., Wilhelms, F., Kipfstuhl, J., Sommer, S. 1998. Little ice age clearly recorded in northern Greenland ice cores. *Geophysical Research Letters*, **25**, pp. 1749-1752.
- Fisher, A.T., Mankoff, K.D., Tulaczyk, S.M., Tyler, S.W., Foley, N., and the WISSARD Science Team, 2015. High geothermal heat flux measured below the West Antarctic Ice Sheet. *Science Advances*, **1**, doi: 10.1126/sciadv.1500093.
- Fox Maule, C., Purucker, M.E., Olsen, N., Mosegaard, K., 2005. Heat Flux Anomalies in Antarctica Revealed by Satellite Magnetic Data. *Science*, **309**, doi: 10.1126/science.1106888.
- Frieler, K., Clark, P.U., He, F., Buizert, C., Reese, R., Ligtenberg, S.R.M., van den Broeke, M.R., Winkelmann, R., Levermann, A. 2015. Consistent evidence of increasing Antarctic accumulation with warming. *Nature Climate Change*, **5**, doi: 10.1038/NCLIMATE2574.
- Fudge, T. J., Markle, B. R., Cuffey, K. M., Buizert, C., Taylor, K. C., Steig, E. J., Waddington, E. D., Conway, H., Koutnik, M. 2016. Variable relationship between accumulation and temperature in West Antarctica for the past 31,000 years. *Geophysical Research Letters*, **43**, pp. 3795–3803, doi:10.1002/2016GL068356.
- Fuhrer, K., Wolff, E.W., Johnsen, S.J. 1999. Timescales for dust variability in the Greenland Ice Core Project (GRIP) ice core in the last 100,000 years. *Journal of Geophysical Research*, **104**, pp. 31043-31052
- Gillet-Chaulet, F., Hindmarsh, R.C.A., Corr, H.F.J., King, E.C., Jenkins, A. 2011. *In-situ* quantification of ice rheology and direct measurement of the Raymond Effect at Summit, Greenland using a phase-sensitive radar. *Geophysical Research Letters*, **38**, doi: 10.1029/2011GL049843.
- Glen, J.W. 1958. The Flow Law of Ice: A discussion of the assumptions made in glacier theory, their experimental foundations and consequences. *Symp. Chamonix, Int. Assoc. Sci. Hydrol./Int. Union Geod. Geophys., IASH Publ.* **47**, pp. 171-183.
- Goosse, H., Masson-Delmotte, V., Renssen, H., Delmotte, M., Fichefet, T., Morgan, V., van Ommen, T., Khim, B.K., Stenni, B. 2004. A late medieval warm period in the Southern Ocean as a delayed response to external forcing? *Geophysical Research Letters*, **31**, doi: 10.1029/2003GH019140.
- Goosse, H., Braida, M., Crosta, X., Mairesse, A., Masson-Delmotte, V., Mathiot, P. Neukom, R., Oerter, H., Philippon, G., Renssen, H., Stenni, B., van Ommen, T., Verleyen, E. 2012. Antarctic temperature changes during the last millennium: evaluation of simulations and reconstructions. *Quaternary Science Reviews*, **55**, pp. 75-90.
- Goosse, H., 2017. Reconstructed and simulated temperature asymmetry between continents in both hemispheres over the last centuries. *Climate Dynamics*, **48**, pp. 1483-1501.

- Goujon, C., Barnola, J.M., Ritz, C., 2003. Modeling the densification of polar firn including heat diffusion: Application to close-off characteristics and gas isotopic fractionation for Antarctica and Greenland sites. *Journal of Geophysical Research*, **108**, DOI:10.1029/2002JD003319
- Goursand, S., Masson-Delmotte, V., Favier, V., Preunkert, S., Fily, M., Gallée, H., Jourdain, B., Legrand, M., Magand, O., Minster, B., Werner, M. 2017. A 60-year ice-core record of regional climate from Adélie Land, coastal Antarctica. *The Cryosphere*, **11**, pp. 343-362.
- Gregory, D. & Morris, D. 1996. The sensitivity of climate simulations to the specification of mixed phase clouds. *Climate Dynamics*, **12**, pp. 641-651.
- Guglielmin, M., Convey, P., Malfasi, F., Cannone, N. 2015. Glacial fluctuations since the “Medieval Warm Period” at Rothera Point (western Antarctic Peninsula). *Holocene*, **26**, pp. 154-158.
- Guillou, H., Singer, B.S., Laj, C., Kissel, C., Scaillet, S., Jicha, B.R., 2004. On the age of the Laschamp geomagnetic excursion. *Earth and Planetary Science*, **227**, pp. 331-343.
- Haefeli, R. 1961. Contribution to the movement and the form of ice sheets in the Arctic and Antarctic. *J. Glacio.*, **3**, pp. 1133-1151.
- Haines, S.A., Mayewski, P.A., Kurbatov, A.V., Maasch, K.A., Sneed, S.B., Spaulding, N.E., Dixon, D.A., Bohleber, P.D. 2016. Ultra-high resolution snapshots of three multi-decadal periods in an Antarctic ice core. *Journal of Glaciology*, **62**, doi: 10.1017/jog.2016.5.
- Hansen, L.B., and Langway, C.C., 1966. Deep core drilling in ice and core analysis at Camp Century, Greenland. *Antarct. J. US*, pp. 207-208.
- Hansson, M. 1994. The Renland ice core. A Northern Hemisphere record of aerosol composition over 120,000 years. *Tellus*, **46B**, pp. 390-418.
- Hays, J. D., Imbrie, J., Shackleton, N.J. 1976. Variations in the Earth's orbit: Pacemaker of the ice ages, *Science*, **194**, pp. 1121-1132.
- Hein, A.S., Marrero, S.M., Woodward, J., Dunning, S.A., Winter, K., Westoby, M.J., Freeman, S.P.H.T., Shanks, R.P., Sugden, D.E. 2016. Mid-Holocene pulse of thinning in the Weddell Sea sector of the West Antarctic ice sheet. *Nature Communications*, **7**, doi: 10.1038/ncomms12511.
- Herron, M.M. & Langway, C.C., 1980. Firn Densification: An empirical model. *Journal of Glaciology*, **25**, pp. 373-385.
- Heuberger, J.C. 1954. *Groenland, glaciology, Forages sur l'inlandis*. Hermann and Cie, Paris.

## References

- Hindmarsh, R.C.A., King, E.C., Mulvaney, R., Corr, H.F.J., Hiess, G., Gillet-Chaulet, F. 2011. Flow at ice-divide triple junctions: 2. Three-dimensional views of isochrone architecture from ice-penetrating radar surveys. *Journal of Geophysical Research*, **116**, doi: 10.1029/2009JF001622.
- Hjartarson, A. 2015. Heat flow in Iceland. Proceedings World Geothermal Congress 2015, Melbourne, Australia.
- Hjort, C., Ingolfsson, O., Moller, P., Manuel Lirio, J. 1997. Holocene glacial history and sea-level changes on James Ross Island, Antarctic Peninsula. *Journal of Quaternary Science*, **12**, pp. 259-273.
- Hjort, C., Bentley, M. J., Ingólfsson, O. 2001. Holocene and pre-Holocene temporary disappearance of the George VI Ice Shelf, Antarctic Peninsula. *Antarctic Science*, **13**, pp. 296-301.
- Hoffman, J.S., Clark, P.U., Parnell, A.C., He, F. 2017. Regional and global sea-surface temperatures during the last interglaciation. *Science*, **355 (6322)**, doi: 10.1126/science.aai8464.
- Holloway, M.D., Sime, L.C., Singarayer, J.S., Tindall, J.C., Bunch, P., Valdes, P.J., 2016. Antarctic last interglacial isotope peak in response to sea ice retreat not ice-sheet collapse. *Nature Communications*, **7**, doi:10.1038/ncomms12293.
- Huybrechts, P. 2002. Sea-level changes at the LGM from ice-dynamic reconstructions of the Greenland and Antarctic ice sheets during the glacial cycles, *Quaternary Science Reviews*, **21 (1)**, pp. 203-231.
- Huybrechts, P., Rybak, O., Pattyn, F., Ruth, U., Steinhage, D., 2007. Ice thinning, upstream advection, and non-climatic biases for the upper 89% of the EDML ice core from a nested model of the Antarctic ice sheet. *Clim. Past*, **3**, pp. 577-589.
- Imbrie, J. and Imbrie, J.Z. 1980. Modeling the climatic response to orbital variations, *Science*, **207**, pp. 943-953.
- Imbrie, J., Boyle, E.A., Clemens, S.C., Duffy, A., Howard, W.R., Kukla, G., Kutzbach, J., Martinson, D.G., McIntyre, A., Mix, A.C., Molfino, B., Morley, J.J., Peterson, L.C., Pisias, N.G., Prell, W.L., Raymo, M.E., Shackleton, N.J., Toggweiler, J.R. 1992. On the structure and origin of major glaciation cycles 1. Linear responses to Milankovitch forcing. *Paleoceanography and Paleoclimatology*, **7**, pp. 701-738.
- Ingolfsson, O., Hjort, C., Bjorck, S., Smith, R. I. L. 1992. Late Pleistocene and Holocene glacial history of James Ross Island, Antarctic Peninsula. *Boreas*, **21**, pp. 209-222.
- Intergovernmental Panel on Climate Change (IPCC). 2013. *Climate change 2013: The physical science basis, in Contribution of Working Group I to the Fourth Assessment Report of the Intergovernmental Panel on Climate Change*, Cambridge University Press, Cambridge.

- Jansen, D., Luckman, A.J., Cook, A., Bevan, S., Kulesa, B., Hubbard, B., Holland, P.R. 2015. Brief communication: Newly developing rift in Larsen C Ice Shelf presents significant risk to stability. *The Cryosphere*, **9**, pp. 1223-1227.
- Johnsen, S.J., White, J.W.C., 1989. The origin of Arctic precipitation under present and glacial conditions. *Tellus*, **41B**, pp. 452-468.
- Joughin, I., Smith, B.E., Howat, I.M., Scambos, T., Moon, T. 2010. Greenland flow variability from ice-sheet-wide velocity mapping. *Journal of Glaciology*, **56**, pp. 415-430.
- Jouzel, J., Merlivat, L., Lorius, C., 1982. Deuterium excess in an East Antarctic ice core suggests higher relative-humidity at the oceanic surface during the last glacial maximum. *Nature*, **299**, pp. 688-691.
- Jouzel, J., Barkov, N.I., Barnola, J.-M., Genthon, C., Korotkevitch, Y.S., Kotlyakov, V.M., Legrand, M., Lorius, C., Petit, J.-P., Petrov, V.N., Raisbeck, G., Raynaud, D., Ritz, C., Yiou, F. 1989. Global change over the last climatic cycle from the Vostok ice core record (Antarctica). *Quaternary International*, **2**, 15-24.
- Jouzel, J., Alley, R.B., Cuffey, K.M., Dansgaard, W., Grootes, P., Hoffman, G., Johnsen, S.J., Koster, R.D., Peel, D., Shuman, C.A., Stievenard, M., Stuiver, M., White, J., 1997. Validity of the temperature reconstruction from water isotopes in ice cores. *Journal of Geophysical Research*, **102**, pp. 26,471 – 26,487.
- Jouzel, J., Masson-Delmotte, V., Cattani, O., Dreyfus, G., Falourd, S., Hoffman, G., Minster, B., Nouet, J., Barnola, J.-M., Chappellaz, J., Fischer, H., Gallet, J.C., Johnsen, S.J., Leuenberger, M., Loulergue, L., Luethi, D., Oerter, H., Parrenin, F., Raisbeck, G., Raynaud, D., Schilt, A., Schwander, J., Selmo, E., Souchez, R., Spahni, R., Stauffer, B., Steffensen, J.P., Stenni, B., Stocker, T.F., Tison, J.L., Werner, M., Wolff, E.W., 2007. Orbital and Millennial Antarctic Climate Variability over the Past 800,000 years. *Science*, **317**, pp. 793-796.
- Jouzel, J. & Masson-Delmotte, V., 2010. Paleoclimates: what do we learn from deep ice cores? *WIREs Climate Change*, **1**, pp. 654-669.
- Jouzel, J. & Merlivat, L., 1984. Deuterium and Oxygen 18 in Precipitation: Modeling of the Isotopic Effects During Snow Formation. *Journal of Geophysical Research*, **89**, pp. 11,749-11,757.
- Jouzel, J. (2013) A brief history of ice core science over the last 50 yr. *Clim. Past*, **9**, pp. 2525-2547.
- Kapsner, W.R., Alley, R.B., Shuman, C.A., Anandakrishnan, S., Grootes, P.M. 1995. Dominant influence of atmospheric circulation on snow accumulation in Greenland over the past 18,000 years. *Nature*, **373**, pp. 52-54.
- Kawamura, K., Aoki, S., Nakazawa, T., Suzuki, K., Parrenin, F., 2012. Accurate age scale of the Dome Fuji ice core, Antarctica from O<sub>2</sub>/N<sub>2</sub> ratio of trapped air. *EGU General Assembly Conference Abstracts*, **14**.

## References

- Kingslake, J., Hindmarsh, R.C.A., Aðalgeirsdóttir, G., Conway, H., Corr, H.F.J., Gillet-Chaulet, F., Martin, C., King, E.C., Mulvaney, R., Pritchard, H.D. 2014. Full-depth englacial vertical ice sheet velocities measured using phase-sensitive radar. *Journal of Geophysical Research: Earth Surface*, **119**, doi: 10.1002/2014JF003275.
- Kingslake, J., Martin, C., Arthern, R.J., Corr, H.F.J., King, E.C. 2016. Ice-flow reorganisation in West Antarctica 2.5 kyr ago dated using radar-derived englacial flow velocities. *Geophysical Research Letters*, **43**, doi: 10.1002/2016GL070278.
- Koutnik, M.R., Fudge, T.J., Conway, H., Waddington, E.D., Neumann, T.A., Cuffey, K.M., Buizert, C., Taylor, K.C. 2016. Holocene accumulation and ice flow near the West Antarctic Ice Sheet Divide ice core site. *Journal of Geophysical Research – Earth Surface*, **121**, pp. 907-924.
- Kreutz, K.J., Mayewski, P.A., Meeker, L.D., Twickler, M.S., Whitlow, S.I., Pittalwala, I.I. 1997. Bipolar Changes in Atmospheric Circulation During the Little Ice Age. *Science*, **277**, pp. 1294-1296.
- Krinner, G., Magand, O., Simmonds, I., Genthon, C., Dufresne, J.-L. 2007. Simulated Antarctic precipitation and surface mass balance at the end of the twentieth and twenty-first centuries. *Climate Dynamics*, **28**, pp. 215-230.
- Kunz, M., King, M.A., Mills, J.P., Miller, P.E., Fox, A.J., Vaughan, D.G., Marsh, S.H. 2012. Multi-decadal glacier surface lowering in the Antarctic Peninsula. *Geophysical Research Letters*, **39**, doi: 10.1029/2012GL052823.
- Lachenbruch, A.H., Marshall, B.V., 1986. Changing climate: geothermal evidence from permafrost in the Alaskan Arctic. *Science*, **234**, pp. 689-696.
- Landais, A., Barnola, J.-M., Kawamura, K., Caillon, N., Delmotte, M., Van Ommen, T., Dreyfus, G., Jouzel, J., Masson-Delmotte, V., Minster, B., Freitag, J., Leuenberger, M., Schwander, J., Huber, C., Etheridge, D., Morgan, V., 2006. Firn-air  $\delta^{15}\text{N}$  in modern polar sites and glacial-interglacial ice: a model-data mismatch during glacial periods in Antarctica? *Quaternary Science Reviews*, **25**, pp. 49-62.
- Landais, A., Masson-Delmotte, V., Capron, E., Langebroek, P.M., Bakker, P., Stone, E.J., Merz, N., Raible, C.C., Fischer, H., Orsi, A., Prie, F., Vinther, B., Dahl-Jensen, D. 2016. How warm was Greenland during the last interglacial period? *Climate of the Past*, **12**, pp. 1933-1948.
- Langway, C.C., 1967. Stratigraphic Analysis of a deep ice core from Greenland. *Geological Society of America (Special Paper)*, **125**.
- Langway, C.C., 2008. The history of early polar ice cores. *Cold Reg. Sci. Technol.*, **52**, pp. 101-117.
- Le Brocq, A.M., Bentley, M.J., Fogwill, C.J., Hubbard, A.L., Sugden, D.E. & Whitehouse, P.L. 2011. Reconstructing the contribution of the Weddell Sea sector, Antarctica, to sea level rise since the last

- glacial maximum, using numerical modelling constrained by field evidence. *Quaternary Science Reviews*, **30**, pp. 2422-2432.
- Le Brocq, A.M., Bentley, M.J., Hubbard, A., Fogwill, C.J., Sugden, D.E., Whitehouse, P.L. 2011. Reconstructing the Last Glacial Maximum ice sheet in the Weddell Sea embayment, Antarctica, using numerical modelling constrained by field evidence. *Quaternary Science Reviews*, **30**, pp. 2422-2432.
- Lemieux-Dudon, B., Blayo, E., Petit, J.-R., Waelbroeck, C., Svensson, A., Ritz, C., Barnola, J.-M., Narcisi, B.M., Parrenin, F. 2010. Consistent dating for Antarctic and Greenland ice cores. *Quaternary Science Reviews*, **29**, pp. 8-20.
- Lewis, R.M., Torczon, V., Trosset, M.W. 2000. Direct Search methods: then and now. *Journal of Computational and Applied Mathematics*, **124**, pp. 191-207.
- Lisiecki, L.E. and Raymo, M.E. 2005. A Pliocene–Pleistocene stack of 57 globally distributed benthic  $\delta^{18}\text{O}$  records. *Paleoceanography*, **20**, doi:10.1029/2004PA001071.
- Lliboutry, L. 1979. A critical review of analytical approximate solutions for steady state velocities and temperature in cold ice sheets. *Z. Gletschekd. Glacialgeol.*, **15(2)**, pp. 135-148.
- Lliboutry, L. and Duval, P. 1985. Various isotropic and anisotropic ices found in glaciers and polar ice caps and their corresponding rheologies. *Annales Geophysicae*, **3**, pp. 207-224.
- Lorius, C., Jouzel, J., Ritz, C., Merlivat, L., Barkov, N.I., Korotkevich, Y.S., Kotlyakov, V.M., 1985. A 150,000 year climatic record from Antarctic Ice. *Nature*, **316**, pp. 591-596.
- Loulergue, L., Schilt, A., Spahni, R., Masson-Delmotte, V., Blunier, T., Lemieux, B., Barnola, J.-M., Raynaud, D., Stocker, T.F., Chappellaz, J. 2008. Orbital and millennial-scale features of atmospheric  $\text{CH}_4$  over the past 800,000 years. *Nature*, **453**, doi:10.1038/nature06950.
- Luthi, D., Le Floch, M., Bereiter, B., Blunier, T., Barnola, J.-M., Siegenthaler, U., Raynaud, D., Jouzel, J., Fischer, H., Kawamura, K., Stocker, T.F. 2008. High-resolution carbon dioxide concentration record 650,000-800,000 years before present. *Nature*, **453**, doi:10.1038/nature06949.
- MacAyeal, D., Firestone, J., Waddington, E. 1991. Paleothermometry by control methods. *Journal of Glaciology*, **37**, pp. 326-338.
- MacMillan, M., Leeson, A., Shepherd, A., Briggs, K., Armitage, T.W.K., Hogg, A., Kuipers Munneke, P., van den Broeke, M., Noël, B., van de Berg, W., Ligtenberg, S., Horwath, M., Groh, A., Muir, A., Gilbert, L. 2016. A high-resolution record of Greenland mass balance. *Geophysical Research Letters*, **43**, doi:10.1002/2016GL069666.

## References

McConnell, J.R., Arthern, R.J., Mosley-Thompson, E., Davis, C.H., Bales, R.C., Thomas, R., Burkhart, J.F., Kyne, J.D. 2000. Changes in Greenland ice sheet elevation attributed primarily to snow accumulation variability. *Nature*, **406**, pp. 877-879.

McConnell, J.R., Lamorey, G.W., Lambert, S.W., Taylor, K. 2002. Continuous ice-core chemical analyses using inductively coupled plasma mass spectrometry. *Environ. Sci. Technol.*, **36**, pp. 7-11.

McConnell, J.R. 2010. New Directions: Historical black carbon and other ice core aerosol records in the Arctic for GCM evaluation. *Atmos. Environ.* **44**, pp. 2665-2666.

McKay, N.P., Overpeck, J.T., Otto-Bleisner, B. 2011. The role of ocean thermal expansion in Last Interglacial sea level rise. *Geophysical Research Letters*, **38**, doi: 10.1029/2011GL048280.

Mani, F.S. 2010. *Measurements of  $\delta^{15}N$  of nitrogen gas and composition of trace gases in air from firn and ice cores*. PhD Thesis, University of East Anglia, UK.

Mann, M.E., Zhang, Z.H., Hughes, M.K., Bradley, R.S., Miller, S.K., Rutherford, S., Ni, F.B. 2008. Proxy-based reconstructions of hemispheric and global surface temperature variations over the past two millennia. *Proceedings of the National Academy of Sciences USA*, **105**, pp. 13252–13257.

Marshall, G.J. 2003. Trends in the Southern Annular Mode from observations and reanalyses. *Journal of Climate*, **16**, pp. 4134–4143.

Martin, C., Hindmarsh, R.C.A., Navarro, F.J. 2006. Dating ice flow change near the flow divide at Roosevelt Island, Antarctica, by using a thermomechanical model to predict radar stratigraphy. *Journal of Geophysical Research*, **111**, doi: 10.1029/2005JF000326.

Martin, C., Mulvaney, R., Gudmundsson, G.H., Corr, H. 2014. Inferring paleo-accumulation records from ice-core data by an adjoint method: application to James Ross Island's ice core. *Clim. Past Discuss.*, **10**, pp. 3821-3845.

Massam, A., Sneed, S., Lee, G., Tuckwell, R., Mulvaney, R., Mayewski, P.A., Whitehouse, P. 2017. A comparison of annual layer thickness model estimates with observational measurements using the Berkner Island ice core, Antarctica. *Antarctic Science*, doi: 10.1017/S0954102017000025.

Masson-Delmotte, V., Hou, S., Ekaykin, A., Jouzel, J., Aristarain, A., Bernado, R.T., Bromwich, D., Cattani, O., Delmotte, M., Falourd, S., Frezzotti, M., Gallee, H., Genoni, L., Isaksson, E., Landais, A., Helsen, M.M., Hoffmann, G., Lopez, J., Morgan, V., Motoyama, H., Noone, D., Oerter, H., Petit, J.R., Royer, A., Uemura, R., Schmidt, G.A., Schlosser, E., Simoes, J.C., Steig, E.J., Stenni, B., Stievenard, M., van den Broeke, M.R., van de Wal, R.S.W., van de Berg, W.J., Vimeux, F., White, J.W.C., 2008. A Review of Antarctic Surface Snow Isotopic Composition: Observations, Atmospheric Circulation and Isotopic Modeling. *Journal of Climate*, **21**, pp. 3359-3387.

- Mayewski, P.A., Sneed, S.B., Birkel, S.D., Kurbatov, A.V., Maasch, K.A. 2014. Holocene warming marked by abrupt onset of longer summers and reduced storm frequency around Greenland. *Journal of Quaternary Science*, **29**, pp. 99-104.
- Medley, B., Joughin, I., Das, S.B., Steig, E.J., Conway, H., Gogineni, S., Criscitiello, A.S., McConnell, J.R., Smith, B.E., van den Broeke, M.R., Lenaerts, J.T.M., Bromwich, D.H., Nicolas, J.P. 2013. Airborne-radar and ice-core observations of annual snow accumulation over Thwaites Glacier, West Antarctica confirm the spatiotemporal variability of global and regional atmospheric models. *Geophysical Research Letters*, **40**, pp. 3649-3654.
- Merlivat, L. & Jouzel, J., 1979. Global climatic interpretation of the Deuterium-Oxygen 18 Relationship for precipitation. *Journal of Geophysical Research*, **84**, pp. 5029 – 5033.
- Miller, M.M., 1954. Juneau Icefield Research Project, Alaska, 1950. JIRP Report 7. *American Geographical Society*.
- Monnin, E., Steig, E.J., Siegenthaler, U., Kawamura, K., Schwander, J., Stauffer, B., Stocker, T.F., Morse, D.L., Barnola, J.-M., Bellier, B., Raynaud, D., Fischer, H. 2004. Evidence for substantial accumulation rate variability in Antarctica during the Holocene, through synchronisation of CO<sub>2</sub> in the Taylor Dome, Dome C, and DML ice cores. *Earth and Planetary Science Letters*, **224**, pp. 45 – 54.
- Morgan, V.I., Wookey, C.W., Li, J., van Ommen, T.D., Skinner, W., Fitzpatrick, M.F., 1997. Site information and initial results from deep ice drilling on Law Dome, Antarctica. *Journal of Glaciology*, **143**, pp. 3-10.
- Müller, W., Shelley, J.M.G., Rasmussen, S.O. 2011. Direct chemical analysis of frozen ice cores by UV laser ablation ICPMS. *J. Anal. At. Spectrom.*, **26**, pp. 2391-2395.
- Mulvaney, R., Oerter, H., Peel, D.A., Graf, W., Arrowsmith, C., Pasteur, E.C., Knight, B., Littot, G.C., Miners, W.D., 2002. 1000 year ice-core records from Berkner Island, Antarctica. *Annals of Glaciology*, **35**, pp. 45-51.
- Mulvaney, R., Alemany, O., Possenti, P. 2007. The Berkner Island (Antarctica) ice-core drilling project. *Annals of Glaciology*, **47**, pp. 115-124
- Mulvaney, R., Abram, N.J., Hindmarsh, R.C.A., Arrowsmith, C., Fleet, L., Triest, J., Sime, L., Alemany, O., Foord, S. 2012. Recent Antarctic Peninsula warming relative to Holocene climate and ice-shelf history. *Nature*, **489**, doi: 10.1038/nature11398.
- Mulvaney, R., Triest, J., Alemany, O. 2014. The James Ross Island and the Fletcher Promontory ice-core drilling projects. *Annals of Glaciology*, **55**, doi: 10.3189/2014AOG68A044.

## References

- Nagornov, O., Kononov, Y.V., Tchijov, V. 2006. Temperature reconstruction for Arctic glaciers. *Palaeogeography, Palaeoclimatology, Palaeoecology*, **236(1)**, pp. 125-134.
- Nakano, S., Suzuki, K., Kawamura, K., Parrenin, F., Higuchi, T. 2016. A sequential Bayesian approach for the estimation of the age-depth relationship of the Dome Fuji ice core. *Nonlinear Processes in Geophysics*, **23**, pp. 31-44.
- Nan, S., and Li, J. 2003. The relationship between summer precipitation in the Yangtze River valley and the previous Southern Hemisphere Annular Mode. *Geophysical Research Letters*, **30(24)**, doi: 10.1029/2003GL018381.
- Näslund, J.-O., Jansson, P., Fastook, J.L., Johnson, J., Andersson, L., 2005. Detailed spatially distributed geothermal heat-flow data for modelling of basal temperatures and meltwater production beneath the Fennoscandian ice sheet. *Annals of Glaciology*, **40**, 95-101.
- NEEM Community Members, 2013. Eemian interglacial reconstructed from a Greenland folded ice core. *Nature*, **493**, pp. 489-494.
- Neftel A., Bales, R.C., Jacob, D.J. 1995. H<sub>2</sub>O<sub>2</sub> and HCHO in Polar Snow and Their Relation to Atmospheric Chemistry. In: Delmas R.J. (ed.). *Ice Core Studies of Global Biogeochemical Cycles. NATO ASI Series (Series I: Global Environmental Change)*. Springer, Berlin, Heidelberg.
- Neukom, R., Luterbacher, J., Villalba, R., Küttel, M., Frank, D., Jones, P.D., Grosjean, M., Wanner, H., Aravena, J.-C., Black, D.E., Christie, D.A., D'Arrigo, R., Lara, A., Morales, M., Soliz-Gamboa, C., Srur, A., Urrutia, R., von Gunten, L. 2011. Multiproxy summer and winter surface air temperature field reconstructions for southern South America covering the past centuries. *Climate Dynamics*, **37**, pp. 35-51.
- Neukom, R., Gergis, J., Karoly, D.J., Wanner, H., Curran, M., Elbert, J., González-Rouco, F., Linsley, B.K., Moy, A.D., Mundo, I., Raible, C.C., Steig, E.J., van Ommen, T., Vance, T., Villalba, R., Zinke, J., Frank, D. 2014. Inter-hemispheric temperature variability over the past millennium. *Nature Climate Change*, **4**, pp. 362-367.
- NGRIP members, 2004. High-resolution record of Northern Hemisphere climate extending into the last interglacial period. *Nature*, **431**, pp. 147-151.
- Nye, J.F., 1963. Correction factor for accumulation measured by the thickness of the annual layers in an ice sheet. *Journal of Glaciology*, **4**, pp. 785-788.
- Oeschger, H. 1985. The contribution of ice core studies to the understanding of environmental processes, in *Greenland Ice Cores: Geophysics, Geochemistry, and the Environment; Geophysical Monograph*, **33**, AGU, Washington, pp. 9-17.

- Ohmura, A., Wild, M., Bengtsson, L. 1996. A possible change in mass balance of Greenland and Antarctic ice sheets in the coming century. *Journal of Climate*, **9**, pp. 2124-2135.
- Orsi, A.J., Cornuelle, B.D., Severinghaus, J.P. 2012. Little Ice Age cold interval in West Antarctica: Evidence from borehole temperature at the West Antarctic Ice Sheet (WAIS) Divide. *Geophysical Research Letters*, **39**, doi: 10.1029/2012GL051260.
- PAGES2k Consortium, 2013. Continental-scale temperature variability during the past two millennia. *Nature Geoscience*, **6**, doi: 10.1038/NGEO1797.
- PAGES2k Consortium, 2017. Data Descriptor: A global multiproxy database for temperature reconstructions of the Common Era. *Scientific Data*, **4**, doi: 10.1038/sdata.2017.88.
- Palerme, C., Kay, J.E., Genthon, C., L'Ecuyer, T., Wood, N.B., Claud, C. 2014. How much snow falls on the Antarctic continent? *The Cryosphere*, **8**, pp. 1577-1587.
- Palerme, C., Genthon, C., Claud, C., Kay, J.E., Wood, N.B., L'Ecuyer, T. 2017. Evaluation of current and projected Antarctic precipitation in CMIP5 models. *Climate Dynamics*, doi: 10.1007/s00382-016-3071-1.
- Parrenin, F., Jouzel, J., Waelbroeck, C., Ritz, C., Barnola, J-M., 2001. Dating the Vostok ice core by an inverse method. *Journal of Geophysical Research*, **106**, pp. 31,837-31,851.
- Parrenin, F., Remy, F., Ritz, C., Siegert, M.J., Jouzel, J., 2004. New modelling of the Vostok ice flow line and implication for the glaciological chronology of the Vostok ice core. *Journal of Geophysical Research*, **109**, DOI: 10.1029/2004JD004561.
- Parrenin, F., Hindmarsh, R.C.A., Rémy, F. 2006. Analytical solutions for the effect of topography, accumulation rate and lateral flow divergence on isochrones layer geometry. *Journal of Glaciology*, **52**, pp. 191-202.
- Parrenin, F. and Hindmarsh, R. 2007. Influence of a non-uniform velocity field on isochrone geometry along a steady flowline of an ice sheet. *Journal of Glaciology*, **53**, pp. 612-622.
- Parrenin, F., Dreyfus, G., Durand, G., Fujita, S., Gagliardini, O., Gillet, F., Jouzel, J., Kawamura, K., Lhomme, N., Masson-Delmotte, V., Ritz, C., Schwander, J., Shoji, H., Uemura, R., Watanabe, O., Yoshida, N., 2007a. 1-D-ice flow modelling at EPICA Dome C and Dome Fuji, East Antarctica. *Clim. Past*, **3**, pp. 243-259.
- Parrenin, F., Barnola, J-M., Beer, J., Blunier, T., Castellano, E., Chappellaz, J., Dreyfus, G., Fischer, H., Fujita, S., Jouzel, J., Kawamura, K., Lemieux-Dudon, B., Loulergue, L., Masson-Delmotte, V., Narcisi, B., Petit, J.R., Raisbeck, G., Raynaud, D., Ruth, U., Schwander, J., Severi, M., Spahni, R., Steffensen, J.P.,

## References

- Svensson, A., Udisti, R., Waelbroeck, C., Wolff, E., 2007b. The EDC3 chronology for the EPICA Dome C ice core. *Clim. Past*, **3**, pp. 485-497.
- Parrenin, F., Barker, S., Blunier, T., Chappellaz, J., Jouzel, J., Landais, A., Masson-Delmotte, V., Schwander, J., Veres, D. 2012. On the gas-ice depth difference ( $\Delta$ depth) along the EPICA Dome C ice core. *Clim. Past*, **8**, pp. 1239-1255.
- Parrenin, F., Bazin, L., Capron, E., Landais, A., Lemieux-Dudon, B., Masson-Delmotte, V. 2015. IceChrono1: a probabilistic model to compute a common and optimal chronology for several ice cores. *Geoscientific Model Development*, **8**, pp. 1473-1492.
- Pasteris, D., McConnell, J.R., Edwards, R., Isaksson, E., Albert, M.R. 2014a. Acidity decline in Antarctic ice cores during the Little Ice Age linked to changes in atmospheric nitrate and sea salt concentrations. *J. Geophys. Res.-Atmos*, **119**, pp. 5640-5652.
- Pasteris, D., McConnell, J.R., Das, S., Criscitiello, A.S., Evans, M.J., Maselli, O.J., Sigl, M., Layman, L. 2014b. Seasonally resolved ice core records from West Antarctica indicate a sea ice source of sea-salt aerosol and a biomass burning source of ammonium. *J. Geophys. Res.-Atmos.*, **119**, pp. 9168-9182.
- Pattyn, F., 2010. Antarctic subglacial conditions inferred from a hybrid ice sheet/ice stream model. *Earth and Planetary Science Letters*, **295**, 451-461, doi: 10.1016/j.epsl.2010.04.025.
- Pedro, J.B., Bostock, H.C., Bitz, C.M., He, F., Vandergoes, M.J., Steig, E.J., Chase, B.M., Krausse, C.E., Rasmussen, S.O., Markle, B.R., Cortese, G. 2016. The spatial extent and dynamics of the Antarctic Cold Reversal. *Nature Geoscience*, **9**, pp. 51-55.
- Petit, J.R., White, J.W.C., Young, N.W., Jouzel, J., Korotkevich, Y.S., 1991. Deuterium excess in recent Antarctic Snow. *Journal of Geophysical Research*, **96**, pp. 5113-5122.
- Petit, J.R., Jouzel, J., Raynaud, D., Barkov, N.I., Barnola, J-M., Basile, I., Bender, M., Chappellaz, J., Davis, M., Delaygue, G., Delmotte, M., Kotlyakov, V.M., Legrand, M., Lipenkov, V.Y., Lorius, C., Pepin, L., Ritz, C., Saltzman, E., Stievenard, M., 1999. Climate and atmospheric history of the past 420,000 years from the Vostok ice core. *Nature*, **399**, pp. 429-436.
- Pettitt, E.C. and Waddington, E.D. 2003. Ice flow at low deviatoric stress. *Journal of Glaciology*, **49**, pp. 359-369.
- Philippe, M., Tison, J.-L., Fjøsne, K., Hubbard, B., Kjaer, H.A., Lenaerts, J.T.M., Drews, R., Sheldon, S.G., De Bondt, K., Claeys, P., Pattyn, F. 2016. Ice core evidence for a 20<sup>th</sup> century increase in surface mass balance in coastal Dronning Maud Land, East Antarctica. *The Cryosphere*, **10**, pp. 2501-2516.
- Pimienta, P. 1987. Etude de comportement mécanique des glaces polycristallines aux faibles contraintes; application aux glaces de calotte polaire. Doctoral thesis, Université Joseph Fourier.

- Poincaré, H. 1892. *Les methods nouvelles de la mécanique celeste*. Paris, Gauthier-Villars et fils.
- Pollard, D. and DeConto, R.M. 2009. Modelling West Antarctic ice sheet growth and collapse through the past five million years. *Nature*, **458**, pp. 329-332.
- Pritchard, H.D., Ligtenberg, S.R.M., Fricker, H.A., Vaughan, D.G., van den Broeke, M.R., Padman, L. 2012. Antarctic ice-sheet loss driven by basal melting of ice shelves. *Nature*, **484**, pp. 502-505.
- Pudsey, C.J. and Evans, J. 2001. First survey of Antarctic sub-ice shelf sediments reveals mid-Holocene ice shelf retreat. *Geology*, **29**, pp. 787-790.
- Pudsey, C.J., Murray, J.W., Appleby, P., Evans, J. 2006. Ice shelf history from petrographic and foraminiferal evidence, Northeast Antarctic Peninsula. *Quaternary Science Reviews*, **25**, pp. 17-18.
- Purucker, M. Geothermal heat flux dataset based on low resolution observations collected by the CHAMP satellite between 2000 and 2010. Available at: <http://websrv.cs.umnt.edu/isis/index.php> (last access 23/08/2016).
- RAISED Consortium, 2014. A community-based geological reconstruction of Antarctic Ice Sheet deglaciation since the Last Glacial Maximum. *Quaternary Science Reviews*. **100**, pp. 1-9.
- Rasmussen, S.O., Andersen, K.K., Svensson, A.M., Steffensen, J.P., Vinther, B.M., Clausen, H.B., Siggaard-Andersen, M.L., Johnsen, S.J., Larsen, L.B., Dahl-Jensen, D., Bigler, M., Rothlisberger, R., Fischer, H., Goto-Azuma, K., Hansson, M.E., Ruth, U. 2006. A new Greenland ice core chronology for the last glacial termination. *Journal of Geophysical Research – Atmospheres*, **111**, doi: 10.1029/2005JD006079
- Rasmussen, S.O., Abbott, P.M., Blunier, T., Bourne, A.J., Brook, E., Buchardt, S.L., Buizert, C., Chappellaz, J., Clausen, H.B., Cook, E., Dahl-Jensen, D., Davies, S.M., Guillevic, M., Kipfstuhl, S., Laepple, T., Seierstadt, I.E., Severinghaus, J.P., Steffensen, J.P., Stowasser, C., Svensson, A., Vallelonga, P., Vinther, B.M., Wilhelms, F., Winstrup, M. 2013. A first chronology for the North Greenland Eemian Ice Drilling (NEEM) ice core. *Climate of the Past*, **9**, pp. 2713-2730.
- Rasmussen, S.O., Bigler, M., Blockley, S.P., Blunier, T., Buchardt, S.L., Clausen, H.B., Cvijanovic, I., Dahl-Jensen, D., Johnsen, S.J., Fischer, H., Gkinis, V., Guillevic, M., Hoek, W.Z., Lowe, J., Pedro, J.B., Popp, T., Seierstad, I.K., Steffensen, J.P., Svensson, A.M., Vallelonga, P., Vinther, B.M., Walker, M.J.C., Wheatley, J.J., Winstrup, M. 2014. A stratigraphic framework for abrupt climatic changes during the Last Glacial period based on three synchronised Greenland ice-core records: refining and extending the INTIMATE event stratigraphy. *Quaternary Science Reviews*, **106**, pp. 14-28.
- Raymond, C.F. 1983. Deformation in the vicinity of ice divides. *J. Glaciol.*, **29 (103)**, pp. 357-373.

## References

- Reeh, N., 1989. Dating by ice flow modelling: a useful tool or an exercise in applied mathematics? In Oeschger, H. & Langway, C.C. (Eds.), *The environmental record in glaciers and ice sheets*. C.J. Wiley & Sons, Chichester, pp. 141-159.
- Reinhardt, H., Kriews, M., Miller, H., Schrems, O., Lüdke, C., Hoffman, E., Skole, J. 2001. Laser ablation inductively coupled plasma mass spectrometry: a new tool for trace element analysis in ice cores. *Fresenius J. Anal. Chem.*, **370**, pp. 629-636.
- Rhodes, R.H., Bertler, N.A.N., Baker, J.A., Steen-Larsen, H.C., Sneed, S.B., Morgenstern, U., Johnsen, S.J. 2012. Little Ice Age climate and oceanic conditions of the Ross Sea, Antarctica from a coastal ice core record. *Climate of the Past*, **8**, pp. 1223-1238.
- Rhodes, R.H., Bertler, N.A.N., Baker, J.A., Steen-Larsen, H.C., Sneed, S.B., Morgenstern, U., Johnsen, S.J. Mt. Erebus Saddle, Antarctica 500 Year Ice Core Glaciochemical Data. Accessed from: <https://www.ncdc.noaa.gov/paleo-search/study/13175> on 21/02/2018.
- Rignot, E., Casassa, G., Gogineni, P., Krabill, W., Rivera, A., Thomas, R. 2004. Accelerated ice discharge from the Antarctic Peninsula following the collapse of the Larsen B ice shelf. *Geophysical Research Letters*, **31**, doi: 10.1029/2004GL020697.
- Rignot, E., Bamber, J.L., Van Den Broeke, M., Davis, C., Li, Y., Van De Berg, W., Meijgaard, E. 2008. Recent Antarctic ice mass loss from radar interferometry and regional climate modelling. *Nature Geoscience*, **1**, pp. 106-110.
- Ritz, C., Rommelaere, V., Dumas, C. 2001. Modeling the evolution of Antarctic ice sheet over the last 420,000 years: Implications for altitude changes in the Vostok region. *Journal of Geophysical Research*, **106**, pp. 31,943-31,964.
- Roberts, S.J., Monien, P., Foster, L.C., Loftfield, L.C., Hocking, E.P., Schnetger, B., Pearson, E.J., Juggins, S., Fretwell, P., Ireland, L., Ochyra, R., Haworth, A.R., Allen, C.S., Moreton, S.G., Davies, S.J., Brumsack, H.J., Bentley, M.J., Hodgson, D.A. 2017. Past penguin colony responses to explosive volcanism on the Antarctic Peninsula. *Nature Communications*, doi: 10.1038/ncomms14914.
- Rothlisberger, R., Hutterli, M.A., Sommer, S., Wolff, E.W., Mulvaney, R. 2000a. Factors controlling nitrate in deep ice cores: evidence from the Dome C deep ice core. *Journal of Geophysical Research*, **105**, pp. 20565-20572.
- Rothlisberger, R., Bigler, M., Hutterli, M., Sommer, S., Stauffer, B. 2000b. Technique for continuous high-resolution analysis of trace substances in firn and ice cores. *Environ. Sci. Technol.*, **34** (2), pp. 338-342.

- Rothlisberger, R., Mulvaney, R., Wolff, E.W., Hutterli, M.A., Bigler, M., de Angelis, M., Hansson, M.E., Steffensen, J.P., Udisti, R. 2003. Limited dechlorination of sea-salt aerosols during the last glacial period: evidence from the European Project for Ice Coring in Antarctica (EPICA) Dome C ice core. *Journal of Geophysical Research*, **108**, doi:10.1029/2003JD003604.
- Ruddiman, W.F. and Raymo, M.E. 2006. A methane-based time scale for Vostok ice. *Quaternary Science Reviews*, **22**, 141-155.
- Ruth, U., Barnola, J.-M., Beer, J., Bigler, M., Blunier, T., Castellano, E., Fischer, H., Fundel, F., Huybrechts, P., Kaufmann, P., Kipfstuhl, S., Lambrecht, A., Morganti, A., Oerter, H., Parrenin, F., Rybak, O., Severi, M., Udisti, R., Wilhelms, F., Wolff, E., 2007. "EDML1": a chronology for the EPICA deep ice core from Dronning Maud Land, Antarctica, over the last 150,000 years. *Clim. Past*, **3**, pp. 475-484.
- Salamatin, A.N., Lipenkov, V.Y., Blinov, K.V., 1994. Vostok (Antarctica) climate record time-scale deduced from the analysis of a borehole-temperature profile. *Ann. Glaciol.* **20**, 207-214.
- Salamatin, A.N., 2000. Paleoclimatic reconstructions based on borehole temperature measurements in ice sheets. Possibilities and limitations. In Hondoh, T (ed.) *Physics of Ice Core Records*, Saporro, Hokkaido University Press, pp. 243-282.
- Schlosser, E., Dittman, A., Stenni, B., Powers, J.G., Manning, K.W., Masson-Delmotte, V., Valt, M., Cagnati, A., Grigioni, P., Scarchilli, C. *In review*. The influence of the synoptic regime on stable water isotopes in precipitation at Dome C, East Antarctica. *The Cryosphere Discussions*, doi: 10.5194/tc-2017-21.
- Schroeder, D.M., Blankenship, D.D., Young, D.A., Quartini, E., 2014. Evidence for elevated and spatially variable geothermal flux beneath the West Antarctic Ice Sheet. *PNAS*, **111**, doi: 10.1073/pnas.1405184111.
- Schwander, J., Sowers, T., Barnola, J.-M., Blunier, T., Fuchs, A., Malaize, B., 1997. Age scale of the air in the summit ice: Implication for glacial-interglacial temperature change. *Journal of Geophysical Research*, **102**, pp. 19,483-19,493.
- Schwander, J., Jouzel, J., Hammer, C.U., Petit, J.R., Udisti, R., Wolff, E., 2001. A tentative chronology for the EPICA Dome Concordia ice core. *Geophysical Research Letters*, **28**, pp. 4243-4246.
- Schytt, V. 1958. Norwegian-British-Swedish Antarctic Expedition 1949-1952. Scientific Results 4. *Glaciology II*. Oslo, Norway: Norsk Polarinstitut
- Severi, M., Becagli, S., Castellano, E., Morganti, A., Traversi, R., Udisti, R., Ruth, U., Fischer, H., Huybrechts, P., Wolff, E., Parrenin, F., Kaufmann, P., Lambert, F., Steffensen, J.P., 2007. Synchronisation

## References

of the EDML and EDC ice cores for the last 52 kyr by volcanic signature matching. *Clim. Past*, **3**, pp. 367-374.

Severinghaus, J. 2009. Southern see-saw seen. *Nature*, **457**, 1093-1094.

Shackleton, N.J. The 100,000 year ice-age cycle identified and found to lag temperature, carbon dioxide, and orbital eccentricity. *Science*, **289**, 1897-1902.

Shapiro, N.M. and Ritzwoller, M.H., 2004. Inferring surface heat flux distributions guided by a global seismic model: particular application to Antarctica. *Earth and Planetary Science. Letters*, **223**, 213-224, doi: 10.1016/j.epsl.2004.04.011.

Shepherd, A., Ivins, E.R., Geruo, A., Barletta, V.R., Bentley, M.J., Srinivas, B., Briggs, K.H., Bronwich, D.H., Forsberg, R., Galin, N., Horwarth, M., Jacobs, S., Joughin, I., King, M.A., Lenaerts, J.T.M., Li, J., Ligtenberg, S.R.M., Luckman, A., Luthcke, S.B., McMillan, M., Meister, R., Milne, G., Mouginit, J., Muir, A., Nicolas, J.P., Paden, J., Payne, A.J., Pritchard, H., Rignot, E., Rott, H., Sandberg Sorensen, L., Scambos, T.A., Scheuchl, B., Schrama, E.J.O., Smith, B., Sundal, A.V., van Angelen, J.H., van de Berg, W.J., van den Broeke, M.R., Vaughan, D.G., Velicogna, I., Wahr, J., Whitehouse, P.L., Wingham, D.J., Yi, D., Young, D., Jay Zwally, H. 2012. A reconciled estimate of ice-sheet mass balance. *Science*, **338**, pp. 1183-1189.

Siegenthaler, U., Monnin, E., Kawamura, K., Spahni, R., Schwander, J., Stauffer, B., Stocker, T.F., Barnola, J.-M., Fischer, H. 2005. EPICA Dronning Maud Land carbon dioxide concentrations for the Last Millennium. doi:10.1594/PANGAEA.472477

Siegert, M., Ross, N., Corr, H., Kingslake, J., Hindmarsh, R. 2013. Late Holocene ice-flow reconfiguration in the Weddell Sea sector of West Antarctica. *Quaternary Science Reviews*, **78**, pp. 98-107.

Sigg, A., Fuhrer, K., Anklin, M., Staffelbach, T., Zurmuhle, D. 1994. A continuous analysis technique for trace species in ice cores. *Environ. Sci. Technol.*, **28(2)**, pp. 204-209.

Sigl, M., McConnell, J.R., Layman, L., Maselli, O., McGwire, K., Pasteris, D., Dahl-Jensen, D., Steffensen, J.P., Vinther, B., Edwards, R., Mulvaney, R., Kipfstuhl, S. 2013. A new bipolar ice core record of volcanism from WAIS Divide and NEEM and implications for climate forcing of the last 2000 years. *Journal of Geophysical Research: Atmospheres*, **118**, pp. 1151-1169.

Sigl, M., Fudge, T.J., Winstrup, M., Cole-Dai, J., Ferris, D., McConnell, J.R., Taylor, K.C., Welten, K.C., Woodruff, T.E., Adolphi, F., Bisiaux, M., Brook, E.J., Buizert, C., Caffee, M.W., Dunbar, N.W., Edwards, R., Geng, L., Iverson, N., Koffman, B., Layman, L., Maselli, O.J., McGwire, K., Muscheler, R., Nishiizumi, K., Pasteris, D.R., Rhodes, R.H., Sowers, T.A. 2016. The WAIS Divide deep ice core WD2014 chronology – part 2: annual layer counting (0 – 31 ka BP). *Clim. Past*, **12**, pp. 769-786.

- Sime, L.C., Marshall, G.J., Mulvaney, R., Thomas, E.R. 2009a. Interpreting temperature information from ice cores along the Antarctic Peninsula: ERA40 analysis. *Geophysical Research Letters*, **36**, doi: 10.1029/2009GL038982.
- Sime, L.C., Wolff, E.W., Oliver, K.I.C., Tindall, J.C. 2009b. Evidence for warmer interglacials in East Antarctic ice cores. *Nature*, **462**, pp. 342-345.
- Sime, L.C., Risi, C., Tindall, J.C., Sjolte, J., Wolff, E.W., Masson-Delmotte, V., Capron, E. 2013. Warm climate isotopic simulations: what do we learn about interglacial signals in Greenland ice cores? *Quaternary Science Reviews*, **67**, pp. 59-80.
- Sneed, S.B., Mayewski, P.A., Sayre, W.G., Handley, M.J., Kurbatov, A.V., Taylor, K.C., Bohleber, P., Wagenbach, D., Erhardt, T., Spaulding, N.E. 2015. New LA-ICP-MS cryocell and calibration technique for sub-millimeter analysis of ice cores. *Journal of Glaciology*, **226**, pp. 233-242.
- Sommer, S., Appenzeller, C., Rothlisberger, R., Hutterli, M.A., Stauffer, B., Wagenbach, D., Oerter, H., Wilhelms, F., Miller, H., Mulvaney, R. 2000. Glacio-chemical study spanning the past 2kyr on three ice cores from Dronning Maud Land, Antarctica 1. Annually resolved accumulation rates. *Journal of Geophysical Research*, **105**, pp. 29411-29421.
- Steffensen, J.P. 1997. The size distribution of microparticles from selected segments of the Greenland Ice Core Project ice core representing different climatic periods. *Journal of Geophysical Research*, **102**, pp. 26755-26763
- Steig, E.J., Schneider, D.P., Rutherford, S.D., Mann, M.M., Comiso, J.C., Shindell, D.T. 2009. Warming of the Antarctic ice-sheet surface since the 1957 International Geophysical Year. *Nature*, **457**, doi: 10.1038/nature07669.
- Steiger, N.J., Steig, E.J., Dee, S.G., Roe, G.H., Hakim, G.J. 2017. Climate reconstruction using data assimilation of water isotope ratios from ice cores. *Journal of Geophysical Research – Atmospheres*, **122**, pp. 1545-1568.
- Steinhart, J.S., and Hart, S.R. 1968. Calibration curves for thermistors. *Deep Sea Research and Oceanographic Abstracts*, **15**, pp. 497-503.
- Svensson, A., Andersen, K.K., Bigler, M., Clausen, H.B., Dahl-Jensen, D., Davies, S.M., Johnsen, S.J., Muscheler, R., Parrenin, F., Rasmussen, S.O. 2008. A 60 000 year Greenland stratigraphic ice core chronology. *Clim. Past*, **4**, pp. 47-57
- Svensson, A., Fujita, S., Bigler, M., Braun, M., Dallmayr, R., Gkinis, V., Goto-Azuma, K., Hirabayashi, M., Kawamura, K., Kipstuf, S., Kjaer, H.A., Popp, T., Simonsen, M., Steffensen, J.P., Vallelonga, P., Vinther,

## References

B.M. 2015. On the occurrence of annual layers in Dome Fuji ice core early Holocene ice. *Clim. Past*, **11**, pp. 1127-1137

Swithinbank, C. 1957. Norwegian-British-Swedish Antarctic Expedition 1949-1952. Scientific Results 3. *Glaciology I*, Oslo Norway: Norsk Polarinstitut.

Tans, P. NOAA/ESRL ([www.esrl.noaa.gov/gmd/ccgg/trends/](http://www.esrl.noaa.gov/gmd/ccgg/trends/)) and Dr. Ralph Keeling, Scripps Institution of Oceanography ([scrippsco2.ucsd.edu/](http://scrippsco2.ucsd.edu/)) (<http://www.esrl.noaa.gov/gmd/ccgg/trends/data.html>) (last accessed 6/12/16).

Tarantola, A. 1987. Inverse problem theory: Methods for data fitting and model parameter estimation. *Elsevier Sci.*, New York.

Tarasov, L. and Peltier, W.R. 2003. Greenland glacial history, borehole constraints, and Eemian extent. *Journal of Geophysical Research*, **108**, doi: 10.1029/2001JB001731.

Thomas, E.R. 2006. *High-resolution analysis of rapid climate change from Greenland ice cores*. PhD Thesis, Open University.

Thomas, E.R., Marshall, G.J., McConnell, J.R. 2008. A doubling in snow accumulation in the western Antarctic Peninsula since 1850. *Geophysical Research Letters*, **35**, doi: 10.1029/2007GL032529.

Thomas, E.R., Wolff, E.W., Mulvaney, R., Johnsen, S.J., Steffensen, J.P., Arrowsmith, C. 2009. Anatomy of a Dansgaard-Oeschger warming transition: high resolution analysis of the North Greenland Ice Core Project ice core. *J. Geophys. Res.*, **114**, DOI: 10.1029/2008JD011215.

Thomas, E.R., Hosking, J.S., Tuckwell, R.R., Warren, R.A., Ludlow, E.C. 2015. Twentieth century increase in snowfall in coastal West Antarctica. *Geophysical Research Letters*, **42**, doi: 10.1002/2015GL065750.

Turner, J., Colwell, S.R., Marshall, G.J., Lachlan-Cope, T.A., Carleton, A.M., Jones, P.D., Lagun, V., Reid, P.A., Iagovkina, S. 2005. Antarctic climate change during the last 50 years. *International Journal of Climatology*, **25**, pp. 279-294.

Turner, J., Lu, H., White, I. King, J.C., Phillips, T., Hosking, J.C., Bracegirdle, T.J., Marshall, G.J., Mulvaney, R., Deb, P. 2016. Absence of 21<sup>st</sup> century warming on Antarctic Peninsula consistent with natural variability. *Nature*, **535**, doi: 10.1038/nature18645.

Ueda, H.T. and Garfield, D.E. 1969. Core drilling through the Antarctic ice sheet. USA CRREL Technical Report 231.

van Liefferinge, B. and Pattyn, F., 2013. Using ice-flow models to evaluate potential sites of million-year old ice in Antarctica. *Clim. Past.*, **9**, doi: 10.5194/cp-9-2335-2013.

- Vaughan, D.G. and Doake, C.S.M. 1996. Recent atmospheric warming and retreat of ice shelves on the Antarctic Peninsula. *Nature*, **379**, pp. 328-331.
- Vaughan, D.G., Marshall, G.J., Connolley, W.M., Parkinson, C., Mulvaney, R., Hodgson, D.A., King, J.C., Pudsey, C.J., Turner, J. 2003. Recent rapid regional climate warming on the Antarctic Peninsula. *Climate Change*, **60**, pp. 243-274.
- Vaughan, D.G., 2006. Recent trends in melting conditions on the Antarctic Peninsula and their implications for ice-sheet mass balance and sea level. *Arctic, Antarctic, and Alpine Research*, **38**, pp. 147-152.
- Vega, C.P., Schlosser, E., Divine, D.V., Kohler, J., Martma, T., Eichler, A., Schwikowski, M., Isaksson, E. 2016. Surface mass balance and water stable isotopes derived from firn cores on three ice rises, Fimbul Ice Shelf, Antarctica. *The Cryosphere*, **10**, pp. 2763-2777.
- Veres, D., Bazin, L., Landais, A., Toyé Mahamadou Kele, H., Lemieux-Dudon, B., Parrenin, F., Martinerie, P., Blayo, E., Blunier, T., Capron, E., Chappellaz, J., Rasmussen, S.O., Severi, M., Svensson, A., Vinther, B., Wolff, E.W. 2013. The Antarctic ice core chronology (AICC2012): an optimised multi-parameter and multi-site dating approach for the last 120 thousand years. *Climate of the Past*, **9**, pp. 1733-1748.
- Vinther, B.M., Clausen, H.B., Johnsen, S.J., Rasmussen, S.O., Andersen, K.K., Buchardt, S.L., Dahl-Jensen, D., Seierstad, I.K., Siggaard-Andersen, M.L., Steffensen, J.P., Svensson, A., Olsen, J., Heinemeier, J. 2006. A synchronized dating of three Greenland ice cores throughout the Holocene. *Journal of Geophysical Research – Atmospheres*, **111**, doi: 10.1029/2005JD006921.
- WAIS Divide Project members, 2014. Precise inter-polar phasing of abrupt climate change during the last ice age. *Nature*, **520**, pp. 661-665.
- Wagenbach, D., Ducroz, F., Mulvaney, R., Keck, L., Minikin, A., Legrand, M., Hall, J.S., Wolff, E.W. 1998. Sea-salt aerosol in coastal Antarctic regions. *Journal of Geophysical Research*, **103**, pp. 10961-10974.
- Wagenbach, D., Graf, W., Minikin, A., Trefzer, U., Kippstuhl, J., Oerter, H., Blindow, N. 1994. Reconnaissance of chemical and isotopic firn properties on top of Berkner Island, Antarctica. *Annals of Glaciology*, **20**, 307-312.
- Weertman, J. 1973. The Creep of Ice. In: Whalley, E., Jones, S.J., Gold, L.W. (Eds.). *Physics and chemistry of ice: papers presented at the Symposium on the Physics and Chemistry of Ice, held in Ottawa, Canada, 14-18 August 1972*, Ottawa, Royal Society of Canada, 320-337.
- Walker, M., Johnsen, S., Rasmussen, S. O., Popp, T., Steffensen, J.-P., Gibbard, P., Hoek, W., Lowe, J., Andrews, J., Björck, S., Cwynar, L. C., Hughen, K., Kershaw, P., Kromer, B., Litt, T., Lowe, D. J., Nakagawa, T., Newnham, R., and Schwander, J. 2009. Formal definition and dating of the GSSP (Global Stratotype Section and Point) for the base of the Holocene using the Greenland NGRIP ice core, and selected auxiliary records. *Journal of Quaternary Science*, **24** pp. 3–17.

## References

- Watanabe, O., Jouzel, J., Johnsen, S.J., Parrenin, F., Shoji, H., Yoshida, N., 2003. Homogenous climate variability across East Antarctica over the past three glacial cycles. *Nature*, **422**, pp. 509-512.
- Weertman, J. 1968. Comparison between measured and theoretical temperature profiles of the Camp Century, Greenland, borehole. *J. Geophys. Res.*, **73**, pp. 2691-2700.
- Winsborrow, M.C.M., Clark, C.D., Stokes, C.R., 2010. What controls the location of ice streams? *Earth-Science Reviews*, 103, 45-59, doi:10.1016/j.earscirev.2010.07.003.
- Wright, A. and Siegert, M., 2012. A fourth inventory of Antarctic subglacial lakes. *Antarctic Science*, 24(6), doi: 10.1017/S095410201200048X.
- Wolff, E.W. and Doake, C.S.M. 1986. Implications of the form of the flow law for vertical velocity and age-depth profiles in polar ice. *Journal of Glaciology*, **32**, pp. 366-370.
- Wolff, E.W., Chappellaz, J., Blunier, T., Rasmussen, S.O., Svensson, A., 2010. Millennial-scale variability during the last glacial: the ice core record. *Quaternary Science Reviews*, **29**, pp. 2828-2838.
- Zagorodnov, V., Nagornov, O., Scambos, T.A., Muto, A., Mosley-Thompson, E., Pettit, E.C., Tyufin, S. 2012. Borehole temperatures reveal details of 20<sup>th</sup> century warming at Bruce Plateau, Antarctic Peninsula. *The Cryosphere*, **6**, pp. 675-686, doi: 10.5194/tc-6-675-2012.